CISM International Centre for Mechanical Sciences 551
Courses and Lectures

Maurizio Angelillo
Editor

Mechanics of Masonry Structures

International Centre
for Mechanical Sciences

Springer

CISM Courses and Lectures

Series Editors:

The Rectors
Friedrich Pfeiffer - Munich
Franz G. Rammerstorfer - Wien
Elisabeth Guazzelli - Marseille

The Secretary General
Bernhard Schrefler - Padua

Executive Editor
Paolo Serafini - Udine

The series presents lecture notes, monographs, edited works and proceedings in the field of Mechanics, Engineering, Computer Science and Applied Mathematics.
Purpose of the series is to make known in the international scientific and technical community results obtained in some of the activities organized by CISM, the International Centre for Mechanical Sciences.

International Centre for Mechanical Sciences

Courses and Lectures Vol. 551

For further volumes:
www.springer.com/series/76

Maurizio Angelillo
Editor

Mechanics of Masonry Structures

Springer

Editor

Maurizio Angelillo
Università di Salerno, Fisciano, Italy

ISSN 0254-1971
ISBN 978-3-7091-1773-6 ISBN 978-3-7091-1774-3 (eBook)
DOI 10.1007/ 978-3-7091-1774-3
Springer Wien Heidelberg New York Dordrecht London

All contributions have been typeset by the authors
Printed in Italy

Printed on acid-free paper

Springer is part of Springer Science+Business Media (www.springer.com)

PREFACE

It is maybe a trivial remark saying that the vast majority of masonry structures (excluding tall towers) exhibit an extraordinary stability under the effect of age and settlements and even under the repeated action of strong winds and heavy earthquakes. Someone may be skeptical about this statement since, lately, collapses of masonry structures are not so infrequent. The point is that, almost invariably, failure is caused by some unaware but diabolic alteration of the natural and pacific equilibrium of masonry. The reason of this pacific stability stems from the so called strength by shape that is typical also of other structures carrying axial forces, such as a cord or a membrane, that is unilateral structures. If pacific-unilateral stability for masonry, does not mean plainly dumb or boring stability, this is actually due to the curved structural elements (arches, vaults and domes) that started to appear systematically in masonry Architecture since the ancient Rome. The unilateral model, which appears as the clue of structural interpretation behind the design of the great Architecture masterpieces of the past, was first rationally introduced in the scientific community by Heyman in 1966, with his mile-stone paper the stone skeleton. *Since then it has been the Italian school of Structural Mechanics to carry the torch of the old masonry tradition, with the contribution of a number of individuals dragged by the charismatic leaderships of Salvatore Di Pasquale, and of whom Lucchesi, Šilhavý and myself are, in some sense, modern followers. The fire of the unilateral model, still burning in Naples in the late seventies, was poked by the unlucky event of the Irpinia earthquake of 1980. At that time I was a young Architect working under the guidance of Giovanni Castellano (a friend and former co-worker of Di Pasquale), and I had the occasion not only to eyewitness the, sometimes turbulent, discussions on the No Tension model for masonry, but also to see the model at work in the wounded body of many masonry buildings and monuments of Naples and of its battered neighbourhoods. But how comes that the unilateral model for masonry, that has been part of the traditional scientific heritage since Mery divulgated the thrust line approach of Moseley in 1840, had to be rediscovered again (and with scant success) in the second half of the twentieth century? Indeed, though the traditional unilateral approach to masonry equilibrium has had an outstanding mentor and*

divulgator in the person of Jaques Heyman, who, after writing the mentioned paper, in 1995 published a crystalline book with the same inspiring title (a book in which the author succeeds in explaining the stone behaviour to the stones themselves by using barely a few equations), it seems that the message of the traditional masonry design has not been welcomed by the modern structural engineers. A reason for this state of affairs is given by Santiago Huerta, in his paper by the provoking title Galileo was wrong *"... any engineer or architect with some formation in structural theory feels more comfortable within the frame of the strength approach of Galileo and the classical theory of structures. It requires an effort, and some study, to overcome our own prejudices and to accept that, for example, the medieval master masons, knowing nothing of mathematics, elastic theory and strength of materials, had a deeper understanding of masonry architecture than we engineers and architects of the twenty-first century do."*

The presentation given by Lucchesi, Šilhavý and myself in the first part of this book represents a modern update of the unilateral model for masonry and a step forward toward the goal of obtaining a useful practical tool for the analysis of masonry structures.

Though we believe that the unilateral model can be useful to practitioners and applied engineers, since it captures the essence of masonry mechanics, still the limits of such a crude model are apparent and there are aspects of masonry behaviour that need to be understood such as damage, degradation, friction, heterogeneity and particularly the role of the interface behaviour in the overall response of masonry. In order to appreciate the limits of validity of the simplified unilateral approach, it is important to study and interpret the experimental results with the "eyes" of more sophisticated models. Actually, all I have said until now refers to the phenomenological modelling of old masonry for which the assessment of the material properties in the detail required by fancy models is virtually impossible. The case of new masonries for which the nature of the blocks and of the mortar and of their arrangement is known and reliable, is a complete different story. A typical case is that of brick-works studied in the present book by Lebon, Sacco and Lourenco & Milani. In the end, these new masonry structures are nothing else than composite structures to which sophisticated techniques of homogenization can be applied. The theoretical and experimental study of these peculiar structures with this

more in depth focus, is not only useful for the closer simulation of their mechanical behaviour, but can put light on the mechanical phenomena that are behind the crude approximations of the Heyman's model, namely the unilateral and the no-sliding assumptions. Unilaterality is an extreme approximation for the brittleness of the material under tensile loads, brittleness being responsible for the softening behaviour of masonry at the macroscopic level. No-sliding is equivalent to assume infinite friction, and friction and sliding are the basic mechanisms in brick-brick, and brick-mortar-brick interactions. Understanding toughness and friction is then obviously a necessary step toward the goal of obtaining a detailed masonry description. Anyone working at some depth in material engineering knows that fracture and friction are still the most difficult challenges of modern Mechanics; the main strength of the simplified unilateral model of Heyman which assumes zero toughness and infinite friction is indeed its ability, while excluding these two tough guys, of being still able to make sound predictions on masonry behaviour.

CONTENTS

Masonry behaviour and modelling

Maurizio Angelillo[‡], Paulo B. Lourenço [*] and Gabriele Milani [†]

[‡] Department of Civil Eng., University of Salerno, Italy
[*] Institute for Sustainability and Innovation in Structural Engineering (ISISE), Department of Civil Engineering, University of Minho, Portugal
[†] Department of Architecture, Built environment and Construction engineering (A.B.C.), Politecnico di Milano, Italy

Abstract In this Chapter we present the basic experimental facts on masonry materials and introduce simple and refined models for masonry. The simple models are essentially macroscopic and based on the assumption that the material is incapable of sustaining tensile loads (No-Tension assumption). The refined models account for the microscopic structure of masonry, modeling the interaction between the blocks and the interfaces.

1 Premise

The first basic question that any course on Masonry Structures should address is: *what we consider as masonry material?*

Masonry structures can be built with a large variety of materials, masonry blocks can be of different types and assembled in many different ways; mortar, if present, can also be of various kinds, and the way it interacts with the blocks depends on workmanship. There is old masonry, new masonry and a peculiar place is taken by brickworks.

There are essentially two ways of approaching the modelling of masonry: the first one is rather ambitious and aims at the modelling of large classes of masonry buildings (e.g. old masonry structures). The second one is more pragmatic and restricts to the mechanical description of very specific types of masonry (masonry structures of regularly arranged blocks, e.g. brickworks of known geometry). Here Silhavi, Lucchesi and myself adopt the first approach and Sacco, Lebon, and Lourenco & Milani propose the second one (also if Sacco has had experiences and papers where the first approach was considered).

M. Angelillo (Ed.), *Mechanics of Masonry Structures*, CISM International Centre for Mechanical Sciences, DOI 10.1007/ 978-3-7091-1774-3_1,

It is evident that with the second approach the models adopted can be very sophisticated and more *close to reality*, whilst the first approach asks for very crude material assumptions and produces predictions on real constructions that are affected by large approximations. The point is that, often, the real geometry and material behaviour of the building is not known in the detail required by the second approach, the definition of even the most primitive material parameters, such as strength and stiffness, being generally difficult and affected by an elevated randomness and uncertainty.

The most basic assumption that can be made, in view of the small and often erratic value of the tensile strength of masonry materials, is that the material behaves unilaterally, that is only compressive stresses can be transmitted (No-Tension assumption). It is generally recognized (since the pioneering work of Heyman (1966)) that such an assumption is the first clue for the interpretation of masonry behaviour; on adopting and applying it, we acquire the *eyes* to appreciate and interpret the fracture patterns, that is the masonry most peculiar manifestation, representing, in a sense, its *breath* (that is the way in which the masonry buildings relieve and can survive also to radical and, sometimes, dramatic changes of the environment).

We call the models based on the No-Tension assumption *simple models* and the models accounting for more sophisticate stress-strain laws (i.e. exhibiting damage, softening, brittleness) or based on the micro/meso-scopic structure of the material, *refined models*. The book is divided into two interconnected but separate parts: Part I, where the simplified models are studied, Part II where the refined models are described.

In the present Chapter we discuss the basic experimental facts on masonry materials justifying the introduction of the simple and refined models for masonry.

2 Basic behaviour of masonry and simplified unilateral models

M. Angelillo

2.1 Local failure modes

There are basically three failure modes that are visible locally in masonry structures.

1. The first one is the one associated to the brittleness of the material and that manifests itself with *detachment* fractures, such as those reported in Figure 1. Such fractures consist in cracks that usually separate neatly two parts of seemingly intact material and are usually

the "good" ones, that is those contributing to the accommodation and release of stress.

Figure 1. Fracture of detachment in brick walls at different scales

2. The second one is a kind of mixed mode in which fractures of detachment alternate to lines of sliding, such as those appearing in the examples of in-plane shear shown in Figure 2. This mode of failure presents usually itself in walls subjected to high compressive loads and shears.

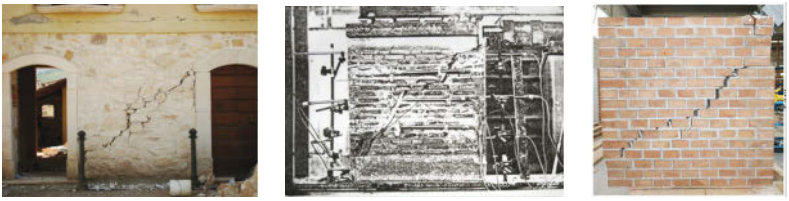

Figure 2. Detachment and sliding due to combined compression and shear.

3. The third failure mode is the so–called crushing of the material (Figure 3) and occurs essentially under compression. By looking closely to this failure mode one can see again that it consists of finer detachment fractures, close together and separated by damaged material, having sometimes the consistence of powder.

The first type of fractures is the most frequent and usually irrelevant. The second and third modes often occur when the load is critical or close to become a collapse load. The third one is the most dangerous since failure under compression is usually sudden.

2.2 Structural failure mechanisms

Besides crushing of compressed members, such as those shown in Figure 3, there are basically other two structural failure mechanisms through

Figure 3. Crushing due to compression.

which a masonry structure (or a part of it) may collapse. The most frequent one, under seismic loads, is out of plane rocking as shown in Figure 4. Such a mechanism can be due to the effect of the self load solely, or can be favoured by the pushing of the roof, or the hammering of a heavy floor or ceiling.

Figure 4. Out of plane rocking.

Both crushing failure and out of plane rocking are usually the result of a poor design, or of unwise modifications of the original construction. To avoid out of plane rocking many regulations prescribe the maximum distance between two consecutive transverse walls. The demolition of such transverse walls is one of the most common examples of risky modifications.

The third failure mechanism, that is in-plane shear, is the one proper of well designed buildings, that is structures sustaining the horizontal actions through the harmonized cooperation of the shear resistant structures (Figure 5), i.e. with local failure modes of their masonry units in their own planes, of the type shown in Figure 2.

Figure 5. In plane failure due to compression and shear.

Figure 6. Incipient failure of a shallow cross vault due to excessive spread of the abutments (aisle vaults of a XVI century chapel in Nocera Inferiore (SA), Italy). Courtesy of Enrico Sicignano.

The reader must be warned that also the detachment fractures, due to settlement or accommodation of the structure to new loads or to environmental changes, usually physiological and not necessarily entailing an imminent danger, may be the precursors of an incipient collapse: if the amplitude of the displacements and the size of the cracks become comparatively large with respect to the overall size of the structure, they could allow for the structure to become unstable. As an example, an arch or a vault may be perfectly comfortable under the action of their own weight, in a fractured and heavily distorted configuration, until the displacements grow to be so large that a mechanism becomes possible and their overall stability is suddenly lost. An example of such extreme conditions is reported in Figure 6. The message is that detachment fractures are usually unwary, but it is wise checking the size of cracks and displacements and their evolution in time.

2.3 Experimental observations: results of typical tests

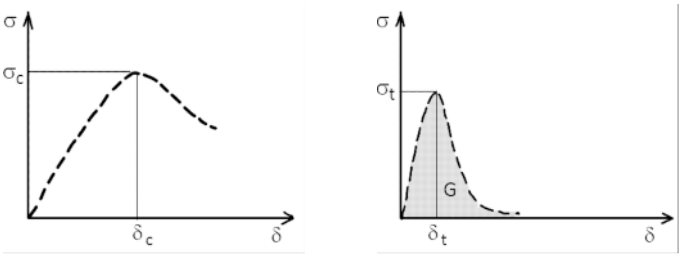

(a) (b)

Figure 7. Typical stress-displacement plot for a masonry material. (a) compression, (b) tension. In (b) the shaded area labelled G is the toughness, that is the surface energy per unit area that must be expended to open a crack. The plots are only qualitative; for any kind of masonry, usually, the values of σ_c and σ_t differ of at least one order of magnitude.

Old master masons could perfectly build without the help of tests on the construction materials. Nowadays the situation, compared to ancient times (when the predominance of metaphysics on physics was absolute, see Benvenuto (1991)), is entirely different and no work on buildings can proceed in absence of an experimental assessment on material performances.

Masonry is a composite material and accurate tests can be performed on the component materials, on masonry assemblies and on small masonry structures. The detailed description of some of these tests will be touched elsewhere in this book (see Sect.3, Ch.1), here I consider the results of typical tests on small masonry walls, in order to extract the main aspects

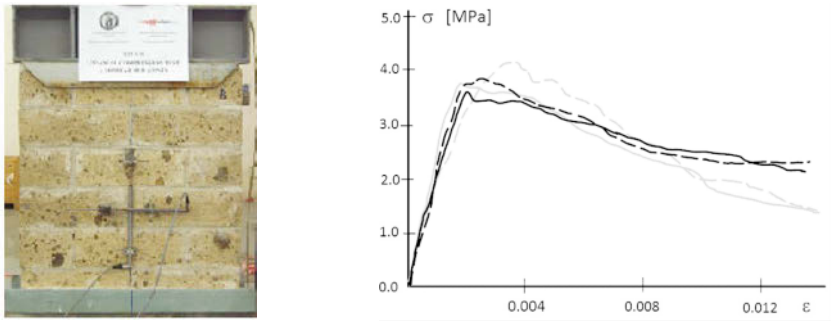

(a) (b)

Figure 8. Simple compression tests on masonry walls made of tuff blocks. (a) test set up, (b) stress strain plots corresponding to four different tests on walls having identical geometry and material components. Courtesy of A. Prota et al. (2008).

of masonry behaviour that can be captured by the simple models.

In Figure 7 the typical aspect of the stress-displacement plots corresponding to simple compression and tension load tests on masonry walls are reported. The strength of the wall depends on the strength of the individual components (masonry units/blocks and mortar): some regulations give formulas to relate the compressive strength of masonry to the compressive strength of the components, also if the reliability of such rules is questionable on many grounds.

As the example reported in Figure 8, relative to compression tests on tuff masonry walls (50 cm $\times$ 60 cm $\times$ 20 cm) made of the same kind of stones and mortar, show, the results are affected by a strong variance, both for strength and stiffness. Such a state of affairs is even worse in the case of tension where a reliable value of strength is hardly identifiable with the standard statistical methods. Therefore we point out that the graphs of Figure 7 have to be interpreted as the uniaxial stress-displacement plots of a highly idealized masonry material.

The main feature of masonry materials is that the tensile strength σ_t is much lower than the compressive strength σ_c: the ratio σ_t/σ_c is usually lower than 0.1 and can be as low as 0.01 or even, locally, vanishingly small.

Masonry behaves essentially as an elastic material in compression up to 80-90 % of the strength, also if due to early microcracking and damage the stress-strain plot is definitely nonlinear. In the post critical phase the material undergoes irreversible deformations, showing a sort of plastic behaviour. Therefore the stress-strain plot of a typical masonry-like bar can

Masonry Type	$\sigma_c(\frac{daN}{cm^2})$	$\tau_s(\frac{daN}{cm^2})$	$E(\frac{daN}{cm^2})$	$\rho(\frac{Kg}{m^3})$
Disarranged masonry of cobbles/boulders	10-18	0.20-0.32	6900-10500	1900
Masonry of roughhewed stones	20-30	0.35-0.51	10200-14400	2000
Masonry of cut stones	26-38	0.56-0.74	15000-19800	2100
Masonry of soft stones	14-24	0.28-0.42	9000-12600	1600
Masonry of squared stone blocks	60-80	0.90-1.20	24000-32000	2200
Brickwork of solid bloks and lime mortar	24-40	0.60-0.92	12000-18000	1800
Brickwork of semisolid blocks and cem. mortar	50-80	2.40-3.20	35000-56000	1500
Brickwork of air bricks (45 %)	40-60	3.00-4.00	36000-54000	1200
Brickwork of air bricks (< 45 %)	30-40	1.00-1.30	27000-36000	1100
Masonry of concrete air-blocks (45-65 %)	30-44	1.80-2.40	24000-35200	1400
Masonry of concrete air-blocks (< 45%)	15-20	0.95-1.25	12000-16000	1200

Table 1. Densities and reference mechanical strength and stiffness of different types of coarse masonry with poor mortar. Strength in compression and shear: σ_c, τ_s, E: Young modulus, ρ: density. Source: Italian Code for Constructions (DM 14.1.2008).

be represented by the graph of Figure 9a.

For book keeping the reference strength and stiffness of some common masonry materials are listed in Table 1. Notice that σ_c is the compressive strength and that the shear strength τ_s is roughly correlated to the tensile strength σ_t through the relation $\tau_s \approx \sigma_t/2$.

2.4 Simplified uniaxial models

In Part I of the present book, basically three simplified models for idealizing the uniaxial masonry-like behaviour will be used. I call them model *zero*, *one* and *two*, these names coming from the number of parameters that are required for their definition. The order in which the models are put, is an order of gradual improvement.

We must observe explicitly that the first model is not, as one usually expects for any canonical solid, the linear elastic material. There is of course the possibility of modelling masonry structures as linearly elastic: masonry material is definitely an elastic brittle material for very small stress and strains, but the point is that the levels of stress and strains at which masonry materials work in real structures, are usually higher.

Model *zero* (RNT). As a first approximation to the behaviour of Figure 9a, the Rigid No-Tension material has been proposed (Figure 9b). This crude unilateral model that describes the material as indefinitely strong and stiff in compression but incapable of sustaining tensile stresses, was first rationally introduced by Heyman (1966) and divulgated and extended in Italy thanks to the effort of Salvatore Di Pasquale (1984) and other distinguished members of the Italian school of Structural Mechanics (see below for an extensive reference). This material is rigid in compression and can elongate freely, a positive deformation of the bar being interpreted as a measure of fracture into the material (either smeared or concentrated). It must be observed that, though the material has a limited repertoire of admissible stresses and strains and exhibits fractures, its uniaxial behaviour in elongation is elastic.

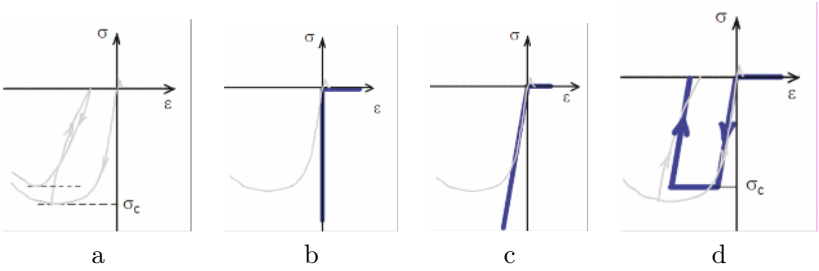

Figure 9. Typical uniaxial behaviour, (a), and simplified models: (b) model *zero*, (c) model *one*, (d) model *two*.

This statement, that may appear "paradoxical", derives from the primitive definition of elasticity: *stress determined by strain*, and the stress has actually a definite value (zero) if the bar elongates. The behaviour is indeed perfectly reversible in elongation, also if deformation occurs without accumulation of elastic energy. We may also notice that there is a *degenerate* elastic energy associated to this material ($\Phi = 0$ if ϵ is non negative, $\Phi = +\infty$ otherwise) and that the constraint on strain makes the compressive stress σ a sort of reaction to this constraint, that is negative values of σ are non-constitutive (in the same way in which pressure is non-constitutive

in incompressible materials). This model requires no material parameters since strength and stiffness in compression are assumed to be infinite whilst they are completely neglected in tension.

Model *one* (ENT). As a first step into the closer modelling of masonry behaviour one can consider to add a finite stiffness in compression: a linear ratio between stress and strain in compression is assumed. Another possibility would have been to add a limited strength in compression still assuming an infinite stiffness (rigid-plastic material), but in the vast majority of applications, the first ingredient to add appears to be elasticity since it allows to study the behaviour of the structure under working conditions, before collapse takes place. Most masonry constructions are indeed in a state of average stress that is well below the crushing strength, but the level of stress is such to trigger not only microscopic but also macroscopic brittle fracture.

Model *one*, described for a 1d bar by the plot of Figure 9c, is the so called Elastic No-Tension material, thoroughly studied since the late 70ties by the Italian school of structural mechanics (Romano and Romano (1979), Baratta and Toscano (1982), Como and Grimaldi (1985), Romano and Sacco (1985), Castellano (1988), Del Piero (1989), Angelillo (1993)).

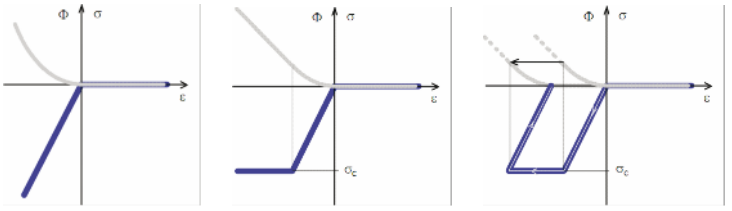

a. b. c.

Figure 10. In (a) elastic energy for model *one*, in (b) elastic energy for NT hyperelastic model with threshold. (c) elastic energy for model *two*.

Now the strain can be positive or negative, positive strain being the fracture part of deformation and negative strain the elastic part. The ENT material is globally elastic, in the sense that strain determines stress for any value of strain: now compressive stress is constitutive. The material is even hyperelastic since there exists a stored elastic energy density Φ such that σ is the derivative of Φ with respect to ϵ. The elastic energy corresponding to model *one* is depicted in Figure 10a. Notice that such energy, though convex, is not strictly convex (major source of mathematical and numerical troubles, see (Giaquinta and Giusti, 1985)).

This model requires only one material parameter: the elastic modulus

E, since strength in compression is assumed to be infinite, whilst strength and stiffness are completely neglected in tension.

Model *two* (ML). A further step can be taken by adding to model *one* the assumption of a limited strength σ_c in compression. In this way the failure modes due to crushing (such as those shown in Figure 3, but also, in a 2-3d formulation, the failure modes and mechanisms represented in Figures 2, 5), can be modelled. Here we shall refer to model *two*, whose uniaxial behaviour is reported in Figure 9d, as the Masonry-Like material. Any attempt to enrich this model for real applications is usually frustrated by the lack of sufficient confidence on the material properties of the real materials and of their assemblages.

As depicted in Figure 9d, it is assumed that the material behaves as perfectly plastic in compression, therefore the constitutive response becomes incremental and the actual stress state is path dependent, being determined by the whole strain history. In Figure 10b the elastic energy of a path independent material having the same stress-strain plot of model *two* under monotone loading (that is a No-Tension hyperelastic material with threshold) is shown.

The incremental model is obviously not hyperelastic, though a sort of "path dependent" elastic energy can still be defined (as shown in Figure 10c for a special loading-unloading cycle). Now the anelastic part of deformation is further decomposed into a reversible fracture part and in a irreversible crushing part. We have to remark that this is a peculiar perfectly plastic material, since, due to the different behaviour in tension (elastic fracture) and compression (incremental plasticity), the plastic deformations cannot be cancelled by reversing the strain. This model requires the setting of two material parameters: the elastic modulus E and the strength in compression σ_c, strength and stiffness being still completely neglected in tension.

Extension to 3d.For real applications the three simplified models need to be extended to 3d. The NT hypothesis translate in 3d into an assumption that the stress $\mathbf{T}$ belongs to the cone Sym^- of negative semidefinite symmetric tensors.

The next step is to introduce convenient rules for the latent part of the deformation, that is for the strain sustaining the unilateral constraint on the stress. The usual simplifying assumption is that there is no sliding along the fracture lines, that is the total fracture strain satisfy a law of normality with respect to the cone Sym^- of admissible stresses (equivalent to require that the stress do no work for the anelastic strain and that the anelastic strain is positive semidefinite).

The law of normality allows for the simple application of the theorems of limit analysis in 3d: the static and the kinematic ones.

For what concerns model *one* the linear elastic assumption in compression is easily generalized if one restricts to isotropy; in such a case the definition of a further parameter: the Poisson ratio ν (a value that is difficult to be assessed through tests and is usually set between 0.1 and 0.2) is required.

The law of normality and the usual restrictions considered on the elastic constants, make the global response of model *one* in 3d elastic, and even hyperelastic (see Del Piero (1989)), that is path independent. Also for model *two* the restriction to isotropy simplify things, but now, besides the material parameter σ_c, it is required to define a material function f, that is the limit surface in compression.

The flow rule for the increments of crushing strain must be also introduced; for simplicity one can choose to adopt an associated flow rule, also if the frictional nature of sliding under compression would require the adoption of a non-associated law.

Remark 1. Though the RNT model (model *zero*) appears as rather rudimentary (notice that it allows only to apply the theorems of limit analysis), it is the opinion of many *master masons* (among which Heyman (1995), Como (2010), and Huerta (2006)) that the RNT model is the only choice for old masonry constructions, the main motivation to this opinion being the impossibility for the elastic models to define correctly the initial state of the structure, due to the uncertainties about the boundary conditions and on the previous history.

Any elastic solution, that, in principle, would allow the definition of the stress state under the given loads, is indeed extraordinarily sensitive to very small variations of the boundary conditions, particularly to the change of the given boundary constraints such as those produced by the unknown settlements of the foundation. The idea for applying the elastic assumption (models *one* and *two*) is that the given settlements have been accommodated by means of a small displacement mechanism, that is a kind of rigid body relative displacement of some parts of the structure. The stress produced during the nucleation and growth of the fracture necessary to activate the mechanism are, in the end, almost completely released, and the final *state* that we see, can be used as an essentially stress free reference state. In the analysis of a real masonry artefact, it is up to the sensitivity of the analyzer, based on the signs that the structure exhibits, to judge if the construction seats or not in this comfortable state.$\diamond$

Remark 2. We have given reasons for adopting the simplified models, but it is obvious that doing so we forget about many mechanical properties of real masonry materials. Such properties can have a more or less fundamental role in the modelling and it is important to know them to fully

appreciate the limits of validity of the simplified models. They are recorded in a "subjective" order of importance in the following list.

- There are signs of damage since the early stages of loading. Effect: non linear $\sigma - \epsilon$ plot and decline of stiffness.
- The behaviour in tension is brittle. Effect: energy is expended to open a crack.
- The anelastic strains and strain rates are not purely normal, sliding is ruled by friction.
- Ductility, if any, is rather limited.
- The elastic and anelastic response is anisotropic.
- The anelastic behaviour, initially of hardening type, turns soon into softening.
- The cyclic response is hysteretic and the stress-strain plots depends on the rates: viscoelastic behaviour is implied.
- The material shows signs of degradation (strength reduction) under long term loading.
- Sometimes the displacements are very large and demand for theories accounting for geometric nonlinearities.

Nowadays there would not be any difficulties, either analytical or numerical, to include all this effects (except brittleness, softening and friction) into a FEM simulation of the masonry structure. The point is that, as already remarked, the knowledge of these fine properties of masonry materials is often lacking, especially for old masonry.$\diamond$

3 Masonry behavior of regularly arranged masonry structures. Homogenization and refined models

P.B. Lourenço and G. Milani

3.1 Introduction

Masonry is a heterogeneous assemblage of units and joints. Units are such as bricks, blocks, ashlars, adobes, irregular stones and others. Mortar can be clay, bitumen, chalk, lime/cement based mortar, glue or other. The huge number of possible combinations generated by the geometry, nature and arrangement of units as well as the characteristics of mortars raises doubts about the accuracy of the term "masonry". Still, much information can be gained from the study of regular masonry structures, in which a periodic repetition of the microstructure occurs due to a constant arrangement of the units (or constant bond).

The difficulties in performing advanced testing of this type of structures are quite large due to the innumerable variations of masonry, the large scatter of in situ material properties and the impossibility of reproducing it all in a specimen. Therefore, most of the advanced experimental research carried out in the last decades concentrated in brick block masonry and its relevance for design. Accurate modelling requires a comprehensive experimental description of the material, which seems mostly available at the present state of knowledge (Rots, 1997; Lourenço, 1998a). The behaviour of masonry is much dependent not only on the composition of units and joints, but also on how they are arranged and treated. Figure 11 shows two results of a set of tests on dry stone masonry joints under shear testing. The adopted stone is granite and the stone has been polished, sawn or artificially made rough with a random impact of a spike. It is clear that the same surface with different treatments has different capacities, with an initial tangent of the friction angle for the polished stone joint (equal to 0.18) much lower than the other surface treatments (about 0.6). The situation is even more dramatic for the initial dilatancy angle, which is about zero for the polished and sawn joints, but provides a dramatic volume loss for each load reversal due to compaction of the joints. This phenomenon contributes to interlocking loss between irregular masonry units and masonry out of plane collapse in case of an earthquake. Another interesting example on how the masonry meso-structure (i.e. the arrangement of units, usually referred to as micro-scale in masonry) influences the response is given in Vasconcelos and Lourenço (2009). Here, three different types of stone masonry walls with the same external geometry are tested under in plane cyclic shear, namely regular dry stone masonry, irregular mortared joints masonry and rubble masonry. Not only the strength and stiffness degradation of the walls is rather different but also the strength envelop found is much different, with a tangent of the friction angle varying between 0.4 (for dry stone masonry), 0.3 (for irregular masonry) and 0.2 (for rubble masonry).

The examples given demonstrate the relevance of the micro-structure of masonry for the structural response. Therefore, the global field of structural analysis of masonry structures encompasses several different approaches and a comprehensive review is given in Lourenço (2002), with a recent update for seismic analysis in Marques and Lourenço (2011) for masonry with box behaviour and in Lourenço et al. (2011) for masonry without box behaviour. Depending on the level of accuracy and the simplicity desired, usually the following representations are possible: (a) micro-modelling, where the geometry of units and joints is directly considered and the constitutive laws are obtained experimentally; (b) macro-modelling, where units and joints are smeared out in the continuum and the constitutive laws are obtained

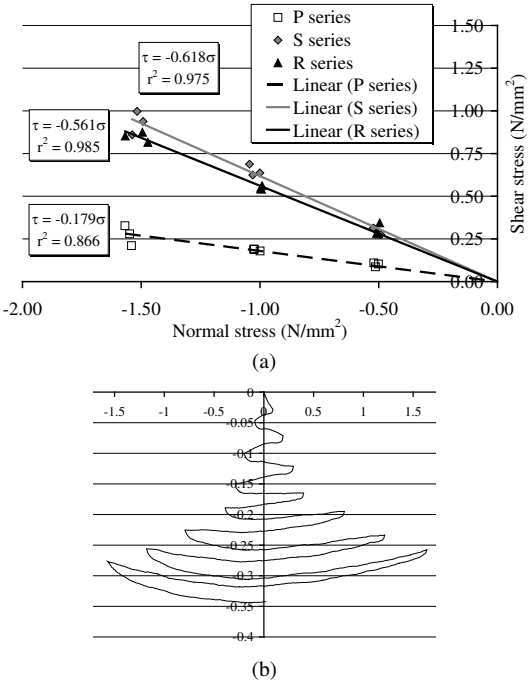

Figure 11. Testing of dry stone masonry joints under cyclic shearing, Lourenço and Ramos (2004): (a) Coulomb friction law for polished "P", sawn "S" and rough "R" surfaces; (b) dilatancy of the joints for "R" surface under reversed cycles, with the horizontal and vertical displacements of the joints in the respective axes, in mm.

experimentally; (c) homogenization, where the micro-structure is handled mathematically in terms of geometry and material data to obtain a smeared continuum model; (d) structural component models, where constitutive laws of structural elements are directly provided in terms of internal forces such as shear force or bending moment (and related generalized displacements), instead of stresses and strains, see Figure 12. The present chapter focuses on masonry behaviour and numerical data, on the analysis of masonry structures making use of homogenization techniques, which has been receiving a growing interest from the scientific community, see also Lourenço et al. (2007), and on the seismic analysis of masonry structures.

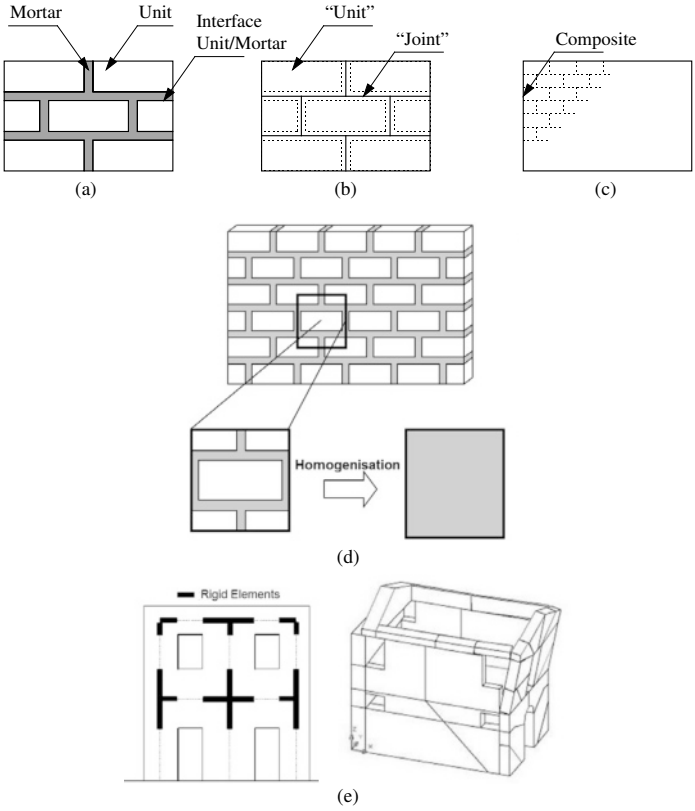

Figure 12. Modelling approaches for masonry: (a) representation of regular staggered or running bond masonry; (b) micro-modelling; (c) macro-modelling; (d) homogenisation; (e) illustrative structural component models, with beam elements or macro-blocks.

3.2 Mechanical Behaviour of Masonry, Observations and Numerical Data

A basic modern notion in the mechanical behaviour of masonry is softening, which is a gradual decrease of mechanical resistance under a continuous increase of deformation forced upon a material specimen or structure, see Figure 13. Softening is a salient feature of brick, mortar, stone or concrete, which fail due to a process of progressive internal crack growth. For tensile failure this phenomenon has been well identified. For shear failure, a softening process is also observed, associated with degradation of the cohesion in Coulomb friction models. For compressive failure, experimental data seems to indicate that both local and continuum fracturing processes govern the behaviour.

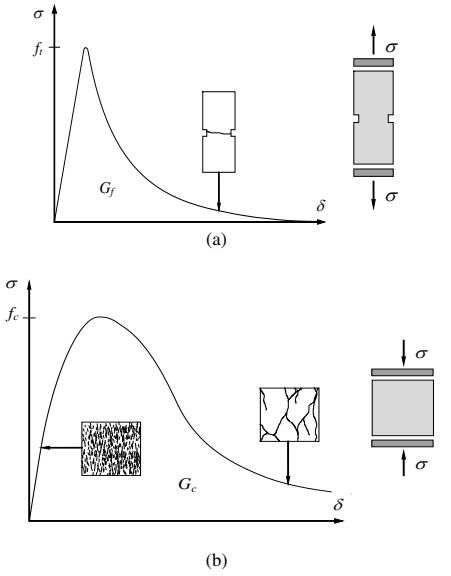

Figure 13. Softening and the definition of fracture energy: (a) tension; (b) compression. Here, f_t equals the tensile strength, f_c equals the compressive strength, G_f equals the tensile fracture energy and G_c equals the compressive fracture energy. It is noted that the shape of the non-linear response is also considered a parameter controlling the structural response. Nevertheless, for engineering applications, this seems less relevant than the other parameters.

Properties of unit and mortar The properties of masonry are strongly dependent upon the properties of its constituents. Compressive strength tests are easy to perform and give a good indication of the general quality of the materials used, but very few results exist in the uniaxial post-peak behaviour of compressed bricks and blocks, or mortar. The values proposed for concrete in the Model Code 90 (CEB-FIP, 1993) are a peak strain of 0.2% and a compressive fracture energy given by a parabolic best fit $G_{f,c} = 15 + 0.43 f_c - 0.0036 f_c^2$, with f_c in N/mm^2 and $G_{f,c}$ in N/mm This curve is only applicable for compressive strength value of f_c between 12 and 80 N/mm^2. The average ductility index in compression $d_{u,c}$ (ratio between fracture energy and strength) is 0.68 mm, even if this value changes significantly and it is recommended to use the above expression. For f_c values lower than 12 N/mm^2, a $d_{u,c}$ value equal to 1.6 mm is suggested and for f_c values higher than 80 N/mm^2, a $d_{u,c}$ value equal to 0.33 mm is suggested. These are the limits obtained from Model Code 90.

It is difficult to relate the tensile strength of the masonry unit to its compressive strength due to the different shapes, materials, manufacture processes and volume of perforations. For the longitudinal tensile strength of clay, calcium-silicate and concrete units, Schubert (1988) carried out an extensive testing program and obtained a ratio between the tensile and compressive strength that ranges from 0.03 to 0.10.

Extensive information on the tensile strength of masonry units and their fracture energy is available, see e.g. van der Pluijm (1999), Lourenço et al. (2005) and Vasconcelos et al. (2008). The ductility index d_u, given by the ratio between the fracture energy G_f and the tensile strength f_t, found for brick was between 0.018 and 0.040 mm. The recommended ductility index d_u, in the absence of more information is the average, 0.029 mm.

For stone granites, a non-linear relation given by $d_u = 0.239 f_t^{-1.138}$ was proposed in Vasconcelos et al. (2008), with d_u in mm and f_t in N/mm^2. For an average granite tensile strength value of 3.5 N/mm^2, the d_u value reads 0.057 mm, which is the double of the suggested value for brick, possibly due to the larger grain structure of granite when compared to clay.

Finally, Model Code 90 (CEB-FIP, 1993) recommends for concrete (maximum aggregate size 8 mm), the value of $G_f = 0.025(f_c/10)^{0.7}$, with G_f in N/mm and the compressive strength f_c in N/mm^2. Assuming that the relation between tensile and compressive strength is about 5%, the following expression is obtained $G_f = 0.04 f_t^{0.7}$.

For the mortar, standard test specimens are cast in steel moulds and the water absorption effect of the unit is ignored, being usually not representative of the mortar inside the composite. Moreover, the interface between mortar and unit controls the behaviour of the joint in a large extent. For the

tensile fracture energy of mortar, very few results are available, see Paulo-Pereira (2012), and the average value of ductility found for different mortar compositions is 0.065 mm.

Properties of the interface The research on masonry has been scarce when compared with other structural materials and experimental data which can be used as input for advanced non-linear models is limited. The bond between the unit and mortar is often the weakest link in masonry assemblages. The non-linear response of the joints, which is then controlled by the unit-mortar interface, is one of the most relevant features of masonry behaviour. Two different phenomena occur in the unit-mortar interface, one associated with tensile failure (mode I) and the other associated with shear failure (mode II).

Different test set-ups have been used for the characterisation of the tensile behaviour of the unit-mortar interface. These include (three-point, four-point, bond-wrench) flexural testing, diametral compression (splitting test) and direct tension testing. For the purpose of numerical simulation, direct tension tests is the one to be adopted as it allows for the complete representation of the stress-displacement diagram and yields the correct strength value, see Figure 14.

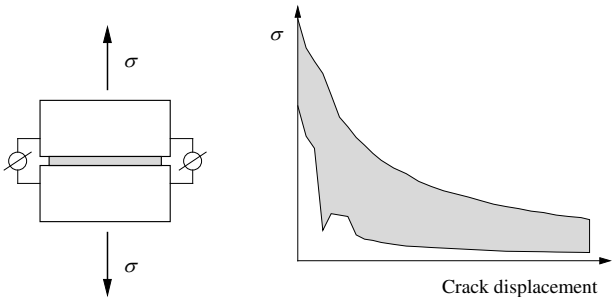

Figure 14. Tensile bond behaviour of masonry: (a) test specimen (direct tension); (b) typical experimental stress-crack displacement results for solid clay brick masonry (the shaded area represents the envelope of four tests), van der Pluijm (1999).

The parameters needed for the tensile mode (Mode I) are similar to the previous section, namely the bond tensile strength ft and the bond fracture energy G_f. The factors that affect the bond between unit and mortar are

highly dependent on the units (material, strength, perforation, size, air dried or pre-wetted, etc.), on the mortar (composition, water contents, etc.) and on workmanship (proper filling of the joints, vertical loading, etc.). A recommendation for the value of the bond tensile strength based on the unit type or mortar type is impossible, but an indication is given in Eurocode 6 (CEN, 2005) for the characteristic value (95% fractile), in the range of 0.1 to $0.4\,\mathrm{N/mm^2}$. The value for Mode I fracture energy $G_{f,I}$ found for different combinations of unit and mortar was between 0.005 mm and 0.035 mm, van der Pluijm (1999). This value is not dependent on the bond strength and the recommended fracture energy is the average value of $0.012\,\mathrm{N/mm}$, in the absence of more information.

An important aspect in the determination of the shear response of masonry joints is the ability of the test set-up to generate a uniform state of stress in the joints. This objective is difficult because the equilibrium constraints introduce non-uniform normal and shear stresses in the joint. Different test set-ups have been used for the characterisation of the shear behaviour of the unit-mortar interface. These include direct shear or couplet test and triplet test, see Figure 15. The triplet test can hardly be used to obtain the post-peak characteristics because the joints do not fail simultaneously and a rotation is obtained, Lourenço et al. (2004), so a couplet test is recommended for this purpose. It is also noted that a key issue for obtaining the post-peak characteristics is to keep constant the stress normal to the bed joint during testing.

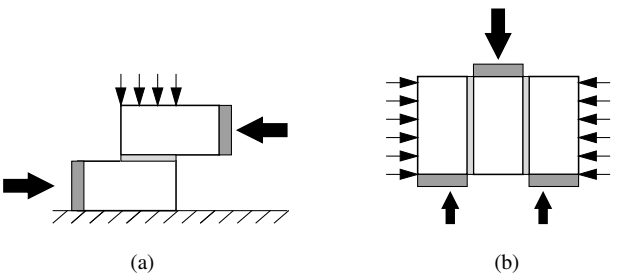

Figure 15. Possible test set-ups for shear strength: (a) couplet test; (b) triplet test.

Experimental results yield typically an exponential shear softening diagram with a residual dry friction level, see Figure 16a. The envelop of the shear strength for different normal stress values provides the cohesion and the friction angle for a Coulomb type friction model, see Figure 16b. A recommendation for the value of the bond shear strength (or cohesion) c based

on the unit type or mortar type is impossible, but an indication is given in Eurocode 6 (CEN, 2005) for the characteristic value (95% fractile), in the range of 0.1 to 0.4 N/mm^2. The ductility index $d_{u,s}$, given by the ratio between the fracture energy $G_{f,II}$ and the cohesion c, found for different combinations of unit and mortar was between 0.062 mm and 0.147 mm, van der Pluijm (1999). The recommended ductility index $d_{u,II}$ is the average value of 0.093 mm. It is noted that the Mode II fracture energy is clearly dependent of the normal stress level and the above values hold for a zero normal stress.

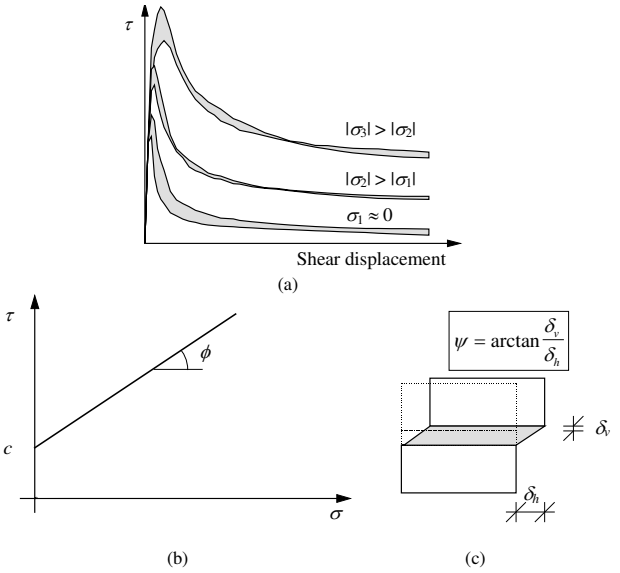

Figure 16. Shear bond behaviour: (a) typical stress-displacement diagram for different normal stress levels (the shaded area represents the envelope of three tests), van der Pluijm (1999); (b) cohesion c and friction angle ϕ, defining the envelop obtained with the shear strength for different compressive stresses; (c) dilatancy angle ψ is the uplift of neighbouring units upon shearing

The friction angle of the joint ϕ, associated with a Coulomb friction model, ranges from 0.7 to 1.2 for different unit-mortar combinations, van der Pluijm (1999), but different values are found in the literature. A value of 0.75 is recommended in the absence of more information. The dilatancy angle ψ measures the uplift of one unit over the other upon shearing, see

Figure 16c. Note that the dilatancy angle decreases to zero with increasing vertical stress and with increasing slip, so a zero value is recommended. The effect of the dilatancy angle is only relevant for applications in which masonry is confined, due to the interlocking effect of the units and the associated stress built-up.

Properties of the masonry The compressive strength of masonry in the direction normal to the bed joints has been traditionally regarded as the most relevant structural masonry property. Since the pioneering work of Hilsdorf (1969) it has been accepted by the masonry community that the difference in elastic properties of the unit and mortar is the precursor of failure. Lourenço and Pina-Henriques (2006) demonstrated that continuum models are inadequate to justify the observed strength values in solid masonry and that there is a need to consider more refined models. Different formulas to predict the compressive strength of masonry based on the properties of the components are available and are compared by these authors. The formula available in Eurocode 6 (CEN, 2005) provides the characteristic value of masonry under uniaxial compression as $f_k = K f_b^{0.7} f_m^{0.3}$, where K is factor about 0.5 for solid units, f_b is the unit compressive strength and f_m is the mortar compressive strength.

Uniaxial compression tests in the direction parallel to the bed joints have received substantially less attention from the masonry community. However, regular masonry is an anisotropic material and, particularly in the case of low longitudinal compressive strength of the units due to high or unfavourable perforation, the resistance to compressive loads parallel to the bed joints can have a decisive effect on the load bearing capacity. According to Hoffman and Schubert (1994), the ratio between the uniaxial compressive strength parallel and normal to the bed joints ranges from 0.2 to 0.8.

For traditional masonry, information is available in PIET-70 (1971) for the compressive strength of stone masonry, varying between 8.0 and 0.5 N/mm^2 depending on the quality of the mortar, the type of stone and the masonry bond, and for different properties of different masonry types in OPCM 3431 (2005), varying between 6.0 and 0.6 N/mm^2.

The relation $E = \alpha f_c$ between the Young's modulus E and the compressive strength f_c is rather variable for masonry, with values of α ranging between 200 and 1000 according to Tomazevic (1999), even if the proposed value in Eurocode 6 (CEN, 2005) is 1000. For dry stone masonry, PIET-70 (1971) proposes a value of $\alpha = 500$, which is in the mid-range of the interval of Tomazevic (1999) and is possibly more adequate for traditional masonry.

3.3 Example of application

Advanced non-linear analyses are not particularly sensitive to the input data, providing that the changes in the material properties are reasonable, see Lourenço (1998b) and Mendes (2012). Therefore, numerical results can be expected to reasonably replicate experimental tests and, in general, to provide a single response to a given combination of geometry, loading and materials. Next, an example of calculation of advanced material properties from basic data of the masonry constituents is given taking as an example a concrete block with two-cells and 10 $\mathrm{N/mm^2}$ compressive strength (f_b) and a mortar with 6 $\mathrm{N/mm^2}$ compressive strength (f_m). The geometry of the block is $0.14 \times 0.39 \times 0.19\,\mathrm{mm^3}(t \times l \times h)$ with a thickness t_s for the shell walls equal to 25 mm.

The properties required for a micro-modelling approach can be estimated as:

1. The bond tensile strength ft can be estimated at $0.2\,\mathrm{N/mm^2}$ which is a minimum value for modern masonry, with the exception of very smooth units. The recommended bond tensile fracture energy is $0.012\,\mathrm{N/mm}$.
2. The cohesion or shear strength can be estimated as 1.5 ft or 0.3 $\mathrm{N/mm^2}$ The recommended ductility index $d_{u,II}$ is 0.093 mm, providing a fracture energy for mode II of $0.028\,\mathrm{N/mm}$. The recommended values for the tangent of the friction and dilatancy angle (in case of a non-associated model) are 0.75 and zero, respectively.
3. The masonry compressive strength (perpendicular to the bed joints) for this type of units can be safely estimated as $0.7f_b$, providing a value of $7\,\mathrm{N/mm^2}$. If the Eurocode 6 (2005) formula is used instead, a lower bound value would be $0.45 \times 10^{0.7} \times 6^{0.3}/0.8 = 6\,\mathrm{N/mm^2}$, where the 0.8 value is adopted to change from the characteristic to the mean value. The recommended ductility index $d_{u,c}$ is 1.6 mm, providing a fracture energy for compression of $9.6\,\mathrm{N/mm}$.

The properties required for a macro-modelling approach using an isotropic model are the same as above, adopting the tensile bond strength and compressive strength. If a macro-modelling approach with an anisotropic model is used, additional material properties are needed:

1. The masonry tensile strength perpendicular to the joints is controlled by the bed joint, being the same as above.
2. The masonry tensile strength parallel to the bed joints can be obtained as indicated next. Assuming a void ratio of 50%, the compressive strength of concrete f_{conc} is $20\,\mathrm{N/mm^2}$. The tensile strength for a straight crack through head joints and blocks can be approximated to the strength of the block given by $10\% \times f_{\mathrm{conc}} \times 2t_s \times h/(t \times 2h) =$

$0.35\,\mathrm{N/mm^2}$. The tensile strength for a stepped crack can be approximated by $c \times l/2/h = 0.29\,\mathrm{N/mm^2}$. The value to be used is the minimum of the two values ($0.29\,\mathrm{N/mm^2}$), being this response in shear fully plastic. Note that the tensile strength of the head joints was not used, as it is rather low and will not reach the peak value simultaneously with the other phenomena involved.

3. The masonry compressive strength perpendicular to the joints is the same as above.
4. The masonry compressive strength parallel to the bed joints for this type of masonry can be estimated as 30% of the vertical strength, as a lower bound. This value can also can be calculated from Eurocode 6 as $0.35 \times (f_{\mathrm{conc}} \times t_s \times 2/t)^{0.7} \times 6^{0.3}/0.8 = 3.0\,\mathrm{N/mm^2}$. The recommended ductility index $d_{u,c}$ is 1.6 mm, providing a fracture energy for compression of $4.8\,\mathrm{N/mm}$.

Bibliography

M. Angelillo. Constitutive relations for no-tension materials. *Meccanica*, 28:195–202. 1993.

A. Baratta and R. Toscano. Stati tensionali in pannelli di materiale non resistente a trazione. In *Atti del VII Congresso Nazionale AIMETA*, 1982 (in Italian).

E. Benvenuto. *An Introduction on the History of Structural Mechanics Part II: Vaulted Structures and Elastic Systems, Springer-Verlag.* Springer Verlag, 1991.

G. Castellano. Un modello cinematico per i materiali non resistente a trazione. In *Cinquantenario della Facoltà di Architettura di Napoli: Franco Jossa e la sua opera*, pages 241–256, 1988 (in Italian).

CEB-FIP. *Model Code 90.* Thomas Telford Ltd., UK, 1993.

CEN. *Eurocode 6: Design of masonry structures, Part 1–1: General rules for reinforced and unreinforced masonry structures.* European Committee for Standardization, Belgium, 2005.

M. Como. *Statica delle costruzioni storiche in muratura, Aracne.* Aracne, 2010 (in Italian).

M. Como and A. Grimaldi. A unilateral model for the limit analysis of masonry walls. In *Unilateral problems in structural analysis, edited by G. Del Piero and F. Maceri, CISM Courses and Lectures 288, Springer.*, pages 25–45, 1985.

G. Del Piero. Constitutive equation and compatibility of the external loads for linear elastic masonry–like materials. *Meccanica*, 24:150–162, 1989.

S. Di Pasquale. Statica dei solidi murari: teorie ed esperienze. *Reports Dipartimento di Costruzioni, Univ. Firenze*, 27, 1984 (in Italian).

M. Giaquinta and E. Giusti. Researches on the equilibrium of masonry structures. *Arch. Rational Mech. Analysis*, 88:359–392, 1985. ISSN 0950-2289.

J. Heyman. The stone skeleton. *Int.J.Solids,Struct.*, 2:249–279, 1966.

J. Heyman. *The stone skeleton: structural engineering of masonry architecture, Cambridge University Press.* Cambridge University Press, 1995.

H.K. Hilsdorf. Investigation into the failure mechanism of brick masonry loaded in axial compression. In F.H. Johnson, editor, *Designing, engineering and constructing with masonry products*, pages 34–41. Gulf Publishing Company, Houston, Texas, 1969.

G. Hoffman and P. Schubert. Compressive strength of masonry parallel to the bed joints. In N.G. Shrive and A. Huizer, editors, *Proc. 10th Int. Brick and Block Masonry Conf.*, pages 1453–1462, Calgary, Alberta, 1994.

S. Huerta. Galileo was wrong: the geometrical design of arches. *Nexus Network Journal*, 8 (2):25–52, 2006.

P.B. Lourenço. Experimental and numerical issues in the modelling of the mechanical behaviour of masonry. In P. Roca and et al., editors, *Proc. Structural analysis of historical constructions II, CIMNE*, pages 57–91, Barcelona, 1998a.

P.B. Lourenço. Sensitivity analysis of masonry structures. In *Proc. 8th Canadian Masonry Symp.*, pages 563–574, Jasper, Canada, 1998b.

P.B. Lourenço. Computations on historic masonry structures. *Progress in Structural Engineering and Materials*, 4(3):301–319, 2002.

P.B. Lourenço and J.L. Pina-Henriques. Validation of analytical and continuum numerical methods for estimating the compressive strength of masonry. *Computers & structures*, 84(29):1977–1989, 2006.

P.B. Lourenço and L.F. Ramos. Characterization of cyclic behavior of dry masonry joints. *Journal of Structural Engineering*, 130(5):779–786, 2004.

P.B. Lourenço, J.O. Barros, and J.T. Oliveira. Shear testing of stack bonded masonry. *Construction and Building Materials*, 18(2):125–132, 2004.

P.B. Lourenço, J.C. Almeida, and J.A. Barros. Experimental investigation of bricks under uniaxial tensile testing. *Masonry International*, 18(1): 11–20, 2005.

P.B. Lourenço, G. Milani, A. Tralli, and A. Zucchini. Analysis of masonry structures: review of and recent trends in homogenization techniques this article is one of a selection of papers published in this special issue on masonry. *Canadian Journal of Civil Engineering*, 34(11):1443–1457, 2007.

P.B. Lourenço, N. Mendes, L.F. Ramos, and D.V. Oliveira. Analysis of masonry structures without box behavior. *International Journal of Architectural Heritage*, 5(4-5):369–382, 2011.

R. Marques and P.B. Lourenço. Possibilities and comparison of structural component models for the seismic assessment of modern unreinforced masonry buildings. *Computers & Structures*, 89(21):2079–2091, 2011.

N. Mendes. *Seismic assessment of ancient masonry buildings: Shaking table tests and numerical analysis*. PhD thesis, University of Minho, Portugal, 2012.

OPCM 3431 . *Technical regulations for the design, assessment and seismic adaptation of buildings*. Gazzetta Ufficiale Serie Generale n.107 del 10/05/2005, Italy, 2005.

M. Paulo-Pereira. *Assessment of the seismic performance of building enclosures (in Portuguese)*. PhD thesis, University of Minho, Portugal, 2012.

PIET-70. *P.I.E.T. 70 Masonry work*. Prescriptions from Instituto Eduardo Torroja. Consejo Superior de Investigaciones CientÃŋficas, Madrid (in Spanish), 1971.

A. Prota, G. Manfredi, F. Nardone. Assessment of formulas for in plane FRP strengthening of masonry walls. *ASCE J. of Composite for Constr.* 12, 6, 643-649, 2008.

G. Romano and M. Romano Sulla soluzione di problemi strutturali in presenza di legami costitutivi unilaterali. *Rend. Accad. Naz. Lincei*, 67: 104–113, 1979 (in Italian).

G. Romano and E. Sacco. Sul calcolo di strutture non resistenti a trazione. In *Atti del VII Congresso Nazionale AIMETA* ., pages 221–233, 1985 (in Italian).

J.G. Rots, editor. *Structural masonry: An experimental/numerical basis for practical design rules*. Balkema, Rotterdam, the Netherlands, 1997.

P. Schubert. The influence of mortar on the strength of masonry. In J.W. de Courcy, editor, *Proc. 8th Int. Brick and Block Masonry Conf.*, pages 162–174, London, 1988. Elsevier Applied Science.

M. Tomazevic. *Earthquake-resistant design of masonry buildings*. Imperial College Press, London, 1999.

R. van der Pluijm. *Out-of-plane bending of masonry: Behavior and Strenght*. PhD thesis, Eindhoven University of Technology, The Netherlands, 1999.

G. Vasconcelos and P.B. Lourenço. In-plane experimental behavior of stone masonry walls under cyclic loading. *Journal of structural engineering*, 135(10):1269–1277, 2009.

G. Vasconcelos, P.B. Lourenço, C.A.S. Alves, and J. Pamplona. Experimental characterization of the tensile behaviour of granites. *International journal of rock mechanics and mining sciences*, 45(2):268–277, 2008.

I Simplified Models

Mathematics of the Masonry–Like model and Limit Analysis

M. Šilhavý
Institute of Mathematics of the AV ČR
Žitná 25
115 67 Prague 1
Czech Republic

1 Introduction

These notes present a brief introduction to the mathematics of equilibrium of no–tension (masonry–like) materials. We first review the constitutive equations using the idea that the stress of the no–tension material must be always negative semidefinite. The strain tensor is naturally split into the sum of the elastic strain and fracture strain. The stress depends linearly on the elastic strain via the fourth–order tensor of elasticities. Then we consider a body made of a no–tension material, introduce the loads and the total energy of the deformation with is the sum of the internal energy and the energy of the loads. Then we examine the question whether the total energy is bounded from below. That brings us to the important notion of the strong compatibility of loads. The loads are strongly compatible if they can be equilibrated (in the sense of the principle of virtual work) by a square integrable negative semidefinite stress field. The total energy is bounded from below if and only if the loads are strongly compatible. The notion of strong compatibility of loads is central in the limit analysis and in a strengthened form in the theory of existence of equilibrium states. Roughly speaking, if the loads are strongly compatible, then the body is safe, while otherwise strongly incompatible loads lead to the collapse of the body. To determine whether the loads are strongly compatible, it is not necessary to solve the full displacement problem, it suffices to find the negative semidefinite square integrable stress field, which is independent of the constitutive theory.

The considerations concerning the limit analysis and strong compatibility of loads are based on the displacements that belong to the Sobolev space of square integrable maps with square integrable gradients. Roughly

M. Angelillo (Ed.), *Mechanics of Masonry Structures*, CISM International Centre for Mechanical Sciences, DOI 10.1007/ 978-3-7091-1774-3_2,

speaking, this means that the fracture part of the strain is always without macroscopic cracks. To obtain the existence theory of equilibrium states, it is necessary to enlarge the class of deformations in which the fracture part of the deformation is a measure in the mathematical sense of that word. This introduces discontinuous displacements with macroscopic cracks. We give a brief introduction to the mathematical theory of such displacements, called displacements with bounded deformation. The full theory of equilibrium states is nontrivial and many assertions are presented without proofs. However, the basic line of thought is preserved.

Then the limit analysis for no–tension materials is presented. The loads of the limit analysis are assumed to be linearly dependent on the loading parameter. The ideal goal of the limit analysis is to determine the largest value of the loading parameter for which the loads are strongly compatible. This value is called the collapse multiplier; the loads corresponding to the loading multiplier bigger than the collapse multiplier lead to the collapse of the body. The loading parameters for which the loads are strongly compatible are called statically admissible loading parameters. By the above, they are characterized by the existence of a square integrable negative semidefinite stress field equilibrating the corresponding loads. For concrete loads, it is often easier to find a stress field represented by a negative semidefinite tensor valued measure equilibrating the loads. We call such loads weakly compatible. The difference between the square integrable stress fields and the stress fields represented by measures is that the latter can contain singular part which is concentrated on surfaces and curves in the body. Of course the strong compatibility implies the weak compatibility but not conversely: there are weakly compatible loads that are not strongly compatible. If the loads happen to be weakly compatible on some interval of the loading parameters, then the averaging procedure to be described in Section 7 may lead to square integrable equilibrating stress fields and hence to the strong compatibility. The last section presents an example of the averaging procedure which leads to an explicit determination of the square integrable averaged stress field.

The mechanical tools to be employed include the notion of stress, the virtual power principle, the notion of weak solution, and the notion of the total energy of the body. These notions are established in detail in the treatment below.

The mathematical tools necessary for the understanding include in particular the notions of the convex cones and orthogonal projection upon them, some elements of the convex analysis, vector valued measures, Sobolev spaces, families of measures, and the basic notions associated with the space of displacements of bounded deformation. The basic definitions of the math-

ematical notions are given in the text below and the basic properties are stated without proof.

2 Constitutive equations

Throughout we use the conventions for vectors and second order tensors identical with those in (Gurtin 1981). Thus Lin denotes the set of all second order tensors on R^n, i.e., linear transformations from R^n into itself, Sym is the subspace of symmetric tensors, Skew is the subspace of skew (antisymmetric) tensors, Sym^+ the set of all positive semidefinite elements of Sym; additionally, Sym^- is the set of all negative semidefinite elements of Sym. The scalar product of $\mathbf{A}, \mathbf{B} \in \mathrm{Lin}$ is defined by $\mathbf{A} \cdot \mathbf{B} = \mathrm{tr}(\mathbf{A}\mathbf{B}^{\mathrm{T}})$ and $|\cdot|$ denotes the associated euclidean norm on Lin. We denote by $\mathbf{1} \in \mathrm{Lin}$ the unit tensor. If $\mathbf{A}, \mathbf{B} \in \mathrm{Sym}$, we write $\mathbf{A} \leq \mathbf{B}$ if $\mathbf{B} - \mathbf{A} \in \mathrm{Sym}^+$.

To describe the stress, we assume that $\mathsf{C} : \mathrm{Sym} \to \mathrm{Sym}$ is a given linear transformation, the fourth order tensor of *elastic constants*, such that

$$\left.\begin{aligned} \mathbf{E} \cdot \mathsf{C}\mathbf{E} > 0 \quad \text{for all} \quad \mathbf{E} \in \mathrm{Sym}, \mathbf{E} \neq \mathbf{0}, \\ \mathbf{E}_1 \cdot \mathsf{C}\mathbf{E}_2 = \mathbf{E}_2 \cdot \mathsf{C}\mathbf{E}_1 \quad \text{for all} \quad \mathbf{E}_1, \mathbf{E}_2 \in \mathrm{Sym}. \end{aligned}\right\} \tag{1}$$

For example, the tensor of elastic constants of an isotropic material is of the form

$$\mathsf{C}\mathbf{E} = \lambda(\mathrm{tr}\,\mathbf{E})\mathbf{1} + 2\mu\mathbf{E}$$

for each $\mathbf{E} \in \mathrm{Sym}$ where λ and μ are constants, Lamé moduli, satisfying

$$\mu > 0, \quad n\lambda + 2\mu > 0$$

where $n = 2, 3$ is the dimension of the underlying space.

In the case of a general C, we introduce the *energetic scalar product* $(\cdot, \cdot)_E$ and the *energetic norm* $|\cdot|_E$ on Sym by setting

$$(\mathbf{A}, \mathbf{B})_E = \mathbf{A} \cdot \mathsf{C}\mathbf{B}, \quad |\mathbf{A}|_E = \sqrt{(\mathbf{A}, \mathbf{A})_E}$$

for each $\mathbf{A}, \mathbf{B} \in \mathrm{Sym}$.

We are now going to review briefly some concepts of convex analysis. We refer to (Rockafellar 1970) and (Ekeland & Temam 1999) for more details.

A nonempty subset K of a vector space V is called a *convex cone* if $tx + sy \in K$ for each $x, y \in K$ and each $t \geq 0$, $s \geq 0$.

Let K be a closed convex cone in a vector space V with scalar product $(\cdot, \cdot)$ and norm $|\cdot|$. We say that a point $y \in K$ is the *(orthogonal) projection* of a point $x \in V$ if y makes the distance $|z - x|$ minimal among all $z \in K$, i.e., if

$$|y - x| \leq |z - x|$$

for all $z \in K$. The projection onto a closed convex cone exists and is uniquely determined.

Let K be a nonempty set in a vector space V with scalar product and $x \in V$. We define the *normal cone* $\mathrm{Norm}(K, x)$ to K at x by

$$\mathrm{Norm}(K, x) = \{y \in V : (z - x, y) \le 0 \text{ for all } z \in K\}.$$

Remark 2.1. Let K be a closed convex cone in a vector space V with scalar product $(\cdot, \cdot)$ and norm $|\cdot|$ and let $x \in K$. Then

$$\mathrm{Norm}(K, x) = \{y \in V : (y, z) \le 0 \text{ for each } z \in K \text{ and } (x, y) = 0\}.$$

Proof. If $y \in \mathrm{Norm}(K, x)$ then $(z - x, y) \le 0$ for all $z \in K$. Replacing z by tz where $t > 0$ in the last inequality, dividing the resulting inequality by t and letting $t \to \infty$ we obtain $(z, y) \le 0$. Similarly, taking $z = 0$ in $(z - x, y) \le 0$ we obtain $(x, y) \ge 0$ and as $x \in K$ we have also $(x, y) \le 0$ by the preceding part of the proof. Thus we have $(x, y) = 0$. Thus $y \in \{y \in V : (y, z) \le 0 \text{ for each } z \in K \text{ and } (x, y) = 0\}$. Conversely, if $y \in \{y \in V : (y, z) \le 0 \text{ for each } z \in K \text{ and } (x, y) = 0\}$ then the inequality $(y, z) \le 0$ and the equality $(x, y) = 0$ provide $(z - x, y) \le 0$ for all $z \in K$. □

Remark 2.2. Let K be a closed convex cone in a vector space V with scalar product $(\cdot, \cdot)$ and norm $|\cdot|$ and let $x \in V$. Then a point $y \in K$ is the projection of x onto K if and only if the following two conditions are satisfied:

(i) $(w, x - y) \le 0$ for all $w \in K$;
(ii) $(x - y, y) = 0$.

Equivalently, a point $y \in K$ is the projection of x onto K if and only if

$$x - y \in \mathrm{Norm}(K, y).$$

Proof. Assume that y is the projection of x onto K. Then for every $z \in K$ we have

$$|z - x| \ge |y - x| \tag{2}$$

which can be rewritten as

$$|z - y + y - x|^2 \ge |y - x|^2$$

which in turn implies

$$|z - y|^2 + 2(z - y, y - x) \ge 0. \tag{3}$$

We now put $z = y + tw$ where $w \in K$ and $t > 0$ to obtain

$$t^2|w|^2 + 2t(w, y - x) \geq 0.$$

Dividing by t and letting $t \to 0$ we obtain (i). Next we put $z = (1 + t)y$ where $t \geq -1$ to obtain

$$t^2|y|^2 + 2t(y, y - x) \geq 0.$$

Dividing by $t > 0$ and letting $t \downarrow 0$ we obtain $(y, y - x) \geq 0$; dividing by $t < 0$ and letting $t \uparrow 0$ we obtain $(y, y - x) \leq 0$ and hence we have (ii).

Conversely, let (i) and (ii) hold. If $z \in K$ then summing the relations $2(z, y - x) \geq 0$, $-2(y, y - x) = 0$ and $|z - y|^2 \geq 0$ we obtain (3) which in turn implies (2) and hence y is the projection of x onto K.

This completes the proof of the characterization by (i) and (ii). The equivalent characterization in terms of the normal cone follows from (i) and (ii) via Remark 2.1. □

Proposition 2.3. *Assume* (1). *If* $\mathbf{E} \in \mathrm{Sym}$, *there exists a unique triplet* $(\mathbf{T}, \mathbf{E}^{\mathrm{e}}, \mathbf{E}^{\mathrm{f}})$ *of elements of* Sym *such that the following three equivalent characterizations hold:*

(i) we have

$$\left.\begin{array}{c} \mathbf{E} = \mathbf{E}^{\mathrm{e}} + \mathbf{E}^{\mathrm{f}}, \\ \mathbf{T} = \mathsf{C}\mathbf{E}^{\mathrm{e}}, \\ \mathbf{T} \in \mathrm{Sym}^{-}, \quad \mathbf{E}^{\mathrm{f}} \in \mathrm{Sym}^{+}, \\ \mathbf{T} \cdot \mathbf{E}^{\mathrm{f}} = 0; \end{array}\right\} \tag{4}$$

(ii) we have equations $(4)_{1,2}$ *and*

$$\left.\begin{array}{c} \mathbf{T} \in \mathrm{Sym}^{-}, \\ (\mathbf{T} - \mathbf{T}^*) \cdot \mathbf{E}^{\mathrm{f}} \geq 0 \quad \textit{for each} \quad \mathbf{T}^* \in \mathrm{Sym}^{-}; \end{array}\right\} \tag{5}$$

(iii) we have equations $(4)_{1,2}$ *and*

$$\mathbf{E}^{\mathrm{e}} \textit{ is the projection of } \mathbf{E} \textit{ onto } \mathsf{C}^{-1}\,\mathrm{Sym}^{-} \textit{ with respect to } (\cdot,\cdot)_E. \tag{6}$$

Proof. Let us first show that the three characterizations of the triplet ($\mathbf{T}$, $\mathbf{E}^{\mathrm{e}}$, $\mathbf{E}^{\mathrm{f}}$) are equivalent.

Proof of (iii) ⇒ (i). Assume that Characterization (iii) holds. Let $\mathbf{E}^{\mathrm{e}}$ be the projection of $\mathbf{E}$ onto the convex cone $\mathsf{C}^{-1}\,\mathrm{Sym}^{-}$ with respect to the energetic scalar product and let $\mathbf{E}^{\mathrm{f}}$ and $\mathbf{T}$ be as in $(4)_{1,2}$. Since $\mathbf{E}^{\mathrm{e}} \in \mathsf{C}^{-1}\,\mathrm{Sym}^{-}$, we have $\mathbf{T} = \mathsf{C}\mathbf{E}^{\mathrm{e}} \in \mathrm{Sym}^{-}$ and by Remark 2.2(i) $(\mathbf{E}^{\mathrm{f}}, \mathsf{C}^{-1}\mathbf{T}^*)_E = (\mathbf{E} - \mathbf{E}^{\mathrm{e}}, \mathsf{C}^{-1}\mathbf{T}^*)_E \leq 0$ for all $\mathbf{T}^* \in \mathrm{Sym}^{-}$ which can be rewritten as $\mathbf{E}^{\mathrm{f}} \cdot \mathbf{T}^* \leq 0$,

which in turn implies that $\mathbf{E}^{\mathrm{f}} \in \mathrm{Sym}^+$. Thus we have $(4)_3$. Finally, by Remark 2.2(ii) we have $(\mathbf{E}^{\mathrm{f}}, \mathsf{C}^{-1}\mathbf{E}^{\mathrm{e}})_E = (\mathbf{E} - \mathbf{E}^{\mathrm{e}}, \mathsf{C}^{-1}\mathbf{T})_E = 0$ which can be rewritten as $\mathbf{E}^{\mathrm{f}} \cdot \mathbf{T} = 0$. Thus we have $(4)_4$. This proves that (iii) $\Rightarrow$ (i).

Proof of (i) $\Rightarrow$ (ii). Assume that Characterization (i) holds. Then we have $(5)_1$. Furthermore, if $\mathbf{T}^* \in \mathrm{Sym}^-$ then $\mathbf{T}^* \cdot \mathbf{E}^{\mathrm{f}} \le 0$ since $\mathbf{E}^{\mathrm{f}} \in \mathrm{Sym}^+$ by $(4)_3$. Combining with $(4)_4$ we obtain $(5)_2$. Thus (i) $\Rightarrow$ (ii).

Proof of (ii) $\Rightarrow$ (iii). Assume that Characterization (ii) holds. Using $(4)_{1,2}$ we can rewrite (5) as

$$\mathbf{E}^{\mathrm{e}} \in \mathsf{C}^{-1}\,\mathrm{Sym}^-$$

$$(\mathbf{E}^* - \mathbf{E}^{\mathrm{e}}, \mathbf{E}^{\mathrm{f}}) \le 0 \quad \text{for each} \quad \mathbf{E}^* \in \mathsf{C}^{-1}\,\mathrm{Sym}^-;.$$

Thus

$$\mathbf{E}^{\mathrm{f}} (\equiv \mathbf{E} - \mathbf{E}^{\mathrm{e}} \in \mathrm{Norm}(\mathsf{C}^{-1}\,\mathrm{Sym}^-, \mathbf{E}^{\mathrm{e}}),$$

and Remark 2.2 asserts (6). Thus we have shown that (ii) $\Rightarrow$ (iii).

Summarizing, we have shown that the three characterizations of the triplet $(\mathbf{T}, \mathbf{E}^{\mathrm{e}}, \mathbf{E}^{\mathrm{f}})$ are equivalent. Characterization (iii) shows that the triplet exists and is unique, because $\mathbf{E}^{\mathrm{e}}$, being the projection of $\mathbf{E}$ on $\mathsf{C}^{-1}\,\mathrm{Sym}^-$ is unique, and the uniqueness of $\mathbf{E}^{\mathrm{f}}$ and $\mathbf{T}$ follows from $(4)_{1,2}$. □

We define the *elastic stress* $\hat{\mathbf{T}} : \mathrm{Sym} \to \mathrm{Sym}$ and *stored energy* $\hat{w} : \mathrm{Sym} \to \mathrm{R}$ of a masonry material by

$$\hat{\mathbf{T}}(\mathbf{E}) = \mathbf{T}, \quad \hat{w}(\mathbf{E}) = \tfrac{1}{2}\hat{\mathbf{T}}(\mathbf{E}) \cdot \mathbf{E} = \tfrac{1}{2}|\mathsf{P}\mathbf{E}|_E^2 \tag{7}$$

for any $\mathbf{E} \in \mathrm{Sym}$ where $(\mathbf{T}, \mathbf{E}^{\mathrm{e}}, \mathbf{E}^{\mathrm{f}})$ is the triplet associated with $\mathbf{E}$ as in Proposition 2.3 and where $\mathsf{P} : \mathrm{Sym} \to \mathsf{C}^{-1}\,\mathrm{Sym}^-$ denotes the projection from Sym onto $\mathsf{C}^{-1}\,\mathrm{Sym}^-$ with respect to the energetic scalar product $(\cdot,\cdot)_E$. The tensors $\mathbf{E}^{\mathrm{e}}$ and $\mathbf{E}^{\mathrm{f}}$ are called the *elastic* and *fracture* parts of the deformation $\mathbf{E}$.

The no–tension materials have been introduced in the eighties in the papers (Di Pasquale 1984), (Anzellotti 1985), (Giaquinta & Giusti 1985), (Del Piero 1989), (Angelillo 1993). The explicit form of the response function $\hat{\mathbf{T}}$ and its further analysis have been given in the case of C isotropic in (Anzellotti 1985), (Giaquinta & Giusti 1985) in dimension 2 and in (Lucchesi et al. 1994), (Lucchesi et al. 1996) in dimension 3; see also (Lucchesi et al. 2008a). We also note for the reader's curiosity that the membranes with continuously distributed wrinkles differ from the no–tension materials by the exchange of the roles of the cones Sym^- and Sym^+ (Epstein 2002), (Barsotti & Vannucci 2013).

If $F : V \to \bar{\mathrm{R}} := \mathrm{R} \cup \{\infty, -\infty\}$ is a function on an inner product space V then $F^* : V \to \bar{\mathrm{R}}$ is the *convex conjugate function* defined by

$$F^*(y) = \sup\{(x, y) - F(x) : x \in V\},$$

$y \in V$, (Ekeland & Temam 1999, Part One).

Proposition 2.4. *The map* $\hat{\mathbf{T}}$ *is monotone and Lipschitz continuous and the function* $\hat{w}$ *is continuously differentiable, convex and* $D\hat{w} = \hat{\mathbf{T}}$; *in fact, we have the following inequalities:*

$$(\hat{\mathbf{T}}(\mathbf{F}) - \hat{\mathbf{T}}(\mathbf{E})) \cdot (\mathbf{F} - \mathbf{E}) \geq k|\hat{\mathbf{T}}(\mathbf{F}) - \hat{\mathbf{T}}(\mathbf{E})|^2, \tag{8}$$

$$|\hat{\mathbf{T}}(\mathbf{F}) - \hat{\mathbf{T}}(\mathbf{E})| \leq k^{-1}|\mathbf{F} - \mathbf{E}|, \tag{9}$$

$$\hat{w}(\mathbf{F}) \geq \hat{w}(\mathbf{E}) + \hat{\mathbf{T}}(\mathbf{E}) \cdot (\mathbf{F} - \mathbf{E}) + \tfrac{1}{2}k|\hat{\mathbf{T}}(\mathbf{F}) - \hat{\mathbf{T}}(\mathbf{E})|^2 \tag{10}$$

for any $\mathbf{E}, \mathbf{F} \in \mathrm{Sym}$ *where*

$$k := \inf\{\mathbf{A} \cdot \mathsf{C}^{-1}\mathbf{A} : \mathbf{A} \in \mathrm{Sym}, |\mathbf{A}| = 1\} > 0. \tag{11}$$

We have

$$\hat{w}^*(\mathbf{T}) = \begin{cases} \frac{1}{2}\mathbf{T} \cdot \mathsf{C}^{-1}\mathbf{T} & \text{if} \quad \mathbf{T} \in \mathrm{Sym}^-, \\ \infty & \text{if} \quad \mathbf{T} \in \mathrm{Sym} \setminus \mathrm{Sym}^- . \end{cases} \tag{12}$$

Cf. Del Piero (Del Piero 1989, Proposition 4.4 and Lemma 5.1) for (8)–(10).

Proof. Let $\mathbf{E}, \mathbf{F} \in \mathrm{Sym}$ and put $\mathbf{T} = \hat{\mathbf{T}}(\mathbf{E}), \mathbf{U} = \hat{\mathbf{T}}(\mathbf{F})$. From $(5)_2$ we obtain

$$(\mathbf{T} - \mathbf{U}) \cdot (\mathbf{E} - \mathsf{C}^{-1}\mathbf{T}) \geq 0, \quad (\mathbf{U} - \mathbf{T}) \cdot (\mathbf{F} - \mathsf{C}^{-1}\mathbf{U}) \geq 0; \tag{13}$$

summing these two inequalities and rearranging we obtain

$$(\mathbf{T} - \mathbf{U}) \cdot \mathsf{C}^{-1}(\mathbf{T} - \mathbf{U}) \leq (\mathbf{T} - \mathbf{U}) \cdot (\mathbf{E} - \mathbf{F});$$

using (11) we obtain (8). Using the Schwarz inequality on the left hand side of (8) we obtain (9). To prove (10), one finds that

$$\hat{w}(\mathbf{F}) - \hat{w}(\mathbf{E}) - \mathbf{T} \cdot (\mathbf{F} - \mathbf{E}) - \tfrac{1}{2}(\mathbf{T} - \mathbf{U}) \cdot \mathsf{C}^{-1}(\mathbf{T} - \mathbf{U}) = (\mathbf{U} - \mathbf{T}) \cdot (\mathbf{F} - \mathsf{C}^{-1}\mathbf{U});$$

the last expression is nonnegative by $(13)_2$ and hence

$$\hat{w}(\mathbf{F}) - \hat{w}(\mathbf{E}) - \mathbf{T} \cdot (\mathbf{F} - \mathbf{E}) - \tfrac{1}{2}(\mathbf{T} - \mathbf{U}) \cdot \mathsf{C}^{-1}(\mathbf{T} - \mathbf{U}) \geq 0;$$

a reference to (11) then yields (10) and hence also the convexity of $\hat{w}$. To prove that $\hat{w}$ is continuously differentiable and $\hat{\mathbf{T}}$ is its derivative, we note that using (10) twice we obtain

$$\hat{\mathbf{T}}(\mathbf{F})\cdot(\mathbf{F}-\mathbf{E})\geq\hat{w}(\mathbf{F})-\hat{w}(\mathbf{E})\geq\hat{\mathbf{T}}(\mathbf{E})\cdot(\mathbf{F}-\mathbf{E})$$

for any $\mathbf{E},\mathbf{F}\in\mathrm{Sym}$; dividing by $|\mathbf{E}-\mathbf{F}|$, letting $\mathbf{F}\to\mathbf{E}$, using $\hat{\mathbf{T}}(\mathbf{F})\to\hat{\mathbf{T}}(\mathbf{E})$ and invoking the definition of the Fréchet derivative we obtain $D\hat{w}(\mathbf{E})=\hat{\mathbf{T}}(\mathbf{E})$. To prove (12), let $\hat{h}:\mathrm{Sym}\to\mathrm{R}\cup\{\infty\}$ be the function defined by the right hand side of (12). We calculate the convex conjugate $\hat{h}^*(\mathbf{E})$ of h at $\mathbf{E}\in\mathrm{Sym}$. We note that if $(\mathbf{T},\mathbf{E}^{\mathrm{e}},\mathbf{E}^{\mathrm{f}})$ is the triplet associated with $\mathbf{E}$ as in Proposition 2.3, then algebraic manipulations show that $(5)_2$ can be rewritten as

$$\mathbf{T}\cdot\mathbf{E}-\hat{h}(\mathbf{T})\geq\mathbf{S}\cdot\mathbf{E}-\hat{h}(\mathbf{S})+\tfrac{1}{2}(\mathbf{T}-\mathbf{S})\cdot\mathsf{C}^{-1}(\mathbf{T}-\mathbf{S})\tag{14}$$

for every $\mathbf{S}\in\mathrm{Sym}^-$ with the equality if $\mathbf{S}=\mathbf{T}$. Since (14) holds also if $\mathbf{S}\notin\mathrm{Sym}^-$ as the right hand side is $-\infty$ in that case, we have

$$\mathbf{T}\cdot\mathbf{E}-\hat{h}(\mathbf{T})\geq\mathbf{S}\cdot\mathbf{E}-\hat{h}(\mathbf{S})$$

for all $\mathbf{S}\in\mathrm{Sym}$ and thus the definition gives $\hat{h}^*(\mathbf{E})=\mathbf{T}\cdot\mathbf{E}-\hat{h}(\mathbf{T})(\equiv\hat{w}(\mathbf{E}))$. Then $\hat{w}^*=\hat{h}^{**}=\hat{h}$ by (Fonseca & Leoni 2007, Theorem 4.92(iii)) since $\hat{h}$ is lowersemicontinuous, convex and bounded from below by an affine (continuous) function. The proof of (12) is complete. □

Proposition 2.5. *The stored energy $\hat{w}$ is decreasing in the sense that*

$$\hat{w}(\mathbf{E}+\mathbf{P})\leq\hat{w}(\mathbf{E})\tag{15}$$

for any $\mathbf{E}\in\mathrm{Sym}$ and any $\mathbf{P}\in\mathrm{Sym}^+$. Moreover, the function $\hat{w}$ is completely characterized by the following two equivalent requirements:

(i) $\hat{w}$ is the largest decreasing function such that

$$\hat{w}(\mathbf{E})\leq\tfrac{1}{2}\mathbf{E}\cdot\mathsf{C}\mathbf{E}\tag{16}$$

for every $\mathbf{E}\in\mathrm{Sym}$;

(ii) we have

$$\hat{w}(\mathbf{E})=\inf\{\tfrac{1}{2}(\mathbf{E}-\mathbf{P})\cdot\mathsf{C}(\mathbf{E}-\mathbf{P}):\mathbf{P}\in\mathrm{Sym}^+\}.\tag{17}$$

Proof. To prove (i), we invoke (10) in which we omit the last term on the right hand side to obtain

$$\hat{w}(\mathbf{E}+\mathbf{P}) - \hat{\mathbf{T}}(\mathbf{E}+\mathbf{P})\cdot\mathbf{P} \le \hat{w}(\mathbf{E}).$$

Noting that $\hat{\mathbf{T}}(\mathbf{E}+\mathbf{P})\cdot\mathbf{P} \le 0$ since $\hat{\mathbf{T}}(\mathbf{E}+\mathbf{P}) \in \mathrm{Sym}^-$ and $\mathbf{P} \in \mathrm{Sym}^+$ completes the proof of (15).

Next let $\hat{w} : \mathrm{Sym} \to \mathrm{R}$ be any function and let us prove that if it is given by (17) then it is the largest decreasing function satisfying (16). Clearly, $\hat{w}$ satisfies (16). Let $\mathbf{E} \in \mathrm{Sym}$ and $\mathbf{Q} \in \mathrm{Sym}^+$. Then

$$\hat{w}(\mathbf{E}-\mathbf{Q}) = \inf\{\tfrac{1}{2}(\mathbf{E}-\mathbf{Q}-\mathbf{P})\cdot\mathsf{C}(\mathbf{E}-\mathbf{Q}-\mathbf{P}) : \mathbf{P} \in \mathrm{Sym}^+\}$$

and noting that $\mathbf{Q}+\mathbf{P} \in \mathrm{Sym}$, we see that $S' := \{\mathbf{Q}+\mathbf{P} : \mathbf{P} \in \mathrm{Sym}^+\} \subset \{\mathbf{P} \in \mathrm{Sym}^+\}$ thus

$$\begin{aligned}
\hat{w}(\mathbf{E}-\mathbf{Q}) &= \{\tfrac{1}{2}(\mathbf{E}-\mathbf{P}')\cdot\mathsf{C}(\mathbf{E}-\mathbf{P}') : \mathbf{P} \in S'\} \\
&\ge \{\tfrac{1}{2}(\mathbf{E}-\mathbf{P})\cdot\mathsf{C}(\mathbf{E}-\mathbf{P}) : \mathbf{P} \in \mathrm{Sym}^+\} \\
&= \hat{w}(\mathbf{E}).
\end{aligned}$$

Thus $\hat{w}$ is decreasing. Next assume that $\hat{w}'$ is a decreasing function satisfying (16) and prove that $\hat{w}'(\mathbf{E}) \le \hat{w}(\mathbf{E})$ for every $\mathbf{E} \in \mathrm{Sym}$. Let $\mathbf{P} \in \mathrm{Sym}^+$. We have

$$\hat{w}'(\mathbf{E}) \le \hat{w}'(\mathbf{E}-\mathbf{P}) \le \tfrac{1}{2}(\mathbf{E}-\mathbf{P})\cdot\mathsf{C}(\mathbf{E}-\mathbf{P}).$$

Taking the infimum over all $\mathbf{P}$ we obtain

$$\hat{w}'(\mathbf{E}) \le \inf\{\tfrac{1}{2}(\mathbf{E}-\mathbf{P})\cdot\mathsf{C}(\mathbf{E}-\mathbf{P})\} = \hat{w}(\mathbf{E}).$$

This proves the equivalence of (i) and (ii).

Let now $\hat{w}$ be the stored energy of a no–tension material and prove that it satisfies (i). We have already seen that $\hat{w}$ is decreasing. To prove (16), we note that

$$\begin{aligned}
\mathbf{E}\cdot\mathsf{C}\mathbf{E} &= \mathbf{E}\cdot\mathsf{C}\mathbf{E}^{\mathrm{e}} + \mathbf{E}\cdot\mathsf{C}\mathbf{E}^{\mathrm{f}} \\
&= \mathbf{E}^{\mathrm{e}}\cdot\mathsf{C}\mathbf{E}^{\mathrm{e}} + (\mathbf{E}^{\mathrm{e}}+\mathbf{E}^{\mathrm{f}})\cdot\mathsf{C}\mathbf{E}^{\mathrm{f}} \\
&= 2\hat{w}(\mathbf{E}) + \mathbf{E}^{\mathrm{e}}\cdot\mathsf{C}\mathbf{E}^{\mathrm{f}} + \mathbf{E}^{\mathrm{f}}\cdot\mathsf{C}\mathbf{E}^{\mathrm{f}} \\
&\ge 2\hat{w}(\mathbf{E}).
\end{aligned}$$

Thus $\hat{w}$ satisfies (16). Furthermore, we have

$$\hat{w}(\mathbf{E}) = \tfrac{1}{2}(\mathbf{E}-\mathbf{E}^{\mathrm{f}})\cdot\mathsf{C}(\mathbf{E}-\mathbf{E}^{\mathrm{f}})$$

and noting that $\mathbf{E}^{\mathrm{f}} \in \mathrm{Sym}^+$ we see that

$$\hat{w}(\mathbf{E}) \geq \inf\{\tfrac{1}{2}(\mathbf{E}-\mathbf{P})\cdot \mathsf{C}(\mathbf{E}-\mathbf{P}) : \mathbf{P} \in \mathrm{Sym}^+\}.$$

Thus $\hat{w}$ is a decreasing function satisfying (16) that is larger than the function defined by the right hand side of (17). However, since this right hand side defines the largest function with this property, we have the equality (17). □

3 Vector valued measures

In this section we introduce the main object which will represent stresses in masonry bodies and loads applied to the bodies. These two classes of objects will be represented by tensor valued measures and vector valued measures, respectively. Among measures there are ordinary functions (up to an identification), i.e., stresses and loads in the usual sense, but most importantly, measures can represent stresses or loads concentrated on lower–dimensional objects–surfaces or curves. The main goal in this section is to introduce the terminology and notation for measures with values in a finite dimensional vector space. We refer to (Ambrosio et al. 2000, Chapter 1) for further details.

Definition 3.1. Let V be a finite-dimensional vector space. By a V *valued measure* in R^n we mean a map m from a system of all Borel sets in R^n to V which is countably additive in the sense that if B_1, B_2, ... is a disjoint family of Borel sets in R^n then

$$\mathsf{m}\big(\bigcup_{i=1}^{\infty} B_i\big) = \sum_{i=1}^{\infty} \mathsf{m}(B_i).$$

Below we need the choices $V = \mathrm{Sym}$ and $V = \mathrm{R}^n$. We call the Sym valued measures tensor valued measures; this particular case is used to model the stress fields over the body. We call the R^n valued measures vector valued measures. These are used to model the loads applied to the body.

We say that a function ϕ defined on the system of all Borel sets in R^n is a *nonnegative measure* if it takes the values from the set $[0,\infty]$ of nonnegative numbers or ∞ which is countably additive in the sense that if B_1, B_2, ... is a disjoint family of Borel sets in R^n then

$$\phi\big(\bigcup_{i=1}^{\infty} B_i\big) = \sum_{i=1}^{\infty} \phi(B_i)$$

and

$$\phi(\emptyset) = 0.$$

If Ω is a Borel subset of R^n and m a V valued measure or a nonnegative measure, we say that m is supported by Ω if $\mathsf{m}(A) = \mathbf{0}$ for any Borel set A such that $A \cap \Omega = \emptyset$. We denote by $\mathcal{M}(\Omega, V)$ the set of all V valued measures supported by Ω.

If $\mathsf{m} \in \mathcal{M}(\Omega, V)$ and if $\alpha : \Omega \to V$ is a bounded Borel function then we have a well defined integral

$$\int_\Omega \alpha \cdot \, d\mathsf{m},$$

which is a real number.

We denote by $\mathcal{L}^n$ the Lebesgue measure in R^n (Ambrosio et al. 2000, Definition 1.52) and if k is an integer, $0 \leq k \leq n$, we denote by $\mathcal{H}^k$ the k-dimensional Hausdorff measure ("k dimensional area") in R^n (Ambrosio et al. 2000, Section 2.8). If ϕ is a nonnegative measure or a V valued measure, we denote by $\phi \llcorner A$ the *restriction* of ϕ to a Borel set $A \subset \mathrm{R}^n$ defined by

$$\phi \llcorner A(B) = \phi(A \cap B)$$

for any Borel subset B of R^n. Thus if $\mathcal{N}$ is an $n-1$ dimensional surface in R^n then $\mathcal{H}^{n-1} \llcorner \mathcal{N}$ is the area measure on $\mathcal{N}$.

If ϕ is a nonnegative measure, we denote by $f\phi$ the *product of the measure* ϕ by a ϕ integrable V valued function f on R^n; one has

$$(f\phi)(A) = \int_A f \, d\phi$$

for any Borel subset A of R^n.

The operations of restriction and multiplication of measures are employed to construct tensor valued measures concentrated on surfaces as follows:

Examples Consider a body $\Omega \subset \mathrm{R}^n$ and an $n-1$ dimensional surface $\mathcal{N} \subset \Omega$ and let $\mathbf{E} : \Omega \to \mathrm{R}^n$ be a bounded continuous function, interpreted as a field of strain over Ω.

(i) The measure $\mathcal{H}^{n-1} \llcorner \mathcal{N}$ is supported by $\mathcal{N}$ and thus if $\mathbf{T}_s : \mathcal{N} \to \mathrm{Sym}$ is an $\mathcal{H}^{n-1}$ integrable tensor field on $\mathcal{N}$, then the measure

$$\mathsf{T}_s := \mathbf{T}_s \mathcal{H}^{n-1} \llcorner \mathcal{N}$$

is a tensor valued measure in $\mathcal{M}(\Omega, \mathrm{Sym})$ concentrated on $\mathcal{N}$. One has

$$\int_\Omega \mathbf{E} \cdot \, d\mathsf{T}_s = \int_\mathcal{N} \mathbf{E} \cdot \mathbf{T}_s \, d\mathcal{H}^{n-1}.$$

(ii) If $\mathbf{T}_r : \Omega \to \mathrm{Sym}$ is an $\mathcal{L}^n$ integrable tensor field, then the tensor valued measure

$$\mathsf{T}_r := \mathbf{T}_r \mathcal{L}^n \llcorner \Omega$$

belongs to $\mathcal{M}(\Omega, \mathrm{Sym})$ and faithfully represents $\mathbf{T}_r$; the measure is distributed over Ω. One has

$$\int_\Omega \mathbf{E} \cdot \, d\mathsf{T}_r = \int_\Omega \mathbf{E} \cdot \mathbf{T}_r \, d\mathcal{L}^n.$$

The measures of the type T_s and T_r and their combinations $\mathsf{T} = \mathsf{T}_r + \mathsf{T}_s$ will be employed in Sections 7–8 where we deal with weakly compatible loads. Vector valued measures will be employed in the following section to define the loads of the body.

The *polar decomposition of measures* (cf. (Rudin 1970, Theorem 6.12)) says that if $\mathsf{m} \in \mathcal{M}(\Omega, V)$, there exists a pair $(r, |\mathsf{m}|)$ consisting of a Borel function $r : \Omega \to V$ and of a nonnegative measure $|\mathsf{m}|$ on Ω such that

$$\mathsf{m} = r|\mathsf{m}|$$

and

$$|r(\mathbf{x})| = 1 \quad \text{for} \quad |\mathsf{m}| \quad \text{almost every} \quad \mathbf{x} \in \Omega.$$

The measure $|\mathsf{m}|$ is unique and the function r is unique up to a change on a $|\mathsf{m}|$ null set. The measure $|\mathsf{m}|$ is called the total variation measure of m, and r the amplitude. We denote by $\mathrm{M}(\mathsf{m})$ the *mass* of m, defined by $\mathrm{M}(\mathsf{m}) = |\mathsf{m}|(\mathrm{R}^n)$.

If Ω is an open subset of R^n, we denote by $C_0(\Omega, V)$ the space of all continuous V valued functions on R^n with compact support that is contained in Ω, and denote by $|\cdot|_{C_0}$ the maximum norm on $C_0(\mathrm{R}^n, V)$.

4 Loads

We consider a continuous body represented by a Lipschitz domain (Adams & Fournier 2003) $\Omega \subset \mathrm{R}^n$ and assume that $\mathcal{D}, \mathcal{S}$ are two disjoint subsets of $\partial\Omega$ such that $\mathcal{D} \cup \mathcal{S} = \partial\Omega$, to be identified below as the set of prescribed boundary displacement and prescribed boundary force. We assume that $\mathcal{D}$ is a closed set.

We put

$$V_0 = \{\mathbf{v} \in C^1(\mathrm{cl}\,\Omega, \mathrm{R}^n) : \mathbf{v} = \mathbf{0} \text{ on } \mathcal{D}\}$$

and

$$V = \{\mathbf{v} \in W^{1,2}(\Omega, \mathrm{R}^n) : \mathbf{v} = \mathbf{0} \text{ almost everywhere on } \mathcal{D}\};$$

here $C^1(\mathrm{cl}\,\Omega, \mathrm{R}^n)$ is the set of all continuously differentiable mappings $\mathbf{v} : \Omega \to \mathrm{R}^n$ such that $\mathbf{v}$ and its derivative $\nabla\mathbf{v}$ have a continuous extension to the closure $\mathrm{cl}\,\Omega$ of Ω and $W^{1,2}(\Omega, \mathrm{R}^n)$ is the Sobolev space of all R^n valued maps such that $\mathbf{v}$ and the weak gradient $\nabla\mathbf{v}$ of $\mathbf{v}$ are square integrable on Ω, i.e.,

$$\int_\Omega |\mathbf{v}|^2 \, d\mathcal{L}^n < \infty, \quad \int_\Omega |\nabla\mathbf{v}|^2 \, d\mathcal{L}^n < \infty,$$

(Adams & Fournier 2003). We assume that V_0 is a dense subset of V. For any $\mathbf{v} \in V$ we define the infinitesimal strain tensor $\hat{\mathbf{E}}(\mathbf{v})$ of $\mathbf{v}$ by

$$\hat{\mathbf{E}}(\mathbf{v}) = \tfrac{1}{2}(\nabla\mathbf{v} + \nabla\mathbf{v}^{\mathrm{T}}).$$

We assume that the body is subjected to loads which consist of a body force acting in the interior of Ω and of the surface force acting on $\mathcal{S}$. We represent both the body and surface forces as vector valued measures supported by Ω and $\mathcal{S}$, respectively. Thus we assume that we are given $\mathsf{b} \in \mathcal{M}(\Omega, \mathrm{R}^n)$ and $\mathsf{s} \in \mathcal{M}(\mathcal{S}, \mathrm{R}^n)$ with the following meaning. For any Borel subset P of Ω the value $\mathsf{b}(P) \in \mathrm{R}^n$ is the body force acting on P from the exterior and for any Borel $S \subset \mathcal{S}$ the value $\mathsf{s}(S) \in \mathrm{R}^n$ is the force acting on the surface S from the exterior of the body. We call the pair (s, b) the *loads* acting on the body. We note that we define the loads as measures, which allows for the concentration of the body force and more importantly surface tractions.

We define for each $\mathbf{u} \in V$ the *internal energy* of the body by

$$\mathsf{E}(\mathbf{u}) = \int_\Omega \hat{w}(\hat{\mathbf{E}}(\mathbf{u})) \, d\mathcal{L}^n$$

and for each $\mathbf{u} \in V_0$ the *energy of the loads* by

$$\langle \mathbf{l}, \mathbf{u} \rangle = \int_\Omega \mathbf{u} \cdot \, d\mathsf{b} + \int_{\mathcal{S}} \mathbf{u} \cdot \, d\mathsf{s}.$$

The *total energy* of the deformation $\mathbf{u} \in V_0$ is defined by

$$\mathsf{F}(\mathbf{u}) = \mathsf{E}(\mathbf{u}) - \langle \mathbf{l}, \mathbf{u} \rangle .$$

An important special case arises when there are square integrable functions $\mathbf{b} \in L^2(\Omega, \mathrm{R}^n)$, $\mathbf{s} \in L^2(\mathcal{S}, \mathrm{R}^n)$ such that

$$\mathsf{b} = \mathbf{b}\mathcal{L}^n \llcorner \Omega, \quad \mathsf{s} = \mathbf{s}\mathcal{H}^{n-1} \llcorner \mathcal{S}. \tag{18}$$

Here $L^2(\Omega, \mathrm{R}^n)$ is the set of all $\mathcal{L}^n$ measurable maps $\mathbf{b} : \Omega \to \mathrm{R}^n$ such that

$$\int_\Omega |\mathbf{b}|^2 \, d\mathcal{L}^n < \infty$$

and $L^2(\mathcal{S},\mathrm{R}^n)$ is the set of all $\mathcal{H}^{n-1}$ measurable maps $\mathbf{s}:\mathcal{S}\to\mathrm{R}^n$ such that

$$\int_{\mathcal{S}}|\mathbf{s}|^2\,d\mathcal{H}^{n-1}<\infty.$$

In the case (18) one can define the potential energy of the loads $\langle\mathbf{l},\mathbf{u}\rangle$ for each $\mathbf{u}$ from the larger space V by

$$\langle\mathbf{l},\mathbf{u}\rangle=\int_\Omega\mathbf{u}\cdot\mathbf{b}\,d\mathcal{L}^n+\int_{\mathcal{S}}\mathbf{u}\cdot\mathbf{s}\,d\mathcal{H}^{n-1}$$

$\mathbf{u}\in V$.

Given the loads (s,b) and $\mathbf{u}\in V$, we say that $\mathbf{u}$ is an *equilibrium state* of Ω under the given loads if

$$\int_\Omega\hat{\mathbf{T}}(\hat{\mathbf{E}}(\mathbf{u}))\cdot\hat{\mathbf{E}}(\mathbf{v})\,d\mathcal{L}^n=\langle\mathbf{l},\mathbf{v}\rangle \tag{19}$$

for each $\mathbf{v}\in V_0$.

We note that if the loads are of the special form (18) with $\mathbf{b}\in L^2(\Omega,\mathrm{R}^n)$, $\mathbf{s}\in L^2(\mathcal{S},\mathrm{R}^n)$ and if $\hat{\mathbf{T}}(\hat{\mathbf{E}}(\mathbf{u}))\in C^1(cl\,\Omega,\mathrm{Sym})$ then the variational equation (19) is equivalent to the strong form

$$div\,\mathbf{T}+\mathbf{b}=\mathbf{0}\text{ in }\ \Omega\quad\text{and}\quad\mathbf{Tn}=\mathbf{s}\text{ on }\ \mathcal{S}$$

where $\mathbf{n}$ is the outer normal to $\partial\Omega$. We note that in general the existence of the equilibrium state is not guaranteed. The existence theory of equilibrium state requires the extension of the states to admit fracture. See Section 5, below. On the other hand, the given loads may admit more than one equilibrium state $\mathbf{u}$.

Remark 4.1. Assume the loads of the special form (18) with $\mathbf{b}\in L^2(\Omega,\mathrm{R}^n)$, $\mathbf{s}\in L^2(\mathcal{S},\mathrm{R}^n)$. Then $\mathbf{u}\in V$ is an equilibrium state under the given loads if and only if $\mathbf{u}$ is a minimizer of the total energy under the given loads.

Proof. Let $\mathbf{u}$ be an equilibrium state under the given loads. Let $\mathbf{v}\in V_0$. Then

$$\begin{aligned}\mathsf{F}(\mathbf{u}+\mathbf{v})&=\textstyle\int_\Omega\hat{w}(\hat{\mathbf{E}}(\mathbf{u})+\hat{\mathbf{E}}(\mathbf{v}))\,d\mathcal{L}^n-\langle\mathbf{l},\mathbf{u}\rangle-\langle\mathbf{l},\mathbf{v}\rangle\\&\geq\textstyle\int_\Omega[\hat{w}(\hat{\mathbf{E}}(\mathbf{u}))+\hat{\mathbf{T}}(\hat{\mathbf{E}}(\mathbf{u})\cdot\hat{\mathbf{E}}(\mathbf{v})]\,d\mathcal{L}^n-\langle\mathbf{l},\mathbf{u}\rangle-\langle\mathbf{l},\mathbf{v}\rangle\\&=\mathsf{F}(\mathbf{u})+[\textstyle\int_\Omega\hat{\mathbf{T}}(\hat{\mathbf{E}}(\mathbf{u})\cdot\hat{\mathbf{E}}(\mathbf{v})\,d\mathcal{L}^n-\langle\mathbf{l},\mathbf{v}\rangle]\end{aligned}$$

by (10). Since $\mathbf{u}$ is an equilibrium state, the square bracket on the last line vanishes and we obtain

$$\mathsf{F}(\mathbf{u}+\mathbf{v})\geq\mathsf{F}(\mathbf{u}) \tag{20}$$

for each $\mathbf{v} \in V_0$. Since V_0 is dense in V and the energy a continuous functional, we have (20) for each $\mathbf{v} \in V$. Thus $\mathbf{u}$ is a point of minimum energy.

Conversely, assume that $\mathbf{u}$ is a point of minimum energy. Let $\mathbf{v} \in V_0$ and $t \in \mathrm{R}$. We have

$$\mathsf{F}(\mathbf{u} + t\mathbf{v}) \geq \mathsf{F}(\mathbf{u})$$

for all $t \in \mathrm{R}$ with the equality sign for $t = 0$ and thus the derivative of the function $t \mapsto \mathsf{F}(\mathbf{u} + t\mathbf{v})$ at $t = 0$ vanishes. One has

$$\mathsf{F}(\mathbf{u} + t\mathbf{v}) = \int_\Omega \hat{w}(\hat{\mathbf{E}}(\mathbf{u}) + t\hat{\mathbf{E}}(\mathbf{v}))\, d\mathcal{L}^n - \langle \mathbf{l}, \mathbf{u} \rangle - t \langle \mathbf{l}, \mathbf{v} \rangle$$

and differentiating under the integral sign we obtain

$$\frac{d}{dt}\mathsf{F}(\mathbf{u} + t\mathbf{v})\big|_{t=0} = \int_\Omega \hat{\mathbf{T}}(\hat{\mathbf{E}}(\mathbf{u})) \cdot \hat{\mathbf{E}}(\mathbf{v}))\, d\mathcal{L}^n - \langle \mathbf{l}, \mathbf{v} \rangle = 0.$$

Hence $\mathbf{u}$ is an equilibrium state of Ω under the given loads. □

Let (s, b) be given loads of Ω and let $\mathbf{T} \in L^2(\Omega, \mathrm{Sym})$ where $L^2(\Omega, \mathrm{Sym})$ is the set of all $\mathcal{L}^n$ measurable maps $\mathbf{T} : \Omega \to \mathrm{Sym}$ such that $\int_\Omega |\mathbf{T}|^2\, d\mathcal{L}^n < \infty$. We say that $\mathbf{T}$ *equilibrates the loads* (s, b) if

$$\int_\Omega \mathbf{T} \cdot \hat{\mathbf{E}}(\mathbf{v})\, d\mathcal{L}^n = \langle \mathbf{l}, \mathbf{v} \rangle$$

for all $\mathbf{v} \in V_0$. We say that $\mathbf{T}$ is *admissible* if $\mathbf{T}(\mathbf{x}) \leq \mathbf{0}$ for $\mathcal{L}^n$ almost every $\mathbf{x} \in \Omega$. We say that the lods (s, b) are *strongly compatible* if there exists an admissible stress field equilibrating the loads. Using this terminology we can say that if $\mathbf{u}$ is an equilibrium state of Ω under the given loads then the stress field corresponding to $\mathbf{u}$ is admissible and equilibrates the loads. Thus the loads must be strongly compatible for an equilibrium state to exist.

Theorem 4.2. *Let $\mathbf{u} \in V_0$ be an equilibrium state under the loads (s, b). Then the stress field $\mathbf{S} := \hat{\mathbf{T}}(\hat{\mathbf{E}}(\mathbf{u}))$ is a minimum point of the complementary energy functional*

$$\mathsf{G}(\mathbf{T}) = \tfrac{1}{2} \int_\Omega \mathbf{T} \cdot \mathsf{C}^{-1}\mathbf{T}\, d\mathcal{L}^n$$

among all admissible stress fields $\mathbf{T}$ equilibrating the loads.

We call G the *complementary energy.*

Proof. Let $\mathbf{T}$ be an admissible stress field equilibrating the loads and let $\mathbf{E}^{\mathrm{e}}$ and $\mathbf{E}^{\mathrm{f}}$ be the elastic and fracture parts of the strain corresponding to $\mathbf{u}$. Using the convexity of the function $\mathbf{U} \mapsto \frac{1}{2}(\mathsf{C}^{-1}\mathbf{U} \cdot \mathbf{U})$ we find

$$\begin{aligned}
\mathsf{G}(\mathbf{T}) - \mathsf{G}(\mathbf{S}) &\geq \textstyle\int_\Omega \mathsf{C}^{-1}\mathbf{S} \cdot (\mathbf{T} - \mathbf{S})\, d\mathcal{L}^n \\
&= \textstyle\int_\Omega \mathbf{E}^{\mathrm{e}} \cdot (\mathbf{T} - \mathbf{S})\, d\mathcal{L}^n \\
&= \textstyle\int_\Omega \mathbf{E}^{\mathrm{e}} \cdot \mathbf{T}\, d\mathcal{L}^n - \langle \mathbf{l}, \mathbf{u} \rangle \\
&= [\textstyle\int_\Omega \hat{\mathbf{E}}(\mathbf{u}) \cdot \mathbf{T}\, d\mathcal{L}^n - \langle \mathbf{l}, \mathbf{u} \rangle] - \textstyle\int_\Omega \mathbf{E}^{\mathrm{f}} \cdot \mathbf{T}\, d\mathcal{L}^n \\
&= - \textstyle\int_\Omega \mathbf{E}^{\mathrm{f}} \cdot \mathbf{T}\, d\mathcal{L}^n \geq 0
\end{aligned}$$

since $\mathbf{u}$ is an equilibrium state and because the square bracket vanishes as $\mathbf{T}$ is a stress field equilibrating the loads. □

As a corollary to Theorem 4.2 we have that while the displacement corresponding to equilibrium may be nonunique, the equilibrium stress is unique as the complementary energy has a unique minimum point. We note also that the complementary energy may admit a minimum among the admissible stress fields equilibrating the given loads, and yet the equilibrium state need not exist.

Let (s, b) be the loads of Ω. We put

$$I_0 = \inf\{\mathsf{F}(\mathbf{u}) : \mathbf{u} \in V_0\}.$$

In general,

$$-\infty \leq I_0 < \infty$$

and we have $I_0 > -\infty$ if and only if the total energy F is bounded from below. Let $H : L^2(\Omega, \mathrm{Sym}) \to \mathrm{R}$ be defined by

$$H(\mathbf{A}) = \int_\Omega \hat{w}(\mathbf{A})\, d\mathcal{L}^n$$

for each $\mathbf{A} \in L^2(\Omega, \mathrm{Sym})$. Let

$$H^*(\mathbf{T}) = \sup\{\mathbf{A} \cdot \mathbf{T} - H(\mathbf{A}) : \mathbf{A} \in L^2(\Omega, \mathrm{Sym})\}$$

for any $\mathbf{T} \in L^2(\Omega, \mathrm{Sym})$. Then (Ekeland & Temam 1999)

$$H^*(\mathbf{T}) = \int_\Omega \hat{w}^*(\mathbf{T})\, d\mathcal{L}^n$$

and hence

$$H^*(\mathbf{T}) = \begin{cases} \frac{1}{2} \int_\Omega \mathbf{T} \cdot \mathsf{C}^{-1}\mathbf{T}\, d\mathcal{L}^n & \text{if} \quad \mathbf{T} \quad \text{is negative semidefinite,} \\ \infty & \text{otherwise,} \end{cases}$$

$\mathbf{T} \in L^2(\Omega, \mathrm{Sym})$, by (12).

Proposition 4.3. *Consider the general loads* (s, b). *Then the loads are strongly compatible if and only if*

$$I_0 > -\infty.$$

Proof. Let $Y := L^2(\Omega, \mathrm{Sym})$ and $X_0 := \{\hat{\mathbf{E}}(\mathbf{v}) : \mathbf{v} \in V_0\}$ so that $X_0 \subset Y$. Assume that $c = I_0 \in \mathrm{R}$. Prove a preliminary result: if $\mathbf{v}_1\ \mathbf{v}_2 \in V_0$ satisfy $\hat{\mathbf{E}}(\mathbf{v}_1) = \hat{\mathbf{E}}(\mathbf{v}_2)$ then $\langle \mathbf{l}, \mathbf{v}_1 \rangle = \langle \mathbf{l}, \mathbf{v}_2 \rangle$. Indeed, let $t \in \mathrm{R}$ and put $\mathbf{v} = (1-t)\mathbf{v}_1 + t\mathbf{v}_2$. Then $\mathbf{v} \in V_0$, $\hat{\mathbf{E}}(\mathbf{v}) = \mathbf{E} := \hat{\mathbf{E}}(\mathbf{v}_1) = \hat{\mathbf{E}}(\mathbf{v}_2)$ and thus

$$\mathsf{F}(\mathbf{v}) = \int_\Omega \hat{w}(\mathbf{E})\, d\mathcal{L}^n - (1-t)\,\langle \mathbf{l}, \mathbf{v}_1 \rangle - t\,\langle \mathbf{l}, \mathbf{v}_2 \rangle \geq c.$$

Assuming $t > 0$, dividing the inequality by t and letting $t \to \infty$ we obtain $\langle \mathbf{l}, \mathbf{v}_1 \rangle - \langle \mathbf{l}, \mathbf{v}_2 \rangle \geq 0$; similarly, assuming $t < 0$, dividing by t and letting $t \to -\infty$ we obtain $\langle \mathbf{l}, \mathbf{v}_1 \rangle - \langle \mathbf{l}, \mathbf{v}_2 \rangle \leq 0$ and thus $\langle \mathbf{l}, \mathbf{v}_1 \rangle = \langle \mathbf{l}, \mathbf{v}_2 \rangle$ which completes the proof of the preliminary result. Let $L_0 : X_0 \to \mathrm{R}$ be defined by

$$L_0(\hat{\mathbf{E}}(\mathbf{v})) = \langle \mathbf{l}, \mathbf{v} \rangle \tag{21}$$

for each $\mathbf{v} \in V_0$, where we use the preliminary result to see that the right hand side of (21) depends only on $\hat{\mathbf{E}}(\mathbf{v})$. Then

$$L_0(\mathbf{A}) \leq H(\mathbf{A}) - c \quad \text{for all} \quad \mathbf{A} \in X_0.$$

The convexity of $\hat{w}$ implies the convexity of H and hence by the version of the Hahn Banach theorem (Fonseca & Leoni 2007, Theorem A.35) there exists a linear extension $L : Y \to \mathrm{R}$ of L_0 such that

$$L(\mathbf{A}) \leq H(\mathbf{A}) - c \quad \text{for all} \quad \mathbf{A} \in Y. \tag{22}$$

The continuity of H on Y, which follows from the properties of $\hat{w}$, implies that H is bounded on the unit ball in Y and hence L is bounded on the unit ball and hence continuous. Thus it can be represented by an element $\mathbf{T} \in Y$ as a scalar product in Y, i.e., there exists a $\mathbf{T} \in Y$ such that

$$L(\mathbf{A}) = \int_\Omega \mathbf{T} \cdot \mathbf{A}\, d\mathcal{L}^n$$

for each $\mathbf{A} \in Y$. Taking in particular $\mathbf{A} \in L^2(\Omega, \mathrm{Sym}^+)$ and noting that then $\hat{w}(\mathbf{A}) = 0$, we find from (22) that

$$L(\mathbf{A}) \leq -c.$$

Repalcing $\mathbf{A}$ by $t\mathbf{A}$ where $t > 0$, dividing by t and letting $t \to \infty$ we obtain $L(\mathbf{A}) \leq 0$ which implies that $\mathbf{T} \leq \mathbf{0}$ for almost all points of Ω. Further, relation (21) gives

$$\int_\Omega \mathbf{T} \cdot \hat{\mathbf{E}}(\mathbf{v})\, d\mathcal{L}^n = \langle \mathbf{l}, \mathbf{v} \rangle$$

for each $\mathbf{v} \in V_0$ and thus $\mathbf{T}$ strongly equilibrates the loads (s, b).

To prove the converse part of the statement, we let $\mathbf{T}$ be a stress field strongly equilibrating the loads (s, b). Since $\mathbf{T}$ is negative semidefinite and square integrable, we have

$$H^*(\mathbf{T}) = \tfrac{1}{2} \int_\Omega \mathbf{T} \cdot \mathsf{C}^{-1}\mathbf{T}\, d\mathcal{L}^n < \infty$$

and hence

$$\infty > H^*(\mathbf{T}) := \sup\{ \int_\Omega \mathbf{T} \cdot \mathbf{A}\, d\mathcal{L}^n - H(\mathbf{A}) : \mathbf{A} \in Y \}$$

from which

$$H(\mathbf{A}) - \int_\Omega \mathbf{T} \cdot \mathbf{A}\, d\mathcal{L}^n \geq -H^*(\mathbf{T}) \quad \text{for all} \quad \mathbf{A} \in Y;$$

taking $\mathbf{A} = \hat{\mathbf{E}}(\mathbf{v})$ where $\mathbf{v} \in V_0$, this is rewritten as

$$\mathsf{F}(\mathbf{v}) \geq c$$

for all $\mathbf{v} \in V_0$ [with $c = -H^*(\mathbf{T})$]. □

5 The existence of equilibrium states

In this section we outline the theory of existence of equilibrium for masonry materials. This theory is due to G. Anzellotti (Anzellotti 1985) and M. Giaquinta & E. Giusti (Giaquinta & Giusti 1985). The presentation below follows (Anzellotti 1985). The reader is referred to the cited paper for further details and proofs. The theories of Anzellotti and Giaquinta & Giusti are based on the existence of uniformly negative definite stress field, see Definition 5.10, below. A theory based on an alternative assumption of the strong absence of collapse mechanism is presented in (Šilhavý 2013).

Definition 5.1. Let $\Omega \subset \mathrm{R}^n$ be an open set. We denote by $BD(\Omega)$ the set of all $\mathbf{u} \in L^1(\Omega, \mathrm{R}^n)$ such that there exist a measure $\hat{\mathbf{E}}(\mathbf{u}) \in \mathcal{M}(\Omega, \mathrm{Sym})$ such that

$$\int_\Omega \mathbf{u} \cdot \mathrm{d}iv\, \mathbf{T}\, d\mathcal{L}^n = -\int_\Omega \mathbf{T} \cdot\, d\hat{\mathbf{E}}(\mathbf{u}) \tag{23}$$

for all $\mathbf{T} \in C_0^\infty(\Omega, \mathrm{Sym})$. Here $C_0^\infty(\Omega, \mathrm{Sym})$ is the set of all $\mathbf{T} : \mathrm{R}^n \to \mathrm{Sym}$ such that the support

$$\operatorname{spt} \mathbf{T} = \mathrm{cl}\{\mathbf{x} \in \mathrm{R}^n : \mathbf{T}(\mathbf{x}) \neq \mathbf{0}\}$$

is contained in Ω and is compact. We denote by $|\mathbf{u}|_{BD(\Omega)}$ the BD norm defined by

$$|\mathbf{u}|_{BD(\Omega)} = |\mathbf{u}|_{L^1(\Omega, \mathrm{R}^n)} + \mathrm{M}(\hat{\mathbf{E}}(\mathbf{u}))$$

where we recall that $\mathrm{M}(\hat{\mathbf{E}}(\mathbf{u}))$ is the mass of $\hat{\mathbf{E}}(\mathbf{u})$ defined in Section 3. We call the elements of $BD(\Omega)$ *displacements of bounded deformation.*

In other words, the strain tensor, being generally a distribution defined by

$$\hat{\mathbf{E}}(\mathbf{u}) = \tfrac{1}{2}(\nabla \mathbf{u} + \nabla \mathbf{u}^{\mathrm{T}}),$$

is a Sym valued measure if $\mathbf{u} \in BD(\Omega)$. If $\varphi \in C_0^\infty(\Omega, \mathrm{R})$ and if we apply (23) with $T_{ij} = T_{ji} = \frac{1}{2}\varphi$ for some pair (i, j) of indices and $T_{kl} = 0$ otherwise we obtain

$$\tfrac{1}{2} \int_\Omega \left(\varphi_{,i} u_j + \varphi_{,j} u_i\right) d\mathcal{L}^n = -\int_\Omega \varphi \, d\hat{E}_{ij}(\mathbf{u}),$$

which is the 'index form' of the definition of the space $BD(\Omega)$.

The space $BD(\Omega)$ endowed with the norm $|\cdot|_{BD(\Omega)}$ is a Banach space.

We refer to (Temam & Strang 1980), (Temam 1983) and (Ambrosio et al. 1997) and the references therein for further details and proofs of displacements with bounded deformation.

Example 5.2 (Fracture in $BD(\Omega)$)**.** Let $\Sigma \subset \Omega$ be a surface of dimension $n-1$ which divides Ω into two open sets Ω_1 and Ω_2. Let $\mathbf{u}$ be a function such that its restriction $\mathbf{u}_k$, $k = 1, 2$, onto Ω_k belongs to $C^1(\mathrm{cl}\,\Omega_k, \mathrm{R}^n)$. Then $\mathbf{u} \in BD(\Omega)$ and

$$\hat{\mathbf{E}}(\mathbf{u}) = \{\hat{\mathbf{E}}(\mathbf{u})\}\mathcal{L}^n \llcorner \Omega + [\mathbf{u}] \odot \mathbf{m}\mathcal{H}^{n-1} \llcorner \Sigma \tag{24}$$

where $\{\hat{\mathbf{E}}(\mathbf{u})\}$ is the function equal to $\hat{\mathbf{E}}(\mathbf{u}_k)$ on Ω_k $(k = 1, 2)$, $[\mathbf{u}](\mathbf{x}) = \mathbf{u}_2(\mathbf{x}) - \mathbf{u}_1(\mathbf{x})$ $(\mathbf{x} \in \Sigma)$, $\mathbf{m}$ is the normal to Σ pointing from Ω_1 to Ω_2, and

$$\mathbf{a} \odot \mathbf{b} = \tfrac{1}{2}(\mathbf{a} \otimes \mathbf{b} + \mathbf{b} \otimes \mathbf{a})$$

for every $\mathbf{a}, \mathbf{b} \in \mathrm{R}^n$.

Proof Let $\mathbf{T} \in C_0^\infty(\Omega, \mathrm{R}^n)$. Applying the divergence theorem to Ω_1 and Ω_2, we obtain

$$\begin{aligned}\int_\Omega \mathbf{u} \cdot \mathrm{d}iv\, \mathbf{T}\, d\mathcal{L}^n &= \int_{\Omega_1} \mathbf{u}_1 \cdot \mathrm{d}iv\, \mathbf{T}\, d\mathcal{L}^n + \int_{\Omega_2} \mathbf{u}_2 \cdot \mathrm{d}iv\, \mathbf{T}\, d\mathcal{L}^n \\ &= -\int_{\Omega_1} \hat{\mathbf{E}}(\mathbf{u}_1) \cdot \mathbf{T}\, d\mathcal{L}^n + \int_\Sigma \mathbf{T}\mathbf{m} \cdot \mathbf{u}_1\, d\mathcal{H}^{n-1} \\ &\quad - \int_{\Omega_2} \hat{\mathbf{E}}(\mathbf{u}_2) \cdot \mathbf{T}\, d\mathcal{L}^n - \int_\Sigma \mathbf{T}\mathbf{m} \cdot \mathbf{u}_2\, d\mathcal{H}^{n-1} \\ &= -\int_\Omega \{\hat{\mathbf{E}}(\mathbf{u})\} \cdot \mathbf{T}\, d\mathcal{L}^n - \int_\Sigma \mathbf{T} \cdot ([\mathbf{u}] \odot \mathbf{m})\, d\mathcal{H}^{n-1}. \quad \square\end{aligned}$$

Theorem 5.3. *Let $\Omega \subset \mathrm{R}^n$ be an open set with Lipschitz boundary. There exists a linear map $\gamma_0 : BD(\Omega) \to L^1(\partial\Omega, \mathrm{R}^n)$ such that we have*

$$\int_\Omega \mathbf{u} \cdot \mathrm{d}iv\, \mathbf{T}\, d\mathcal{L}^n + \int_\Omega \mathbf{T} \cdot\, d\hat{\mathbf{E}}(\mathbf{u}) = \int_{\partial\Omega} \mathbf{T}\mathbf{n} \cdot \gamma_0(\mathbf{u})\, d\mathcal{H}^{n-1}$$

for each $\mathbf{u} \in BD(\Omega)$ and $\mathbf{T} \in C^1(\mathrm{cl}\,\Omega, \mathrm{Sym})$. One has

$$|\gamma_0(\mathbf{u})|_{L^1(\partial\Omega, \mathrm{R}^n)} \le c|\mathbf{u}|_{BD(\Omega)}$$

for each $\mathbf{u} \in BD(\Omega)$ and some $c \in \mathrm{R}$.

The function $\gamma_0(\mathbf{u})$ represents the boundary values of $\mathbf{u}$. We often simplify the notation and write $\mathbf{u}$ for $\gamma_0(\mathbf{u})$. With this notation we have

$$\int_\Omega \mathbf{u} \cdot \mathrm{d}iv\, \mathbf{T}\, d\mathcal{L}^n + \int_\Omega \mathbf{T} \cdot\, d\hat{\mathbf{E}}(\mathbf{u}) = \int_{\partial\Omega} \mathbf{T}\mathbf{n} \cdot \mathbf{u}\, d\mathcal{H}^{n-1}.$$

Theorem 5.4. *Let $\Omega \subset \mathrm{R}^n$ be an open set with Lipschitz boundary. If $\mathbf{u} \in BD(\Omega)$ then one has $\mathbf{u} \in L^{n/(n-1)}(\Omega, \mathrm{R}^n)$ and there exists a $c \in \mathrm{R}$ such that*

$$|\mathbf{u}|_{L^{n/(n-1)}(\Omega, \mathrm{R}^n)} \le c|\mathbf{u}|_{BD(\Omega)}$$

for all $\mathbf{u} \in BD(\Omega)$.

Theorem 5.5. *$\Omega \subset \mathrm{R}^n$ be an open set with Lipschitz boundary. The operator imbedding $BD(\Omega)$ into $L^p(\Omega, \mathrm{R}^n)$, $1 \le p < n/(n-1)$, is compact; i.e., if $\mathbf{u}_j \in BD(\Omega)$ is a sequence bounded in the $|\cdot|_{BD(\Omega)}$ norm and $1 \le p < n/(n-1)$ then there exists a subsequence of $\mathbf{u}_j$, still denoted by $\mathbf{u}_j$, such that*

$$\mathbf{u}_j \to \mathbf{u} \quad \textit{in} \quad L^p(\Omega, \mathrm{R}^n)$$

for some $\mathbf{u} \in BD(\Omega)$.

Theorem 5.6. *Let $\Omega \subset \mathrm{R}^n$ be an open connected set and $\mathbf{u} \in BD(\Omega)$. Then $\hat{\mathbf{E}}(\mathbf{u}) = \mathbf{0}$ if and only if $\mathbf{u}$ is of the form*

$$\mathbf{u}(\mathbf{x}) = \mathbf{W}\mathbf{x} + \mathbf{a} \tag{25}$$

for all $\mathbf{x} \in \Omega$ where $\mathbf{a} \in \mathrm{R}^n$ and $\mathbf{W} \in \mathrm{Skew}$.

If $n = 3$ and $\mathbf{b}$ is the polar vector of $\mathbf{W}$, we can write

$$\mathbf{u}(\mathbf{x}) = \mathbf{b} \times \mathbf{x} + \mathbf{a}.$$

We call any $\mathbf{u}$ of the form (25) a rigid body displacement and denote by $\mathcal{R}(\Omega)$ the linear space of all rigid body displacements of Ω.

Theorem 5.7. *Let $\Omega \subset \mathrm{R}^n$ be an open connected set. There exists a linear map $\mathbf{u} \mapsto \mathbf{r}(\mathbf{u})$ from $BD(\Omega)$ to $\mathcal{R}(\Omega)$ such that $\mathbf{r}(\mathbf{u}) = \mathbf{u}$ for $\mathbf{u} \in \mathcal{R}(\Omega)$ and*

$$|\mathbf{u} - \mathbf{r}(\mathbf{u})|_{L^{n/(n-1)}(\Omega, \mathrm{R}^n)} \leq c\mathrm{M}(\hat{\mathbf{E}}(\mathbf{u}))$$

for all $\mathbf{u} \in BD(\Omega)$ and some $c \in \mathrm{R}$.

Recall from Section 2 that $\mathsf{P} : \mathrm{Sym} \to \mathsf{C}^{-1}\,\mathrm{Sym}^-$ denotes the orthogonal projection from Sym onto $\mathsf{C}^{-1}\,\mathrm{Sym}^-$ with respect to the energetic scalar product $(\cdot, \cdot)_E$. Endow Sym with the energetic scalar product. Let $\mathbf{u} \in BD(\Omega)$ and write

$$\hat{\mathbf{E}}(\mathbf{u}) = \mathbf{D}|\hat{\mathbf{E}}(\mathbf{u})|$$

for the polar decomposition of the measure $\hat{\mathbf{E}}(\mathbf{u})$, with $|\hat{\mathbf{E}}(\mathbf{u})|$ a nonnegative measure on Ω and $\mathbf{D} : \Omega \to \mathrm{Sym}$ a function satisfying $|\mathbf{D}|_E = 1$ for $|\hat{\mathbf{E}}(\mathbf{u})|$ almost every point of Ω. We denote by $\mathcal{P}\hat{\mathbf{E}}(\mathbf{u})$ the measure defined by

$$\mathcal{P}\hat{\mathbf{E}}(\mathbf{u}) = (\mathsf{P}\mathbf{D})|\hat{\mathbf{E}}(\mathbf{u})|.$$

Definition 5.8. We denote by $\mathcal{U}(\Omega)$ the set of all $\mathbf{u} \in BD(\Omega)$ such that the measure $\mathcal{P}\hat{\mathbf{E}}(\mathbf{u})$ is absolutely continuous with respect to the Lebesgue measure, with the density $\tilde{\mathcal{P}}\hat{\mathbf{E}}(\mathbf{u})$ such that $\tilde{\mathcal{P}}\hat{\mathbf{E}}(\mathbf{u}) \in L^2(\Omega, \mathrm{Sym})$. We call the elements of $\mathcal{U}(\Omega)$ *admissible displacements.* We define the internal energy of the admissible displacement $\mathbf{u}$ by

$$\mathsf{E}(\mathbf{u}) = \int_\Omega |\tilde{\mathcal{P}}\hat{\mathbf{E}}(\mathbf{u})|_E^2 \, d\mathcal{L}^n.$$

Example 5.9 (Fracture in $\mathcal{U}(\Omega)$)**.** The set $\mathcal{U}(\Omega)$ is the basic set of competitors for the equilibrium problem. Note that $\mathcal{U}(\Omega)$ is not a linear space

since if $\mathbf{u} \in \mathcal{U}(\Omega)$ then it may happen that $-\mathbf{u} \notin \mathcal{U}(\Omega)$. As an example, let $\mathbf{u} \in BD(\Omega)$ be as in Example 5.2. Let us show that $\mathbf{u} \in \mathcal{U}(\Omega)$ if and only if there exists a function $\lambda : \Sigma \to [0, \infty)$ such that

$$[\mathbf{u}] = \lambda \mathbf{m} \quad \text{on} \quad \Sigma, \tag{26}$$

i.e., the jump in $\mathbf{u}$ across Σ is positively proportional to the normal to Σ. This seems to be in agreement with the observation of fractured masonry structures.

Proof. Assume that there exists a point $\mathbf{x}$ on Σ such that $[\mathbf{u}]$ and $\mathbf{m}$ are not positively proportional. Then by the continuity there exists a neighborhood N of $\mathbf{x}$ in Σ such that $[\mathbf{u}]$ and $\mathbf{m}$ are not positively proportional. One easily finds that in this case the tensor $[\mathbf{u}] \odot \mathbf{m}$ has a nonzero negative definite part, which further implies

$$\mathsf{P}([\mathbf{u}] \odot \mathbf{m}) \neq \mathbf{0} \quad \text{on} \quad N,$$

since otherwise $[\mathbf{u}] \odot \mathbf{m}$ would be positive semidefinite. Equation (24) then gives

$$\mathcal{P}\hat{\mathbf{E}}(\mathbf{u}) = \mathsf{P}\{\hat{\mathbf{E}}(\mathbf{u})\}\mathcal{L}^n \llcorner \Omega + \mathsf{P}([\mathbf{u}] \odot \mathbf{m})\mathcal{H}^{n-1} \llcorner \Sigma$$

and thus $\mathcal{P}\hat{\mathbf{E}}(\mathbf{u})$ has a nonzero singular part, in contradiction with the definition of $\mathcal{U}(\Omega)$. Therefore we have (26) with a nonnegative λ. The converse implication: under (26) we have $\mathsf{P}([\mathbf{u}] \odot \mathbf{m}) = \mathbf{0}$ and thus

$$\mathcal{P}\hat{\mathbf{E}}(\mathbf{u}) = \mathsf{P}\{\hat{\mathbf{E}}(\mathbf{u})\}\mathcal{L}^n \llcorner \Omega$$

and hence $\mathcal{P}\hat{\mathbf{E}}(\mathbf{u})$ is absolutely continuous with respect to $\mathcal{L}^n$ with a square integrable density. □

We shall deal with the existence of solution for the Neumann problem. Thus we assume that $\mathcal{D} = \emptyset$. We call a pair $(\mathbf{s}, \mathbf{b})$ loads for the system if $\mathbf{s} \in L^\infty(\partial\Omega, \mathrm{R}^n)$, $\mathbf{b} \in L^n(\Omega, \mathrm{R}^n)$. In view of the fact that for any $\mathbf{u} \in BD(\Omega)$ we have $\gamma_0(\mathbf{u}) \in L^1(\partial\Omega)$, $\mathbf{u} \in L^{n/(n-1)}(\Omega, \mathrm{R}^n)$, by the Hölder inequality we have a well defined energy of the loads

$$\langle \mathbf{l}, \mathbf{u} \rangle = \int_{\partial\Omega} \mathbf{u} \cdot \mathbf{s} \, d\mathcal{H}^{n-1} + \int_\Omega \mathbf{u} \cdot \mathbf{b} \, d\mathcal{L}^n$$

for any $\mathbf{u} \in BD(\Omega)$ and in particular for any $\mathbf{u} \in \mathcal{U}(\Omega)$. We define the total energy of $\mathbf{u} \in \mathcal{U}(\Omega)$ by

$$\mathsf{F}(\mathbf{u}) = \mathsf{E}(\mathbf{u}) - \langle \mathbf{l}, \mathbf{u} \rangle .$$

We say that $\Omega \subset \mathrm{R}^n$ is an *admissible domain* if for any $\mathbf{u} \in \mathcal{U}(\Omega)$ there exists a sequence $\mathbf{u}_j \in C^1(cl\,\Omega, \mathrm{R}^n)$ such that

$$\mathbf{u}_j \to \mathbf{u} \quad \text{in} \quad L^{n/(n-1)}(\Omega, \mathrm{R}^n),$$

$$\mathrm{M}(\hat{\mathbf{E}}(\mathbf{u}_j)) \to \mathrm{M}(\hat{\mathbf{E}}(\mathbf{u})),$$

$$\tilde{\mathcal{P}}(\mathbf{u}_j) \to \tilde{\mathcal{P}}(\mathbf{u}) \quad \text{in} \quad L^2(\Omega, \mathrm{Sym}).$$

It turns out that all Lipschitz domains in R^2 are admissible and that for any n all star shaped Lipschitz domains are admissible.

Definition 5.10. We say that a stress field $\mathbf{T} \in L^2(\Omega, \mathrm{Sym})$ is *safe* if there exists an $\alpha > 0$ such that

$$-\mathbf{T}(\mathbf{x}) \cdot \mathbf{A} \geq \alpha |\mathbf{A}|$$

for all $\mathbf{A} \in \mathrm{Sym}^+$ and $\mathcal{L}^n$ almost every $\mathbf{x} \in \Omega$.

In other words, $\mathbf{T}$ is uniformly negative definite over Ω, which in particular implies that $\mathbf{s} \cdot \mathbf{n} \leq -\alpha < 0$ on $\partial\Omega$, i.e., the body must be uniformly compressed on the boundary. As before we say that a stress field $\mathbf{T}$ equilibrates the loads $(\mathbf{s}, \mathbf{b})$ if

$$\langle \mathbf{l}, \mathbf{v} \rangle = \int_\Omega \mathbf{T} \cdot \hat{\mathbf{E}}(\mathbf{v})\, d\mathcal{L}^n$$

for every $\mathbf{v} \in C^1(\mathrm{cl}\,\Omega, \mathrm{R}^n)$.

Theorem 5.11. *Let Ω be an admissible Lipschitz domain in R^n and consider loads $(\mathbf{s}, \mathbf{b})$. If there exists a safe stress field $\mathbf{T}$ equilibrating the loads then the functional F is coercive on $\mathcal{U}(\Omega)$ in the sense that*

$$\mathsf{F}(\mathbf{u}) \geq c_1 \Big\{ \int_\Omega |\tilde{\mathcal{P}}(\hat{\mathbf{E}}(\mathbf{u}))|_E^2\, d\mathcal{L}^n + \mathrm{M}(\hat{\mathbf{E}}(\mathbf{u})) \Big\} + c_2$$

for some constants c_1, c_2 with $c_1 > 0$ and all $\mathbf{u} \in \mathcal{U}(\Omega)$.

We say that a sequence $\mathbf{u}_j \in \mathcal{U}(\Omega)$ *converges weakly* to $\mathbf{u} \in BD(\Omega)$ if we have the relations

$$\left.\begin{array}{c} \mathbf{u}_j \to \mathbf{u} \quad \text{in} \quad L^1(\Omega, \mathrm{R}^n), \\ \mathbf{u}_j \rightharpoonup \mathbf{u} \quad \text{in} \quad L^{n/(n-1)}(\Omega, \mathrm{R}^n), \\ \mathrm{M}(\hat{\mathbf{E}}(\mathbf{u}_j)) \leq M, \\ \int_\Omega |\tilde{\mathcal{P}}(\hat{\mathbf{E}}(\mathbf{u}_j))|_E^2\, d\mathcal{L}^n \leq M \end{array}\right\} \tag{27}$$

for some $M \in \mathrm{R}$.

Theorem 5.12. *Let Ω be an admissible Lipschitz domain in R^n and consider loads $(\mathbf{s},\mathbf{b})$. Assume that there exists a stress field $\mathbf{S}\in L^2(\Omega,\mathrm{Sym}^-)$ and a function $\mathbf{c}\in L^n(\Omega,\mathrm{R}^n)$ such that $\mathbf{S}$ is bounded and $\mathbf{S}$ equilibrates the loads $(\mathbf{s},\mathbf{c})$. Then the functional F is weakly sequentially lowersemicontinuous in the sense that for any sequence $\mathbf{u}_j\in\mathcal{U}(\Omega)$ which converges weakly to $\mathbf{u}\in\mathcal{U}(\Omega)$, we have*

$$\liminf_{j\to\infty}\mathsf{F}(\mathbf{u}_j)\geq\mathsf{F}(\mathbf{u}).$$

Proposition 5.13. *The set $\mathcal{U}(\Omega)$ is closed under the weak convergence of sequences, i.e., if $\mathbf{u}_j\in\mathcal{U}(\Omega)$ converges weakly to $\mathbf{u}\in BD(\Omega)$ then $\mathbf{u}\in\mathcal{U}(\Omega)$.*

Theorem 5.14. *Let Ω be an admissible Lipschitz domain in R^n and consider loads $(\mathbf{s},\mathbf{b})$. Assume that there exists a safe stress field equilibrating the loads and moreover there exists a stress field $\mathbf{S}$ as in Theorem 5.12. Then there exists in $\mathcal{U}(\Omega)$ a minimizer of F on $\mathcal{U}(\Omega)$.*

Proof. There exists a sequence $\mathbf{u}_j\in\mathcal{U}(\Omega)$ such that

$$\lim_{j\to\infty}\mathsf{F}(\mathbf{u}_j)=\inf\{\mathsf{F}(\mathbf{u}):\mathbf{u}\in\mathcal{U}(\Omega)\}.$$

Since the energy functional F is coercive by Theorem 5.11, the boundedness of the sequence $\mathsf{F}(\mathbf{u}_j)$ implies that there exists a $M\in\mathrm{R}$ such that

$$\mathrm{M}(\hat{\mathbf{E}}(\mathbf{u}_j))\leq M,$$

$$\int_\Omega|\tilde{\mathcal{P}}(\hat{\mathbf{E}}(\mathbf{u}_j))|_E^2\,d\mathcal{L}^n\leq M$$

If $\mathbf{u}\mapsto\mathbf{r}(\mathbf{u})$ is the map from Theorem 5.7, we have

$$|\mathbf{u}_j-\mathbf{r}(\mathbf{u}_j)|\leq\mathrm{M}(\hat{\mathbf{E}}(\mathbf{u}_j))\leq M$$

and thus the sequence $\mathbf{v}_j:=\mathbf{u}_j-\mathbf{r}(\mathbf{u}_j)$ is bounded in $L^{n/(n-1)}(\Omega,\mathrm{R}^n)$ and hence it contains a subsequence, again denoted by $\mathbf{v}_j$, such that

$$\mathbf{v}_j\rightharpoonup\mathbf{v}\quad\text{in}\quad L^{n/(n-1)}(\Omega,\mathrm{R}^n)\tag{28}$$

for some $\mathbf{v}\in L^{n/(n-1)}(\Omega,\mathrm{R}^n)$. Since $\hat{\mathbf{E}}(\mathbf{v}_j)=\hat{\mathbf{E}}(\mathbf{u}_j)$, we also have

$$\mathrm{M}(\hat{\mathbf{E}}(\mathbf{v}_j))\leq M,\tag{29}$$

$$\int_\Omega|\tilde{\mathcal{P}}(\hat{\mathbf{E}}(\mathbf{v}_j))|_E^2\,d\mathcal{L}^n\leq M.\tag{30}$$

Since the sequence $\mathbf{v}_j$ is bounded in $L^{n/(n-1)}(\Omega, \mathrm{R}^n)$, it is also bounded in $L^1(\Omega, \mathrm{R}^n)$. Thus we conclude that $|\mathbf{v}_j|_{BD(\Omega)}$ is bounded. The compactness of the imbedding of $BD(\Omega)$ into $L^1(\Omega, \mathrm{R}^n)$ by Theorem 5.5 implies that we have

$$\mathbf{v}_j \to \mathbf{v} \quad \text{in} \quad L^1(\Omega, \mathrm{R}^n). \tag{31}$$

We thus summarize (28)–(31) by saying that the sequence $\mathbf{v}_j \in \mathcal{U}(\Omega)$ converges weakly to $\mathbf{v} \in BD(\Omega)$. The weak closedness of $\mathcal{U}(\Omega)$ (Proposition 5.13) then says that $\mathbf{v} \in \mathcal{U}(\Omega)$. Moreover, one easily finds that $\mathsf{F}(\mathbf{v}_j) = \mathsf{F}(\mathbf{u}_j)$ and thus

$$\lim_{j\to\infty} \mathsf{F}(\mathbf{v}_j) = \min\{\mathsf{F}(\mathbf{u}) : \mathbf{u} \in \mathcal{U}(\Omega)\}.$$

On the other hand, the functional F is sequentially weakly lowersemicontinuous (Theorem 5.12) and thus

$$\lim_{j\to\infty} \mathsf{F}(\mathbf{v}_j) \geq \mathsf{F}(\mathbf{v}).$$

This gives

$$\mathsf{F}(\mathbf{v}) \leq \inf\{\mathsf{F}(\mathbf{u}) : \mathbf{u} \in \mathcal{U}(\Omega)\}$$

and thus

$$\mathsf{F}(\mathbf{v}) = \min\{\mathsf{F}(\mathbf{u}) : \mathbf{u} \in \mathcal{U}(\Omega)\}. \qquad \square$$

6 Limit analysis

The limit analysis deals with the loads that depend linearly (affinely) on a scalar parameter $\lambda \in \mathrm{R}$, see (Del Piero 1998). Accordingly, we thus assume (Lucchesi et al. 2008b), (Lucchesi et al. 2011) that the body and surface forces $\mathsf{b}^\lambda \in \mathcal{M}(\Omega, \mathrm{R}^n)$ and $\mathsf{s}^\lambda \in \mathcal{M}(\mathcal{S}, \mathrm{R}^n)$ corresponding to λ are given by

$$\mathsf{b}^\lambda = \mathsf{b}_0 + \lambda \mathsf{b}_1, \quad \mathsf{s}^\lambda = \mathsf{s}_0 + \lambda \mathsf{s}_1 \tag{32}$$

where

$$\mathsf{b}_0, \mathsf{b}_1 \in \mathcal{M}(\Omega, \mathrm{R}^n) \quad \mathsf{s}_0, \mathsf{s}_1 \in \mathcal{M}(\mathcal{S}, \mathrm{R}^n).$$

We call $(\mathsf{s}(\lambda), \mathsf{b}(\lambda)) = (\mathsf{s}^\lambda, \mathsf{b}^\lambda)$ the loads corresponding to λ. If $\mathbf{v} \in V_0$ then the work of the loads $(\mathsf{s}(\lambda), \mathsf{b}(\lambda))$ corresponding to $\mathbf{v}$ is

$$\langle \mathbf{l}(\lambda), \mathbf{v} \rangle = \int_{\mathcal{S}} \mathbf{v} \cdot d\mathsf{s}^\lambda + \int_\Omega \mathbf{v} \cdot d\mathsf{b}^\lambda.$$

If the loads have square integrable densities, i.e., if

$$\mathsf{b}_0 = \mathbf{b}_0 \mathcal{L}^n, \quad \mathsf{b}_1 = \mathbf{b}_1 \mathcal{L}^n, \quad \mathsf{s}_0 = \mathbf{s}_0 \mathcal{H}^{n-1}, \quad \mathsf{s}_1 = \mathbf{s}_1 \mathcal{H}^{n-1},$$

where

$$\mathbf{b}_0,\, \mathbf{b}_1 \in L^2(\Omega, \mathrm{R}^n), \quad \mathbf{s}_0,\, \mathbf{s}_1 \in L^2(\mathcal{S}, \mathrm{R}^n),$$

then one can extend the definition of $\mathbf{l}(\lambda)$ to elements $\mathbf{v}$ of V.

In the general context of loads represented by measures we define the total energy $\mathsf{F}(\mathbf{v}, \lambda)$ of the body corresponding to the loads $(\mathsf{s}(\lambda), \mathsf{b}(\lambda))$ and displacement $\mathbf{v} \in V_0$ by

$$\mathsf{F}(\mathbf{v}, \lambda) = \mathsf{E}(\mathbf{v}) - \langle \mathbf{l}(\lambda), \mathbf{v} \rangle$$

so that $\mathsf{F}(\cdot, \lambda) : V_0 \to \mathrm{R}$. Central to our considerations is the *infimum energy* $I_0(\lambda) \in \mathrm{R} \cup \{-\infty\}$ of the loads $(\mathsf{s}(\lambda), \mathsf{b}(\lambda))$ defined by

$$I_0(\lambda) = \inf\{\mathsf{F}(\mathbf{v}, \lambda) : \mathbf{v} \in V_0\}.$$

We denote by $\mathcal{A}(\lambda)$ the set of all admissible stress fields equilibrating the loads $(\mathsf{s}(\lambda), \mathsf{b}(\lambda))$. Recal that the loads $(\mathsf{s}(\lambda), \mathsf{b}(\lambda))$ are strongly compatible if $\mathcal{A}(\lambda) \neq \emptyset$.

We now follow (Lucchesi et al. 2010).

Proposition 6.1.

(i) The loads $(\mathsf{s}(\lambda), \mathsf{b}(\lambda))$ are strongly compatible if and only if $I_0(\lambda) > -\infty$.

(ii) The function $I_0 : \mathrm{R} \to \mathrm{R} \cup \{-\infty\}$ is concave and uppersemicontinuous, i.e.,

$$I_0(\alpha\lambda + (1-\alpha)\mu) \geq \alpha I_0(\lambda) + (1-\alpha) I_0(\mu)$$

for every $\lambda, \mu \in \mathrm{R}$ and $\alpha \in [0, 1]$ and

$$I_0(\lambda) \geq \limsup_{k \to \infty} I_0(\lambda_k)$$

for every $\lambda \in \mathrm{R}$ and every sequence $\lambda_k \to \lambda$. Hence the set

$$\Lambda = \{\lambda \in \mathrm{R} : I_0(\lambda) > -\infty\} (\equiv \{\lambda \in \mathrm{R} : \mathcal{A}(\lambda) \neq \emptyset\} \tag{33}$$

is an interval.

Since the notion of compatibility of loads is independent of the tensor of elastic constants C, also the finiteness of $I_0(\lambda)$ is independent of C [within the class specified by (1)], even though the concrete value of $I_0(\lambda)$ depends on C. We emphasize the role of the square integrability requirement of the stress field in the definition of strongly compatible loads; there are loads $(\mathsf{s}(\lambda), \mathsf{b}(\lambda))$ with $I_0(\lambda) = -\infty$ and yet with $(\mathsf{s}(\lambda), \mathsf{b}(\lambda))$ being weakly equilibrated by a stress field $\mathbf{T} \in L^1(\Omega, \mathrm{Sym}) \setminus L^2(\Omega, \mathrm{Sym})$ with values in Sym^-.

Proof.
(i): This follows from Proposition 4.3.
(ii): The affine dependence of $\mathbf{l}(\lambda)$ on λ implies that the function $\lambda \mapsto \mathsf{F}(\mathbf{u}, \lambda)$ is affine for each $\mathbf{u} \in V_0$; thus the function $\lambda \mapsto I_0(\lambda)$, being the lower envelope of the family of affine continuous functions over the parameter set $\{\mathbf{u} \in V_0\}$, is concave and uppersemicontinuous (Ekeland & Temam 1999, Chapter I, Section 2). □

Definition 6.2. Let Λ be given by (33). A loading multiplier $\lambda \in \mathrm{R}$ is said to

(i) be *statically admissible* if $\lambda \in \Lambda$; otherwise λ is said to be *statically inadmissible*;
(ii) be a *collapse multiplier* if it is a finite endpoint of Λ;
(iii) be *kinematically admissible* if there exists a $\mathbf{v} \in V_0$ such that $\hat{\mathbf{E}}(\mathbf{v}) \geq \mathbf{0}$, $\langle \bar{\mathbf{l}}, \mathbf{v} \rangle = 1$ and
$$\lambda = -\langle \mathbf{l}_0, \mathbf{v} \rangle ; \tag{34}$$
(iv) *admit a collapse mechanism* if λ is kinematically admissible and $\lambda \leq \sup \Lambda$.

Remark 6.3.
(i) The collapse multiplier can be statically admissible as well as statically inadmissible.
(ii) The notion of collapse multiplier can be given a dynamical meaning. The paper (Padovani et al. 2008) considers no–tension bodies in dynamical situations with a viscous perturbation of the equations of motion. It turns out that if $I_0(\lambda) > -\infty$ then the motion with arbitrary initial data stabilizes in the sense that the kinetic energy satisfies $K(t) \to 0$ as $t \to \infty$ while if $I_0(\lambda) = -\infty$ then the total energy, given by the sum of the total potential energy and the kinetic energy, $T(t) = F(t) + K(t)$, satisfies $T(t) \to -\infty$ as $t \to \infty$.
(iii) If λ admits a collapse mechanism then there exists a $\mathbf{v} \in V$ with $\hat{\mathbf{E}}(\mathbf{v}) \geq \mathbf{0}$, $\langle \bar{\mathbf{l}}, \mathbf{v} \rangle = 1$ and $\langle \mathbf{l}(\lambda), \mathbf{v} \rangle = 0$; each such a $\mathbf{v}$ is said to be a *collapse mechanism for the loads* $(\mathsf{s}(\lambda), \mathsf{b}(\lambda))$.
(iv) If λ admits a collapse mechanism and if additionally λ is statically admissible then each admissible equilibrating stress field for $(\mathsf{s}(\lambda), \mathsf{b}(\lambda))$ is called a *collapse stress field.* A stronger version of the definition of collapse mechanism $\mathbf{v}$ in (Del Piero 1998) requires that $\mathbf{v}$ be as in (iii) and that additionally λ be statically admissible.

Remark 6.4. If $\mathbf{T} \in L^2(\Omega, \mathrm{Sym})$, we denote the normal cone to the set $L^2(\Omega, \mathrm{Sym}^-)$ at $\mathbf{T}$ by $\mathrm{Norm}(L^2(\Omega, \mathrm{Sym}^-), \mathbf{T})$ and applying the definition from Section 2 we obtain

$$\begin{aligned}
&\mathrm{Norm}(L^2(\Omega, \mathrm{Sym}^-), \mathbf{T}) \\
&\quad = \{\mathbf{D} \in L^2(\Omega, \mathrm{Sym}) : \textstyle\int_\Omega \mathbf{D} \cdot (\mathbf{T} - \mathbf{S})\, d\mathcal{L}^n \geq 0 \\
&\qquad\qquad\qquad\qquad \text{for each admissible stress field } \mathbf{S}\} \\
&\quad = \{\mathbf{D} \in L^2(\Omega, \mathrm{Sym}) : \mathbf{D} \cdot (\mathbf{T} - \mathbf{U}) \geq 0 \\
&\qquad\qquad \text{for every } \mathbf{U} \in \mathrm{Sym}^- \text{ and } \mathcal{L}^n \text{ almost every point of } \Omega\}.
\end{aligned}$$

Let $\lambda \in \mathrm{R}$. If $\mathbf{v} \in V$ satisfies

$$\hat{\mathbf{E}}(\mathbf{v}) \in \mathrm{Norm}(L^2(\Omega, \mathrm{Sym}^-), \mathbf{T}), \quad \langle \bar{\mathbf{l}}, \mathbf{v} \rangle = 1 \tag{35}$$

and

$$\lambda = -\langle \mathbf{l}_0, \mathbf{v} \rangle \tag{36}$$

for some $\mathbf{T} \in \mathcal{A}(\lambda)$ then $\mathbf{v}$ is a collapse mechanism for the loads $(\mathsf{s}(\lambda), \mathsf{b}(\lambda))$. Indeed, the second characterization of $\mathrm{Norm}(L^2(\Omega, \mathrm{Sym}^-), \mathbf{T})$ implies that $\hat{\mathbf{E}}(\mathbf{v}) \geq \mathbf{0}$ almost everywhere on Ω.

The number of collapse multipliers ranges from 0 to 2. In applications, one is interested in the larger of the possibly two collapse multipliers. Motivated by this, we introduce the multiplier

$$\lambda_{\mathrm{c}}^+ := \sup\{\lambda \in \mathrm{R} : \lambda \text{ is statically admissible } \} \tag{37}$$

$-\infty \leq \lambda_{\mathrm{c}}^+ \leq \infty$; thus if λ_{c}^+ is finite, then λ_{c}^+ is a collapse multiplier, and if there are two collapse multipliers, then λ_{c}^+ is the larger of these two. Also, we consider the multiplier

$$\bar{\lambda}_{\mathrm{c}}^+ = \inf\{\lambda \in \mathrm{R} : \lambda \text{ is kinematically admissible } \}. \tag{38}$$

Remark 6.5. The above definitions of λ_{c}^+ and $\bar{\lambda}_{\mathrm{c}}^+$ are based on the square integrability: in the definition of λ_{c}^+ the admissible equilibrating stresses are square integrable and in the definition of $\bar{\lambda}_{\mathrm{c}}^+$ we consider mechanisms that are square integrable with the square integrable gradients. The definitions of the analogs of λ_{c}^+ and $\bar{\lambda}_{\mathrm{c}}^+$ using different function spaces is treated in detail in (Lucchesi et al. 2012). However, it must be emphasized that the definitions based on the square integrability are well motivated by Proposition 4.3.

Remark 6.6. It turns out (Lucchesi et al. 2012) that the definition of the kinematic multiplier (38) can be reformulated to the format of the variational problem by Ekeland & Temam (Ekeland & Temam 1999) and then the static multiplier (37) takes the form of the dual problem in the sense of the cited reference.

Our first result shows that our definition of the collapse multiplier generalizes that based on the collapse mechanism:

Theorem 6.7.
(i) We have $\lambda_c^+ \le \bar{\lambda}_c^+$.
(ii) If $\lambda \in \mathrm{R}$ *admits a collapse mechanism then* $\lambda = \lambda_c^+ = \bar{\lambda}_c^+$.

Proof.
(i): Let $\lambda \in \mathrm{R}$ be kinematically admissible, i.e., there exists a $\mathbf{v} \in V_0$ such that $\hat{\mathbf{E}}(\mathbf{v}) \ge \mathbf{0}$ almost everywhere on Ω, $\langle \bar{\mathbf{l}}, \mathbf{v} \rangle = 1$, and $\langle \mathbf{l}(\lambda), \mathbf{v} \rangle = 0$. Then $\lambda = -\langle \mathbf{l}_0, \mathbf{v} \rangle$ and thus

$$\bar{\lambda}_c^+ = \inf\{-\langle \mathbf{l}_0, \mathbf{v} \rangle : \mathbf{v} \in V_0,\ \hat{\mathbf{E}}(\mathbf{v}) \ge \mathbf{0},\ \langle \bar{\mathbf{l}}, \mathbf{v} \rangle = 1\}. \tag{39}$$

Let $\lambda \in \mathrm{R}$ be statically admissible with the admissible equilibrating stress field $\mathbf{T}$ and let $\mathbf{v} \in V_0$ be such that $\hat{\mathbf{E}}(\mathbf{v}) \ge \mathbf{0}$ almost everywhere on Ω and $\langle \bar{\mathbf{l}}, \mathbf{v} \rangle = 1$. Then we have

$$0 \ge \int_\Omega \mathbf{T} \cdot \hat{\mathbf{E}}(\mathbf{v})\, d\mathcal{L}^n = \langle \mathbf{l}(\lambda), \mathbf{v} \rangle = \lambda + \langle \mathbf{l}_0, \mathbf{v} \rangle ,$$

Thus

$$\lambda \le -\langle \mathbf{l}_0, \mathbf{v} \rangle .$$

Taking the infimum over all $\mathbf{v}$ with the indicated properties and using (39) we find $\lambda \le \bar{\lambda}_c^+$ and taking the supremum over all $\mathbf{T}$ with the indicated properties, we obtain the inequality in (i).

(ii): Assume that $\lambda \in \mathrm{R}$ admits a collapse mechanism. Prove first that $\lambda = \lambda_c^+$. Since λ admits a collapse mechanism, λ is kinematically admissible and hence there exists a $\mathbf{v} \in V_0$ with

$$\hat{\mathbf{E}}(\mathbf{v}) \ge \mathbf{0}, \quad \langle \bar{\mathbf{l}}, \mathbf{v} \rangle = 1 \quad \text{and} \quad \langle \mathbf{l}(\lambda), \mathbf{v} \rangle = 0. \tag{40}$$

Prove that $I_0(\mu) = -\infty$ for all $\mu > \lambda$. We have $\mathsf{E}(t\mathbf{v}) = 0$ and hence

$$\begin{aligned} \mathsf{F}(t\mathbf{v}, \mu) &= -\langle \mathbf{l}(\mu), t\mathbf{v} \rangle \\ &= -\langle \mathbf{l}(\lambda), t\mathbf{v} \rangle - (\mu - \lambda) \langle \bar{\mathbf{l}}, t\mathbf{v} \rangle = -(\mu - \lambda) t \langle \bar{\mathbf{l}}, \mathbf{v} \rangle = -(\mu - \lambda) t. \end{aligned}$$

Letting $t \to \infty$ we thus obtain $\mathsf{F}(t\mathbf{v}, \mu) \to -\infty$ as $t \to \infty$ for all $\mu > \lambda$. Hence $\lambda_c^+ \le \lambda$; on the other hand, $\lambda \le \lambda_c^+$ as part of the definition of the multiplier admitting a collapse mechanism. This completes the proof of $\lambda = \lambda_c^+$.

On the other hand, λ is kinematically admissible as part of the definition of the property of λ admitting a collapse multiplier. Thus $\bar{\lambda}_c^+ \le \lambda = \lambda_c^+$ and Item (i) completes the proof. □

7 Families of measures and the weak compatibility of loads

In this section we introduce the generalized compatibility of loads called weak compatibility. This involves balancing the loads by a stressfield represented by a measure T from $\mathcal{M}(\Omega, \mathrm{Sym})$. Thus in contrast to the strong compatibility, which is based on balancing by a square integrable function, we here admit concentrations of stress on objects of dimension lower than the dimension n of the physical space R^n, see Example 3(i). In many concrete cases, it is easier to prove the weak compatibility than the strong compatibility. However, Proposition 4.3 on the boundedness below of the total energy requires strong compatibility. In the case of the limit analysis, where we deal with the loads depending on the loading parameter λ, we have the balancing measures depending on λ as well. Then we can use a procedure of integrating the balancing stress measures with respect to the loading parameter to smear out the singularities of the stress measure to obtain a square integrable function.

We say that $\mathsf{T} \in \mathcal{M}(\Omega, \mathrm{Sym})$ is admissible if T takes the values in the set Sym^- of the negative semidefinite symmetric tensors, i.e., if $\mathsf{T}(A)\mathbf{a}\cdot\mathbf{a} \le 0$ for any Borel set $A \subset \Omega$ and for any $\mathbf{a} \in \mathrm{R}^n$. We say that T *weakly equilibrates the loads* (s, b) if

$$\int_\Omega \hat{\mathbf{E}}(\mathbf{v}) \cdot d\mathsf{T} = \int_\Omega \mathbf{v} \cdot d\mathsf{b} + \int_{\mathcal{N}} \mathbf{v} \cdot d\mathsf{s}$$

for any $\mathbf{v} \in V_0$. We say that the loads (s, b) are *weakly compatible* if there exists an admissible $\mathsf{T} \in \mathcal{M}(\Omega, \mathrm{Sym})$ which weakly equilibrates them. The reader is referred to (Šilhavý 2008) for the general properties of stresses represented by measures.

If the loads are strongly compatible then they are weakly compatible; however, there are examples of loads that are weakly compatible but not strongly compatible.

Example 7.1. Consider a stress measure of the form

$$\mathsf{T} = \mathsf{T}_r + \mathsf{T}_s, \quad \text{where} \quad \mathsf{T}_r = \mathbf{T}_r \mathcal{L}^n \llcorner \Omega, \quad \mathsf{T}_s = \mathbf{T}_s \mathcal{H}^{n-1} \llcorner \mathcal{N}$$

where $\mathbf{T}_r : cl\,\Omega \to \mathrm{Sym}$ is a smooth $\mathcal{L}^n$ integrable function over the body and $\mathbf{T}_s : cl\,\mathcal{N} \to \mathrm{Sym}$ is a smooth $\mathcal{H}^{n-1}$ integrable function over a smooth surface $\mathcal{N}$ contained in Ω. Assume furthermore given the loads (s, b) of the form (18) with $\mathbf{b}$ and $\mathbf{s}$ continuous integrable functions over Ω and $\mathcal{S}$, respectively. Then T weakly equilibrates the loads (s, b) if and only if the following two conditions hold:

(i) we have
$$div\,\mathbf{T}_r + \mathbf{b} = \mathbf{0} \text{ in } \Omega \setminus \mathcal{N}, \tag{41}$$
where div is the classical divergence operator;

(ii) the stress field $\mathbf{T}_s$ is superficial in the sense that $\mathbf{T}_s\mathbf{m} = \mathbf{0}$ where $\mathbf{m}$ is the normal to $\mathcal{N}$ and we have
$$[\mathbf{T}_r]\mathbf{m} + div^{\mathcal{N}}\,\mathbf{T}_s = \mathbf{0} \text{ on } \mathcal{N} \tag{42}$$
where $[\mathbf{T}_r] = \mathbf{T}_r^+ - \mathbf{T}_r^-$ is the jump discontinuity of $\mathbf{T}_r$ on $\mathcal{N}$ and $div^{\mathcal{N}}$ is the superficial divergence (Lucchesi et al. 2006, Section 4);

(iii) we have
$$\mathbf{T}_r\mathbf{n} = \mathbf{s} \quad \text{on} \quad \mathcal{S}$$
where $\mathbf{n}$ is the outer normal to $\partial\Omega$.

We now pass to the details of the integration procedure.

Definition 7.2.
An *integrable parametric measure* (see (Lucchesi et al. 2008b)) is a family $\{\mathsf{m}^\lambda : \lambda \in \Lambda\}$ of V valued measures on R^n where $\Lambda \subset \mathrm{R}$ is a $\mathcal{L}^1$ measurable set of parameters such that

(i) for every continuous V valued function f on R^n with compact support the function $\lambda \mapsto \int_{\mathrm{R}^n} f \cdot d\mathsf{m}^\lambda$ is $\mathcal{L}^1$ measurable on Λ;

(ii) we have
$$c := \int_\Lambda \mathrm{M}(\mathsf{m}^\lambda)\, d\lambda < \infty.$$

We note that parametric measures similar to those defined above occur in the context of disintegration (slicing) of measures (Ambrosio et al. 2000, Section 2.5) and, what is related, in the context of Young's measures (Müller 1999, Chapter 5).

Proposition 7.3. *If* $\{\mathsf{m}^\lambda : \lambda \in \Lambda\}$ *is an integrable parametric measure then there exists a unique* V *valued measure* m *on* R^n *such that*

$$\int_{\mathrm{R}^n} f \cdot d\mathsf{m} = \int_\Lambda \int_{\mathrm{R}^n} f \cdot d\mathsf{m}^\lambda \, d\lambda \tag{43}$$

for each continuous V *valued function* f *on* R^n *with compact support.*

We write

$$\mathsf{m} = \int_\Lambda \mathsf{m}^\lambda \, d\lambda \tag{44}$$

and call m the integral of the family $\{\mathsf{m}^\lambda : \lambda \in \Lambda\}$ with respect to λ.

Proof. We note that for each continuous V valued function f on R^n with compact support the right hand side of (43) is a well defined real number: indeed

$$\begin{aligned} \left| \textstyle\int_\Lambda \int_{\mathrm{R}^n} f \cdot d\mathsf{m}^\lambda \, d\lambda \right| &\le \textstyle\int_\Lambda \int_{\mathrm{R}^n} |f| \, d|\mathsf{m}^\lambda| \, d\lambda \\ &\le \max\{|f(\mathbf{x})| : \mathbf{x} \in \mathrm{R}^n\} \textstyle\int_\Lambda \mathrm{M}(\mathsf{m}^\lambda) \, d\lambda \\ &\le c \max\{|f(\mathbf{x})| : \mathbf{x} \in \mathrm{R}^n\}. \end{aligned}$$

Thus by the Riesz representation theorem (Ambrosio et al. 2000, Theorem 1.54) there exists a measure m such that (43) holds. □

The following two propositions give two important examples of integrable parametric measures. In both cases the corresponding integral (44) is absolutely continuous with respect to the Lebesgue measure.

Proposition 7.4. *Let* $\{\mathbf{T}_r^\lambda : \lambda \in \Lambda\}$ *be a family of* Sym *valued functions on* $\Omega \subset \mathrm{R}^n$ *defined for all* λ *from a* $\mathcal{L}^1$ *measurable set* $\Lambda \subset \mathrm{R}$ *such that the mapping* $(\mathbf{x}, \lambda) \mapsto \mathbf{T}_r^\lambda(\mathbf{x})$ *is* $\mathcal{L}^{n+1}$ *integrable on* $\Omega \times \Lambda$, *i.e.,*

$$\int_\Lambda \int_\Omega |\mathbf{T}_r^\lambda(\mathbf{x})| \, d\mathbf{x} \, d\lambda < \infty. \tag{45}$$

If we define a Sym *valued measure* T_r^λ *by*

$$\mathsf{T}_r^\lambda = \mathbf{T}_r^\lambda \mathcal{L}^n \llcorner \Omega$$

then $\{\mathsf{T}_r^\lambda : \lambda \in \Lambda\}$ *is an integrable parametric measure and we have*

$$\int_\Lambda \mathsf{T}_r^\lambda \, d\lambda = \mathbf{T}_r \mathcal{L}^n \llcorner \Omega$$

where

$$\mathbf{T}_r(\mathbf{x}) = \int_\Lambda \mathbf{T}_r^\lambda(\mathbf{x})\, d\lambda$$

for $\mathcal{L}^n$ *almost every* $\mathbf{x} \in \Omega$.

Proof. This follows directly from Fubini's theorem. □

Proposition 7.5. *Let* $\Omega_0 \subset \mathrm{R}^n$ *be open, let* $\varphi : \Omega_0 \to \mathrm{R}$ *be locally Lipschitz continuous and let* $\mathbf{T}_s : \Omega_0 \to \mathrm{Sym}$ *be* $\mathcal{L}^n$ *measurable on* Ω_0, *with*

$$\int_{\Omega_0} |\mathbf{T}_s||\nabla\varphi|\, d\mathcal{L}^n < \infty. \tag{46}$$

Then for $\mathcal{L}^1$ *almost every* $\lambda \in \mathrm{R}$ *the function* $\mathbf{T}_s$ *is* $\mathcal{H}^{n-1} \llcorner \varphi^{-1}(\lambda)$ *integrable; denoting by* Λ *the set of all such* λ *we define the measure* m^λ *by*

$$\mathsf{T}^\lambda := \mathbf{T}_s \mathcal{H}^{n-1} \llcorner \varphi^{-1}(\lambda)$$

for each $\lambda \in \Lambda$. *Then* $\{\mathsf{T}^\lambda : \lambda \in \Lambda\}$ *is an integrable parametric measure and we have*

$$\int_\Lambda \mathsf{T}^\lambda\, d\lambda = \mathbf{T}_s |\nabla\varphi| \mathcal{L}^n \llcorner \Omega_0. \tag{47}$$

Proof. Let T be given by

$$\mathsf{T} = \int_\Lambda \mathsf{T}^\lambda\, d\lambda. \tag{48}$$

If $\mathbf{E} \in C_0(\mathrm{R}^n, \mathrm{Sym})$ then by the coarea formula (Ambrosio et al. 2000, Section 2.12) we have

$$\begin{aligned} \textstyle\int_{\Omega_0} \mathbf{E} \cdot \mathbf{T}_s |\nabla\varphi|\, d\mathcal{L}^n &= \textstyle\int_{\mathrm{R}} \int_{\varphi^{-1}(\lambda)} \mathbf{E} \cdot \mathbf{T}_s\, d\mathcal{H}^{n-1} d\lambda \\ &= \textstyle\int_\Lambda \int_{\mathrm{R}^n} \mathbf{E} \cdot\, d\mathsf{T}^\lambda d\lambda \\ &= \textstyle\int_{\mathrm{R}^n} \mathbf{E} \cdot d\mathsf{T}. \end{aligned}$$ □

We now assume that the loads depend affinely on the loading parameter as in (32), thus we have loads $(\mathsf{s}^\lambda, \mathsf{b}^\lambda)$ defined for each $\lambda \in \mathrm{R}$. It may happen that there exists an interval $(\lambda - \epsilon, \lambda + \epsilon)$ such that each load $(\mathsf{s}^\mu, \mathsf{b}^\mu)$, with μ from this interval, is weakly equilibrated by a stress field $\mathsf{T}^\mu \in \mathcal{M}(\Omega, \mathrm{Sym})$ in such a way that

$$\{\mathsf{T}^\mu, \mu \in \Lambda\} \tag{49}$$

is an integrable parametric measure. In this situation, we have

Remark 7.6. The measure U defined by

$$\mathsf{U} = \frac{1}{2\epsilon}\int_{\lambda-\epsilon}^{\lambda+\epsilon} \mathsf{T}^\mu \, d\mu$$

weakly equilibrates the loads $(\mathsf{s}^\lambda, \mathsf{b}^\lambda)$. However, depending on the nature of the family (49), it may happen that the measure U is such that

$$\mathsf{U} = \mathbf{U}\mathcal{L}^n \llcorner \Omega \quad \mathbf{U} \in L^2(\Omega, \mathrm{Sym}^-),$$

i.e., the loads $(\mathsf{s}^\lambda, \mathsf{b}^\lambda)$ are strongly equilibrated by the stress field $\mathbf{U}$. Such a situation arises when the family (49) satisfies the hypothesis of Proposition 7.4 or Proposition 7.5, or is a sum of families such that one satisfies Proposition 7.4 and the other Proposition 7.5. In many concrete cases, it is hard to evalueate U explicitly but for the analysis it suffices to know that U is represented by a square integrable function.

8 Integration with gravity

In this section we consider a rectangular panel made of a no-tension material that is fixed at its base and subject to both the weight $\mathbf{b}$ which constitutes the permanent part of the loads, and a horizontal compressive load $\mathbf{s}^\lambda$ of intensity λ, which is uniformly distributed on the right lateral side of the panel and constitutes the variable part of the loads. Then, for every λ in an appropriate interval $(0, \lambda_c)$, we determine a negative semidefinite and square integrable stress field $\mathbf{T}^\lambda$ which is in equilibrium with the given loads and we conclude that every $\lambda \in (0, \lambda_c)$ is statically admissible (see Definition 6.2). Let

$$\Omega = (0, B) \times (0, H) \subset \mathrm{R}^2$$

be the rectangular panel. We introduce the coordinate system x, y in R^2 with the origin in the upper right corner of the panel and with the x axis pointing to the left and the y axis pointing downward. We denote a general point of Ω by $\mathbf{r} = (x, y)$ and the coordinate vectors along the axes x, y by $\mathbf{i}$, $\mathbf{j}$, respectively. We put

$$\mathcal{D} = (0, B) \times \{H\}, \quad \mathcal{S} = \partial\Omega \setminus \mathcal{D}$$

and consider the loads $(\mathbf{s}^\lambda, \mathbf{b}^\lambda)$ where, for $b > 0$, $\mathbf{b}^\lambda = b\mathbf{j}$ in Ω, and for $\mathbf{r} = (x, y) \in \mathcal{S}$ and $\lambda > 0$,

$$\mathbf{s}^\lambda(\mathbf{r}) = \begin{cases} \lambda\mathbf{i} & \text{on} \quad \{0\} \times (0, H), \\ \mathbf{0} & \text{elsewhere.} \end{cases} \tag{50}$$

The stress field $\mathbf{T}^\lambda$ will be constructed in two steps. Firstly, for every $\lambda \in (0, \lambda_c)$ we determine a measure stress field $\mathsf{T}^\lambda \in \mathcal{M}(\Omega, \mathrm{Sym}^-)$ that is in equilibrium with the loads, i.e., such that

$$\int_\Omega \hat{\mathbf{E}}(\mathbf{v}) \cdot d\mathsf{T}^\lambda = b \int_\Omega \mathbf{v} \cdot \mathbf{j}\, d\mathcal{L}^2 + \lambda \int_{\{0\}\times(0,H)} \mathbf{v} \cdot \mathbf{i}\, d\mathcal{H}^1$$

for every $\mathbf{v} \in V = W^{1,2}(\Omega, \mathrm{R}^2)$ (we recall that $\mathcal{L}^2$ stands for the Lebesgue measure and $\mathcal{H}^1$ for the 1-dimensional Hausdorff measure in R^2). This expression is well defined because the loads are of the special form (18). Secondly, we determine a square integrable negative semidefinite and equilibrated stress field $\mathbf{T}^\lambda$ for every $\lambda \in (0, \lambda_c)$ by the integration procedure described in Section 7, i.e. $\mathbf{T}^\lambda \in \mathcal{A}(\lambda)$. This will prove that the loads $(\mathbf{s}^\lambda, \mathbf{b}^\lambda)$ are strongly compatible for every $\lambda \in (0, \lambda_c)$ (see (6.2)).

To determine the stress measure T^λ, we use the results of the paper (Lucchesi et al. 2009). We consider a smooth curve $\mathcal{N}^\lambda$ which starts at the upper right corner and ends at the bottom of the panel, and which is the graph of an increasing function $\omega^\lambda : [0, t^\lambda] \to [0, H]$ to be specified below. In this way, Ω is divided into the regions Ω^λ_+ (on the left) and Ω^λ_- (on the right) by the curve $\mathcal{N}^\lambda$. We are looking for a weakly equilibrated measure stress field T^λ which is absolutely continuous with respect to the Lebesgue measure in Ω^λ_+ and Ω^λ_- with a piecewise continuously differentiable density $\mathbf{T}^\lambda_r$ and has a concentration on $\mathcal{N}^\lambda$ with a continuously differentiable density $\mathbf{T}^\lambda_s$, i.e.,

$$\mathsf{T}^\lambda = \mathbf{T}^\lambda_r \mathcal{L}^2 \llcorner \Omega + \mathbf{T}^\lambda_s \mathcal{H}^1 \llcorner \mathcal{N}^\lambda.$$

The equilibrium condition (41) implies that

$$div\, \mathbf{T}^\lambda_r + \mathbf{b}^\lambda = \mathbf{0} \text{ in } \Omega \setminus \mathcal{N}^\lambda. \tag{51}$$

Furthermore, $\mathbf{T}^\lambda_s$ is superficial by Item (ii) of Example 7.1, which means here

$$\mathbf{T}^\lambda_s = \sigma^\lambda \mathbf{t}^\lambda \otimes \mathbf{t}^\lambda, \tag{52}$$

where $\mathbf{t}^\lambda$ is the unit tangent vector to $\mathcal{N}^\lambda$ and σ^λ is a scalar function on $\mathcal{N}^\lambda$. By (42) we have

$$[\mathbf{T}^\lambda_r]\mathbf{m} + div^{\mathcal{N}}\, \mathbf{T}^\lambda_s = \mathbf{0} \text{ on } \mathcal{N}^\lambda \tag{53}$$

where $[\mathbf{T}^\lambda_r]$ is the jump discontinuity $\mathbf{T}^\lambda_r$ on $\mathcal{N}^\lambda$, $\mathbf{m}$ is the unit normal to $\mathcal{N}^\lambda$ pointing toward Ω^λ_+.

Following the method presented in (Lucchesi et al. 2009) we obtain (see (Lucchesi et al. 2009, Eqs. (4.6), (4.7) and (3.1)))

$$\mathbf{T}^\lambda_r(\mathbf{r}) = \begin{cases} -by\mathbf{j} \otimes \mathbf{j} & \text{if} \quad \mathbf{r} \in \Omega^\lambda_+, \\ -\lambda \mathbf{i} \otimes \mathbf{i} - 2bx\mathbf{i} \odot \mathbf{j} - \frac{b^2x^2}{\lambda}\mathbf{j} \otimes \mathbf{j} & \text{if} \quad \mathbf{r} \in \Omega^\lambda_- \end{cases} \tag{54}$$

which satisfies the equilibrium equation (51) and the boundary conditions (50). From (53) we deduce the equation of $\mathcal{N}^\lambda$ (see (Lucchesi et al. 2009, Eq. (4.16)) with $\lambda = \beta H$ and $p_0 = 0$)

$$\omega^\lambda(x) = cbx^2/\lambda, \quad c = 1/2 + \sqrt{3}/6 \tag{55}$$

which has the unit tangent vector

$$\mathbf{t}^\lambda(\mathbf{r}) = \frac{x\mathbf{i} + 2y\mathbf{j}}{\sqrt{x^2 + 4y^2}} \tag{56}$$

Moreover, from (55) and (53) we obtain (see (Lucchesi et al. 2009, Eq. (2.19)), with $s_0 = 0$, and $f(x, y)$ at the end of page 229)

$$\sigma^\lambda(\mathbf{r}) = -\frac{\sqrt{3}}{6} bx\sqrt{x^2 + 4y^2} \tag{57}$$

$\mathbf{r} \in \mathcal{N}^\lambda$. If $\lambda \in (0, \lambda_c)$, with $\lambda_c = cbB^2/H$, then $\mathcal{N}^\lambda$ is contained in Ω, except for the endpoints and the measure stress field $\mathbf{T}^\lambda$ is well defined by relations (54)–(57).

The parametric measure $\mathbf{T}^\lambda_r \mathcal{L}^2 \llcorner \Omega$ is of the form considered in Proposition 7.4 and the integrability condition (45) is satisfied because we have

$$\int_0^{\lambda_c} \int_\Omega |\mathbf{T}^\lambda_r(\mathbf{r})| \, d\mathbf{r} \, d\lambda < \infty$$

Hence for $0 < \lambda < \lambda_c$ and $\epsilon > 0$ such that

$$\Lambda = (\lambda - \epsilon, \lambda + \epsilon) \subset (0, \lambda_c) \tag{58}$$

the measure

$$\bar{\mathsf{T}}^\lambda_r = \frac{1}{2\epsilon} \int_\Lambda \mathsf{T}^\mu_r \, d\mu \tag{59}$$

is an absolutely continuous measure with respect to $\mathcal{L}^2 \llcorner \Omega$,

$$\bar{\mathsf{T}}^\lambda_r = \mathbf{U}^\lambda_r \mathcal{L}^2 \llcorner \Omega.$$

To compute $\mathbf{U}^\lambda_r$, let us put

$$A = \{\mathbf{r} = (x, y) : bcx^2/y \in \Lambda\}. \tag{60}$$

We obtain

$$\mathbf{U}^\lambda_r(\mathbf{r}) = \begin{cases} -by\mathbf{j} \otimes \mathbf{j} & \text{if } \mathbf{r} \in \Omega^\lambda_+ \setminus A, \\ -\lambda\mathbf{i} \otimes \mathbf{i} - 2bx\mathbf{i} \odot \mathbf{j} - (2\epsilon)^{-1} b^2 x^2 \ln\left(\frac{\lambda+\epsilon}{\lambda-\epsilon}\right) \mathbf{j} \otimes \mathbf{j} & \text{if } \mathbf{r} \in \Omega^\lambda_- \setminus A, \\ (2\epsilon)^{-1} \left(\xi_1(\mathbf{r})\mathbf{i} \otimes \mathbf{i} + 2\xi_2(\mathbf{r})\mathbf{i} \odot \mathbf{j} + \xi_3(\mathbf{r})\mathbf{j} \otimes \mathbf{j}\right) & \text{if } \mathbf{r} \in A, \end{cases} \tag{61}$$

where

$$\xi_1(\mathbf{r}) = \frac{b^2c^2x^4}{2y^2} - \frac{1}{2}(\lambda+\epsilon)^2$$

$$\xi_2(\mathbf{r}) = bx(\frac{bcx^2}{y} - \lambda - \epsilon),$$

$$\xi_3(\mathbf{r}) = by(\lambda-\epsilon) - b^2x^2\left(c + \ln\frac{y(\lambda+\epsilon)}{bcx^2}\right).$$

In order to verify the first two regimes in (61) we note that if $\mathbf{r} \in \Omega_+^\mu \setminus A$ or $\mathbf{r} \in \Omega_-^\mu \setminus A$ then, for all values of μ in Λ, the expression of $\mathsf{T}_r^\mu(\mathbf{r})$ is that given by $(54)_1$ and $(54)_2$, respectively. Thus, $(61)_1$ and $(61)_2$ can be immediately obtained from (55). For $\mathbf{r} \in A$, we have $\mathbf{r} \in \Omega_+^\mu$ for $\mu \in (\lambda-\epsilon, bcx^2/y)$ and $\mathbf{r} \in \Omega_-^\mu$ for $\mu \in (bcx^2/y, \lambda+\epsilon)$. Therefore

$$\begin{aligned}
\mathbf{U}_r^\lambda(\mathbf{r}) &= (2\epsilon)^{-1}\int_{\lambda-\epsilon}^{\lambda+\epsilon} \mathsf{T}_r^\mu \, d\mu \\
&= (2\epsilon)^{-1}\Big\{\int_{\lambda-\epsilon}^{bcx^2/y} -by\mathbf{j}\otimes\mathbf{j}\, d\mu \\
&+ \int_{bcx^2/y}^{\lambda+\epsilon}(-\mu\mathbf{i}\otimes\mathbf{i} - 2bx\mathbf{i}\odot\mathbf{j} - \tfrac{b^2x^2}{\mu}\mathbf{j}\otimes\mathbf{j})\, d\mu\Big\} \\
&= (2\epsilon)^{-1}\Big\{\Big(\tfrac{b^2c^2x^4}{2y^2} - \tfrac{1}{2}(\lambda+\epsilon)^2\Big)\mathbf{i}\otimes\mathbf{i} + 2bx\Big(\tfrac{bcx^2}{y} - \lambda - \epsilon\Big)\mathbf{i}\odot\mathbf{j} \\
&\qquad + \Big[by(\lambda-\epsilon) - b^2x^2\Big(c + \ln\tfrac{y(\lambda+\epsilon)}{bcx^2}\Big)\Big]\mathbf{j}\otimes\mathbf{j}\Big\}.
\end{aligned}$$

The density $\mathbf{U}_r^\lambda$ is bounded in Ω (we note that for $\mathbf{r}\in A$ we have $\lambda-\epsilon < cbx^2/y < \lambda+\epsilon$ by (56)).

Next we consider the measures $\mathbf{T}_s^\lambda$. Let $\varphi : \Omega \to \mathrm{R}$ be defined by

$$\varphi(\mathbf{r}) = cbx^2/y, \tag{62}$$

$\mathbf{r} = (x, y) \in \Omega$. Then, for any $\lambda \in (0, \lambda_c)$, the curve $\mathcal{N}^\lambda$ is the level set of φ corresponding to the value of λ, i.e.

$$\mathcal{N}^\lambda(\mathbf{r}) = \{\mathbf{r} \in \Omega : \varphi(\mathbf{r}) = \lambda\}.$$

Moreover, φ is continuously differentiable and

$$|\nabla\varphi(\mathbf{r})| = \frac{cbx\sqrt{x^2+4y^2}}{y^2} \tag{63}$$

Firstly we note that

$$|\nabla\varphi(\mathbf{r})||\mathbf{T}_s^\lambda(\mathbf{r})| = |\nabla\varphi(\mathbf{r})||\sigma^\lambda(\mathbf{r})| = \frac{\sqrt{3}}{6}c^2b^2(4x^2 + \frac{x^4}{y^2})$$

is bounded in

$$\Omega_0 = \{\mathbf{r} = (x, y) : cbx^2/y \in (0, \lambda_c)\} = \varphi^{-1}(0, \lambda_c),$$

in view of (63), (52) and (57). Then, Proposition 7.5 says that for any interval Λ as in (58) the measure

$$\bar{\mathsf{T}}^\lambda_s = \frac{1}{2\epsilon}\int_\Lambda \mathsf{T}^\mu_s \, d\mu$$

is $\mathcal{L}^2$ absolutely continuous over Ω, i.e.,

$$\bar{\mathsf{T}}^\lambda_s = \mathbf{U}^\lambda_s(\mathbf{r})\mathcal{L}^2 \llcorner \Omega_0,$$

with the density given by (47), i.e.

$$\mathbf{U}^\lambda_s(\mathbf{r}) = \begin{cases} (2\epsilon)^{-1}\mathbf{T}^\lambda_s(\mathbf{r})|\nabla\varphi(\mathbf{r})| & if \quad \mathbf{r} \in A, \\ \mathbf{0} & \text{otherwise.} \end{cases} \tag{64}$$

Note that $\varphi(\mathbf{r}) \in \Lambda$ if and only if $\mathbf{r} \in A$, by (62) and (60). In the present case we have

$$\begin{aligned} \mathbf{T}^\lambda_s(\mathbf{r})\,|\nabla\varphi(\mathbf{r})| &= \sigma^\lambda(\mathbf{r})\mathbf{t}^\lambda(\mathbf{r}) \otimes \mathbf{t}^\lambda(\mathbf{r})\,|\nabla\varphi(\mathbf{r})| \\ &= -\tfrac{\sqrt{3}cb^2x^2}{6y^2}(x\mathbf{i} + 2y\mathbf{j}) \otimes (x\mathbf{i} + 2y\mathbf{j}) \\ &= -\tfrac{\sqrt{3}cb^2x^2}{6y^2}(x^2\mathbf{i}\otimes\mathbf{i} + 4xy\mathbf{i}\odot\mathbf{j} + 4y^2\mathbf{j}\otimes\mathbf{j}) \end{aligned}$$

$\mathbf{r} \in A$, by (63), (52) and (57).

Finally, we obtain the negative semidefinite and square integrable (in fact bounded) stress field $\mathbf{U}^\lambda = \mathbf{U}^\lambda_r + \mathbf{U}^\lambda_s$,

$$\mathbf{U}^\lambda(\mathbf{r}) = \begin{cases} -by\mathbf{j}\otimes\mathbf{j} & \text{if } \mathbf{r} \in \Omega^\lambda_+ \setminus A, \\ -\lambda\mathbf{i}\otimes\mathbf{i} - 2bx\mathbf{i}\odot\mathbf{j} - (2\epsilon)^{-1}b^2x^2\ln\left(\frac{\lambda+\epsilon}{\lambda-\epsilon}\right)\mathbf{j}\otimes\mathbf{j} & \text{if } \mathbf{r} \in \Omega^\lambda_- \setminus A, \\ \mathbf{s}(\mathbf{r}) & \text{if } \mathbf{r} \in A, \end{cases}$$

where

$$\begin{aligned} \mathbf{s}(\mathbf{r}) \quad &= -(2\epsilon)^{-1}\Big\{\Big[-\tfrac{b^2x^4}{12y^2} + \tfrac{1}{2}(\lambda+\epsilon)^2\Big]\mathbf{i}\otimes\mathbf{i} \\ &\quad + 2\Big[-\tfrac{b^2x^3}{3y} + bx(\lambda+\epsilon)\Big]\mathbf{i}\odot\mathbf{j} \\ &\quad + \Big[(\tfrac{\sqrt{3}}{2} + \tfrac{5}{6} + \ln\tfrac{y(\lambda+\epsilon)}{bcx^2})b^2x^2 - by(\lambda-\epsilon)\Big]\mathbf{j}\otimes\mathbf{j} \end{aligned}$$

by (61) and (64). It is an easy matter to verify that, for every $\lambda \in (0, \lambda_c)$, $\mathbf{U}^\lambda$ verifies the equilibrium equation $div\,\mathbf{U}^\lambda + b\mathbf{j} = \mathbf{0}$ in Ω and the boundary conditions (50), so that λ is statically admissible and the loads $(\mathbf{s}^\lambda, \mathbf{b}^\lambda)$ are strongly compatible.

Acknowledgment. The research of M. Šilhavý was supported by RVO: 67985840. The support is gratefully acknowledged.

Bibliography

[Adams & Fournier 2003] Adams, R. A.; Fournier, J. J. F. 2003. *S*obolev spaces (Second edition). New York: Academic Press.

[Ambrosio et al. 1997] Ambrosio, L.; Coscia, A.; Dal Maso, G. 1997. Fine properties of functions with bounded deformation. *A*rch. Rational Mech. Anal., Vol. 139: 201–238.

[Ambrosio et al. 2000] Ambrosio, L.; Fusco, N.; Pallara, D. 2000. *F*unctions of bounded variation and free discontinuity problems. Oxford: Clarendon Press.

[Angelillo 1993] Angelillo, M. 1993. Constitutive relations for no-tension materials. *M*eccanica (Milano), Vol. 28: 195–202.

[Anzellotti 1985] Anzellotti, G. 1985. A class of convex non-corecive functionals and masonry-like materials. *A*nn. Inst. Henri Poincaré, Vol. 2: 261–307.

[Barsotti & Vannucci 2013] Barsotti, R.; Vannucci, P. 2013. Wrinkling of Orthotropic Membranes: An Analysis by the Polar Method. *J.* Elasticity. To appear. DOI 10.1007/s10659-012-9408-z

[Del Piero 1989] Del Piero, G. 1989. Constitutive equations and compatibility of the external loads for linear elastic masonry-like materials. *M*eccanica, Vol. 24: 150–162.

[Del Piero 1998] Del Piero, G. 1998. Limit analysis and no-tension materials. *I*nt. J. Plasticity, Vol. 14: 259–271.

[Di Pasquale 1984] Di Pasquale, S. 1984. Statica dei solidi murari teorie ed esperienze. Dipartimento di Costruzioni, Pubblicazione n. 27

[Ekeland & Temam 1999] Ekeland, I.; Temam, R. 1999. *C*onvex analysis and variational problems. Philadelphia: SIAM.

[Epstein 2002] Epstein, M. 2002. From Saturated Elasticity to Finite Evolution, Plasticity and Growth. *M*athematics and mechanics of solids, Vol. 7: 255–283.

[Fonseca & Leoni 2007] Fonseca, I.; Leoni, G. 2007. *M*odern Methods in the Calculus of Variations: L^p Spaces. New York: Springer.

[Giaquinta & Giusti 1985] Giaquinta, M.; Giusti, E. 1985. Researches on the equilibrium of masonry structures. *A*rch. Rational Mech. Anal., Vol. 88: 359–392.

[Gurtin 1981] Gurtin, M. E. 1981. *A*n introduction to continuum mechanics. Boston: Academic Press.

[Lucchesi et al. 1994] Lucchesi, M.; Padovani, C.; Pagni, A. 1994. A numerical method for solving equilibrium problems of masonry–like solids. *M*eccanica, Vol. 24: 175–193.

[Lucchesi et al. 1996] Lucchesi, M.; Padovani, C.; Zani, N. 1996. Masonry–like materials with bounded compressive strength. *I*nt J. Solids and Structures, Vol. 33: 1961–1994.

[Lucchesi et al. 2008a] Lucchesi, M.; Padovani, C.; Pasquinelli, G.; Zani, N. 2008. *M*asonry Constructions: Mechanical Models and Numerical Applications. Berlin: Springer.

[Lucchesi et al. 2010] Lucchesi, M.; Padovani, C.; Šilhavý, M. 2010. An energetic view on the limit analysis of normal bodies. *Q*uart. Appl. Math., Vol. 68: 713–746.

[Lucchesi et al. 2006] Lucchesi, M.; Šilhavý, M.; Zani, N. 2006. A new class of equilibrated stress fields for no–tension bodies. *J*ournal of Mechanics of Materials and Structures, Vol. 1: 503–539.

[Lucchesi et al. 2008b] Lucchesi, M.; Šilhavý, M.; Zani, N. 2008. Integration of measures and admissible stress fields for masonry bodies. *J*ournal of Mechanics of Materials and Structures, Vol. 3: 675–696.

[Lucchesi et al. 2009] Lucchesi, M.; Šilhavý, M.; Zani, N. 2009. Equilibrated divergence measure stress tensor fields for heavy masonry bodies. *E*uropean Journal of Mechanics A/Solids, Vol. 28: 223–232.

[Lucchesi et al. 2011] Lucchesi, M.; Šilhavý, M.; Zani, N. 2011. Integration of parametric measures and the statics of masonry panels. *A*nnals of Solid and Structural Mechanics, Vol. 2: 33–44.

[Lucchesi et al. 2012] Lucchesi, M.; Šilhavý, M.; Zani, N. 2012. On the choice of functions spaces in the limit analysis for masonry bodies. *J*ournal of Mechanics of Materials and Structures, Vol. 7: 795–836.

[Müller 1999] Müller, S. 1999. Variational Models for Microstructure and Phase Transitions. Pp. 85–210 in S. Hildebrandt, M. Struwe (ed.), In Calculus of variations and geometric evolution problems (Cetraro, 1996) Lecture notes in Math. 1713 Springer, Berlin.

[Padovani et al. 2008] Padovani, C.; Pasquinelli, G.; Šilhavý, M. 2008. Processes in masonry bodies and the dynamical significance of collapse. *M*ath. Mech. Solids, Vol. 13: 573–610.

[Rockafellar 1970] Rockafellar, R. T. 1970. *C*onvex analysis. Princeton: Princeton University Press.

[Rudin 1970] Rudin, W. 1970. *R*eal and complex analysis. New York: McGraw-Hill.

[Šilhavý 2008] Šilhavý, M. 2008. Cauchy's stress theorem for stresses represented by measures. *C*ontinuum Mechanics and Thermodynamics, Vol. 20: 75–96.

[Šilhavý 2013] Šilhavý, M. 2013. Collapse mechanisms and the existence of equilibrium solutions for masonry bodies. To appear in Mathematics and Mechanics of Solids.

[Temam 1983] Temam, R. 1983. *P*roblémes mathématiques en plasticité. Paris: Gauthier–Villars.

[Temam & Strang 1980] Temam, R.; Strang, G. 1980. Functions of Bounded Deformation. *A*rch. Rational Mech. Anal., Vol. 75: 7–21.

A numerical method for solving BVP of masonry-like solids

Massimiliano Lucchesi*
* Dipartimento di Ingegneria Civile e Ambientale
University of Florence
via S. Marta 3, 50139 Florence

1 Introduction

In this chapter, we shall first explicitly determine the solution to the constitutive equation of isotropic masonry-like materials (i.e., find the stress tensor $\mathbf{T}$ and the fracture strain $\mathbf{E}^f$ corresponding to a prescribed strain tensor $\mathbf{E}$, so as to satisfy relations (2.4)). The problem can be solved by observing that the stress in the isotropic case is coaxial not only with the fracture strain, but with the elastic strain as well. This enables representing all these tensors with respect to the same principal system and then expressing the constitutive equation as a function of their eigenvalues. In this way, (2.4) can be transformed into a linear complementarity problem (7), (27), (28) whose solution is unique because the tensor of the elastic constants has been assumed to be positive definite. As the solution to the constitutive equation depends on the number of principal stresses that vanish, in order to construct the stress function we need to consider a partition of the strain space into four different regions, each of which corresponds to different material behavior. We then calculate the derivative of the stress function with respect to the strain, as this will be used to construct the tangent stiffness matrix when dealing with numerical solution of the equilibrium problem. The derivative of the stress function turns out to be smooth in each region and its jump has no tangential component at the interfaces between the different regions.

In Section 2 we consider the equilibrium problem of a body made of masonry-like material. We limit ourselves to considering loads that are square integrable functions (i.e. measures that are absolutely continuum with a square integrable density). Thus, we can suppose that the displacement field belongs to the Sobolev space V of all vector fields which are square integrable with their first weak derivative and satisfy the prescribed

M. Angelillo (Ed.), *Mechanics of Masonry Structures*, CISM International Centre for Mechanical Sciences, DOI 10.1007/ 978-3-7091-1774-3_3,

boundary conditions. Then, for given loads, solving the equilibrium problem involves finding an equilibrium state, i.e., a displacement field in V which satisfies the equation of virtual work for every displacement field in V (see (22) below). As already established in the previous chapter, for general loads the equilibrium state cannot exist and, if it does exist it cannot be unique; on the other hands, the stress fields corresponding to different equilibrium states coincide. We say that the loads are admissible if there exists at least one equilibrium state, and that all such equilibrium state are regular admissible if they are admissible and the corresponding stress field is continuously differentiable. Because numerical applications require assigning the loads incrementally, we define a (regular) admissible loading process, that is, a piecewise continuously differentiable path in the space of loads which starts at the origin, ends at the assigned loads and whose points are (regular) admissible loads. Because masonry-like material is hyperelastic, it turns out that the solution is independent of the choice of the process, at least for the stress. Next, we briefly describe a numerical method for solving the equilibrium problem. The approach is based on a displacement formulation of the finite element method (1), (5), (6) and uses the Newton Raphson method to solve the non-linear algebraic system that is obtained by the discretization. (See also (8) and (2) for different approaches).

In Section 3, in order to make a comparison between the explicit and numerical solutions, we consider a trapezoidal panel that is fixed at its base and whose horizontal displacements are prevented at its vertical lateral side. The panel undergoes normal and tangential loads that are distributed on its top (see Fig. 1 below). Due to the constraint conditions used, in this case the solution is unique also in terms of displacement and strain. This makes the comparison between explicitly and numerically determined displacement fields meaningful (see Figures 2 and 3 below).

With the aim of illustrating the possible applications of the constitutive equation of masonry-like materials and the numerical method presented in the foregoing, Section 4 reports on a case study. The cross vault of the Church of San Ponziano in Lucca was analysed using the NOSA code (16) at the Laboratory of Mechanics of Materials and Structures of the ISTI-CNR Institute (25).

Lastly, Section 5 addresses the study of the dynamic behavior of slender masonry structures. In order to overcome the difficulties inherent in performing dynamic analyses of continuous bodies made of masonry-like materials, a constitutive equation for masonry structures that can be represented by one-dimensional elements has been formulated (4), (30). By assuming that the longitudinal fibers of the beam have no resistance under tension and bounded compressive strength, the generalized stresses (normal

force and bending moment) are expressed as functions of the generalized strains (extensional strain and the change of curvature). It has been proved that, under suitable hypotheses on the range of the corresponding stress field, the equilibrium state turns out to be unique (21). In order to study the dynamic behavior of age-old masonry towers, the constitutive equation has been formulated for hollow, rectangular cross-sectional beams (19). As the application example shows, the effects of horizontal and vertical accelerations applied to the base of the tower can be evaluated in terms of crushed and cracked volume.

1.1 Explicit expression for the stress function for isotropic masonry-like materials and its derivative

In this Section we study the constitutive equation of masonry-like materials in order to characterize the mechanical behavior of a class of isotropic materials that are incapable of withstanding tensile stresses and have infinite compressive strength. See (20), Chap. 2 for a constitutive equation that takes into account the limited compressive strength of the material.

We say that a masonry-like material, whose constitutive equation is defined in (2.4), is isotropic if the tensor of the elastic constant $\mathbb{C}$ is isotropic, i.e., if

$$\mathbb{C}\left(\mathbf{Q}\mathbf{E}\mathbf{Q}^T\right) = \mathbf{Q}\mathbb{C}\left(\mathbf{E}\right)\mathbf{Q}^T$$

for all orthogonal tensors $\mathbf{Q}$. In the following we suppose that the material is isotropic and that (2.1) is satisfied. Thus, we have (13) p. 235

$$\mathbf{T} = \mathbb{C}\mathbf{E}^e = 2\mu E^e + \lambda(\mathrm{tr}\mathbf{E}^e)\mathbf{1} \tag{1}$$

where the Lamé moduli of the material satisfy the conditions

$$\mu > 0, 2\mu + 3\lambda > 0. \tag{2}$$

We say that two tensors $\mathbf{A}, \mathbf{B} \in$Sym are coaxial if they have the same eigenvectors; as has been proved in (13), p. 12, this is the case if and only if they commute, i.e. if $\mathbf{AB} = \mathbf{BA}$.

The following proposition is the basis for explicit solution of the constitutive equation (2.4); its simple proof can be found in (20), p.22.

Proposition 1.1. If $\mathbb{C}$ is isotropic, then $\mathbf{E}$, $\mathbf{T}$, $\mathbf{E}^e$ and $\mathbf{E}^f$ are coaxial.

Let $\{\mathbf{q}_1, \mathbf{q}_2, \mathbf{q}_3\}$ be orthonormal eigenvectors of $\mathbf{E}$, $\mathbf{T}$, $\mathbf{E}^e$ and $\mathbf{E}^f$ and $\mathbf{e}= (e_1, e_2, e_3)$, $\mathbf{t}= (t_1, t_2, t_3)$, $\mathbf{e}^e = (e_1^e, e_2^e, e_3^e)$ and $\mathbf{e}^f = (e_1^f, e_2^f, e_3^f)$ the lists of the corresponding eigenvalues. Therefore, system (2.4) can be rewritten as

$$\mathbf{t} = D\mathbf{e}^e,$$
$$\mathbf{t} \leq \mathbf{0},$$
$$\mathbf{e}^f \geq \mathbf{0},$$
$$\mathbf{t} \cdot \mathbf{e}^f = 0, \tag{3}$$

where

$$D = \begin{pmatrix} 2\mu+\lambda & \lambda & \lambda \\ \lambda & 2\mu+\lambda & \lambda \\ \lambda & \lambda & 2\mu+\lambda \end{pmatrix}. \tag{4}$$

This is a linear complementarity problem which, given $\mathbf{e}$, has a unique solution $\mathbf{t}$ and $\mathbf{e}^f$, because D is positive definite by (2) (see (7)).

In order to write the explicit solution of system (3), we define

$$\mathcal{R} = \{\mathbf{e} = (e_1, e_2, e_3) \in \mathbb{R}^3 : e_1 \leq e_2 \leq e_3\} \tag{5}$$

and consider the partition of $\mathcal{R}$ made up of the following four subsets

$$\mathcal{R}_1 = \{\mathbf{e} \in \mathcal{R} : 2\mu e_3 + \lambda(e_1 + e_2 + e_3) \leq 0\},$$
$$\mathcal{R}_2 = \{\mathbf{e} \in \mathcal{R} : e_1 \geq 0\},$$
$$\mathcal{R}_3 = \{\mathbf{e} \in \mathcal{R} : e_1 < 0,\ \lambda e_1 + 2(\lambda+\mu)e_2 \geq 0\},$$
$$\mathcal{R}_4 = \{\mathbf{e} \in \mathcal{R} : \lambda e_1 + 2(\lambda+\mu)e_2 < 0,\ 2\mu e_3 + \lambda(e_1 + e_2 + e_3) > 0\}. \tag{6}$$

If $\mathbf{e} \in \mathcal{R}_1$, the normal component of the stress is compressive in all directions and the material behaves in a linear elastic manner. In $\mathcal{R}_2$ the stress tensor is zero and the material can fracture in all directions. In $\mathcal{R}_3$ and $\mathcal{R}_4$ there are two and one principal stresses that are zero, respectively, and the material can fracture orthogonally to these directions. Therefore, we have if $\mathbf{e} \in \mathcal{R}_1$ then

$$t_i = 2\mu e_i + \lambda(e_1 + e_2 + e_3) \quad e_i^f = 0, \tag{7}$$

if $\mathbf{e} \in \mathcal{R}_2$ then

$$t_i = 0, e_i^f = e_i, \quad i = 1, 2, 3; \tag{8}$$

if $\mathbf{e} \in \mathcal{R}_3$ then

$$t_1 = \frac{\mu(2\mu+3\lambda)}{\lambda+\mu} e_1, \quad e_1^f = 0,$$

$$t_i = 0,\ e_i^f = e_i + \frac{\lambda}{2(\lambda+\mu)}e_1, \quad i = 2,3; \tag{9}$$

if $\mathbf{e}\in \mathcal{R}_4$ then

$$t_1 = \frac{2\mu}{\lambda+2\mu}(\lambda e_2 + 2(\lambda+\mu)e_1), e_1^f = 0,$$

$$t_2 = \frac{2\mu}{\lambda+2\mu}(\lambda e_1 + 2(\lambda+\mu)e_2), e_2^f = 0, t_3 = 0, e_3^f = e_3 + \frac{\lambda}{2(\lambda+\mu)}(e_1+e_2). \tag{10}$$

Thus, given a symmetric tensor $\mathbf{E}= \sum_{i=1}^3 e_i\mathbf{q}_i\otimes\mathbf{q}_i$, we can calculate the corresponding stress

$$\mathbf{T} = \widehat{\mathbf{T}}(\mathbf{E}) = \sum_{i=1}^{3} t_i\mathbf{q}_i \otimes \mathbf{q}_i \tag{11}$$

and the corresponding fracture strain

$$\mathbf{E}^f = \sum_{i=1}^{3} e_i^f \mathbf{q}_i \otimes \mathbf{q}_i. \tag{12}$$

Note that stress function $\widehat{\mathbf{T}} : Sym \to \mathrm{Sym}^-$ is isotropic, i.e.,

$$\widehat{\mathbf{T}}(\mathbf{Q}\mathbf{E}\mathbf{Q}^T) = \mathbf{Q}\widehat{\mathbf{T}}(\mathbf{E})\mathbf{Q}^T. \tag{13}$$

Moreover, for the stored energy function $\widehat{w}(\mathbf{E}) = \frac{1}{2}\widehat{\mathbf{T}}(\mathbf{E})\cdot\mathbf{E}$ we have (20), p. 30
if $\mathbf{e}\in\mathcal{R}_1$ then

$$\widehat{w}(\mathbf{E}) = \mu \parallel \mathbf{E}\parallel^2 + \frac{1}{2}\lambda(\mathrm{tr}\mathbf{E})^2; \tag{14}$$

if $\mathbf{e}\in\mathcal{R}_2$ then

$$\widehat{w}(\mathbf{E}) = 0; \tag{15}$$

if $\mathbf{e}\in\mathcal{R}_3$ then

$$\widehat{w}(\mathbf{E}) = \frac{1}{2}\frac{\mu(2\mu+3\lambda)}{\lambda+\mu}e_1^2; \tag{16}$$

if $\mathbf{e}\in\mathcal{R}_4$ then

$$\widehat{w}(\mathbf{E}) = \frac{2\mu}{\lambda+2\mu}((\lambda+\mu)(e_1^2+e_2^2) + \lambda e_1 e_2). \tag{17}$$

In order to compute the derivative of the stress function $\widehat{\mathbf{T}}$ with respect to $\mathbf{E}$ we need to compute the derivatives of the principal stresses t_i with respect to $\mathbf{E}$. To this end, we first state the following proposition, whose proof can be found in (20) , p. 16. Let Sym^* be the subset of Sym made of all symmetric tensors having distinct eigenvalues. Consider the functions

$$a_i : \mathrm{Sym}^* \to \mathbb{R}, \quad \mathbf{A} \mapsto a_i(\mathbf{A}), i = 1, 2, 3$$

which associate each $\mathbf{A}\in\mathrm{Sym}^*$ with its eigenvalues, with $a_1 < a_2 < a_3$, denote by $\mathbf{g}_1$, $\mathbf{g}_2$, $\mathbf{g}_3$ a triad of corresponding normalized eigenvectors, and put

$$\mathbf{G}_{ij} = \frac{1}{2}(\mathbf{g}_i \otimes \mathbf{g}_j + \mathbf{g}_j \otimes \mathbf{g}_i), \quad i, j = 1, 2, 3.$$

Proposition 1.2. We have

$$D_{\mathrm{A}} a_i = \mathbf{G}_{ii} \quad i = 1, 2, 3,$$
$$D_{\mathrm{A}} \mathbf{G}_{ii} = \sum_{i \neq j} \frac{2}{a_i - a_j} \mathbf{G}_{ij} \otimes \mathbf{G}_{ij}, \quad i = 1, 2, 3.$$

Now we are in a position to give the explicit expression for the derivative $D_E\widehat{\mathbf{T}}$ of $\widehat{\mathbf{T}}$ with respect to $\mathbf{E}$ in the interior $\mathring{\mathcal{R}}_i$ of each region $\mathcal{R}_i$. Let $\mathbb{I}$ and $\mathbb{O}$ be the identity and the null fourth order tensor, respectively. Moreover, let us put

$$\mathbf{O}_{ij} = \frac{1}{2}(\mathbf{q}_i \otimes \mathbf{q}_j + \mathbf{q}_j \otimes \mathbf{q}_i), i, j = 1, 2, 3.$$

Proposition 1.3. If $\mathbf{e}$ belongs to $\mathring{\mathcal{R}}_i$, $i = 1, 2, 3, 4$, then $\widehat{\mathbf{T}}$ is differentiable with respect to $\mathbf{E}$ and we have
if $\mathbf{e} \in \mathcal{R}_1$ then

$$D_E\widehat{\mathbf{T}} = 2\mu\mathbb{I} + \lambda\mathbf{1} \otimes \mathbf{1}; \tag{18}$$

if $\mathbf{e} \in \mathcal{R}_2$ then

$$D_E\widehat{\mathbf{T}} = \mathbb{O}; \tag{19}$$

if $\mathbf{e} \in \mathcal{R}_3$ then

$$D_E\widehat{\mathbf{T}} = \frac{2\mu(2\mu + 3\lambda)}{\lambda + \mu}\Big(\mathrm{O}_{11} \otimes \mathrm{O}_{11} - \frac{e_1}{e_2 - e_1}\mathrm{O}_{12} \otimes \mathrm{O}_{12} - \frac{e_1}{e_3 - e_1}\mathrm{O}_{13} \otimes \mathrm{O}_{13}\Big); \tag{20}$$

if $\mathbf{e} \in \mathcal{R}_4$ then

$$D_E\widehat{\mathbf{T}} = 4\mu O_{12} \otimes O_{12} - \frac{4\mu}{\lambda+2\mu}\frac{2(\lambda+\mu)e_1+\lambda e_2}{e_3-e_1}O_{13}\otimes O_{13}$$

$$-\frac{4\mu}{\lambda+2\mu}\frac{2(\lambda+\mu)e_2+\lambda e_1}{e_3-e_2}O_{23}\otimes O_{23}+\frac{2\mu(3\lambda+2\mu)}{\lambda+2\mu}(O_{11}+O_{22})\otimes(O_{11}+O_{22})$$

$$+2\mu(O_{11}-O_{22})\otimes(O_{11}-O_{22}). \tag{21}$$

For the proof, which follows from (1.11), (1.7)-(1.10) and Proposition 1.2, see [20, p. 45]. □

Further properties of $D_E\widehat{\mathbf{T}}$ can be found in (20). In particular, it can be proved that on the interfaces between the different regions $\mathcal{R}_i$, $i = 1, 2, 3, 4$ the jump of the derivative $D_E\widehat{\mathbf{T}}$ has no tangential component (see (20), Prop. 2.22).

1.2 The equilibrium problem and a numerical method for its solution

Let $\Omega \subset \mathbb{R}^3$ be a continuous body represented by an open and bounded set with Lipschitz boundary (9), p. 38 and let $\mathcal{D}$, $\mathcal{S}$ be two disjoint subsets of $\partial\Omega$ such that $\mathcal{D}\cup\mathcal{S} = \partial\Omega$, which will be interpreted as the set of prescribed boundary displacements and prescribed boundary forces. Moreover, let us put

$$V = \{\mathbf{v} \in W^{1,2}(\Omega, \mathbb{R}^3) : \mathbf{v} = \mathbf{0} \quad \text{a.e. on} \quad \mathcal{D}\},$$

and for any $\mathbf{v} \in V$ let

$$\widehat{\mathbf{E}}(\mathbf{v}) = \frac{1}{2}(\nabla\mathbf{v} + \nabla\mathbf{v}^{\mathrm{T}})$$

be the corresponding infinitesimal strain tensor. We assume that the body force $\mathbf{b}$ acting in Ω and the surface force $\mathbf{s}$ acting on $\mathcal{S}$ are square integrable functions as in (2.18), i.e.,

$$\mathbf{b} \in L^2(\Omega, \mathbb{R}^3), \qquad \mathbf{s} \in L^2(\mathcal{S}, \mathbb{R}^3)$$

and call ($\mathbf{b}$,$\mathbf{s}$) the load applied to Ω. Thus, the internal energy of the body

$$\mathrm{E}(\mathbf{u}) = \int_\Omega \widehat{w}(\widehat{\mathbf{E}}(\mathbf{u}))d\mathcal{L}^3,$$

the energy of the load

$$< \mathbf{l}, \mathbf{u} >= \int_{\Omega} \mathbf{b} \cdot \mathbf{u}\, d\mathcal{L}^3 + \int_{\mathcal{S}} \mathbf{s} \cdot \mathbf{u}\, d\mathcal{H}^2$$

and the total energy of deformation

$$\mathrm{F}(\mathbf{u}) = \mathrm{E}(\mathbf{u}) - < \mathbf{l}, \mathbf{u} >= \int_{\Omega} \widehat{w}(\widehat{\mathbf{E}}(\mathbf{u}))d\mathcal{L}^3 - \int_{\Omega} \mathbf{b} \cdot \mathbf{u} d\mathcal{L}^3 - \int_{\mathcal{S}} \mathbf{s} \cdot \mathbf{u}, d\mathcal{H}^2$$

can be defined for each $\mathbf{u} \in V$.

The equilibrium problem for the masonry-like body Ω with stress function $\widehat{\mathbf{T}}$, under the load ($\mathbf{b}$,$\mathbf{s}$), is to find a displacement field $\mathbf{u} \in V$ such that

$$\int_{\Omega} \widehat{\mathbf{T}}(\widehat{\mathbf{E}}(\mathbf{u})) \cdot \widehat{\mathbf{E}}(\mathbf{v}) d\mathcal{L}^3 =< \mathbf{l}, \mathbf{v} > \tag{22}$$

for each $\mathbf{v} \in V$. Such a displacement field, if it exists, is called an equilibrium state of Ω.

As already noted in Chapter 2, Sec 3, if $\mathbf{u}$ satisfies (22) and it happens that $\widehat{\mathbf{T}}(\widehat{\mathbf{E}}(\mathbf{u})) \in C^1(\mathrm{cl}\Omega,\mathrm{Sym})$, then we have

$$\mathrm{div}\mathbf{T} + \mathbf{b} = \mathbf{0} \quad \text{in} \quad \Omega \qquad \text{and} \quad \mathbf{T}\mathbf{n} = \mathbf{s} \quad \text{on} \quad \mathcal{S} \tag{23}$$

where $\mathbf{T} = \widehat{\mathbf{T}}(\widehat{\mathbf{E}}(\mathbf{u}))$ and $\mathbf{n}$ is the outer normal to $\partial\Omega$. Indeed, from formula (13)

$$\mathbf{T} \cdot \nabla \mathbf{v} = \mathrm{div}(\mathbf{T}^{\mathrm{T}}\mathbf{v}) - \mathbf{v} \cdot \mathrm{div}\mathbf{T},$$

the symmetry of $\mathbf{T}$, and because $\mathbf{v} = \mathbf{0}$ on $\mathcal{D}$, by using the divergence theorem, we obtain

$$\begin{aligned} &\int_{\Omega} \mathbf{T} \cdot \widehat{\mathbf{E}}(\mathbf{v}) d\mathcal{L}^3 = \int_{\Omega} \mathbf{T} \cdot \nabla \mathbf{v} d\mathcal{L}^3 = \\ &\int_{\Omega} \mathrm{div}(\mathbf{T}\mathbf{v}) d\mathcal{L}^3 - \int_{\Omega} \mathbf{v} \cdot \mathrm{div}\mathbf{T} d\mathcal{L}^3 = \\ &\int_{\mathcal{S}} \mathbf{T}\mathbf{n} \cdot \mathbf{v} d\mathcal{H}^2 - \int_{\Omega} \mathbf{v} \cdot \mathrm{div}\mathbf{T} d\mathcal{L}^3. \end{aligned} \tag{24}$$

By comparing (22) and (24) we obtain equation (23) due to the arbitrariness of $\mathbf{v}$.

In general, the existence of an equilibrium state is not guaranteed for equilibrium problems of masonry-like solids (see Chapter 2, Sec 3 for the

existence theory). Moreover, it may happen that there more than one equilibrium state exists. However, if $\mathbf{u}_1$ and $\mathbf{u}_2$ are two equilibrium states then

$$\widehat{\mathbf{T}}(\widehat{\mathbf{E}}(\mathbf{u}_1)) = \widehat{\mathbf{T}}(\widehat{\mathbf{E}}(\mathbf{u}_2)). \tag{25}$$

This follows from the fact that if $\mathbf{u}$ is an equilibrium state, then $\widehat{\mathbf{T}}(\widehat{\mathbf{E}}(\mathbf{u}))$ is a minimum point of the complementary energy functional among all admissible stress fields equilibrating the loads, and this minimum point is unique, as the complementary energy functional is convex. This has been proved in Chapter 2, Theorem 3.3 (see also (20), Prop. 3.1 for a simple direct proof of (2.4)). We say that the load $(\mathbf{b}, \mathbf{s})$ is admissible if there is at least one equilibrium state, that is, a displacement field $\mathbf{u}$ which satisfies (2.1); we moreover say that $(\mathbf{b}, \mathbf{s})$ is a regular admissible load if $\widehat{\mathbf{T}}(\widehat{\mathbf{E}}(\mathbf{u})) \in C^1(\mathrm{cl}\Omega,\mathrm{Sym})$.

In order to solve the equilibrium problem by using the finite element method, we have to assign the load incrementally. Therefore, given a regular admissible load ($\mathbf{b}$, $\mathbf{s}$), we consider a piecewise continuously differentiable loading process $\tau \mapsto(\mathbf{b}(\tau)$, $\mathbf{s}(\tau))$, where $\tau \in [0, \bar{\tau}]$ is a loading parameter, such that $(\mathbf{b}(0)$, $\mathbf{s}(0))= (\mathbf{0}, \mathbf{0})$, $(\mathbf{b}(\bar{\tau})$, $\mathbf{s}(\bar{\tau}))=(\mathbf{b}$, $\mathbf{s})$, $(\mathbf{b}(\tau)$, $\mathbf{s}(\tau))$ is a regular admissible load for each $\tau \in [0, \bar{\tau}]$ and, moreover, the map $\tau \mapsto \widehat{\mathbf{T}}(\widehat{\mathbf{E}}(\mathbf{u}(\tau)))$ is piecewise continuously differentiable. We call a map $\tau \mapsto(\mathrm{b}(\tau)$, $\mathrm{s}(\tau))$ with such characteristics a regular loading process.

Given a regular loading process, from (22) we deduce that

$$\int_\Omega \widehat{\mathbf{T}}(\widehat{\mathbf{E}}(\mathbf{u}(\tau))) \cdot \widehat{\mathbf{E}}(\mathbf{v}) d\mathcal{L}^3 = \int_\Omega \mathbf{b}(\tau) \cdot \mathbf{v} d\mathcal{L}^3 + \int_\mathcal{S} \mathbf{s}(\tau) \cdot \mathbf{v} d\mathcal{H}^2 \tag{26}$$

for each $\mathbf{v} \in V$ and $\tau \in [0, \bar{\tau}]$. We assume the initial conditions

$$\mathbf{u}(\mathbf{x}, 0) = \mathbf{0}, \qquad \mathbf{E}(\mathbf{x}, 0) = \mathbf{0}, \mathbf{T}(\mathbf{x}, 0) = \mathbf{0} \quad \text{on} \quad \Omega.$$

By differentiating (26) with respect to τ, we obtain the incremental equilibrium equation

$$\int_\Omega D_E \widehat{\mathbf{T}}(\widehat{\mathbf{E}}(\mathbf{u}))[\dot{\mathbf{E}}(\mathbf{u})] \cdot \widehat{\mathbf{E}}(\mathbf{v}) d\mathcal{L}^3 = \int_\Omega \dot{\mathbf{b}} \cdot \mathbf{v}, d\mathcal{L}^3 + \int_\mathcal{S} \dot{\mathbf{s}} \cdot \mathbf{v} d\mathcal{H}^2 \tag{27}$$

where a dot denotes differentiation with respect to τ and $\dot{\mathbf{E}}(\mathbf{u}) = \frac{1}{2}(\nabla\dot{\mathbf{u}} + \nabla\dot{\mathbf{u}}^{\mathrm{T}})$. Note that, in view of (23), variational equation (27) is equivalent to

$$\dot{\mathbf{T}} = D_E \widehat{\mathbf{T}}(\widehat{\mathbf{E}}(\tau)[\dot{\mathbf{E}}(\tau)],$$

$$\text{div}\dot{\mathbf{T}} + \dot{\mathbf{b}} = \mathbf{0} \quad \text{on} \quad \Omega$$
$$\dot{\mathbf{u}} = \mathbf{0} \quad \text{on} \quad \mathcal{D},$$
$$\dot{\mathbf{T}}\mathbf{n} = \dot{\mathbf{s}} \quad \text{on} \quad \mathcal{S}.$$

It is easy to see that, given a regular admissible load ($\mathbf{b}$, $\mathbf{s}$), the solution to the equilibrium problem does not depend on the (regular) loading process, at least with regard to the stress.

By using the finite element method (see e.g., (3), (5), (6), (24)), the equilibrium equation (26) and the incremental equilibrium equation (27) are transformed into the non-linear algebraic equilibrium system

$$[K\{\mathbf{u}\}]\{\mathbf{u}\} = \{\mathbf{f}\} \tag{28}$$

and into the non-linear evolution system

$$[K_T[\{\mathbf{u}\}]\{\dot{\mathbf{u}}\} = \{\dot{\mathbf{f}}\} \tag{29}$$

where $\{\mathbf{u}\}$ and $\{\mathbf{f}\}$ are the arrays of the nodal displacements and the equivalent nodal forces, respectively, and $\{\dot{\mathbf{u}}\}$ and $\{\dot{\mathbf{f}}\}$ are their derivatives with respect to τ. K and K_T are the stiffness and tangent stiffness matrix, which, as usual, are obtained from the assembly of the corresponding elemental matrices. The elemental tangent stiffness matrices are computed by using the derivatives of the stress function (18)-(21) (see also (20) for the plane cases). For each load increment, equilibrium is reached by following a suitable iterative procedure. In the following we describe the Newton-Raphson procedure. Let us suppose that in correspondence to $\tau \in (0, \bar{\tau})$, equation (26) holds and the body is thus in equilibrium under the load ($\mathbf{b}(\tau)$, $\mathbf{s}(\tau)$). We assign a nodal load increment $\{\Delta\mathbf{f}\}$ and have to solve the system

$$[K_T]\{\Delta\mathbf{u}\} = \{\Delta\mathbf{f}\}. \tag{30}$$

Let $\{\mathbf{u}^{(i)}\}$, $\{\Delta\mathbf{u}^{(i)}\}$ be the nodal vectors corresponding to the $i-th$ iteration, and denote by $\{\mathbf{f}^{(i)}\}$ the nodal forces corresponding to $\{\Delta\mathbf{f}\}$ for $i = 0$, and the vector of residual load if $i > 0$. We solve the linear system

$$[K_T\{\mathbf{u}^{(i)}\}]\{\Delta\mathbf{u}^{(i)}\} = \{\mathbf{f}^{(i)}\} \tag{31}$$

in order to determine the displacement $\{\mathbf{u}^{(i+1)}\} = \{\mathbf{u}^{(i)}\} + \{\Delta\mathbf{u}^{(i)}\}$ corresponding to the $(i+1)-th$ iteration, and the tangent matrix $[K_T\{\mathbf{u}^{(i+1)}\}]$ that can be used in the next iteration or in the next load increment.

In order to avoid the occurence of null pivot during solution of system (31), at the integration points at which $D_E\widehat{\mathbf{T}}(\widehat{\mathbf{E}}(\mathbf{u}))$ vanishes (see (19)) we

use (18), with the right-hand side multiplied by a small positive number (see (1) for a slightly different technique).

After solving system (31), we calculate the vector of the residual load

$$\{\mathbf{f}^{(i+1)}\} = \{\bar{\mathbf{f}}\} - [K\{\mathbf{u}^{(i+1)}\}]\{\mathbf{u}^{(i+1)}\}$$

where $\{\bar{\mathbf{f}}\}$ is the vector of overall loads assigned up to the current iteration, including the reaction forces. We then perform a convergence check

$$\frac{\left\|\{\mathbf{f}^{(i+1)}\}\right\|}{\{\bar{\mathbf{f}}\}} \leq \xi \tag{32}$$

where ξ is a suitable parameter. If (32) is verified, we assign a new load increment, otherwise we solve system (31) with the vector of residual load $\{\mathbf{f}^{(i+1)}\}$. The convergence check (32) guarantees that the calculated stress field is (negative semidefinite) and in equilibrium with the assigned load.

Before closing this section we briefly describe how this numerical technique can be applied to the study of masonry vaults. Let us consider a vault with (not necessarily constant) thickness h and denote by S the mean surface with Gaussian coordinates η_1 and η_2, corresponding unit tangent vectors $\mathbf{g}_1$ and $\mathbf{g}_2$ and normal unit vector $\mathbf{n}$. Let $\zeta \in [-h/2, h/2]$ be the coordinate in the normal direction $\mathbf{n}$. We assume that the stress tensor $\mathbf{T} = \mathbf{T}(\eta_1, \eta_2, \zeta)$ is negative semidefinite and satisfies the condition

$$\mathbf{T}(\eta_1, \eta_2, \zeta)\mathbf{n}(\eta_1, \eta_2) = \mathbf{0}. \tag{33}$$

For each $(\eta_1, \eta_2) \in \mathsf{S}$ we define the tensors

$$\mathbf{N}(\eta_1, \eta_2) = \int_{-h/2}^{h/2} \mathbf{T}(\eta_1, \eta_2, \zeta)d\zeta, \quad \mathbf{M}(\eta_1, \eta_2) = \int_{-h/2}^{h/2} \mathbf{T}(\eta_1, \eta_2, \zeta)\zeta d\zeta. \tag{34}$$

Moreover, for each $\gamma \in [-\pi/2, \pi/2)$ let $\mathbf{g}(\gamma)$ be the unit tangent vector to S which forms an angle γ with $\mathbf{g}_1$. Thus,

$$\begin{aligned} N(\eta_1, \eta_2, \gamma) &= \mathbf{g}(\gamma) \cdot \mathbf{N}(\eta_1, \eta_2)\mathbf{g}(\gamma), \\ M(\eta_1, \eta_2, \gamma) &= \mathbf{g}(\gamma) \cdot \mathbf{M}(\eta_1, \eta_2)\mathbf{g}(\gamma) \end{aligned} \tag{35}$$

are the normal force and bending moment per unit length corresponding to the direction γ. Because $\mathbf{T}$ is negative semidefinite, it is an easy matter to verify that N is non-positive and that M satisfies the condition

$$|M(\eta_1, \eta_2, \gamma)| \leq \frac{h}{2} |N(\eta_1, \eta_2, \gamma)|. \tag{36}$$

Now let us consider the subset S' of S , where $\mathbf{N} \neq 0$, and for each $\gamma \in [-\pi/2, \pi/2)$ let us consider the corresponding eccentricity

$$e(\eta_1, \eta_2, \gamma) = \frac{M(\eta_1, \eta_2, \gamma)}{N(\eta_1, \eta_2, \gamma)}. \tag{37}$$

If, for some γ, we have $N(\eta_1, \eta_2, \gamma) = 0$, the corresponding eccentricity is not well-defined, but it can be proved that in this case $e(\eta_1, \eta_2, \gamma) = \alpha$ is a constant function of γ. Thus, $e(\eta_1, \eta_2, \gamma)$ can be extended by continuity (20), Prop. 5.1. Let $(\eta_1, \eta_2) \in \mathsf{S}'$ and $\bar{e}(\eta_1, \eta_2)$ be such that

$$|\bar{e}(\eta_1, \eta_2)| = \sup\{|e(\eta_1, \eta_2, \gamma)| : \gamma \in [-\pi/2, \pi/2)\}.$$

The surface

$$\mathcal{M} = \{\mathbf{p} : \mathbf{p} = (\eta_1, \eta_2) + \bar{e}(\eta_1, \eta_2)\mathbf{n}, (\eta_1, \eta_2) \in \mathsf{S}'\}$$

is called the maximum modulus eccentricity surface (m.m.e.s.). It can be proved that (20), Prop. 5.2

$$\bar{e}(\eta_1, \eta_2) = \begin{cases} \omega_1 & \text{if } \det\mathbf{N}(\eta_1, \eta_2) \neq 0 \text{ and } |\omega_1| \geq |\omega_2|, \\ \omega_2 & \text{if } \det\mathbf{N}(\eta_1, \eta_2) \neq 0 \text{ and } |\omega_2| \geq |\omega_1|, \\ \alpha & \text{if } \det\mathbf{N}(\eta_1, \eta_2) = 0, \end{cases} \tag{38}$$

where, for $\beta = \mathrm{tr}(\mathbf{N}^{-1}\mathbf{M})(\det\mathbf{N})$,

$$\omega_1 = \frac{\beta - \sqrt{\beta^2 - 4\,(\det\mathbf{N})\,(\det\mathbf{M})}}{2\det\mathbf{N}}, \quad \omega_2 = \frac{\beta + \sqrt{\beta^2 - 4\,(\det\mathbf{N})\,(\det\mathbf{M})}}{2\det\mathbf{N}}. \tag{39}$$

Note that, in view of inequality (36), the m.m.e.s corresponding to a negative semidefinite stress field is entirely contained within the vault. The m.m.e.s. allows concise, effective rendering of the results of finite elements analyses. In dealing with masonry vaults the m.m.e.s. plays a role analogous to that of the line of thrust for arches (15), (16).

1.3 Comparison between the explicit and numerical solutions

Let $b > 0$ and $\alpha > 0$. In the Cartesian reference system shown in Figure 1, with $\mathbf{i}$ and $\mathbf{j}$ the unit vectors corresponding to the x and y axes, respectively, let us consider a trapezoidal masonry panel

$$\Omega = \{\mathbf{r} = (x, y) \in \mathbb{R}^2 : 0 < x < \alpha y,\ b/2\alpha < y < b/\alpha\}. \tag{40}$$

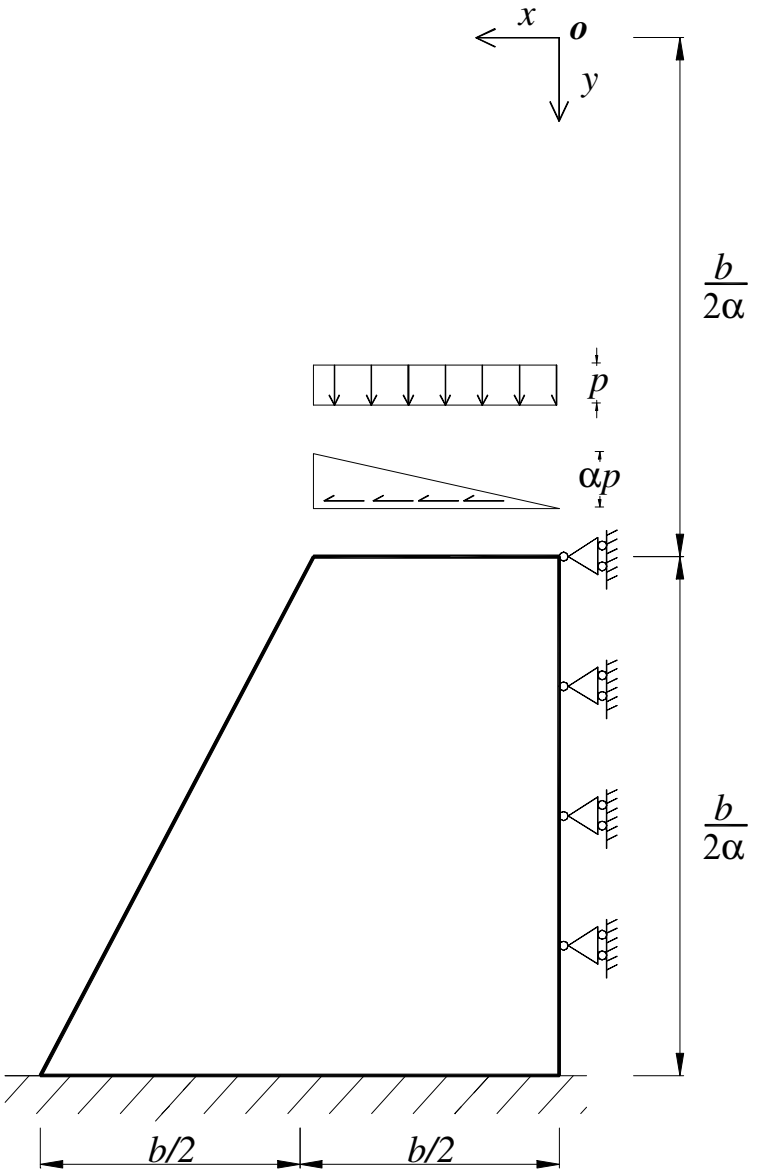

Figure 1. Trapezoidal masonry panel.

The panel is fixed at its base $(0,b)\times\{b/\alpha\}$ and, moreover, horizontal displacements are prevented on its right-hand side $\{0\}\times(b/2\alpha, b/\alpha)$. In the absence of gravity, the panel is subjected to a uniform vertical load p and a linear tangential load $q(x) = 2\alpha px/b$ which are distributed on its top $(0,b/2)\times\{b/2\alpha\}$. We now try to solve the BVP with a stress field $\mathbf{T}:\Omega\to\mathrm{Sym}^-$,

$$\mathbf{T} = \sigma_x \mathbf{i}\otimes\mathbf{i} + \tau_{xy}(\mathbf{i}\otimes\mathbf{j} + \mathbf{j}\otimes\mathbf{i}) + \sigma_y \mathbf{j}\otimes\mathbf{j}, \tag{41}$$

such that $\det\mathbf{T} = 0$. Thus, if we denote by κ the cotangent of the angle between the active isostatic lines and the x axis, and σ_y by σ, we can write (17)

$$\mathbf{T} = \kappa^2\sigma\mathbf{i}\otimes\mathbf{i} + \kappa\sigma(\mathbf{i}\otimes\mathbf{j} + \mathbf{j}\otimes\mathbf{i}) + \sigma\mathbf{j}\otimes\mathbf{j}, \tag{42}$$

where κ and σ have to satisfy the system of PDE

$$\begin{cases} \kappa\kappa_{,x} + \kappa_{,y} = 0, \\ \kappa\sigma_{,x} + \sigma\kappa_{,x} + \sigma_{,y} = 0 \end{cases} \tag{43}$$

with the boundary conditions

$$\kappa(x, b/2\alpha) = 2\alpha x/b \quad \text{and} \quad \sigma(x, b/2\alpha) = -p, \tag{44}$$

for $0 < x < b/2$.

From $(43)_1$ and $(44)_1$ we obtain

$$\kappa = \frac{x}{y} \tag{45}$$

and then, in view of $(43)_2$ and $(44)_2$, we have

$$\frac{x}{y}\sigma_{,x} + \frac{1}{y}\sigma + \sigma_{,y} = 0 \tag{46}$$

whose solution is

$$\sigma = -\frac{pb}{2\alpha y} \tag{47}$$

Therefore, we can write

$$\mathbf{T} = -\frac{pb}{2\alpha y^3}(x^2\mathbf{i}\otimes\mathbf{i} + xy(\mathbf{i}\otimes\mathbf{j} + \mathbf{j}\otimes\mathbf{i}) + y^2\mathbf{j}\otimes\mathbf{j}) = -\frac{pb}{2\alpha y^3}\mathbf{r}\otimes\mathbf{r}, \tag{48}$$

with $\mathbf{r} = (x, y)$.

If we denote by

$$E = \frac{\mu(2\mu + 3\lambda)}{\mu + \lambda} \quad \text{and} \quad \nu = \frac{\lambda}{2(\mu + \lambda)}$$

the Young's modulus and Poisson' s ratio of the material, from (2) and (48) we obtain the elastic strain

$$\mathbf{E}^e = -\frac{pb}{2\alpha E y^3}(\mathbf{r} \otimes \mathbf{r} - \nu \mathbf{r}^\perp \otimes \mathbf{r}^\perp)$$

with $\mathbf{r}^\perp = (y, -x)$. Moreover, because the inequalities $\mathbf{E}^f \geq \mathbf{0}$, $\mathbf{T} \leq \mathbf{0}$ and the condition $\mathbf{T} \cdot \mathbf{E}^f = 0$ imply $\mathbf{T}\mathbf{E}^f = \mathbf{0}$, from (48) we deduce the expression for the fracture strain

$$\mathbf{E}^f = \frac{1}{y^2} a(\mathbf{r}) \mathbf{r}^\perp \otimes \mathbf{r}^\perp$$

with $a : \Omega \to \mathbb{R}^+$ and we have

$$\mathbf{E} = \mathbf{E}^e + \mathbf{E}^f = -\frac{pb}{2\alpha E y^3}(\mathbf{r} \otimes \mathbf{r} - \nu \mathbf{r}^\perp \otimes \mathbf{r}^\perp) + \frac{1}{y^2} a(\mathbf{r}) \mathbf{r}^\perp \otimes \mathbf{r}^\perp. \tag{49}$$

In order that the strain $\mathbf{E}$ satisfy the compatibility condition a, once it has been expressed as a function of y and κ, has to satisfy the ODE (17)

$$a_{,yy} + \frac{2}{y} a_{,y} = \frac{\phi}{y^3}, \tag{50}$$

where

$$\phi = \frac{2pb(1 + 3\kappa^2)}{\alpha E}.$$

From (50) we obtain

$$a(y, \kappa) = -\frac{1}{y}(\phi(1 + \ln y) + a_0(\kappa)) + a_1(\kappa) \tag{51}$$

with a_0 and a_1 arbitrary functions.

Let $\boldsymbol{u}(\mathbf{r}) = (u(\mathbf{r}), v(\mathbf{r}))$ be the displacement field. If we require

$$u(b/\alpha, x) = v(b/\alpha, x) = 0, \quad \text{for} \quad 0 < x < b,$$

$$u(0, y) = 0, \text{for} \frac{b}{2\alpha} < y < \frac{b}{\alpha},$$

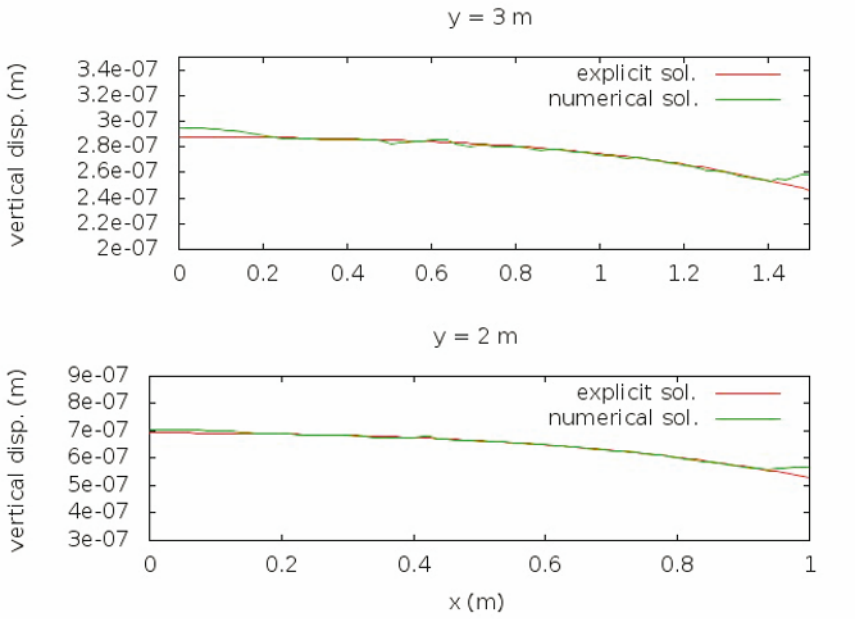

Figure 2. Vertical displacement for $y = 2$ m and $y = 3$ m.

and, for the sake of simplicity we put $\nu = 0$, then from (49) and (51) we obtain

$$u(\mathbf{r}) = \frac{pbx(x^2+y^2)}{\alpha E y^3}(-2\ln(\frac{\alpha y}{b}) + \frac{\alpha y}{b} - 1),$$

$$v(\mathbf{r}) = \frac{pb(x^2+y^2)}{\alpha E y^4}(\frac{1}{2}(3x^2-y^2)\ln(\frac{\alpha y}{b}) + x^2(1-\frac{\alpha y}{b})). \tag{52}$$

In order to compare the explicit and numerical solutions, the panel has been discretized into 6400 four-node isoparametric rectangular finite elements and the following parameter values have been used.

$$b = 2m, \alpha = .5, p = 10^3 Pa, E = 2 \cdot 10^9 Pa, \nu = 0. \tag{53}$$

Figures 2 and 3 show the behavior of u and v, respectively, for $y = 2$ m and 3 m.

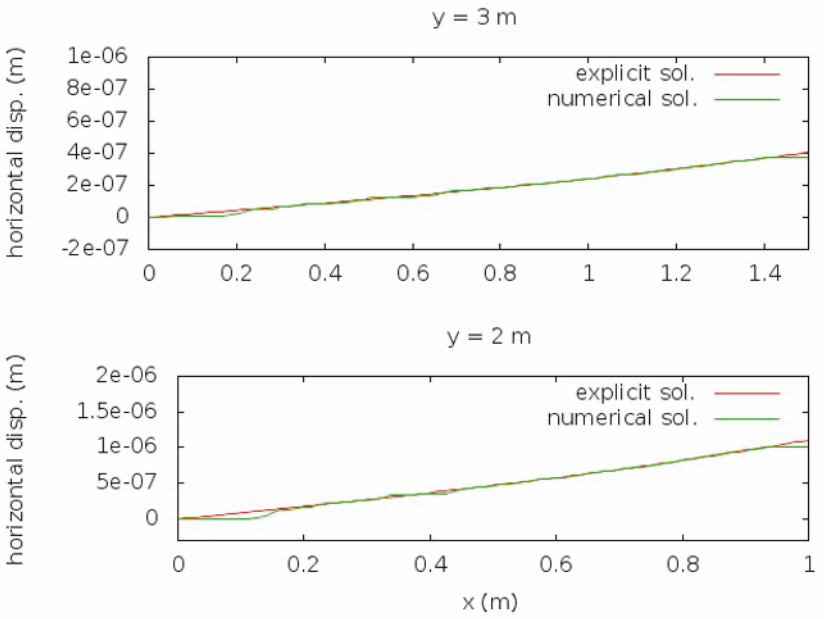

Figure 3. Horizontal displacement for $y = 2$ m and $y = 3$ m.

1.4 Example applications

In the early 1990s, the numerical method described in Section 2 was implemented in the finite element code named NOSA (16), (20), p. 145 by the Mechanics of Materials and Structures Laboratory of the ISTI-CNR Institute. Since then, the code has been applied to the study of several historical monuments (see (20), Ch. 7 and the bibliography for an account of these applications). The results of these numerical analyses were visualized using the graphic code MSC Mentat®. More recently, within the framework of the NOSA-ITACA project, funded by the Regione Toscana (23), the code has been integrated with the open-source platform SALOME (29).

Herein, we briefly describe an analysis of the cross vault of the Church of San Ponziano in Lucca. This study has been conducted by researchers at the ISTI-CNR Institute, who kindly made their results available to us, a contribution which we gratefully acknowledge (25).

The church (Fig. 4), which dates back to the 9th century, has recently undergone a complex series of restorations and functional adjustments. In

particular, the roofing structures, which had deteriorated over the centuries, were consolidated and partially reconstructed. Structurally, the church is constructed of load-bearing masonry with a rectangular plan divided into three aisles. The central aisle (nave) in correspondence to the presbytery area is covered by a constant-thickness cross, or groin, vault (Fig. 4), which is the focus of the present study. Sometime in the past a number of small solid-brick walls were built to support the beams, which therefore unloaded the weight of the roofing, the beams themselves and associated joists onto the cross vault, thereby giving rise to an asymmetrical distribution of concentrated loads.

The NOSA code has been used to study the compound structure made up of the cross vault overlying the altar, which represents the intersection of two toroidal surfaces, the arches delimiting it from the nave and lateral aisles, and the wall overlying the barrel vault of the apse area. The dimensions of the compound structure under examination are 9 m x 13.8 m in plan and 6.4 m in height. Static analyses of the structure were conducted by discretising it into 6040 nonconforming "shell" elements (12), subjected to their own weight and the concentrated loads on the extrados due to the walls, while at the same time accounting for the presence of reinforcement chains in the arches (fig. 7). The relevant values of Young's modulus and Poisson's ratio have respectively been assumed to be $5 \cdot 10^9$ Pa and 0.1, while the specific weight has been taken to be $2 \cdot 10^4$ N/m^3, and the thickness of the vault and arches 0.25 m and 0.60 m, respectively.

Regarding the boundary conditions, the vault's springers were considered to be immovably wedged onto the supporting pillars, and no movement of the arch extremities was moreover allowed in the direction of the generatices. This last condition was imposed by assuming that the stiffness of the vault's supporting and surrounding structures is such that any movement of the constraining bonds is severely limited.

Initially, an analysis was made of the structure subjected to its own weight alone. Analysis of the displacement field reveals a lowering of the vault in its central area and, regarding the arches, a lowering at the keystone accompanied by bulging in the area of the haunches. In any event, the relative displacement did not exceed 1.25 mm. An analysis of the entire compound structure enables concluding that the compressive stresses are below $13 \cdot 10^5$ Pa, a value considered acceptable. Analysis of the fracture strain components moreover excludes the presence of cracking in the cross vault.

Figures 8, 9 and 10 show plots of the maximum modulus eccentricities surface respectively for the arch towards the nave, for one of the arches towards a lateral aisle and for the cross vault. In all three cases, the surface

Figure 4. Transverse section of the Church of San Ponziano.

Figure 5. The roof vault of the presbytery area.

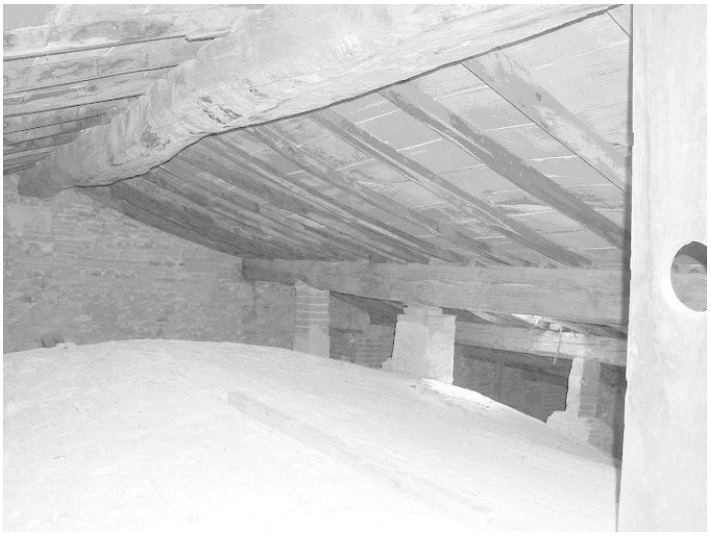

Figure 6. Extrados of the cross vault.

remains well within the thickness of the considered structural elements, thereby confirming the good overall static conditions of the vault.

Subsequently, a further analysis was conducted in order to evaluate the effects on the displacement and stress fields in the structure of the metal reinforcement chains in the arches toward the nave and the apse. The finite elements analysis reveals that the presence of the chains, modelled via 3 x 3 cm cross-sectional steel "beam" elements, has no significant influence on either the displacement or the stress field. The negligible effect of the chains is also highlighted by the modest degree of tension that they exert, below 11000 N.

Lastly, an analysis was conducted to account for both the self-weight of the structure, as well as the concentrated loads transmitted by the roof's load-bearing beams set on the walls arranged along the vault extrados. The arrangement of the walls is shown in the plan view illustration in figure 11. The analysis of the loads showed that each of the small walls transmits a vertical load of 37500 N to the vault. All told, the load due to the presence of the walls is about 12% of the weight of the entire structure, which is equal to $1.59\ 10^6$ N.

Figures 12 and 13 show plots of the vertical displacement of the vault

Figure 7. Finite element model of the cross vault and connected arches.

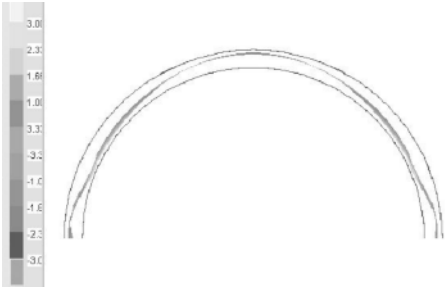

Figure 8. Maximum modulus eccentricities surface of the arch toward the nave.

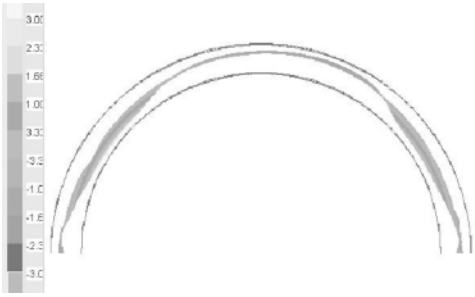

Figure 9. Maximum modulus eccentricities surface of the arch toward a lateral aisle.

Figure 10. Maximum modulus eccentricities surface of the cross vault.

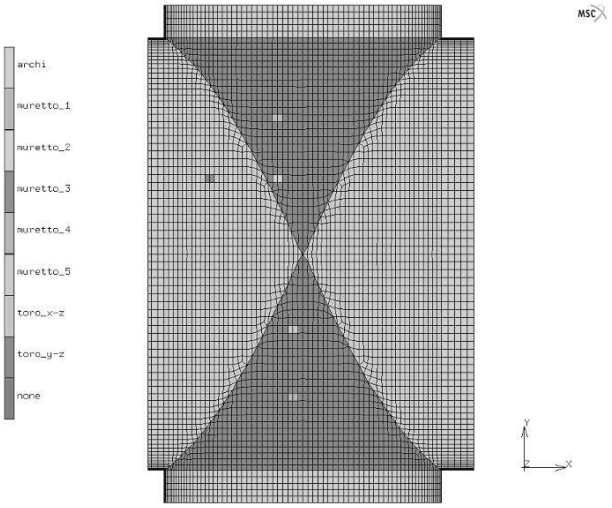

Figure 11. Plan of the cross vault with the walls sustaining the roof beams.

subjected to its self-weight alone, and when subjected to its self-weight plus the loads transmitted by the walls. A fair degree of variation is evident, especially in correspondence to the group of walls indicated as muretto_1, muretto_2 and muretto_3 in figure 11. In any case, the displacement values are very small and their variation quite unlikely to cause any significant changes in the fracture stress and strain fields. Moreover, once again under these loading conditions, the maximum modulus eccentricities surface is contained well within the thickness of the arches and the cross vault.

The study shows the potentials of the constitutive equation and numerical techniques described in the foregoing for analysing the structural behaviour of historical buildings and modelling any consolidation operations before undertaking them.

1.5 A numerical method for dynamic analysis of slender masonry structures

Due to the difficulties inherent in performing dynamic analyses of continuous masonry-like bodies (10), (11), recent research efforts have been directed at developing simplified constitutive models for masonry structures by representing them through one-dimensional elements. Such efforts have

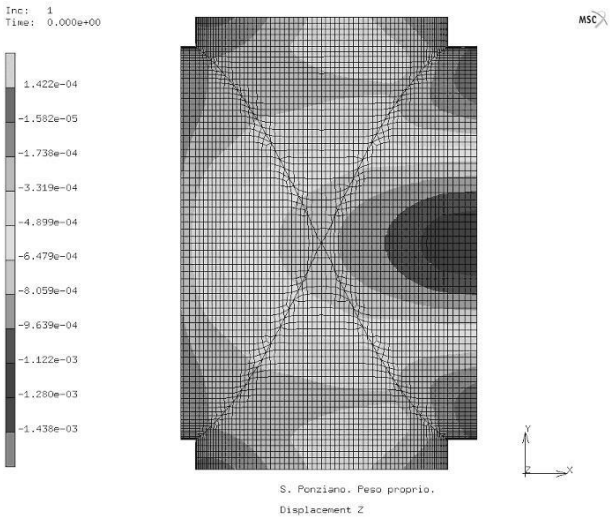

Figure 12. Vertical displacement (m) under self-weight alone.

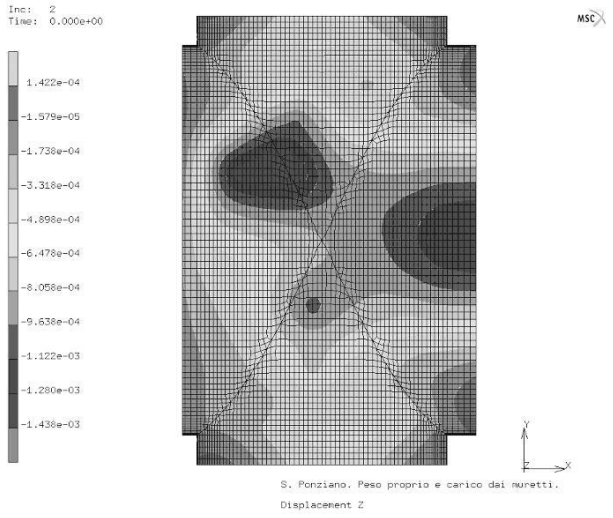

Figure 13. Vertical displacement (m) under both self-weight and loads transmitted by the walls.

given rise to a nonlinear constitutive equation for beams, which furnishes the generalized stress (normal force and bending moment) as a function of the generalized strain (extensional strain and curvature change of the beams longitudinal axis), by making the assumption that the material does not withstand tensile stresses in the longitudinal direction; variants of the model take into account the cases of unbounded, as well as bounded compressive strength (21).

This constitutive equation has revealed to be suitable for formulating and refining a simple numerical model which, implemented in the finite-element code MADY, developed at the Dipartimento di Costruzioni e Restauro, University of Florence (22), render almost effortless to perform non-linear dynamic analyses of slender masonry structures which exhibit primarily a flexural behaviour. Specifically, the model has been developed for both solid and hollow rectangular cross-sections in order to study masonry arches as well as free-standing masonry towers (19), (26).

From a practical standpoints, the proposed model has shown to be particularly suitable for the seismic analysis of slender towers: although it represents towers as one-dimensional continuum, it is refined enough to reveal the effects of the higher vibration modes that often affect them. Moreover, coupling phenomena between transverse and axial vibrations, which are widely recognized as an important factor in the seismic behaviour of slender towers, are also taken into account by the model, as they are embedded in the constitutive equation. The vertical components of earthquake excitations, often significant sources of additional damage to these structures, can also be introduced as input ground motions.

Furthermore, since the model accounts for the material's non-linear behaviour in all sections along the structure's height, it can be useful to obtain measures of local and global damage. Because the damage to such structures tends to be distributed along their height, rather than concentrated at the base alone, such measures can be meaningful, even if the assumed elasticity of the material does not allow for assessing the irreversibility of the damage process.

Firstly, we introduce the constitutive equation formulated for hollow, rectangular cross-section beams made of a non-linear elastic material with no resistance to tension and limited compressive strength σ_o.

By making the usual assumption of plane sections, according to the classical Euler-Bernoulli hypothesis, and accounting for axial stresses alone, the relation between generalized stress and strain can be determined as follows. For each longitudinal fiber, the considered constitutive equation is

$$\sigma(\bar{y}) = \begin{cases} \sigma_0 & \text{if } \epsilon(\bar{y}) \leq \epsilon_0, \\ E\epsilon(\bar{y}) & \text{if } \epsilon_0 \leq \epsilon(\bar{y}) \leq 0, \\ 0 & \text{if } \epsilon(\bar{y}) > 0, \end{cases} \tag{54}$$

where $\epsilon_0 = \sigma_0/E$ with E the Young modulus of the material. Thus, the pattern of the axial stress component σ in any given transverse section of the beam may be one of those described - with reference to the case $M < 0$, - in Fig. 14, plus the trivial cases for which σ is equal to zero or to σ_o over the entire section. The various cases differ from each other with regard to the position of the neutral axis - denoted as y_n - and the position of the axis where the stress reaches its limit value σ_o - denoted as y_s -, with respect to the section geometry. In Case 1, neither axis crosses the section, and the constitutive behaviour is linear elastic. In each of the Cases 2, 3 and 4, for which y_n crosses the section differently with respect to the hollow, cracking of the section occurs. Conversely, in Cases 5, 6 and 7, y_s crosses the section in three different positions, and the corresponding portion of the section is crushed. Lastly, the remaining cases represent all the possible situations in which cracking and crushing occur at the same time.

By the Euler-Bernoulli hypothesis, the ordinate of both y_n and y_s can be simply expressed as a function of ϵ and κ, that is

$$\epsilon(y_n) = \epsilon + \kappa y_n = 0, \epsilon(y_s) = \epsilon + \kappa y_s = \epsilon_o. \tag{55}$$

In order to define the constitutive relations, it is helpful to introduce the non-dimensionalized strains η and χ, given by

$$\eta = \frac{\epsilon}{\epsilon_o}, \quad \chi = \frac{\kappa h}{\epsilon_o}, \tag{56}$$

and to describe the geometric properties of the sections via the non-dimensionalized parameters

$$\alpha = \frac{h-t}{h}, \quad \beta = \frac{b-s}{b} \tag{57}$$

where b and $2h$ denote the section's dimensions, while $(b-s)$ and $2(h-t)$ denote those of the hollow in the x and y directions, respectively (Fig. 14, Case 1). Analogously, regarding the generalized stresses, it is useful to refer to the non-dimensionalized quantities

$$n = \frac{2N}{bh\sigma_o} \quad m = \frac{6M}{bh^2\sigma_o}. \tag{58}$$

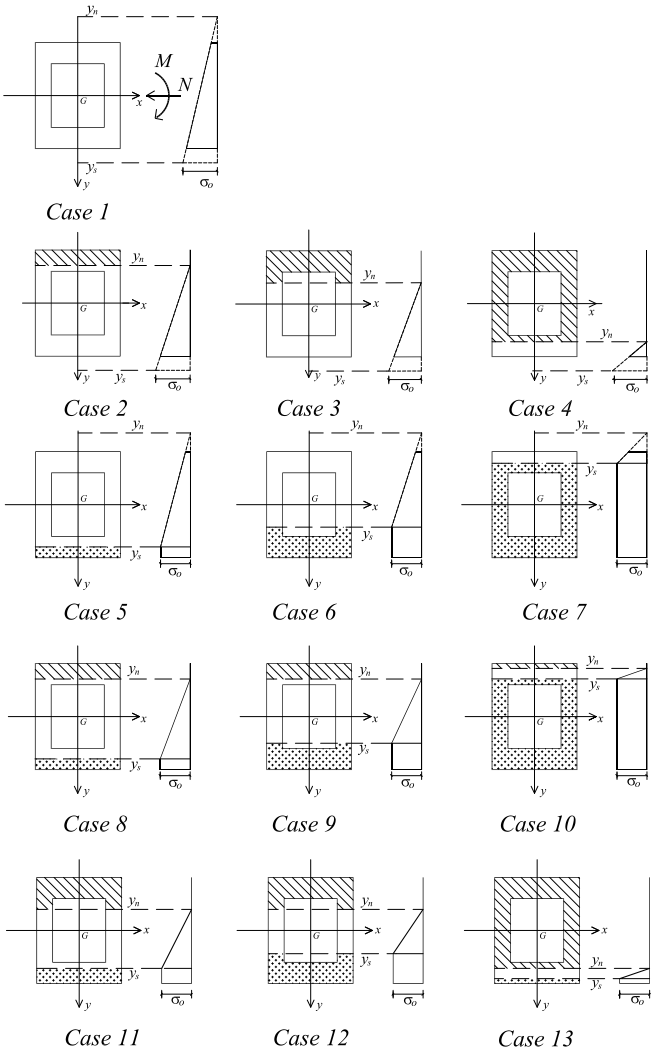

Figure 14. σ patterns over the cross-section.

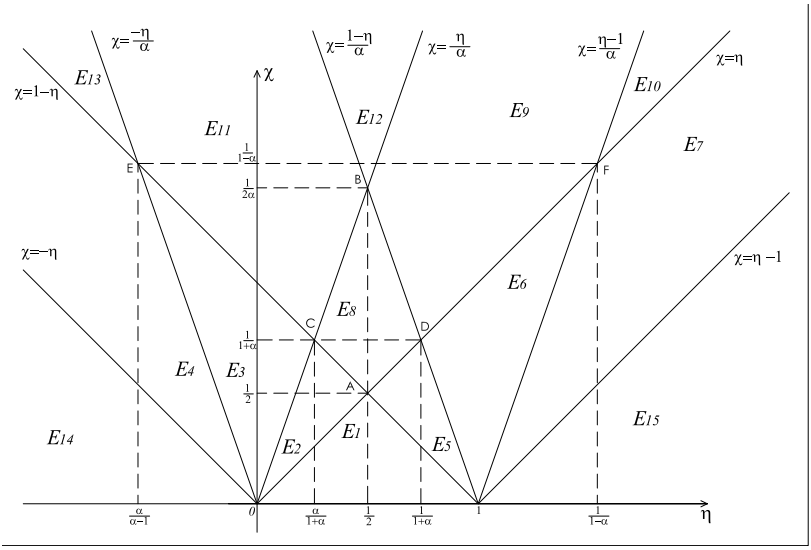

Figure 15. Partition in the half-plane (η, χ).

In view of (55), we can define different regions in the plane (η, χ), in which each of the illustrated σ patterns occur (Fig. 15). Due to the different distributions of σ, distinct constitutive relations expressing n and m as a function of η and χ hold for each region.

Thus, since from (55) and (56) we have

$$y_n = -\frac{\eta}{\chi}h, \quad y_s = \frac{1-\eta}{\chi}h, \tag{59}$$

in view of relations

$$\begin{cases} y_{\mathrm{n}} \leq -h \\ y_{\mathrm{s}} \geq h \end{cases} \tag{60}$$

identifying Case 1, the region of linear elastic behaviour is

$$E_1 = \{\chi \geq 0,\, \chi \leq \eta,\, \chi \leq 1-\eta\}\,.$$

In the same way for each of the twelve regions of non-linear behaviour $E_i, i = 2, ..13$, we obtain

$$\text{Case 2}: \begin{cases} -h \le y_n \le -\alpha h \\ y_s \ge h \end{cases} \quad E_2 = \left\{ \chi \ge 0, \chi \ge \eta, \chi \le \frac{\eta}{\alpha}, \chi \le 1-\eta \right\}$$

$$\text{Case 3}: \begin{cases} -\alpha h \le y_n \le \alpha h \\ y_s \ge h \end{cases} \quad E_3 = \left\{ \chi \ge 0, \chi \ge \frac{\eta}{\alpha}, \chi \ge -\frac{\eta}{\alpha}, \chi \le 1-\eta \right\}$$

$$\text{Case 4}: \begin{cases} \alpha h \le y_n \le h \\ y_s \ge h \end{cases} \quad E_4 = \left\{ \chi \ge 0, \chi \ge -\eta, \chi \le -\frac{\eta}{\alpha}, \chi \le 1-\eta \right\}$$

$$\text{Case 5}: \begin{cases} y_n \le -h \\ \alpha h \le y_s \le h \end{cases} \quad E_5 = \left\{ \chi \ge 0, \chi \le \eta, \chi \le \frac{1-\eta}{\alpha}, \chi \ge 1-\eta \right\}$$

$$\text{Case 6}: \begin{cases} y_n \le -h \\ -\alpha h \le y_s \le \alpha h \end{cases} \quad E_6 = \left\{ \chi \ge 0, \chi \le \eta, \ \chi \ge \frac{\eta-1}{\alpha}, \chi \ge \frac{1-\eta}{\alpha} \right\}$$

$$\text{Case 7}: \begin{cases} y_n \le -h \\ -\alpha h \le y_s \le \alpha h \end{cases} \quad E_7 = \left\{ \chi \ge 0, \chi \le \eta, \ \chi \ge \eta - 1, \chi \le \frac{\eta-1}{\alpha} \right\}$$

$$\text{Case 8}: \begin{cases} -h \le y_n \le -\alpha h \\ \alpha h \le y_s \le h \end{cases}$$

$$E_8 = \left\{ \chi \ge 0, \chi \ge \eta, \chi \le \frac{\eta}{\alpha}, \ \chi \le \frac{1-\eta}{\alpha}, \chi \ge 1-\eta \right\}$$

$$\text{Case 9}: \begin{cases} -h \le y_n \le -\alpha h \\ -\alpha h \le y_s \le \alpha h \end{cases}$$

$$E_9 = \left\{ \chi \ge 0, \chi \ge \eta, \chi \le \frac{\eta}{\alpha}, \chi \ge \frac{1-\eta}{\alpha}, \chi \ge \frac{\eta-1}{\alpha} \right\}$$

$$\text{Case 10}: \begin{cases} y_n \ge -h \\ y_s \le -\alpha h \end{cases} \quad E_{10} = \left\{ \chi \ge 0, \chi \ge \eta, \chi \le \frac{\eta-1}{\alpha} \right\}$$

$$\text{Case 11}: \begin{cases} -\alpha h \le y_n \le \alpha h \\ \alpha h \le y_s \le h \end{cases}$$

$$E_{11} = \left\{ \chi \ge 0,\, \chi \ge \frac{\eta}{\alpha}, \chi \ge -\frac{\eta}{\alpha},\, \chi \le \frac{1-\eta}{\alpha}, \chi \ge 1-\eta \right\}$$

$$\text{Case 12}: \begin{cases} y_n \ge -\alpha h \\ y_s \le \alpha h \end{cases} \quad E_{12} = \left\{ \chi \ge 0,\, \chi \ge \frac{\eta}{\alpha},\, \chi \ge \frac{1-\eta}{\alpha} \right\}$$

$$\text{Case 13}: \begin{cases} y_n \ge \alpha h \\ y_s \le h \end{cases} \quad E_{13} = \left\{ \chi \ge 0,\, \chi \le -\frac{\eta}{\alpha},\, \chi \ge 1-\eta \right\}$$

The partition of $E^- = \{(\eta, \chi) \mid \chi \le 0\}$ that corresponds to $M \ge 0$ is symmetric to that of E^+ with respect to η-axis.

For (η, χ) belonging to each region, n and m can be evaluated by means of simple equilibrium considerations, and the following cases can be distinguished:

$$(\eta, \chi) \in E_1 : \; n = 4\eta(1-\alpha\beta); \quad m = 4\chi(1-\alpha^3\beta).$$

$$(\eta, \chi) \in E_2 : \; n = \tfrac{\eta^2 + 2\eta\chi\,(1-2\alpha\beta) + \chi^2}{\chi}; \quad m = \tfrac{2\chi^3(1-2\alpha^3\beta) + 3\eta\chi^2 - \eta^3}{\chi^2}.$$

$$(\eta, \chi) \in E_3 : \; n = \frac{\eta^2(1-\beta) + 2\eta\chi(1-\alpha\beta) + \chi^2(1-\alpha^2\beta)}{\chi};$$

$$m = \frac{2\chi^3(1-\alpha^3\beta) + 3\eta\chi^2(1-\alpha^2\beta) - \eta^3(1-\beta)}{\chi^2}.$$

$$(\eta, \chi) \in E_4 : \; n = \frac{(\eta+\chi)^2}{\chi}; \quad m = \frac{2\chi^3 + 3\eta\chi^2 - \eta^3}{\chi}.$$

$$(\eta, \chi) \in E_5 : \{ n = -\frac{(\eta-1)^2 + 2\chi(2\alpha\beta\eta - \eta - 1) + \chi^2}{\chi};$$

$$m = \frac{2\chi^3(1-2\alpha^3\beta) + 3\chi^2(1-\eta) + (\eta-1)^3}{\chi^2}.$$

$$(\eta, \chi) \in E_6 : \; n = \frac{(\eta-1)^2(\beta-1) + 2\chi(\eta+1)(1-\alpha\beta) - \chi^2(1-\alpha^2\beta)}{\chi};$$

$$m = \frac{2\chi^3(1-\alpha^3\beta) + 3\chi^2(\alpha^2\beta(\eta-1) - \eta + 1) + (1-\beta)(\eta-1)^3}{\chi^2}.$$

$$(\eta,\chi)\in E_7: n=\frac{-(\eta-1)^2+2\chi(\eta+1-2\alpha\beta)-\chi^2}{\chi};$$

$$m=\frac{2\chi^3+3\chi^2(1-\eta)+(\eta-1)^3}{\chi^2}.$$

$$(\eta,\chi)\in E_8:\ n=\frac{2\eta(1-2\alpha\beta\chi)+2\chi-1}{\chi};$$

$$m=\frac{-4\alpha^3\beta\chi^3+3\chi^2-3\eta^2+3\eta-1}{\chi^2}.$$

$$(\eta,\chi)\in E_9: n=\frac{\beta\eta^2-2\eta(\alpha\beta\chi+\beta-1)+\alpha^2\beta\chi^2+2\chi(1-\alpha\beta)+(\beta-1)}{\chi};$$

$$m=\frac{-2\alpha^3\beta\chi^3+3\chi^2(\alpha^2\beta(\eta-1)+1)-\beta(\eta-1)^3-3\eta^2+3\eta-1}{\chi^2}.$$

$$(\eta,\chi)\in E_{10}:\ n=\frac{2\eta-4\alpha\beta\chi+2\chi-1}{\chi};\quad m=\frac{3\chi^2-3\eta^2+3\eta-1}{\chi^2}.$$

$$(\eta,\chi)\in E_{11}:\ n=\frac{-\beta\eta^2-2\eta(\alpha\beta\chi-1)-\alpha^2\beta\chi^2+2\chi-1}{\chi};$$

$$m=\frac{-2\alpha^3\beta\chi^3-3\chi^2(\alpha^2\beta\eta-1)+\beta\eta^3-3\eta^2+3\eta-1}{\chi^2}.$$

$$(\eta,\chi)\in E_{12}:\ n=\frac{2\eta(1-\beta)-2\chi(\alpha\beta-1)-(1-\beta)}{\chi};$$

$$m=\frac{3\chi^2(1-\alpha^2\beta)+(\beta-1)(3\eta^2-3\eta+1)}{\chi^2}.$$

$$(\eta,\chi)\in E_{13}: n=\frac{2\eta+2\chi-1}{\chi};\quad m=\frac{3\chi^2-3\eta^2+3\eta-1}{\chi^2}. \tag{61}$$

Once all the expressions for $\chi>0$ have been defined, the corresponding ones for $\chi<0$ can be easily obtained by using the appropriate symmetry properties.

It should be noted that for α or β equal to zero, i.e., when the section is solid, the constitutive equation defined above corresponds to that formulated in (30) for a rectangular cross-section beam. Moreover for $\sigma_o\to\infty$, we obtain the constitutive equation for no-tension beam with infinite compressive strength.

Regarding the admissible domain in the plane (n,m), it is a simple matter to verify that in order for the axial component σ of the stress to satisfy the inequality $\sigma_o\le\sigma\le 0$ at each point in the section, n must belong to

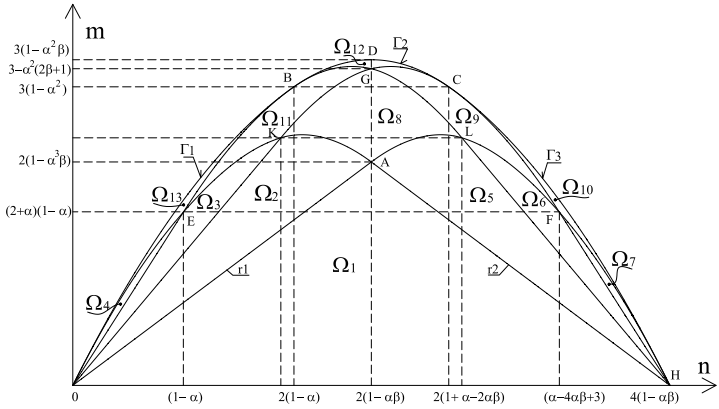

Figure 16. Admissible range in the (n, m) plane.

the interval $0 \leq n \leq 4(1-\alpha\beta)$. For each value of n, m must take on an expression that depends on the relation between the σ pattern and the section's geometry. Precisely, it assumes three different expressions, defining curves Γ_1, Γ_2, and Γ_3 which, as shown in Fig. 16, bound the admissible region $\Omega^+ = \{(n,m)\, 0 \leq n \leq 4(1-\alpha\beta), m \geq 0\}$.
Furthermore, the partition defined in region E^+ determines a partitioning of Ω^+ into thirteen regions, where the stress distributions are those identified by the thirteen different Cases in Fig. 14.
Equations of curves which bound regions shown in Fig. 16 have been omitted here for the sake of brevity.

Now, we briefly describe the method used to numerically integrate equations of motion considering the constitutive relation presented in the foregoing.
The well-known equations for transverse and axial vibrations of a beam (which as formulated herein includes the axial-force effects) are

$$m\frac{\partial^2 v}{\partial t^2} + \frac{\partial}{\partial z}\left(\frac{\partial M}{\partial z} + N\frac{\partial v}{\partial z}\right) - q = 0\,, m\frac{\partial^2 u}{\partial t^2} - \frac{\partial N}{\partial z} - p = 0 \qquad (62)$$

where z denotes the abscissa along the beam's axis, t the time; $M(z,t)$ and $N(z,t)$ denote the bending moment and axial forces, $v(z,t)$ and $u(z,t)$ the transverse and longitudinal displacements, $q(z,t)$ and $p(z,t)$ the trans-

verse and axial distributed loads, and m the mass per unit length of beam. The dynamic problem of the beam is governed by the equations (62) together with the strain-displacement relations

$$\chi = -\frac{\partial^2 v}{\partial z^2}\frac{h}{\epsilon_o}, \eta = \frac{\partial u}{\partial z}\frac{1}{\epsilon_o} \tag{63}$$

and the constitutive relations (61). Equations (62) and (63) together with (61) are solved numerically. Beams are discretized into finite elements and each node has three degrees of freedom: axial and transverse displacement plus rotation. The flexural problem is addressed by using Hermite shape functions, which guarantee the continuity of both the transverse displacement and rotation, while for the axial displacement linear shape functions are adopted (24). Moreover, the Newmark and the Newton-Raphson methods are used to obtain the numerical solution. As most of these techniques are standard, a detailed explanation has been omitted. Nevertheless, it should be noted that defining the element stiffness matrix $\hat{\mathbf{K}}^E$ requires calculating the derivatives of the generalized stress with respect to the generalized strain in each of the domain regions. Moreover, it should mentioned that two different contributions are accounted for defining $\hat{\mathbf{K}}^E$: the tangent stiffness matrix of the element $\hat{\mathbf{K}}_s^E$ and the so-called geometric-stiffness matrix $\hat{\mathbf{K}}_g^E$, which represents the tendency toward buckling induced by axial loads, with consequent reduction of the total stiffness matrix. In this regard, it is interesting to point out that, while the stiffness matrix $\hat{\mathbf{K}}_s^E$ is symmetrical in all regions of the admissible domain, $\hat{\mathbf{K}}_g^E$ is not, as detailed in (26).

Lastly, regarding the effects of viscous damping, these have been accounted for by including in the motion equation a constant viscous damping matrix, C, which is obtained as a linear combination of M and the initial elastic stiffness matrix K, as per the Rayleigh assumption.

Finally, an example application of the proposed model is presented. By referring to some of the typical characteristics of age-old, free-standing towers in Italy, the constant squared cross sectional tower is 40 m in height and 5.5 m in width, with walls of constant 1.5 m thickness. For the Youngs modulus, the mass density and the maximum compressive stress the values of E = 3000 MPa, ρ = 1900 kg/m^3 and σ_o = - 2.0 MPa have been chosen. The first flexural and axial periods of the structure in the linear elastic range are 1.19s and 0.12s, respectively. By way of example, the tower is subjected to the (main) horizontal and vertical components of the classical El Centro earthquake: the horizontal accelerogram (El Centro S00E, 18/05/1940) has a duration of 53.40 s and a PGA of 3.41 m/s^2, while the vertical com-

ponent exhibits a PGA of 2.02 m/s^2. The dynamic non-linear analysis is performed by assuming a viscous damping coefficient ν of 0.02 over the two flexural modes. The results are given in terms of y- and z-displacements at the tower's top, as well as two damage parameters F_v/V and C_v/V as a function of time. Such parameters represent, respectively, the volumes of cracked and crushed portions, non-dimensionalized to the tower's total volume. Figures 17 and 18 show comparisons of the response for the different cases: (i) the heavy line represents the response to the earthquake's actions obtained via the proposed model (LCS masonry), (ii) the dashed line indicates the response obtained via the proposed model when an unbounded compressive strenght is considered (UCS masonry).
Non-resistance to tension leads to amplifications of the horizontal displacements and elongation of the lateral period, which are caused by formation of the first cracked zones and the consequent loss of stiffness. When limited compressive strength is also considered, further amplification of the displacements occurs, together with elongated transverse and axial vibration periods. It is also interesting to note that significant coupling occurs between the axial and transversal vibrations in the non-linear range, as evinced by the time histories of the vertical displacements. Lastly, Figure 19 shows the distribution of the areas subjected to craking and crushing along the tower height at the instant of time at which the maximum of the C_v/V parameter occurrs.

Acknowledgement This research has been supported by the Regione Toscana (project tools for modelling and assessing the structural behaviour of ancient constructions: the NOSA-ITACA code, PAR FAS 2007-2013). This support is gratefully acknowledged. I would also like to thank C. Padovani, A. Pagni and G. Pasquinelli of the ISTI-CNR Laboratory of Mechanics of Materials and Structures for providing the study reported on in Section 4, as well as B. Pintucchi and N. Zani for their precious collaboration on drafting Section 5.

Bibliography

[1] Alfano G., Rosati L., Valoroso N., A numerical strategy for finite element analysis of no-tension materials. *Int. J. Numer. Meth. Engng*, vol. 48, pp. 317-350, 2000.

[2] Angelillo M., Cardamone L., Fortunato A., A new numerical model for masonry structures. J Mech. Mater. Stuct. 5, 583-615 (2010).

[3] Bathe K. J., Wilson E. L., *Numerical methods in finite element analysis*, Prentice-Hall, Inc., Englewood Cliffs, New Jersey, 1976.

[4] Bennati S., Barsotti R.: Optimum radii of circular masonry arches.

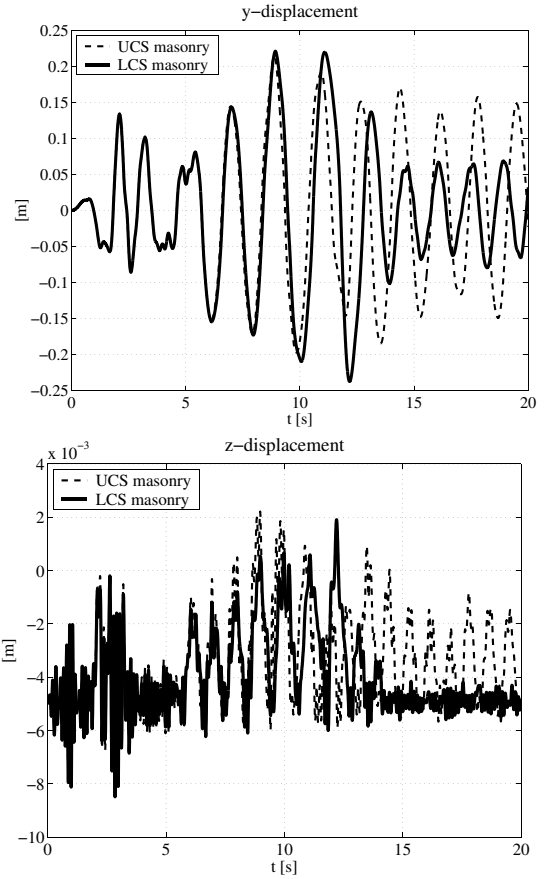

Figure 17. Time history of the trasversal and longitudinal displacements.

Proc. Third Int. Arch Bridges Confer., Paris (2001).

[5] Brenner S. C., Scott L. R. *The mathematical theory of finite element method*, Second edition, Springer 2002.

[6] Ciarlet P. G., *The finite element method for elliptic problems*. North-Holland Publishing Company, 1978.

[7] Cottle R. W., Pang J. S., Stone R. E., *The linear complementarity problem*. Academic Press Inc. 1992.

[8] Cuomo M., Ventura G., A complementary energy formulation of no tension masonry-like solids. *Computer Methods in Applied Mechanics and Engineering* 189, pp. 313-339, 2000.

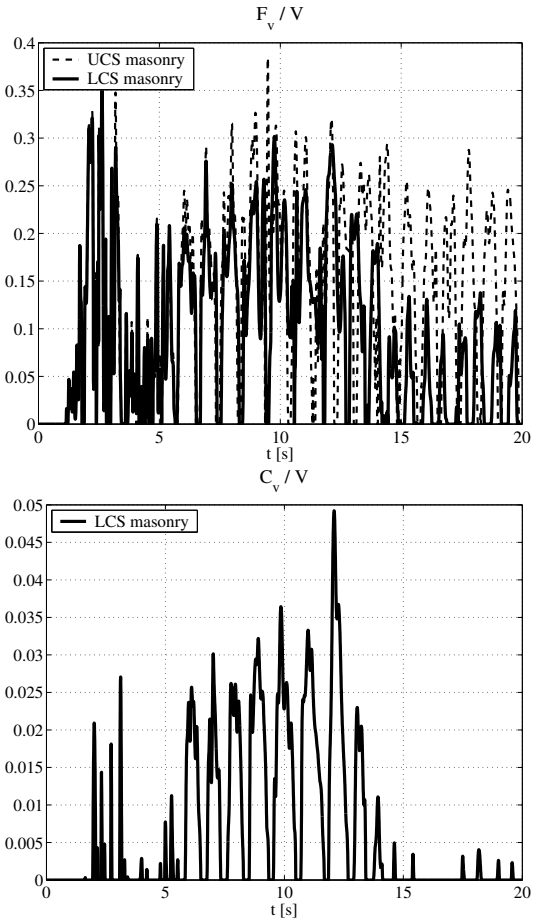

Figure 18. Time history of the damage parameters F_v/V and C_v/V.

[9] Dacorogna B.: Introduction to the Calculus of Variations. Imperial College Press, (2004).

[10] Degl'Innocenti S., Lucchesi M., Padovani C., Pagni A., Pasquinelli G., Zani N.: Dynamical analysis of masonry pillars. Proc. Third Int. Cong. on Science and Technology for the Safeguard of Cultural Heritage in the Mediterranean Basin, Alcalá de Henares, (2001).

[11] Degl'Innocenti, S., Padovani, C., Pagni, A., Pasquinelli, G.: Dynamic analysis of age-old masonry constructions. Proc. Eighth Inter. Conf. on Computational Structures Technology, B.H.V. Topping, G. Montero

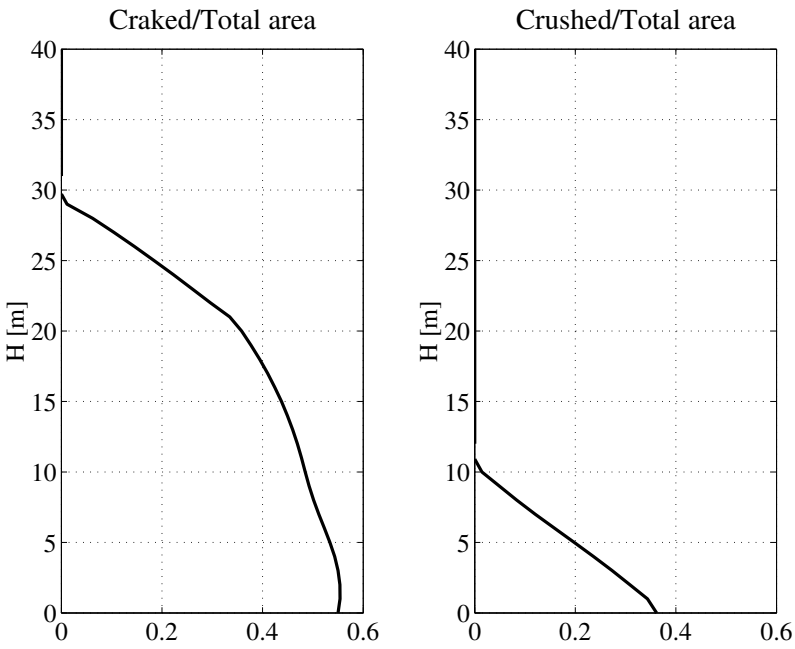

Figure 19. Distribution of the areas subjected to craking and crushing along the tower height.

and R. Montenegro(Editors), Civil-Comp Press, Stirlingshire, Scotland 2006. Las Palmas de Gran Canaria 12-15 Sept., (2006).

[12] Guidotti P., Lucchesi M., Pagni A., Pasquinelli G., *Application of shell theory to structural problem using the finite element method*. CNR-Quaderni de "La Ricerca Scientifica", 115, 1986.

[13] Gurtin M. E., *An introduction to continuum mechanics*. Academic Press, Boston, 1981.

[14] Lucchesi M., Padovani C., Pagni A., A numerical method for solving equilibrium problems of masonry-like solids. *Meccanica*, vol. 29, pp. 175-193, 1994.

[15] Lucchesi M., Padovani C., Pasquinelli G., Zani N., The maximum modulus eccentricity surface for masonry vaults and limit analysis. *Mathematics and Mechanics of Solids*, 4, pp. 71-87, 1999.

[16] Lucchesi M., Padovani C., Pagni A., Pasquinelli G., Zani N: COMES-NOSA A finite element code for non-linear structural analysis. Report CNUCE-B4-2000-003 (2000).

[17] Lucchesi M., Zani N., Some explicit solution to plane equilibrium problem for no-tension bodies. *Structural Engineering and Mechanics*, vol. 16, pp. 295-316, 2003.
[18] Lucchesi M., Padovani C., Pasquinelli G., Zani N., Static analysis of masonry vaults, constitutive model and numerical analysis. *Journal of Mechanics of Materials and Structures*, 2(2), pp. 211-244, 2007.
[19] Lucchesi M., Pintucchi B.: A numerical model for non-linear dynamic analysis of slender masonry structures. Eur. J. Mech. A. Solids, 26, 88-105, (2007).
[20] Lucchesi M., Padovani C., Pasquinelli G., Zani N.: Masonry Constructions: Mechanical Models and Numerical Applications. Lectures notes in applied and computational mechanics, Vol. 39, Springer Verlag (2008).
[21] Lucchesi M., Silhavy M., Zani N.: Equilibrium problems and limit analysis of masonry beams. J. Elasticity, 106, 165-188, (2012).
[22] Lucchesi M., Pintucchi B. Zani N.: MADY, a finite element code for dynamic analysis of slender masonry structures: Mathematical specifications and user manual (In preparation) (2013).
[23] http://www.nosaitaca.it/en/
[24] Oden J. T., Carey G. F., *Finite elements-Special problems in solid mechanics*, Vol. 5. Prenctice-Hall, Inc., Englewood Cliffs, New Jersey, 1984.
[25] Padovani C., Pagni A., Pasquinelli G.: Un codice di calcolo per l'analisi statica e il consolidamento di volte in muratura. Proc. WONDERmasonry - Workshop on design for rehabilitation of masonry structures, 145 - 153, P. Spinelli (ed.), (2006).
[26] Pintucchi B, Zani N.: Effects of material and geometric non-linearities on the collapse load of masonry arches. Eur. J. Mech. A. Solids, 28, 45-61, (2009).
[27] Romano G., Sacco E., Sulla proprietà di coassialità del tensore di fessurazione. Atti Ist. Scienza delle Costruzioni, Facoltà di Ingegneria, Napoli, n. 351, 1984.
[28] Sacco E., Modellazione e calcolo di strutture in materiale non resistente a trazione. *Rend. Mat. Acc. Lincei*, s. 9, vol. 1, pp. 235-258, 1990.
[29] http://www.salome-platform.org
[30] Zani N.: A constitutive equation and a closed form solution for no-tension beams with limited compressive strength. Eur. J. Mech. A. Solids, 23, 467-484, (2004).

Practical applications of unilateral models to Masonry Equilibrium

Maurizio Angelillo[‡]
[‡] Dipartimento di Ingegneria Civile, University of Salerno, Italy

Abstract This Chapter is devoted to the application of unilateral models to the stress analysis of masonry structures. Some 2d applications of what we call the simplified models for masonry, are discussed and studied. Though the essentially unilateral behaviour of masonry is largely recognized, some prejudices still persist on the possibility of making the No-Tension (NT) assumption a practical model for designing engineers. The results here presented demonstrate that the unilateral model for masonry can be a useful tool for modeling real masonry structures. In the exposition the critical points are emphasized and strategies to handle them are suggested, both for the most primitive model (namely the Rigid NT material), and for the more accurate Normal Elastic NT and Masonry-Like (ML)materials. The first tool here introduced for applying the No-Tension model to structures is the systematic use of singular stress and strain fields. Next a number of closed form solutions for NENT and ML materials is discussed. Finally a numerical approach based on descent is proposed for handling the zero-energy modes typical of unilateral materials. Some numerical solutions and comparisons with analytical solutions and test results are also presented.

This Chapter is dedicated to Giovanni Castellano who inspired most of my work on masonry since my early steps.

1 Basic tools

In this section the main notation and the basic notions of equilibrium and compatibility, in presence of singular stress and strain fields, are introduced. Singular strains are usually considered in perfect plasticity, and the use of singular stress fields (though in a mathematically unconscious way) has been around since the nineteenth century (see Mery (1840)). It is only fairly recently that Šilhavý, Lucchesi et al (see Lucchesi and Zani (2005)) , have put forward a rigorous mathematical formulation of stress field singularities. Chapters 2 and 3 of the present book are partly devoted to the mathematical exposition of these clever concepts within the theory of measures.

M. Angelillo (Ed.), *Mechanics of Masonry Structures*, CISM International Centre for Mechanical Sciences, DOI 10.1007/ 978-3-7091-1774-3_4, © CISM, Udine 2014

The formulation that is given here, instead, is rather informal and based mainly on geometrical arguments. A substantial knowledge of the mathematical theory of linear elasticity, such as that given in the monograph by Gurtin (1972), to which I refer for notations, is presumed. Familiarity with functional analysis is not strictly required, though some previous experience with elementary functional analysis in Sobolev spaces and variational methods (as can be found, for example, in the books by Kreyszig (1989) and Dym and Shames (1973)) would be of help.

The matter treated and analysed here is not entirely new. Much of what is reported, apart from the classical and more recent sources cited throughout the text, leans on a number of papers recently published, or under print or review, by myself or my reserch group. In particular, on singular stress: Angelillo et al. (2012) and Angelillo et al. (2013); on Limit Analysis for masonry: Angelillo and Fortunato (2013); on semianalitical solutions for panels: Fortunato (2010); on numerical methods for unilateral materials Angelillo et al. (2010).

1.1 Preliminaries

It is assumed that the body, a domain $\Omega \in \Re^n$ (here n=2), loaded by the given tractions $\underline{\mathbf{s}}$ on the part $\partial\Omega_N$ of the boundary, and subject to given displacements $\underline{\mathbf{u}}$ on the complementary, constrained part of the boundary $\partial\Omega_D$, is in equilibrium under the given surface displacements, tractions and body loads $(\underline{\mathbf{u}}; \underline{\mathbf{s}}, \mathbf{b})$[1] and undergoes displacements $\mathbf{u}$ and local deformations, so small that the infinitesimal strain $\mathbf{E}(\mathbf{u})$ is a proper strain measure.

Vectors and tensors are represented in Cartesian components, in a fixed frame $(0; x_1, x_2)$. Summation convention is adopted throughout the text.

1.2 Equilibrated stress fields, regularity of T

A stress field $\mathbf{T}$ is said to be *equilibrated* with $(\underline{\mathbf{s}}, \mathbf{b})$, if it satisfies the equilibrium equations

$$div\mathbf{T} + \mathbf{b} = \mathbf{0} \,,$$

and the traction boundary conditions

$$\mathbf{T}\mathbf{n} = \underline{\mathbf{s}} \,, \; on \; \partial\Omega_N \,,$$

$\mathbf{n}$ denoting the unit outward normal to $\partial\Omega$.

[1] Other possible data are the eigenstrains $\underline{\mathbf{E}}$; here I omit them from the analysis to simplify the exposition, though some special eigenstrains will be considered as data in some of the examples which follow.

$\mathbf{T}$ is a tensor function of $\mathbf{x} \in \Omega$, for which some kind of regularity must be assumed. If the differential equations of equilibrium are considered in a *strong sense*, the stress field $\mathbf{T}$ must be differentiable and its divergence must be continuous.

On adopting a variational formulation, if the material is linearly elastic, the minimal request for $\mathbf{T}$ is to be square summable, that is

$$\sqrt{\int_\Omega \mathbf{T} \cdot \mathbf{T} da} < \infty \, .$$

For some rigid perfectly plastic materials (such as rigid unilateral materials), less regular and even singular stresses may be admitted. The minimal request for such materials is that $\mathbf{T}$ be summable

$$\int_\Omega \sqrt{\mathbf{T} \cdot \mathbf{T}} da < \infty \, .$$

If one admits stress fields that are only summable, the set of competing functions enlarges to bounded measures, that is to summable distributions $\widetilde{\mathbf{T}}$:

$$\int_\Omega \left| \widetilde{\mathbf{T}} \right| < \infty \, ,$$

which, in general, can be decomposed into the sum of two parts

$$\widetilde{\mathbf{T}} = \widetilde{\mathbf{T}}_r + \widetilde{\mathbf{T}}_s \, ,$$

where $\widetilde{\mathbf{T}}_r$ is absolutely continuous with respect to the area measure (that is $\widetilde{\mathbf{T}}_r$ is a density per unit area) and $\widetilde{\mathbf{T}}_s$ is the singular part.

In the examples, the analysis will be restricted to bounded measures $\widetilde{\mathbf{T}}$ whose singular part is concentrated on a finite number of regular arcs, that is bounded measures admitting on such curves a density $\widetilde{\mathbf{T}}_s$ with respect to the length measure (that is special bounded measures with void Cantor part; for reference to these function spaces see Ambrosio et al. (2000)).

Remark 1. If the stress field is summable (and also if it is square summable), it is not differentiable in strong sense, and the equilibrium equations have to be reformulated in variational form (e.g. through the Virtual Work equation). Singular stresses require also special modifications of the boundary conditions; the trace of the stress $\mathbf{T}$ on the loaded part of the boundary is not given by $\mathbf{Tn}$ if $\mathbf{T}$ is singular. I shall come to this point later.$\diamond$

1.3 Compatible displacement fields, regularity of u

The displacement field $\mathbf{u}$ is said to be compatible if, besides being *regular enough* for the corresponding strain $\mathbf{E}(\mathbf{u})$ to exist [2], $\mathbf{u}$ satisfies the boundary conditions on the constrained part $\partial\Omega_D$ of the boundary

$$\mathbf{u} = \underline{\mathbf{u}} \ , \ on \ \partial\Omega_D \ .$$

For linearly elastic bodies, on adopting a variational formulation, the usual assumption is that $\mathbf{E}$ be square summable, that is

$$\sqrt{\int_\Omega \mathbf{E} \cdot \mathbf{E} da} < \infty \ .$$

For some rigid, perfectly plastic (or rigid unilateral) materials, it is sufficient to assume that $\mathbf{E}$ be summable

$$\int_\Omega \sqrt{\mathbf{E} \cdot \mathbf{E}} da < \infty \ .$$

As before, the set of competing functions enlarges to bounded measures, that is to summable distributions $\widetilde{\mathbf{E}}$; then the displacement $\mathbf{u}$ can admit finite discontinuities, i.e. $\mathbf{u}$ can be a function with bounded variation. If $\mathbf{E}$ were the whole gradient of $\mathbf{u}$, the summability of $\mathbf{E}$ would entail: $\mathbf{u} \in BV(\Omega)$, exactly. Since $\mathbf{E}$ is only the symmetric part of $\nabla\mathbf{u}$, $\mathbf{u}$ must belong to a larger space: $BD(\Omega)$. The strain corresponding to $\mathbf{u}$ is again a bounded measure

$$\int_\Omega \left|\widetilde{\mathbf{E}}\right| < \infty \ ,$$

which, in general, can be decomposed into the sum of two parts

$$\widetilde{\mathbf{E}} = \widetilde{\mathbf{E}}_r + \widetilde{\mathbf{E}}_s \ ,$$

where $\widetilde{\mathbf{E}}_r$ is absolutely continuous with respect to the area measure (that is $\widetilde{\mathbf{E}}_r$ is a density per unit area) and $\widetilde{\mathbf{E}}_s$ is the singular part.

$\widetilde{\mathbf{E}}_s$ has support on the union of a set of linear 1d measure (the jump set of $\mathbf{u}$) and a set of fractional measure.

For simplicity, in the examples, I shall restrict to bounded measures $\widetilde{\mathbf{E}}$ whose singular part is concentrated on a finite number of regular arcs, that is bounded measures admitting on such curves a density $\widetilde{\mathbf{E}}_s$ with respect

[2] Recall that, here, $\mathbf{E}(\mathbf{u})$ is the infinitesimal strain

to the length measure (that is special bounded measures with void Cantor part).

Remark 2. If $\mathbf{u} \in BD(\Omega)$, that is $\mathbf{u}$ can be discontinuous, the b.c. $\mathbf{u} = \underline{\mathbf{u}}$ on $\partial\Omega_D$ makes no sense. A way to keep alive the b.c. of Dirichelet type is to identify the masonry body rather than with the domain Ω (usually an open set) with the set $\Omega \cup \partial\Omega_D$ and to assume that $\mathbf{u}$ must comply with the constraint $\mathbf{u} = \underline{\mathbf{u}}$ on the *skin* $\partial\Omega_D$, admitting possible singularities of the strain at the constrained boundary. Then, from here on, I shall deviate from standard notation referring to Ω as to the set $\Omega \cup \partial\Omega_D$. $\diamond$

Given the displacement field $\mathbf{u}$ of $\mathbf{x}$, by taking the gradient of $\mathbf{u}$, in a classical sense if $\mathbf{u}$ is regular, and in a generalized sense if $\mathbf{u}$ is singular, the strain $\mathbf{E}(\mathbf{u})$ is derived. *Vice versa*, if $\mathbf{E}$ of $\mathbf{x}$ is given, the possibility of integrating the components $E_{\alpha\beta}$ to get the (possibly discontinuous) components u_α of $\mathbf{u}$, is submitted to the necessary compatibility conditions (also sufficient if Ω is simply connected)

$$E_{11,22} + E_{22,11} - 2E_{12,12} = 0 \ ,$$

where a comma followed by an index, say α, means differentiation with respect to x_α.

The reader will see in what follows, that, on admitting discontinuous displacements, this condition can be reinterpreted in a generalized sense and applied (with some care), also to discontinuous, and even singular, strains.

1.4 Dirac deltas: a familiar example

For the unilateral models that here are adopted for masonry materials, it makes sense to admit singular stresses and strains, that is stress fields $\mathbf{T}$ and strain fields $\mathbf{E}$ that can be concentrated on lines (line Dirac deltas). In mathematical terms these are not functions in a strict sense, since they assign finite values to all points $\mathbf{x} \in \Omega$, except to those belonging to a set of lines of $\Omega \cup \partial\Omega_D$, to which infinite values are associated. Anyway, these infinite values must be such that these stresses or strains be summable, that is

$$\int_\Omega |\mathbf{T}| < \infty \ , \ \int_\Omega |\mathbf{E}| < \infty \ ,$$

or, in other words, $\mathbf{T}$ and $\mathbf{E}$ must be bounded measures. Here I call $M(\Omega)$ the set of bounded measures on $\Omega \cup \partial\Omega_D$. Line Dirac deltas are special bounded measures; a simple example of a Dirac delta in 1d, is the concentrated load on a beam, that is a point Dirac delta (Figure 1).

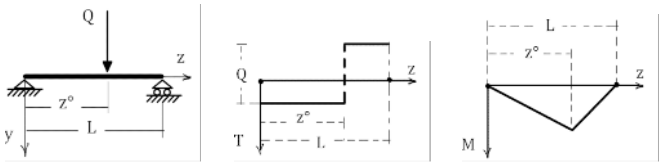

Figure 1. Concentrated transverse force Q on a beam: (a). Corresponding internal shear force T: (b), and bending moment M: (c).

From elementary beam theory the internal moment M, the shear force T and the transverse load per unit length q, are related by the differential equilibrium relations

$$M' = T\,,\ T' = -q\,,$$

where *prime* denotes differentiation with respect to z.

The previous equilibrium conditions admit also the following integral form

$$T(z) = T(0) - \int_0^z q\ ,\ M(z) = M(0) + \int_0^z T\ .$$

The second set of equations have sense also if q is a concentrated force, that is a Dirac delta:

$$q(z) = Q\delta(z^o)\ ,$$

Q being the intensity of the load, $\delta(.)$ the unit Dirac delta, z^o the point of application of the force.

The unit point Dirac delta applied at z^o is defined as follows

$$\int_{z^o-\epsilon}^{z^o+\epsilon} \delta(z^o) = 1\ ,\ \forall \epsilon > 0\ .$$

The differential equations can be extended to the case of singular loads by interpreting -q in Figure 1a as the generalized derivative of T in Figure 1b.

More generally, in 1d, the generalized derivative of a piecewise constant function f is a distribution whose regular part is zero and whose singular part has support on the jump set of f. Therefore a piecewise constant function is a special BV function whose singular part consists of point Dirac deltas applied at the points of discontinuity of f. The integral of such Dirac deltas across any point of discontinuity gives the value of the jump of f, at that point.

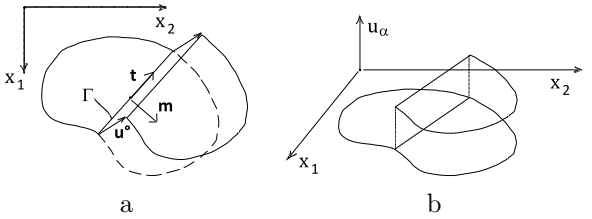

Figure 2. Discontinuous displacement alog a straight line Γ, unit tangent **t** and normal **m** to Γ: (a). Graph of the generic component u_α, a BV function: (b).

1.5 Singular stress and strain as line Dirac deltas

In what follows I will restrict to consider stress and strain fields that are special bounded measures, namely Dirac deltas with support on a finite number of regular arcs, and look at the restrictions imposed on these singular fields by equilibrium and compatibility, respectively.

Strain. In what follows, special displacement fields of bounded variation will be considered. In particular, restricting to discontinuous displacement fields **u** having finite discontinuities on a finite number of regular arcs Γ, the strain $\mathbf{E}(\mathbf{u})$ consists of a regular part $\mathbf{E}_r$, that is a diffuse deformation over $\Omega - \Gamma$, and a singular part $\mathbf{E}_s$ in the form of a line Dirac delta, concentrated on Γ.

The jumps of **u** along Γ, can be interpreted as fractures. In Figure 2a, to which I refer for notations, a crack separating the body Ω into two parts, $\wp_1$ and $\wp_2$, along a straight interface Γ, is represented. On such a line, the jump of **u**:

$$[[\mathbf{u}]] = \mathbf{u}^+ - \mathbf{u}^- \ .$$

due to a relative translation of the two parts, is considered. Here $\mathbf{u}^+$ is the displacement on the side of Γ where **m** points

The displacement field is a piecewise constant vector field, discontinuous on Γ; the graph of a generic Cartesian component of **u**, is depicted in Figure 2b.

The jump of **u** can be decomposed into normal and tangential components

$$\Delta v = [[\mathbf{u}]] \cdot \mathbf{m} \ , \ \Delta w = [[\mathbf{u}]] \cdot \mathbf{t} \ ,$$

where $\mathbf{t}, \mathbf{m}$ are the unit tangent and normal to Γ, represented in Figure 2a. Notice that, on any crack, incompenetrability of matter requires $\Delta v \geq 0$ (a unilateral restriction).

The strain $\mathbf{E}$ corresponding to the piecewise constant field $\mathbf{u}$ depicted in Figure 2b, is zero everywhere on $\Omega - \Gamma$ and is singular on Γ:

$$\mathbf{E}(\mathbf{u}) = \delta(\Gamma)(\Delta v \mathbf{m} \otimes \mathbf{m} + \frac{1}{2}\Delta w \mathbf{t} \otimes \mathbf{m} + \frac{1}{2}\Delta w \mathbf{m} \otimes \mathbf{t}) \ .$$

Stress. If the stress field $\mathbf{T}$ is non-singular (say $\mathbf{T} \in L^2(\Omega)$), on a possible discontinuity line Γ, for equilibrium, the stress emerging on Γ must be continuous. Then at any regular point of Γ, denoting $\mathbf{m}$ the unit normal to Γ, the stress $\mathbf{T}$ must satisfy the condition

$$(\mathbf{T}^+ - \mathbf{T}^-)\mathbf{m} = \mathbf{0} \ ,$$

$\mathbf{T}^+$ being the stress on the side of Γ where $\mathbf{m}$ points. Then, if $\mathbf{T} \in L^2(\Omega)$, the possible jumps of $\mathbf{T}$ must be restricted to the part of $\mathbf{T}$ non-emerging on Γ.

If $\mathbf{T}$ is singular, say a Dirac delta on Γ, also the part of $\mathbf{T}$ emerging on Γ can be discontinuous. The unbalanced emerging stress

$$\mathbf{q} = (\mathbf{T}^+ - \mathbf{T}^-)\mathbf{m} \ ,$$

in equilibrium, must be balanced by the stress concentrated on Γ (Figure 3). Referring for notations to Figure 3, the representation of the singular part $\mathbf{T}_s$ of $\mathbf{T}$ on Γ, is

$$\mathbf{T}_s = N\delta(\Gamma)\mathbf{t} \otimes \mathbf{t} \ .$$

For equilibrium, calling p, q the components of $\mathbf{q}$ in the tangential and normal directions, and denoting ρ the curvature of Γ, the following equations must hold

$$N' + p = 0 \ , \ N\,\rho + q = 0 \ .$$

Therefore q must be zero if Γ is straight.

Kinks. Though the singularity lines Γ, for the stress $\mathbf{T}$, that I consider are a.e. smooth, they can have kinks and multiple points. At such nodes the equilibrium of forces transmitted to the nodes must be satisfied; then if the node is inside the body and there are no concentrated external forces applied to the node there must be at least a triple junction.

Airy's stress function and singular stresses. In absence of body forces ($\mathbf{b}$=$\mathbf{0}$), the equilibrium equations admit the following solution in terms of a scalar function F:

$$T_{11} = F_{,22} \ , \ T_{22} = F_{,11} \ , \ T_{12} = -F_{,12} \ .$$

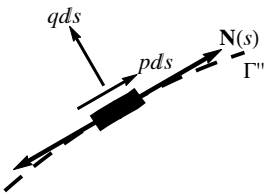

Figure 3. Stress singularity: forces acting on the curve Γ.

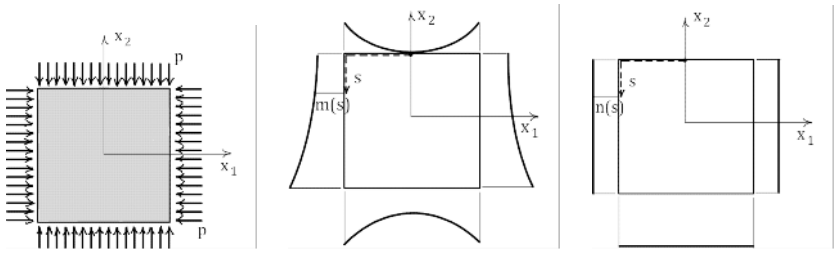

Figure 4. Square panel under uniform pressure: (a). Corresponding boundary value $m(s)$: (b), and normal slope $n(s)$: (c).

This is the general solution of the equilibrium equations, if the loads are *self-balanced* on any closed boundary delimiting Ω (see Gurtin (1972)).

The b.c. $\mathbf{T}\ \mathbf{n} = \underline{\mathbf{s}}$ on $\partial\Omega_N$, must be reformulated in terms of F. Denoting $\mathbf{x}(s)$ the parametrization of $\partial\Omega_N$ with the arc length, the b.c. on F are:

$$F(s) = m(s)\ ,\ \frac{dF}{d\nu} = n(s)\ ,\ on\ \partial\Omega_N\ ,$$

in which $dF/d\nu$ is the normal derivative of F at the boundary (that is the slope of F in the direction of $\mathbf{n}$) and $m(s)$, $n(s)$ are the moment of contact and the axial force of contact produced by the tractions $\underline{\mathbf{s}}(s)$, on a beam structure having the same shape of $\partial\Omega$, and cut at the point s=0.

A simple example is shown in Figure 4.

Regular and singular equilibrated stress fields can be derived by stress functions meeting the prescribed b.c. on F and $dF/d\nu$. A regular stress field is represented by a smooth F (see Figure 5a), a singular stress field by a continuous but folded F (Figure 5b). The projection of a fold of F on Ω is

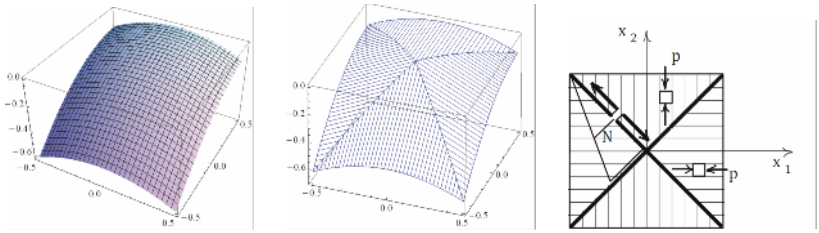

a b c

Figure 5. Square panel under uniform pressure. Smooth Airy's stress function giving homogeneous pressure inside the body: (a); folded Airy's function: (b); representation of the uniaxial and singular stress field corresponding to the folded Airy's function: (c).

called folding line and is denoted Γ. On a fold of F, the second derivative of F, with respect to the normal $\mathbf{m}$ to the folding line Γ, is a Dirac delta with support on Γ. Therefore, along Γ the Hessian $\mathbf{H}(F)$ of the stress function F is a dyad of the form

$$\mathbf{H}(F) = \Delta_m F \delta(\Gamma) \mathbf{m} \otimes \mathbf{m} \, ,$$

$\Delta_m F$ denoting the jump of slope of F in the direction of the normal $\mathbf{m}$ to Γ (see Figure 5c). Recalling the Airy's relation, the corresponding singular part of the stress is

$$\mathbf{T}_s = N \delta(\Gamma) \mathbf{t} \otimes \mathbf{t} \, ,$$

where the axial contact force N is given by

$$N = \Delta_m F \, .$$

2 Model *zero* (RNT)

In this section the main ingredients of the theory concerning the most primitive model for masonry materials, namely the Rigid No-Tension (RNT) material, are presented. After introducing the constitutive assumptions, the definitions of statically admissible and kinematically admissible fields are given, and the compatibility of loads and distortions is discussed. The RNT model allows for the application of the theorems of Limit Analysis: the formulation of the static and kinematic theorems for rigid-unilateral materials is given and a number of illustrative examples is developed.

2.1 Constitutive restrictions and equilibrium problem

It is assumed that the body $\Omega \in \Re^n$ (here $n = 2$), loaded by the given tractions $\underline{\mathbf{s}}$ on the part $\partial\Omega_N$ of the boundary, and subject to given displacements $\underline{\mathbf{u}}$ on the complementary, constrained part of the boundary $\partial\Omega_D$, is in equilibrium under the action of such given surface displacements and tractions, besides body loads $\mathbf{b}$ and distortions $\underline{\mathbf{E}}$ (the set of data being denoted: $(\underline{\mathbf{u}}, \underline{\mathbf{E}}; \underline{\mathbf{s}}, \mathbf{b})$), and undergoes small displacements $\mathbf{u}$ and strains $\mathbf{E}(\mathbf{u})$[3].

I point out that here the masonry structure is identified with the set: $\Omega = \Omega \cup \partial\Omega_D$, i.e. it is considered closed on $\partial\Omega_D$ and open on the rest of the boundary.

I consider that the body Ω is composed of Rigid No-Tension material, that is the stress $\mathbf{T}$ is negative semidefinite

$$\mathbf{T} \in Sym^{-} \ , \tag{1}$$

the effective strain $\mathbf{E}^* = \mathbf{E}(\mathbf{u}) - \underline{\mathbf{E}}$ is positive semidefinite

$$\mathbf{E}^* \in Sym^{+} \ , \tag{2}$$

and the stress $\mathbf{T}$ does no work for the corresponding effective strain $\mathbf{E}^*$

$$\mathbf{T} \cdot \mathbf{E}^* = 0 \ . \tag{3}$$

The effective strain E^* is a positive definite tensor field doing no work for the corresponding stress, and representing detachment fractures (that is type 1. fractures, see Sect.2, Chap.1). E^* is a sort of "reaction" deformation associated to the constraint on stress (1), and, therefore, is also called latent strain. In order to avoid trivial incompatible loads ($\underline{\mathbf{s}}$,$\mathbf{b}$), it is assumed that the tractions $\underline{\mathbf{s}}$ satisfy the condition

$$\underline{\mathbf{s}} \cdot \mathbf{n} < 0 \ , \ or \ \underline{\mathbf{s}} = \mathbf{0}, \ \forall \mathbf{x} \in \partial\Omega_N \ . \tag{4}$$

Notice that in the plane case (n=2) conditions (1), (2), can be rewritten as

$$tr\,\mathbf{T} \leq 0 \ , \ det\,\mathbf{T} \geq 0 \ , \tag{5}$$

$$tr\,\mathbf{E}^* \geq 0 \ , \ det\,\mathbf{E}^* \geq 0 \ . \tag{6}$$

[3]When eigenstrains are considered, under the small strain assumption, the total strain $\mathbf{E}(\mathbf{u})$ is decomposed additively as follows: $\mathbf{E}(\mathbf{u}) = \mathbf{E}^* + \underline{\mathbf{E}}$, $\mathbf{E}^*$ being the *effective* strain of the material.

2.2 Statically admissible stress fields

An equilibrated stress field $\mathbf{T}$ (that is a stress field $\mathbf{T}$ balanced with the prescribed body forces $\mathbf{b}$ and the tractions $\underline{\mathbf{s}}$ given on $\partial\Omega_N$) satisfying the unilateral condition (1) (that is conditions (5)), is said *statically admissible* for a RNT body. The set of statically admissible stress fields is denoted H and is defined as follows

$$H = \left\{ \mathbf{T} \in S(\Omega) \; s.t. \; div\mathbf{T} + \mathbf{b} = \mathbf{0} \; , \; \mathbf{Tn} = \underline{\mathbf{s}} \; on \; \partial\Omega_N \; , \; \mathbf{T} \in Sym^- \right\} \; , \quad (7)$$

$S(\Omega)$ being a function space of convenient regularity. Since for RNT materials, discontinuous and even singular stress fields will be considered, one can assume $S(\Omega) = M(\Omega)$, that is the set of bounded measures.

For Elastic No-Tension (ENT) materials a sensible choice is $S(\Omega) = L^2(\Omega)$, that is the function space of square summable functions.

Actually the space $M(\Omega)$ contains $L^2(\Omega)$ and is much larger than it, that is the set of functions which compete for equilibrium is richer for RNT than for ENT materials; this fact makes easier for RNT materials the search of s.a. stress fields.

The differential equations of equilibrium must be reformulated for non smooth $\mathbf{T}$, since the derivatives of $\mathbf{T}$ do not exist in a classical sense[4]. One way to do it is to impose equilibrium in a variational form, namely by using the Virtual Work Principle.

On introducing the set of virtual displacements

$$\delta K = \{ \delta\mathbf{u} \in S^*(\Omega) \; s.t. \; \delta\mathbf{u} = \mathbf{0} \; on \; \partial\Omega_D \} \; , \quad (8)$$

the stress field $\mathbf{T}$ is balanced with ($\underline{\mathbf{s}}$,$\mathbf{b}$) if and only if

$$\int_{\partial\Omega_N} \underline{\mathbf{s}} \cdot \delta\mathbf{u} + \int_\Omega \mathbf{b} \cdot \delta\mathbf{u} = \int_\Omega \mathbf{T} \cdot \mathbf{E}(\delta\mathbf{u}) \; , \; \forall \delta\mathbf{u} \in \delta K \, . \quad (9)$$

$S^*(\Omega)$ is a function space of convenient regularity. If $\mathbf{T} \in L^2(\Omega)$, then $S^*(\Omega) = H^1(\Omega)$ guarantees the finiteness of the internal work. If $\mathbf{T} \in M(\Omega)$, the choice $S^*(\Omega) = C^1(\Omega)$ ensures the possibility of computing the internal virtual work.

[4] For singular stress fields, even the b.c. on the emerging tractions must be changed, since the *Cauchy argument* leading to them, is restricted to absolutely continuous stress vectors.

2.3 Fundamental partition

To any statically admissible stress field $\mathbf{T}$ one can associate the following partition of the domain $\Omega = \Omega \cup \partial\Omega_D$:

$$\Omega_1 = \{\mathbf{x} \in \Omega \; s.t. \; tr\mathbf{T} \leq 0 \; , \; det\mathbf{T} \geq 0\} \; , \tag{10}$$

$$\Omega_2 = \{\mathbf{x} \in \Omega \; s.t. \; tr\mathbf{T} \leq 0 \; , \; det\mathbf{T} = 0\} \; , \tag{11}$$

$$\Omega_3 = \{\mathbf{x} \in \Omega \; s.t. \; \mathbf{T} = 0\} \; . \tag{12}$$

On introducing the spectral decomposition of $\mathbf{T}$:

$$\mathbf{T} = \sigma_1 \, \mathbf{k}_1 \otimes \mathbf{k}_1 + \sigma_2 \, \mathbf{k}_2 \otimes \mathbf{k}_2 \; ,$$

in Ω_1 the stress is of biaxial compression, that is $\sigma_1 < 0$, $\sigma_2 < 0$; in Ω_2 the stress is of uniaxial compression, that is $\mathbf{T}{=}\sigma \, \mathbf{k} \otimes \mathbf{k}$, $\sigma < 0$; Ω_3 is inert.

Notice that the form and the regularity of these regions depend on the smoothness of $\mathbf{T}$, and that such regions can be rather weird if one admits $\mathbf{T} \in M(\Omega)$. We will see in what follows that, on admitting only special bounded measures (i.e. Dirac deltas with support on a finite number of regular arcs), the regions Ω_i can degenerate, but the *fundamental partition* can be still easily identified.

Remark 3. In the Ω_2 regions, that is where the stress is of uniaxial compression, a classical theorem of *Tension Field Theory* (see *Subsection* 3.8 and Remark 9), states that (as the intuition suggests, see below and Figure 6) the lines of principal compression (tension in the case of TFT) form a family of straight lines if the body forces vanish.

A simple geometrical proof of this statement can be obtained by observing that, the equilibrium of a material tube contained in between two such infinitesimally spaced principal lines, is possible only if the tube is straight and the internal axial force of contact N is constant (see Figure 6).

If the two contiguous lines are parallel the stress itself is constant. If the two lines converge, on denoting R the distance between the point P and the point of intersection of the two lines, and introducing the arc length s along the ray from the origin P, calling $\sigma(s)$ and σ° the stress at Q and the stress at P, for equilibrium, the stress along the ray takes the form

$$\sigma(s) = \frac{R}{R-s}\sigma^\circ \; .$$

$\diamond$

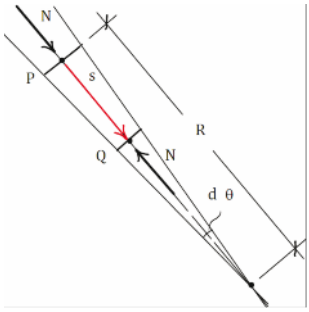

Figure 6. Stress along a compression ray.

2.4 Concavity of the Airy's stress function

In absence of body forces, a statically admissible stress field can be expressed[5] in terms of a scalar function F (called *Airy's solution*, see *subsection* 1.5).

The constraint (5), translated in terms of F, reads

$$tr\,\mathbf{T} = F_{,11} + F_{,22} \leq 0\ ,\ det\,\mathbf{T} = F_{,11}\,F_{,22} - F_{,12}^2 \geq 0\ , \tag{13}$$

then the Hessian $\mathbf{H}(F)$ of F, is negative semidefinite and the stress function F must be concave. Therefore, in absence of body forces $\mathbf{b}$, the equilibrium problem for a NT material, can be formulated as the search of a concave function F, taking on the part $\partial\Omega_N$ of the boundary, a specified value and a specified slope.

Example. As a simple example of an *equilibrium problem*, I consider the traction problem depicted in Figure 7a. Smooth and singular statically admissible stress fields can be easily derived from simple stress functions matching the given boundary data.

A smooth solution can be derived from the stress function (here L=1 is assumed):

$$F = \begin{cases} -\frac{3}{2}p + 2px_2\ ,\ x_2 < \frac{1}{2}(1-x_1^2)\ , \\ -\frac{1}{2}px_1^2 - 2p\frac{(1-x_2^2)^2}{1+x_1^2}\ ,\ x_2 \geq \frac{1}{2}(1-x_1^2)\ . \end{cases}$$

This F is a composite surface, flat in the region denoted Ω_3 in Figure 7c, and strictly concave in Ω_1. The graph of such F is depicted in Figure 7b. I

[5] Univocally, if the body is simply connected or loaded by self balanced tractions on any closed boundary.

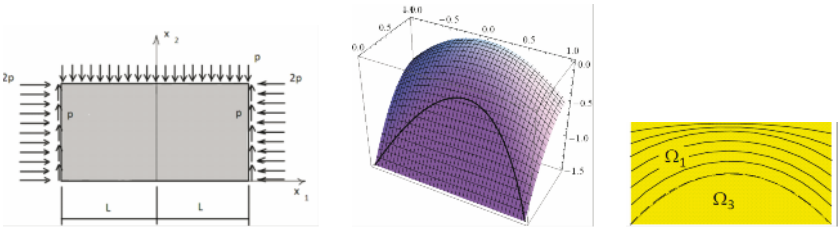

a b c

Figure 7. Wall beam under uniform transverse load: (a). Graph of the Airy's stress function, corresponding to the smooth solution: (b). Domain partition and one of the families of compression lines corresponding to the smooth solution: (c).

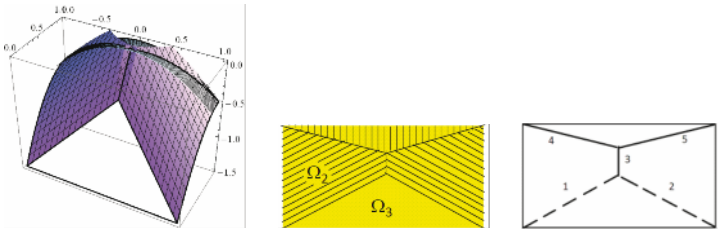

a b c

Figure 8. Graph of the folded Airy's function, showing the intersection of the generating surfaces: (a). Corresponding domain partition and principal lines of compression: (b). Support of the singular stress (solid lines 3, 4, 5): (c).

leave to the reader to verify that the corresponding $\mathbf{T}$ is statically admissible, that is that such $\mathbf{T}$ matches the boundary data and belongs to Sym^-.

A singular statically admissible stress field is derived from the stress function F depicted in Figure 8a. F is a continuous non-smooth function: the surface F, making (concave) folds along the lines indicated with 3, 4, 5 in Figure 8c, can be easily produced by prolongating the datum $F|_{\partial\Omega}$ with ruled surfaces having the prescribed slope $\frac{dF}{d\nu}|_{\partial\Omega}$ at the boundary. The intersections of the four ruled surfaces emanating from the boundary (see Figure 8a) give the folding lines; the jump of slope hortogonal to the folding line gives the value of the axial force along the line:

$$\mathbf{T}_s = N\delta(\Gamma)\mathbf{t} \otimes \mathbf{t} \, .$$

Since the fold is concave the jump of slope is negative, then

$$N = \Delta_m F \, < \, 0 \, .$$

In Figure 8b the principal lines of uniaxial compression corresponding to the non smooth solution are reported.

2.5 Kinematically admissible displacement fields

A compatible displacement field $\mathbf{u}$, that is a displacement $\mathbf{u}$ matching the given displacements $\underline{\mathbf{u}}$ on $\partial\Omega_D$ for which $(\mathbf{E}(\mathbf{u})$ - $\underline{\mathbf{E}}) \in Sym^+$, i.e. such that the *effective strain* satisfies the unilateral conditions (6), is said to be *kinematically admissible* for a RNT body.

The set of kinematically admissible displacement fields is denoted K and is defined as follows:

$$K = \left\{ \mathbf{u} \in T(\Omega) \; s.t. \; \mathbf{u} = \underline{\mathbf{u}} \; on \; \partial\Omega_D \; , \; \mathbf{(E(u)\text{-}\underline{E})} \in Sym^+ \right\} \; , \qquad (14)$$

where $\Omega = \Omega \cup \partial\Omega_D$ and $T(\Omega)$ is a function space of convenient regularity. Since for RNT materials, discontinuous displacements can be considered, one can assume $T(\Omega) = BV(\Omega)$, that is the set of functions of bounded variation (the functions whose gradient belongs to $M(\Omega)$, i.e. functions $\mathbf{u}$ admitting finite discontinuities). I restrict to the subset of $BV(\Omega)$, consisting of displacement fields $\mathbf{u}$ having finite jumps on a finite number of regular arcs. Actually, as we shall see, I will need only to consider discontinuous functions $\mathbf{u}$ whose jump set is the union of a finite number of segments.

The differential relation between $\mathbf{E}$ and $\mathbf{u}$, likewise the displacement b.c., must be reformulated in a weak form, since the derivative of $\mathbf{u}$ does not exist in a classical sense, and the trace of $\mathbf{u}$ on $\partial\Omega_D$ is not well defined. One way to do it is to impose compatibility in a variational form, namely by using the Complementary Virtual Work Principle.

On introducing the set of virtual stress fields

$$\delta H = \{ \delta\mathbf{T} \in T^*(\Omega) \; s.t. \; div\delta\mathbf{T} = \mathbf{0} \; , \; \delta\mathbf{T}\mathbf{n} = \mathbf{0} \; on \; \partial\Omega_N \} \; , \qquad (15)$$

the displacement field $\mathbf{u}$ is compatible with $(\underline{\mathbf{u}}, \underline{\mathbf{E}})$ if and only if

$$\int_{\partial\Omega_D} (\delta\mathbf{T}\mathbf{n}) \cdot \underline{\mathbf{u}} - \int_\Omega \delta\mathbf{T} \cdot \underline{\mathbf{E}} = \int_\Omega \delta\mathbf{T} \cdot \mathbf{E}(\mathbf{u}) \; , \; \forall \delta\mathbf{T} \in \delta H \, . \qquad (16)$$

$T^*(\Omega)$ is a function space of convenient regularity. If $\mathbf{u} \in H^1(\Omega)$ (as it is assumed in linear elasticity), then $T^*(\Omega) = L^2(\Omega)$ guarantees the finiteness of the internal virtual work. If $\mathbf{u} \in BV(\Omega)$, the choice $T^*(\Omega) = C^\circ(\Omega)$ ensures the possibility of computing the internal virtual work.

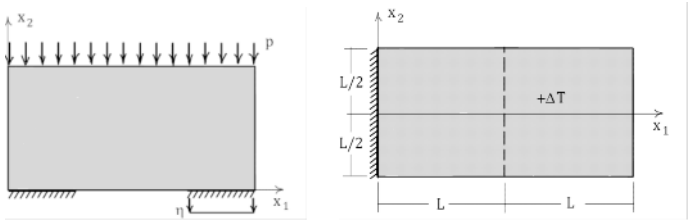

a b

Figure 9. Examples of kinematical problems. Wall loaded by uniform vertical load at the top and subjected to a given uniform settlement of the right foot: (a). Masonry panel subject to uniform thermal expansion of the right half: (b).

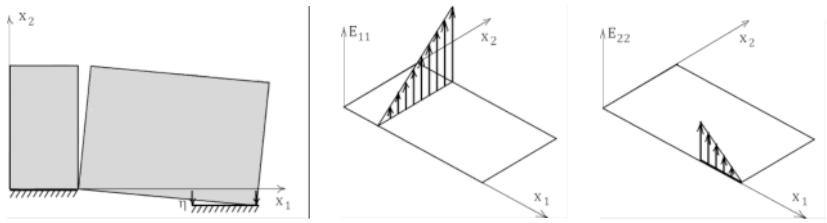

a b c

Figure 10. Compatible solution for the problem of Figure 9a: (a). Corresponding (singular) strain components: (b), (c).

Examples. As a simple illustration of typical *kinematical problems*, I construct some admissible deformations for the two example problems reported in Figure 9. In (a) the effect of a given settlement η of the right foot, is considered. In (b) the constraints are fixed and the effect of the distortion $\underline{\mathbf{E}} = \alpha \Delta T \, \mathbf{I}$, due to the uniform, positive increment of temperature ΔT, applied to the right half of the strip, is studied.

A kinematically admissible displacement, compatible with the given settlement, is shown in Figure 10a; in Figures 10b,c the strain components E_{11}, E_{22} are graphically represented.

A kinematically admissible displacement for the second example is

$$u_1 = \begin{cases} \alpha \Delta T x_1 (1 - x_2^2/L^2) \ , \ x_1 < L \ , \\ \alpha \Delta T x_1 \ , \ x_1 \geq L \ , \end{cases}$$

$$u_2 = \begin{cases} \alpha \Delta T x_2 x_1^2/L^2 \ , \ x_1 < L \ , \\ \alpha \Delta T x_2 \ , \ x_1 \geq L \ . \end{cases}$$

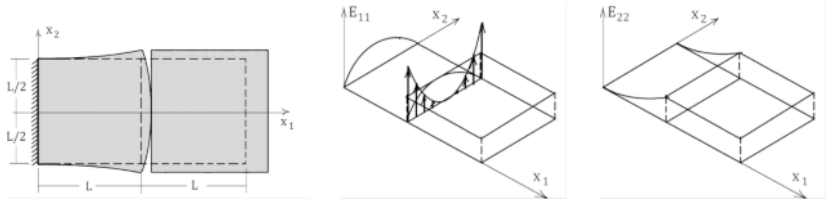

a b c

Figure 11. Compatible solution for the problem of Figure 10b: (a). Corresponding (regular and singular) strain components: (b), (c).

The corresponding deformation and the strain components E_{11}, E_{22}, are graphically represented in Figure 11. I leave to the reader to verify that the effective strain ($\mathbf{E}(\mathbf{u})$-$\underline{\mathbf{E}}$) belongs to Sym^{+}[6] and that the strain $\mathbf{E}$, whose non-vanishing components are depicted in Figures 11b c, satisfy the compatibility conditions (6) in a generalized sense.

2.6 Compatibility of loads and distortions

The data of a general BVP for a RNT body can be split into two parts

$$\ell \leftrightarrow (\underline{\mathbf{s}}, \mathbf{b}) \approx \textit{loads} ,$$

$$\ell^* \leftrightarrow (\underline{\mathbf{u}}, \underline{\mathbf{E}}) \approx \textit{distortions} .$$

The *equilibrium problem* and the *kinematical problem* for RNT materials, namely the search of admissible stress or displacement fields for given data, are essentially independent, in the sense that they are uncoupled but for condition (3).

It has to be pointed out that, for RNT bodies, there are non-trivial compatibility conditions, both on the loads and on the distortions; that is the existence of statically admissible stress fields for given loads, and the existence of kinematically admissible displacement fields for given distortions, is submitted to special conditions on the data (for a thorough study of compatibility conditions on the loads see Del Piero (1989) and Angelillo and Rosso (1995)).

[6] The assumption that the effective strain has to belong to Sym^{+}, implies that, on a crack Γ, the form of the singular strain be

$$\mathbf{E}^s = \delta(\Gamma)\Delta v \mathbf{m} \otimes \mathbf{m} , \ \textit{with} \ \Delta v > 0 ,$$

that is shearing discontinuities are forbidden.

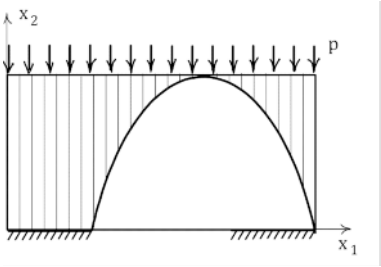

Figure 12. Statically admissible solution reconcilable with the compatible mechanism of Figure 11a, and corresponding to the BVP depicted in Figure 10a. An arch carrying a concentrated axial force is formed, springing from the two *hinges* of Figure 10a. The stress field is regular and uniaxial above the arch.

The definition of compatible loads and distortions is rather straightforward:

$$\{\ell \; is \; compatible\} \; \Leftrightarrow \{H \neq \emptyset\} \; , \tag{17}$$

$$\{\ell^* \; is \; compatible\} \; \Leftrightarrow \{K \neq \emptyset\} \; . \tag{18}$$

Therefore the more direct way to prove compatibility, both for loads and distortions, is to construct a s.a. stress field or a k.a. displacement field, as done in the previous examples.

To prove the existence of a solution to the BVP for a No-Tension body, the compatibility of ℓ and ℓ^* is necessary but not sufficient, since the further condition

$$\mathbf{T} \cdot \mathbf{E}^*(\mathbf{u}) = 0 \; ,$$

must be satisfied (this is the material restriction (3)). Then one can say that a possible solution to the BVP is given, if there exist a s.a. stress field and and a k.a. dispalcement field, which are reconcilable in the sense of condition (3).

As a simple example in Figure 12, a s.a. stress field giving, together with the mechanism of Figure 10a, a possible solution to the simple problem depicted in Figure 9a, is reported.

Examples. In the examples of Figure 13, the possible solution of two classical mixed BVP for RNT materials is pictorially presented. Notice that both the stress solution and the displacement solution present singularities.

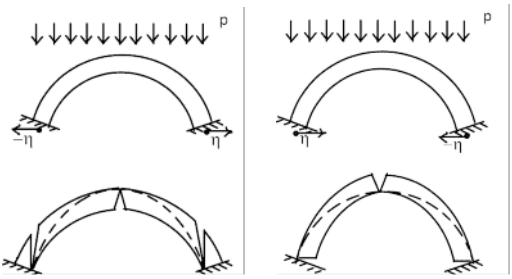

a b

Figure 13. Examples of solutions of typical BVP's for NENT materials. Arch loaded by a uniform (per-unit projection) vertical load at the extrados and subjected to a given uniform settlement of its abutments. In (a) the supports spread, in (b) they get closer. The strain is singular at the supports and at the key-stone; two different arches form in the two cases.

The examples reported in Figures 13, that can be found also in the milestone book by Heyman (1995), testify the need, in order to solve a BVP for Rigid No-Tension materials, to consider at the same time singular stress and strain fields, and call for an *extended* formulation of the theorems of Limit Analysis.

2.7 Incompatibility of loads and distortions

The way to verify the incompatibility of the data is less straightforward, requiring the definition of two new sets

$$H^\circ = \left\{ \mathbf{T}^\circ \in S(\Omega) \; s.t. \; div\mathbf{T}^\circ = \mathbf{0} \; , \; \mathbf{T}^\circ\mathbf{n} = \mathbf{0} \; on \; \partial\Omega_N \; , \; \mathbf{T}^\circ \in Sym^- \right\} \; ,$$

and

$$K^\circ = \left\{ \mathbf{u}^\circ \in T(\Omega) \; s.t. \; \mathbf{u}^\circ = \mathbf{0} \; on \; \partial\Omega_D \; , \; \mathbf{E}(\mathbf{u}^\circ) \in Sym^+ \right\} \; .$$

Both H° and K° can reduce to the sets $H^{\circ\circ}$ and $K^{\circ\circ}$ corresponding to null stress and strain fields, depending on the geometry of the boundary, of the loads and of the constraints.

Remark 4. The fact that $H^\circ - H^{\circ\circ}$ can be void and that $K^\circ - K^{\circ\circ}$ can be non-void is kind of peculiar of RNT materials; indeed we are used to think to 2d continua as overdetermined and deprived of rigid, *zero-energy*, internal modes.

One way to see overdeterminacy is to add to any s.a. stress field a, non zero, self balanced stress field $\mathbf{T}^\circ$. The fact that $H^\circ - H^{\circ\circ}$ can be void,

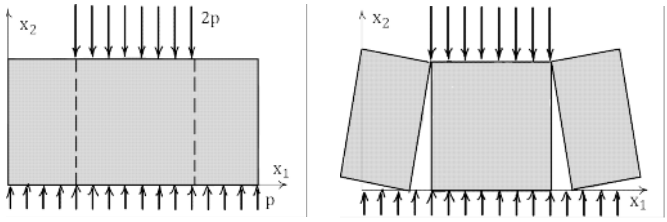

a b

Figure 14. Example of incompatible loads: in (a) wall loaded by uniform vertical loads at the top and bottom bases. K.a. displacement field for which the load performs positive work: (b).

means that overdeterminacy depends on the loads. There also can be loads for which the structure becomes statically admissible. The fact that the overdeterminacy/underdeterminacy of the structure depends on the load is typical also of *discrete* structures with unilateral constraints.

The absence of degrees of freedom is proved, for discrete structures, by denying the possibility of zero energy mechanisms. $\mathbf{u}^\circ \in K^\circ - K^{\circ\circ}$ is indeed a non trivial mechanism requiring, for the RNT body, zero energy expended. The underdeterminacy of the structure, descending from the fact that $K^\circ - K^{\circ\circ}$ can be non-void, demands for non trivial compatibility conditions on the loads. $\diamond$

The incompatibility of the data can be assessed as follows

$$\{\ell \; \textit{incompatible}\} \Leftarrow \left\{\exists \mathbf{u}^\circ \in K^\circ \; s.t. \; \langle \ell, \mathbf{u}^\circ \rangle > 0\right\} \; , \tag{19}$$

$$\{\ell^* \; \textit{incompatible}\} \Leftarrow \left\{\exists \mathbf{T}^\circ \in H^\circ \; s.t. \; \langle \ell^*, \mathbf{T}^\circ \rangle > 0\right\} \; , \tag{20}$$

where $\langle \ell, \mathbf{u}^\circ \rangle$, $\langle \ell^*, \mathbf{T}^\circ \rangle$ represent the work of the loads and distortions for $\mathbf{u}^\circ$, $\mathbf{T}^\circ$, respectively.

Examples. The load of Figure 14a is incompatible, since it makes positive work for the mechanism $\mathbf{u}^\circ$ depicted in Figure 14b.

The distortion represented in Figure 15a is incompatible, since it makes positive work for the self stress $\mathbf{T}^\circ$ depicted in Figure 15b.

Remark 5. The incompatibility of a given set of loads means that equilibrium is not possible and that acceleration of the structure must take place[7]. The incompatibility of a given set of distortions means that the given

[7] A trivial compatibility condition for all kinds of bodies, under pure traction conditions,

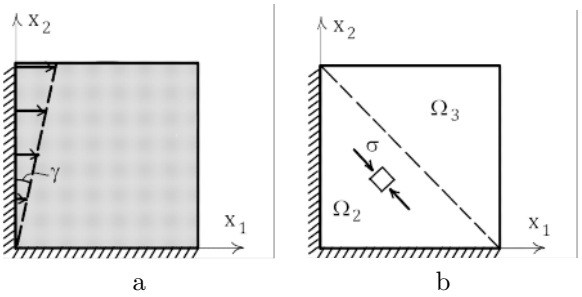

Figure 15. Example of incompatible distortions: in (a) panel subject to a given displacement of the left constraint. S.a. stress field for which the distortion performs positive work: (b).

kinematical data cannot be accomodated with a zero energy mechanism and demand for more complex material models (i.e. elastic NT, elastic NT-plastic, etc). ⋄

2.8 Limit Analysis

We have seen in the preceding sections that, for RNT bodies, both force and displacement data are subject to compatibility conditions, that is the existence of a statically admissible stress field and the existence of a kinematically admissible displacement field, are subordinated to some necessary or sufficient conditions on the given data. Here I concentrate on necessary or sufficient conditions for the compatibility of a given set of loads $(\underline{\mathbf{s}}, \mathbf{b})$, restricting to the case of zero kinematical data $(\underline{\mathbf{u}}, \underline{\mathbf{E}})$. The definition of safe, limit and collapse loads are given first, and the propositions defining the compatibility of the loads, that are essentially a special form of the theorems of Limit Analysis (LA), are then discussed.

Theorems of Limit Analysis. Recalling the definition of RNT materials, we can observe that the restrictions (2), (3) are equivalent to a rule of normality of the total strain to the cone of admissible stress states. Normality is the essential ingredient allowing for the application of the two theorems of Limit Analysis (see Del Piero (1998)). In order to avoid the possibility of trivial incompatible loads (and simplify the formulation of the two theorems), assumption (4) (i.e. that the tractions $\underline{\mathbf{s}}$ applied at the

is load balance. Load balance is only a necessary compatibility condition for unilateral bodies.

boundary are either compressive or zero) is made.

Admissible fields. The rigorous proof of the two theorems of Limit Analysis requires to set the problem in proper functions spaces. For RNT materials is appropriate and convenient to define the sets of statically admissible stress fields H and kinematically admissible displacement fields K, as follows

$$H = \left\{ \mathbf{T} \in S(\Omega) \; s.t. \; div\mathbf{T} + \mathbf{b} = \mathbf{0} \; , \; \mathbf{Tn} = \underline{\mathbf{s}} \; on \; \partial\Omega_N \; , \; \mathbf{T} \in Sym^- \right\} \; , \quad (21)$$

$$K = \left\{ \mathbf{u} \in T(\Omega) \; s.t. \; \mathbf{u} = \mathbf{0} \; on \; \partial\Omega_D \; , \; \mathbf{E}(\mathbf{u}) \in Sym^+ \right\} \; , \quad (22)$$

where a convenient choice for the function spaces $S(\Omega)$ and $T(\Omega)$ is

$$S(\Omega) = SMF(\Omega) \; ,$$

$$T(\Omega) = \{ \mathbf{u} \; s.t. \; grad\mathbf{u} \in SMF^*(\Omega) \} \; ,$$

SMF being the set of Special Measures (that is measures with null Cantor part) whose jump set is Finite, in the sense that the support of their singular part consists of a finite number of regular $(n-1)$d arcs[8].

With SMF^* I denote the subset of SMF for which the support of the singular part is restricted to a finite number of $(n-1)$d segments.

Notice that, depending on the geometry of the structure $\Omega = \dot{\Omega} \cup \partial\Omega_N$ and on the given loads, the set H can be void. If H is void the load $(\underline{\mathbf{s}}, \mathbf{b})$ is incompatible, in the sense previously specified (no possibility of equilibrium with purely compressive stresses).

Strictly admissible stress fields and load classification. In order to formulate the theorems of Limit Analysis, I need to introduce the following definitions.

On denoting$\langle \ell, \mathbf{u} \rangle$ the work of the load $\ell = (\underline{\mathbf{s}}, \mathbf{b})$ for the displacement $\mathbf{u}$, the load can be classified as follows:

1. (ℓ is a collapse load)$\Leftrightarrow$ ($\exists \mathbf{u}^* \in K s.t. \langle \ell, \mathbf{u}^* \rangle > 0$),
2. (ℓ is a limit load)$\Leftrightarrow$ ($\langle \ell, \mathbf{u} \rangle \leq 0$, $\forall \mathbf{u} \in K$ and $\exists \mathbf{u}^* \in K - K^{\circ\circ}$ s.t. $\langle \ell, \mathbf{u}^* \rangle = 0$),
3. (ℓ is a safe load)$\Leftrightarrow$ ($\langle \ell, \mathbf{u} \rangle < 0 \; , \; \forall \mathbf{u} \in K$).

[8] We suggest the reader to consult the book (Ambrosio et al., 2000)for a complete essay on SBV functions and measure spaces.

I now introduce a useful definition. A stress field $\mathbf{T} \in H$ such that $tr\mathbf{T} < 0$ and $det\mathbf{T} > 0$, $\forall \mathbf{x} \in \Omega$, is said to be *strictly admissible*.

Notice that, if $\mathbf{T}$ is strictly admissible, then at each point of Ω (that is the open set $\dot{\Omega}$ to which the fixed part of the boundary $\partial\Omega_D$ is added) it results:

$$\sigma_1 < 0 \ , \ \sigma_2 < 0 \ ,$$

σ_1, σ_2 being the eigenvalues of $\mathbf{T}$ at the point $\mathbf{x}$.

Kinematic Theorem. If ℓ is a collapse load (in the sense of item (1) above) then H is void.

Static Theorem. If a strictly admissible stress field $\mathbf{T}$ exists, then the load ℓ is safe (in the sense of item (3) above).

Limit Theorem. If H is not void and there exists $\mathbf{u}^* \in K - K^{\circ\circ}$ $\langle \ell, \mathbf{u}^* \rangle = 0$, then the load ℓ is limit (in the sense of item (2) above).

For the proof of these theorems I refer to the paper (Del Piero, 1998). The reader must be warned that the proofs given by Del Piero refer to a similar function space for the displacement but to a different functional setting for the stress (namely $L^2(\Omega)$). In the present paper I assume that these theorem are still valid in the present larger setting for the stress and smaller setting for the displacement[9].

2.9 Simple applications of the theorems of Limit Analysis

Example 1. Compressed wall/pier. The two simple BVP depicted in Figure 16 are considered. The first one (Figure 16a) refers to a rectangular wall compressed at the two bases by uniform normal tractions. The second example (Figure 16b) is a wall compressed at the top base by a uniform pressure load and fixed at the bottom base. By employing the Airy's representation and by using the static and kinematic theorems, it can be shown that in case (a) the load is limit and in the second case the load is safe.

The data for F and $dF/d\nu$ at the boundary, in case (a), are shown in Figure 16c. In this case the only concave surface that can possibly satisfy

[9]For general stress and strain fields that can be line Dirac deltas on a finite number of regular arcs the internal work $\int_\Omega \mathbf{T} \cdot \mathbf{E}$ is not defined. Considering the restrictions which define the sets H and K, that is taking into account the constraints on $\mathbf{T}$ and $\mathbf{E}$, the only case in which there are troubles in computing the internal work (if $\mathbf{T}$ and $\mathbf{E}$ are so restricted) is when both the stress and the strain are singular on the same line Γ, the line is curved and there is a stress discontinuity in the direction of the normal $\mathbf{m}$ to Γ. A way to avoid this is to allow stress singularities on curved lines but to assume that the support of the jumps of $\mathbf{u}$ is a segmentation, that is a line formed by the union of a finite number of straight arcs.

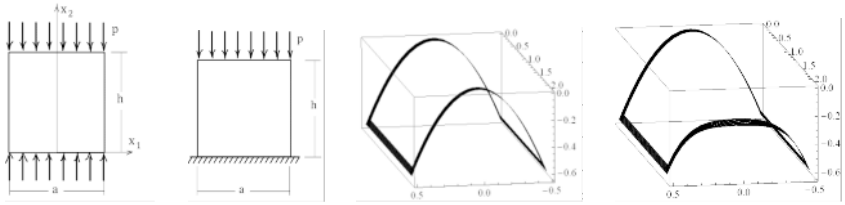

a b c d

Figure 16. Compressed pier (wall). Pure traction problem: (a), Mixed problem: (b). Corresponding data for F and dF/ν for the two cases.

the data shown in Figure 16c is the parabolic cylinder defined by

$$F = -\frac{px_1^2}{2} .$$

The uniqueness of this F can be proved by observing that the surface defined by it coincides with the upper part of the convex hull of the curve carrying the boundary datum for F. The properties of minimality of the convex hull ensure the uniqueness of F and of the corresponding stress (see Angelillo and Rosso (1995)), that is of the uniform uniaxial stress

$$\{\mathbf{T}\} = \left\{ \begin{array}{cc} 0 & 0 \\ 0 & -p \end{array} \right\} .$$

Since this is the only statically admissible stress field, H is a singleton and we can say that the structure, with this load, is statically determined (see Remark 4). Notice that based on the definition (3) above and on the theorems of LA, the load is not safe. It is actually limit (see Limit Theorem above) since by splitting the panel into two parts along any vertical line Γ with a normal crack, the strain corresponding to this mechanism is a horizontal uniaxial Dirac delta whose intensity has the value of the displacement jump along Γ: the work of the load for this non-zero mechanism is zero. Notice that the strain corresponding to this mechanism and the unique statically admissible stress field are reconcilable in the sense of condition (3), that is they represent a possible solution for the BVP. The fact that, under these conditions, strain can increase indefinitely at constant load is a typical feature of limit loads.

In case (b) the previous stress function can be corrected by adding a term to it. Notice that the boundary is loaded only on the lateral sides and on the top base (with the same load of case (a)), and that both the value and the slope of the stress function can be modified along the bottom base

of the panel (see Figure 16d). The simplest correction with polinomia one can think of, is

$$F = -\frac{p\,x_1^2}{2} - \beta\,\frac{(a^2 - x_1^2)^2\,x_2^2}{a^4}\ .$$

The corresponding stress is

$$\{\mathbf{T}\} = \left\{ \begin{array}{cc} -\beta\,\frac{2(a^2-x_1^2)^2}{a^4} & -\beta\,\frac{8(a^2-x_1^2)x_1x_2}{a^4} \\ -\beta\,\frac{8(a^2-x_1^2)x_1x_2}{a^4} & -p+\beta\,\frac{4(a^2-3x_1^2)x_2^2}{a^4} \end{array} \right\}\ .$$

The trace and the determinant of $\mathbf{T}$ are then

$$tr\mathbf{T} = -p + \beta\,\left(-2 + \frac{4a^2x_1^2 + 4a^2x_2^2 - 2x_1^4 - 12x_1^2x_2^2}{a^4}\right)\ ,$$

$$det\mathbf{T} = \beta\frac{2(a^2 - x_1^2)^2}{a^8}\left(pa^4 - \beta(4a^2 + 20x_1^2)x_2^2\right)\ .$$

If $h \leq \frac{\sqrt{2}}{2}\,a$ then $tr\mathbf{T}$ is always negative. If $h > \frac{\sqrt{2}}{2}\,a$ then $tr\mathbf{T}$ is negative on Ω if

$$\beta < \frac{pa^2}{4h^2 - 2a^2}\ ,$$

and $det\mathbf{T}$ is positive on Ω if

$$\beta < \frac{pa^2}{24h^2}\ .$$

Then $\mathbf{T}$ is negative definite on Ω, and the load is safe, on the base of the Static Theorem of LA, if the second inequality holds. For example, for a square panel, if one takes $\beta < \frac{p}{96}$, then the stress given by the above expression is strictly admissible and the load is safe. In Figure 17 the stress functions emploied for cases (a) and (b) are shown side by side for comparison, in the special case $h = 2a$, and putting for case (b), $\beta = \frac{p}{400}$.

Notice that the negative definiteness of $\mathbf{T}$ in case (b) is not uniform, since on the lateral sides we must have $det\mathbf{T} = 0$ and one of the two eigenvalues of $\mathbf{T}$ must tend to zero as that part of the boundary is approached.

Remark 6. The bounds found on β give values of β vanishingly small with respect to p, as the ratio h/a increases; if one takes β/p as a sort of measure of the safety level of the load with respect to collapse: then slender walls, under this kind of loading, tend to become less and less safe, as the ratio h/a is increased.$\diamond$

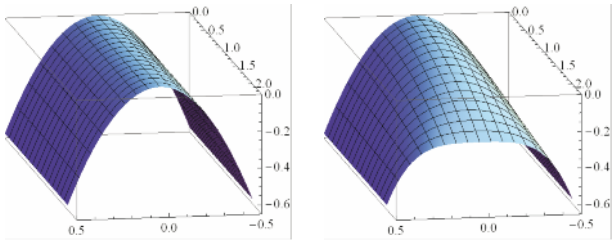

a b

Figure 17. Compressed pier (wall): in (a) Airy's stress function for the traction problem. In (b) Airy's stress function adopted for the mixed case.

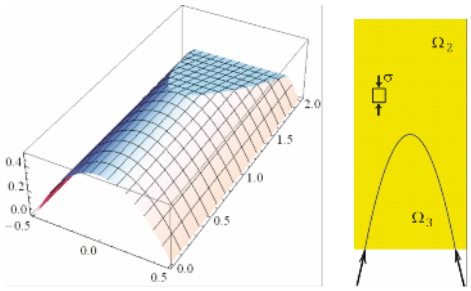

a b

Figure 18. In (a) Airy's folded stress function for the mixed problem. In (b) a scheme of the corresponding stress is reported.

Remark 7. It is worth pointing out that the existence of a strictly admissible stress field does not imply that the actual state of stress in the body be of biaxial compression. If the material is rigid in compression, any statically admissible stress has the same dignity and is theoretically admissible for equilibrium.

The choice among these fields requires the introduction of more advanced constitutive restrictions, allowing for shortening strains. When elasticity is assumed it happens that s.a. stress fields which are not strictly admissible are preferable, on an energetic ground, to strictly admissible ones. Therefore the material exhibits both biaxial and uniaxial stress states (and fractures) despite the existence of a strictly admissible stress field (see *Exact solution 4*, *Subsection* 3.7).◇

By using the Airy's formulation singular s.a. stress fields can be easily generated. By modifying, with some care, these singular fields, strictly

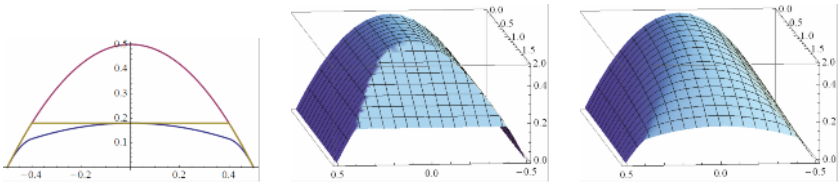

a b c

Figure 19. Smoothing of the folded stress function of Figure 18. Sections of the folded surface and its smoothed transformation at $x_2 = 0$: (a); the section of the parabolic cylinder corresponding to the solution of the traction problem is reported for reference. In (b), (c) a 3d view of the folded and smoothed surfaces is shown

admissible stress fields can be obtained. A non smooth F satisfying the b.c. for case (b) of Figure 16 is depicted in Figure 18a.

The stress field corresponding to the non smooth Airy's function depicted in Figure 18a, is reported schematically in Figure 18b. The way in which such a composite surface can be generated by the boundary data is explained in detail in the next example. Notice that the half-span αa and the rise βh of the arch-like structure depicted in Figure 18b can be chosen arbitrarily provided that α, β vary in the interval $[0, 1]$.

The process through which the singular statically admissible stress field depicted in Figure 18 can be smoothed out and transformed into a strictly admissible stress field is not discussed here for brevity. A 3d view of the folded F and of its strictly admissible modification (together with the stress function of case (a) used as a reference surface) is shown pictorially in Figure 19.

Example 2. Rocking of a rectangular panel. This is perhaps the most classical problem for unilateral masonry-like materials, for which the determination of the limit load under a horizontal force is trivial; therefore this is the ideal example to understand how the theorems of limit analysis can be applied to NT materials and how one can take advantage of singular stress fields and of the stress function formulation.

The vertical load is fixed to the value $q = \frac{P}{L}$ and the intensity of the concentrated horizontal force is taken as $H = \alpha P$, α being a load parameter. A trivial upper bound for α ($\alpha^\circ = \frac{1}{3}$) in the case shown in Figure 20a, is found by considering the rocking mechanism of the panel (shown in Figure 20b) and applying the kinematic theorem. If one can find a statically admissible stress field for the same value of α then α° is the limit value of the load parameter.

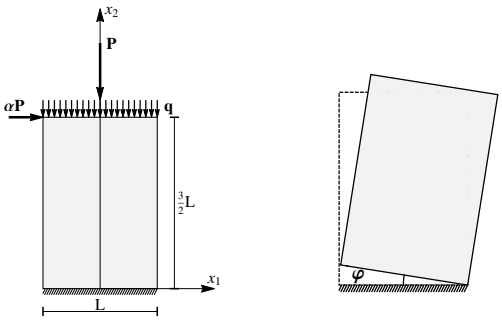

Figure 20. Rectangular panel loaded by vertical and horizontal forces. Loading scheme: (a). Rocking mechanism: (b)

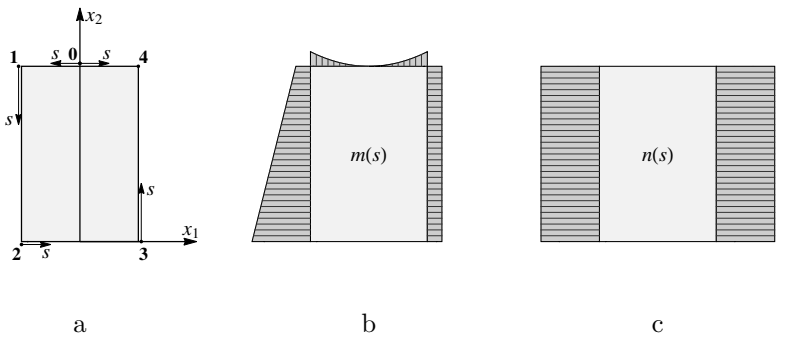

Figure 21. Rectangular panel loaded by vertical and horizontal forces. Parametrization of the boundary: (a). Boundary value for F (moment $m(s)$): (a). Boundary value for the normal derivative of F (axial force $n(s)$): (c)

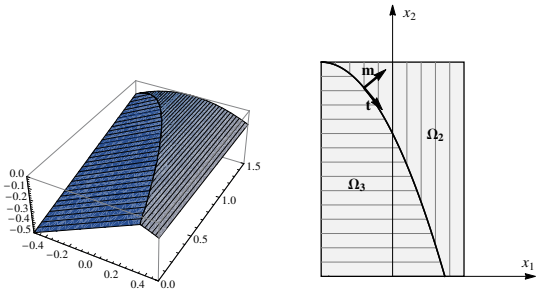

Figure 22. Rectangular panel loaded by vertical and horizontal forces for $\alpha = 1/4$. Composite stress function: (a). Corresponding support of the singular stress on the planform and domain partition: (b).

For $\alpha < \frac{1}{3}$, say $\alpha = \frac{1}{4}$, a strictly admissible stress field can be constructed. To use the Airy's formulation the loaded boundary is divided into five parts (see Figure 21a where $L = 1$ is set).

1. The boundary is parametrized with the arc length s. The data $m(s)$ and $n(s)$ are defined in terms of the load on the segments 0-1 and 1-2 (see Figure 21b, c). From them the curve carrying the datum for F and the gradient $gradF$ at the boundary are computed.

Segment 0-1.

Parametrization: $\mathbf{x}(s) = \{-s, \frac{3}{2}\}$;

Moment: $m(s) = -\frac{qs^2}{2}$;

Axial force: $n(s) = 0$;

Curve of boundary data: $\mathbf{X}(s) = \{-s, \frac{3}{2}, -\frac{qs^2}{2}\}$;

Gradient of F at the boundary: $gradF^{\circ}(s) = \{-m'(s), n(s)\} = \{qs, 0\}$.

Segment 1-2.

Parametrization: $\mathbf{x}(s) = \{-\frac{1}{3}, \frac{3}{2} - s\}$;

Moment: $m(s) = -\frac{q}{8} - \frac{qs}{4}$;

Axial force: $n(s) = -\frac{q}{2}$;

Curve of boundary data: $\mathbf{X}(s) = \{-\frac{1}{2}, \frac{3}{2} - s, -\frac{q}{8} - \frac{qs}{4}\}$;

Gradient of F at the boundary: $gradF^{\circ}(s) = \{-n(s), m'(s)\} = \{\frac{q}{2}, \frac{q}{4}\}$.

2. The data are extended inside the body with a uniaxial prolongation. Such a prolongation is obtained by constructing on each part γ_i of the boundary, a ruled surface having as generating curve, the curve $\mathbf{X}(s)$ carrying the Dirichelet data, and formed by the straight lines r directed as the given loads and whose slope is specified by $gradF^{\circ}(s)$. If the load is zero, the direction of the line r is taken as the inward normal -**n**.

Segment 0-1
Load direction: $\mathbf{k} = \{0, -1\}$;
Propagation vector: $\mathbf{v}(s) = \{k_1, k_2, gradF \cdot \mathbf{k}\} = \{0, -1, 0\}$;
Parametric form of F^1: $\mathbf{y}(s, \nu) = \mathbf{X}(s) + \nu\mathbf{v}(s) = \{-s, \frac{3}{2} - \nu, -\frac{qs^2}{2}\}$;
F^1 in terms of x_1, x_2: $F^1(x1, x_2) = -\frac{qx_1^2}{2}$.
Segment 1-2
Load direction: $\mathbf{k} = \{1, 0\}$;
Propagation vector: $\mathbf{v}(s) = \{k_1, k_2, gradF \cdot \mathbf{k}\} = \{1, 0, \frac{q}{2}\}$;
Parametric form of F^2: $\mathbf{y}(s, \nu) = \mathbf{X}(s) + \nu\mathbf{v}(s) =$
$\{-\frac{1}{2} + \nu, \frac{3}{2} - s, -\frac{p}{8}(1 - 2qs + 4\nu q)\}$;
F^2 in terms of x_1, x_2: $F^2(x1, x_2) = -\frac{q}{4}(1 - 2x_1 - x_2)$.

3. The two surfaces F^1 and F^2 intersect along a curve (represented in Figure 22a) whose projection Γ on the "planform" is determined, in explicit form. By solving the equation $F^1 = F^2$, one obtains the following equation for Γ:

$$x_2 = 1 - 2x_1 - 2x_1^2 \, .$$

The curve Γ is a parabola, passing through the point $\{-\frac{1}{2}, \frac{3}{2}\}$ and intersecting the base at $x_1^\circ = \frac{1}{2}(\sqrt{3} - 1)$. Γ splits the rectangle into two parts Ω_2, Ω_3(Figure 22b).

4. Along Γ the stress is singular: it is a concentrated axial force N whose intensity is determined by the jump of slope ΔF of the composite surface F in the direction of $\mathbf{h}$ (Figure 22ab). Since the gradient jump across Γ is $gradF^1 - gradF^2 = -q\{\frac{1}{2} + x_1, \frac{1}{4}\}$ and the unit normal $\mathbf{h}$ to Γ is $\mathbf{h} = \{2 + 4x_1, 1\}/\sqrt{5 + 16x_1 + 16x_1^2}$, we have

$$\Delta F = (gradF^1 - gradF^2) \cdot \mathbf{h} = -\frac{1}{4} q \sqrt{5 + 16x_1 + 16x_1^2} \, .$$

The stress corresponding to this composite F is zero in Ω_1, uniaxial inside Ω_2, and a Dirac delta stress of intensity $N = \Delta F$, balancing the stress jump on Γ due to the stress discontinuity, at the interface between Ω_1 and Ω_2 (Figure 23a). The graph of N along the curve Γ, in the interval $\left[-\frac{1}{2}, \frac{1}{2}(\sqrt{3} - 1)\right]$, is shown in Figure 23b.

Remark 8. Notice that the concentrated force emerging at the bottom edge is the trace of the singular stress field $\mathbf{T}(x_1) = N(x_1)\delta(\Gamma)\mathbf{t}(x_1) \otimes \mathbf{t}(x_1)$, $\mathbf{t}$ being the unit tangent vector to Γ: $\{\mathbf{t}\} = \{h_2, -h_1\}$. The value of such force is $\mathbf{R} = N(x_1^\circ)\delta(x_1^\circ)\mathbf{t}(x_1^\circ)$, i.e. it is not given by the Cauchy formula $\mathbf{s}(\mathbf{n}) = \mathbf{T}\mathbf{n}$, valid for absolutely continuous stress vectors $\mathbf{s}$.$\diamond$

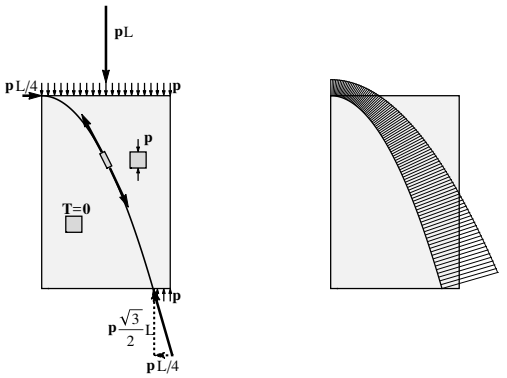

a b

Figure 23. Rectangular panel loaded by vertical and horizontal forces for $\alpha = 1/4$. Stress corresponding to the stress function of Figure 22: (a). Graph of the axial force along the arch: (b).

A s.a. stress field for $\alpha = \frac{1}{3}$ is obtained by following the same steps as before. The two functions F^1 and F^2 are in this case:

$$F^1(x_1, x_2) = -q\frac{x_1^2}{2} \ , F^2(x_1, x_2) = -\frac{1}{24}q(9 - 12x_1 - 8x_2) \ .$$

They intersect along the curve Γ depicted in Figure 24a, whose projection on the planform is given by the equation:

$$x_2 = \frac{3}{8}(3 - 4x_1 - 4x_1^2) \ .$$

Γ is a parabola passing through the points $[-1/2, 3/2]$, $[1/2, 0]$ (thus is the two opposite top and bottom corners of the rectangle: Figure 24b). The jump of slope along Γ is

$$\Delta F(x_1) = (gradF^1 - gradF^2)|_\Gamma \cdot \mathbf{h}(x_1) = -\frac{1}{6}q\sqrt{13 + 36x_1 + 36x_1^2} \ .$$

the corresponding axial force N along Γ, in the interval $[-0.5, 0.5]$, is reported in Figure 24d.

In Figure 24c the stress field corresponding to the composite surface F^1, F^2 is reported. Such a field is not strictly admissible and does zero work for the mechanism of Figure 20b, therefore $\alpha = 1/3$ is the limit load.

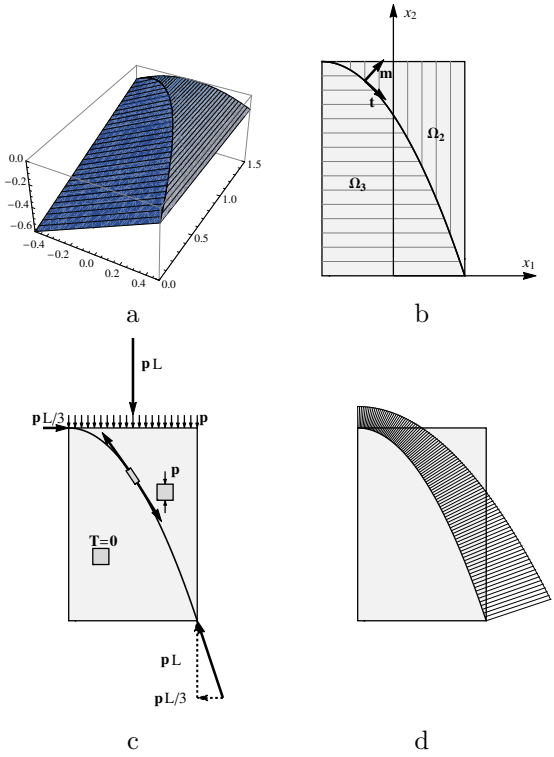

Figure 24. Rectangular panel loaded by vertical and horizontal forces for $\alpha = 1/3$. Strees function: (a). Support of the singular stress on the planform and domain partition: (b). Stress corresponding to the stress function depicted in (a): (c). Graph of the axial force along the arch: (d).

The stress field that was constructed for $\alpha = 1/4$ is not strictly admissible (actually the stress that we derived from the folded stress function is on the boundary of the cone Sym^- all over Ω), but, for any value of the load parameter $\alpha < \frac{1}{3}$, the previous construction can be used to generate a strictly admissible stress field. The method proceeds as follows:

Assume that a value of the parameter, say $\widetilde{\alpha} < \frac{1}{3}$, is given. If one removes a portion $p = q(1 - 3\widetilde{\alpha})$ from the given uniform load, the load becomes limit, that is the parabola hits the right corner of the rectangle and, as before, a stress field $\mathbf{T}^1$ can be constructed. Now I consider the panel under the action of the uniform vertical load p applied at the top base, and take the strictly admissible solution, say $\mathbf{T}^2$, constructed for the

previous example (the compressed wall). The sum of the two stress fields $\mathbf{T}^1 + \mathbf{T}^2$ is strictly statically admissible, since Sym^- is convex, the second stress state is strictly inside the cone, and then the sum of the two stress fields is also strictly inside the cone for any $\mathbf{x} \in \Omega$.

Remark 9. In the previous example statically admissible stress fields were produced through the stress function formulation. The overdetermined problem of equilibrium was reduced to a determined problem by restricting the search to a special class of stress functions, namely that of ruled surfaces (that is surfaces composed of straight lines). The stress fields corresponding to these surfaces are either uniaxial or null, that is the stress is limit *almost everywhere* in the body and the equilibrium problem is determined, since to the two differential equations of equilibrium the algebraic condition that the stress is uniaxial ($det\mathbf{T} = 0$) is added[10]. Any statically admissible uniaxial stress field balanced with zero body forces $\mathbf{b}$, has one family of isostatic lines (the ones corresponding to the negative eigenvalue) composed of straight lines (see Remark 3 and Figure 6). These straight lines, being actually the projections of the straight lines generating the ruled stress surface associated to $\mathbf{T}$, are called *compression rays* [11].

The differential problem is parabolic, and the stresses inside Ω are determined by the boundary data. By propagating the loads from opposite parts of the boundary the corresponding stress fields are usually unbalanced at the interface between the two fields: singular stress fields must be admitted along the interface. Both the value of the singular stress and the shape and location of the interface is determined by equilibrium. With the stress function formulation both the form and the location of the interface, besides the intensity of the axial contact force along Γ, are derived by intersecting two contiguous stress surfaces.$\diamond$

Example 3. Lintel under vertical and horizontal loads. A rectangular wall beam, supported at the bottom corners A, B, submitted to vertical and horizontal loads applied along its top edge, is shown in Figure 25a to which I refer for notations. This element can be representative of lintels, that is the transverse structures connecting the piers in masonry portals or in sequences of arches, when the effect of the loads transmitted to the arch from other parts of the structure, prevails on the self load, and

[10] This assumption is the basic hypothesis of the *Tension Field Theory* (see (Mansfield, 1969)), a simplified unilateral model for thin elastic membranes, analogous to the NT model for masonry structures (see Remark 3 and *Subsection* 3.8).

[11] This is a terminology similar to that adopted in *Tension Field Theory*, see Fortunato (2010).

the diffuse effect of body forces will be neglected. In Example 5 below the effect of uniform vertical body forces is considered.

The lintel's lower edge is actually often curved (see dashed line in Figure 25a), this feature being in keeping with the kind of stress state that I wish to consider in the element, as we shall see below. The presence of this arched intrados is necessary for equilibrium, if vertical body forces are considered.

By adopting the previous approach, in the case at hand I formulate the equilibrium problem of the lintel as follows.

The loads acting on Ω consists of a distributed load $\mathbf{q}$, applied along the top edge of Ω and having two components $\{q_1, q_2\}$ (see Figure 25b). The supports A, B reacts with two forces $\mathbf{R}_A, \mathbf{R}_B$, whose components are denoted $\{H(A), V(A)\}$, $\{-H(B), V(B)\}$; the lateral and the lower edges are unloaded.

Restricting to at most uniaxial stress fields and denoting $g = q_1/q_2$ the slope of the applied load with respect to x_2, the stress field, in the upper part of the domain, is a uniaxial field in the direction of the compression rays emanating from the top edge, whose slope with respect to x_2 is g. Calling τ the length along the (straight) top edge of the domain, measured from O, I also assume that the slope g is so restricted:

$$g(0) = 0 \ , \ g(L) = 0 \ , \ -\frac{\tau}{h^\circ} \leq g(\tau) \leq \frac{L-\tau}{h^\circ} \ , \ |g(\tau)| \ ,$$

that is the initial and final slopes are zero (then the two extreme compression rays run along the lateral edges), and the compression rays go from base to base and do not cross each other inside the rectangle enclosing Ω.

The stress field in the lower part of the domain is zero. The upper and the lower regions are separated by a common boundary Γ, passing through A and B, that is parametrized in terms of τ as follows

$$\Gamma = \{\{\mathbf{x}_\Gamma\} = \{\tau + g(\tau)y(\tau), y(\tau)\} \ , \ \tau \in \{0, L\}\} \ ,$$

carrying a concentrated axial force.

We denote H and V the horizontal and vertical components of the axial contact force N, arising on Γ in order to equilibrate the stress jump [12]. By imposing the equilibrium of the piece $\wp$ of Ω represented in Figure 25a, the following set of differential equations is obtained

$$H' = q_1 \ , \ V' = q_2 \ , \ V = H\frac{y'}{1 + gy' + g'y} \ ,$$

[12] For the positive sign of these two components I refer to the choice reported in Figure 25a.

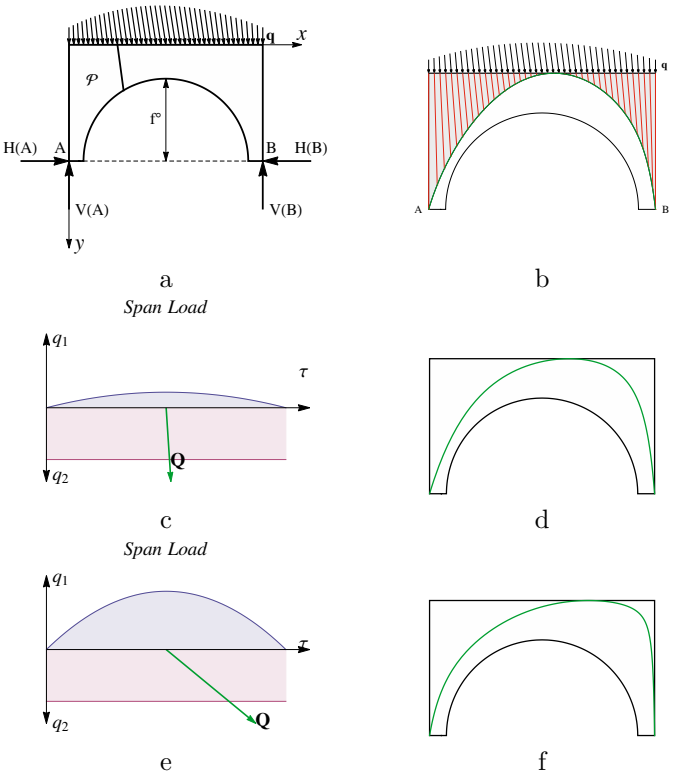

Figure 25. Lintel loaded by vertical and horizontal forces. Geometry of the panel: (a). Forces acting on the panel, compression rays and arch: (b). Horizontal and vertical load for two special cases (c, e) corresponding to the equilibrium solutions (d, f).

to be solved for H, V, y with the boundary conditions

$$y(0) = h^\circ \ , \ y(L) = h^\circ \ , \ y(\tau^\circ) = 0 \ , \ y'(\tau^\circ) = 0 \ ,$$

τ° being an unknown position along the upper edge. In the special case in which the horizontal and vertical loads have the form

$$q_1(\tau) = \frac{6q^\circ(L-\tau)^2\tau}{L^3} \ , \ q_2(\tau) = q^\circ \ ,$$

that is the vertical load is uniform, the horizontal load is parabolic, and the horizontal load resultant is half of the vertical resultant, the solution is

$$H = q^\circ \left(\frac{(h^\circ - L)^2}{8h^\circ} + \frac{6L^2\tau^2 - 8L\tau^3 + 3\tau^4}{2L^3} \right) ,$$

$$V = \frac{1}{2} q^\circ (h^\circ - L + 2\tau) ,$$

$$y = \frac{h^\circ L^3 (h^\circ - L + 2\tau)^2}{L^5 + (h^\circ)^2 a(\tau) - 2h^\circ b(\tau)} ,$$

where

$$a(\tau) = L^3 - 24L^2\tau + 48L\tau^2 - 24\tau^3 ,$$
$$b(\tau) = L^4 - 12L^3\tau + 36L^2\tau^2 - 44L\tau^3 + 18\tau^4 .$$

The solution of this special case for $h^\circ = \frac{L}{2}$ is reported in Figure 25.

Example 4. Lintel under a vertical uniform load and a horizontal concentrated force. Here I apply the stress function method to solve a problem similar to the previous one, namely the equilibrium of a rectangular, simply supported panel under a vertical uniform load applied along the top edge and a horizontal concentrated force acting at the left upper corner (Figure 26a). Again it is assumed that the supports in A and B react with two concentrated forces passing through A and B. These two forces are expressed in the form

$$\{\mathbf{R}(A)\} = \left\{ H, \frac{q^\circ L}{2} - \frac{Fh^\circ}{L} \right\} ,$$

$$\{\mathbf{R}(B)\} = \left\{ -H - F, \frac{q^\circ L}{2} + \frac{Fh^\circ}{L} \right\} ,$$

The corresponding boundary data for the stress function are reported pictorially in Figure 26b. Prolongating the data with ruled surfaces having the prescribed slope and direction at the boundary, a surface composed by three parts, a parabolic cylinder and two planes, is generated. Notice that the value of the thrust H could be chosen arbitrarily, within some limits, and that, in Figure 26b, it is set to a value such that the intersection of the lower plane with the parabolic cylinder, touches the upper boundary (minimal thrust).

The intersection of the three surfaces (Figure 26c) determines the 1d structure depicted in Figure 26d. The stress is uniaxial between the top edge and the structure Γ, null below the estrados of the arch; the singular part of it is concentrated on the support of the folds of F, that is on the structure Γ.

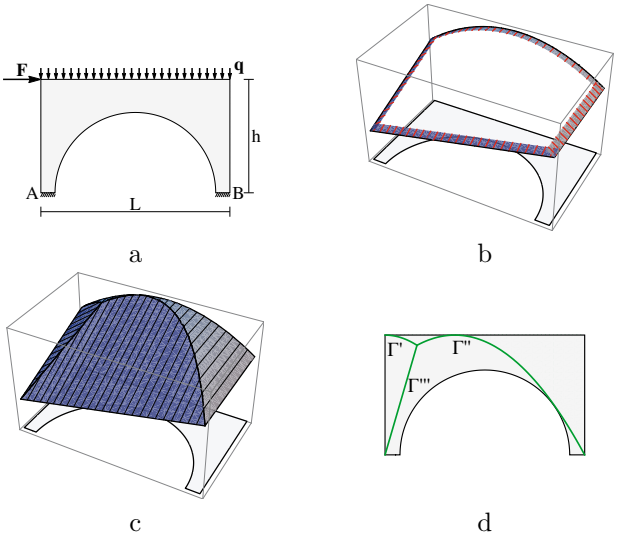

Figure 26. Lintel loaded by vertical and horizontal forces: (a). Boundary data: (b). Composite stress function: (c). Support of the singular stress, arch structure: (d).

Example 5. Lintel under homogeneous vertical body forces. A rectangular wall beam of heigth h° and width L, supported at the bottom corners A, B and submitted to homogeneous vertical body forces, is shown in Figure 27a, to which I refer for notations. This element is representative of lintels for which the effect of body forces is not negligible. The parameter $p^\circ = \frac{2h^\circ}{L}$ defines the aspect ratio of the lintel.

The lintel's lower edge is actually considered as symmetric (with respect to the center line) and curved (see dashed line in Figure 27a). For now the shape of this symmetric curve Γ is not specified, whilst its rise is fixed and called $f^\circ = (1-\alpha)h^\circ$, α being a parameter ranging in the open interval $(0,1)$. Notice that αh° is the thickness of the arch at the keystone.

The curve is described parametrically, in the Cartesian frame depicted in Figure 27a, as follows

$$\Gamma = \{\{\mathbf{x}_\Gamma\} = \{x, f(x)\}\ ,\ x \in [-L/2, L/2]\}\ ,$$

with

$$f(L/2) = f(-L/2) = 0, f(0) = (1-\alpha)h^\circ\ .$$

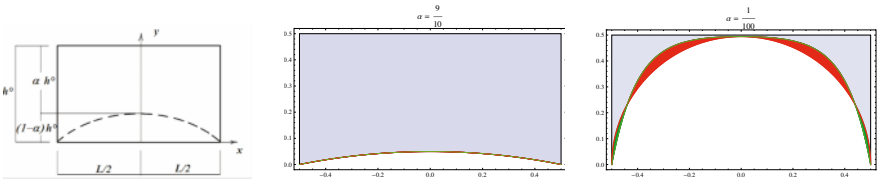

a b c

Figure 27. Lintel loaded by uniform body forces. Geometry of the panel: (a). Lower arch for $\alpha = 9/10$: (b) and for $\alpha = 1/100$: (c).

I construct two different statically admissible solutions for the equilibrium problem of the lintel as described in what follows.

First solution: maximal thrust. With the first solution I assume that inside the body the stress field is a.e. uniaxial and vertical, and an arch, on which the normal stress is concentrated, forms along the bottom boundary curve Γ. The loads acting on the wall produce a resultant vector $\mathbf{Q}$, having components $\{0, -Q\}$, with $Q = -\gamma\ area(\Omega)$, and located at the center of the wall. The supports A, B react with two forces $\mathbf{R}_A, \mathbf{R}_B$, whose components are denoted $\{H(A), V(A) = Q/2\}$, $\{-H(B), V(B) = Q/2\}$, where $H(A) = H(B) = H$, H being the unknown thrust of the arch; the rest of the boundary is unloaded.

The uniaxial stress field of simple compression in the vertical direction, has a non-vanishing component of the form

$$\sigma = -\gamma(h^\circ - y)\ .$$

Therefore the arch Γ is subjected to the vertical distributed load (per unit horizontal length) $q = -\gamma(h^\circ - f(x))$, $f(x)$ being the vertical coordinate of the arch Γ. For equilibrium the shape of the arch must satisfy the equation

$$f'' = -\gamma\frac{h^\circ - f}{H}\ .$$

that one can solve (for f and H) with the boundary conditions

$$f(L/2) = f(-L/2) = 0, f(0) = (1-\alpha)h^\circ\ .$$

The solution is

$$f = \frac{\left(1 + e^{L\sqrt{\frac{\gamma}{H}}} - e^{\frac{(L-2x)}{2}\sqrt{\frac{\gamma}{H}}} - e^{\frac{(L+2x)}{2}\sqrt{\frac{\gamma}{H}}}\right)\mathrm{h}^\circ}{1 + e^{L\sqrt{\frac{\gamma}{H}}}}\ ,$$

$$H = \gamma \frac{L^2}{\mathrm{Log}^2\left(\frac{2-\alpha^2-2\sqrt{1-\alpha^2}}{\alpha^2}\right)} \ .$$

The value of the force resultant is then

$$Q = \gamma p^\circ \frac{2L^2\left(1-\alpha^2+\sqrt{1-\alpha^2}\right)\left(\mathrm{Log}\left(2-\alpha^2-2\sqrt{1-\alpha^2}\right)-2\mathrm{Log}(\alpha)\right)}{\left(-1+\sqrt{1-\alpha^2}\right)\mathrm{Log}^2\left(\frac{2-\alpha^2+2\sqrt{1-\alpha^2}}{\alpha^2}\right)} \ .$$

In Figures 27b,c the shape of the lower curve determined through equilibrium is compared to the actual shape of the intrados of the lintel, for two extreme special cases ($\alpha = 0.9$, $\alpha = 0.01$). From these two pictures one can see that, in the first case, the statically admissible stress field here constructed can be accepted as an approximate equilibrated solution (by neglecting the slight geometrical difference between the two curves); whilst, in the second case, there is a large portion of the domain (located below the arch) that remains out of the picture.

It is to be pointed out that for $\alpha \to 1$, the thrust force tends to $+\infty$.

Second solution: reducing the thrust.The domain Ω is divided into two parts: the part Ω' comprised between the curve Γ and the curve

$$\Gamma' = \{\{\mathbf{x}_\Gamma\} = \{\{x, g(x)\} \ , \ x \in [-L/2, L/2]\}\} \ ,$$

with

$$g(x) = \frac{1}{1-\alpha} f(x) \ ,$$

and the part Ω'', that is the part of Ω located above Γ' (see Figure 28). A solution of the equilibrium problem for the region Ω' is constructed first; the problem of equilibrium of the region Ω'' is solved in a second phase, and superimposed to the previous stress field.

Again I restrict to at most uniaxial stress fields, assuming that the stress field is convected to one of the two families of curvilinear lines $\vartheta^1 = x, \vartheta^2 = \lambda$, defined by

$$x_1 = x \ , \ x_2 = h(x, \lambda) \ ,$$

with

$$h(x, \lambda) = (1 - \alpha + \lambda\alpha)\, g(x) \ ,$$

where, $x \in [-L/2, L/2]$, $\lambda \in (0, 1)$ and

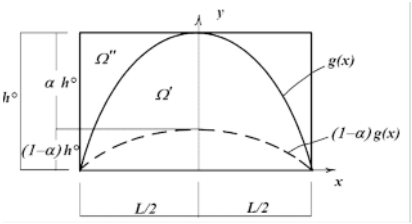

Figure 28. Lintel loaded by uniform body forces: geometry of the panel and domain partition for the second solution.

$$g(x) = \frac{1}{1-\alpha} f(x)$$

is the function describing the upper curve Γ'.

The natural and reciprocal base vectors associated to this curvilinear system, in components in the Cartesian reference depicted in Figure 28, are

$$\{\mathbf{a}_1\} = \{1, h_{,1}\} \ , \ \{\mathbf{a}_2\} = \{0, h_{,2}\} \ ,$$

$$\left\{\mathbf{a}^1\right\} = \{1, 0\} \ , \ \left\{\mathbf{a}^2\right\} = \left\{-\frac{h_{,1}}{h_{,2}}, \frac{1}{h_{,2}}\right\} \ .$$

The uniaxial stress field here considered has the form

$$\mathbf{T} = \sigma \mathbf{a}_1 \otimes \mathbf{a}_1 \ ,$$

σ being a function of (x, λ), describing the intensity of the stress field, to be found, together with f, by solving the equilibrium equation

$$\frac{\partial}{\partial \vartheta^\alpha} \left(\sigma \mathbf{a}_1 \otimes \mathbf{a}_1\right) \mathbf{a}^\alpha + \mathbf{b} = \mathbf{0} \ .$$

By projecting this vector equation along the natural bases, after some algebra, the following system of second order differential equations, is obtained:

$$\sigma_{,1} + \sigma \frac{h_{,12}}{h_{,2}} = 0 \ ,$$

$$-\frac{\gamma}{h_{,2}} + \sigma \frac{h_{,11}}{h_{,2}} = 0 \ ,$$

Recalling that $h_{,2} = \frac{\partial h}{\partial \lambda} = \alpha g$, since $h_{,2}$ is always different from zero inside Ω', integrating the first equation, one obtains

$$\sigma = \frac{m(\lambda)}{h_{,2}} \ ,$$

$m(\lambda)$ being an unknown function of λ. Substituting into the second equation one obtains

$$\gamma = m(\lambda)\frac{h_{,11}}{h_{,2}} \ .$$

Therefore, taking into account that $h_{,2} = \frac{\partial h}{\partial \lambda} = \alpha g$ and $h_{,11} = \frac{\partial^2 h}{\partial x^2} = (1 - \alpha + \alpha\lambda)g''$, the following two conditions are obtained:

$$g'' = -kg \ , \ m(\lambda) = -\gamma \frac{\alpha}{k(1 - \alpha + \alpha\lambda)} \ ,$$

k being a constant that I will assume positive.

By solving the first equation with the boundary conditions $g(-L/2) = 0, g(0) = h^\circ$ the following solution is obtained

$$g^\circ = \mathrm{h}^\circ \left(\cos\left(\sqrt{k}x\right) + \cot\left(\frac{\sqrt{k}L}{2}\right) \sin\left(\sqrt{k}x\right) \right) \ .$$

By imposing the condition $g'(0) = 0$ the value of the constant k is determined:

$$k = \frac{\pi^2}{L^2} \ ,$$

and then the form of the curve Γ' is given by

$$g^\circ = h^\circ cos\left(\frac{\pi x}{L}\right) \ ,$$

that is

$$\Gamma' = \left\{ \{\mathbf{x}\} = \left\{ x, h^\circ cos\left(\frac{\pi x}{L}\right) \right\} \ , \ x \in \left[-\frac{L}{2}, \frac{L}{2} \right] \right\} \ .$$

The *physical* uniaxial stress component

$$\sigma = T_{(11)} = \mathbf{T} \cdot \left(\frac{\mathbf{a}_1}{|\mathbf{a}_1|} \otimes \frac{\mathbf{a}_1}{|\mathbf{a}_1|} \right) = -\frac{L^2 \gamma \mathrm{Sec}\left(\frac{\pi x}{L}\right)}{\mathrm{h}^\circ \pi^2 (1 + \alpha(-1 + \lambda))} \ ,$$

along the ϑ^1 curves, is depicted in the graphic of Figure 29.

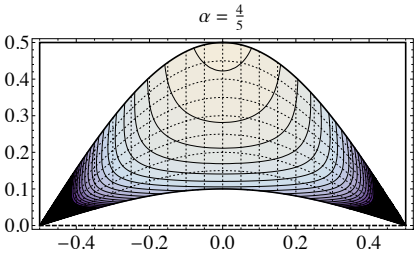

Figure 29. Contour plot of the stress σ in the region Ω'.

It is assumed that the load which is given above the curve Γ', is taken by an arch Γ'', that is by a concentrated stress with support on Γ''. The form of this curve, springing from the points A, B, determined by the form of the load through equilibrium, should be located below the load (that is below the curve Γ') and contained inside the masonry (that is above the curve Γ). In this way, the load can be transmitted to the arch by compressive uniaxial vertical stresses, linearly varying inside Ω'', and constant outside it.

The vertical load that I consider acting on Γ''' is then

$$q = \gamma(s + h^\circ - g^\circ) \ ,$$

γs being the effect of a given uniform over-load. By solving the equilibrium equation for the arch, with the conditions that the arch passes through the points A and B, and through the point P of coordinates $\{0, \mathrm{h}_y\}$, one obtains

$$\Gamma''' = \left\{ \left\{ x, \frac{\mathrm{h}_y \left(\pi^2 (L\mathrm{p}^\circ + 2s)\left(L^2 - 4x^2\right) - 8L^3 \mathrm{p}^\circ \cos\left(\frac{\pi x}{L}\right)\right)}{L^2 \left(L\left(-8 + \pi^2\right)\mathrm{p}^\circ + 2\pi^2 s\right)} \right\}, \right.$$
$$\left. x \in (-L/2, L/2) \right\} \ ,$$

where $p^\circ = \frac{2h^\circ}{L}$ is the *aspect ratio* of the lintel. In Figure 30 the form of the arch for $p^\circ = 1$, $s = L/8$ and three special cases is reported.

Finally the values of the vertical reactions and of the thrust forces in A and B, due to the compound effect of the first and the second equilibrium solutions are:

$$Q/2 = \frac{(\pi - 4p^\circ + 2\pi p^\circ)\gamma}{8\pi} + \frac{p^\circ \alpha \gamma}{2\pi} \ , \tag{23}$$

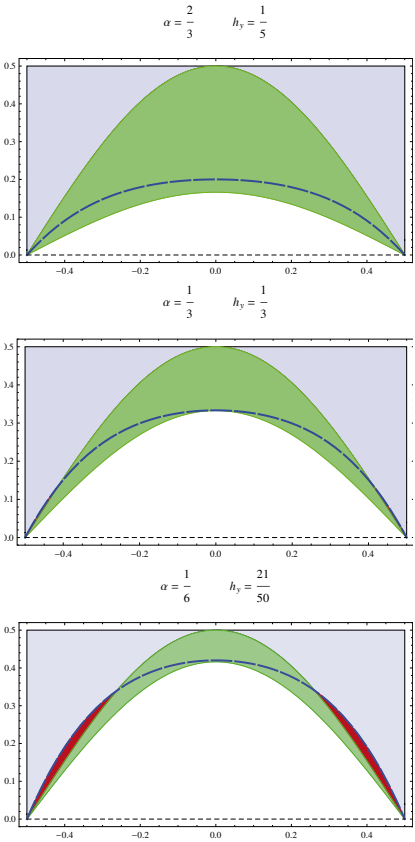

Figure 30. Lintel loaded by uniform body forces: geometry of the arch Γ''' carrying the load of the part Ω'' for three special cases: from top top to bottom, $\alpha = 2/3$, $\alpha = 1/3$, $\alpha = 1/6$.

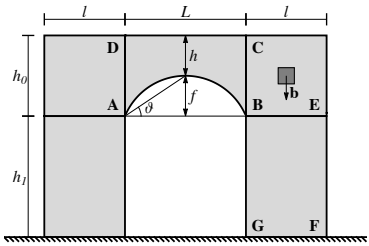

Figure 31. Typical masonry portal. L: span of the arch, f: rise, h: thickness. $ABCD$: lintel, $h_\circ$: height of the lintel. $GFEB$: pier, h_1: height of the pier, ℓ: width of the pier.

$$H = \frac{\left(-16p^\circ + \pi^2(1+2p^\circ)\right)\gamma}{32h_y\pi^2} - \frac{\gamma \mathrm{Log}(1-\alpha)}{\pi^2}\,. \tag{24}$$

2.10 Derand's rule

Based on the unilateral model the safety of the structure is a matter of geometry rather than of strength of materials, in keeping with the spirit of the "rules of proportion" used by the ancient architects for masonry design. The essential characteristic of all these rules is that they are proportional and that they control the overall form of the structure of the building, regardless of its size.

Most of these rules, being not written, have faded and progressively been forgotten, but it is evident that the great buildings of the past could not have been built without some kind of rich and complex knowledge, because its application resulted in astonishing realizations such as the Pantheon and the Gothic cathedrals. One of the rules that is survived, is the Derand's rule (see Benvenuto (1991) and Huerta (2008)), and here I try to assess the safety margins it assures on the basis of singular stress fields for the masonry-like model. The results here obtained confirm that this often criticized rule is actually a sharp technical tool.

The rule applied to a portal. In 1643 François Derand published his monumental work on vaults (Derand (1643)), where the rule for determining the thickness of the walls, needed to support the thrust of the vaults, appears. Here I apply the rule to a simple masonry portal.

If Figure 31, a masonry panel Ω, having the form of a portal, fixed at the base and unloaded on the rest of the boundary, is depicted. The panel

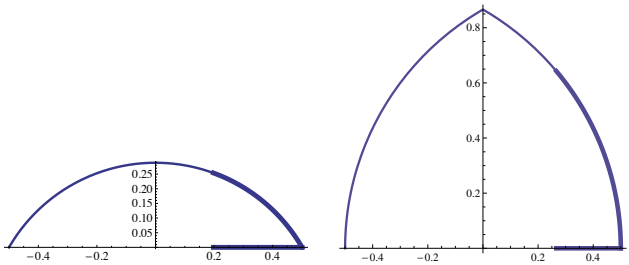

Figure 32. Derand's rule for shallow and pointed arches.

is loaded by its own weight **b**, considered uniform and acting vertically downward, and by a small uniform vertical load applied along the top edge. The main nomenclature concerning such a typical structure is reported in Figure 31, to which I refer for notations. For simplicity I take the unit of length and force in such a way that $L = 1$ and $|\mathbf{b}| = \gamma = 1$.

Derand's rule applies both to segmental and pointed arches as illustrated in Figure 32a,b, to which I refer for notations. Based on this rule the thickness of the wall is the segment ℓ_c indicated as a thick line in Figure 32a,b, that is given by the projection of the arch segment, reported in the same figure, on the horizontal line. The rule is that the arch segment whose projection determines ℓ_c, is $\frac{1}{3}$ of the total length of the intrados.

On introducing the angle $\vartheta = artan(2(1-\alpha)h^\circ)$ (in which α is the parameter introduced in the previous example) and noticing that the radii for the segmental ($\vartheta < \pi/4$) and pointed ($\vartheta > \pi/4$) arches are

$$r' = \frac{L}{2sin2\vartheta} \ , \ r'' = \frac{L}{2(1+cos2\vartheta)} \ ,$$

the rule gives

$$\ell_c = \begin{cases} \frac{L}{2} - r' sin\frac{2}{3}\vartheta \ , \\ r'' \left(1 - cos\frac{2}{3}(\pi - 2\vartheta)\right) \ . \end{cases} \tag{25}$$

Limit Analysis solution We analyze the equilibrium of the portal considering separately the equilibrium of the lintel ABCD and of the pier BEFG, and then assembling the two parts.

Lintel. The effect of the dead load **b** on the lintel depicted in Figure 33a is analyzed by adopting the second s.a. stress field, introduced in the previous Section. Based on this solution the forces transmitted to the piers at

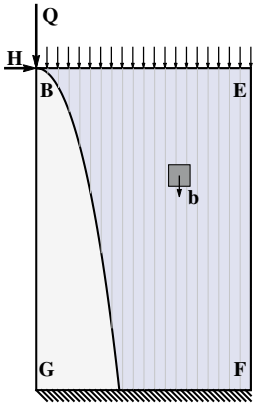

Figure 33. Forces acting of the pier. **Q**, **H** are the vertical and horizontal forces trasmitted by the lintel; the uniformly distributed load at the top base is the effect of the weight of the part BEC; **b** is the body force.

the points A, B, have the vertical and horizontal components given by (23) and (24).

The concentrated and distributed forces acting on the right pier of the portal, are depicted in Figure 33a.

Pier. These forces and their slope can be used as data for the equilibrium of the pier, as shown in Figure 33. In the pier $BEFG$ I consider an arch Γ springing from the point B with the slope given by $2H/Q$. The arch Γ is represented by its graph $z(x)$ in a right handed reference $\{O; x, y\}$ with origin in B and y directed vertically, downward. The arch Γ carries the inclined thrust force coming from the lintel and the weight of the part of the wall above it, besides the over-load s. A uniaxial stress field, linearly varying with y, and balancing the, constant, vertical load $\mathbf{b}$ ($|\mathbf{b}| = \gamma = 1$), is considered both above and below the arch: the upper part is sustained by the arch; the part below is supported by the soil. The equilibrium conditions give, in this case, the following equation for z:

$$z'' = \frac{1}{H}(s + h^\circ + z) \, .$$

This equation can be integrated with the conditions

$$z(0) = 0, z'(0) = \frac{2H}{Q} \, .$$

The solution is

$$z^\circ = \frac{1}{2}\left((p^\circ\frac{L}{2}+s)(1-e^{-\beta x})(-1+e^{\beta x})+\frac{2H}{Q\beta^2}(1+e^{\beta x})\right) ,$$

where $\beta = \sqrt{1/H}$. The form taken by the arch Γ depends on the aspect ratio, p°, of the lintel, and on the parameter α defining the thickness of the arch at the key stone. To compare the results with the rule of Derand, I introduce the parameter

$$\lambda = tan(\vartheta) ,$$

and notice that

$$\lambda = \frac{(1-\alpha)2h^\circ}{L} = (1-\alpha)p^\circ .$$

Then z° can be expressed as a function of p° and λ and the limit length ℓ_c, that is the intersection of the arch Γ' with the base, can be determined for different values of the heigth h.

Effect of the heigth: Gil's rule. Derand'rule makes no reference to the heigth of the pier, though other rules of proportion relating the shape of the arch to the heigth of the piers are known. One of these is the seventh rule of Gil (Rodrigo Gil de Hontanon, see Huerta (2004)) for which the heigth of the pier is approximately twice the rise of the arch.

In Figure 34 a comparison between the values of ℓ_c given by Derand's rule with that obtained with the RNT model under Gil's prescription (that is by putting for the heigth: $h = 2f$), is presented. The values of ℓ_c are plotted against the parameter λ, for a few values of the parameter p°, in the range of practical interest: $\{\frac{1}{10}, \frac{9}{10}\}$. The different curves refer to different values of p°.

The values of ℓ_c predicted with the unilateral model (which being obtained with the static theorem of LA are *safe* and then upper bounds to the limit length ℓ_c) are always smaller than the values prescribed by Derand in the range of values of the aspect ratio p° here explored. Notice that the range considered covers both the cases of shallow and pointed arches and that, based on the NT theory, Derand's prescription appears as a rather sharp rule.

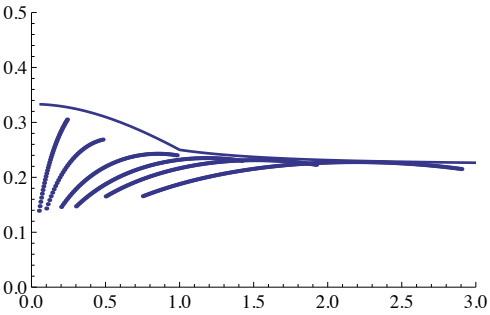

Figure 34. Comparison of Derand's (and Gil's) rule with LA predictions. The continuous upper curve represents the graphic of Derand's rule (25). The sequence of curves represents the LA predictions of ℓ_c for (from left to right) $p^\circ = \{\frac{1}{8}, \frac{1}{4}, \frac{1}{2}, 1, 2, 3\}$.

3 Model *one* (NENT)

In this section the main ingredients of the theory concerning model *one* for masonry materials, namely the Normal Elastic No-Tension (NENT) material, that is the $n > 1$ version of the 1d model introduced in Chapter 1, are presented. The constitutive assumptions, the balance equations and the boundary conditions are introduced and the boundary value problem for NENT materials is formulated. On introducing a proper form of stored elastic energy, the minimum problem for the potential energy functional provides the existence of the solution for this boundary value problem. The main issues connected with energy minimization and a number of illustrative exact solutions and examples are discussed.

3.1 A Premise on Minimum problems and the peculiarity of NT materials

Several problems in physics and Engineering can be formulated as a minimum search: a functional describing the energy of the system and depending on an unknown function has to be minimized over the set of all admissible functions. In the context of elasticity, denoting $\mathbf{u}$ the displacement vector describing the deformation from a given configuration Ω, of a material body subject to a system of applied forces and given boundary displacements, the energy can be written in the form

$$E(\mathbf{u}) = -\langle \ell, \mathbf{u} \rangle + U(\mathbf{u}) \,, \tag{26}$$

where -$\langle \ell, \mathbf{u} \rangle$ is the linear form describing the potential energy of the load, that is minus the work of the load $\ell = (\underline{\mathbf{s}}, \mathbf{b})$ for the displacement $\mathbf{u}$, and U($\mathbf{u}$) is the stored energy functional. The simplest case in which existence theorems for the minimum problem

$$\min_{\mathbf{u} \in K} E(\mathbf{u}) \ , \tag{27}$$

K being the subset of a convenient Banach space $T(\tilde{\Omega})$, occurs when $E(\mathbf{u})$ is lower semicontinuous and coercive, in the sense that $E(\mathbf{u}) \to \infty$ as $\|\mathbf{u}\|_S \to \infty$. Unfortunately, as we shall see, the energy functional for masonry-like materials is not coercive (see also the form that the strain energy density takes in the 1d case (see Figure 10.a of Chapter 1) and therefore some supplementary hypotheses have to be added in order to get existence. For instance, existence of solution in the case of Normal Elastic No-Tension materials, under small strains and in the 2d context, has been established by Giaquinta and Giusti (in Giaquinta and Giusti (1985)), under a so called *safe load condition*. Specifically the form of energy to be minimized in the case of NENT materials is

$$E(\mathbf{u}) = -\int_{\partial\Omega_N} \underline{\mathbf{s}} \cdot \mathbf{u} - \int_{\Omega} \mathbf{b} \cdot \mathbf{u} + \int_{\Omega} \Phi(\mathbf{E}(\mathbf{u})) \ , \tag{28}$$

where $\mathbf{E}(\mathbf{u})$ is the infinitesimal strain associated to $\mathbf{u}$, $\Phi(\mathbf{E}(\mathbf{u}))$ is the elastic energy density, and the stress $\mathbf{T}$ is related to $\mathbf{E}$ through the relation

$$\mathbf{T} = \frac{\partial \Phi}{\partial \mathbf{E}} \ . \tag{29}$$

The minimizer of $E(\mathbf{u})$ is searched for $\mathbf{u} \in S(\Omega)$ (a Banach space) and $\mathbf{u} = \underline{\mathbf{u}}$ on $\partial\Omega_D$. Concerning the nature of such Banach space, that is the regularity of $\mathbf{u}$, actually it seems reasonable to expect, based on the non coercivity of Φ (see Figure 10.a of Chapter 1) and on the at most linear growth of the energy $E(\mathbf{u})$, that $\mathbf{u}$ be possibly discontinuous and the corresponding deformation not to be absolutely continuous. A popular choice for $S(\Omega)$ is the space $BD(\Omega)$ of bounded deformations, though one expects that, apart from very special cases and away from the case of collapse loads, the minimizers should be much more regular. We shall return to the variational formulation of equilibrium for masonry materials after the BVP in its strong form is considered.

3.2 The Boundary Value Problem for NENT materials

Constitutive restrictions. It is assumed that the structure $\Omega \in \Re^n$ (here $n = 2$), loaded by the given tractions $\underline{\mathbf{s}}$ on the part $\partial\Omega_N$ of the boundary, and

subject to given displacements $\underline{\mathbf{u}}$ on the complementary, constrained part of the boundary $\partial\Omega_D$, is in equilibrium under the action of the given surface and body loads ($\underline{\mathbf{s}}$, $\mathbf{b}$) and distortions $\underline{\mathbf{E}}$, and undergoes small displacements $\mathbf{u}$ and strains $\mathbf{E}(\mathbf{u})$[13].

Notice again that Ω is considered closed on $\partial\Omega_D$ and open on the rest of the boundary.

We consider that the structure Ω is composed of Normal Elastic No-Tension material, that is the stress $\mathbf{T}$ is negative semidefinite

$$\mathbf{T} \in Sym^{-} \ , \tag{30}$$

the effective strain, that is the total infinitesimal strain $\mathbf{E}(\mathbf{u})$ minus the eigenstrains $\underline{\mathbf{E}}$, is decomposed additively into the sum of an elastic part $\mathbf{E}^e$ and an anelastic part $\mathbf{E}^a$, namely:

$$\mathbf{E}(u) = \mathbf{E}^e + \mathbf{E}^a + \underline{\mathbf{E}} \ , \tag{31}$$

the elastic part being linearly related to the stress $\mathbf{T}$:

$$\mathbf{E}^e = \mathbf{A}\,[\mathbf{T}] \ , \tag{32}$$

the latent anelastic part (a measure for fracture) being positive semidefinite

$$\mathbf{E}^a \in Sym^{+} \ , \tag{33}$$

and the stress $\mathbf{T}$ doing no work for the corresponding latent strain $\mathbf{E}^a$

$$\mathbf{T} \cdot \mathbf{E}^a = 0 \ . \tag{34}$$

Notice that in the plane case (n=2) conditions (30), (33), can be rewritten as

$$tr\,\mathbf{T} \leq 0 \ , \ det\,\mathbf{T} \geq 0 \ , \tag{35}$$

$$tr\,\mathbf{E}^a \geq 0 \ , \ det\,\mathbf{E}^a \geq 0 \ . \tag{36}$$

Remark 10. It is to be pointed out that a NENT material, that is a material defined by the restrictions (30) through (34), is elastic in the sense that, given the total strain $\mathbf{E}(\mathbf{u})$, the stress can be univocally determined. The material is actually hyperelastic as we shall see later in what follows.$\diamond$

[13]When eigenstrains are considered, under the small strain assumption, the total strain $\mathbf{E}(\mathbf{u})$ is decomposed additively as follows: $\mathbf{E}(\mathbf{u})=\mathbf{E}^* + \underline{\mathbf{E}}$, $\mathbf{E}^*$ being the *effective* strain of the material.

Equilibrium problem. In order to avoid trivial incompatible loads ($\underline{\mathbf{s}}$,$\mathbf{b}$), I assume again that the tractions $\underline{\mathbf{s}}$ satisfy condition (4).

In equilibrium, the stress field $\mathbf{T}$ must be balanced with $\mathbf{b}$, that is

$$div\mathbf{T} + \mathbf{b} = \mathbf{0} \,, \tag{37}$$

and the stress $\mathbf{T}$ and the displacement $\mathbf{u}$ must comply with the boundary conditions

$$\mathbf{T}\mathbf{n} = \underline{\mathbf{s}} \,, \; on \; \partial\Omega_N \,, \mathbf{u} = \underline{\mathbf{u}} \,, \; on \; \partial\Omega_D \,. \tag{38}$$

Boundary Value Problem. The boundary value problem for NENT materials can be formulated as follows:

Given a bounded open set Ω *and the partition* $\partial\Omega = \partial\Omega_D \cup \partial\Omega_N$, *find the fields* $\mathbf{u}$, $\mathbf{T}$ *defined over* $\Omega \cup \partial\Omega_D$, *such that the material restrictions* (30) through (34), *the balance equations* (37) *and the b.c.* (38) *are satisfied.*

Peculiar features of the fracture field for NENT materials, in the three sets of the Fundamental Partition. As it was already observed in the previous Chapter concerning the RNT model, to each statically admissible stress field $\mathbf{T}$ defined over $\Omega \cup \partial\Omega_D$, is associated a Fundamental Partition of the domain: $\Omega = \Omega_1 \cup \Omega_2 \cup \Omega_3$, of biaxial, uniaxial and zero stress (see Section 2.3).

In Ω_2 the equilibrium equations and the condition $det\mathbf{T} = 0$, form a system of three equations in the three unknown independent components of $\mathbf{T}$. The differential problem is parabolic and the stress is determined by equilibrium regardless of the material response.

In Ω_1 fractures are not possible, that is $\mathbf{E}^a = \mathbf{0}$.

In Ω_3, where $\mathbf{T} = \mathtt{0}$, any positive semidefinite fracture field is possible.

Also in Ω_2 the material can be fractured. The necessity of fractures is naturally produced by the problem being statically determined: the elastic strain associated to the statically determined stress is generally not compatible and fracture strains are required to restore compatibility. The normality condition requires that in Ω_2 the fractures must open up orthogonally to the isostatic compression lines, therefore, as a consequence of normality, on a crack line (that is a line where the strain is a line Dirac delta) the jump of displacement must be purely orthogonal to the crack line. If the strain is regular, in a curvilinear frame with natural bases $\mathbf{a}_1, \mathbf{a}_2$ coincident with the eigenvectors of $\mathbf{T}$, $\mathbf{T}$ admits the representation

$$\mathbf{T} = \sigma \frac{\mathbf{a}_1 \otimes \mathbf{a}_1}{\mathbf{a}_1 \cdot \mathbf{a}_1} ,$$

σ being the only non zero, negative eigenvalue of $\mathbf{T}$. Normality implies the following form for the fracture strain $\mathbf{E}^a$:

$$\mathbf{E}^a = \lambda \frac{\mathbf{a}_2 \otimes \mathbf{a}_2}{\mathbf{a}_2 \cdot \mathbf{a}_2} ,$$

λ being the only non zero, non negative eigenvalue of $\mathbf{E}^a$. Then, regardless of the possible elastic anisotropy of the material, the principal directions of stress and anelastic strain of a NENT material are always coincident all over Ω.

3.3 Strain energy density in 2d

Most of the features illustrated by the 1d ENT model (that is *Model 1* introduced in *Chapter* 1) are transposed to the 2d case, except that to obtain hyperelasticity there is a price to pay: the assumption of normality (that is the constituitve assumptions (33), (34)) must be made on the total latent strain $\mathbf{E}^a$. Such an assumption implies that on a discontinuity line Γ for the displacement $\mathbf{u}$, that is on the support of a concentrated fracture, the jump of displacement must be orthogonal to Γ. Therefore sliding is forbidden on fracture lines. It is shown by Del Piero in Del Piero (1989) that, for NENT materials, the major symmetry of $\mathbf{A}$ is necessary and sufficient to get existence of an elastic energy function. In the isotropic case the form of the energy density Φ can be constructed explicitly[14] in terms of the eigenvalues e_1, e_2 of $\mathbf{E}$ (here $e_1 < e_2$ is assumed). In the case of generalized plane stress, one has (see Figure 35)

$$\Phi = \begin{cases} 0 , & e_1 \geq 0 \text{ and } e_2 \geq 0 , \\ \frac{1}{2} E e_1^2 , & e_1 < 0 \text{ and } e_2 \geq -\nu e_1 , \\ \frac{1}{2} \frac{E}{1-\nu^2} \left(e_1^2 + e_2^2 + 2\nu e_1 e_2 \right) & e_1 < 0 \text{ and } e_2 < -\nu e_1 , \end{cases}$$

E, ν being the Young modulus and the Poisson ratio. Notice that the stress $\mathbf{T}$ derived from Φ satisfies identically the no-tension restriction (30), that is there is no need to impose it as a constraint.

[14] In the general anisotropic case the explicit symbolic form of Φ is not known and must be constructed numerically, case by case.

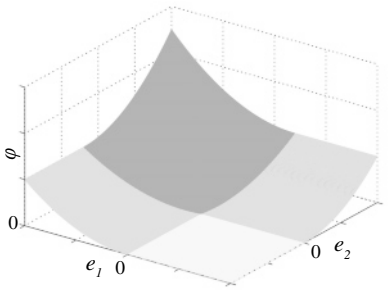

Figure 35. Strain energy density of isotropic NENT materials: zero energy region: light grey; parabolic energy region: grey; elliptic energy region: dark grey.

3.4 Function spaces for the potential energy functional.

For hyperelastic materials equilibrium states of the body can be searched as minimizers of the total potential energy (28)

$$\min_{\mathbf{u}\in K} E(\mathbf{u}) \ , \tag{39}$$

K being the set of kinematically admissible displacement fields for NENT materials, defined as follows

$$K = \{\mathbf{u} \in T(\Omega) \ s.t. \ \mathbf{u} = \underline{\mathbf{u}} \ on \ \partial\Omega_D \ \} \ , \tag{40}$$

where $\Omega = \dot{\Omega} \cup \partial\Omega_D$ and $T(\Omega)$ is a convenient Banach space. As it is evident from the picture of Figure 35, the strain energy function characterizing NENT materials is not coercive.

Coercivity of the total potential energy can be restored by considering the following *supersafe load condition* on the applied forces (here I consider for simplicity the case of fixed boundary constraints: $\mathbf{u} = 0$, *on* $\partial\Omega_D$)

Supersafe load condition. The load $\mathbf{p}, \mathbf{b}$ is said to be *supersafe* if there exists at least one stress field $\overline{\mathbf{T}} \in H$, H being the set of statically admissible stress fields for NT materials defined in (7):

$$H = \left\{\mathbf{T} \in S(\Omega) \ s.t. \ div\mathbf{T} + \mathbf{b} = \mathbf{0} \ , \ \mathbf{Tn} = \underline{\mathbf{s}} \ on \ \partial\Omega_N \ , \ \mathbf{T} \in Sym^- \right\} \ , \tag{41}$$

such that

$$(\overline{\mathbf{T}} + \beta \mathbf{I}) \in Sym^{-} \ , \tag{42}$$

for some constant $\beta > 0$. In other words the load is supersafe if $\overline{\mathbf{T}}$ is strictly statically admissible over the set Ω in a uniform way, that is independently of $\mathbf{x}$. The definition of supersafe loads depends on the choice of the function space $S(\Omega)$. For NENT materials one can assume

$$S(\Omega) \equiv L^2(\Omega) \ . \tag{43}$$

If the load is supersafe then the potential energy associated to the external forces can be expressed in terms of $\overline{\mathbf{T}}$ and of any displacement $\mathbf{u} \in K$, in the form

$$-\int_{\partial\Omega_N} \underline{\mathbf{s}} \cdot \mathbf{u} - \int_{\Omega} \mathbf{b} \cdot \mathbf{u} = -\int_{\Omega} \overline{\mathbf{T}} \cdot \mathbf{E}(\mathbf{u}) \ .$$

Then the total potential energy can be rewritten in terms of this super safe s.a. stress field $\overline{\mathbf{T}}$ as

$$E(\mathbf{u}) = -\int_{\Omega} \overline{\mathbf{T}} \cdot \mathbf{E}(\mathbf{u}) + \frac{1}{2} \int_{\Omega} \mathbf{C}[\mathbf{E}^e(\mathbf{u})] \cdot \mathbf{E}^e(\mathbf{u}) \ .$$

Recalling that $\mathbf{E}(\mathbf{u}) = \mathbf{E}^e(\mathbf{u}) + \mathbf{E}^a(\mathbf{u})$, on using the safe load assumption one can write

$$E(\mathbf{u}) \geq -\int_{\Omega} \overline{\mathbf{T}} \cdot \mathbf{E}^e(\mathbf{u}) + \frac{1}{2} \int_{\Omega} \mathbf{C}[\mathbf{E}^e(\mathbf{u})] \cdot \mathbf{E}^e(\mathbf{u}) + \beta \int_{\Omega} |\mathbf{E}^a(\mathbf{u})| \ ,$$

that is the energy has at least a linear growth with respect to the norm of the space $BD(\Omega)$: the space of functions $\mathbf{u}$ whose corresponding infinitesimal deformation $\mathbf{E}$ is a bounded measure. For full information on this function space I refer to the paper by Temam and Strang (1994). Here I notice only that, since the infinitesimal strain $\mathbf{E}$ can be a bounded measure, then $\mathbf{u}$ can be discontinuous and $\mathbf{E}$ can be decomposed in its absolutely continuous and singular parts with respect to the 2d Lebesgue measure:

$$\mathbf{E}(\mathbf{u}) = \mathbf{E}_r + \mathbf{E}_s \ .$$

Recalling the decomposition of $\mathbf{E}$ into its elastic and fracture parts, since the potential energy grows quadratically with respect to the elastic part of the deformation, then only the fracture part $\mathbf{E}^a$ can be singular,

that is only fracture discontinuities are admitted. In other words the elastic deformation must be regular and the anelastic deformation can be either regular or singular. In Giaquinta and Giusti (1985) (theorem 6.8, p 381), the authors show the existence of the solution for the minimum problem with $T(\Omega) = BD(\Omega)$ under the supersafe load condition (and some supplementary technical conditions) in the special case of traction problems and isotropic elastic behaviour. Since the energy is not strictly convex the solution is in general non unique.

3.5 Complementary energy functional.

Also a dual energy principle based on the Complementary Energy can be proved (see Giaquinta and Giusti (1985)). The stress state $\mathbf{T}^\circ$ that corresponds to the solution of the boundary value problem for NENT materials can be characterized as the minimizer of the energy functional

$$E_c(\mathbf{T}) = -\int_{\partial\Omega_D} \mathbf{T}\mathbf{n}\cdot\underline{\mathbf{u}} + \frac{1}{2}\int_\Omega \mathbf{A}[\mathbf{T}]\cdot\mathbf{T}\ , \tag{44}$$

over the set H of statically admissible stress fields

$$H = \left\{\mathbf{T}\in S(\Omega)\ s.t.\ div\mathbf{T}+\mathbf{b}=\mathbf{0}\ ,\ \mathbf{T}\mathbf{n}=\underline{\mathbf{s}}\ on\ \partial\Omega_N\ ,\ \mathbf{T}\in Sym^-\right\}\ , \tag{45}$$

$S(\Omega)$ being a convenient Banach space. $S(\Omega)$ can be assumed as the Hilbert space $L^2(\Omega)$: in other words H is represented by the symmetric second order tensors $\mathbf{T}$ of $L^2(\Omega)$, such that $\mathbf{T}$ is negative semidefinite and balanced with $\underline{\underline{\mathbf{s}}}, \mathbf{b}$. Obviously on considering $\mathbf{T}\in L^2(\Omega)$ the balance conditions must be considered in a generalized sense (see (8), (9)).

The choice of $L^2(\Omega)$ as the function space for the stress field seems natural considering the quadratic term which represents the stress energy in the complementary energy (44). Since the Complementary Energy functional is strictly convex over the convex set H, the existence and the uniqueness of the minimizer $\mathbf{T}^\circ$ of such functional is guaranteed whenever H is not void (that is there exist at least one square summable stress field $\mathbf{T}$ such that $\mathbf{T}$ is negative semidefinite and balanced with $\underline{\underline{\mathbf{s}}}, \mathbf{b}$, or, in other words, the loads are compatible in the sense of definition (17)). Therefore though the solution $\mathbf{u}^\circ$ may be non unique the elastic part $\mathbf{E}^e$ of the strain solution is unique. Non uniqueness is restricted to the anelastic part $\mathbf{E}^a$ of the deformation $\mathbf{E}$, and to special arrangements of the boundary conditions. This circumstance makes the displacement and stress approach to the equilibrium of NENT materials non symmetric, in the sense that existence of the minimizer $\mathbf{T}^\circ$ for the complementary energy. is not sufficient for the existence of the minimizer $\mathbf{u}^\circ$ of the potential energy E. The existence of $\mathbf{T}^\circ$

requires only the existence of an admissible stress field, existence of $\mathbf{u}^\circ$, with the known theorems, requires instead the existence of a uniformly strictly admissible stress field. There are indeed counterexamples for the existence of $\mathbf{u}^\circ$ in the case the loads do not satisfy the safe load condition, in which a s.a. stress field $\mathbf{T}^\circ$ can be found; two of them are reported in the next *Subsection*.

3.6 Examples of non-existence.

To my knowledge there are no examples of non existence, for traction problems, in the case in which the loads do not satisfy the safe load condition but there exists a strictly admissible stress field $\mathbf{T}$. The only known counterexamples refer to the case in which the loads do not satisfy the safe load condition and there exists a balanced and admissible, but not strictly admissible, stress field $\mathbf{T}$. In the known examples there are parts of the domain that can be taken away and transplaced rigidly, without paying any energy price. Therefore $E = 0$ as $|\mathbf{u}| \to +\infty$, and I can say that the loads are collapse loads, in the sense that the deformation can increase indefinitely at constant load. Some trivial examples of non-existence are considered in what follows.

Two examples of non existence. The NENT material is a peculiar model for a continuum, some care in the imposition of the data must be exercised to avoid nasty results, that is lack of solution or very large displacements for small loads. The idea is that the material is rather delicate and loads and displacements must be applied cautiously to allow for the material to accept them. This aspect is somehow in keeping with the behaviour of real masonry structures which suffer from the application of concentrated loads or from the abrupt changes of loads or given displacements. The message is that the data of a BVP relative to a body made of NENT material must be specially disposed and coordinated.

The two following examples are two, more or less famous, examples of non existence. The first case (Figure 36a) refers to a traction problem, the second (Figure 36b) to a mixed BVP.

These two examples suggest that a *finite* normal crack develops on a line: the assumption of infinitesimal displacements and strains is violated.

3.7 Elementary analytical solutions

A number of closed form solutions for NENT materials were first presented in Angelillo and Giliberti (1988); here I report some of them.

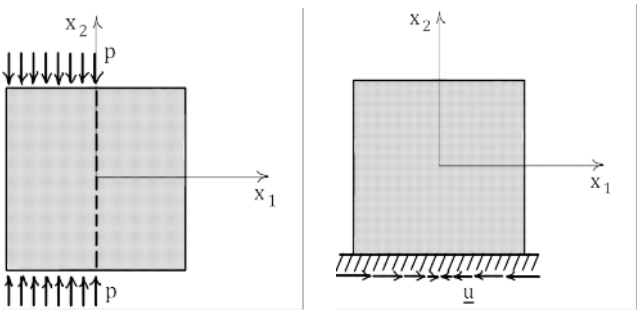

Figure 36. Examples of non existence of the solution for the NENT BVP. (a) : the displacement corresponding to the only statically admissible state cannot possibly verify the normality condition at the interface Γ (the vertical center line), unless the normal displacement jump on Γ tends to $+\infty$. (b): since the only statically admissible stress field is $\mathbf{T} = \mathbf{0}$, any k.a. displacement field cannot possibly satisfy the normality condition at the base for the given tangential displacements, unless the normal displacement jump at the base tends to $+\infty$.

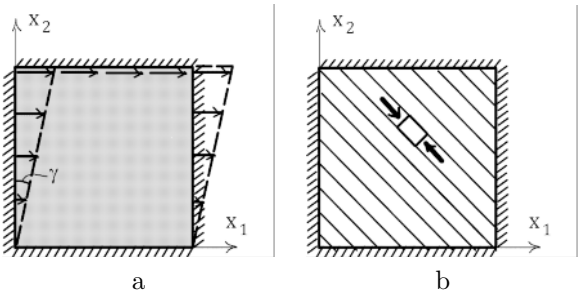

Figure 37. Pure shear: (a). Stress field solution: (b).

Exact solution 1: Pure shear. The very first simple, non trivial solution (i.e. distinct from elementary solutions of linear elasticity), for NENT materials is pure shear (Figure 37).

The solution, in terms of displacements, is identical to the universal solution for homogeneous linearly elastic materials, that is

$$u_1 = \gamma x_2 \ , \ u_2 = 0 \ .$$

The corresponding strain decomposition into elastic and anelastic strains: $\mathbf{E} = \mathbf{E}^e + \mathbf{E}^a$, for a homogeneous and isotropic NENT material, is

$$\left\{ \begin{array}{cc} 0 & \frac{\gamma}{2} \\ \frac{\gamma}{2} & 0 \end{array} \right\} = \left\{ \begin{array}{cc} -\frac{\gamma}{4} & \frac{\gamma}{4} \\ \frac{\gamma}{4} & -\frac{\gamma}{4} \end{array} \right\} + \nu \left\{ \begin{array}{cc} \frac{\gamma}{4} & \frac{\gamma}{4} \\ \frac{\gamma}{4} & \frac{\gamma}{4} \end{array} \right\} + (1-\nu) \left\{ \begin{array}{cc} \frac{\gamma}{4} & \frac{\gamma}{4} \\ \frac{\gamma}{4} & \frac{\gamma}{4} \end{array} \right\} ,$$

where

$$\{\mathbf{E}^a\} = (1-\nu) \left\{ \begin{array}{cc} \frac{\gamma}{4} & \frac{\gamma}{4} \\ \frac{\gamma}{4} & \frac{\gamma}{4} \end{array} \right\} .$$

The associated stress field, trivially balanced with zero body loads inside Ω is (see Figure 37b)

$$\{\mathbf{T}\} = E \left\{ \begin{array}{cc} -\frac{\gamma}{4} & \frac{\gamma}{4} \\ \frac{\gamma}{4} & -\frac{\gamma}{4} \end{array} \right\} .$$

With this solution the whole domain is of the Ω_2 type, the material being uniformly compressed along a family of compression rays parallel to a diagonal of the square panel; uniformly distributed fractures open up in the direction of the other diagonal. Therefore, in a real masonry panel, one may expect a pattern of parallel cracks in the direction of the compression rays.

Exact solution 2: Simple flexure. The second problem I consider is the flexure of a rectangular strip. The geometry and the boundary conditions are depicted in Figure 38a to which I refer for notations. A simple solution of the problem exists if the material is isotropic and one assumes $\nu = 0$ (an assumption that, though far from being realistic, produces easy analytical solution that one can use as benchmark problems for numerical approximations).

In this case the displacement field $\mathbf{u} = u\hat{\mathbf{e}}_1 + v\hat{\mathbf{e}}_2$ with

$$u = \frac{\varphi}{L}(L - 2x_1)x_2 ,$$

$$v = -\frac{\varphi}{L}(L - x_1)x_1 ,$$

solves all the field and boundary equations, for a homogeneous and isotropic NENT material, with $\nu = 0$. Indeed the corresponding total strain is

$$\{\mathbf{E}\} = \left\{ \begin{array}{cc} -2\frac{\varphi x_2}{L} & 0 \\ 0 & 0 \end{array} \right\} ,$$

that is easily decomposed into the elastic and fracture parts:

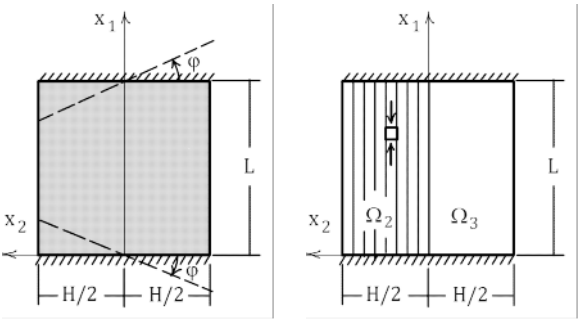

a b

Figure 38. Pure flexure of a rectangular strip. Boundary data: (a), stress and domain partition corresponding to the first solution: (b).

$$\{\mathbf{E}^e\} = \begin{cases} \left\{ \begin{array}{cc} -2\frac{\varphi x_2}{L} & 0 \\ 0 & 0 \end{array} \right\} & , \; x_2 > 0 \, , \\ \\ \left\{ \begin{array}{cc} 0 & 0 \\ 0 & 0 \end{array} \right\} & , \; x_2 \leq 0 \, , \end{cases} \tag{46}$$

$$\{\mathbf{E}^a\} = \begin{cases} \left\{ \begin{array}{cc} 0 & 0 \\ 0 & 0 \end{array} \right\} & , \; x_2 > 0 \, , \\ \\ \left\{ \begin{array}{cc} -2\frac{\varphi x_2}{L} & 0 \\ 0 & 0 \end{array} \right\} & , \; x_2 \leq 0 \, . \end{cases} \tag{47}$$

The corresponding stress field is

$$\{\mathbf{T}\} = E \begin{cases} \left\{ \begin{array}{cc} -2\frac{\varphi x_2}{L} & 0 \\ 0 & 0 \end{array} \right\} & , \; x_2 > 0 \, , \\ \\ \left\{ \begin{array}{cc} 0 & 0 \\ 0 & 0 \end{array} \right\} & , \; x_2 \leq 0 \, . \end{cases} \tag{48}$$

This stress field is obviously balanced with the prescribed body load $\mathbf{b} = \mathbf{0}$ at the interior and with the surface tractions $\underline{\mathbf{s}} = \mathbf{0}$ given at the loaded part of the boundary ($x = \mp H/2$). Based on this solution for the

stress, the domain Ω is divided into two zones of the type Ω_2, Ω_3, as depicted in Figure 38b.

For this example I can also give a different solution, namely the same stress field but a different fracture field, under the same boundary conditions. The second solution (see Figure 39) to the same problem is defined by the displacement field $\mathbf{u} = u\hat{\mathbf{e}}_1 + v\hat{\mathbf{e}}_2$, as follows

$$u = \begin{cases} \frac{\varphi}{L}(L - 2x_1)x_2 & , \ x_2 > 0 \ , \\ \varphi x_2 & , \ x_2 < 0 \text{ and, } \ x_1 < L/2 \ , \\ -\varphi x_2 & , \ x_2 < 0 \text{ and, } \ x_1 > L/2 \ , \end{cases}$$

$$v = \begin{cases} -\frac{\varphi}{L}(L - x_1)x_1 & , \ x_2 > 0 \ , \\ -\varphi x_1 & , \ x_2 < 0 \text{ and, } \ x_1 < L/2 \ , \\ \varphi(x_1 - L) & , \ x_2 < 0 \text{ and, } \ x_1 > L/2 \ . \end{cases}$$

The corresponding total strain is composed of absolutely continuous and singular parts: $\mathbf{E} = \mathbf{E}_r + \mathbf{E}_s$ with

$$\{\mathbf{E}_r\} = \begin{cases} \left\{ \begin{array}{cc} -2\frac{\varphi x_2}{L} & 0 \\ 0 & 0 \end{array} \right\} & , \ x_2 > 0 \ , \\ \left\{ \begin{array}{cc} 0 & 0 \\ 0 & 0 \end{array} \right\} & , \ x_2 \leq 0 \ , \end{cases}$$

$$\{\mathbf{E}_s\} = \begin{cases} \left\{ \begin{array}{cc} -2\varphi x_2 & 0 \\ 0 & 0 \end{array} \right\} \delta & , \ x_1 = L/2 \text{ and } x_2 \leq 0 \ , \\ \left\{ \begin{array}{cc} 0 & 0 \\ 0 & \frac{\varphi x_1^2}{L} \end{array} \right\} \delta & , \ x_1 < L/2 \text{ and } x_2 = 0 \ , \\ \left\{ \begin{array}{cc} -2\varphi x_2 & 0 \\ 0 & \frac{\varphi(x_1 - L)^2}{L} \end{array} \right\} \delta & , \ x_1 > L/2 \ \& \ x_2 = 0 \ . \end{cases}$$

where δ denotes the unit Dirac delta. The total strain is then decomposed in its elastic and anelastic parts as follows:

$$\mathbf{E}^e = \mathbf{E}_r \ , \ \mathbf{E}^a = \mathbf{E}_s \ .$$

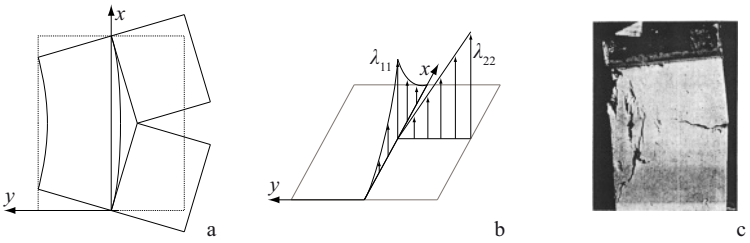

Figure 39. Deformed configuration corresponding to the second solution: (a). Graph of the non zero Cartesian components of $\mathbf{E}^a$:(b). Flexure test on a masonry panel (courtesy G. Castellano): (c).

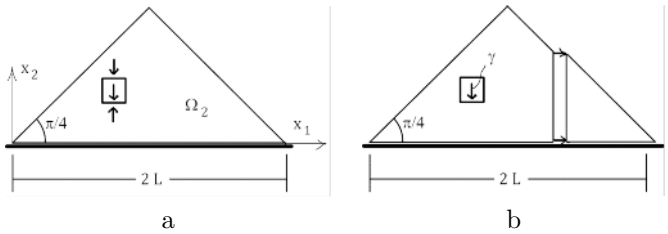

Figure 40. Heap under uniform body forces resting on a smooth foundation: (a). Mechanism for which the load does zero work: (b).

Therefore the stress $\mathbf{T}$ coincides with that of the first solution and determines the same partition of the domain Ω, as described in Figure 38b.

The fracture strain is singular and describes the cracks exhibited by the deformed configuration depicted in Figure 39a. A graph of the E_{11} and E_{22} components of $\mathbf{E}^a$ is reported in Figure 39b. In the absence of any energy price to pay to open up fractures, the two solutions reported are perfectly equivalent and the body can choose any of the two. It could be of some interest to look at the result of the flexure test performed on a masonry-like material (a mixture of lime and gypsum with a ratio between tensile and compressive strength of $\frac{1}{20}$) shown in Figure 39c.

Exact solution 3: 2d heap of masonry stones on a smooth foundation. The third problem I consider concerns a triangle of NENT material, simply supported at the base on a rigid, perfectly smooth interface (see Figure 40). The only external forces I consider are represented by a uniform gravitational load $\mathbf{b} = -\gamma \hat{\mathbf{e}}_2$ directed vertically.

A solution to this problem can be easily found since there exists only

one admissible stress field for this geometry and for these data.

The load is a collapse load since the resultant stress across any vertical section of the triangle (see Figure 40b) is zero and any two parts divided by a vertical section, can be separated horizontally with a vertical crack, corresponding to a zero energy mode and consisting into a horizontal uniaxial strain, concentrated on the line of separation.

Setting the length scale in such a way that $L = 1$, the one and only s.a. stress field, negative semidefinite and in equilibrium with the load, is written as follows

$$\{\mathbf{T}\} = \left\{ \begin{array}{cc} 0 & 0 \\ 0 & \sigma(x_1, x_2) \end{array} \right\} ,$$

with

$$\sigma(x_1, x_2) = \left\{ \begin{array}{cc} \gamma(x_2 - x_1) & , \ x_1 \leq 1 \ , \\ \gamma(x_2 + x_1 - 2) & , \ x_1 \geq 1 \end{array} \right\} .$$

To this stress field (considering for simplicity the case $\nu = 0$) is associated the elastic strain

$$\{\mathbf{E}^e\} = \left\{ \begin{array}{cc} 0 & 0 \\ 0 & \epsilon(x_1, x_2) \end{array} \right\} ,$$

with

$$\epsilon(x_1, x_2) = \left\{ \begin{array}{cc} \frac{\gamma}{E}(x_2 - x_1) & , \ x_1 \leq 1 \ , \\ \frac{\gamma}{E}(x_2 + x_1 - 2) & , \ x_1 \geq 1 \end{array} \right\} .$$

Therefore, taking into account the normality condition $\mathbf{T}.\mathbf{E}^a$, the anelastic strain takes the form

$$\{\mathbf{E}^a\} = \left\{ \begin{array}{cc} \lambda(x_1, x_2) & 0 \\ 0 & \end{array} \right\} ,$$

the total strain being

$$\{\mathbf{E}\} = \left\{ \begin{array}{cc} \lambda(x_1, x_2) & 0 \\ 0 & \epsilon(x_1, x_2) \end{array} \right\} .$$

Such total strain is compatible if and only if

$$\frac{\partial^2 \lambda(x_1, x_2)}{\partial x_2^2} + \frac{\partial^2 \epsilon(x_1, x_2)}{\partial x_1^2} = 0 \, .$$

The function $\epsilon(x_1, x_2)$ is not smooth and its second derivatives must be interpreted in a generalized sense. The 3d graph of $\epsilon(x_1, x_2)$ depicted in

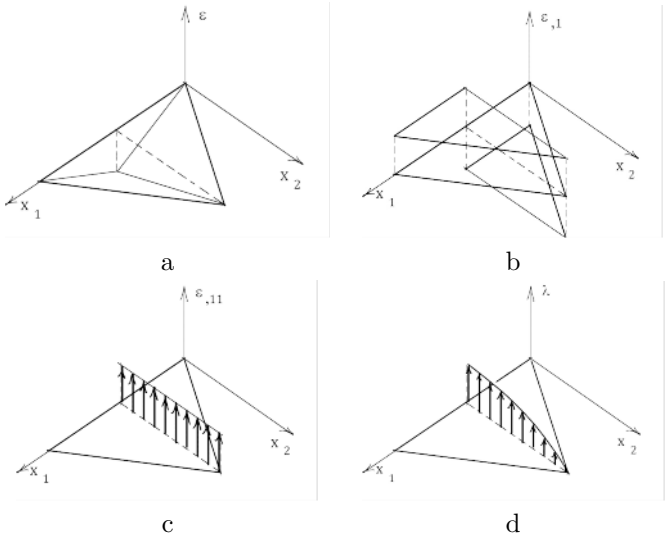

Figure 41. 3d plot of the elastic uniaxial strain $\epsilon(x_1, x_2)$: (a). In (b): first derivative of $\epsilon(x_1, x_2)$ with respect to x_1: piecewise constant field. In (c): second derivative; a constant line Dirac delta with support on the center line Γ. In (d) the anelastic strain $\lambda(x_1, x_2)$ restoring compatibility: a parabolic line Dirac delta with support on the center line Γ

Figure 41a, can help to visualize the first and second derivatives of $\epsilon(x_1, x_2)$ with respect to x_1 reported in Figures 41b,c.

A function $\lambda(x_1, x_2)$ that solves the compatibility equation and is non negative is

$$\lambda(x_1, x_2) = \frac{\gamma}{E}(L - x_2^2)\,\delta(\Gamma)\,,$$

where $\delta(\Gamma)$ is the line Dirac delta defined on the line Γ of equation $x_1 = 1$ (see the graph depicted in Figure 41d).

The displacement $\mathbf{u} = u\hat{\mathbf{e}}_1 + v\hat{\mathbf{e}}_2$ is then obtained integrating the total deformation. In components

$$u = \begin{cases} \frac{\gamma}{2E}(x_2^2 - 1) & ,\ x_1 < 1\,, \\ \frac{\gamma}{2E}(1 - x_2^2) & ,\ x_1 > 1\,, \end{cases}$$

$$v = \begin{cases} \frac{\gamma}{2E}x_2(x_2 - x_1) & ,\ x_1 < 1\,, \\ \frac{\gamma}{2E}x_2(x_2 + x_1 - 2) & ,\ x_1 > 1\,, \end{cases}$$

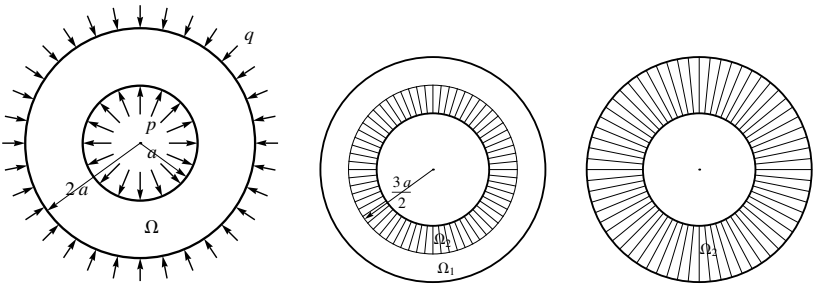

Figure 42. Ring under external and internal pressures: (a). Fundamental partition of the domain corresponding to the solution for $\alpha = 25/48$: (b). Fundamental partition corresponding to $\alpha = 1/2$: (c).

The deformation corresponding to this discontinuous displacement field, singular on the center line Γ, gives a concentrated fracture varying parabolically with x_2.

Exact solution 4: Ring under internal and external pressures. The fourth problem I consider concerns a ring of internal radius a and external radius $2a$, composed of NENT material and subjected to an internal pressure p and an external pressures $q = \alpha\, p$ (see Figure 42).

The real number α is a load parameter varying in the interval $[1/2, 1]$. Notice that the case $\alpha = 1$ corresponds to the elastic solution of uniform pressure.

First Case: supersafe load. First I consider the case in which $1/2 < \alpha < 1$. To fix the ideas I consider the special case $\alpha = \frac{25}{48}$.

In this case the load is *supersafe* since there exists a strictly s.a. stress field, uniformly bounded from above by a uniform compression of value $-p/18$. Such s.a. stress field, in physical components in the polar coordinate system $\{r, \vartheta\}$ with origin in the center of the ring, takes the form

$$T_{rr} = -p\left(\frac{a}{r} + \frac{r^2 - a^2}{36r^2}\right) ,$$

$$T_{\vartheta\vartheta} = -p\frac{r^2 + a^2}{36r^2} ,$$

$$T_{r\vartheta} = 0 .$$

The existence of a purely compressive s.a. stress field does not imply that the solution of the BVP is necessarily of pure biaxial compression. In the case at hand we shall see that both uniaxial and biaxial stress states, and fractures open up in the inner part of the domain.

With reference to the linear elastic solution for an isotropic pressurized ring, recalling the formula for the stress (see Timoshenko and Goodier (1951)), one easily finds that: in the region $\Omega_1 = \{\{r, \vartheta\}\ s.t.\ \frac{3}{2}a < r < 2a\}$, the stress coincides with the classical elastic solution; in the region $\Omega_2 = \{\{r, \vartheta\}\ \text{ s.t. }\ a < r < \frac{3}{2}a\}$, the stress is uniaxial and radial (see Figure 42b). Namely:

$$T_{rr} = \begin{cases} -\frac{p\,a}{r} & ,\ a \le r \le \frac{3}{2}a\ , \\ -\frac{p\left(9a^2+4r^2\right)}{12r^2} & ,\ \frac{3}{2}a \le r \le 2a\ , \end{cases}$$

$$T_{\vartheta\vartheta} = \begin{cases} 0 & ,\ a \le r \le \frac{3}{2}a\ , \\ -\frac{p\left(4r^2-9a^2\right)}{12r^2} & ,\ \frac{3}{2}a \le r \le 2a\ , \end{cases}$$

$$T_{r\vartheta} = 0\ .$$

We leave to the reader to verify that this stress field verifies the balance equations with zero body forces, matches the given pressures at the inner and outer boundary, and is compressive. In the region Ω_1 the stress field being coincident with the elastic solution, gives compatible strains and the physical components$\{u_r, 0\}$ of the displacement $\mathbf{u}$, can be easily found through the relations:

$$E_{\vartheta\vartheta} = T_{\vartheta\vartheta} - \nu T_{rr}\ ,\ E_{\vartheta\vartheta} = \frac{u_r}{r}\ .$$

In Ω_2, u_r can be found, modulo a constant, through the equations

$$E_{rr} = T_{rr} - \nu T_{\vartheta\vartheta}\ ,\ E_{rr} = \frac{\partial u_r}{\partial r}\ .$$

The constant is finally determined by imposing the continuity condition

$$u_r\left(r^-\right) = u_r\left(r^+\right)\ ,$$

at $r = \frac{3}{2}a$. Then the displacement u_r takes the following form

$$u_r = \begin{cases} \frac{p\,a}{E}\left(log\left(\frac{3a}{2r}\right) + \nu\right) & ,\ a \le r \le \frac{3}{2}a\ , \\ \frac{p\left(4r^2(-1+\nu)+9a^2(1+\nu)\right)}{12Er} & ,\ \frac{3}{2}a \le r \le 2a\ , \end{cases}$$

In Ω_2 the elastic deformations $E^e_{rr} = T_{rr}$, $E^e_{\vartheta\vartheta} = -\nu T_{rr}$, left alone, are not compatible. To restore compatibility I must add the fracture field

$$E^a_{\vartheta\vartheta} = \frac{\partial u_r}{\partial r} - E^e_{\vartheta\vartheta} \ ,$$

that is

$$E^a_{\vartheta\vartheta} = \begin{cases} \frac{p\,a}{Er}\, log\left(\frac{3a}{2r}\right) & , \ a \le r \le \frac{3}{2}a \ , \\ 0 & , \ \frac{3}{2}a \le r \le 2a \ . \end{cases}$$

Then the fracture field is described by a regular deformation consisting into a diffuse uniaxial circumferential strain taking place in the internal ring Ω_2, of outer radius $\frac{3}{2}a$, and becoming vanishingly small at the boundary between Ω_1 and Ω_2 (as shown pictorially in Figure 42b).

Second case: Limit load. Consider now the case in which $\alpha = \frac{1}{2}$ (see Figure 42c).

In this case the load is *limit* since there exists at the same time, a stress field belonging to H, that is a statically admissible (but not strictly admissible) stress field, and also a non-zero displacement field belonging to K° for which the load does zero work.

This s.a. stress field, in physical components in the polar coordinate system $\{r, \vartheta\}$ with origin in the center of the ring, is

$$T_{rr} = -p\frac{a}{r} \ ,$$

$$T_{\vartheta\vartheta} = 0 \ ,$$

$$T_{r\vartheta} = 0 \ .$$

Notice that, in this case, this is also the unique statically admissible solution, that is the set H of s.a. stress fields is a singleton (with the language of Structural Mechanics one may say that the *structure*, with this kind of load, is statically determined).

The given loads do zero work for the *mechanism* described by the following physical components of displacement:

$$u_r = \overline{u} \ , \ u_\vartheta = 0 \ ,$$

where $\overline{u}$ is an arbitrary positive constant.

The solution of the BVP in terms of displacements reads

$$u_r = \overline{u} + \frac{p\,a}{E}\left(log\left(\frac{2a}{r}\right) + \nu\right) \ , \ u_\vartheta = 0 \ ,$$

and the corresponding fracture strain is

$$E^a_{\vartheta\vartheta} = \frac{\overline{u}}{r} + \frac{p\,a}{Er}\,log\left(\frac{2a}{r}\right)\ .$$

We point out that, being $\overline{u}$ an unknown positive parameter, the solution, in terms of strains and displacements, is not unique.

3.8 Masonry-like panels under flexure, shear and compression: Mansfield-Fortunato semi-analytical solutions

The problem of equilibrium for normal elastic no-tension materials can be formulated as a minimum problem for the complementary energy functional over the set of statically admissible stress fields H.

Masonry facades are often formed by an assembly of units in the form of rectangular panels; an example of a wall with openings in which rectangular panels can be devised in the masonry, is shown in Figure 43. A special class of mixed boundary value problem for such units can be solved by minimizing the complementary energy over the subset $\tilde{H}$ of H defined by the admissible stress fields that are of rank one. These minimal uniaxial stress states represent often the exact solution of such BVP's in some parts of the domain. This can be verified by deriving the corresponding fracture strains through the compatibility equations and checking the boundary conditions for the associated displacements.

These approximate solutions for rectangular panels have some relevance both for masonry structures as well as for elastic membranes due to simplified models which impose unilateral constraints on the normal stress, namely the No-Tension theory (NT-T) for masonry (see Fortunato (2010))and the *Tension Field Theory* (TF-T) for membranes (see Mansfield (1969) and Steigmann (1990) and references therein). Solutions of similar problems, consisting of uniaxial stress fields directed along a one parameter family of rays[15], can be found in the technical literature dating back to sixties.

The first to analyze the *shearing* problem, under the ad hoc assumptions of TF-T, in mathematically rigorous terms, was Mansfield (Mansfield, 1969). In Mansfield (1989) he considers more general boundary conditions. For NT materials, the shearing case was also studied with a variational approach by Angelillo and Olivito (1995) in the general case of unilateral, anisotropic elastic materials.

In a recent paper, Fortunato (2010), a comprehensive study, valid for any relative rigid displacements of the bases (including rotations), is presented;

[15] We recall that (see Remark 3, Remark 9 and Figure 6), in the regions of uniaxial stress and under vanishing body forces, a classical result of TF-T is that the lines of principal traction (compression for NT-T) form a family of straight lines.

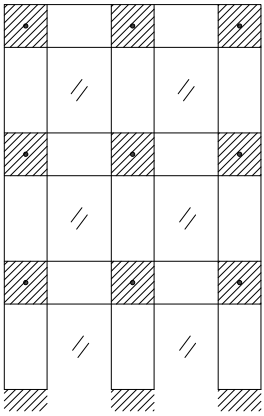

Figure 43. Structural scheme of a masonry wall with openings (in a simplified model dashed parts can be considered as rigid).

on introducing a curvilinear coordinate system convected with the compression rays, the problem is reduced to an ordinary differential equation for the ray distribution (that is the Euler equation of the minimum problem for the complementary energy over the set $\tilde{H}$), without the need of any ad hoc assumptions besides energy minimization. The basic tension field assumption (that is the restriction to $\tilde{H}$), in the present context, reduces the compression ray solution to an approximate solution of the minimum problem for the complementary energy, and gives a lower bound for the *stiffness* of the panel. A definition of the partition of the domain Ω into uniaxial stress part Ω_2 and slack part Ω_3, explicit in terms of the relative displacement parameters, is given. Simple ordinary differential equations are obtained from the compatibility condition, from which the anelastic strain (that is the fracture strain for NT-T and the wrinkling strain for TF-T) can be computed through integration.

Unilateral models for masonry and wrinkling. The last result has significant relevance for the problem of wrinkling of thin membranes. When a thin panel is forced into the post-buckling range by loads applied to its edges, load is transmitted primarily along one of the principal axes of stress, while bending effects remain secondary. The panel deforms into a wavy or wrinkly surface, the crests of the waves coinciding approximately with the trajectories of the tensile stresses (see Figure 44b).

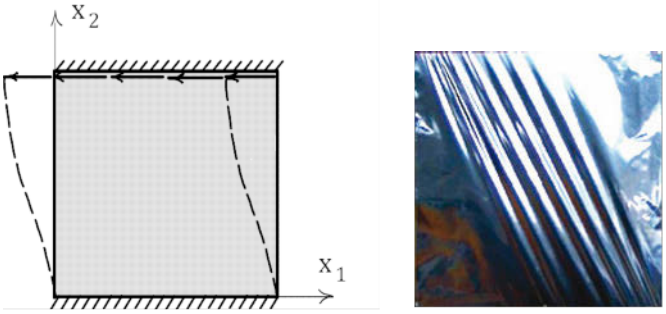

a b

Figure 44. Wrinkling of a rectangular sheet under relative shearing of the bases and free on the lateral sides. Boundary conditions: (a) . In (b) wrinkles developing in an alluminium sheet subject to the b.c. described in (a).

TF-T defines approximately the magnitude and direction of the stress in the wrinkled zone. The anelastic strains, in TF-T, are a measure of wrinkling, in the sense that they may be viewed as limits of sequences of ordinary deformations whose gradients oscillate finely on any interval. The definition of the wave length and the amplitude of the wrinkles is of vital importance in many applications (such as sails or space solar panels). In recent works, some authors (Epstein (1999), Wong and Pellegrino (2006)) propose approximate formulas for estimating the amplitude as well as the wave length of wrinkles, based on the knowledge of the TFT stress field and the corresponding anelastic strain. Then the knowledge of the anelastic strain can be used to test the adherence of such formulas to the description of known experimental results on panels.

Basic Boundary Value Problem for a Masonry Panel In this Section I summarize the main results of the analysis given by Fortunato in (Fortunato, 2010). Consider a masonry-like rectangular panel, traction free on the lateral sides and subject to zero body forces and prescribed rigid body displacements of the top and bottom bases. A Cartesian frame of reference $\{O;\ x_1 = x,\ x2 = y\}$ (Figure 45a) is introduced, with associated unit base vectors $(\mathbf{e}_1, \mathbf{e}_2)$; let us define $\{u_A,\ v_A,\ \varphi_A\}$ as the translation and rotation parameters of the block R_A relative to the pole A°, $\{u_B,\ v_B,\ \varphi_B\}$ as the translation and rotation parameters of the block R_B relative to the pole B°, $\{U, V, \Phi\}$ as the relative rigid displacement parameters between the top and bottom bases.

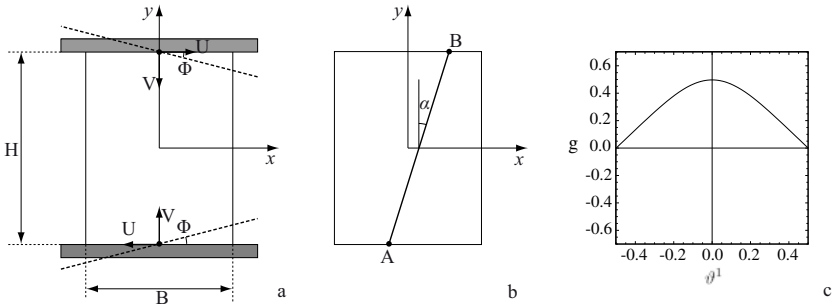

Figure 45. Masonry panel undergoing rigid relative displacements of the bases: a. Slope g of a compression ray: (b). Typical minimizing slope g as a function of $\vartheta^1 = x$: (c).

Modulo an ineffective rigid body displacement, it is straightforward to relate the displacement components at the top and bottom bases a, b with the relative (rigid) displacement parameters, written

$$\mathbf{u}_a = u_a\mathbf{e}_1 + v_a\mathbf{e}_2 = U\mathbf{e}_1 + (V + \Phi x)\mathbf{e}_2 \ ,$$

$$\mathbf{u}_b = u_b\mathbf{e}_1 + v_b\mathbf{e}_2 = -U\mathbf{e}_1 - (V + \Phi x)\mathbf{e}_2 \ .$$

Based on the complementary energy principle stated in *Subsection* 3.5, the equilibrium solution can be searched by minimizing the complementary energy over the set H defined in (45). In keeping with the spirit of TF-T, an approximate solution is looked for in the restricted set $\tilde{H}$ obtained by considering stress fields $\mathbf{T} \in H$ such that $\mathbf{T}$ is of rank-one.

Remark 11. As shown by some of the elementary solutions previously discussed, the displacement solution, in the closure of the regions $\Omega_2 \cup \Omega_3$, can exhibit singularities affecting the latent strain. These singularities correspond to discontinuities in the displacement through lines that can be interpreted as fracture lines. The normality assumptions (34), (36), imply that displacement discontinuities be orthogonal to the discontinuity line. $\diamond$

Remark 12. On the interface between Ω_2 and Ω_3 the stress must be continuous in order to avoid shear discontinuities (violating the normality rule). As a consequence the stress along the interface between the regions Ω_2 and Ω_3 must be zero, the interface itself a straight unextended line. $\diamond$

The minimizer $\mathbf{T}^\circ$ of the complementary energy over the restricted set $\tilde{H}$ is generally not the exact solution of the problem, rather an approximate solution.

For any $\mathbf{T} \in \tilde{H}$ one has $\Omega = \Omega_2 \cup \Omega_3$, that is $\Omega_1 = \emptyset$. Once the free boundary between Ω_2 and Ω_3 is identified, the solution of the equilibrium problem is reduced to the search of the stress field solution in Ω_2. As already remarked, in Ω_2 one of the two families of principal stress curves (i.e., the integral curves of the stress eigenvectors) is made of straight lines, that are called *compression rays*. The compression rays carry the non zero stress and do not overlap. Since the lateral sides of the panel are stress free the compression rays intersect the boundary along the bases. Therefore the definition of the behaviour of a single panel, under the above assumptions, is reduced to finding in Ω_2 the optimal compression ray distribution, with the optimal choice being determined by energy convenience.

In what follows, I summarize the results of the analysis given by Fortunato in (Fortunato, 2010), omitting all the proofs and referring to the cited paper for the detailed derivations. The main results contained in Fortunato (2010) concern: 1. the explicit definition of the partition $\Omega = \Omega_2 \cup \Omega_3$, in terms of the data $\{U, V, \Phi\}$. 2. The explicit definition of the stress and complementary energy to be minimized, in terms of the slope of the rays g. 3. The formalization of the Euler equations and boundary conditions for all the possible data. 4. The explicit definition of the anelastic strains (fractures) in terms of the slope g.

Partition of the panel and free boundary between Ω_2 and Ω_3 Consider the rectangular panel of base $B_\circ$ and height $H_\circ$. In the sequel a rectangular normalized panel is considered, which is a rectangular panel whose base is of unit length and whose height is $H = H_\circ/B_\circ$. The slope function g of a compression ray is introduced; the compression ray intersects the bottom and top bases at the abscissae x_A, x_B and the horizontal axis at $\vartheta_1 = \frac{x_A + x_B}{2}$, and the slope is defined as a function of ϑ^1

$$[-1/2, 1/2] \ni \vartheta^1 \to g(\vartheta^1) := tan(\alpha(\vartheta^1)$$

where α is the angle between such ray and the y axis, as shown in Figure 45b, to which I refer for notations.

In order that the rays belong entirely to Ω, the geometrical constraints on g

$$-\frac{1-2\vartheta^1}{H} \leq g(\vartheta^1) \leq \frac{1-2\vartheta^1}{H} \; s.t. \; \vartheta^1 > 0 \,, \tag{49}$$

$$-\frac{1+2\vartheta^1}{H} \leq g(\vartheta^1) \leq \frac{1+2\vartheta^1}{H} \; s.t. \; \vartheta^1 \leq 0 \,, \tag{50}$$

must be satisfied.

On observing that, for compatibility (that is in order that the strain satisfies the elasticity relations for shortening and the normality conditions for lengthening), the interface between the regions Ω_2, Ω_3, if any, must be an unextended ray, the following equation definining such class of rays is derived:

$$g(\vartheta^1) = -\frac{V}{U} - \frac{\Phi}{U}\vartheta^1 \ . \tag{51}$$

The free boundary must be chosen in this class.

It is easy to show that all the rays satisfying the constraint (51) pass through a common centre C whose coordinates $\{x_\circ, y_\circ\}$ depend only on the parameters $\{U, V, \Phi\}$. The expressions for the coordinates of the centre C are

$$x_\circ = -\frac{V}{\Phi} \ , \ y_\circ = \frac{U}{\Phi} \ .$$

The partition of the panel into the disjoint regions Ω_2 and Ω_3, and in particular their free boundary (necessarily made by rays that satisfy the constraint (51)), can be obtained by the position of the center C, and is independent of the size of the rigid displacement parameters, provided the ratios $\frac{U}{\Phi}$ and $\frac{V}{\Phi}$ stay constant.

If $U > 0$ the inequality

$$g(\vartheta^1) < -\frac{V}{U} - \frac{\Phi}{U}\vartheta^1 \ . \tag{52}$$

defines the ray passing through the points P and Q on the top and bottom bases which are shortened for the given rigid displacements parameters $\{U, V, \Phi\}$ of the bases.

This is a kinematic constraint on the slope g for the existence of the compression rays, that is for the existence of the region Ω_2.

In the case $U = 0$, $g(\vartheta^1)$ is not restricted and the rays are shortened, as long as $\vartheta^1 > -\frac{V}{\Phi}$ if $\Phi > 0$ and $\vartheta^1 < -\frac{V}{\Phi}$ if $\Phi < 0$. In the case $U < 0$ then $g(\vartheta^1) > -\frac{V}{\Phi} - \frac{\Phi}{U}\vartheta^1$.

Summing up, the restrictions on $g(\vartheta^1)$ that have been introduced can be reformulated as follows:

Given the rigid boundary displacement parameters $\{U, V, \Phi\}$, find the pair $\{\vartheta^1, g(\vartheta^1)\}$, so that the geometrical constraints (49), (50) and the kinematical constraint (52) hold.

These five inequalities define a feasible region for the pair $(\{\vartheta^1, g(\vartheta^1)\}$ that can be easily visualized with a graph through which the interface between the Ω_2 and Ω_3 regions can be located.

Depending on the values of the triplet $\{U, V, \Phi\}$, the feasible region for g can be either empty or not empty. In the latter case the region is a polygon with three to five sides whose extrema, with respect to the ϑ^1 component, define the boundary of the Ω_2 region. These extrema are called $\underline{\vartheta}^1$ and $\overline{\vartheta}^1$.

Based on the values of U, V, Φ, there are essentially five representative cases to be considered:

(i) Shearing, shortening, flexure: $U \neq 0\ , V > 0,\ \Phi \neq 0$;
(ii) Shearing, elongation, flexure: $U \neq 0\ , V < 0,\ \Phi \neq 0$;
(iii) Shortening: $U = 0\ , V > 0,\ \Phi = 0$;
(iv) Shearing: $U \neq 0\ , V = 0,\ \Phi = 0$;
(v) Shortening, flexure: $U = 0\ , V < 0,\ \Phi \neq 0$.

Figure 46 shows the admissible repertoire of $g(\vartheta^1)$ in the range $[-1/2, 1/2]$ for one of these cases.

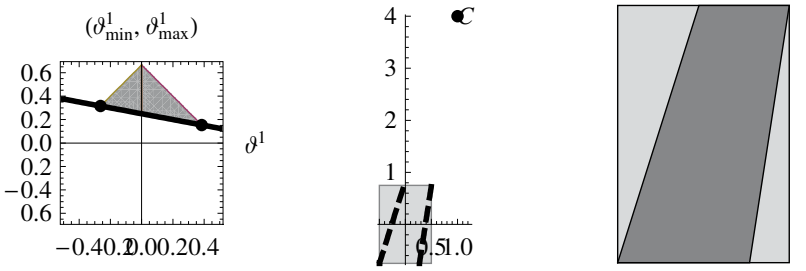

Figure 46. Definition of the taut region for the case of shearing, elongation, flexure. Restrictions on g and limit slopes: (a). Position of the center C: (b). Taut region: (c).

Curvilinear Coordinates in Ω_2 In Ω_2 it is convenient to introduce a system of curvilinear coordinates $\{\vartheta^1, \vartheta^2\}$ with one of the curvilinear lines, say ϑ^2, convected to the compression rays. In terms of the Cartesian coordinates $x_1 = x, x_2 = y$, with associated base vectors $\mathbf{e}_1, \mathbf{e}_2$, the curvilinear coordinates $\{\vartheta^1, \vartheta^2\}$ are defined as follows

$$x_1 = \vartheta^1 + g\vartheta^2\ ,\ x_2 = \vartheta^2\ ,$$

g being the slope of the rays, a function of ϑ^1 alone.

A physical reference system, that is a variable orthonormal base $\{\mathbf{e}_{1'}, \mathbf{e}_{2'}\}$, with $\mathbf{e}_{2'}$ tangent to the compression rays at any point of Ω_2, is also introduced.

Strain and Stress in Ω_2 Calling u_α, the covariant components of the displacement field $\mathbf{u}$ in the curvilinear system $\{\vartheta^1, \vartheta^2\}$, the local infinitesiamal strain $\mathbf{E}$ has the following covariant components in the same curvilinear system

$$E_{11} = u_{1,1} - \frac{g''\vartheta^2}{1 + g'\vartheta^2} u_1 \ ,$$

$$E_{22} = u_{2,2} \ ,$$

$$E_{12} = \frac{1}{2}(u_{1,2} - u_{2,1}) - \frac{g'}{1 + g'\vartheta^2} u_1 \ .$$

The physical component of strain in the ray direction, that is the strain component in the direction of $\mathbf{e}_{2'} \otimes \mathbf{e}_{2'}$, is related to the covariant component E_{22} through the relation

$$E_{(2'2')} = E_{22} \frac{1}{1 + g^2} \ .$$

Notice that the total strain $\mathbf{E}$, in the variable hortonormal base $\{\mathbf{e}_{1'}, \mathbf{e}_{2'}\}$, is described by the matrix

$$\{\mathbf{E}\} = \left\{ \begin{array}{cc} \lambda(\vartheta^1, \vartheta^2) - \nu\epsilon(\vartheta^1, \vartheta^2) & 0 \\ 0 & \epsilon(\vartheta^1, \vartheta^2) \end{array} \right\} \ .$$

where ν is the Poisson ratio, $\epsilon = E_{(2'2')}$ is the elastic strain component and λ is the unknown fracture field.

The decomposition of the total strain into its anelastic and elastic parts is then

$$\{\mathbf{E}^a\} = \left\{ \begin{array}{cc} \lambda(\vartheta^1, \vartheta^2) & 0 \\ 0 & 0 \end{array} \right\} \ ,$$

$$\{\mathbf{E}^e\} = \left\{ \begin{array}{cc} -\nu\epsilon(x_1, x_2) & 0 \\ 0 & \epsilon(x_1, x_2) \end{array} \right\} \ .$$

The uniaxial stress $\mathbf{T}$, in order to satisfy the equilibrium with zero body forces, must take the form (for a pictorial description of equilibrium along a compression ray see Remark 3 and Figure 6)

$$\mathbf{T} = \sigma \mathbf{e}_{2'} \otimes \mathbf{e}_{2'} \ ,$$

with

$$\sigma = \frac{f(1+g^2)}{1+g'\vartheta^2} \ .$$

The elastic part ϵ of the deformation, is easily obtained, through the Hooke's law, in the form

$$\epsilon = \frac{\sigma}{E} \ ,$$

E being the Young modulus of the material.

Energy The complementary energy (44) can be written in the form

$$E_c = -\int_{\underline{\vartheta}^1}^{\overline{\vartheta}^1} 2f(Ug+V+\Phi\vartheta^1)d\vartheta^1 + \frac{1}{2}\int_{\underline{\vartheta}^1}^{\overline{\vartheta}^1}\int_{-\frac{H}{2}}^{\frac{H}{2}} \frac{f^2}{E}\frac{(1+g^2)^2}{1+g'\vartheta^2}d\vartheta^1 d\vartheta^2 \ . \quad (53)$$

The complementary energy, depending parametrically on $\{U, V, \Phi\}$ is a functional of f, g, that is of two unknown numeric functions of ϑ^1. The function f can be determined explicitly by pre-minimizing E_c with rewspect to f. Such a minimizer is

$$f = \frac{Eg'}{(1+g^2)^2}\frac{2(Ug+V+\Phi\vartheta^1}{log(1-g'\frac{H}{2}) - log(1-g'\frac{H}{2})} \ .$$

By substituting the previous expression into the stress, one has

$$\sigma = \frac{1}{1+g'\vartheta^2}\frac{Eg'}{1+g^2}\frac{2(Ug+V+\Phi\vartheta^1}{log(1-g'\frac{H}{2}) - log(1-g'\frac{H}{2})} \ ,$$

and substituting back into the energy, after some algebra, the following reduced expression of E_c is obtained

$$E_c = -2E\int_{\underline{\vartheta}^1}^{\overline{\vartheta}^1} \frac{(Ug+V+\Phi\vartheta^1)^2 g'^2}{(1+g^2)^2 \log\frac{1+g'\frac{H}{2}}{1-g'\frac{H}{2}}}d\vartheta^1 \ . \quad (54)$$

This is a functional of the sole unknown function g, to be minimized for g with the boundary conditions

$$g(\underline{\vartheta}^1) = \underline{g} \ , \ g(\overline{\vartheta}^1) = \overline{g} \ .$$

The solution, that is called $g_\circ$, can be determined by finding the zeroes of the derivative (the Euler equation) associated to the minimum problem for (54) (see equation (58), p.101 of Fortunato (2010)). The Euler equation

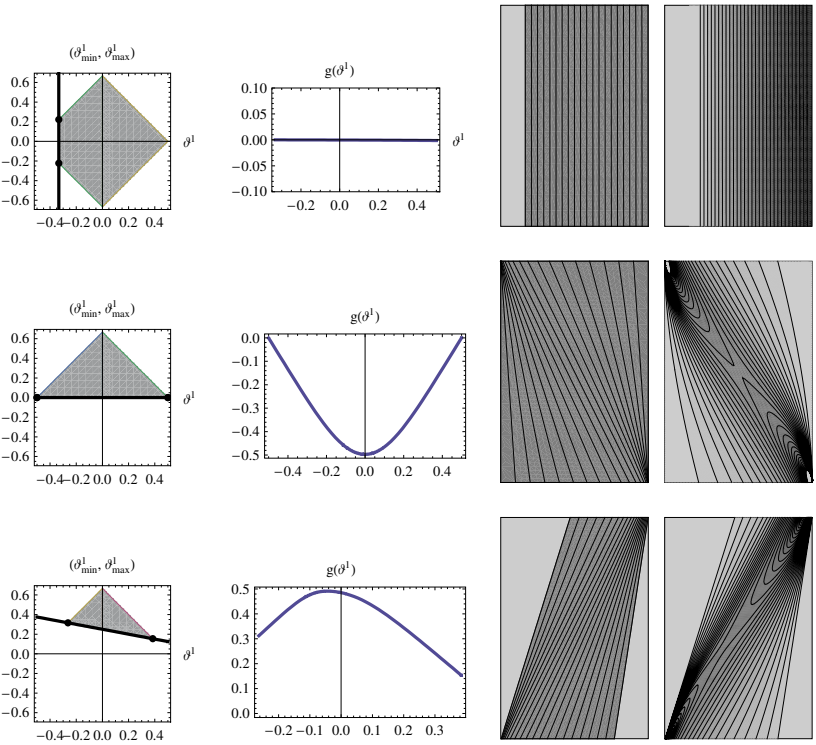

Figure 47. Numerical solution of three special cases. In column a: fundamental partition and minimizing slope g. In column b: compression rays corresponding to the minimizing g and level curves of the principal stress. First row: shortening and flexure. Second row: pure relative shearing. Third row: shearing, elongation and flexure.

is a second order non-linear differential equation for g that, due to the precence of *log* terms in g', results rather stiff. The equation is integrated by Fortunato in (Fortunato, 2010) for some special cases, by employing a multi-shooting technique and a Gauss-Kronrod quadrature formula.

Compatibility, Anelastic Deformation The stress field $\mathbf{T}_\circ$ corresponding to the minimizer $g_\circ$, that is the uniaxial stress field directed as the compression rays for which the principal stress component is

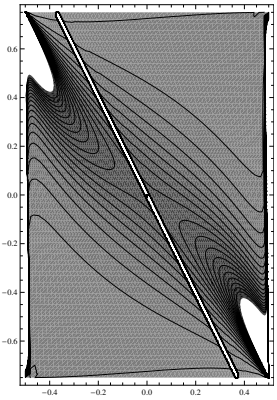

Figure 48. Level curves for of the fracture strain for the case of pure relative shearing.

$$\sigma = \frac{1}{1+g'_\circ\vartheta^2}\frac{Eg'_\circ}{1+g_\circ^2}\frac{2(Ug_\circ+V+\Phi\vartheta^1}{log(1-g'_\circ\frac{H}{2})-log(1-g'_\circ\frac{H}{2})}\ ,$$

can be either an approximation to the exact solution or the solution of the BVP. In order to check that $\mathbf{T}_\circ$ is the exact solution of the BVP, compatibility of the strain $\mathbf{E}$, and compatibility of the corresponding displacements on the part $\partial\Omega_D$ of the boundary, must be verified. Actually a continuous displacement field $\mathbf{u}$ of which $\mathbf{E}$ is the symmetric part of its gradient exists in Ω_2 if and only if

$$E_{11/22}+E_{22/11}-2E_{12/12}=0\ , \tag{55}$$

where / followed by indices denotes covariant differentiation with respect to those indices.

Recalling that the total strain $\mathbf{E}$ admits the representation

$$\mathbf{E}=(\lambda-\nu\epsilon)\mathbf{e}_{1'}\otimes\mathbf{e}_{1'}+\epsilon\mathbf{e}_{2'}\otimes\mathbf{e}_{2'}\ ,$$

and that ϵ is the elastic stretch determined by the known stress $\mathbf{T}_\circ$, the unknown fracture strain field λ can be found by solving the differential equation (55).

In Fortunato (2010) the author finds the explicit solution of this differential equation in terms of $g_\circ$. The solution is

$$\lambda=\frac{z(1+g_\circ^2)}{1+g'_\circ\vartheta^2}+\nu\epsilon+g_\circ^2\epsilon$$

where z is the solution of the differential equation

$$z_{,22} = \frac{p}{1 + g_\circ \vartheta^2}$$

p being a specified function of f, g, that is of $g_\circ$ (see (73), p.103 Fortunato (2010)).

Rectangular panels under elongation, flexure and shearing: examples In this section the solution of some peculiar cases is presented. A rectangular panel of normalized lengths and Poisson ratio $\nu = 0$, subject to three different combinations of the given displacements $\{U, V, \Phi\}$ is considered. The Euler equation is solved numerically for each of the three cases with a multi-shooting technique. In Figure 47 the fundamental partition, the minimizer $g(\vartheta^1)$, the compression rays and the principal stress levels are shown. In particular for the example of pure shearing the contour plot of the fracture λ, that is the only non vanishing component of the anelastic strain in Ω_2, is shown in Figure 48. Since the solution of the Euler equation is obtained numerically the optimal g, and the corresponding σ, are affected by numerical errors depending essentially on the integration scheme chosen. In the examples, an adaptive algorithm has been adopted: the function g is integrated over the interval $[\underline{\vartheta}^1, \overline{\vartheta}^1]$, by using a Gauss-Kronrod quadrature formula, from which an integral value (usually overestimated) and an error estimate are obtained. If the estimation is too big, the interval is divided in half and the integration is performed over each of the halves using the quadrature formula. If the total error is still too big, the interval with the biggest error is again bisected. The process is repeated until the desired precision is reached. For the integration scheme adopted the anelastic strain is always non negative all over Ω_2. This outcome gives an indication that the compression ray solution is the exact solution for the cases considered ($\nu = 0$).

4 Model *two* (ML)

In this section the main ingredients of the theory concerning model *two* for masonry materials, namely the Masonry-Like (ML) material, that is the $n > 1$ version of the 1d model introduced in Chapter 1, are presented. The constitutive assumptions, the balance equations and the boundary and initial conditions are given and the evolutionary boundary value problem for ML materials is formulated. A number of illustrative exact solutions and examples are discussed and a new technique for handling numerically the solution of specific ML problems, is introduced.

4.1 The equilibrium problem for ML materials

The crushing behaviour of masonry, that is its limited strength in compression, is modeled as perfectly plastic, then the crushing behavior of the material is assumed to be represented within the classical framework of a convex elastic domain coupled with the normality law, the yield surface being fixed in the stress space (no hardening or softening).

The initial-boundary value problem describing the quasi-static evolution of a NT elasto-plastic body occupying a bounded domain Ω with boundary $\partial\Omega$ is then considered.

The first to propose and analyse this model for masonry materials were Lucchesi and Zani (1996).

Plastic behaviour is described in terms of strain rates and the problem is not merely a BVP but rather an evolutionary problem. The evolution is assumed to be quasi-static, that is, to occur so slowly that inertial effects may be ignored.

The initial-boundary value problem in two dimensions. Again I assume small strains and restrict to 2d problems.

Time dependent data are considered, such as the fields $\mathbf{b}(\mathbf{x},t)$ (body forces per unit volume), $\underline{\mathbf{s}}(\mathbf{x},t)$ (surface tractions per unit area), and $\underline{\mathbf{u}}(\mathbf{x},t)$ (surface displacements):

$$\mathbf{b}:\ (\mathbf{x},t)\in\Omega\times[0,\underline{t})\to\mathbf{b}(\mathbf{x},t)\in V^2\ ,$$

$$\underline{\mathbf{s}}:\ (\mathbf{x},t)\in\partial\Omega_N\times[0,\underline{t})\to\underline{\mathbf{s}}(\mathbf{x},t)\in V^2\ ,$$

$$\underline{\mathbf{u}}:\ (\mathbf{x},t)\in\partial\Omega_D\times[0,\underline{t})\to\underline{\mathbf{u}}(\mathbf{x},t)\in V^2\ ,$$

with $T=[0,\underline{t})$ the time interval in which the evolution is considered and $\underline{t}$ the final instant of the evolution. Usually it is assumed that

$$\mathbf{b}(\mathbf{x},0)=0\ ,\ \underline{\mathbf{s}}(\mathbf{x},0)=0\ ,\ \underline{\mathbf{u}}(\mathbf{x},0)=0\ .$$

We consider that the body Ω is composed of NT material, that is the stress $\mathbf{T}$ is negative semidefinite ($\mathbf{T}\in Sym^-$).

We further assume that the stress cannot be arbitrarily large but is confined to belong to a bounded convex set K of Sym containing the origin. Then the interior of K $\cap Sym^-$ is the elastic region:

$$\mathbf{T}\in \mathrm{K}\cap Sym^-\ , \tag{56}$$

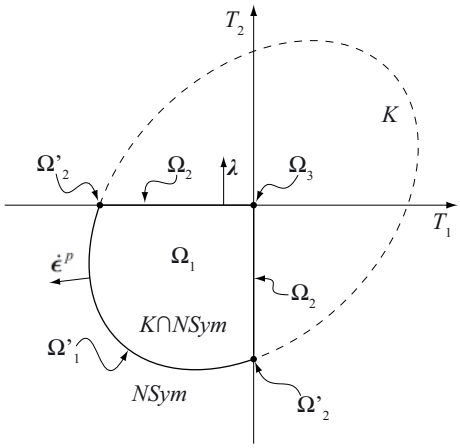

Figure 49. Section of the Elastic Domain in the stress space Sym with the plane $T_{12} = 0$.

while its boundary is the yield surface. Notice that K $\cap Sym^-$ is convex but need not to be smooth. The boundary of K may be represented by a level set of a function f, called the crushing function, so that

$$\mathrm{K} = \{\mathbf{T} \in Sym \ : \ f(\mathbf{T}) \leq 0\} \ .$$

For simplicity I consider

$$f(\mathbf{T}) = \tilde{\Phi}(\mathbf{T}) - \frac{\sigma_\circ^2}{2E} \ , \tag{57}$$

where $\tilde{\Phi}$ is the strain energy density of the isotropic NENT material, expressed as a function of the stress $\mathbf{T}$, and $\sigma_\circ$ is the crushing stress in uni-axial compression; that is the boundary of K is a level set of the free energy of the NENT material. In Figure 49 the intersection of the elastic domain with the plane $T_{12} = 0$, is depicted.

Under the small strain hypothesis, the total deformation is again described by the tensor $\mathbf{E}$, and an additive decomposition of the total strain can be considered in the form

$$\mathbf{E} = \mathbf{E}^* + \mathbf{E}^p \ , \tag{58}$$

where $\mathbf{E}^p$ is the plastic strain. Notice that now $\mathbf{E}^*$ represents the reversible part of the deformation, in turn composed itself of two parts:

$$\mathbf{E}^* = \mathbf{E}^e + \mathbf{E}^a \ , \tag{59}$$

the elastic part being linearly related to the stress $\mathbf{T}$:

$$\mathbf{E}^e = \mathbf{A}\,[\mathbf{T}] \ . \tag{60}$$

For the latent anelastic part (a measure for fracture) of the reversible strain, again normality to the cone Sym^- is assumed

$$(\mathbf{T}' - \mathbf{T}) \cdot \mathbf{E}^a \leq 0 \ , \forall \mathbf{T}' \in Sym^- \ . \tag{61}$$

For the time rate $\dot{\mathbf{E}}^p$ of the plastic strain the associative flow rule

$$(\mathbf{T}' - \mathbf{T}) \cdot \dot{\mathbf{E}}^p \leq 0 \ , \forall \mathbf{T}' \in \mathrm{K} \ , \tag{62}$$

is considered.

Notice that the reversible part of the strain $\mathbf{E}^*$ can still be derived by an energy density:

$$\mathbf{T} = \frac{\partial \Phi}{\partial \mathbf{E}^*} \ .$$

In the isotropic case the form of the energy density Φ can be constructed explicitly in terms of the eigenvalues e_1^*, e_2^* of $\mathbf{E}^*$ (here $e_1^* < e_2^*$ is assumed). In the case of generalized plane stress this form is

$$\Phi = \begin{cases} 0 \ , & e_1^* \geq 0 \text{ and } e_2^* \geq 0 \ , \\ \frac{1}{2} E (e_1^*)^2 \ , & e_1^* < 0 \text{ and } e_2^* \geq -\nu e_1^* \ , \\ \frac{1}{2} \frac{E}{1-\nu^2} \left((e_1^*)^2 + (e_2^*)^2 + 2\nu e_1^* e_2^* \right) & e_1^* < 0 \text{ and } e_2^* < -\nu e_1^* \ , \end{cases} \tag{63}$$

E, ν being the Young modulus and the Poisson ratio. Notice that the stress $\mathbf{T}$ derived from Φ satisfies identically the unilateral restriction (30), that is there is no need to impose it as a constraint.

Energy formulation, internal variables. The problem is described in terms of the total strain and of the recorded history of mechanical behaviour, by introducing as an internal variable the total plastic strain $\mathbf{E}^p$. If I consider that the form of $\Phi(\mathbf{E} - \mathbf{E}^p)$ is prescribed and that $\mathbf{T} = \frac{\partial \Phi}{\partial \mathbf{E}^*}$, the instantaneous values of $\mathbf{T}$ are known if $\mathbf{E}$ is given and the entire process

of plastic strain is known. Obviously $\mathbf{E}^p = \int_0^t \dot{\mathbf{E}}^p dt$, and $\dot{\mathbf{E}}^p$ is described by the flow rule (62).

Notice that, based on the ML model, fracture strains are reversible and are perfectly recoiled upon load inversion. Crushing strains, by contrast, cannot be healed and, being totally irreversible, can either stay or grow. In other words, smeared fractures cannot cancel crushing strains; the two mechanisms being completely independent.

4.2 Numerical minimization strategy

The numerical method I adopt to solve approximately the BVP for NENT materials is to search for the minimum of the potential energy (26) and is based on the direct minimization of such a functional through a descent method. The search is carried out in the subset of the set of statically admissible displacements K defined by the C° displacement fields obtained by employing a standard finite element approximation based on a triangular finite element discretization $\Pi^h(\Omega)$ of the domain Ω, where h denotes the mesh size. This kind of discretization excludes discontinuities in $\mathbf{u}$, that is, real cracks. The reason for considering such a simplification is twofold:

Firstly, I believe that fractures in NENT materials will appear smeared within the domain if the loads are safe (that is they are not collapse loads) in the sense specified in *Subsection* 2.9.

Secondly, in limit cases in which the loads approach the collapse limit the fracture strain may accumulate in narrow bands indicating the occurrence of real cracks in the limit.

Descent methods for NENT materials. The convenience of descent methods, favoured in recent years by the widespread availability of computational power, is recovered in the case of unilateral and non-smooth energy shapes. In the specific case of NENT materials the method is particularly indicated since the problem becomes unconstrained, the potential energy is a convex function of its arguments and the method of descent is insensitive to *zero-energy modes* (source of major troubles with standard FEM based on updated stiffness matrices, see Alfano et al. (2000)).

Several numerical tests performed on simple problems, for which the exact solutions are known, show the competitiveness of the descent approach with respect to more classical techniques. Some of these benchmark problems are reported in what follows, a larger number of examples can be found in the recent paper by Angelillo et al. (2010). Comparisons with numerical solutions obtained by other developing codes (see Lucchesi and Zani (2008)) and commercial programs (Abaqus, 6.12) indicate that the descent method

seems to be the right choice to overcome the difficulties which are inherent to the NT constraint.

The energy functional E is approximated with the function $\widetilde{E}(\{u_h\})$ of the nodal displacements $\{u_h\}$:

$$\widetilde{E}(\{u_h\}) = -\sum_r L_r \underline{\mathbf{s}}(\mathbf{x}_r)\cdot\mathbf{u}_r - \sum_m \mathbf{f}_m\cdot\mathbf{u}_m - \sum_n A_n \mathbf{b}(\mathbf{x}_n)\cdot\mathbf{u}_n - \sum_q A_q \Phi(\mathbf{x}_q) \tag{64}$$

where $\mathbf{u}_r$ is the displacement at the midpoint $\mathbf{x}_r$ of the r-th edge of length L_r on $\partial\Omega_N$, $\mathbf{u}_m$ the displacement of the m-th mesh node where the concentrated force $\mathbf{f}_m$ is applied, $\mathbf{u}_n$ the displacement at the Gauss point $\mathbf{x}_n$ of the n-th mesh triangle with area A_n, and $\mathbf{x}_q$ the Gauss point of the q-th mesh triangle of area A_q, where the strain energy density Φ is evaluated for integration. In the discretized version (64) of the potential energy, all the displacements $\mathbf{u}_j$, as well as the strain energy density $\Phi(\mathbf{x}_q)$ of the q-th triangle, are clearly explicit functions of the nodal displacements $\{u_h\}$, via the linear shape functions of a standard triangular mesh.

The iterative procedure adopted to minimize the function (64) is based on a step-by-step minimization method. Let us denote $\{u_h\}_j$ the nodal displacements at the j-th minimization step. The force acting on the mesh nodes is given by the negative gradient of the energy $\mathbf{f}_j = -\nabla_j \widetilde{E}$. The descent method implemented computes the current velocity $\mathbf{p}_j$ employing the nodal forces at the current and previous step as

$$\mathbf{p}_j = \eta_j \mathbf{p}_{j-1} + \mathbf{f}_j \ ,$$

where the scalar η_j is

$$\eta_j = Max\left\{\frac{\mathbf{f}_j\cdot(\mathbf{f}_j - \mathbf{f}_{j-1})}{\mathbf{f}_{j-1}\cdot\mathbf{f}_{j-1}}, 0\right\} \ ,$$

in the Polak-Ribiere version of the conjugate gradient method, and

$$\eta_j = \frac{\mathbf{f}_j\cdot\mathbf{f}_j}{\mathbf{f}_{j-1}\cdot\mathbf{f}_{j-1}} \ ,$$

if the Fletcher-Reeves variant of the method is employed (the Polak-Ribiere method is usually adopted in the applications reported herein).

If the nodes of the mesh are constrained, the velocity $\mathbf{p}_j$ is projected onto the tangent space of the constraint equations to obtain the compatible velocity $\mathbf{p}_j^*$. The velocity $\mathbf{p}_j^*$ gives the direction for the minimization motion while obeying all the constraints imposed on the nodes. The nodal displacement $\{u_h\}_j$ is computed as

$$\{u_h\}_j = \{u_h\}_j + \kappa_j \mathbf{p}_j^* \ ,$$

where κ_j is the amplitude of the minimization step in the direction of $\mathbf{p}_j^*$ and is computed via a line search method[16] to minimize the energy $\widetilde{E}(\{u_h\})$ in the direction of the velocity $\mathbf{p}_j^*$. The iteration process stops when a suitable norm of the energy gradient becomes sufficiently small (for the decrease conditions see for example (Kelley, 1999)).

Descent methods for ML (dissipative) materials. When considering ML materials, that is, adding to the NENT model a crushing strength criterion (of elasto-plastic associative type), it seems that the proposed numerical technique, based on energy minimization (extremely efficient for unilateral materials) should be abandoned. The elastoplastic behavior is indeed inherently path-dependent: the stress state at time t depends, in general, on the whole strain history in the interval $T = [0, \underline{t})$ rather than on the strain at time t. Then the equilibrium problem for such a material is essentially a dissipative evolution problem whose solution cannot be obtained by simply minimizing an energy functional. The proposed technique can still be applied to this evolutive problem considering the exact trajectory as the limit of a sequence of minimum problems. This is done by discretizing the time interval into steps and updating the energy in a suitable way. The evolutive problem is then approximated as a sequence of a discrete number of minimizing movements. The evolutive solution is obtained as the limit of the discrete evolution by letting the time step go to zero (see De Giorgi (1996) for the general formulation, Mielke and Ortiz (2008) for the convergence proofs in the general case of rate independent materials and Dal Maso et al. (2004) in the specific case of perfect elastoplasticity).

The time interval $T = [0; \underline{t})$ is discretized into k subintervals by means of the instants $0 = t_\circ \leq t_1 \leq .. \leq t_i \leq .. \leq t_k = \underline{t}$. The idea is approximate the exact trajectory $(\mathbf{u}(t), \mathbf{T}(t), \mathbf{E}^a(t), \mathbf{E}^p(t))$ (which solves the initial-boundary value problem defined above), with a sequence of states obtained by solving, at each time step t_i, the minimum problem for a suitably defined, updated energy functional, characteristic of an evolving hyper-elastic NT material. To model perfect plasticity in compression, I assume a linearly-growing extension of the strain energy function defined in (63), beyond the yield surface defined in (57) (see Figure 50).

[16] The line search method calculates the energy for several values of the scale factor κ_j (doubling or halving each time) until the minimum energy is passed. The optimum scale is then calculated by quadratic interpolation.

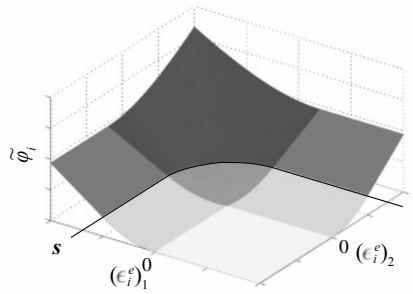

Figure 50. Linear prolongation of the strain energy beyond the crushing limit.

Namely, at any time step t_i, the functional form implemented in the finite element code is

$$\widetilde{\Phi}_i(\mathbf{E}_i^*) = \begin{cases} 0\ , & (e_1^*)_i \geq 0\ ,\ (e_2^*)_i \geq 0\ , \\ \frac{1}{2}E(e_1^*)_i^2\ , & (e_1^*)_i < 0\ ,\ (e_2^*)_i \geq -\nu(e_1^*)_i\ ,\ f(\mathbf{E}_i^*) \leq 0\ , \\ \alpha\sqrt{\frac{1}{2}E(e_1^*)_i^2} + \beta\ , & (e_1^*)_i < 0\ ,\ (e_2^*)_i \geq -\nu(e_1^*)_i\ ,\ f(\mathbf{E}_i^*) > 0\ , \\ \varphi((e_j^*)_i) & (e_1^*)_i < 0\ ,\ (e_2^*)_i < -\nu(e_1^*)_i\ ,\ f(\mathbf{E}_i^*) \leq 0\ , \\ \alpha\sqrt{\varphi((e_j^*)_i)} + \beta & (e_1^*)_i < 0\ ,\ (e_2^*)_i < -\nu(e_1^*)_i\ ,\ f(\mathbf{E}_i^*) > 0\ , \end{cases}$$

where

$$\varphi((e_j^*)_i) = \frac{1}{2}\frac{E}{1-\nu^2}\left((e_1^*)_i^2 + (e_2^*)_i^2 + 2\nu(e_1^*)_i(e_2^*)_i\right)\ ,$$

$(e_1^*)_i, (e_2^*)_i$ $((e_1^*)_i < (e_2^*)_i)$ are the principal values of $\mathbf{E}_i^*$, and the elastic strain at time t_i is given by the difference between the total strain $\mathbf{E}_i$ at the same time step and the plastic strain $\mathbf{E}_{i-1}^p$ inherited from the previous solution step, that is $\mathbf{E}_i^* = \mathbf{E}_i - \mathbf{E}_{i-1}^p$; by using this relation $\widetilde{\Phi}_i(\mathbf{E}_i^*)$ can be expressed as a function of $\mathbf{E}_i$ and becomes $\widehat{\Phi}_i(\mathbf{E}_i)$. The constants

$$\alpha = \sqrt{\frac{2}{E}}\sigma_\circ\ ,\ \beta = -\frac{\sigma_\circ^2}{2E}$$

are introduced to preserve the C^1 regularity of $\widetilde{\Phi}_i(\mathbf{E}_i^*)$. A representation of $\widetilde{\Phi}_i(\mathbf{E}_i^*)$ in the space of principal elastic strains is depicted in Figure 50.

The descent procedure finds the minimum of the total potential energy at time t_i, defined as

$$E_i(\mathbf{u}_i) = -\int_{\partial\Omega_N} \underline{\mathbf{s}} \cdot \mathbf{u}_i - \int_\Omega \mathbf{b} \cdot \mathbf{u}_i + \int_\Omega \widehat{\Phi}(\mathbf{E}_i(\mathbf{u}_i)) \,, \tag{65}$$

via a finite element discretization of the domain and descent minimization. The solution at the previous loading step is used as the initial condition for the minimization of the function

$$\widehat{E}(\{u_h\}) = -\sum_r L_r \underline{\mathbf{s}}(\mathbf{x}_r) \cdot \mathbf{u}_r - \sum_m \mathbf{f}_m \cdot \mathbf{u}_m - \sum_n A_n \mathbf{b}(\mathbf{x}_n) \cdot \mathbf{u}_n - \sum_q A_q \widehat{\Phi}(\mathbf{x}_q) \tag{66}$$

representing the finite element approximation of the total potential energy (65), as in the case of NENT materials (see (64)). At each step i, the minimization of the function $\widehat{E}(\{u_h\})$ is performed via the descent method described previously for NENT materials.

A plastic strain update is then performed at each Gauss point. The yield condition $f(\mathbf{E}_i^*) = 0$ defines, in the space of principal reversible strains $\mathbf{E}^*$, a curve whose position vector is $\mathbf{y}$, of coordinates $\{y_j\}$. It is useful to give a parametric description $\mathbf{y}(\gamma)$ of the yielding curve in the space of principal elastic strain, γ being the parameter. The return mapping algorithm, according to the principle of minimum dissipation imposed by the assumption of associated plasticity (Ortiz and Simo, 1986), consists in finding the value of the parameter giving the minimum distance (in the energy norm) of the current elastic strain $\mathbf{E}_i^*$ from the curve $\mathbf{y}(\gamma)$:

$$min_\gamma \Phi(\mathbf{y}(\gamma) - \mathbf{E}_i^*) \,.$$

This minimum problem can be easily formulated as

$$\frac{d}{d\gamma}\Phi(\mathbf{y}(\gamma) - \mathbf{E}_i^*) = 0 \,,$$

that can be solved for γ, at each Gauss point, via the Newton–Raphson method. The tensor of plastic strain rate $\dot{\mathbf{E}}^p$ at time t_i is coaxial to the reversible strain tensor $\mathbf{E}_i^*$, therefore the principal components $(\Delta e_j^p)_i$ (with j=1,2) of the plastic strain increment $\Delta\mathbf{E}_i^p$ (i.e., the discrete version of $(\dot{\mathbf{E}}^p)_i$) are simply computed as

$$(\Delta e_j^p)_i = (e_j^*)_i - y_j(\gamma_i^\circ) \,.$$

Once the plastic strain has been updated in the global reference frame, i.e. $\mathbf{E}_i^p = \mathbf{E}_{i-1}^p + \Delta\mathbf{E}_i^p$ (a backward Euler finite difference scheme), the

energy density dissipation at the given Gauss point, at time step t_i, can be computed as

$$D_i = \widehat{\Phi}(\mathbf{E}_i, \mathbf{E}^p_{i-1}) - \widehat{\Phi}(\mathbf{E}_i, \mathbf{E}^p_i) = \widehat{\Phi}(\mathbf{E}_i, \mathbf{E}^p_{i-1}) - \frac{1}{2}\mathbf{T}_i \cdot \mathbf{A}[\mathbf{T}_i]$$

from which one sees that the plastic strain increments produce energy loss.

4.3 Numerical examples

The ability of descent methods to approximate the solution of boundary value problems for NENT and ML materials is tested in the paper (Angelillo et al., 2010) in two ways: the numerical solutions are compared first with some simple exact solutions, then with some experimental results; finally the numerical solutions obtained with our code for more complex boundary value problems concerning masonry facades are presented. Here I report some of those results.

Example 1: Simple Flexure. In Angelillo et al. (2010), we solved numerically the problem of Flexure (whose exact solution is described in Subsection 3.7) both for the isotropic NENT material and for the isotropic ML material, by putting $\nu = 0$, $H = B = 2$ m.

For the first case (NENT material), we assumed for the Young modulus $E = 660$ MPa; the value of the rotation was set to $\Phi = 0.001$ radiants. To test convergence a sequence of structured discretizations of decreasing mesh size h was considered. By introducing the normalized mesh size h/D, D being the diameter of the domain, the four values $\sqrt{2}\{1/16, 1/32, 1/64, 1/128\}$ were considered. In Figure 51a, the contour plot of the maximum principal fracture strain obtained with the finest mesh, is reported. Fractures are non-zero in the region indicated as Ω_3 in Figure 38b, and their distribution suggests that the numerical solution is close to the rigid-block displacement represented in Figure 51b, which can be thought of as an energetically-equivalent alternative to the two analytical solutions described in *Subsection* 3.7 (see also Figure 39).

The numerical experiment was repeated for a ML panel by assuming for the maximum compressive stress in uniaxial compression, the value $\sigma_\circ = 19.8$ MPa. The value of the given rotation $\Phi = 0.006$ radiants is selected in such a way that, for the exact solution, the strip $y > B/4$ is forced into the yielding regime. For this value of Φ the exact stress solution is

$$\mathbf{T}_\circ = \begin{cases} -\sigma_\circ \mathbf{e}_1 \otimes \mathbf{e}_1 \ , \ y \geq B/4 \ , \\ -4\sigma_\circ \frac{y}{B} \mathbf{e}_1 \otimes \mathbf{e}_1 \ , \ B/4 > y \geq 0 \ , \\ 0 \ , \ 0 > y \ , \end{cases}$$

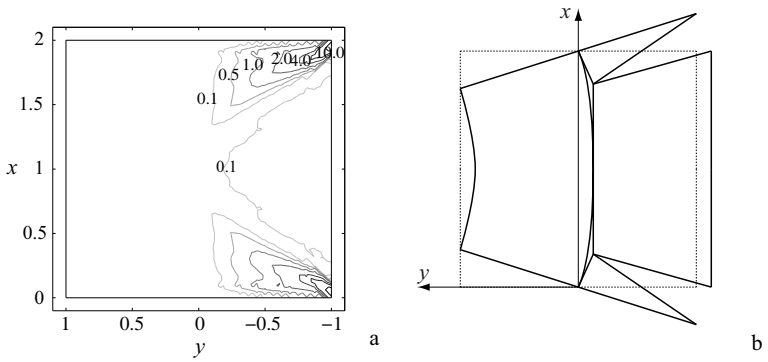

Figure 51. Numerical solution of the flexure problem for an isotropic NENT material. In (a): maximum fracture strain [$\times 10^{-3}$.]. Deformation on the right and rigid-block displacement on the right, close to the solution obtained numerically through descent.

Again the same sequence of discretizations of decreasing mesh size is considered. Figure 52a shows the computed isostatic curves for the finest mesh. They are very close to being vertical lines as expected. In Figure 52b the contour plot of the computed maximum compressive stress (solid lines) is comapared with the exact solution (dash-dotted lines). The numerical solution shows, graphically, good qualitative accuracy. The maximum fracture strain is reported in Figure 52c, and it can be noticed that the fracture distribution in the strip $y < 0$ (region Ω_3 in Figure 38b) is similar to the one observed in the NENT material (see Figure 51a). The distribution of fracture strain in the Ω_2 region resembles closely the crushing vertical fractures that appear in the experiment shown in Figure 52d.

For this example,both for the NENT and ML materials, we performed a numerical convergence study on the stress, by considering the sequence of discretizations of decreasing mesh size h described above. In Figure 53 a plot of the approximation error for the stress

$$e_h = \frac{\|\mathbf{T}_h - \mathbf{T}_{circ}\|_{L^2}}{\|\mathbf{T}_h\|_{L^2}} ,$$

versus the dimensionless mesh size h/D ($\mathbf{T}_0$, $\mathbf{T}_h$, being the exact stress solution snd the stress field computed for the mesh of size h) is reported. A linear convergence of the method is obtained in both cases.

Example 2: Pure relative shearing. The simple rectangular panel depicted in Figure 54 subject to a given relative horizontal translation of the bases (of value $2U$) and vanishing tractions on the lateral sides is considered.

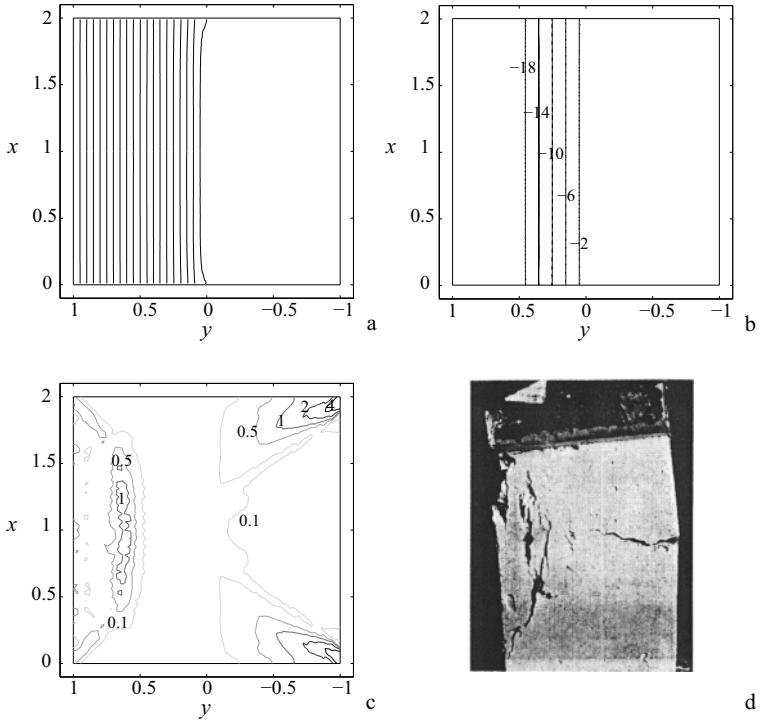

Figure 52. Numerical solution of the flexure problem for an isotropic ML material. In (a), (b): isostatic lines of compression and contour plot of the minimum principal stress (the other principal stress is almost zero). In (c): contour plot of the maximum anelastic strain component (fracture strain). Flexure test on a masonry panel (courtesy G. Castellano): (d).

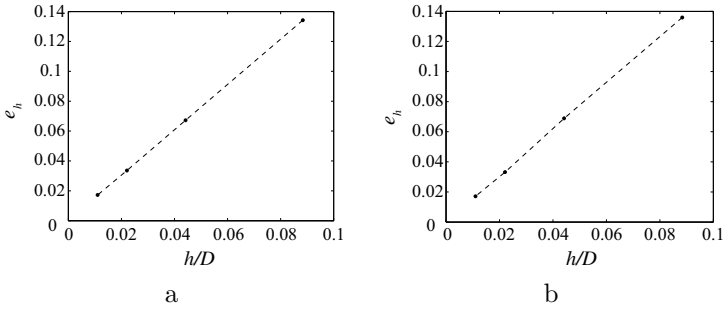

Figure 53. Flexure: convergence diagram. In (a): NENT material; in (b): ML material.

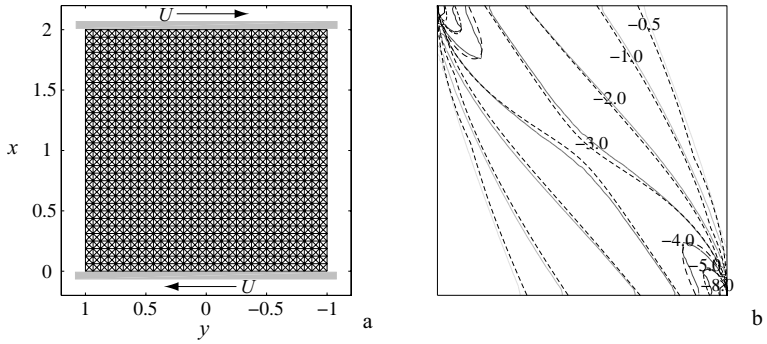

Figure 54. Pure relative shearing of a NENT panel. In (a): boundary conditions and mesh used in the numerical simulation. In (b): Comparison of the minimum principal compressive stress levels corresponding to the numerical (solid lines) and exact solution (dotted lines).

NENT material. The material parameters and the geometry are the same adopted in the previous *Section*. The value $U = 1$mm is considered. In Figures 54 and 55 the numerical solution is compared with the semi-analytical solution described in *Subsection* 3.8.

The distribution of the maximum compressive stress, the fracture strain, and the form of the isostatic lines computed numerically for the NENT panel are in good agreement with the results of the semi-analytical method of Fortunato (2010), as summarized in Figures 54 and 55.

ML material. The numerical experiment was repeated for a ML panel, by assuming the same material parameters adopted for the NENT material and putting for the limit stress: $\sigma_\circ = 19.8$ MPa. The value of the displacement at the boundary, $U = 1$ mm, previously considered, is small enough to give very limited yielding (mainly located in the vicinity of the corners, and is used as the first step in the discretized loading of the ML panel, whose evolution and crushing spreading is followed approximately, as the relative shearing U is gradually increased, by discretizing the real trajectory into steps.

In Figure 56 three stages of the evolving solution are reported. As the boundary displacement increases, a diagonal band, uniaxially and uniformly compressed at the limit stress of 19.8 MPa, forms progressively, and the isostatic lines of compression (compression rays) become more and more parallel.

The contour plots in Figure 57 represent the maximum fracture strain, which concentrates on two sub-diagonal lines, and the maximum plastic

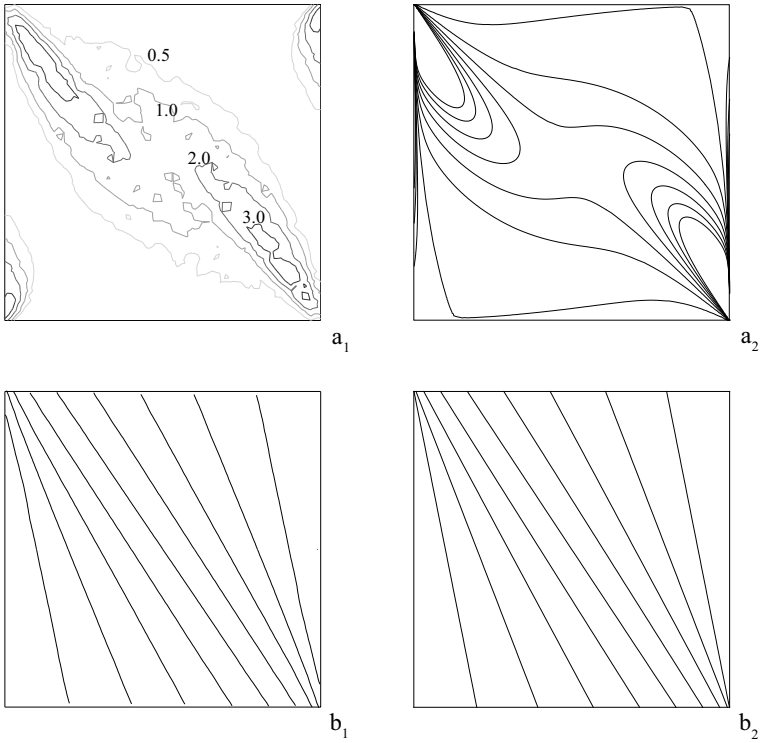

Figure 55. Pure relative shearing of a NENT panel. Fracture strain for the numerical: (a) and for the exact: (b) solutions. Compression rays for the numerical: (c) and the exact: (d) solutions.

strain, which concentrates at the constrained boundary, near two opposite corners. Concentration of plastic strain is expected, due to the assumed perfect plasticity of the material.

In Figure 58, a plot of the energy as a function of the step-wise increment of the boundary displacement U is reported, where: black circles denote the energy level of the computed solution at the beginning of the time step i, open circles denote the energy level due to the loading increment, and diamond marks denote the energy level reached after convergence.

Therefore the upward jump in energy represents the effect of updating the given disploacement from the value at time i to the one at time $i + 1$; the jump back of the energy is the effect of the numerical minimization of the updated energy, and the last smaller drop is the effect of the numerical

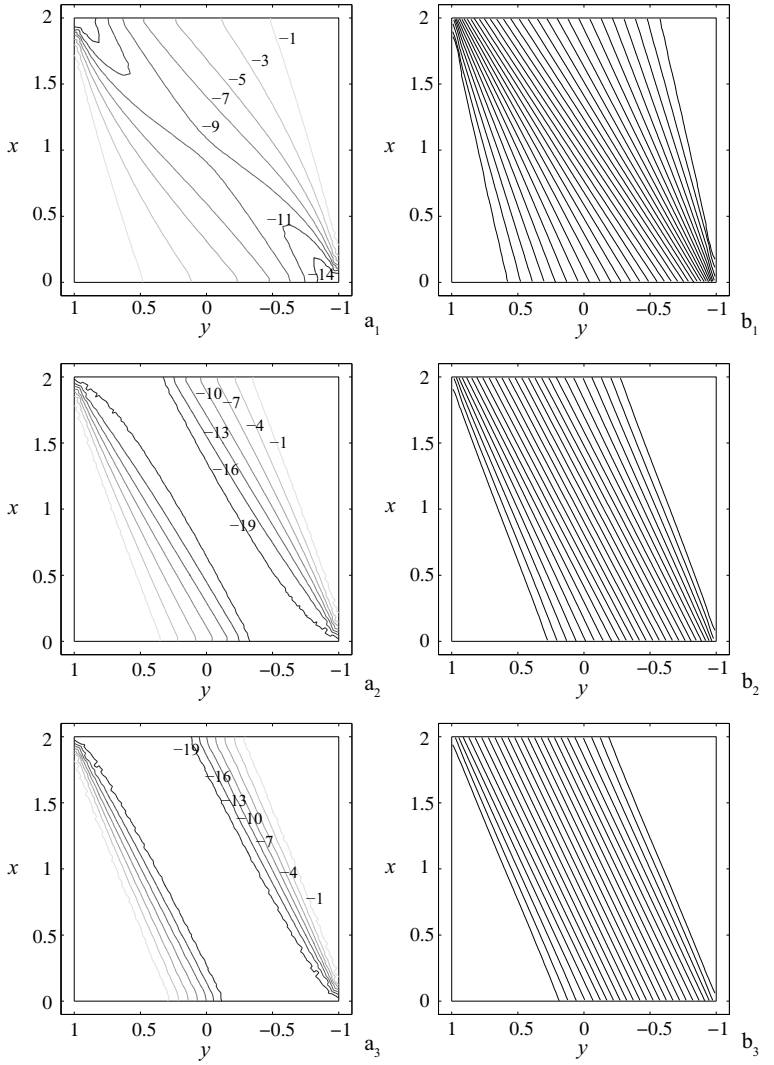

Figure 56. Pure shearing of a ML panel. Evolution of the contour plot of the minimum principal compressive stress and of the compression rays at three steps of the loading process.

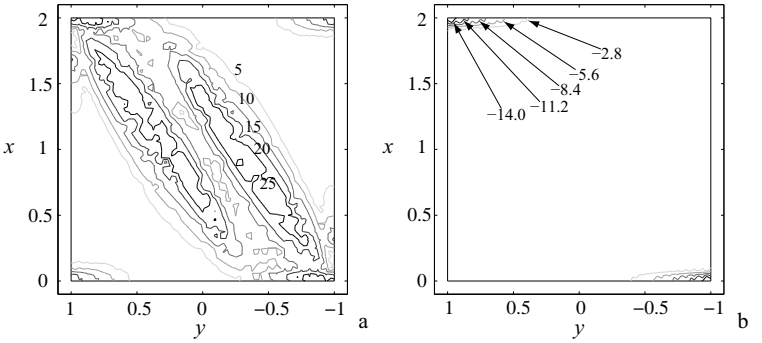

Figure 57. Pure shearing of a ML panel. Contour plot of the maximum principal fracture strain: (a), and minimum plastic strain: (b), for the final value of the relative displacement.

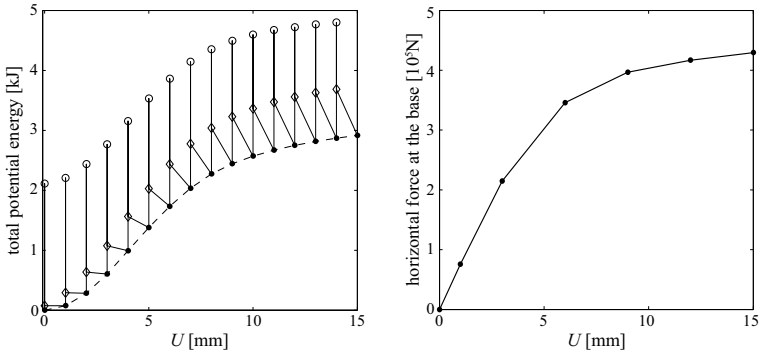

Figure 58. Pure shearing of a ML panel. Energetics.

update of the plastic strain that gives the approximate solution at time $i+1$.

This energy loss represents energy dissipation due to plastic work, and gives evidence of spreading of plastic deformation as the load is increased. The dashed line (that is the envelope of the solution points) represents the numerical approximation to the exact time history of the total potential energy of the body. In Figure 58b the push-over plot, that is the evolution of the horizontal component of the computed reaction at the base (horizontal force) as the displacement U increases, is depicted. The shear force plateaus, as expected for a perfectly plastic structure approaching collapse.

Validation against experimental tests. Here the ML material model is validated against independent sets of experimental results from Benedetti

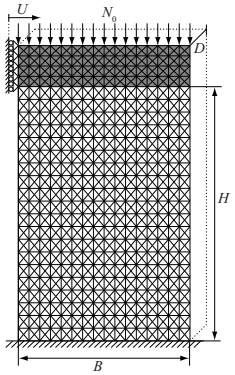

Figure 59. Loading scheme in the experiments by Benedetti and Steli (2008) and Eucentre (2010)

and Steli (2008) and Eucentre (2010), performed on different types of masonry. Figure 59 reports the constraints and the load scheme used in the numerical analysis to simulate the experimental setup.

A masonry panel of width B, height H, and thickness D is fixed to the ground at the bottom and to a steel beam at the top (the gray strip in Figure 59). A uniform load is distributed at the top part of the steel beam and the horizontal load is applied in incremental steps by imposing the horizontal displacement U of the left edge of the steel beam. Neither Benedetti and Steli (2008) and Eucentre (2010) report measurements of the Poisson's ratio, and because of that $\nu = 0$ is assumed in the simulations, since, parametric studies, not reported here, show that the simulated force-displacement curves, under shear, manifest very low sensitivity to the Poisson's ratio. The graphs in the top row of Figure 60 compare the numerical simulations and the experimental results for specimens (1A-08,2C-03) of the experiments by Benedetti and Steli (2008). In these tests, the masonry is composed of crushed stones and injected crushed stones. Our model reproduces quantitatively the substantial features of the measured force-displacement curves, with a slight overestimation of the force for higher levels of the horizontal displacement U.

The graphs of Figure 60c,d report the comparison between experimental data and numerical simulations for the specimens CS00, CS02, and CT01 of (Eucentre, 2010), all composed of stone masonry. Specimen CS00 differs from the other two because the mortar has been reinforced with 20% sand in mass fraction. This might explain the flatness of the force-displacement curve for experiment CS00 which is very well captured by the model. The

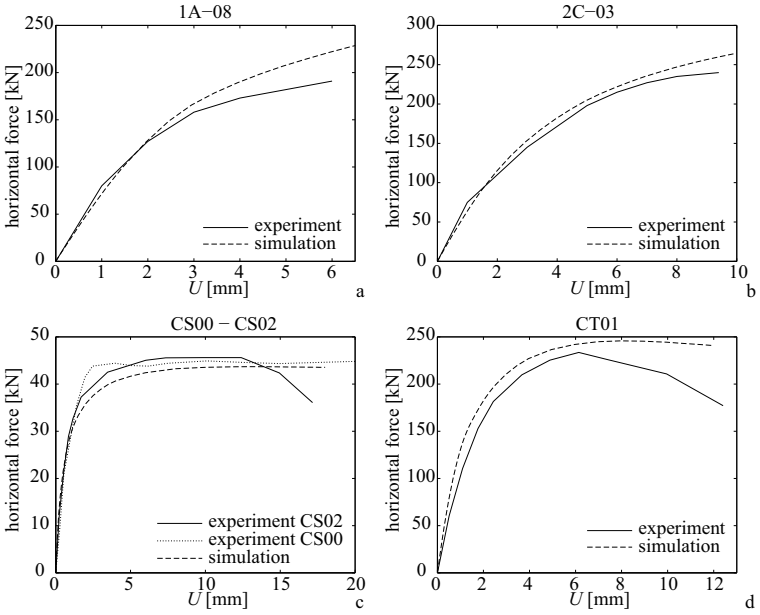

Figure 60. Comparison of numerical simulations with the experimental results of Benedetti and Steli (2008) (1A-08,2C-03) and Eucentre (2010) (CS00-CS02, CT01)

marked reduction of the horizontal force at higher levels of the displacement U might be due to softening effects induced in the masonry by the unreinforced mortar, an effect that is not captured by the ML model as presented here.

Example 3: Masonry walls with regular openings. In this section I apply the ML material model to simulate the response of a simple two-storey facade to vertical loads, seismic loads, and differential foundation subsiding. The geometry of the facade, the applied loads, and the boundary conditions are summarized in Figure 61a.

The facade is provided, above the openings, with 25 cm-thick wood beams and is assumed to be made of tuff and mortar of good quality. Wood is modeled as elastic, with Young's modulus $E = 11$ GPa, Poisson's ratio $\nu = 0.35$, and density $\rho = 800$ kg/m^3. For the tuff wall we assumed a Young's modulus $E = 0.66$ GPa, Poisson's ratio $\nu = 0.2$, density 1800 kg/m^3, and compression limit $\sigma^\circ = 1.98$ MPa. The whole structure is assumed to be 0.5 m thick.

Working loads. Working loads are represented by the weight of masonry

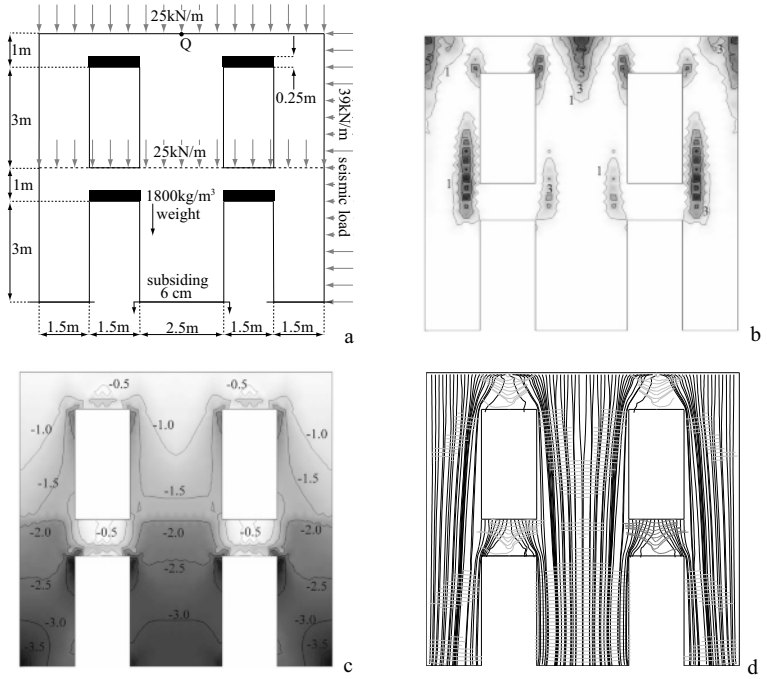

Figure 61. Masonry wall with openings. Loading schemes: (a). Numerical results for vertical loads: b,c,d. Contour plot of maximum principal fracture strain: (b). Minimum principal stress: (c). Isostatic lines: (d)

and the force transmitted by the floors (25 kN/m); the results of the simulation are reported in Figure 61b,c,d. The structure sustains the working loads without detectable crushing. The value of the maximum stress at the base of the wall is about 0.35 MPa. The partition of the domain can be inferred from Figure 61d: in Ω_1 both families of isostatic lines are depicted; in $Omega_2$ the family of isostatic lines corresponding to zero stress are not reported.

Horizontal loads. We simulated the response of the facade to a uniform horizontal force per unit length of 39 kN/m, distributed on the right side of the structure and superimposed to the structure subject to working loads (see Figure 61a). The total horizontal load is equivalent to 70% of the weight of the structure and is applied in ten steps. This kind of loading can be adopted to simulate seismic loads if horizontal ties or connections are present. Crushing strain accumulates in very localized regions near the

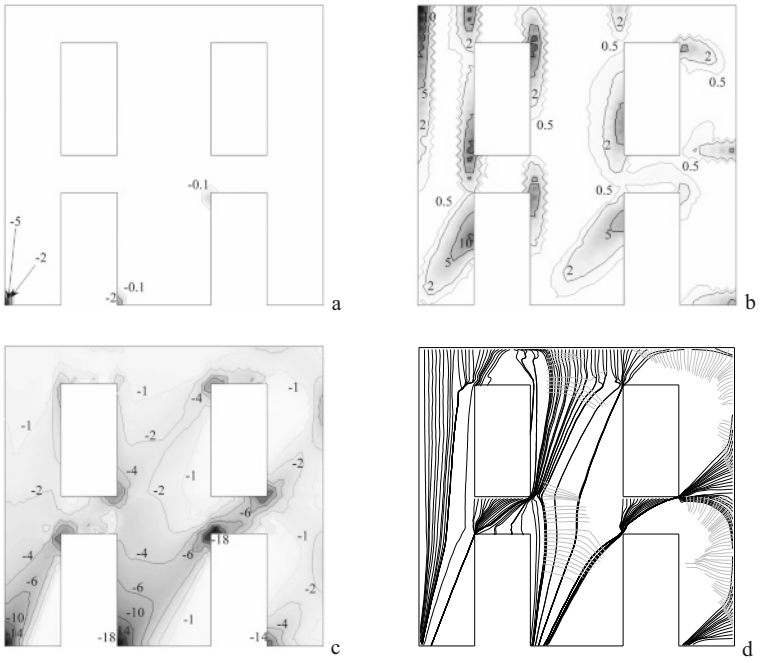

Figure 62. Numerical results for vertical and horizontal loads. Contour plot of maximum principal plastic strain: (a). Contour plot of maximum principal fracture strain: (b). Minimum principal stress: (c). Isostatic lines: (d)

corners (see Figure 62a). The formation of a compressed diagonal truss element, in the panels in between the openings, is evident from Figures 62c and 62d.

The force-displacement curve, depicted in Figure 64, shows that the structure is approaching collapse for the maximum horizontal load applied.

Differential foundation subsiding. A 6 cm subsiding of the base of the central wall is imposed in fifteen steps.This action is superimposed to the effect of working loads. The structure shows a peculiar kinematical effect, consisting in a vertical displacement of the central wall and an outward rotation of the lateral walls around the corner points of the bases, where the plastic strain concentrates (see Figure 63).

The computed vertical component of the reaction of the central wall drops from about 390 kN to 240 kN after the subsiding. This computation indicates that the vertical loads migrate from the central panel to the lateral ones. Such a stress redistribution is also highlighted from the com-

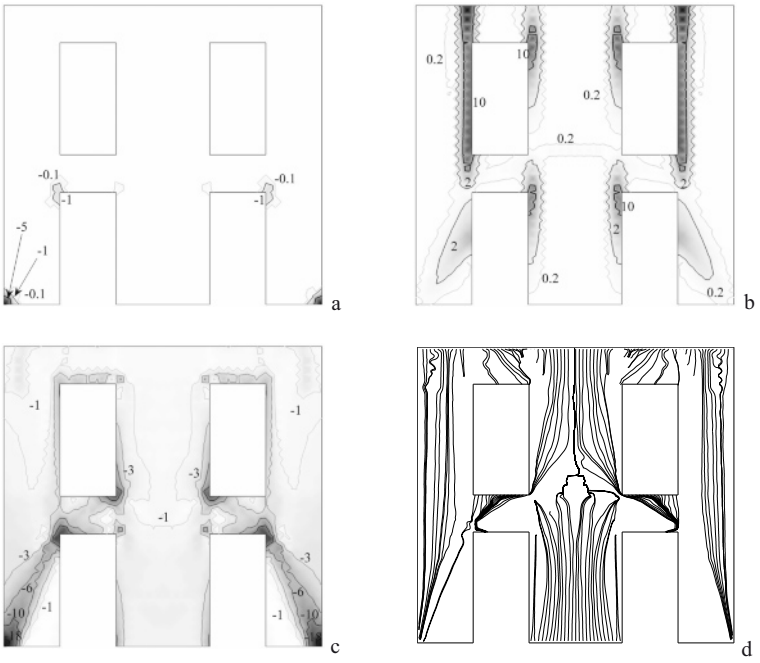

Figure 63. Masonry walls with openings under the effect of vertical loads and a vertical settlement of the central pier: mumerical results. Contour plot of maximum principal plastic strain: (a). Contour plot of maximum principal fracture strain: (b). Minimum principal stress: (c). Isostatic lines: (d)

parison of the isostatic lines depicted in Figure 63d with the ones reported in Figure 61d.

Bibliography

Dassault Systemes Abaqus, ver. 6.12 `http://www.3ds.com/fileadmin/PRODUCTS/SIMULIA`

G. Alfano, L. Rosati and N. Valoroso. A numerical strategy for finite element analysis of no-tension materials. *Int. J. Numer. Methods Eng.*, 48 (3): 317–350, 2000.

L. Ambrosio, N. Fusco and D. Pallara . *Functions of bounded variation and free discontinuity problems, Clarendon Press.* 2000.

M. Angelillo and A. Fortunato. Compatibility of loads and distortions for unilateral materials. *In preparation.*

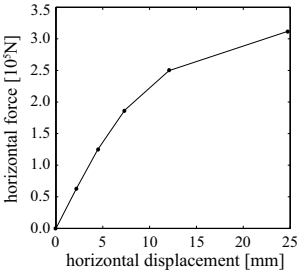

Figure 64. Masonry walls with openings under vertical and horizontal loads: shearing force versus roof displacement

M. Angelillo and L. Giliberti. Statica delle strutture murarie. *Giornale del genio Civile*, 1988 (in Italian).

M. Angelillo and R.S. Olivito. Experimental analysis of masonry walls loaded horizontally in plane. *Masonry International*, 8 (3):91–100, 1995.

M. Angelillo and F. Rosso. On statically admissible stress fields for a plane masonry-like structure. *Quarterly Of Applied Mathematics*, 53 (4):731–751, 1995.

M. Angelillo, L. Cardamone, and A. Fortunato. A numerical model for masonry-like structures. *Journal of Mechanics of Materials and Structures*, 5:583–615, 2010.

M. Angelillo, E. Babilio, and A. Fortunato. Singular stress fields for masonry-like vaults. *Continuum Mechanics And Thermodynamics*, 2012.

M. Angelillo, A. Fortunato, M. Lippiello, and A. Montanino. Singular stress fields and the equilibrium of masonry walls. *Meccanica*, under revision, 2013.

A. Benedetti and E. Steli. Analytical models for shear-displacement curves of unreinforced and frp reinforced masonry panels. *Constr. Build. Mater.*, 22 (3):175–185, 2008.

E. Benvenuto. *An Introduction on the History of Structural Mechanics Part II: Vaulted Structures and Elastic Systems, Springer-Verlag.* Springer Verlag, 1991.

G. Dal Maso, A. De Simone, and M.G. Mora. Quasistatic evolution problems for linearly elastic perfectly plastic materials. *Arch. Rat. Mech. Anal.*, 2004.

E. De Giorgi. Congetture riguardanti alcuni problemi di evoluzione. *Duke Math. J.*, 81(2):255–268, 1996.

G. Del Piero. Constitutive equation and compatibility of the external loads for linear elastic masonry–like materials. *Meccanica*, 24:150–162, 1989.

G. Del Piero. Limit analysis and no–tension materials. *Int. J. Plasticity*, 14:259–271, 1998.

F. Derand. *L'architecture des voutes, Cramoisy.* 1643.

C. L. Dym and I. H. Shames. *Solid Mechanics: a variational approach, Mc Graw Hill.* 1973.

M. Epstein. On the wrinkling of anisotropic elastic membranes. *J. Elast.*, 55:99–108, 1999.

Eucentre. Prove murature. 2010. URL `http://www.eucentre.it/provemurature`.

A. Fortunato. Elastic solutions for masonry-like panels. *J. Elas.*, 98:87–110, 2010.

M. Giaquinta and E. Giusti. Researches on the equilibrium of masonry structures. *Arch. Rational Mech. Analysis*, 88:359–392, 1985. ISSN 0950-2289.

E. M. Gurtin. *The linear theory of elasticity, in Handbuch der Physik, band VIa/2, Springer-Verlag.* 1972.

J. Heyman. *The stone skeleton: structural engineering of masonry architecture.* Cambridge University Press, 1995.

S. Huerta. Arcos, bovedas y cupulas. geometria y equilibrio en el calculo tradicional de estructuras de fabrica. *Report: Instituto Juan de Herrera*, 2004 (in Spanish).

S. Huerta. The analysis of masonry architecture: a historical approach. *Arch. Sc. Review*, 51(4):297–328, 2008.

C. T. Kelley. *Iterative Methods for Optimization", Frontiers in Applied Mathematics 18, SIAM.* 1999.

E. Kreyszig. *Introductory Functional Analysis with Applications, John Wiley.* 1989.

C. Padovani M. Lucchesi and N. Zani. Masonry-like solids with bounded compressive stress. *Int. J. Solids Struct.*, 33 (14):1961–1964, 1996.

M. Šilhavý M. Lucchesi and N. Zani. Singular equilibrated stress fields for no-tension panels. In *Lecture Notes in Applied and Computational Mechanics, 23, Springer*, pages 255–265, 2005.

G. Pasquinelli M. Lucchesi, C. Padovani and N. Zani. *Masonry constructions: mechanical models and numerical applications, Lecture Notes in Applied and Computational Mechanics 39, Springer.* 2008.

E. H. Mansfield. Tension field theory. In *Proc. 12th Int. Cong. App. Mech., M. Hetenyi and W. G. Vincenti (eds.), Springer*, 1969.

E. H. Mansfield. *The bending and stretching of plates, Cambridge University Press.* 1989.

E. Mery. Memoire sur l'equilibre des voutes en berceau. *Annales des pontes et chausees*, 1 (2):50–57, 1840.

A. Mielke and M. Ortiz. A class of minimum principles for characterizing the trajectories and the relaxation of dissipative systems. *ESAIM Control Optim. Calc. Var.*, 14 (3):494–516, 2008.

M. Ortiz and J. C. Simo. An analysis of a new class of integration algorithms for elastoplastic constitutive relations. *Int. J. Numer. Methods Eng.*, 23 (3):353–366, 1986.

D. J. Steigmann. Tension–field theory. *Proc. R. Soc. Lond. A*, 429:141–173, 1990.

R. Temam and G. Strang. Functions of bounded deformation. *Arch. Rat. Mech. Anal.*, 75 (1):57–73, 1994. ISSN 1980.

S. Timoshenko and J. N. Goodier. *Theory of elasticity, Mc Graw Hill.* 1951.

Y. W. Wong and S. Pellegrino. Wrinkled membranes ii: analytical models. *J. Mech. Mater. Struct.*, 1:27–60, 2006.

II Refined Models

Modeling the interfaces in masonry structures

Frédéric Lebon*
Aix-Marseille University, LMA, UPR7051, CNRS, Centrale Marseille, 13402
Marseille, France
frederic.lebon@univ-amu.fr

Abstract This chapter deals with some models for interfaces in the case of masonry structures. Some experimental studies are recalled in the first part. In the second part, four interface models are presented.

1 Introduction

The aim of the chapter is to present some ideas for modeling interfaces in masonry structures. Devising means of modeling interfaces between solids in structural assemblies is obviously now of great importance in the fields of mechanical technology and civil engineering. These interfaces contribute crucially to the strength of many structures, such as optics lenses, airplanes, asphalt pavements and masonry, for example. It is therefore necessary to develop rather fine models. One of the main problems which often arises in this context is that of developing a unified theory: from the tribological point of view, the contact is often unique, in the sense that it depends on the materials, roughness, wear, etc., and especially on the mechanical system involved. The problem of cracking in pavements is obviously quite different from that of the cornering of an airplane tire. Another problem is due to the smallness of the interface in comparison with the size of the structure, as well as the possibly weak mechanical characteristics (in the case of old mortar, for example). A large number of studies have been devoted to the behavior of interfaces. Two main modeling approaches used for this purpose are phenomenological modeling and deductive modeling. In the first approach, the thickness of the interface is taken to be zero and the mechanical properties are obtained from physical considerations and experiments (see for example Frémond (1987); Point and Sacco (1996); Freddi and Frémond (2006); Raous (2011); Bonetti and Frémond (2011) and references therein). The

*The author thanks F. Fouchal, C. Pelissou, A. Rekik, R. Rizzoni and I. Titeux for their contribution in this work

M. Angelillo (Ed.), *Mechanics of Masonry Structures*, CISM International Centre for Mechanical Sciences, DOI 10.1007/ 978-3-7091-1774-3_5, © CISM, Udine 2014

second approach consists in focusing on the thin layers of material at the micro-mechanical level, which are usually called the interphase. The mechanical parameters of the interface model, characterized by zero thickness, are identified on the basis of the parameters of the material constituting this interphase. These boundary conditions have been extensively used to model imperfect interface properties. One of the method commonly used to model interface conditions is based on the use of asymptotic techniques (see for example Klarbring (1991); Licht and Michaille (1997); Lebon et al. (1997, 2004); Lebon and Ronel (2007); Lebon and Rizzoni (2008) and references therein), in order to include microscopic considerations in the interface model.

Figure 1. Irregular type of masonry a) b) d) Typical Lozerian structures, France c) Miramas-Le-Vieux, France.

Obviously, one of the problem which arises when modeling interfaces in masonry is due to the the irregularity of the structures (see figure 1). In this chapter, we will deal only with fairly regular structures (see figure 2). Another problem arises with the constitutive equation for the blocks because stones are quite rigid blocks (see Lucchesi et al. (2008); Como (2010)). In

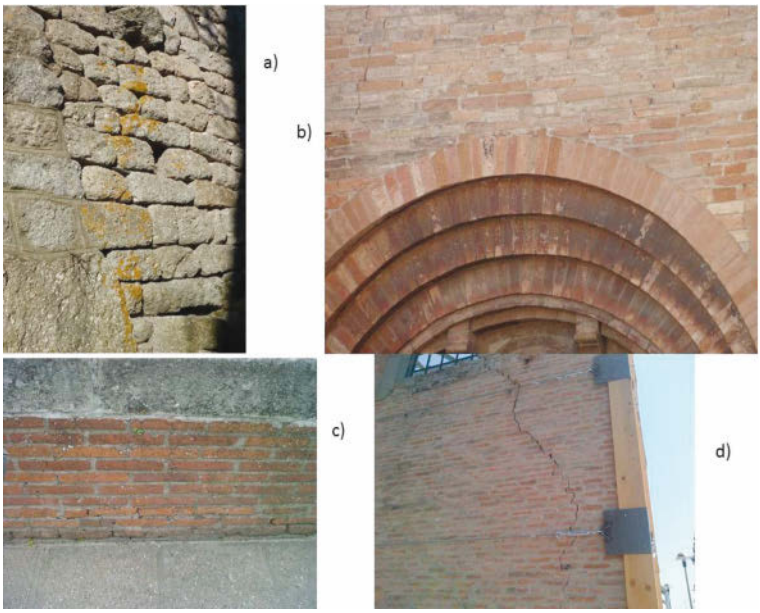

Figure 2. Examples of regular masonry a)Lozere, France b) Bologne, Italy c) Albi, France d) Ferrara, Italy.

what follows, we will deal only with deformable elastic bricks.
The last main problem depends on whether or not mortar is present in the structure and if so, how to write the constitutive equation for the mortar. If there is no mortar, the contact between blocks can be assimilated to dry friction. In the presence of mortar, it is necessary to model this component. The thickness of the mortar is also an important modeling parameter. If the mortar is thin, an interface law can be used directly for this purpose (see figure 3). If the thickness of the mortar is not negligible, it is necessary to introduce some additional considerations in order to account for the interactions between the bricks and the mortar (see figure 4).

In this chapter, it is proposed to present some interface laws. In the first part, the classical phenomenological law of unilateral contact with dry friction is recalled. In the second part, a phenomenological law of adhesion is presented and modeled based on the adhesion variable introduced by Fremond (Frémond (1987)). Two deductive interface laws are presented: the first one is linear and the second one is non linear and takes the damage which occurs at interface of this kind into account. The last modeling

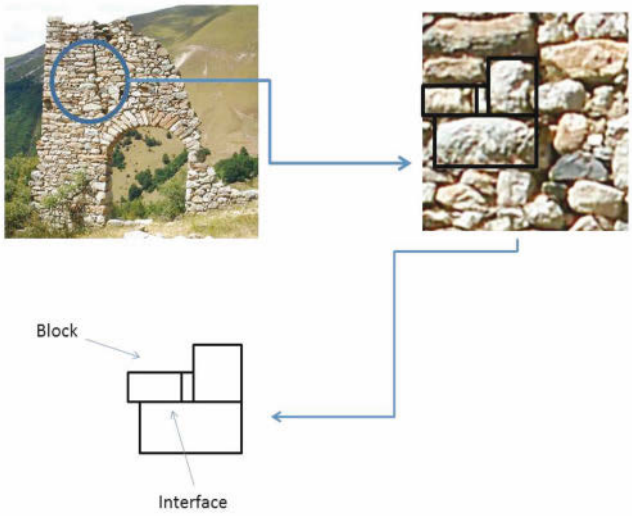

Figure 3. A wall without mortar: a study at local level.

approach presented here includes mechanical processes responsible for the failure, such as the unilateral contact, the friction at the microscopic scale and the normal and tangential damage. The four models discussed in this chapter were developed in the context of multibody mechanics.

This paper is composed of three parts. In the first part, experimental results are recalled. The second part is devoted to the modeling of friction between blocks with no mortar. In the third part of the paper, the phenomenological model of adhesion is presented in the form of two imperfect interface models based on the use of asymptotic techniques. Some numerical examples are provided.

2 Some comments on experimental results

2.1 Brick-brick interactions: dry friction

Michel Jean (Jean and Moreau (1994)) conducted experiments on a small wall (figure 5) consisting of 105 rigid blocks. each of which was 49 mm high, and 124 mm wide (62 mm in the case of half bricks). The wall was set on

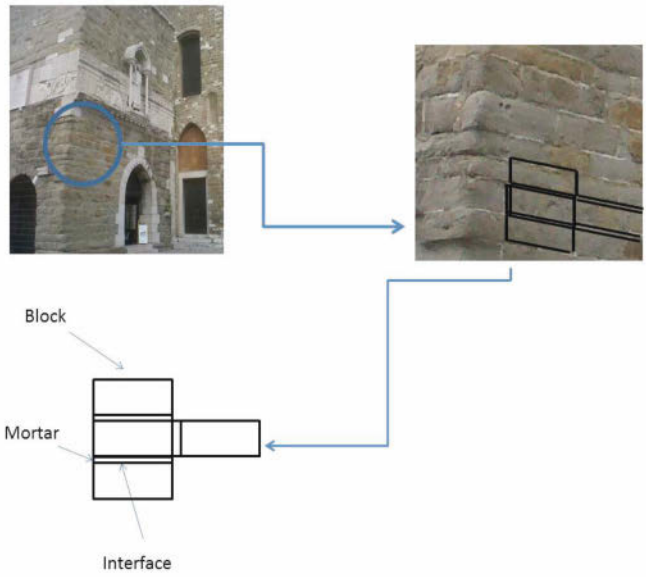

Figure 4. A wall with mortar: a study at local level.

a rigid foundation. The left half of the rigid foundation could be moved down. The total possible displacement was 6 cm.

Figure 5 shows the displacement of the blocks. Note that the interactions between the blocks are limited to contact (there is no penetration) and dry friction. The displacement of the blocks is strongly heterogeneous, especially along the diagonal.

2.2 Brick-mortar interactions

This section deals with the behavior of deformable blocks. The local behavior of the interfaces between full and hollow bricks and mortar joints, which are typical quasi-brittle interfaces (see Gabor (2002); Gabor et al. (2006)), has been studied by various authors. We will attempt here to summarize the results obtained.

The experimental device developed by Fouchal (2006); Fouchal et al. (2009) (figures. 6 and 7) was designed to study on the local scale the shear behavior of a simple assembly consisting of two and three full or hollow bricks (210×50 mm) connected by a mortar joint 10 mm thick. The samples were subjected to a monotonous increasing load up to failure.

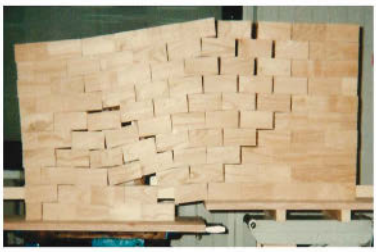

Figure 5. Experimental device involving 105 blocks (Jean and Moreau (1994))

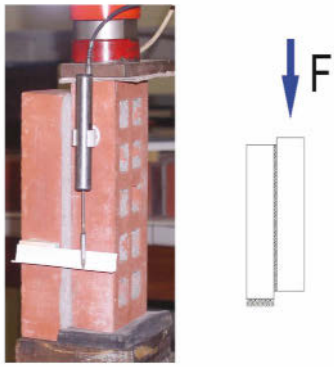

Figure 6. Experimental device involving two bricks

The following findings were obtained (see also figure 8):

- rigid elastic behavior up to the failure, followed by friction sliding behavior;
- the behavior of full bricks was fragile beyond the limit strength;
- the behavior of hollow bricks was quasi-fragile beyond the limit strength;
- hollow brick samples showed great dispersion, mainly due to the non uniform distribution of the mortar spikes and local defects in the com-

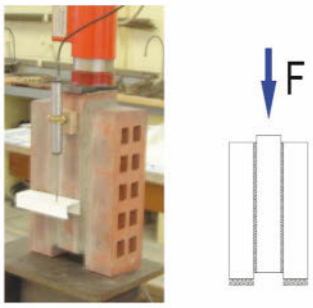

Figure 7. Experimental device involving three bricks

ponents of the bricks;

- samples consisting of two and three bricks showed similar behavior. The choice of basic cell therefore has no effect on the local scale.

3 Masonry structures without mortar: dry friction modeling (model 1)

This section focuses on structures devoid of mortar, or including mortar with a very low stiffness. In a first approach, the contact is assumed to involve dry friction with no penetration between the blocks.

For the sake of simplicity, we have adopted the framework of contact between two deformable solids (see figure 9). The contact can be defined by a punctual correspondence between two surfaces in contact Γ_c^1 and Γ_c^2 belonging to the domains Ω^1 and Ω^2 of $\Re^d$ $(d = 2, 3)$, respectively. We assume that initially $\Gamma_c = \Gamma_c^1 = \Gamma_c^2$. The relative displacement between two points located on the two surfaces in contact is denoted by $[u]$ with $[u] = u^1 - u^2$. Let F be the density of the contact forces. We take n^1 and n^2 to denote the external unit normal vectors to the boundaries of the two domains. The decomposition into normal and tangential parts is written:

$$[u] = [u_N]n^1 + [u_T] \quad \text{with} \quad [u_N] = [u].n^1 \tag{1}$$

$$F = F_N n^1 + F_T \quad \text{with} \quad F_N = F.n^1 \tag{2}$$

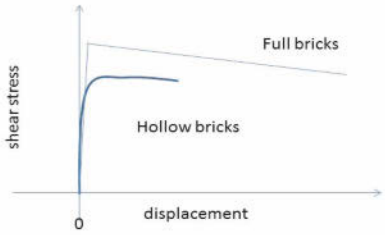

Figure 8. Typical behavior of the mortar/brick interface (with full and hollow bricks)

3.1 Unilateral contact

The contact conditions (Signorini conditions) are written:

$$F_N \geq 0; \quad [u_N] \geq 0; \quad F_N[u_N] = 0 \tag{3}$$

3.2 Dry Friction

The friction conditions (Coulomb's law) are written:

$$\begin{array}{lcll} ||F_T|| & \leq & \mu|F_N| & \\ ||F_T|| & < & \mu|F_N| \quad \Rightarrow & [\dot{u_T}] = 0 \\ ||F_T|| & = & \mu|F_N| \quad \Rightarrow & \exists\lambda \geq 0, \qquad [\dot{u_T}] = \lambda F_T \end{array} \tag{4}$$

where μ is the friction coefficient.

3.3 Formulations

The bodies are assumed to be elastic and the deformations are assumed to be small. In this case, formulation of three kinds can be used: primal (the unknowns are the displacements), dual (the unknowns are the stresses) and mixed formulations (the unknowns are the displacements and the stresses).

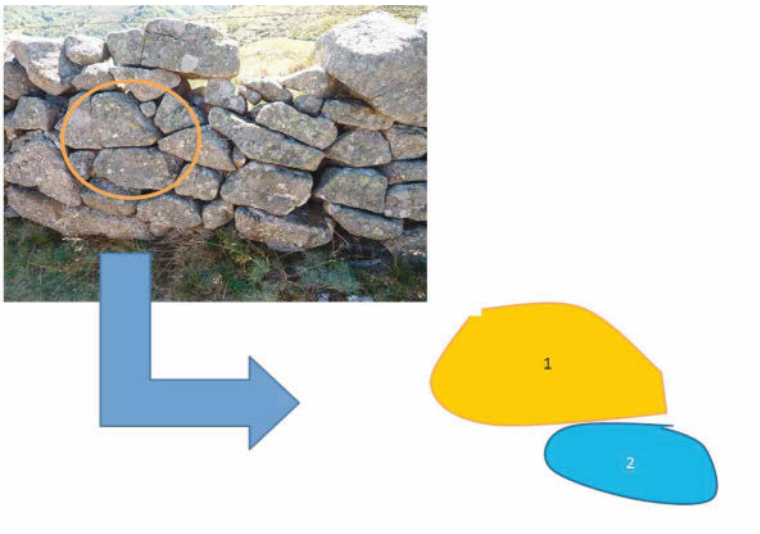

Figure 9. Dry contact between two blocks

In this chapter, two kinds of formulations are presented. Note that there exists a large class of methods for solving problems of this kind (see Raous et al. (1988); Lebon and Raous (1992); Chabrand et al. (1998); Lebon (2003); Fortin et al. (2002); Alart and Curnier (1991); Alart and Lebon (1995); Wriggers (2006) and references therein). Two corresponding algorithms are presented below.

Primal formulation (see Cocu et al. (1995))

Let us take $H^1(\Omega)$ to denote the order 1 Sobolev space, and H and H_0 to denote the subspaces of $(H^1(\Omega))^2$ defined by

$$\begin{aligned} H &= \{v \in (H^1(\Omega))^2, v = U \ on \ \Gamma_d\}, \\ H_0 &= \{v \in (H^1(\Omega))^2, v = 0 \ on \ \Gamma_d\}, \end{aligned} \tag{5}$$

We define $\mathcal{K}$ as the convex of contact of kinematically admissible fields $\mathcal{K} = \{v \in H, [v_N] \geq 0 \ on \ \Gamma_c\}$. u_0 is taken to denote the initial displacements

fields.

$$\begin{cases} u_0 \in H \text{ be given, find } u \in V = H^1(0,T;\mathcal{K}) \text{ such that } u(0) = u_0 \text{ in } \Omega \\ a(u, v - \dot{u}) + j(u, v) - j(u, \dot{u}) \leq l(v - \dot{u}), \ \ \forall v \in H_0 \\ \int\limits_{\Gamma_c} \sigma_N(u)([z_N] - [u_N])dl \leq 0, \ \ \forall z \in \mathcal{K} \end{cases} \tag{6}$$

with

$$\begin{aligned} j(u,v) &= -\int\limits_{\Gamma_c} \mu\sigma_N(u)||[\dot{v}_T]||dl, \\ l(v) &= \int\limits_{\Omega} Fvdx + \int\limits_{\Gamma_f} fvdl \\ a(u,v) &= \int\limits_{\Omega} e(u)Ae(v)dx. \end{aligned} \tag{7}$$

Using a finite difference, $\dot{u}(t^{k+1}) \simeq \frac{u^{k+1}-u^k}{\Delta t} = \frac{\Delta u^k}{\Delta t}$, with $u^k = u(t_k)$, at time t_{k+1}, we have

$$\begin{cases} \text{Find } \ u^{k+1} = u^k + \Delta u^k \in \mathcal{K} \ \text{ such that} \\ a(u^{k+1}, v - \Delta u^k) + j(u^{k+1}, v) - j(u^{k+1}, \Delta u^k) \leq l(v - \Delta u^k), \ \ \forall v \in \mathcal{K}. \end{cases} \tag{8}$$

Note that the results obtained on the existence, unicity and regularity of the solution for this problem have been discussed in Cocu (1984). An example of non uniqueness is given in Hild (2003).

Fixed point Method FPM (see Raous et al. (1988); Lebon and Raous (1992)) In the following sections, the indices k (time) will be omitted (this is a static formulation). The above problem is expressed as a fixed point problem on the sliding limit (Duvaut and Lions (1976); Cocu (1984))

$$\lambda \longrightarrow -\mu\sigma_N(u(\lambda)), \tag{9}$$

u is the solution of a variational inequation similar to the above one, where $j(.,.)$ is replaced by $j(.)$ defined by

$$j(v) = \int\limits_{\Gamma_c} \lambda|v_T|dl. \tag{10}$$

The latter problem is equivalent to the minimization of $L(v) = \frac{1}{2}a(v,v) - l(v) + j(v)$ in $\mathcal{K}$. It is possible to regularize the non-differentiable term

in the minimization problem, by replacing the absolute value by a smooth function. For example, a suitable value of $\sqrt{x^2+\epsilon^2}$ or $\epsilon Ln(ch(x/\epsilon))$ can be chosen (Lebon (1995)). This regularization procedure does not affect numerical structures. The problem is usually discretized by a linear interpolation (Finite Element Method). Let h be the discretization step. The displacement gives to a vector of dimension N_h. If I_h is the set of degrees of freedom involved in the friction, the fixed point iteration consists in finding the vector of dimension I_h, λ_h, which is the fixed point of the previously discretized problem. The algorithm, which is convergent, is written:

0 Initialization u^0 be given
1 Fixed Point (Iteration k) $\lambda^k \longrightarrow -\mu\sigma_N(u(\lambda^{k-1}))$
2 Minimization (Relaxation)

A Initialization $u^{k,0} = u^k$

B Resolution (iteration n, (a_{ij}) is the stiffness matrix)

Case 1 With a normal component of a contact node

$$u_i^{k,n+\frac{1}{2}} = \tfrac{1}{a_{ii}}(f_i - \sum_{j=1}^{j=i-1} a_{ij}u_j^{k,n} - \sum_{j=i+1}^{j=N_h} a_{ij}u_j^{k,n+1}) \qquad If\ u_i^{k,n+\frac{1}{2}} \geq 0\ then\ u_i^{k,n+1} = 0. \tag{11}$$

Case 2 With a tangential component of a contact node

$$u_i^{k,n+1} = \frac{1}{a_{ii}}(f_i - \sum_{j=1}^{j=i-1} a_{ij}u_j^{k,n} - \sum_{j=i+1}^{j=N_h} a_{ij}u_j^{k,n+1} + \lambda_i^k\epsilon(u_i^{k,n+1})) \qquad \text{If } x \geq 0, \epsilon(x) = 1, \text{ if } x \leq 0, \epsilon(x) = -1, \text{ if } x = 0, \epsilon(x) = 0. \tag{12}$$

Case 3 With a component of a free node (not involved in the contact)

$$u_i^{k,n+1} = \frac{1}{a_{ii}}(f_i - \sum_{j=1}^{j=i-1} a_{ij}u_j^{k,n} - \sum_{j=i+1}^{j=N_h} a_{ij}u_j^{k,n+1}). \tag{13}$$

C Convergence test : Yes : $u^{k+1} = u^{k,n+1}$, Go to 3; No : Go to B
3 Convergence Test Yes = End; No = Go to 1

At each iteration k, the energy present in the discretized convex $\mathcal{K}_h$ has to be minimized. This step is performed using the relaxation procedure presented above. Since the functional is strictly convex, the minimization procedure has a unique solution.

Mixed formulation (see Alart and Curnier (1991); Alart and Lebon (1995))

The idea underlying this method is to write the problem as an equilibrium equation,

$$\left\{ \begin{array}{c} Find\ u\ and\ \lambda\ such\ that \\ F^{int}(u) + F^{ext} + \mathcal{F}([u], F) = 0, \\ a(F - \mathcal{F}([u], F)) = 0, \end{array} \right. \tag{14}$$

where a is a given coefficient, F^{ext} are the given external forces, F^{int} are internal forces which depend on the constitutive equation and the kinematics, and $\mathcal{F}([u], \lambda)$ is the friction map. In the case of a node in contact with a rigid obstacle (i.e. $[u] = u$), in elasto-statics, we have (see Alart and Curnier (1991); Alart and Lebon (1995))

$$\mathcal{F}(u, F) = proj_{R_-}(\tau_N)n + proj_{C(proj_{R_-}(\tau_N))}(\tau_T), \tag{15}$$

proj is the projection operator, $C(F_N)$ is the Coulomb's cone and r is a parameter (usually equal to $-r^{-1}$). τ_N et τ_T are given by

$$\tau_N = F_N + ru_N \quad , \quad \tau_T = F_T + ru_T. \tag{16}$$

The non-linear problem is then written

$$\mathcal{D}(x) + \mathcal{U}(x) = 0 \tag{17}$$

where

$$\mathcal{D}(x) = \left[\begin{array}{c} Au + f^{ext} \\ aF \end{array} \right] \ and\ \mathcal{U}(x) = \left[\begin{array}{c} \mathcal{F}(u, F) \\ -a\mathcal{F}(u, F) \end{array} \right]. \tag{18}$$

This system is solved using a Generalized Newton method

$$x^{i+1} = x^i - (\bigtriangledown \mathcal{D}(x^i) + \partial \mathcal{U}(x^i))^{-1}(\mathcal{D}(x^i) + \mathcal{U}(x^i)) \tag{19}$$

$\partial \mathcal{U}(x^i)$ is a point in the Jacobian set of matrices. The linearized system (19) is solved by a solver dedicated to non symmetric systems. The algorithm can be summed up as follows:

0 Initialization $x^0 = (u^0, \lambda^0)$ be given
1 Resolution (Non-symmetric linear system)
$y^{i+1} = (\bigtriangledown \mathcal{D}(x^i) + \partial \mathcal{U}(x^i))^{-1}(\mathcal{D}(x^i) + \mathcal{U}(x^i))$
2 Updating $x^{i+1} = x^i - y^{i+1}$
3 Convergence Test Yes = End; No = Go to Step 1

Concluding comment The numerical problem can be solved using the open computer code LMGC90 (http://www.lmgc.univ-montp2.fr/~dubois-/LMGC90/). This code is a numerical platform dedicated to the modeling and simulation of dynamic multibody problems. Problems are approached in the general framework of dynamics (see Moreau (1988); Jean (1999)). The discretized equations involved in the problem are written:

$$\begin{array}{rcl} M\ddot{q} & = & F(q,\dot{q}) \; + \; P(t) \; + \; r, \\ & + & \text{interface conditions} \\ & + & \text{initial conditions and boundary conditions} \end{array} \tag{20}$$

where q is a parametrization of the system (degrees of freedom), M is the mass matrix, $F(q,\dot{q}) + P(t)$ are the internal and external loading vectors, and r is the vector of contact forces.
The problem of the 105 blocks presented in the previous section can be solved using this technique. The results are presented in figure 10. These results were obtained by J. J. Moreau (Jean and Moreau (1994)). The correspondence observed seems to be perfect.

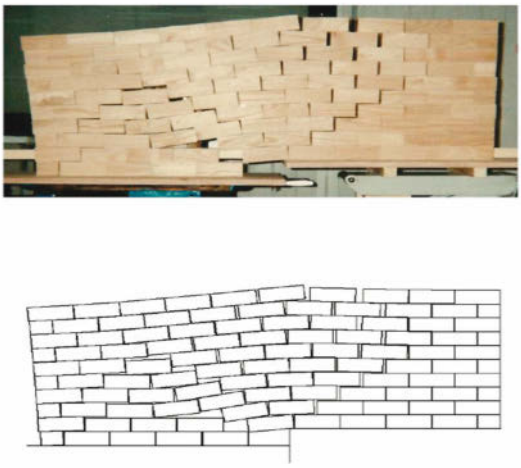

Figure 10. Comparison between experimental and numerical findings on the example of 105 blocks (Jean and Moreau (1994))

4 Masonry blocks with mortar

4.1 A phenomenological model taking the adhesion into account (model 2)

In this section, the RCCM model is presented (Raous et al. (1999); Monerie and Raous (2000)). This adhesion model was used to model mortar/brick interfaces in Fouchal et al. (2009). In this model, the unilateral contact conditions (non penetration between the mortar and the brick, as in the previous section) are combined with dry friction and adhesion between bricks and mortar. The local constitutive equations required for this model are deduced from thermodynamic considerations and based on a material surface hypothesis on the contact zone. The basic idea underlying this model is to introduce a new state variable describing the contact state. This adhesion intensity variable, denoted b, was initially introduced by Frémond (1987). This variable gives the relative proportion of the active links between two bodies in contact. This variable is chosen so that:

- $b = 1$, total adhesion
- $0 < b < 1$, partial adhesion
- $b = 0$, no adhesion

As in the previous section, we are working in the framework of the contact between two deformable solids, and the same notations are adopted here. w is taken to denote the Dupré energy, and C_N (resp. C_T) to denote the initial normal (resp. tangential) stiffness of the interface. In what follows, p, q and r are three given numbers. The constitutive equations of the interface are given by the following equations, based on state laws and complementarity laws:

Unilateral contact with adhesion

$$R_N - C_N[u_N]b^p \geq 0; \quad [u_N] \geq 0; \quad (R_N - C_N[u_N]b^p)[u_N] = 0 \tag{21}$$

Friction with adhesion

$$\begin{array}{rcll} ||R_T - C_T[u_T]b^q|| & \leq & \mu|R_N - C_N[u_N]b^p| & \\ ||R_T - C_T[u_T]b^q|| & < & \mu|R_N - C_N[u_N]b^p| & \Rightarrow \quad [\dot{u_T}] = 0 \\ ||R_T - C_T[u_T]b^q|| & = & \mu|R_N - C_N[u_N]b^p| & \Rightarrow \quad \exists\lambda \geq 0, \\ & & & [\dot{u_T}] = \lambda(R_T - C_T[u_T]b^q) \end{array} \tag{22}$$

Evolution of the intensity of adhesion

$$0 \quad = \quad -(w - (\tfrac{1}{2}C_N[u_T]^2 + \tfrac{1}{2}C_T|[u_T]|^2)b^r)^- \quad if \quad b \in [0,1[\tag{23}$$

Note that if there is no adhesion ($b = 0$), this model involves the classical Signorini-Coulomb problem.

A graphic interpretation of the normal part of this RCCM model given in figure 11 (for $(p, q, r) = (2, 2, 1)$) shows the changes with time in the normal forces depending on the normal displacement jump. The changes in b lead to irreversible effects. If b decreases, the adhesive forces will decrease and eventually disappear. In the case of pure traction ($[u_N] > 0$), the adhesion resistance ($R_N = C_N[u_N]^p$) is activated (elasticity without damage). b decreases when the displacement becomes sufficiently large for the elastic energy to become larger than the adhesion limit w.

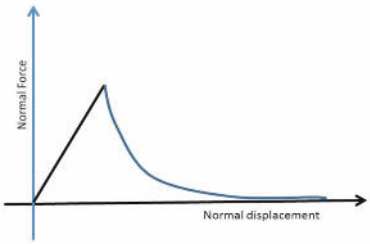

Figure 11. Normalized normal forces versus the normalized normal jump in the displacement

A numerical example (see Fouchal et al. (2009))

Problems are usually approached using θ-methods and the Non-Smooth Contact Dynamics (NSCD) method (Moreau (1988); Jean (1999)). Due to the contact conditions, a fairly small time-step is chosen and the problem is condensed in the local frame associated with the contact nodes. The local problem is solved using a non-linear Gauss-Seidel method.

The interface is governed by the RCCM law presented above. Contact between bodies is defined by contact nodes. Contact nodes are located between two nodes in the mesh of an element in contact at distances of 0.2 and 0.8, respectively, along each of the segments in contact.

The bodies (bricks and mortar) are modeled using $Q4$ quadrangular finite elements. The numerical tests are performed with a constant time step equal to $\Delta t = 0.5 * 10^{-3}$ s. The computations require 2000 increments in

order to reach values resembling the experimental data, and θ (in the time integration method) is fixed and taken to be equal to 0.55.
The example presented shows the evolution of a triplet of full bricks and comparisons are made in figures 12 and 13 between two experiments and the numerical results.

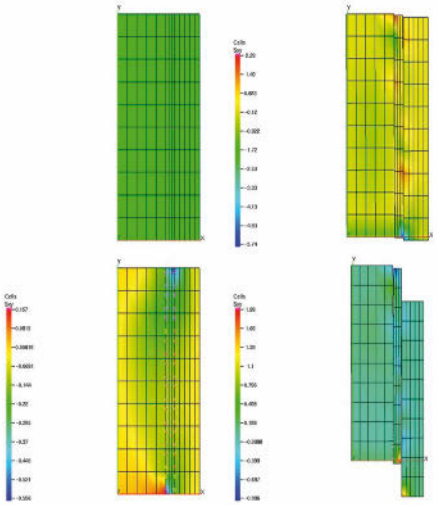

Figure 12. Damage evolution in a triplet of full-bricks

4.2 Deductive models: linear (and non linear) multi-scale models

Generalities on asymptotic methods There exist a large class of asymptotic methods, such as matched asymptotic expansions (Eckhaus (1979); Sanchez-Hubert and Sanchez-Palencia (1992)). The general idea is to dilate (blow up) the interphase from the thickness η to 1 (see Figure 14). We have two expansions of the displacement u^η, the strain $e(u^\eta)$ and the stress σ^η in the powers of η, that is, an external one in the adherents and an internal in the joint. We have to connect these two expansions along the interface. In what follows, we study a problem in 2 dimensions in order to simplify the computations. The relations obtained in the internal expansions will be expressed using values that intervene in the external expansions.

a) External expansions The external expansion is a classical expansion

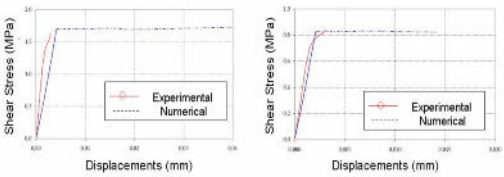

Figure 13. Comparison between experimental and numerical results obtained on full brick triplets

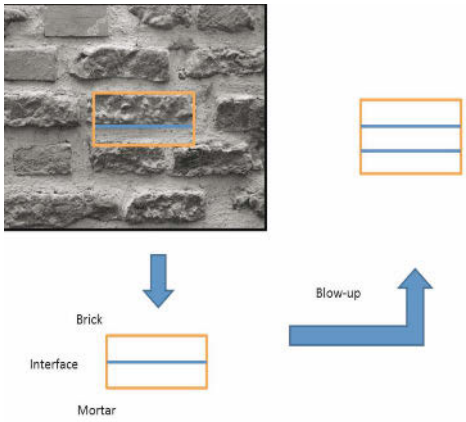

Figure 14. Blow-up process

in powers of η

$$\begin{array}{rcl} u^\eta(x_1,x_2) & = & u^0(x_1,x_2)+\eta u^1(x_1,x_2)+..., \\ e_{ij}(u^\eta)(x_1,x_2) & = & e^0_{ij}+\eta e^1_{ij}+..., \\ e^l_{ij} & = & \frac{1}{2}(\frac{\partial u^l_i}{\partial x_j}+\frac{\partial u^l_j}{\partial x_i}), \\ \sigma^\eta_{ij}(x_1,x_2) & = & \sigma^0_{ij}(x_1,x_2)+e\sigma^1_{ij}(x_1,x_2)+... \end{array} \tag{24}$$

b) Internal expansions In the internal expansion, we perform a blow-up of the second variable. Let $y_2=\frac{x_2}{e}$. The internal expansion gives

$$\begin{array}{rcl} u^\eta(x_1,x_2) & = & v^0(x_1,y_2)+\eta v^1(x_1,y_2)+..., \\ \varepsilon_{ij}(u^\eta)(x_1,y_2) & = & \eta^{-1}e^{-1}_{ij}+e^0_{ij}+e\varepsilon^1_{ij}+..., \\ e^l_{11} & = & \frac{\partial v^l_1}{\partial x_1}, \\ e^l_{22} & = & \frac{\partial v^{l+1}_2}{\partial y_2}, \\ e^l_{12} & = & \frac{1}{2}(\frac{\partial v^l_2}{\partial x_1}+\frac{\partial v^{l+1}_1}{\partial y_2}), \\ \sigma^\eta_{ij}(x_1,y_2) & = & \eta^{-1}\tau^{-1}_{ij}(x_1,y_2)+\tau^0_{ij}(x_1,y_2)+\eta\tau^1_{ij}(x_1,y_2)+..., \\ \sigma^\eta_{ij,j} & = & \sum_{l=-2}^{\infty}\eta^l(\frac{\partial\tau^l_{i1}}{\partial x_1}+\frac{\partial\tau^{l+1}_{i2}}{\partial y_2}). \end{array} \tag{25}$$

We use the convention

$$v^l=0, l<0, \tau^l=0, l<-1. \tag{26}$$

c) Continuity conditions The third step in the method consists in the connecting of the two expansions. If the interface between the mortar and the brick is perfect, we have continuity of the displacement and of the stress tensor along this interface. This gives:

$$\begin{array}{rcl} (i)\ v^0(x_1,\pm 1/2) & = & u^0(x_1,\pm 1/2), \\ (ii)\ \tau^{-1}(x_1,\pm\pm 1/2) & = & 0, \\ (ii)\ \tau^0(x_1,\pm 1/2).e_2 & = & \sigma^0(x_1,\pm 1/2).e_2. \end{array} \tag{27}$$

A linear multi-scale model (model 3) The equilibrium equation becomes:

$$(\eta^{-1}\tau^{-1}_{ij}+\tau^0_{ij}+\eta\tau^1_{ij}+...)_{,j} = 0 \tag{28}$$

We obtain

$$\begin{array}{rcl} \tau^{-1}_{ij} & = & 0 \\ \tau^0_{i2,2} & = & 0 \end{array} \tag{29}$$

that is

$$\left[\tau_{i2}^{0}.e_2\right] = 0 \tag{30}$$

The interphase is assumed to be linearly elastic, and the above theory is applied to this kind of material. We have

$$\eta^{-1}\tau_{ij}^{-1} + \tau_{ij}^{0} + \eta\tau_{ij}^{1} + ... = C_{ijkl}\left(\eta^{-1}e_{kl}^{-1} + e_{kl}^{0} + \eta e_{kl}^{1} + \right) \tag{31}$$

where C denotes the stiffness tensor.

We obtain:

$$\begin{array}{rcl} \tau_{12}^{0} & = & C_{1212}v_{1,2}^{0} \\ \tau_{22}^{0} & = & C_{2222}v_{2,2}^{0} \end{array} \tag{32}$$

that is

$$\begin{array}{rcl} \tau_{12}^{0} & = & C_{1212}\left[v_1^0\right] \\ \tau_{22}^{0} & = & C_{2222}\left[v_2^0\right] \end{array} \tag{33}$$

Using the continuity conditions, we obtain

$$\begin{array}{rcl} \sigma_{ij}^{0} & = & 0 \text{ in the brick and the mortar} \\ \sigma^{0}.e_2 & = & \widehat{C}\left[u^0\right] \text{ along the interface} \end{array} \tag{34}$$

where $\widehat{C}$ is a matrix consisting of C_{1212} and C_{2222}. Note that this technique was used in Rekik and Lebon (2010) and Rekik and Lebon (2012).

An example of a non linear multi-scale model including micro-cracks (model 4) (see Pelissou and Lebon (2009))

General considerations and notations

The model described in this section is an extension of the bulk model introduced in Gambarotta and Lagomarsino (1997), which takes the damage to the mortar joint into account. The interface modeling procedure (figure 15) consists of three steps:

- Let us take a macroscopic bulk model for quasi-fragile materials;
- The structure is assumed to consist of three phases: material 1 (brick, for example), material 2 (mortar, for example) and a thin interphase between the two materials, consisting of the material described in the first step;
- Since the interphase is thin, an interface model is developed by performing an asymptotic analysis, as described above (Geymonat and Krasucki (1997); Lebon and Ronel-Idrissi (2004)) (the thickness of the interface tends to zero).

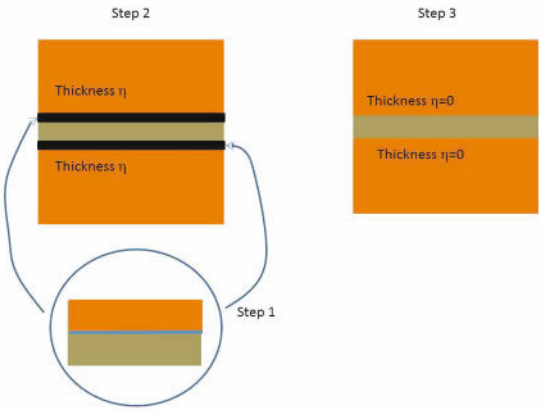

Figure 15. Interface modeling in three steps

The model obtained memorizes some of the geometrical and mechanical characteristics of the interphase, such as the thickness, elastic coefficients, normal and tangential stress, damage variable, etc.

For the sake of simplicity, the structure is taken to occupy an open bounded set Ω of $\Re^2$ with a smooth boundary $\partial\Omega$. The two dimensional space is referred to the orthonormal frame (O, x_1, x_2).

First step: The bulk model

In this section, the bulk model introduced by Gambarotta and Lagomarsino (1997) is briefly described. In this model dedicated to masonry structures, the masonry is regarded as a "material" showing nonlinear damage behavior. The macroscopic behavior is accounted for by applying averaging process based on microscopic considerations. In the line with the classical procedure, the strain tensor is decomposed in its linear and nonlinear (anelastic) parts:

$$e = e^{el} + e^{an} \tag{35}$$

where

$$\sigma = Ce^{el} \text{ and } e^{an} = S_\sigma \sigma \tag{36}$$

At the local level (in an elementary volume, see figure 16), the stress vector is decomposed into its normal σ_N and tangential σ_T parts, and the normal and tangential components of $\boldsymbol{e^{an}}$ are expressed by (37) :

$$\begin{cases} e_N^{an} = h\alpha H(\sigma_N)\sigma_N \\ e_T^{an} = k\alpha(\sigma_T - f) \end{cases} \tag{37}$$

where $f = \sigma_T$ if $\sigma_T \in I =]-\mu\sigma_N\ ,\ +\mu\sigma_N[$and $f = \pm\mu\sigma_N$ if $\sigma_T \notin I$ (figure 17), H is the Heaviside function of the unilateral response of the joint and α is the damage variable. h and k are positive coefficients standing for the opening and sliding compliances of the mortar joint and μ is the internal friction coefficient.

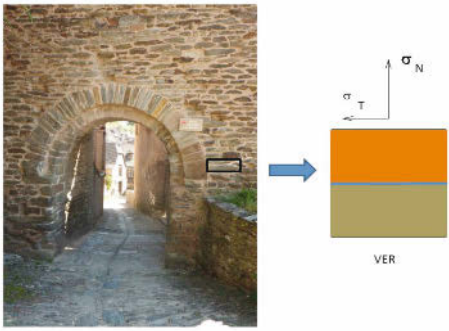

Figure 16. Normal and tangential stress vector components

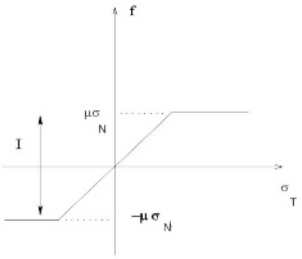

Figure 17. Relation between f and σ_T (friction threshold)

We can write

$$e_t^{an} = k\alpha\chi_I(\sigma_T)(\sigma_T \pm \mu\sigma_N) \tag{38}$$

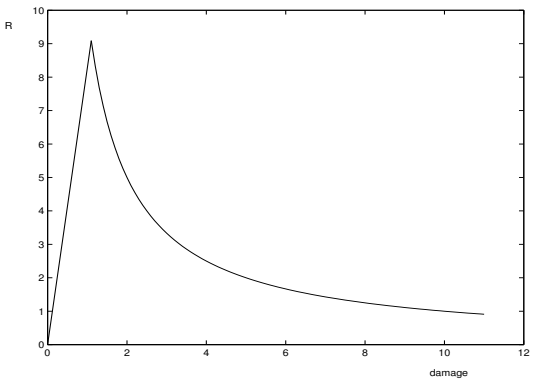

Figure 18. Evolution of $R(\alpha)$

where χ_I is the characteristic function of the tangential damage undergone by the set I, such that:

- If $\sigma_T \in I$, $\chi_I(\tau) = 1$, there is tangential damage.
- If $\sigma_T \notin I$, $\chi_I(\sigma_T) = 0$, there is no tangential damage.

Therefore S_σ is given locally in matrix form by:

$$S_\sigma = \begin{pmatrix} h\alpha\, H(\sigma_N) & 0 \\ \pm\, k\alpha\, \chi_I(\sigma_T)\, \mu & k\alpha\, \chi_I(\sigma_T) \end{pmatrix} \tag{39}$$

The damage is governed by a yield condition $\Phi(\alpha) \leq 0$, where

$$\begin{aligned} \Phi(\alpha) &= Y - R(\alpha) \\ Y &= \frac{1}{2} h H(\sigma_N) \sigma_N^2 + \frac{1}{2} k \chi_I(\sigma_T) \sigma_T^2 \end{aligned} \tag{40}$$

where R is the toughness of the material defined by (see figure 18)

$$\begin{aligned} R(\alpha) &= R_0 \alpha, \ \text{ if } 0 \leq \alpha \leq 1 \\ R(\alpha) &= R_0/\alpha, \ \text{ if } \alpha \geq 1 \end{aligned} \tag{41}$$

Second step: The interphase

In this section, the structure is taken to consist of two materials separated by a thin interphase which is a "mixture" of the other two materials. The interphase is assumed to be parallel to the x_1-axis and the thickness, which is constant, is denoted by η. In what follows, the constitutive equations are those given in the previous section, i.e., the interface consists of a

quasi-brittle material. The elastic part is assumed to be isotropic, and in view of the external normal vector x_2, the constitutive equation is

$$\sigma = \Big(Id + CS_\sigma\Big)^{-1} Ce = C_\sigma \varepsilon \tag{42}$$

Upon introducing the Lamé's coefficients, λ and G, we can write:

$$C_\sigma = \begin{pmatrix} \lambda + 2G - \frac{\lambda^2 h\alpha H}{1+(\lambda+2G)h\alpha H} & \lambda - \frac{\lambda(\lambda+2G)h\alpha H}{1+(\lambda+2G)h\alpha H} & 0 \\ \frac{\lambda}{1+(\lambda+2G)h\alpha H} & \frac{\lambda+2G}{1+(\lambda+2G)h\alpha H} & 0 \\ -\frac{\pm\mu\lambda Gk\alpha\chi_I}{(1+(\lambda+2G)h\alpha H)(1+Gk\alpha\chi_I)} & -\frac{\pm\mu(\lambda+2G)Gk\alpha\chi_I}{(1+(\lambda+2G)h\alpha H)(1+Gk\alpha\chi_I)} & \frac{G}{1+Gk\alpha\chi_I} \end{pmatrix} \tag{43}$$

Interface behavior

Using this asymptotical approach (see the previous section or Lebon and Ronel-Idrissi (2004) in another context), and substituting the asymptotic expansions into the constitutive equations and the equilibrium equations, we obtain expressions linking the stress vector to the jump in the displacement denoted $[u]$. This gives:

$$\begin{aligned} \tau_{22}^0 &= \lim_{e\to 0} \frac{\lambda+2G}{1+(\lambda+2G)h\alpha H} \frac{\partial v_2^0}{\partial y_2} \\ \tau_{12}^0 &= \lim_{e\to 0} \frac{\pm\mu(\lambda+2G)Gk\alpha\chi_I}{(1+(\lambda+2G)h\alpha H)(1+Gk\alpha\chi_I)} \frac{\partial v_2^0}{\partial y_2} + \lim_{e\to 0} \frac{G}{1+Gk\alpha\chi_I} \frac{\partial v_1^0}{\partial y_2} \end{aligned} \tag{44}$$

By integration, the A-GL (Asymptotic Gambarotta-Lagomarsino) model is therefore given by the following system (in the terms of the normal and tangential components):

$$\begin{cases} \sigma_N = \dfrac{C_N}{1 + C_N \bar{h}\alpha H(\sigma_N)} [u_N] \\ \sigma_T = \dfrac{\pm C_N C_T \mu \bar{k}\alpha \chi_I}{(1 + C_N \bar{h}\alpha H(\sigma_N))(1 + C_T \bar{k}\alpha\chi_I)} [u_N] + \dfrac{C_T}{1 + C_T \bar{k}\alpha \chi_I} [u_T] \end{cases} \tag{45}$$

where

$$\begin{aligned} C_N &= (\lambda + 2G)/e \\ C_T &= G/e \\ \bar{h} &= he \\ \bar{k} &= ke \end{aligned} \tag{46}$$

The resulting matrix is not diagonal, contrary to the classical case: a non symmetric coupling term occurs between the normal compliance term C_N and the tangential compliance term C_T. It can be noted that the configuration of traction when $f = 0$ is combined in this general expression with

that of the compression when $f = \sigma_T$ and when the friction threshold is reached at $f = \pm\mu\,\sigma_N$.

The damage is governed by a yield condition $\bar{\Phi}(\alpha) = \bar{Y} - \bar{R}(\alpha) \leq 0$, where

$$\left\{\begin{array}{l} \bar{Y} = \dfrac{1}{2}\,\bar{h}\,H(\sigma_N)\,\sigma_N^2 \;+\; \dfrac{1}{2}\,\bar{k}\,\chi_I(\sigma_T)\,(\sigma_T - \pm\mu\sigma_N)^2 \\ \bar{R}\,(\alpha) = \lim\limits_{e\to 0}\; R\,e = \left\{\begin{array}{ll} \bar{R}_0\,\alpha & \text{if } 0 < \alpha < 1 \\ \dfrac{\bar{R}_0}{\alpha} & \text{if } \alpha > 1 \end{array}\right. \end{array}\right. \tag{47}$$

A numerical example: shear test on a simple brick Let us perform an academic shear test on a single rectangular piece. The piece is bonded at the bottom and subjected to horizontal forces on the left. Details of this test are presented in figure 19. This horizontal force which is equal to 20 kN, is applied progressively. The load is applied on the right and left sides. The (academic) coefficients are $C_N = C_T = 500\ kNcm^{-3}$, $\mu = 0.3$, $\bar{h} = \bar{k} = 0.04kN^{-1}cm^3, \bar{R}_0 = 10kNcm^{-1}$.

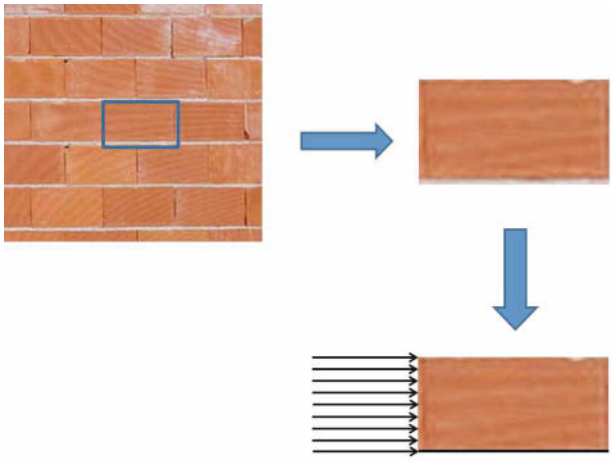

Figure 19. Shear test

Due to the geometry and the loading conditions, the behavior of the contact zone is very complex. Figure 20 shows the evolution of the damage along the contact zone, which is strongly non linear. In particular,

the damage increases strongly in an intermediate zone, which is subjected to both shear and traction forces. Note that the tangential displacement shows a linear pattern of evolution in the first phase and a non linear pattern corresponding to the failure, in the second phase, as was to be expected.

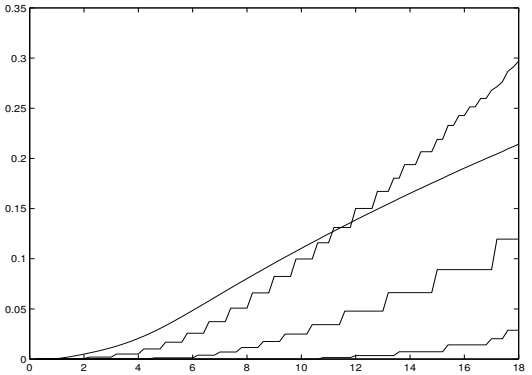

Figure 20. Damage evolution for four typical elements (shear test).

5 Conclusion

In this chapter, four of the many existing interface models are presented. It is quite difficult to solve large problems using this approach. In Rekik and Lebon (2010, 2012), we established that it can be possible to solve larger problems (small walls), however. It will obviously be necessary in future studies to review all the existing models (a simple look at Science Direct^{TM} with the keywords "masonry" and "interface" gives more than 2500 papers), in order to choose the most suitable one and use efficient solvers (DDM, MG, etc.) before it will be possible to solve real physical problems.

Bibliography

P. Alart and A. Curnier. A mixed formulation for frictional contact problems prone to Newton like solution methods. *Computer Methods in Applied Mechanics and Engineering*, 92:353–375, 1991.

P. Alart and F. Lebon. Solution of frictional contact problems using ILU and coarse/fine preconditioners. *Computational Mechanics*, 16:98–105, 1995.

E. Bonetti and M. Frémond. Analytical results on a model for damaging in domains and interfaces. *ESAIM-Control Optimisation and calculus of Variations*, 17:955–974, 2011.

P. Chabrand, F. Dubois, and M. Raous. Various numerical methods for solving unilateral contact problems with friction. *Mathematical Computer and Modeling*, 28(4-8):97–108, 1998.

M. Cocu. Existence of solutions of Signorini problems with friction. *International Journal of Engineering Science*, 22:567–575, 1984.

M. Cocu, E. Pratt, and M. Raous. Formulation and approximation of quasistatic frictional contact. *Comptes Rendus Académie des Sciences, Paris, Série I*, 320:1413–1420, 1995.

M. Como. *Statica delle costruzioni storiche in muratura*. Aracne, 2010.

G. Duvaut and J. L Lions. *Inequalities in mechanics and physics*. Springer Verlag, 1976.

W. Eckhaus. *Asymptotic analysis of singular perturbations*. North-Holland, 1979.

J. Fortin, M. Hjiaj, and G. De Saxcé. An improved discrete element method based on a variational formulation of the frictional contact law. *Computers and Geotechnics*, 29:609–640, 2002.

F. Fouchal. *Contribution à la modélisation numérique des interfaces dans les structures maçonnées*. PhD thesis, Université de Reims Champagne Ardennes, 2006.

F. Fouchal, F. Lebon, and I. Titeux. Contribution to the modeling of interfaces in masonry construction. *Construction and Building Materials*, 23:2428–2441, 2009.

F. Freddi and M. Frémond. Damage in domains and interfaces: A coupled predictive theory. *Journal of Mechanics of Materials and Structures*, 1: 1205–1233, 2006.

M. Frémond. Adhesion of solids. *Journal de Mécanique Théorique et Appliquée*, 6:383–407, 1987.

A. Gabor. *Contribution à la caractérisation et à la modélisation des maçonneries non renforcées et renforcées par materiaux composites*. PhD thesis, Université Claude-Bernard Lyon I, 2002.

A. Gabor, A. Bennani, E. Jacquelin, and F. Lebon. Modelling approaches of the in-plane shear behaviour of unreinforced and frp strengthened masonry panels. *Composites Structures*, 74:277–288, 2006.

L. Gambarotta and S. Lagomarsino. Damage models for the seismic response of brick masonry walls. part i : The continuum model and its application. *Earthquake Engineering and Structural Dynamics*, 26:441–462, 1997.

G. Geymonat and F. Krasucki. Analyse asymptotique du comportement en flexion de deux plaques collées. *Compte Rendu Académie des Sciences Série I*, 325:307–314, 1997.

P. Hild. An example of nonuniqueness for the continuous static unilateral contact model with coulomb friction. *Comptes Rendus Académie des Sciences, Paris, Série I*, 337:685–688, 2003.

M. Jean. The non-smooth contact dynamics method. *Computer Methods in Applied Mechanics and Engineering*, 177:235–257, 1999.

M. Jean and J. J. Moreau. Monuments under seismic action. Technical report, Commission of the European Communities, November 1994. Environment Programme, Contract n° EV5V CT93 0300.

A. Klarbring. Derivation of the adhesively bonded joints by the asymptotic expansion method. *International Journal of Engineering Science*, 29: 493–512, 1991.

F. Lebon. Two-grid method for regularized frictional elastostatics problems. *Engineering Computations*, 12:657–664, 1995.

F. Lebon. Contact problems with friction: Models and simulations. *Simulation, Modelling, Practice and Theory*, 11:449–464, 2003.

F. Lebon and M. Raous. Friction modelling of a bolted junction under internal pressure loading. *Computers and Structures*, 43:925–933, 1992.

F. Lebon and R. Rizzoni. Asymptotic study of soft thin layer: the non convex case. *Mechanics of Advanced Materials and Structures*, 15:12–20, 2008.

F. Lebon and S. Ronel. First order numerical analysis of linear thin layers. *ASME Journal of Applied Mechanics*, 74:824–828, 2007.

F. Lebon and S. Ronel-Idrissi. Asymptotical analysis of Mohr-Coulomb and Drucker-Prager soft thin layers. *Steel and Composite Structures*, 4: 133–147, 2004.

F. Lebon, A. Ould-Khaoua, and C. Licht. Numerical study of soft adhesively bonded joints in finite elasticity. *Computational Mechanics*, 21:134–140, 1997.

F. Lebon, R. Rizzoni, and S. Ronel. Analysis of non-linear soft thin interfaces. *Computers and Structures*, 82:1929–1938, 2004.

C. Licht and G. Michaille. A modeling of elastic adhesive bonded joints. *Advances in Mathematical Sciences and Applications*, 7:711–740, 1997.

M. Lucchesi, C. Padovani, G. Pasquinelli, and N. Zani. *Masonry constructions: mechanical models and numerical applications*. Springer, 2008.

Y. Monerie and M. Raous. A model coupling adhesion to friction for the intercation between a crack and a fiber/matrix interface. *ZAMM*, 80: 205–209, 2000.

J. J. Moreau. *Unilateral contact and dry friction in finite freedom dynamics*, volume 302 of *CISM - Courses and Lectures*, pages 1–82. Springer, 1988.

C. Pelissou and F. Lebon. Asymptotic modeling of quasi-brittle interfaces. *Computers and Structures*, 87:1216–1223, 2009.

N. Point and E. Sacco. A delamination model for laminated composite. *International Journal of Solids and Structures*, 33:483–509, 1996.

M. Raous. Interface models coupling adhesion and friction. *Comptes Rendus Mécanique*, 339:491–501, 2011.

M. Raous, P. Chabrand, and F. Lebon. Numerical methods for solving unilateral contact problem with friction. *Journal of Theoretical and Applied Mechanics*, 7:111–128, 1988.

M. Raous, L. Cangémi, and M. Cocou. A consistent model coupling adhesion, friction and unilateral contact. *Compututer Methods in Applied Mechanics and Engineering*, 177:383–399, 1999.

A. Rekik and F. Lebon. Identification of the representative crack length evolution in a multi-level interface model for quasi-brittle masonry. *International Journal of Solids and Structures*, 47:3011–3021, 2010.

A. Rekik and F. Lebon. Homogenization methods for interface modeling in damaged masonry. *Advances in Engineering Software*, 46:35–42, 2012.

J. Sanchez-Hubert and E. Sanchez-Palencia. *Introduction aux méthodes asymptotiques et à l'homogénisation.* Masson, 1992.

P. Wriggers. *Computational Contact Mechanics.* Springer, 2006.

Micro, Multiscale and Macro Models for Masonry Structures

Elio Sacco
Dipartimento di Ingegneria Civile e Meccanica
Università di Cassino e del Lazio Meridionale

1 Introduction

The development of adequate stress analyses for masonry structures represents an important task not only for verifying the stability of masonry constructions, as old buildings, historical town and monumental structures, but also to properly design effective strengthening and repairing interventions. The analysis of masonry structures is not simple at least for two reasons: the masonry material presents a strong nonlinear behavior, so that linear elastic analyses generally cannot be considered as adequate; the structural schemes, which can be adopted for the masonry structural analyses, are more complex than the ones adopted for concrete or steel framed structures, as masonry elements require often to be modeled by two- or three-dimensional elements. As a consequence, the behavior and the analysis of masonry structures still represents one of the most important research field in civil engineering, receiving great attention from the scientific and professional community.

Several numerical techniques have been developed to investigate and to predict the behavior of masonry structures. In fact, in the last decades, the scientific community has demonstrated great interest in the development of sophisticated numerical tools as an opposition to the tradition of rules-of-thumb or empirical and geometrical formulas adopted to evaluate the safety of masonry buildings. In particular, nonlinear models implemented in suitable finite elements formulations currently represent the most common advanced strategy to simulate the structural behavior of masonry structures. The main problem in the development of accurate stress analyses for masonry structures is the definition and the use of suitable material constitutive laws.

M. Angelillo (Ed.), *Mechanics of Masonry Structures*, CISM International Centre for Mechanical Sciences, DOI 10.1007/ 978-3-7091-1774-3_6,

Taking into account the heterogeneity of the masonry material, which results from the composition of blocks connected together by mortar joints, several modeling approaches have been proposed in literature.

Micro-models consider the units and the mortar joints separately, characterized by different constitutive laws; thus, the structural analysis is performed considering each constituent of the masonry material. The mechanical properties that characterize the models adopted for units and mortar joints, are obtained through experimental tests conducted on the single material components (compressive test, tensile test, bending test, etc.). This approach leads to structural analyses characterized by great computational effort; in fact, in a finite element formulation framework, both the unit blocks and the mortar beds have to be discretized, obtaining a problem with a high number of nodal unknowns.

Micro-macro, i.e. multiscale, models consider different constitutive laws for the units and the mortar joints; then, a homogenization procedure is performed obtaining a macro-model for masonry which is used to develop the structural analysis. Also in this case, the mechanical properties of units and mortar joints are obtained through experimental tests. The micro-macro models appear very appealing, as they allow to derive in a rational way the stress-strain relationship of the masonry, accounting in a suitable manner for the mechanical properties of each material component. Moreover, this approach can lead to effective models.

Macro-models, or macroscopic models, are based on the use of phenomenological constitutive laws for the masonry material; i.e. the stress-strain relationships adopted for the structural analysis are derived performing tests on masonry, without distinguishing the blocks and the mortar behavior. A macroscopic model could be unable to describe in a detailed manner some micromechanisms occurring in the damage evolution of masonry, but it is very effective from a computational point of view when structural analyses are performed.

In the following, the micromechanical, the multiscale and the macromechanical approaches are presented, giving some details for specific models proposed in the last years. In particular, the discussion is limited to three models (micro, micro-macro and macro) framed in the 2D small strain and displacement approach.

2 Micromechanical modeling

The micromechanical analysis of masonry elements is performed considering different constitutive laws for the bricks and for the mortar. Moreover, the adhesion between the mortar and the brick can play a fundamental role

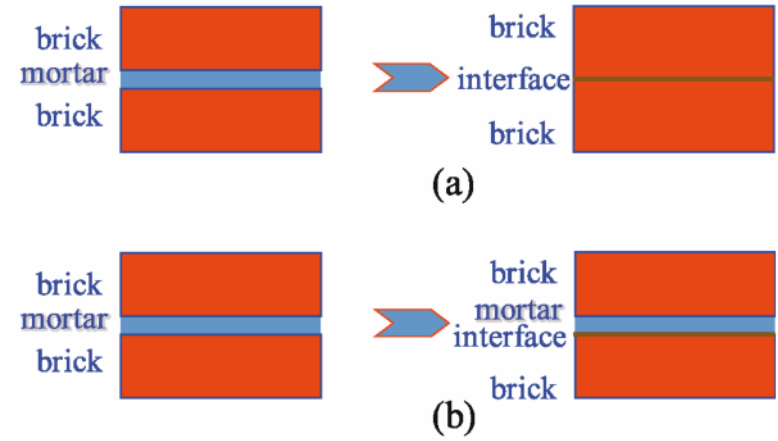

Figure 1. (a) the interface models the mortar and the adhesion mortar-brick; (b) the interface models only the adhesion mortar-brick.

in the overall response of the masonry texture. Thus, the modeling of the response of the mortar-brick interface can be necessary in order to reproduce the possible decohesion of the mortar from the brick.

In the micromechanical modeling of the masonry, at least two possible approaches can be distinguished, schematically illustrated in figure 1:

- the mortar and the adhesion surfaces between the mortar and the brick are modeled as a unique interface, characterized by a mechanical response which accounts for the behavior of the mortar and of the mortar-brick adhesion; in this case, as the interface has zero thickness, the units are expanded in both the directions by the mortar thickness (37);
- the mortar is modeled as a continuum material, eventually characterized by nonlinear response, and the adhesion surface between the mortar and the brick is modeled by a specific interface (59).

In both cases, the interface models are characterized by constitutive laws relating the stress acting at the interface with the displacement discontinuity. Several interface models have been presented in literature; in particular some of them have been developed to reproduce the gradual process of crack opening, in which the incipient separation of the two edges of the crack is constrained by cohesive stresses due to interaction and friction between aggregate or bridging phenomena. It is the salient feature of the quasi-brittle materials like clay brick, mortar, ceramics, rock or concrete, which

fail because of a process of progressive internal crack growth. The idea of developing a cohesive model interface was introduced by Dugdale (20) and Barenblatt (7), who proposed several distributions of the cohesive stresses.

In order to model the behavior of masonry mortar joints, Lofti and Shing (36) proposed a dilatant interface constitutive model capable of simulating the initiation and the propagation of interface fracture under combined normal and shear stress in both tension-shear and compression-shear regions. Giambanco and Di Gati (29) formulated a simple cohesive interface model adopting a yield surface expressed by the classical bi-linear Coulomb condition with a tension cut-off and with a non-associated flow law. Gambarotta and Lagomarsino (27) postulated the constitutive equation of interface model in term of two internal variables representing the frictional sliding and the damage occurring in the mortar joint because of cyclic load. Lourenço and Rots (38) and, then, Oliveira and Lourenço (51) implemented a constitutive interface model, based on an incremental formulation of plasticity theory, able to simulate the cyclic behavior of the cohesive zone by reproducing the nonlinear response during unloading. Giambanco and Mroz (31) proposed a model of interface for which the contact stresses and strains interact with the internal stresses or strains within the joint, separated by two interfaces from the adjacent material. Alfano and Sacco (5) and Alfano et al. (4) introduced a new method to combine interface damage and friction in a cohesive-zone model on the basis of a simplified micromechanical formulation. They showed the effectiveness of the proposed model to predict the failure mechanisms and the response of a masonry structure. In particular, the experimental behavior of a masonry wall subjected to a compression and shear load was reproduced (5). The developed interface model was able to simulate the progressive damage and failure of the mortar layers as well as the possible fracture initiation and propagation within the bricks. Then, this model has been properly modified by Sacco and Toti (59) and applied to describe the brick-mortar interface response. The interface model was utilized by Fouchal et al. (25) to simulate the experimental behavior of the mortar-brick adhesion zones of the masonry structures, remarking that the decohesion between the constituents of masonry is the main responsible of its nonlinear response. Numerical analyses of the masonry unit cell and of a simple masonry structure have been recently developed by Giambanco et al. (30), making use of a new interphase model implemented in a finite element framework. An innovative deductive approach based on a micromechanical analysis and on a homogenization procedure has been proposed recently by Sacco and Lebon (58). A homogenization technique has been presented and applied to derive the interface model considering the brick–mortar interaction.

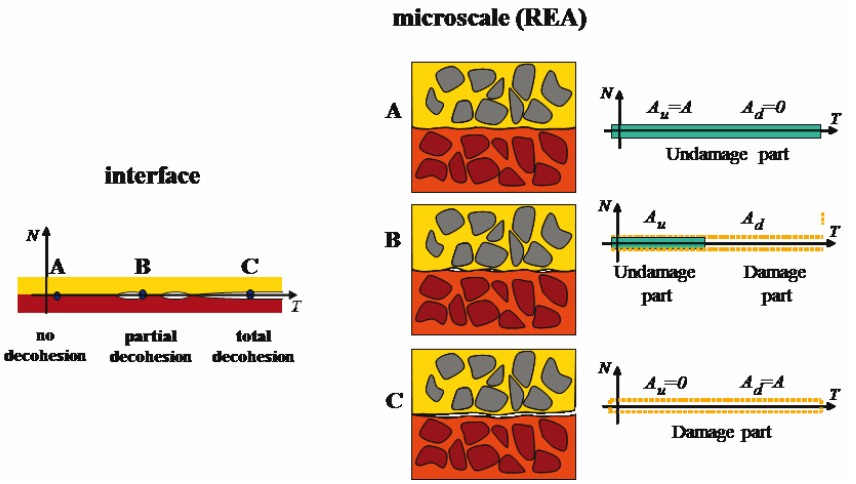

Figure 2. Micromechanical scheme of the interface.

In the following the model proposed in (5) and (4) and reviewed in (59) is presented.

2.1 Interface model

The interface cohesive model combining damage and friction is described in this section. The interface model, developed on the basis of mechanical model proposed in (5; 4; 59), adopts a micromechanical approach. With reference to a typical interface zone, as represented in figure 2, a micromechanical analysis of the damaging process is performed. Three different states can be recognized at the interface: point A, the mortar-brick connection is absolutely undamaged; point B, partial decohesion between the two contact surfaces occurred; point C, the decohesion phenomenon is complete.

At each point of the interface a representative element area (REA) is introduced. At the point A, the interface does not present any detachment and the associated REA results undamaged. The REA corresponding to point B contains partial decohesion due to the presence of micro-cracks, so that the representative area can be schematically split in two parts: an undamaged part and a damaged one. In the REA corresponding to point C the coalescence of micro-cracks occurred and a total decohesion is present, so that a macro-crack appears into the representative element which results completely damaged. Summarizing, the total area A of the REA can be

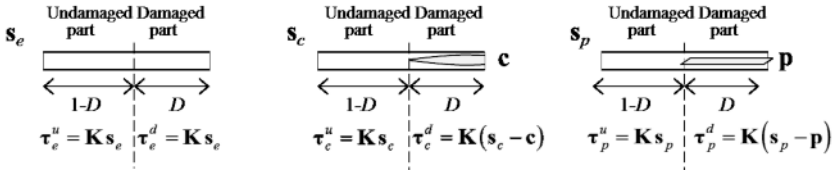

Figure 3. Scheme of the REA at a typical point of the interface.

decomposed into a undamaged part A_u and a completely damaged part A_d, such that $A = A_u + A_d$. Following standard arguments of continuum damage mechanics, the damage parameter D is introduced as ratio between the damaged part and the whole area:

$$D = \frac{A_d}{A} \tag{1}$$

the two parts of the total area A, i.e. A_u and A_d can be recovered as:

$$A_u = (1 - D)A, \qquad A_d = A\,D \tag{2}$$

According to this definition, D can vary in the range $[0, 1]$, where the case $D = 0$ corresponds to the virgin material state and the case $D = 1$ to the total damaged state.

The relative displacement vector at the typical point of the interface is denoted by $\mathbf{s}$. Thus, the vector $\mathbf{s}$ represents in the REA the relative displacement of the two surfaces in contact, as schematically illustrated in figure 2. Denoting with the subscripts $_N$ and $_T$ the components in the normal and tangential direction to the interface, respectively, according to the local coordinate system illustrated in figure 1 and in figure 2, the relative displacement can be written as $\mathbf{s} = \{s_N \; s_T\}^T$.

As schematically illustrated in figure 3, the overall behavior of the REA can be obtained as the superposition of three schemes: the first scheme considers the REA subjected to a relative displacement $\mathbf{s}_e$ of the interface, assuming the crack mouths opening equal to zero; in the second scheme, a relative displacement $\mathbf{c}$, corresponding to a crack opening, is prescribed, which leads to the overall relative displacement $\mathbf{s}_c$ of the interface; in the third scheme, the REA is subjected to a relative displacement $\mathbf{p}$ at the crack mouths, due to the frictional sliding, which induces an overall relative displacement $\mathbf{s}_p$. In such a way, the overall relative displacement is obtained as:

$$\mathbf{s} = \mathbf{s}_e + \mathbf{s}_c + \mathbf{s}_p \tag{3}$$

The overall constitutive response of the REA is determined developing a simplified micro-mechanical analysis. In fact, the behavior of the contact zone is modeled considering the different mechanical responses of the undamaged and damaged parts of the REA, associated to the typical point of the interface.

On both parts of the REA, i.e. on the undamaged part A_u and on the damaged part A_d, the interface stress is supposed to be constant. In particular, on A_u the stress is a linear function of the relative displacement, while on A_d inelastic effects are accounted for:

$$\begin{array}{lll} \boldsymbol{\tau}_e^u = \mathbf{K}\,\mathbf{s}_e & \boldsymbol{\tau}_c^u = \mathbf{K}\,\mathbf{s}_c & \boldsymbol{\tau}_p^u = \mathbf{K}\,\mathbf{s}_p \\ \boldsymbol{\tau}_e^d = \mathbf{K}\,\mathbf{s}_e & \boldsymbol{\tau}_c^d = \mathbf{K}\,(\mathbf{s}_c - \mathbf{c}) & \boldsymbol{\tau}_p^d = \mathbf{K}\,(\mathbf{s}_p - \mathbf{p}) \end{array} \tag{4}$$

where the inelastic displacement vectors $\mathbf{c}$ and $\mathbf{p}$ account for the unilateral nature of the contact and for the friction phenomenon, while $\mathbf{K}$ is the diagonal matrix collecting the stiffness values in the normal and tangential directions to interface:

$$\mathbf{K} = \begin{bmatrix} K_N & 0 \\ 0 & K_T \end{bmatrix} \tag{5}$$

Then, the stress vectors in the undamaged and damaged parts of the REA are obtained as:

$$\begin{array}{rcl} \boldsymbol{\tau}^u & = & \boldsymbol{\tau}_e^u + \boldsymbol{\tau}_c^u + \boldsymbol{\tau}_p^u \\ & = & \mathbf{K}\,\mathbf{s}_e + \mathbf{K}\,\mathbf{s}_c + \mathbf{K}\,\mathbf{s}_p = \mathbf{K}\,\mathbf{s} \\ \boldsymbol{\tau}^d & = & \boldsymbol{\tau}_e^d + \boldsymbol{\tau}_c^d + \boldsymbol{\tau}_p^d \\ & = & \mathbf{K}\,\mathbf{s}_e + \mathbf{K}\,(\mathbf{s}_c - \mathbf{c}) + \mathbf{K}\,(\mathbf{s}_p - \mathbf{p}) = \mathbf{K}\,[\mathbf{s} - (\mathbf{c} + \mathbf{p})] \end{array} \tag{6}$$

respectively. The overall interface stress vector on the REA is denoted by $\boldsymbol{\tau}$ and it is obtained by suitably weighting the two stresses $\boldsymbol{\tau}^u$ and $\boldsymbol{\tau}^d$ given by equations (6):

$$\boldsymbol{\tau} = (1 - D)\,\boldsymbol{\tau}^u + D\boldsymbol{\tau}^d \tag{7}$$

The inelastic relative displacements $\mathbf{c}$, due to the unilateral contact, is defined by the relationship:

$$\mathbf{c} = H\,(s_N) \left\{ \begin{array}{c} s_N \\ 0 \end{array} \right\} \tag{8}$$

where $H\,(s_N)$ denotes the Heaviside function, i.e. $H\,(s_N) = 0$ if $s_N \leq 0$ and $H\,(s_N) = 1$ if $s_N > 0$.

The evolution of the inelastic slip relative displacement $\mathbf{p}$, occurring on the damaged part of the REA, is assumed to be governed by the classical Coulomb yield function:

$$\phi\left(\tau^d\right) = \mu\left\langle \tau_N^d \right\rangle_- + \left|\tau_T^d\right| = \mu\tau_N^d + \left|\tau_T^d\right| \tag{9}$$

where μ is the friction coefficient and $\langle \tau_N^d \rangle_-$ denotes the negative part of the normal stress τ_N^d. The evolution law of $\mathbf{p}$ is governed by the relationships:

$$\dot{\mathbf{p}} = \dot{\lambda} \left\{ \begin{array}{c} 0 \\ \dfrac{d\phi}{d\tau_T^d} \end{array} \right\} = \dot{\lambda} \left\{ \begin{array}{c} 0 \\ \dfrac{\tau_T^d}{\left|\tau_T^d\right|} \end{array} \right\} \qquad \begin{array}{lll} \dot{\lambda} \geq 0, & \phi\left(\tau^d\right) \leq 0, & \dot{\lambda}\phi\left(\tau^d\right) = 0 \end{array} \tag{10}$$

with λ the plastic multiplier.

About the evolution of the damage parameter, a model which accounts for the coupling of mode I of mode II of fracture is considered. In fact, the two quantities η_N and η_T, defined as the ratios between the first cracking relative displacements s_N^0 and s_T^0 and the full damage relative displacements s_N^f and s_T^f, respectively, are introduced:

$$\eta_N = \frac{s_N^0}{s_N^f} = \frac{s_N^0 \tau_N^0}{2\, G_{cN}}, \qquad \eta_T = \frac{s_T^0}{s_T^f} = \frac{s_T^0 \tau_T^0}{2\, G_{cT}} \tag{11}$$

where τ_N^0 and τ_T^0 are the peak stresses corresponding to the first cracking relative displacements and G_{cN} and G_{cT} are the specific fracture energies in mode I and mode II, respectively. Then, the parameter η, which relates the two modes of fracture, is defined as follows:

$$\eta = \frac{\langle s_N \rangle_+^2}{\|\tilde{\mathbf{s}}\|^2} \eta_N + \frac{s_T^2}{\|\tilde{\mathbf{s}}\|^2} \eta_T \tag{12}$$

where $\tilde{\mathbf{s}} = \left\{ \langle s_N \rangle \;\; s_T \right\}^T$, with the McCauley bracket $\langle . \rangle$ selecting the positive part of a number. The equivalent relative displacement ratio is introduced as:

$$Y = \sqrt{Y_N^2 + Y_T^2} \qquad \text{with} \quad Y_N = \frac{\langle s_N \rangle_+}{s_N^0}, \quad Y_T = \frac{s_T}{s_T^0} \tag{13}$$

The damage parameter is assumed to be function of η and of the history of the equivalent relative displacement Y as:

$$D = \max_{history} \left\{ 0, \min \left\{ 1, \frac{Y-1}{Y\,(1-\eta)} \right\} \right\} \tag{14}$$

The damage evolution law given by equation (14) allows to obtain a linear stress - relative displacement softening when the ratio s_N/s_T is assigned (59).

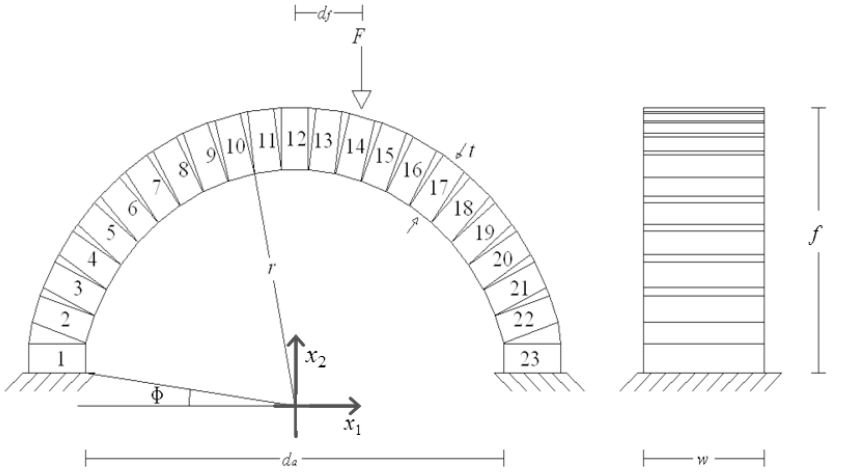

Figure 4. Geometry of the arch.

2.2 Numerical applications

The proposed interface model is implemented in a research version of the finite element code FEAP (66). In particular, a four-node interface element is developed, integrating the evolutive equations through a step by step algorithm. The time step is solved at a typical point of the interface, adopting a predictor-corrector algorithm through a displacement-based formulation. In order to ensure the quadratic rate of asymptotic convergence that characterizes the use of the Newton's iterative method at the global level in the FEAP code, the consistent tangent interface stiffness matrix is computed and implemented in the program, accordingly to the local integration algorithmic scheme.

In particular, two structural applications are performed; the first application concerns the study of a masonry arch, while the second one deals with the analysis of a masonry panel.

Analysis of a masonry arch In this section, numerical analyses concerning a masonry arch are developed. The numerical results are compared with the experimental ones, recovered from the experimental campaign carried out by Cancelliere et al. (11).

The geometrical data of the round arch, schematically reported in figure 4, are the following: internal radius $r = 456\,\text{mm}$, width $w = 255\,\text{mm}$,

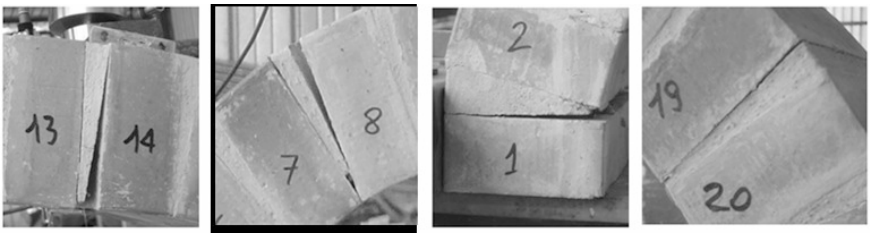

Figure 5. Position of the four hinges for the arch.

thickness $t = 120\,\text{mm}$, height $f = 510\,\text{mm}$, abutment angle $\Phi = 8°$ and span $d_a = 900\,\text{mm}$. The arch was built in the experimental laboratory using 23 standard clay bricks joined by 22 mixed mortars; the conventional numeration of bricks is clearly shown in figure 4. During the experimental tests, the arch in addition to its weight was subjected to a point-wise load applied with an eccentricity $d_f = 140\,\text{mm}$ with respect to the keystone; in particular, the load was applied on the 14-th brick by the action of a hydraulic jack. The arch was restrained at the springs by rigid steel elements, in order to avoid horizontal sliding.

The experimental test of the arch showed that (figure 5): the first hinge arose on the extrados between the mortar number 13 and the clay brick number 14, the second hinge formed on the intrados between the mortar number 7 and the clay brick number 8, the third hinge formed between on the extrados the clay brick number 1 and between the mortar number 1 and the fourth hinges formed on the intrados between the clay brick number 19 and the mortar number 19.

Finite element analyses are developed in order to reproduce the mechanical response of the arch. In particular, the clay bricks and the mortar joints are modeled by four nodes quadrilateral elements, while the mortar-brick interface and the brick-support interface by the developed four node interface elements. Experimental evidences showed that the decohesion phenomenon between a mortar joint and two adjacent bricks is activated mainly on only one of the two interfaces, as illustrated in figure 5. For this reason and in order to simplify the finite element model of the arch, only one nonlinear interface is considered for each mortar bed. Figure 6 illustrates the numerical model of the arch, emphasizing that the interface elements are positioned on only one of the two surfaces joining the mortar with the bricks, while a perfect mortar-brick adhesion is assumed for the other surface.

In the numerical simulations the geometrical cross-section of the arch was reduced of 6 mm in height and width with respect to the nominal size

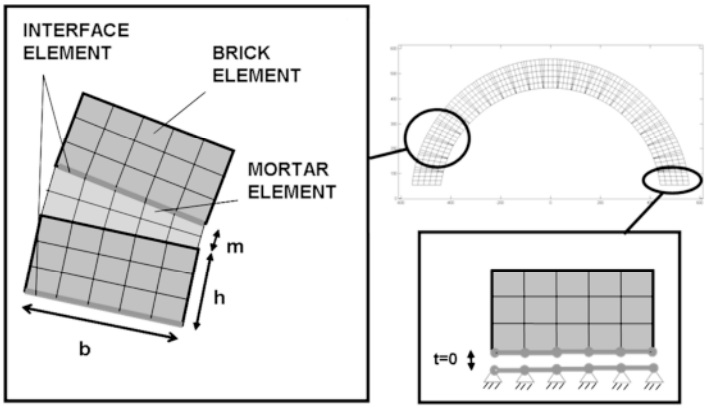

Figure 6. Finite element mesh and constraints adopted for the analyses.

of the cross-section; this choice is justified by the presence of defects and irregularities of construction of the beds mortar, which make smaller the contact surface between brick and mortar joint.

Linear elastic constitutive laws are adopted for both mortar and bricks to simulate the behavior of the arch. This choice is due to the observation that the collapse mechanism for the arch is mainly governed by the unilateral and frictional behavior of the mortar-brick interface, while no material failure due to compressive stresses has been noted during the experimental tests, as it was reasonably expected. The mechanical properties of the brick and mortar materials, adopted for the computations, are determined by experimental tests described in (11):

$$E_b = 16000\,\text{MPa}, \quad \nu_b = 0.2$$
$$E_m = 1500\,\text{MPa}, \quad \nu_m = 0.2$$

where E_b, ν_b and E_m, ν_m are the elastic modulus and the Poisson ratio of the brick and the mortar, respectively. The following values of the mechanical properties, derived by the experimental evidences, are adopted for the interface elements:

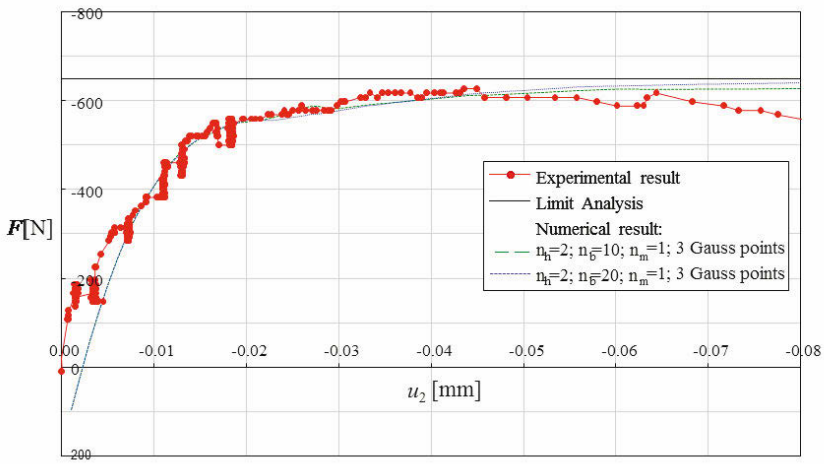

Figure 7. Limit load, experimental results and numerical results obtained considering different meshes for the arch.

$$\begin{aligned} &\tau_N^0 = 0.3\,\text{MPa}, \quad G_{cN} = 0.3\,\text{N/mm}, \quad K_N = 1500\,\text{N/mm}^3, \\ &\tau_T^0 = 3.0\,\text{MPa}, \quad G_{cT} = 0.3\,\text{N/mm}, \quad K_T = \ 750\,\text{N/mm}^3, \\ &\mu = 0.5 \end{aligned}$$

Three different discretizations are considered for the arch; they are obtained introducing the three discretization parameters n_h, n_b end n_m, representing the number of subdivisions along the height of the brick, along the base of the brick and in the thickness of mortar joint, respectively, as illustrated in figure 6. In particular, the computations are performed setting $n_h = 2$ and $n_m = 1$, while different values for the parameter n_b are considered, $n_b = 5$, 10 and 20. In the numerical simulations, the arc-length technique is adopted in order to be able to capture the possible softening branch of the equilibrium path. In particular, the incremental negative displacement u_2 along the x_2-direction (see figure 4) of the loaded node is chosen as control parameter.

In the graph of figure 7 the results of the numerical simulations, plotted in term of nodal force F versus the negative displacement u_2 of the loaded node, are compared with the experimental data provided in (11). In same figure the value of the failure load (650 N) deduced by applying the kine-

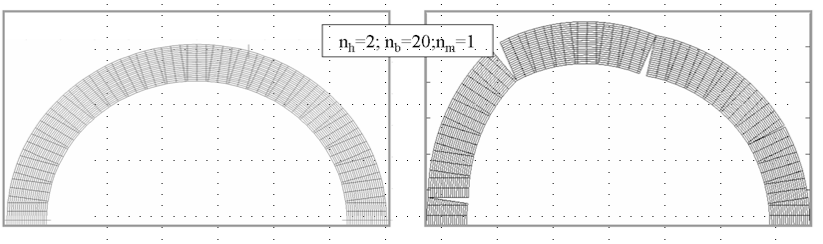

Figure 8. Equilibrium configuration for $v = -0.1\,\text{mm}$.

matic theorem of the limit analysis is also reported. It can be remarked that:

- the three numerical models satisfactory approximate the experimental behavior of the arch and the theoretical limit load;
- increasing the discretization along the base of the clay brick, the numerical result tends to the experimental one;
- the analyses are stable;
- the collapse load deduced by the limit analysis represents the upper bound of the ultimate strength of the arch.

It can be remarked that finer meshes lead to better evaluations of the limit load, because of the improvement in the reproduction of the stress profile at mortar-brick interface. Indeed, the elastic deformation of both bricks and mortar does not play any role in the determination of the limit load of the arch, but it can influence only the first part of the response of the structure.

In figure 9, the finest discretization adopted for the computations is reported with the corresponding deformed configuration when the vertical displacement of the loaded node reaches the value $u_2 = -0.1\,\text{mm}$. It can be remarked that the numerical simulation is able to predict the collapse mechanism of the arch.

Raijmakers-Vermeltfoort panel The second analyzed micromechanical problem is the masonry wall loaded in compression and shear studied by Lourenço (37) on the basis of the experimental tests performed by Raijmakers and Vermeltfoort (55).

The geometry and loading are shown in figure 9. The initial compression is obtained by prescribing the vertical displacement of the top of the wall where a steel beam is positioned until the total sum of the vertical reactions is equal to $\text{Q} = 30\,\text{kN}$; such vertical displacements are then kept constant

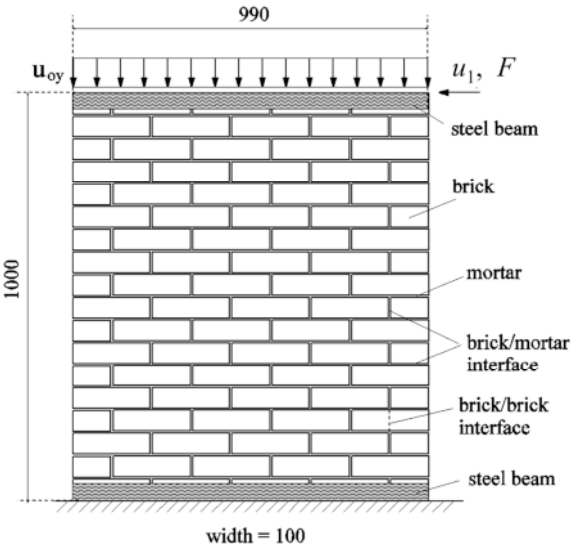

Figure 9. Masonry panel loaded in compression and shear: geometry and loading (dimensions in mm).

during the rest of the analysis, in which the horizontal displacement of the top-right corner, u_1, is incremented left-ward.

Computations are performed modeling the mortar and the adhesion-contact surface mortar-brick by means of the interface element. Thus, the numerical model is constituted by bricks, suitably enlarged, directly joined by interfaces.

Interface elements have even been placed in the middle of each brick to take into account the possible failure of a brick by allowing a crack to initiate and propagate vertically on its middle. A regular finite-element discretization is adopted for the computations. In particular, each half brick is discretized with 2×2 4-noded, plane stress elements with enhanced strains.

The material properties of the brick, adopted for the computations, are:

$$E_b = 17600\,\text{MPa}, \quad \nu_b = 0.15$$

while the following values of the mechanical properties are adopted for the interface elements:

- mortar joint

$$\begin{array}{lll} \tau_N^0 = 0.25\,\text{MPa}, & G_{cN} = 0.018\,\text{N/mm}, & K_N = 82\,\text{N/mm}^3, \\ \tau_T^0 = 0.35\,\text{MPa}, & G_{cT} = 0.125\,\text{N/mm}, & K_T = 36\,\text{N/mm}^3, \\ \mu = 0.75 & & \end{array}$$

- brick-brick interface

$$\begin{array}{lll} \tau_N^0 = 2.00\,\text{MPa}, & G_{cN} = 0.080\,\text{N/mm}, & K_N = 1E6\,\text{N/mm}^3, \\ \tau_T^0 = 4.00\,\text{MPa}, & G_{cT} = 0.200\,\text{N/mm}, & K_T = 1E6\,\text{N/mm}^3, \\ \mu = 0.75 & & \end{array}$$

In figure 10, the numerically computed horizontal reaction F is plotted versus the horizontal prescribed displacement u_1 of the top-right corner, and compared with the experimental data. The numerical and experimental results appear in good agreement. Computations are performed combining the local-control arc-length method with the displacement control. The special numerical procedure adopted, described in details in (5), is able to determine the complex load-displacement equilibrium curve.

Figure 11(a) reports the contour plot of the shear stress component on the deformed configuration, when the prescribed displacement is equal to 4.24 mm, with a magnification factor of 20, showing the corresponding crack pattern. Figure 11(b) shows the experimentally found crack pattern in two tested walls (37); it can be remarked the good agreement of the crack path determined numerically with the ones obtained from experimental tests.

3 Multiscale modeling

The masonry is a composite, material; for this reason, in the last twenty years, several models derived from homogenization approaches have been proposed in the literature. Different assumptions have been considered in the development of the models.

The differences among the models concern: the arrangement of the masonry, i.e. regular or irregular texture; the constitutive model adopted for the brick, i.e. rigid, deformable with linear or nonlinear response, including damage and/or plasticity effects; the model adopted for the mortar, i.e. interface or continuum material characterized by linear or nonlinear response; the macroscopic model obtained by homogenization, i.e. Cauchy, Cosserat or higher order continua.

Moreover, various homogenization techniques have been proposed and applied for the masonry material. Thus, selecting among the different possible mechanical assumptions and adopting different homogenization tech-

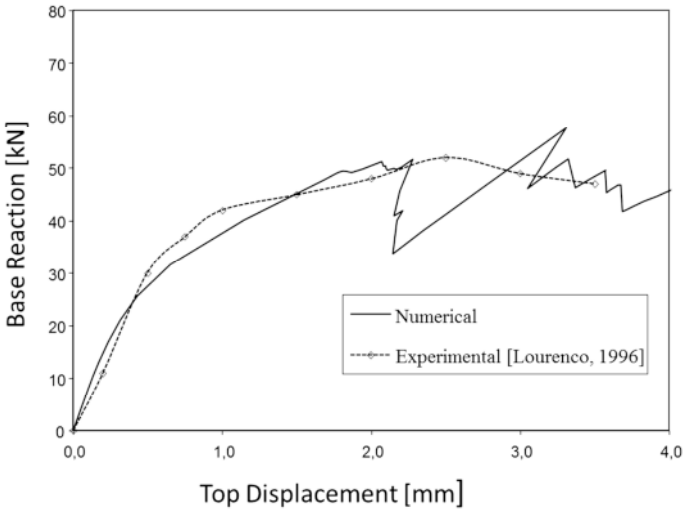

Figure 10. Load-displacement curve: comparison between the numerical and the experimental results reported in Reference (37).

niques, many masonry models and numerical procedures have been proposed in literature.

Among the others, Cauchy models have been derived for the particular microstructural geometry of masonry material, developing simplified homogenization techniques by Kralj et al. (33), by Pietruszczak and Niu (54) and by Gambarotta and Lagomarsino (27; 28), considering the nonlinear behavior of the constituents. Periodic homogenization techniques have been proposed by Anthoine (6) and by Luciano and Sacco (41), considering the elastic behavior of both brick and mortar. Pegon and Anthoine (52) derived the in-plane macroscopic nonlinear behavior of masonry considering a damage model for the brick and the mortar in the framework of the plane stress and generalized plane strain states. The effect of the head joints in the overall nonlinear response of the masonry has been remarked. Luciano and Sacco (40) derived a damage model for masonry material characterized by periodic micro-structure. As for old masonry the strength of the mortar is much lower than the strength of the bricks, it has been assumed that damage can develop only in the mortar material. Uva and Salerno

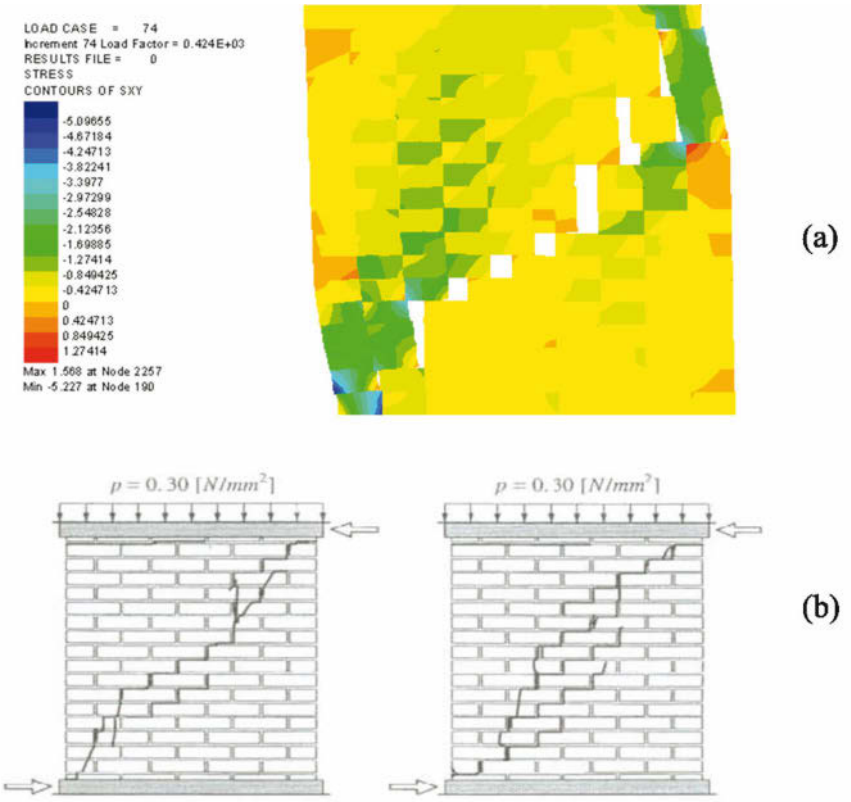

Figure 11. Contour-plot and deformed shape at $u_1 = 4.24$ mm (a) and crack pattern reported in Reference (37) (b).

(67) presented the homogenized response of the masonry accounting for the damage development within the bed joints and the frictional dissipation over cracks' faces. Multiscale FE (finite element) analyses of large-scale panels have been shown. Massart et al. (46) proposed an enhanced multiscale model using nonlocal implicit gradient isotropic damage models for both the constituents, describing the damage preferential orientations and employing at the macroscopic scale an embedded band model. Zucchini and Lourenço (70) proposed an improved micromechanical model for masonry homogenization in the nonlinear domain, incorporating suitably chosen deformation mechanisms coupled with damage and plasticity models. Wei and Hao (68) developed a continuum damage model for masonry account-

ing for the strain rate effect, using a homogenization theory implemented in a numerical algorithm. Sacco (60) presented a nonlinear homogenization procedure for the masonry, considering a linear elastic behavior for the blocks and a nonlinear constitutive law for the mortar joints. In particular, the mortar constitutive law accounted for the coupling of the damage and friction phenomena occurring in the mortar joints during the loading history.

In the framework of the Cosserat continuum models, Masiani et al. (44) and Masiani and Trovalusci (45) studied the case of two-dimensional periodic rigid block assemblies joined by elastic mortar, deducing the macroscopic characterization of the equivalent medium by equating the virtual power of the coarse model with the virtual power of the internal actions of the discrete fine model. Casolo (12) considered isotropic linear elastic models both for the brick and the mortar and used a computational approach to identify the homogenized elastic tensor of the equivalent Cosserat medium. Salerno and de Felice (61) investigated the accuracy of various identification schemes for Cauchy and Cosserat continua, showing that in the case of non-periodic deformation states micropolar continuum better reproduces the discrete solutions, due to its capability to take scale effects into account. Addessi et al. (3) developed a two scales model, characterized by the Cosserat micropolar continuum at the macro level and the classical Cauchy medium at the micro level. Nonlinear response of the mortar joints was considered by using a cohesive-friction constitutive model. The nonlinear behavior for both brick and mortar has been considered by De Bellis and Addessi (17). A full multiscale model for the structural analysis of the in-plane response of masonry panels has been presented by Addessi and Sacco (2).

Micro-macro, i.e. multiscale, analysis based on nonlocal Cauchy-Cauchy modeling has been presented by Marfia and Sacco (42), where an effective homogenization procedure is developed and implemented at Gauss point level, in 2D plane state finite element. A nonlocal integral model is adopted in order to overcome problems due to the localization of strain and damage.

An interesting numerical procedure, based on a multilevel computational approach, has been proposed by Brasile et al. (9), (10) for the static and dynamic multiscale analysis of masonry walls.

Most of the existing models for masonry concern periodic microstructures. A non-periodic masonry, typical of historical buildings, has been analyzed in (14) by means of a perturbation approach, while the evaluation of the strength domain for non-periodic masonry using a random media micromechanical approach is discussed in (13).

The out-of-plane analysis of masonry panels is a very important and

interesting issue. In fact, recent earthquakes show that the out-of-plane failure of masonry walls is the main responsible of the loss of human lives. Mercatoris and Massart (47) presented a multiscale framework for the failure of periodic quasi-brittle thin planar shells, using a shear-enhanced element with the Reissner - Mindlin description and employing it for the failure of out-of-plane loaded masonry walls.

When softening behavior is considered for the masonry constituents, the classical Cauchy model leads to the well-known localization and mesh-dependency problems. On the contrary, the Cosserat continuum model accounts for a material length scale into the constitutive description, providing a natural way to obtain a dependence of the overall response of the composite material on the absolute size of the constituents and to achieve a realistic description of a micro-structurally triggered macroscopic localization. In fact, the Cosserat model is able to overcome the localization problems for shear loaded panels.

In this section, the two scales model, characterized by the Cosserat micropolar continuum at the macro level and the classical Cauchy medium at the micro level (3; 2), is reviewed and illustrated. The model is presented together with numerical applications.

In the following, quantities identified in the macro and in the micro scales are denoted with capital and small letters, respectively.

3.1 Macro-level model

At the macro-level, where the Cosserat continuum model is employed, the displacement vector $\mathbf{U} = \{U_1\, U_2\, \Phi\}^T$ contains three independent kinematic fields, representing the translations U_1 and U_2 and the rotation Φ, at each point $\mathbf{X} = \{X_1\, X_2\}^T$ of the body volume. The compatibility equations, relating the deformation components to the displacement fields, are introduced in the compact form of Voigt notation as:

$$\mathbf{E} = \mathbf{D}\,\mathbf{U} \qquad \text{with} \quad \mathbf{D} = \begin{bmatrix} \frac{\partial}{\partial X_1} & 0 & 0 \\ 0 & \frac{\partial}{\partial X_2} & 0 \\ \frac{\partial}{\partial X_2} & \frac{\partial}{\partial X_1} & 0 \\ -\frac{\partial}{\partial X_2} & \frac{\partial}{\partial X_1} & -2 \\ 0 & 0 & \frac{\partial}{\partial X_1} \\ 0 & 0 & \frac{\partial}{\partial X_2} \end{bmatrix} \tag{15}$$

where $\mathbf{E} = \left\{ \begin{array}{cccccc} E_1 & E_2 & \Gamma_{12} & \Theta & K_1 & K_2 \end{array} \right\}^T$ is the strain vector and $\mathbf{D}$ the compatibility operator. The first three components of $\mathbf{E}$ are the in-plane Cauchy extensional and symmetric shear strains, $\Theta = 2(W - \Phi)$ is the rotational deformation, representing two times the difference between

the rigid rotation

$$W = \frac{1}{2}\left(\frac{\partial U_2}{\partial X_1} - \frac{\partial U_1}{\partial X_2}\right)$$

and the Cosserat rotation field Φ, and K_1 and K_2 are the curvatures.

Accordingly, the stress vector is expressed as

$$\mathbf{\Sigma} = \left\{ \begin{array}{cccccc} \Sigma_1 & \Sigma_2 & \Sigma_{12} & Z & M_1 & M_2 \end{array} \right\}^T,$$

where Σ_1 and Σ_2 are the normal stresses, Σ_{12} is the symmetric shear stress, Z is the stress component associated to the rotational deformation Θ and M_1 and M_2 are the couples.

In order to derive the constitutive response in each macroscopic material point a homogenization procedure is applied by means of the analysis of the corresponding RVE (representative volume element). In particular, for each RVE a boundary value problem is solved and the constitutive relationship is determined, deriving the macroscopic elastic 6×6 constitutive matrix $\mathbf{C}$.

3.2 Micro-level model

At the micromechanical level, the compatibility, equilibrium and constitutive equations governing the behavior of the masonry RVE are introduced in the $2D$ plane strain framework. The analysis is limited to the case of periodic masonry made of regular textures of bricks and mortar joints.

The displacement vector $\mathbf{u} = \{u_1\, u_2\}^T$ at each point $\mathbf{x} = \{x_1\, x_2\}^T$ of the RVE occupying the volume ω is introduced in a representation form as the superposition of a prescribed field $\bar{\mathbf{u}}$, defined as function the macroscopic deformation $\mathbf{E}$, and an unknown periodic fluctuation $\tilde{\mathbf{u}}$, satisfying proper periodicity conditions on the RVE boundary (65; 41), namely:

$$\mathbf{u} = \bar{\mathbf{u}}\,(\mathbf{x}) + \tilde{\mathbf{u}}(\mathbf{x}) \quad \text{in} \quad \omega \tag{16}$$

The strain $\boldsymbol{\varepsilon} = \{\varepsilon_1\, \varepsilon_2\, \gamma_{12}\}^T$ is obtained from the compatibility equation as:

$$\boldsymbol{\varepsilon} = \mathbf{d}\mathbf{u} \quad \text{in} \quad \omega \qquad \text{with} \quad \mathbf{d} = \begin{bmatrix} \frac{\partial}{\partial x_1} & 0 \\ 0 & \frac{\partial}{\partial x_2} \\ \frac{\partial}{\partial x_2} & \frac{\partial}{\partial x_1} \end{bmatrix} \tag{17}$$

and according to equation (16) $\boldsymbol{\varepsilon}$ is expressed as:

$$\boldsymbol{\varepsilon} = \bar{\boldsymbol{\varepsilon}}\,(\mathbf{x}) + \tilde{\boldsymbol{\varepsilon}}\,(\mathbf{x}) \tag{18}$$

being $\bar{\boldsymbol{\varepsilon}}$ and $\tilde{\boldsymbol{\varepsilon}}$ the strain fields compatible with $\bar{\mathbf{u}}$ and $\tilde{\mathbf{u}}$, respectively.

Linear elastic stress-strain relationship is adopted for the brick:

$$\boldsymbol{\sigma}^B = \mathbf{C}^B \boldsymbol{\varepsilon} \tag{19}$$

where $\mathbf{C}^B$ is the elastic matrix and $\boldsymbol{\sigma}^B = \left\{\sigma_1^B, \sigma_2^B, \tau_{12}^B\right\}^T$ is the stress vector in the brick.

Regarding the mortar material a coupled damage-plasticity constitutive model is adopted. Indeed, the stress-strain relationship can be considered as the extension to the case of continuum material of the constitutive law presented in the previous section for the interface. It is able to conjugate the damage due to the evolution of the micro-cracks and the plasticity due to the unilateral and friction effects. Herein, the model is enriched introducing a limit compressive stress in order to take into account the crushing mechanism of the masonry. Indeed, the crushing of the masonry panel is generally due to the failure of the bricks; in order to work with a simple model, leaving a linear elastic stress-strain relationship for the bricks, the compressive crushing is introduced in the mortar constitutive law.

The proposed nonlinear model for the masonry, described in detail in (58; 2), can be obtained by a suitable modification of the interface model presented in section 2. An additive decomposition of the stress vector $\boldsymbol{\sigma}^M$ at a typical point of the mortar is assumed as follows:

$$\boldsymbol{\sigma}^M = (1 - D)\, \boldsymbol{\sigma}^u + D\boldsymbol{\sigma}^d \tag{20}$$

with D the scalar damage parameter. The two stress vectors $\boldsymbol{\sigma}^u$ and $\boldsymbol{\sigma}^d$ are given by the relationships:

$$\boldsymbol{\sigma}^u = \mathbf{C}^M \left(\boldsymbol{\varepsilon} - \boldsymbol{\varepsilon}^\kappa\right), \qquad \boldsymbol{\sigma}^d = \mathbf{C}^M \left(\boldsymbol{\varepsilon} - \boldsymbol{\varepsilon}^p - \boldsymbol{\varepsilon}^\kappa\right) \tag{21}$$

where:

$$\mathbf{C}^M = \begin{bmatrix} C_{TT}^M & C_{NT}^M & 0 \\ C_{NT}^M & C_{NN}^M & 0 \\ 0 & 0 & G^M \end{bmatrix} \tag{22}$$

represents the elasticity matrix of the mortar, $\boldsymbol{\varepsilon}^p$ is the inelastic strain vector accounting for the possible unilateral opening effect and for the friction sliding, while $\boldsymbol{\varepsilon}^\kappa$ is the plastic strain due to the crushing.

Taking into account the constitutive equations (21), the relationship (20) becomes:

$$\boldsymbol{\sigma}^M = \mathbf{C}^M \left(\boldsymbol{\varepsilon} - \boldsymbol{\pi}\right) \tag{23}$$

where $\boldsymbol{\pi}$ is the vector collecting all the inelastic strains:

$$\boldsymbol{\pi} = \begin{Bmatrix} \pi_T \\ \pi_N \\ \pi_{NT} \end{Bmatrix} = \begin{Bmatrix} 0 \\ \varepsilon_N^\kappa \\ 0 \end{Bmatrix} + D \begin{Bmatrix} H\left(\varepsilon_N - \varepsilon_N^\kappa\right) \varepsilon_T \\ H\left(\varepsilon_N - \varepsilon_N^\kappa\right) \left(\varepsilon_N - \varepsilon_N^\kappa\right) \\ \gamma_{NT}^p \end{Bmatrix} \tag{24}$$

accounting for the crushing, ε_N^κ, the damage, D, the unilateral contact by means of the component $H\left(\varepsilon_N - \varepsilon_N^\kappa\right)\left(\varepsilon_N - \varepsilon_N^\kappa\right)$ and the slip by means of the component γ_{NT}^p; $H\left(\varepsilon_N - \varepsilon_N^\kappa\right)$ is the Heaviside function, which assumes the following values: $H\left(\varepsilon_N - \varepsilon_N^\kappa\right) = 0$ if $\left(\varepsilon_N - \varepsilon_N^\kappa\right) \leq 0$ and $H\left(\varepsilon_N - \varepsilon_N^\kappa\right) = 1$ if $\left(\varepsilon_N - \varepsilon_N^\kappa\right) > 0$. Because of the simplified form of the inelastic strain (24), the constitutive law (21) is able to provide zero normal stress in transversal direction, $\sigma_N^d = 0$, as well as in longitudinal direction, $\sigma_T^d = 0$, when opening of the mortar joint occurs.

The crushing and the friction effects are modeled as classical plasticity problems. The evolution law of the crushing inelastic strain component ε_N^κ is stated as:

$$\dot{\varepsilon}_N^\kappa = -\dot{\lambda}_\kappa \tag{25}$$

and it is ruled by the Kuhn-Tucker conditions, being λ_κ the inelastic multiplier:

$$\dot{\lambda}_\kappa \geq 0 \quad \psi\left(\boldsymbol{\sigma}\right) \leq 0, \quad \dot{\lambda}_\kappa \; \psi\left(\boldsymbol{\sigma}\right) = 0 \tag{26}$$

The yield function is assumed as:

$$\psi\left(\boldsymbol{\sigma}\right) = -\left(\sigma_N + \sigma_y + \kappa\xi\right) \tag{27}$$

where σ_y is the compressive yield threshold, $\kappa \leq 0$ is the softening parameter and ξ is the accumulated plastic strain evaluated as:

$$\xi = \int_0^t \left|\dot{\varepsilon}_N^\kappa\right| d\tau \tag{28}$$

As concerning the friction mechanism, the evolution of the inelastic slip strain component γ_{NT}^p is governed by the Coulomb yield function:

$$\varphi\left(\boldsymbol{\sigma}^d\right) = \mu\, \sigma_N^d + \left|\tau_{NT}^d\right| \tag{29}$$

where μ is the friction parameter. A non-associated flow rule is considered as:

$$\dot{\gamma}_{NT}^p = \dot{\lambda}_\mu \frac{\tau_{NT}^d}{\left|\tau_{NT}^d\right|} \tag{30}$$

with the following loading-unloading Kuhn-Tucker conditions:

$$\dot{\lambda}_\mu \geq 0 \quad \varphi\left(\boldsymbol{\sigma}^d\right) \leq 0, \quad \dot{\lambda}_\mu \; \varphi\left(\boldsymbol{\sigma}^d\right) = 0 \tag{31}$$

where λ_μ is the inelastic multiplier.

A model which accounts for the coupling of mode I and mode II of fracture is considered for the evolution of the damage parameter D. The two quantities η_N and η_{NT}, which depend on the first cracking strains ε_N^0

and γ^0_{NT}, on the peak values of the stresses σ^0_N and τ^0_{NT} and on the fracture energies G_{cN} and G_{cNT}, respectively, are introduced in the form:

$$\eta_N = \frac{\varepsilon^0_N \, \sigma^0_N}{2\, G_{cN}}, \qquad \eta_{NT} = \frac{\gamma^0_{NT} \, \tau^0_{NT}}{2\, G_{cNT}} \tag{32}$$

The equivalent strain measures Y_N and Y_{NT} are defined as:

$$Y_N = \left(\langle \varepsilon_N - \varepsilon^{\kappa}_N \rangle\right)^2 \;, \quad Y_{NT} = \left(\gamma_{NT}\right)^2 \tag{33}$$

where the bracket operator $\langle \bullet \rangle$ gives the positive part of the quantity $\bullet$. Then, the strain ratios are determined as:

$$\eta = \frac{1}{\alpha^2}\left(Y_N \; \eta_N + Y_{NT} \; \eta_{NT}\right), \quad \beta = \sqrt{\frac{Y_N}{\varepsilon^2_{N,0}} + \frac{Y_{NT}}{\gamma^2_{NT,0}}}, \quad \alpha = \sqrt{Y_N + Y_{NT}} \tag{34}$$

Finally, the damage is evaluated according to the following law:

$$D = \max_{history} \left\{ 0, \min \left\{ 1, \frac{\beta - 1}{(1-\eta)\,\beta} \right\} \right\} \tag{35}$$

3.3 Homogenization technique

Different homogenization procedures have been proposed in the literature in order to evaluate the nonlinear behavior of composites. An interesting approach is the Transformation Field Analysis (TFA) proposed initially by Dvorak (21) and adopted and extended to plasticity and viscoplasticity problems by Fish and Shek (23). According to TFA approach, the inelastic strain, i.e. the transformation strain, is assumed to be uniform within each individual phase in the composite. Dvorak et al. (22) and Chaboche et al. (15) improved the TFA for deriving the nonlinear behavior of damaging composites, subdividing each phase into subdomains, at the expense of increasing the complexity of the model. Michel and Suquet (48) proposed a nonuniform TFA, where the inelastic strain field is considered as nonuniform and described as the superposition of functions, called inelastic modes and determined numerically by simulating the response of the composite along monotone loading paths. The technique was then modified and implemented for the analysis of the morphological anisotropy of microheterogeneous materials with particle reinforcement by Fritzen and Böhlke (26). A new approach for the nonuniform TFA has been recently proposed by Sepe et al. (62).

The use of the TFA requires the computation of localization and transformation tensors. To this end, numerical techniques based on generalizations

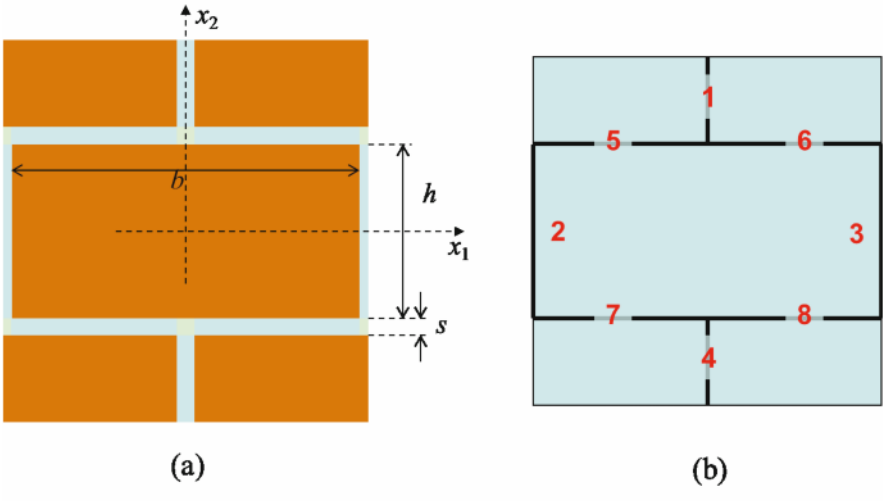

Figure 12. Selected RVE for the running bond masonry texture (a); numbering of the mortar joints (b).

of the Eshelby method (50) can be quite successfully adopted for composites characterized by random microstructure. When the geometry of the microstructure is complex, as in the case of masonry material, numerical techniques, most often based on the assumption of microstructure periodicity, can be adopted. In fact, finite element methods or fast Fourier transform solutions are able to describe accurately local stress and strain fields, so that the correct nonlinear behavior of the phases can be determined.

A RVE is selected; it is characterized by rectangular shape with dimensions $2a_1$ and $2a_2$, parallel to the coordinate axes x_1 and x_2, mortar thickness denoted by s and brick sizes by b and h, as shown in figure 12(a). The RVE accounts for all the geometrical and constitutive properties of the masonry components.

A kinematic map linking the macro-and micro-level is established. Herein, following the methodology proposed by Forest and Sab (24), third order polynomial expansions are assumed for the assigned part of the microscopic displacement $\bar{\mathbf{u}}(\mathbf{x})$, which allows to take into account all the macroscopic Cosserat deformation components. In the case of a rectangular cell, the following form of the assigned displacement $\bar{\mathbf{u}}$ is adopted in compact notation:

$$\bar{\mathbf{u}} = \mathbf{A}\,(\mathbf{x})\;\mathbf{E} \tag{36}$$

where

$$\mathbf{A} = \begin{bmatrix} x_1 & 0 & \frac{1}{2}x_2 & -a(x_2^3 - 3\rho^2 x_1^2 x_2) & -x_1 x_2 & -\frac{1}{2}x_2^2 \\ 0 & x_2 & \frac{1}{2}x_1 & -\rho^2 a(\rho^2 x_1^3 - 3x_1 x_2^2) & \frac{1}{2}x_1^2 & x_1 x_2 \end{bmatrix} \tag{37}$$

with

$$a = \frac{5}{4}\frac{a_1^2 + a_2^2}{a_1^4} \qquad \rho = \frac{a_2}{a_1} \tag{38}$$

In order to activate the Cauchy deformation modes independently from the Cosserat ones, in equation (36) the fourth component of the Cosserat strain vector $\mathbf{E}$ is redefined as:

$$\hat{\Theta} = \Theta + \frac{1}{2}\,\frac{\rho^2 - 1}{\rho^2 + 1}\,\Gamma_{12} \tag{39}$$

The stress variable conjugated to $\hat{\Theta}$ is denoted with $\hat{Z}$.

The strain vector at the micro-level, equation (18), can now be expressed as:

$$\boldsymbol{\varepsilon} = \mathbf{B}(\mathbf{x})\mathbf{E} + \tilde{\boldsymbol{\varepsilon}}(\mathbf{x}) \tag{40}$$

where $\boldsymbol{\varepsilon}(\mathbf{x})$ is the periodic strain, satisfying null average condition in the RVE volume ω, and:

$$\mathbf{B} = \begin{bmatrix} 1 & 0 & 0 & 6\,a\,\rho^2 x_1 x_2 & -x_2 & 0 \\ 0 & 1 & 0 & 6\,a\,\rho^2 x_1 x_2 & 0 & x_1 \\ 0 & 0 & 1 & 3\,a\,\left(\rho^2 - 1\right)\left(x_2^2 - \rho^2 x_1^2\right) & 0 & 0 \end{bmatrix} \tag{41}$$

The in-plane periodicity and continuity conditions lead to the following boundary conditions:

$$\begin{array}{ll} \tilde{\mathbf{u}}(a_1, x_2) = \tilde{\mathbf{u}}(-a_1, x_2) & \forall x_2 \in [-a_2, a_2] \\ \tilde{\mathbf{u}}(x_1, a_2) = \tilde{\mathbf{u}}(x_1, -a_2) & \forall x_1 \in [-a_1, a_1] \end{array} \tag{42}$$

The masonry RVE is subjected to the macroscopic Cosserat strain $\mathbf{E}$ applied to the whole RVE and to the inelastic strain $\boldsymbol{\pi}^i$, with $i = 1, \ldots, m$, applied to each of the m mortar joints illustrated in figure 12(b). Note that the inelastic strain is assumed to be uniform in each mortar joint.

The micromechanical problem of the RVE subjected to the prescribed value of the six components of $\mathbf{E}$ and to the three components of the inelastic strains $\boldsymbol{\pi}^i$ in the m mortar joints, have to be solved. The micromechanical strain field, resulting after solving the boundary value problem for the RVE subjected to $\mathbf{E}$, can be written in the following representation form:

$$\mathbf{e} = \mathbf{R}_e\,(\mathbf{x})\,\mathbf{E} \tag{43}$$

where the localization matrix $\mathbf{R}_e(\mathbf{x})$ is introduced. Consequently, the average strain in the brick and in each mortar joint M^i results as:

$$\bar{\mathbf{e}}^B = \bar{\mathbf{R}}_e^B \mathbf{E}, \quad \bar{\mathbf{e}}^{M^i} = \bar{\mathbf{R}}_e^{M^i} \mathbf{E} \tag{44}$$

where $\bar{\mathbf{R}}_e^B$ and $\bar{\mathbf{R}}_e^{M^i}$ denote the average localization matrices in the brick volume and in the mortar joint volume, respectively.

The homogenized Cosserat stress in the whole RVE volume ω is obtained by applying the generalized Hill-Mandel principle, resulting:

$$\boldsymbol{\Sigma}_e = \mathbf{C}\,\mathbf{E} \tag{45}$$

where the overall elastic constitutive matrix is defined as (3):

$$\mathbf{C} = \frac{1}{\omega}\left[\int_B \mathbf{R}_e^T \mathbf{C}^B\,\mathbf{e}\,d\omega + \sum_{j=1}^{m}\int_{M^j} \mathbf{R}_e^T \mathbf{C}^{M^j}\,\mathbf{e}\,d\omega\right] \tag{46}$$

Moreover, the average stress in the mortar joint M^i may be evaluated as $\boldsymbol{\sigma}_e^{M^i} = \mathbf{C}^M \bar{\mathbf{e}}^{M^i} = \mathbf{C}^M \bar{\mathbf{R}}_e^{M^i} \mathbf{E}$, as well as in the brick $\bar{\boldsymbol{\sigma}}_e^B = \mathbf{C}^B \bar{\mathbf{e}}^B = \mathbf{C}^B \bar{\mathbf{R}}_e^B \mathbf{E}$.

Similarly, after solving the micromechanical problem of the RVE subjected to an inelastic strain $\boldsymbol{\pi}^i$ prescribed in the mortar joint M^i, the resulting local strain field is expressed in the form:

$$\mathbf{q}^i = \mathbf{R}_\pi^i(\mathbf{x})\,\boldsymbol{\pi}^i \tag{47}$$

being $\mathbf{R}_\pi^i(\mathbf{x})$ the associated localization matrix. Note that the local strain field $\mathbf{q}^i$ is characterized by null average. The elastic strain in the mortar joint M^j results:

$$\boldsymbol{\eta}^{i,M^j} = \mathbf{q}^{i,M^j} - \delta_{ij}\boldsymbol{\pi}^i = \left(\mathbf{R}_{\pi^i}^{M^j} - \delta_{ij}\mathbf{I}\right)\boldsymbol{\pi}^i \qquad \text{(no sum)} \tag{48}$$

where $\mathbf{q}^{i,M^j}$ and $\mathbf{R}_{\pi^i}^{M^j}$ are the restriction to the mortar M^j of the fields $\mathbf{q}^i$ and $\mathbf{R}_{\pi^i}$, respectively. The elastic strain $\boldsymbol{\eta}^{i,B}$ in the brick coincides with the total strain.

The corresponding overall Cosserat stress can be obtained again by applying the generalized Hill-Mandel principle in the form:

$$\boldsymbol{\Sigma}_{\pi^i} = \frac{1}{\omega}\left[\int_B \left(\mathbf{R}_{\pi^i}^B\right)^T \mathbf{C}^B \mathbf{R}_{\pi^i}^B\,d\omega + \sum_{j=1}^{m}\int_{M^j}\left(\mathbf{R}_{\pi^i}^{M^j}\right)^T \mathbf{C}^{M^j}\left(\mathbf{R}_{\pi^i}^{M^j} - \delta_{ij}\mathbf{I}\right)d\omega\right]\boldsymbol{\pi}^i \tag{49}$$

When the RVE is subjected to the overall elastic strain $\mathbf{E}$ and to the inelastic strains $\boldsymbol{\pi}^i$, $i = 1, 2, \ldots, m$, the superposition of the effects can be performed. In such a way, it is possible to compute the overall stress:

$$\boldsymbol{\Sigma} = \boldsymbol{\Sigma}_e + \sum_{i=1}^{m} \boldsymbol{\Sigma}_{\pi^i} = \mathbf{C}\mathbf{E} + \sum_{i=1}^{m} \boldsymbol{\Sigma}_{\pi^i} \tag{50}$$

and the average stress in the m mortar joints:

$$\boldsymbol{\sigma}^{M^j} = \mathbf{C}^M \left(\boldsymbol{\varepsilon}^{M^j} - \boldsymbol{\pi}^j \right) \tag{51}$$

The nonlinear behavior of the RVE is assumed to depend on the average stresses and strains evaluated in each of the m mortar joints.

3.4 Numerical applications

The FE method is used to solve the macro and micromechanical problems. In particular, the multiscale solution procedure is implemented in a research version of the finite element code FEAP (69).

The proposed homogenization procedure initially requires the evaluation of the overall constitutive matrix $\mathbf{C}$ and of the localization matrices $\bar{\mathbf{R}}_e^{M^j}$ and $\bar{\mathbf{R}}_{\pi^i}^{M^j}$. They are computed by solving $6 + 3m$ FE linear elastic micromechanical problems at the RVE level.

A standard Cauchy 4-node quadrilateral FE is adopted to model the RVE with two translational degrees of freedom at each node. At the macro-level a $2D$ 4-node quadrilateral FE is implemented to discretize the Cosserat medium, with three degrees of freedom at each node, two translational and one rotational. A step-by-step solution technique based on the classical backward-Euler algorithm (64) is adopted for the time integration of the governing equations. The nonlinear problem at each time step is solved by means of the Newton-Raphson technique.

The multiscale procedure is employed to analyze the structural response of two masonry panels for which experimental results are available.

Masonry panel under vertical load The masonry panel acting as a deep beam shown in figure 13 was experimentally investigated by Milani et al. (49).

The dimensions of the panel are: width $B = 290$ mm, eight $H = 270$ mm, thickness $T = 30$ mm. In the experimental tests the panel was restrained at the bottom side with two steel rollers and the vertical external load was applied through steel plates located on the top side of the panel as shown in figure 13. The geometrical parameters of bricks and mortar are the

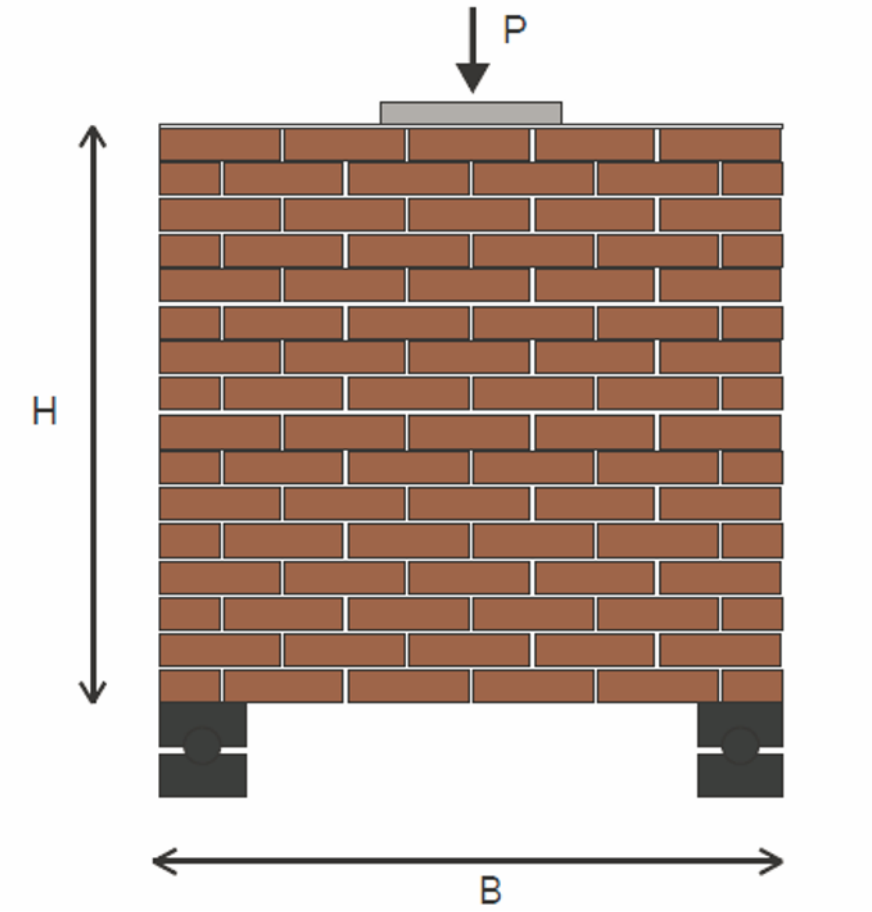

Figure 13. Masonry panel subjected to a vertical load: geometry and boundary conditions.

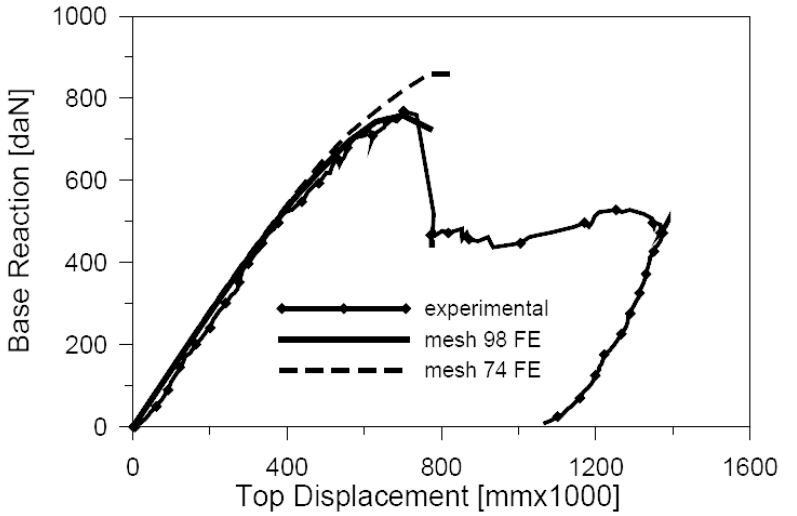

Figure 14. Force-displacement equilibrium path for the masonry panel subjected to a vertical load.

following: size of the brick $b = 56$ mm, $h = 15$ mm; thickness of the mortar joints $s = 2$ mm. Furthermore, the material mechanical parameters are:

- brick

$$E = 1850\,\text{MPa} \qquad \nu = 0.15$$

- mortar

$$E = 233\,\text{MPa} \qquad \nu = 0.15 \qquad \varepsilon_{N,0} = 0.0015 \qquad \gamma_{NT,0} = 0.007$$
$$G_{cI} = 0.0013\,\text{MPa} \qquad G_{cII} = 0.0013\,\text{MPa} \qquad \sigma_y = 5\,\text{MPa} \qquad \kappa = 0$$
$$\mu = 0.1$$

where E and ν are Young's and Poisson moduli, respectively. Due to the symmetry of the problem, only one half of the panel is analyzed and a mesh with 108 FEs is adopted. The three nodes of the right-top side, close to the symmetry axis, are subjected to the same vertical displacement. The support steel rollers are discretized by means of 4-node quadrilateral FEs, assuming a linear elastic constitutive law with Young's modulus equal to 210000 MPa and Poisson modulus 0.3.

In figure 14 the global response curve of the panel is shown, i.e. the global vertical reaction computed at the restrained node of the bottom side versus the top applied displacement is depicted. Three curves are reported; they refer to the numerically obtained results, obtained with two different

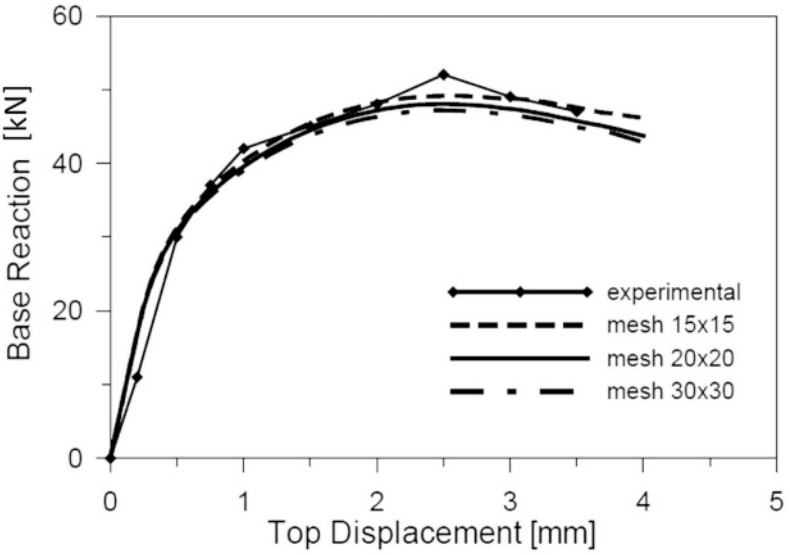

Figure 15. Load-displacement curve: comparison between the numerical and the experimental results reported in Reference (37).

meshes (solid line and dashed line), and to the experimental ones (line with diamond symbols). As it can be noted the numerical curves are in a very good agreement with the experimental one.

Raijmakers-Vermeltfoort panel The masonry wall shown in figure 9, yet analyzed adopting a micromechanical model, is studied performing the multiscale procedure. The material mechanical parameters adopted for the computations are:

- brick

$$E = 16700\,\text{MPa} \qquad \nu = 0.15$$

- mortar

$$E = 798\,\text{MPa} \qquad \nu = 0.11 \qquad \varepsilon_{N,0} = 0.0003 \qquad \gamma_{NT,0} = 0.001$$
$$G_{cI} = 0.00179\,\text{MPa} \qquad G_{cII} = 0.0126\,\text{MPa} \qquad \sigma_y = 5\,\text{MPa} \qquad \kappa = 0$$
$$\mu = 0.75$$

Three different meshes are considered with 15×15, 20×20 and 30×30 FEs.

In figure 15 the global response curve of the wall is reported. In particular, the global horizontal reaction computed at the bottom side versus the top applied displacement is depicted. Four different curves are shown

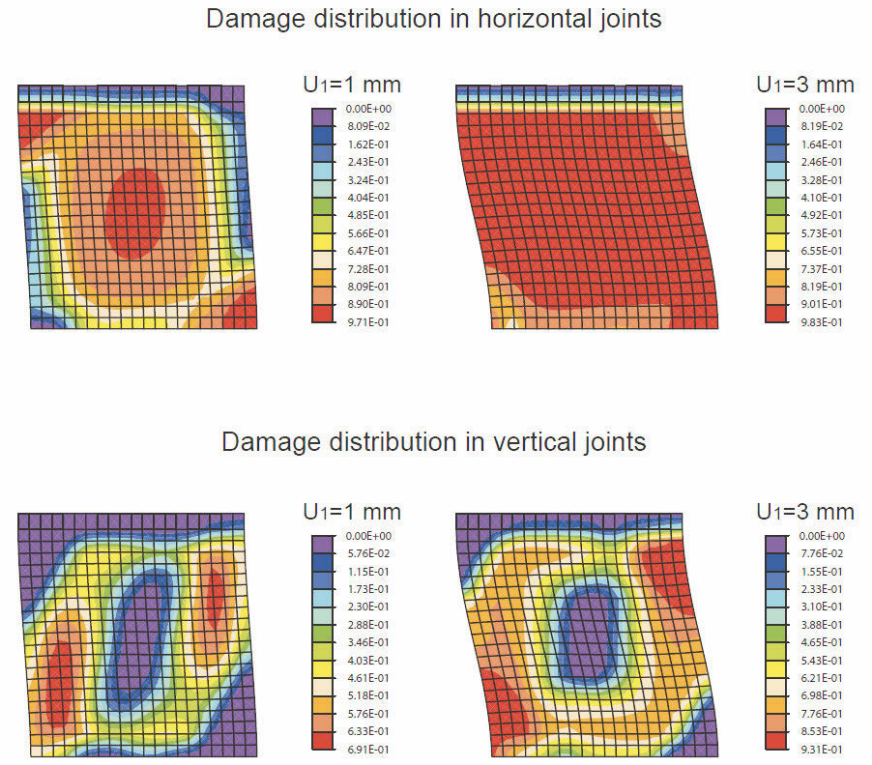

Figure 16. Damage distributions in horizontal (first line) and vertical joints (second line) evaluated at different values of the applied horizontal displacement.

referring to the numerically obtained results and the experimental ones (line with diamond symbols). It is evident that the numerical curves match very well the experimental one. Furthermore, the dashed line curve referring to the 15×15 mesh is not a perfectly converged solution, while the solid and dash-dot line curves referring to the finer mesh are indistinguishable, so proving the capability of the Cosserat model adopted at the macro-level to lead to mesh-independent FE results. After the initial linear elastic behavior, the nonlinear mechanisms are activated and the global response curve reaches a peak load of about 48 N, a little lower than the experimental one, at the applied displacement value of 2.5 mm. Then, the global response curve shows a softening trend.

In figure 16 the map of the macroscopic damage variable is reported for the horizontal bed joints (first line) and the vertical head joints (second line), respectively, at two values of the top applied displacement, $U_1 = 1$ mm and $U_1 = 3$ mm. By observing the first line, it can be seen that damage starts in the bed joints located at the bottom left and top right of the wall, where it experiences the most severe bending deformation state. After, damage spreads involving also the bed joints located near the center of the wall, where the shear mechanisms are predominant. As for the damage in the vertical joints, it is mainly concentrated into two vertical bands. The map of the damage distributions can be compared with the crack pattern obtained during the experimental tests and illustrated in figure 11(b); the satisfactory agreement between the fracture path obtained from the experiments and the damage map recovered using the multiscale masonry model can be noted.

4 Macromechanical modeling

Masonry is a cohesive material characterized by softening response. Indeed, his nonlinear behavior is due to the damage and plastic micromechanical processes. From a microscopic point of view the damage is linked to the growth and coalescence of microcracks, leading to the formation of macrocracks which can induce the collapse of the structure. The plasticity can simulate the presence of irreversible displacements due, for instance, to the effects of the friction. Various phenomenological nonlinear models have been proposed in the literature to describe the softening response of structural elements made of masonry material. The available models adopted for structural computations are mainly based on macromechanical approaches using damage mechanics (34) and plasticity theory (39).

Among the others, Lotfi and Shing (35) developed smeared crack finite element analyses of masonry structures in order to assess the capability of this approach in capturing the strength and various failure mechanisms of masonry shear walls. They compared the numerical results with experimental data, investigating the objectivity of numerical results with respect to mesh size. Lourenço (37) presented an anisotropic continuum model based on multisurface plasticity, considering a Rankine type yield surface for tension and a Hill type yield surface for compression. The proposed model is completed with a computational algorithm which is used to perform comparisons between numerical and experimental results, available in the literature. Berto et al. (8) proposed an orthotropic damage model for the analysis of brittle masonry subjected to in-plane loading. The material model is governed by four independent internal damage parameters, one in compression and one in tension for each of the two natural axes of the masonry, and

it is able to account for the stiffness recovery at crack closure. Comparison between numerical results and experimental data are reported both for masonry shear panels and for a large-scale masonry wall. Dhanasekar and Haider (19) presented an explicit finite element analysis of masonry shear walls containing reinforcements. Ramalho et al. (56) developed a nonlinear finite element model to simulate the nonlinear response of a masonry construction, considering a nonlinear constitutive law governed by a damage tensor, which allows the damage-induced anisotropy accompanying the cracking process. The results of the numerical computations concerning the analysis of a three-leaf masonry specimens was put in comparison with the experimental data, remarking the effectiveness of the approach. Reyes et al. (57) presented a numerical procedure for fracture of brickwork masonry based on the strong discontinuity approach. The model, which takes into account the anisotropy of the material, has been implemented into a commercial code by means of a user subroutine. Comparison between numerical and experimental results have been provided, remarking that the proposed numerical procedure is able to accurately predict the experimental mixed-mode fracture for different orientations of the brick layers on masonry panels. Marques and Lourenço (43) presented a simple design tool based on structural component models for investigating the seismic assessment of a two-storey masonry building using pushover analysis. They demonstrated that macro-modeling can be adequate approaches for the seismic design of unreinforced masonry buildings, as the tool requires very low computational resources, allowing easy interpretation of results and provides satisfactory accuracy. Grande et al. (32) developed a simple beam finite element for the nonlinear analysis of masonry structures in the context of the "equivalent frame model". Numerical applications have been presented to assess the reliability of the proposed approach, performing comparisons between experimental results available in literature and the numerical predictions. Pelá et al. (53) presented a numerical model for nonlinear analysis of masonry structural elements based on orthotropic continuum damage mechanics. The capabilities of the model for representing the behavior of different types of brickwork masonry has been illustrated by means of simulations of experimental tests.

In the following, a phenomenological model for studying the mechanical response of masonry structural elements is presented. In particular, the plastic nonlocal damage model, resulting effective and computationally efficient, proposed in (1) is presented.

In order to take into account the mechanical properties degradation, a damage scalar variable is introduced in the constitutive law of the material. The damage is isotropic, i.e. the damage variable has the same influence on

all the stiffness matrix components.

As remarked in section 3, the softening constitutive relationships for cohesive materials lead to strain localization and produce mesh dependent results in finite element analyses. The nonlocal models are based on the introduction of a characteristic length that determines the size of the neighborhood of a typical point of the body which affects the nonlocal constitutive equation. A quite wide review of the nonlocal approaches can be found in (18). They can be based on integral models, gradient models and rate dependent damage models.

Herein, a regularization technique, based on the introduction of the damage Laplacian in the damage limit function, is adopted in order to account for the nonlocal effects in the material response.

4.1 Plastic-nonlocal damage model

Let the displacement, the strain and the stress fields defined in the two-dimensional body Ω, be denoted as $\mathbf{u} = \{u_1\ u_2\}^T$, $\boldsymbol{\varepsilon} = \{\varepsilon_1\ \varepsilon_2\ \gamma_{12}\}^T$ and $\boldsymbol{\sigma} = \{\sigma_1\ \sigma_2\ \tau_{12}\}^T$, respectively.

Next, a plastic-damage model, based on the following assumptions, is proposed:

- the damage evolution process is controlled by the elastic strain $\boldsymbol{\varepsilon}^e$ in tension, since experimental tests demonstrate that plastic response under tensile loading is negligible for cohesive materials, like masonry;
- the damage evolution process is controlled by the total strain $\boldsymbol{\varepsilon}$ in compression; in fact, plasticity plays a fundamental role in the material behavior in compression**;**
- the plastic deformation flow is governed by the effective stress $\widetilde{\boldsymbol{\sigma}}$, defined in the following.

The adopted stress-strain law is:

$$\begin{aligned} \boldsymbol{\sigma} &= (1-D)^2\ \mathbf{C}\ \boldsymbol{\varepsilon}^e \\ &= (1-D)^2\ \mathbf{C}\ (\boldsymbol{\varepsilon} - \boldsymbol{\varepsilon}^p) \end{aligned} \tag{52}$$

where $\boldsymbol{\varepsilon}^p$ is the plastic deformation, $\mathbf{C}$ is the elastic isotropic constitutive matrix and D is the damage variable.

Damage model The damage variable D is defined as the amount of microstructural defects in a typical section of the representative volume element and hence it represents a measure of the material degradation. For the isotropic damage model, as considered in the following, the variable D is a function only of the material point and it does not depend on the particular direction of the normal section.

From the relation between the stress and the strain (52), the effective constitutive matrix $\widetilde{\mathbf{C}}$, deduced by the complementary energy equivalence principle proposed by Sideroff (63), is defined as:

$$\widetilde{\mathbf{C}} = (1-D)^2\,\mathbf{C} \tag{53}$$

It can be pointed out that, since the damage variable D has an equal influence on all the components of the isotropic matrix $\mathbf{C}$, the relation (53) define an isotropic constitutive matrix during the whole damage process. The effective stress is defined as:

$$\widetilde{\sigma} = \frac{\sigma}{(1-D)^2} \tag{54}$$

The proposed model, able to describe the damage processes both in tension and in compression by means of a unique damage scalar variable D, is derived introducing a proper definition of the equivalent tensile and compressive deformations Y_t and Y_c as:

$$Y_t = \sqrt{< e_1^e >^2 + < e_2^e >^2} \qquad Y_c = \sqrt{< -e_1 >^2 + < -e_2 >^2} \tag{55}$$

The equivalent elastic and total strains e_i^e and e_i are defined as:

$$e_i^e = (1-2\nu)\hat{\varepsilon}_i^e + \nu(\hat{\varepsilon}_1^e + \hat{\varepsilon}_2^e) \qquad e_i = (1-2\nu)\hat{\varepsilon}_i + \nu(\hat{\varepsilon}_1 + \hat{\varepsilon}_2) \tag{56}$$

with $\hat{\varepsilon}_i^e$ and $\hat{\varepsilon}_i$ the elastic and total principal strains.

Then, the variable $\tilde{Y}$ is defined as:

$$\tilde{Y} = \frac{Y_t}{Y_t^0} + \frac{Y_c}{Y_c^0} \tag{57}$$

where $Y_t^0 > 0$ and $Y_c^0 > 0$ are the initial damage thresholds in tension and in compression, respectively. Hence, the quantity $\tilde{Y}$, defined by formula (57), represents an equivalent deformation, function of the principal positive and negative strains.

A suitable choice for the damage limit function is proposed:

$$F = \left(\tilde{Y} - 1\right) - \left(\tilde{a}\tilde{Y} + \tilde{K}\right) D + h^* \nabla^2 D \tag{58}$$

where $\nabla^2(\bullet) = \partial^2(\bullet)/\partial x_1^2 + \partial^2(\bullet)/\partial x_2^2$ is the Laplacian operator. The model constants $\tilde{K}$ and $\tilde{a}$ are defined on the basis of the material characteristic parameters K_t, K_c, a_t and a_c as:

$$\begin{array}{rcl} \tilde{a} & = & \alpha_t a_t + \alpha_c a_c \\ \tilde{K} & = & \alpha_t K_t / Y_{0t} + \alpha_c K_c / Y_{0c} \end{array} \tag{59}$$

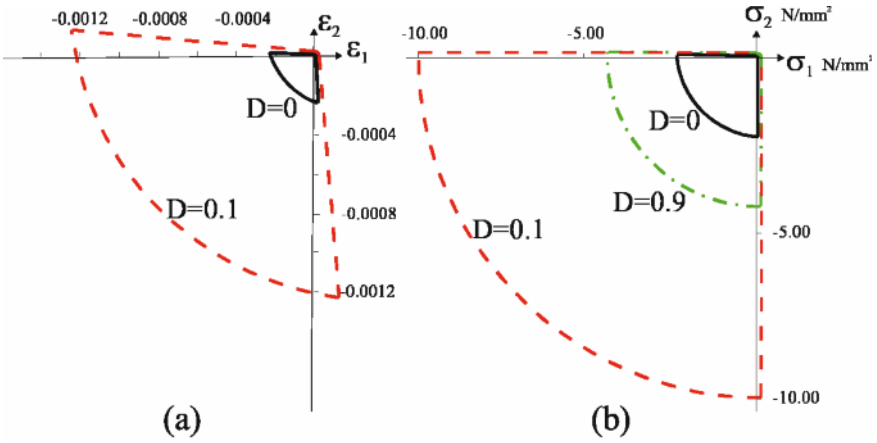

Figure 17. Evolution of the damage yield function in the strain (a) and stress plane (b).

where $K_{t/c} \geq 0$ and $0 \leq a_{t/c} \leq 1$ control the damage rate growth and the softening branch slope, respectively. The quantity $\alpha_{t/c}$ is defined as:

$$\alpha_t = \frac{\eta_t}{\eta_t + \eta_c} \quad , \quad \alpha_c = \frac{\eta_c}{\eta_t + \eta_c} \quad \Rightarrow \quad \alpha_t + \alpha_c = 1 \tag{60}$$

with

$$\eta_t = \frac{Y_t}{Y_{0t} + (a_t Y_t + K_t)\, D} \quad , \quad \eta_c = \frac{Y_c^e}{Y_{0c} + (a_c Y_c^e + K_c)\, D} \tag{61}$$

where

$$Y_c^e = \sqrt{< -e_1^e >^2 + < -e_2^e >^2} \tag{62}$$

In the figure 17(a) the damage function is schematically represented in the principal strain plane $\hat{\varepsilon}_1 - \hat{\varepsilon}_2$ and in the principal stress plane $\hat{\sigma}_1 - \hat{\sigma}_2$, for different values of the damage variable. Figure 17(b) shows the stress hardening and softening phases occurring during the damage evolution.

The nonlocal parameter h^*, linked to the characteristic length of the material, controls the size of the localization region. The determinations of the dimension of the internal length ℓ is an important and interesting issue. A procedure for the definition of h^* as function of ℓ is discussed in (1).

In the proposed model, the value of h^* is set as:

$$h^* = h \left(\frac{\alpha_t}{Y_{0t}} + \frac{\alpha_c}{Y_{0c}} \right) \tag{63}$$

where h is the constant nonlocal parameter used for the pure tensile and compressive states. Thus, h^* depends on the equivalent deformation Y. By substituting equations (59) and (63) into relation (58), the limit function takes the explicit form:

$$\begin{aligned} F &= \left(\frac{Y_t}{Y_{0t}} + \frac{Y_c}{Y_{0c}} - 1\right) \\ &- \left[(\alpha_t\, a_t + \alpha_c\, a_c)\left(\frac{Y_t}{Y_{0t}} + \frac{Y_c}{Y_{0c}}\right) + \left(\alpha_t \frac{K_t}{Y_{0t}} + \alpha_c \frac{K_c}{Y_{0c}}\right)\right] \\ &+ h\left(\frac{\alpha_t}{Y_{0t}} + \frac{\alpha_c}{Y_{0c}}]\right)\ \nabla^2 D \end{aligned} \tag{64}$$

The damage evolution is ruled by the consistency condition:

$$\dot{F}\dot{D} = 0 \tag{65}$$

together with the classical Kuhn-Tucker conditions:

$$\dot{D} \geq 0 \quad F \leq 0 \quad F\dot{D} = 0 \tag{66}$$

Equations (66) translates in mathematical form the mechanical condition of the irreversibility of the damage process. According to formulas (65) and (66) the points inside F represent the material states without damage evolution ($\dot{D} = 0$), while the points on the boundary of F represent possible damage evolution states ($\dot{D} > 0$). The damage parameter rate $\dot{D}$ is explicitly determined using the consistency condition (65) in the form:

$$\dot{F} = 0 \qquad \text{when} \quad \dot{D} > 0 \tag{67}$$

Applying the consistency condition (67) to the nonlocal limit function (64), the following partial differential equation is obtained:

$$\frac{\partial F}{\partial D}\dot{D} + \frac{\partial F}{\partial Y}\dot{Y} + \frac{\partial F}{\partial \nabla^2 D}\nabla^2 \dot{D} = 0 \qquad \text{with} \quad \dot{D} > 0 \tag{68}$$

where, it is:

$$\frac{\partial F}{\partial Y} = \frac{\partial F}{\partial Y_t}\frac{\partial Y_t}{\partial Y} + \frac{\partial F}{\partial Y_c}\frac{\partial Y_c}{\partial Y} = \frac{\partial F}{\partial Y_t}Y_{0t} + \frac{\partial F}{\partial Y_c}Y_{0c} \tag{69}$$

It can be remarked that the equation (69) contains the term $\nabla D \partial h^*/\partial Y$, i.e the adopted nonlocal regularization leads to a damage evolution process governed by the differential equation (68). Hence, the evaluation of the damage increment requires a resolution of a differential equation.

Note that the proposed damage model is based on a single damage parameter and, as consequence, crack closure effects cannot accounted for. In order to take into account the crack closure a two damage variables model, one in tension and one in compression, has to be formulated.

4.2 Plastic model

A plastic model with isotropic hardening, which accounts for the different material strength in tension and in compression is introduced. A plastic limit function $F_P = F_P(\widetilde{\sigma}, q)$, which depends on the effective stress $\widetilde{\sigma}$ defined in equation (54) and on the thermodynamic force q, is considered. The force q is associated to the internal variable α by the relation:

$$q = -\chi\ \alpha \tag{70}$$

where χ is the hardening parameter.

The evolution laws are ruled by the equations:

$$\dot{\varepsilon}^P = \dot{\lambda}_P \frac{\partial F_P}{\partial \widetilde{\sigma}} \tag{71}$$

$$\dot{\alpha} = \dot{\lambda}_P \frac{\partial F_P}{\partial q} \tag{72}$$

$$F_P \leq 0 \qquad \dot{\lambda}_P \geq 0 \qquad F_P \dot{\lambda}_P = 0 \tag{73}$$

where $\dot{\lambda}_P$ is the plastic multiplier rate.

The following yield function F_P is considered:

$$F_P\left(\widetilde{\sigma}, q\right) = 3J_2 + \left(\sigma_c - \sigma_t\right)\ I_1 - \sigma_c\ \sigma_t + q \tag{74}$$

where σ_c and σ_t are the compressive and tensile yield stresses, respectively, I_1 is the first stress tensor invariant and J_2 is the second deviatoric stress invariant, defined as:

$$I_1 = \widetilde{\sigma}_1 + \widetilde{\sigma}_2 \tag{75}$$

$$J_2 = \frac{1}{6}\left[\left(\widetilde{\sigma}_1 - \widetilde{\sigma}_2\right)^2 + \widetilde{\sigma}_1^2 + \widetilde{\sigma}_2^2 + 6\widetilde{\tau}_{12}^2\right]$$

4.3 Plastic-damage rate problem

According to the proposed plastic-damage model, the rate problem is governed by the plastic and damage evolution laws:

$$\dot{\sigma} = (1-D)^2\ \mathbf{C}\ \left(\dot{\varepsilon} - \dot{\varepsilon}^P\right) - 2\ (1-D)\dot{D}\ \mathbf{C}\ \left(\varepsilon - \varepsilon^P\right) \tag{76}$$

$$\begin{aligned} &\dot{\varepsilon}^P = \dot{\lambda}_P \frac{\partial F_P}{\partial \widetilde{\sigma}} = \dot{\lambda}_P \left[\left(\sigma_c - \sigma_t\right)\ \frac{\partial I_1}{\partial \widetilde{\sigma}} + 3\frac{\partial J_2}{\partial \widetilde{\sigma}}\right] \\ &\dot{\alpha} = \dot{\lambda}_P \frac{\partial F_P}{\partial q} = \dot{\lambda}_P \\ &F_P \leq 0 \qquad \dot{\lambda}_P \geq 0 \qquad F_P \dot{\lambda}_P = 0 \end{aligned} \tag{77}$$

$$\begin{aligned} F &\leq 0 \qquad \dot{D} \geq 0 \qquad F\dot{D} = 0 \\ \dot{F} &= -(aY + K)\dot{D} + \left(1 - aD + \nabla^2 D \frac{\partial h^*}{\partial Y}\right)\dot{Y} \\ &\quad + h^* \nabla^2 \dot{D} = 0 \qquad\qquad \text{with } \dot{D} > 0 \end{aligned} \tag{78}$$

As already underlined, a differential equation has to be solved to evaluate $\dot{D}$, because of the presence of Laplacian in the limit function F. Moreover, it can be pointed out that the plastic deformation increment can be evaluated locally, also for the nonlocal damage model.

The rate damage law (78) can be rewritten in weak form (16), resulting as:

$$0 = \int_{\Omega_D} \dot{F}\ \delta\dot{D}\ d\Omega \quad \text{with } \dot{D}\ > 0 \tag{79}$$

where $\delta\dot{D}$ represents the virtual variation of the damage variable and Ω_D represents the part of the whole domain Ω where damage evolution is occurring at the current time, i.e.:

$$\Omega_D = \left\{ X \in \Omega \qquad / \qquad \dot{D}\,(X) > 0 \right\}$$

with X typical point of the material body Ω.

Integrating by parts equation (79), it results:

$$\begin{aligned} 0 &= \int_{\Omega_D} \left[-(aY + K)\dot{D} + \left(1 - aD + \nabla^2 D \frac{\partial h^*}{\partial Y}\right)\dot{Y} \right] \delta\dot{D}\ dV \\ &\quad - \int_{\Omega_D} h^* \nabla\dot{D} \cdot \delta\nabla\dot{D}\ dV + \int_{\partial\Omega_D} \left(\nabla\dot{D} \cdot \mathbf{n}\right) \delta\dot{D}\ dA \end{aligned} \tag{80}$$

The following boundary conditions arise from equation (80):

$$\left(\nabla\dot{D} \cdot \mathbf{n}\right) \dot{D} = 0 \qquad \text{on } \partial\Omega_D \tag{81}$$

leading to:

$$\begin{aligned} &\text{if } X \in \partial\Omega_D \text{ and } X \notin \partial\Omega \qquad \text{then} \quad \dot{D} = 0 \\ &\text{if } X \in \partial\Omega_D \text{ and } X \in \partial\Omega \qquad \text{then} \quad \nabla\dot{D} \cdot \mathbf{n} = 0 \end{aligned} \tag{82}$$

The damage evolution equation (79) is formulated as the stationary condition of a constrained minimization problem of a convex functional (16; 1).

In fact, it can be proved that equation (80) is equivalent to the minimization problem:

$$\min \left\{ L\left(\dot{D}\right) \qquad / \qquad \dot{D} \geq 0 \right\} \tag{83}$$

where the functional L is defined as:

$$L\left(\dot{D}\right) = \int_{\Omega} \left[\left(aY + K\right) \frac{\dot{D}^2}{2} - \left(1 - aD + \nabla^2 D \frac{\partial h^*}{\partial Y}\right) \dot{D}\dot{Y} + \frac{h^*}{2} \nabla\dot{D} \cdot \nabla\dot{D} \right] d\Omega \tag{84}$$

Note that, the problem (83) is completed with the further constraint:

$$0 \leq D \leq 1 \qquad\qquad \text{in } \Omega \tag{85}$$

Finally, the solution of the evolution elasto-plastic nonlocal damage problem is determined solving the plasticity evolution problem (77) and the minimization problem (83) under the constraint (82) and (85).

In order to solve the evolutionary equations (76), (77) and the minimization problem (83), a predictor-corrector solution procedure based on the splitting method within a time discretization algorithm, is adopted.

In the predictor phase, the elasto-plastic problem is solved, taking the damage evolution frozen. On the other hand, in the corrector phase, the damage field increment is evaluated solving the minimization constrained problem and considering the total and the plastic deformation as constant. Hence, the solution algorithm consists in the following two steps:

- an elasto-plastic predictor phase, with a plastic corrector; in this phase, the consistent elasto-plastic tangent operator is computed,
- a damage evaluation phase; in this phase, the total and plastic strains are assumed as frosen.

The integration of the evolutionary equations (76), (77) and (83) is performed developing a backward-Euler implicit integration procedure (64).

4.4 Numerical applications

Some numerical applications are developed to analyze the mechanical response of two-dimensional structural elements made of masonry material.

The proposed elasto-plastic nonlocal damage model is adopted to reproduce the constitutive behavior of the masonry material. The following values for the model parameters are assumed:

- **elastic parameters**:

  $$E = 1.0 \cdot 10^4 \,\text{MPa} \qquad \nu = 0.1$$

  where E and ν are the Young's modulus and the Poisson ratio, respectively

- **damage parameters**:

$$\begin{array}{ll} Y_{0t} = 1.0 \cdot 10^{-5} & Y_{0c} = 2.0 \cdot 10^{-4} \\ K_t = 1.0 \cdot 10^{-4} & K_c = 8.0 \cdot 10^{-3} \\ a_t = 0.9 & a_c = 0.9 \end{array}$$

- **plastic parameters**:

$$\begin{array}{ll} \sigma_t = 10.0\,\text{MPa} & \sigma_c = 10.0\,\text{MPa} \\ \chi = 1.0 \cdot 10^6\,\text{MPa} & \end{array}$$

The value of the damage parameter h is related to the internal length ℓ of the material. For masonry walls it can be set $\ell = 300$ mm, which corresponds about to $h = 100\,\text{mm}^2$.

Three masonry panels, schematically reported in figure 18, subjected to pure shear loading are analyzed. They are characterized by the following geometrical parameters:

$$\begin{array}{lll} \text{wall1} & H = 4000\,\text{mm} & B = 6000\,\text{mm} \\ \text{wall2} & H = 4000\,\text{mm} & B = 4000\,\text{mm} \\ \text{wall3} & H = 6000\,\text{mm} & B = 4000\,\text{mm} \end{array}$$

The adopted material properties of the masonry are reported above. Meshes obtained adopting 4-node elements are considered for the computations. In particular, wall1 is discretized by 15×20 elements, wall2 by 15×15 elements and wall3 by 20×15 elements.

In figures 19, 20 and 21, the damage and the minimum principal stress maps for the prescribed displacement $u_1 = 6\,\text{mm}$ are plotted for wall1, wall2 and wall3, respectively (figure 18). It can be noted that the failure mechanism is characterized by the formation, growth and propagation of inclined damage bands, as it typically occurs in masonry panels subjected to horizontal forces, e.g. seismic loading.

Because of the different geometrical properties of the three walls, the damaging process in wall1 and wall2 is concentrated in a single band, while in the widest panel, denoted as wall3, two damage bands appear. Then, as it can be seen in figures 19(b), 20(b) and 21(b), the resistant part of the walls consists in compressive inclined trusses carrying the external applied load. These compressive zones are separated by the damage bands.

In figure 22, the load versus the prescribed displacement is plotted for wall1 adopting three different discretizations, consisting in $15 \times 20 = 300$, $20 \times 30 = 600$ and $30 \times 40 = 1200$ quadrilateral elements. According to the adopted discretizations, the minimum and maximum element dimensions

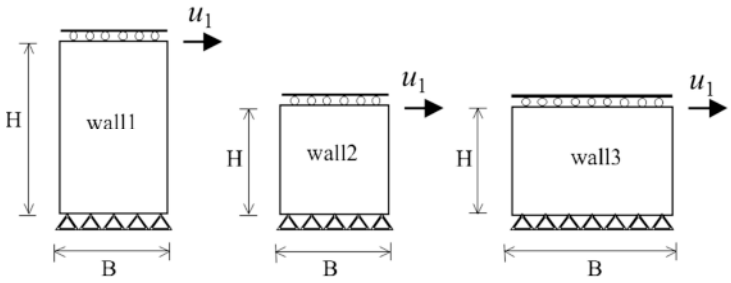

Figure 18. Masonry walls subjected to shear action.

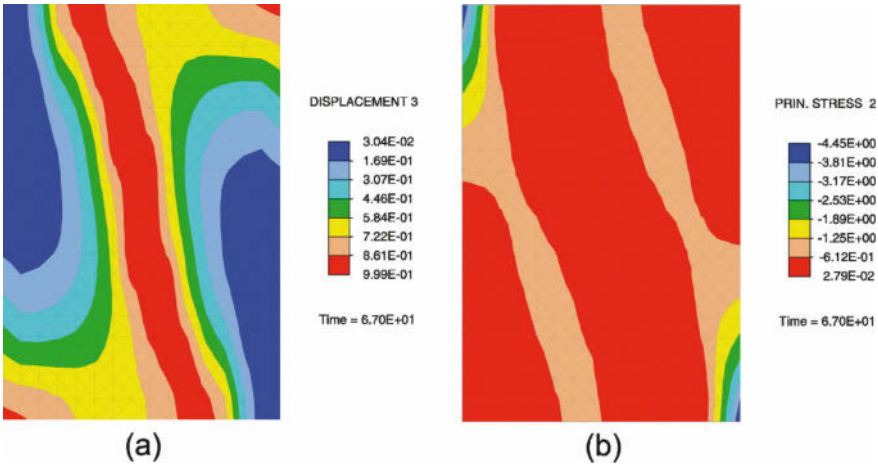

Figure 19. Damage (a) and minimal normal stress distribution (b) for the wall1.

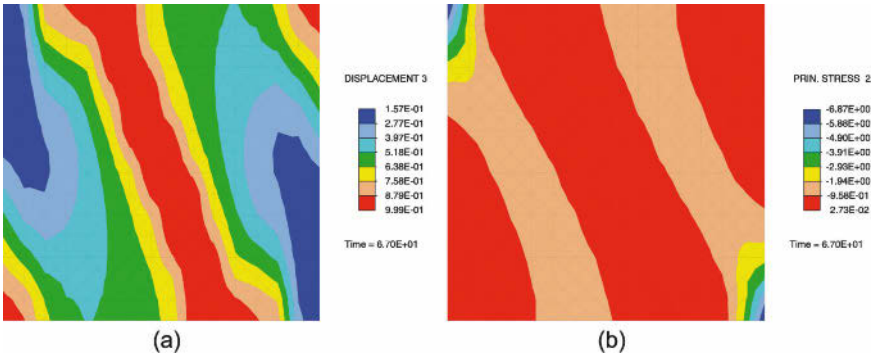

Figure 20. Damage (a) and minimal normal stress distribution (b) for the wall2.

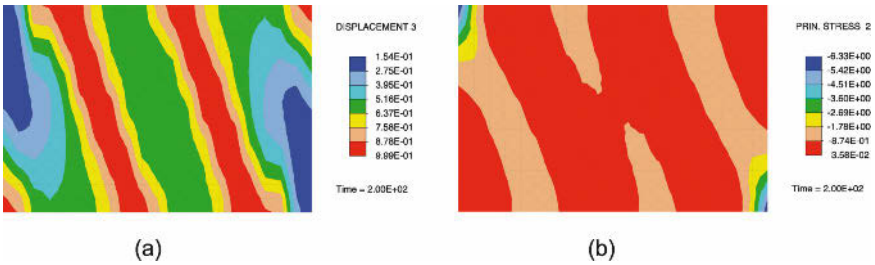

Figure 21. Damage (a) and minimal normal stress distribution (b) for the wall3.

are 133.33 mm and 266.67 mm, respectively; since the masonry damage localization size is taken 600 mm, it results that the mesh size is lower than the damage length.

It can be noted that the mechanical response of wall1 subjected to shear loading is characterized by:

- an initial elastic response;
- a damage phase characterized by hardening response;
- a first steep softening branch due to the damage propagation, concentrated where the maximum tensile strains occur;
- a hardening phase during which the plastic evolution process becomes more significant than the damage one;
- a softening branch due to the formation and growth of the damage band.

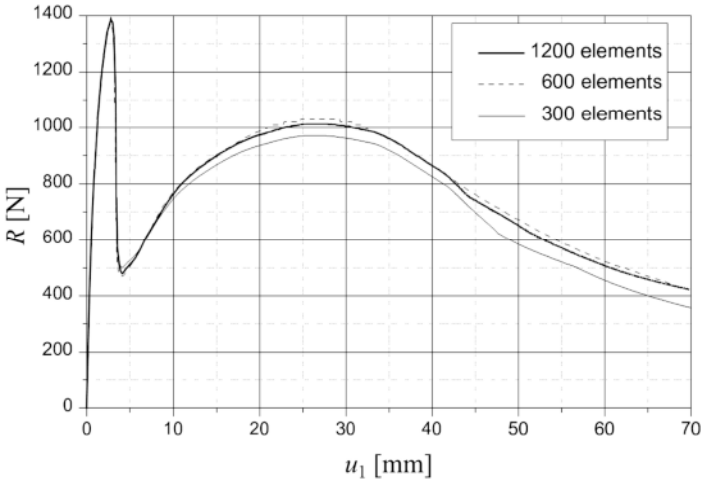

Figure 22. Mechanical response of wall1 in terms of base force vs top displacement for three different discretizations.

It can be remarked that the regularization technique, herein adopted, leads to numerical results characterized by a satisfactory mesh independence.

In figure 23 the load versus the prescribed displacement is plotted for wall1, wall2 and wall3. It can be noted that the different geometrical properties of the three walls lead to different shear strength and compliance. In particular, wall3 is characterized by a shear strength significantly higher than the other two walls, while wall1 is the most deformable. Finally, it can be pointed out that the overall response of wall2 and wall3 is similar to that of wall1 described above.

5 Conclusions

The modeling of masonry structures is an interesting and important problem related both to the safety of historical and monumental constructions and to the safeguard of the human lives of many people who live in masonry buildings.

Even limiting the interest only to the computational modeling of ma-

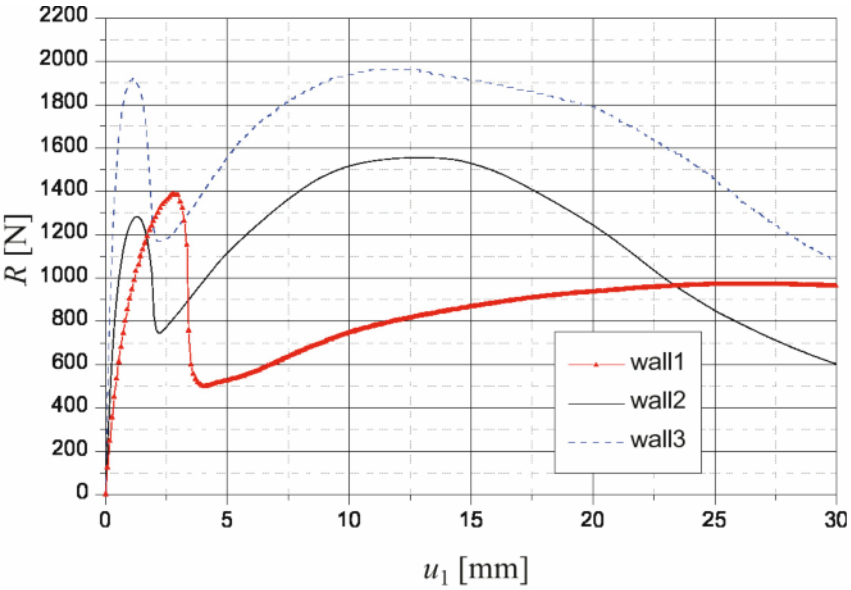

Figure 23. Mechanical response of the three walls in terms of base force vs top displacement.

sonry structures, the approaches illustrated in this chapter are absolutely not exhaustive. In fact, other approaches can be found in literature; for instance, one of the most adopted for design intents is the so-called macro-element approach, which has not been treated herein.

Moreover, for each considered approach only one (specific) model is presented, while a great variety of models are available within each approach. For instance, in the framework of the macro-models it is neither discussed nor presented the no-tension model which can lead to very interesting results and can be considered very effective in several cases; on the other hand, the no-tension model is object of other chapters in this book.

The main conclusion of the discussion on the different modeling approaches for masonry constructions is that all the approaches can satisfactory reproduce the response of specific masonry elements, there is no one that can be considered in absolute better than the others. On the contrary, each approach can be more appropriate for specific typologies of masonry structures. For instance, the micromechanical approach can be satisfactory adopted to reproduce the response of small size (laboratory) elements or of

structures characterized by big blocks, in which the size of the blocks has the same order of magnitude of the size of the structural element. On the contrary, it is less suitable for the analysis of large structures because of the required great computational effort and for the difficulty in adequately describing the specific geometry of the whole masonry texture, i.e. the position of each brick or block in the structure.

As consequence, the most suitable approach for the stress analysis depends on the typology and on the characteristics of masonry elements; the choice of the most appropriate approach and, then, of the most suitable model depends on masonry construction, on the specific masonry behavior and on the knowledge of the material parameters of the material.

Acknowledgments

This chapter contains the results of the researches developed together with Daniela Addessi, Giulio Alfano, Sonia Marfia and Jessica Toti, who are deeply and kindly thanked for their nice and fruitful collaboration. Without their work this chapter would be not written.

Bibliography

[1] D. Addessi, S. Marfia, and E. Sacco. A plastic nonlocal damage model. *Computer Methods in Applied Mechanics and Engineering*, 191:1291–1310, 2002.

[2] D. Addessi and E. Sacco. A multi-scale enriched model for the analysis of masonry panels. *International Journal of Solids and Structures*, 49:865–880, 2012.

[3] D. Addessi, E. Sacco, and A. Paolone. Cosserat model for periodic masonry deduced by nonlinear homogenization. *European Journal of Mechanics - A/Solids*, 29:724–737, 2010.

[4] G. Alfano, S. Marfia, and E. Sacco. A cohesive damage-friction interface model accounting for water pressure on crack propagation. *Computer Methods in Applied Mechanics and Engineering*, 196:192–209, 2006.

[5] G. Alfano and E. Sacco. Combining interface damage and friction in a cohesive-zone model. *International Journal for Numerical Methods in Engineering*, 68(5):542–582, 2006.

[6] A. Anthoine. Derivation of the in-plane elastic characteristics of masonry through homogenization theory. *International Journal of Solids and Structures*, 32(2):137–163, 1995.

[7] G. I. Barenblatt. The mathematical theory of equilibrium cracks in the brittle fracture. *Advances in Applied Mechanics*, 7:55–129, 1962.

[8] L. Berto, A. Saetta, R. Scotta, and R. Vitaliani. An orthotropic damage model for masonry structures. *International Journal for Numerical Methods in Engineering*, 55:127–157, 2002.

[9] S. Brasile, R. Casciaro, and G. Formica. Multilevel approach for brick masonry walls part i: A numerical strategy for the nonlinear analysis. *Computer Methods in Applied Mechanics and Engineering*, 196:4934–4951, 2007.

[10] S. Brasile, R. Casciaro, and G. Formica. Multilevel approach for brick masonry walls part ii: On the use of equivalent continua. *Computer Methods in Applied Mechanics and Engineering*, 196:4801–4810, 2007.

[11] I. Cancelliere, M. Imbimbo, and E. Sacco. Numerical and experimental study of masonry arches. *Engineering Structures*, 32:776–792, 2010.

[12] S. Casolo. Macroscopic modelling of structured materials: Relationship between orthotropic Cosserat continuum and rigid elements. *International Journal of Solids and Structures*, 43(3-4):475–496, 2006.

[13] N. Cavalagli, F. Cluni, and V. Gusella. Strength domain of non-periodic masonry by homogenization in generalized plane state. *European Journal of Mechanics A/Solids*, 30:113–126, 2011.

[14] Antonella Cecchi and Karam Sab. Discrete and continuous models for in plane loaded random elastic brickwork. *European Journal of Mechanics - A/Solids*, 28:610–625, 2009.

[15] J.L. Chaboche, S. Kruch, J.F. Maire, and T. Pottier. Towards a micromechanics based inelastic and damage modeling of composites. *International Journal of Plasticity*, 17:411–439, 2001.

[16] C. Comi. Computational modelling of gradient-enhanced damage in quasi-brittle materials. *Mech Coh.-Frictional Mater.*, 4:17–36, 1999.

[17] M.L. De Bellis and D. Addessi. A Cosserat based multi-scale model for masonry structures. *International Journal of Computational Engineering*, 9:543–563, 2011.

[18] Francesco Marotti de Sciarra. A nonlocal model with strain-based damage. *International Journal of Solids and Structures*, 46(22-23):4107 – 4122, 2009.

[19] M. Dhanasekar and W. Haider. Explicit finite element analysis of lightly reinforced masonry shear walls. *Computers and Structures*, 86:15–26, 2008.

[20] D.S. Dugdale. Yielding of steel sheets containing slits. *J. Mech. Phys. Solids*, 8:100–104, 1960.

[21] G.J. Dvorak. Transformation field analysis of inelastic composite materials. *Proceedings of the Royal Society of London A*, 437:311–327, 1992.

[22] G.J. Dvorak and A. Bahei-El-Din. Inelastic composite materials: transformation field analysis and experiments. In P. Sequet, editor, *Continuum Micromechanics, CISM Course and Lecture 377*, pages 1 – 59. Springer, Berlin, 2005.

[23] J. Fish and K. Shek. Multiscale analysis of composite materials and structures. *Composites Science and Technology*, 60:2547–2556, 2000.

[24] S. Forest and K. Sab. Cosserat overall modelling of heterogeneous materials. *Mechanics Research Communications in Numerical Methods in Engineering*, 4:449–454, 1998.

[25] F. Fouchal, F. Lebon, and I. Titeux. Contribution to the modelling of interfaces in masonry construction. *Construction and Building Materials*, 23:2428–2441, 2009.

[26] F. Fritzen and T. Bhlke. Nonuniform transformation field analysis of materials with morphological anisotropy. *Composites Science and Technology*, 71:433–442, 2011.

[27] L. Gambarotta and S. Lagomarsino. Damage models for the seismic response of brick masonry shear walls part i: the mortar joint model and its application. *Earthquake Engineering and Structural Dynamics*, 26:423–439, 1997.

[28] L. Gambarotta and S. Lagomarsino. Damage models for the seismic response of brick masonry shear walls part ii: the continuum model and its application. *Earthquake Engineering and Structural Dynamics*, 26:441–462., 1997.

[29] G. Giambanco and L. Di Gati. A cohesive interface model for the structural mechanics of block masonry. *Mechanics Research Communications*, 24(5):503–512, 1997.

[30] G. Giambanco, G. Fileccia Scimemi, and A. Spada. The interphase finite element. *Computational Mechanics*, 50:353–366, 2012.

[31] G. Giambanco and Z. Mroz. The interphase model for the analysis of joints in rock masses and masonry structures. *Meccanica*, 36:111–130, 2001.

[32] E. Grande, M. Imbimbo, and E. Sacco. A beam finite element for nonlinear analysis of masonry elements with or without fiber-reinforced plastic (frp) reinforcements. *International Journal of Architectural Heritage*, 5:693–716, 2011.

[33] B. Kralj, G.K. Pande, and J. Middleton. On the mechanics of frost damage to brick masonry. *Computers and Structures*, 41:53–66, 1991.

[34] J. Lemaitre and J.L. Chaboche. *Mechanics of Solid Materials*. Cambridge University Press, 1990.

[35] H.R Lofti and B.P. Shing. An appraisal of smeared crack models for masonry shear wall analysis. *Computers and Structures*, 41:413–425, 1991.

[36] H.R Lofti and B.P. Shing. Interface model applied to fracture of masonry structures. *Journal of Structural Engineering*, 120:63–80, 1994.

[37] P. B. Lourenço. *Computational Strategies for Masonry Structures*. PhD thesis, Delft University of Technology, 1996.

[38] P. B. Lourenço and J. G. Rots. Multisurface interface model for analysis of masonry structures. *Journal of Engineering Mechanics*, 123(7):660–668, 1997.

[39] J. Lubliner. *Plasticity Theory*. Macmillan Publishing Company, New York, 1990.

[40] R. Luciano and E. Sacco. Homogenization technique and damage model for old masonry material. *International Journal of Solids and Structures*, 32(24):3191–3208, 1997.

[41] R. Luciano and E. Sacco. Variational methods for the homogenization of periodic heterogeneous media. *European Journal of Mechanics - A/Solids*, 17(4):599–617, 1998.

[42] S. Marfia and E. Sacco. Multiscale damage contact-friction model for periodic masonry walls. *Computer Methods in Applied Mechanics and Engineering*, 205-208:189–203, 2012.

[43] R. Marques and P.B. Lourenço. Possibilities and comparison of structural component models for the seismic assessment of modern unreinforced masonry buildings. *Computers and Structures*, 89:2079–2091, 2011.

[44] R. Masiani, R. Rizzi, and P. Trovalusci. Masonry as structured continuum. *Meccanica*, 30(6):673–683, 1995.

[45] R. Masiani and P. Trovalusci. Cauchy and Cosserat materials as continuum models of brick masonry. *Meccanica*, 31(4):421432., 1996.

[46] T. J. Massart, R. H. J. Peerlings, and M. G. D. Geers. An enhanced multi-scale approach for masonry wall computations with localization of damage. *International Journal for Numerical Methods in Engineering*, 69(5):1022–1059, 2007.

[47] B.C.N. Mercatoris and T.J. Massart. A coupled two-scale computational scheme for the failure of periodic quasi-brittle thin planar shells and its application to masonry. *International Journal for Numerical Methods in Engineering*, 85:1177–1206, 2011.

[48] J.C. Michel and P. Suquet. Nonuniform transformation field analysis. *International Journal for Solids and Structures*, 40:6937–6955, 2003.

[49] G. Milani, P. B. Lourenço, and Tralli. Homogenization approach for the limit analysis of out-of-plane loaded masonry walls. *Journal of Structural engineering*, 132:1650–1663, 2006.

[50] T. Mura. *Micromechanics of defects in solid*. Martinus, 1987.

[51] D.V. Oliveira and Lourenço P.B. Implementation and validation of a constitutive model for the cyclic behaviour of interface elements. *Computers & Structures*, 82:1451–1461, 2004.

[52] P. Pegon and A. Anthoine. Numerical strategies for solving continuum damage problems with softening: application to the homogenization of masonry. *Computers & Structures*, 64:623–642, 1997.

[53] L. Pel, M. Cervera, and P. Roca. An embedded cohesive crack model for finite element analysis of brickwork masonry fracture. *Construction and Building Materials*, http://dx.doi.org/10.1016/j.conbuildmat.2012.07.014, 2012.

[54] S. Pietruszczak and X. Niu. A mathematical description of macroscopic behaviour of brick masonry. *International Journal of Solids and Structures*, 29(5):531–546, 1992.

[55] T. M. J. Raijmakers and A. T. Vermeltfoort. *Deformation controlled tests in masonry shear walls, In: Report B-92-1156*. TNO-Bouw, Delft, The Netherlands, 1992.

[56] M.A Ramalho, A. Taliercio, A. Anzani, L. Binda, and E. Papa. A numerical model for the description of the nonlinear behaviour of multileaf masonry walls. *Advances in Engineering Software*, 39:249–257, 2008.

[57] E. Reyes, J.C. Galvez, M.J. Casati, D.A. Cendon, J.M. Sancho, and J. Planas. An embedded cohesive crack model for finite element analysis of brickwork masonry fracture. *Engineering Fracture Mechanics*, 76:1930–1944, 2009.

[58] E. Sacco and F. Lebon. A damage-friction interface model derived from micromechanical approach. *International Journal of Solids and Structures*, 49:3666–3680, 2012.

[59] E. Sacco and J. Toti. Interface elements for the analysis of masonry structures. *International Journal for Computational Methods in Engineering Science and Mechanics*, 11:354–373, 2010.

[60] Elio Sacco. A nonlinear homogenization procedure for periodic masonry. *European Journal of Mechanics - A/Solids*, 28(2):209–222, 2009.

[61] G. Salerno and G. de Felice. Continuum modeling of periodic brickwork. *International Journal of Solids and Structures*, 46(5):1251–1267, 2009.

[62] V. Sepe, S. Marfia, and E. Sacco. A nonuniform tfa homogenization technique based on piecewise interpolation functions of the inelastic field. *International Journal of Solids and Structures*, 50:725–742, 2013.

[63] F. Sideroff. Description of anisotropic damage application to elasticity. In *Proceeding of IUTAM Colloquium on Physical Nonlinearrities in Structural Analysis*, pages 237–244. Springer. Berlin, 1981.

[64] J.C. Simo and T. J. R. Hughes. *Computational Inelasticity*. New Yok: Springer, 1998.

[65] P. Suquet. *Elements of homogenization for inelastic solid mechanics. In Homogenization Techniques for Composite Media*. Springer-Verlag, Berlin., 1987.

[66] R.L. Taylor. *FEAP-A finite element analysis program, Version 8.3*. Department of Civil and Environmental Engineering, University of California at Berkeley, California, 2011.

[67] G. Uva and G. Salerno. Towards a multiscale analysis of periodic masonry brickwork: A fem algorithm with damage and friction. *International Journal of Solids and Structures*, 43:3739–3769, 2006.

[68] X. Wei and H. Hao. Numerical derivation of homogenized dynamic masonry material properties with strain rate effects. *International Journal of Impact Engineering*, 36:522–536, 2009.

[69] O. C. Zienkiewicz and R. L. Taylor. *The finite element method. Fourth edition*, volume 1. McGraw-Hill Publ., New York, 1991.

[70] A. Zucchini and P.B. Lourenço. A micromechanical homogenisation model for masonry: Application to shear walls. *International Journal of Solids and Structures*, 46(3-4):871 – 886, 2009.

Homogenization and Seismic Assessment: Review and Recent Trends

Paulo B. Lourenço * and Gabriele Milani †

* Institute for Sustainability and Innovation in Structural Engineering (ISISE), Department of Civil Engineering, University of Minho, Portugal

† Department of Architecture, Built environment and Construction engineering (A.B.C.), Politecnico di Milano, Italy

Abstract The mechanics of masonry structures has been for long underdeveloped in comparison with other fields of knowledge. Presently, non-linear analysis is a popular field in masonry research and advanced computer codes are available for researchers and practitioners. The chapter presents a discussion of masonry behaviour and clarifies how to obtain the non-linear data required by the computations. The chapter also addresses different homogenisation techniques available in the literature in the linear and rigid-plastic case, aiming at defining a catalogue and at discussing the advantages and disadvantages of the different approaches. Special attention is given to stress assumed models based either on a polynomial expansion of the micro-stress field or in the discretization of the unit cell by means of a few constant stress finite elements CST with joints reduced to interfaces. Finally, the aspects of seismic assessment are presented and case studies involving the use of macro-block analysis, static (pushover) analysis and time integration analysis are discussed.

Keywords: masonry, non-linear data, homogenisation, limit analysis, Finite Elements, seismic assessment

1 Homogenization Theory, Basic Assumptions

This section briefly recalls the basis of the theory of homogenization applied to masonry structures, with particular emphasis on running bond texture. Consider a masonry wall Ω, constituted by the periodic arrangements of masonry units and mortar joints as shown in Figure 1. The periodicity

M. Angelillo (Ed.), *Mechanics of Masonry Structures*, CISM International Centre for Mechanical Sciences, DOI 10.1007/ 978-3-7091-1774-3_7,

allows to regard Ω as the repetition of a representative element of volume Y (REV or elementary cell).

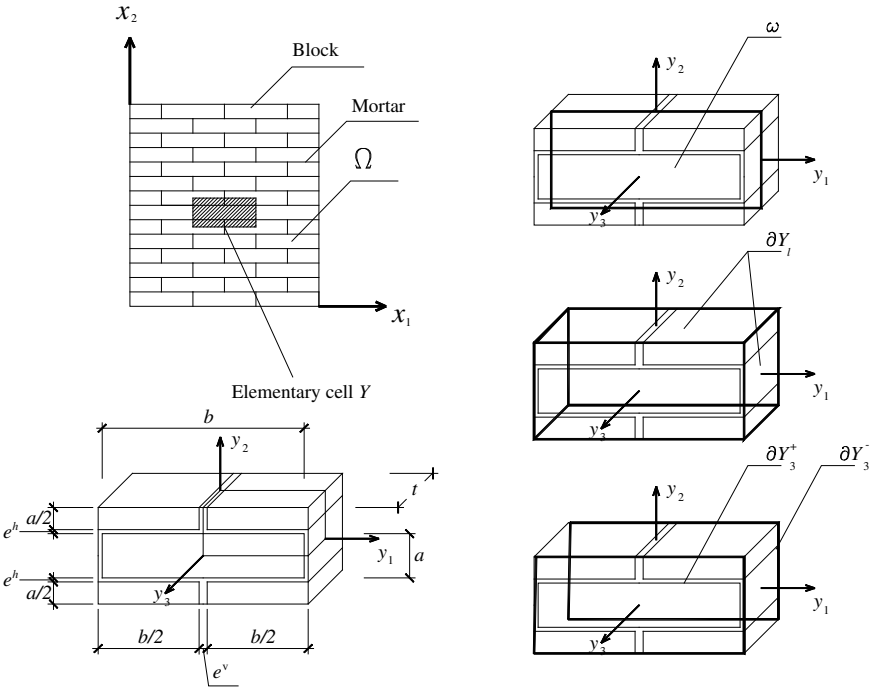

Figure 1. Representative Element of Volume (REV) for running bond masonry

Let $\mathbf{x} = [x_1, x_2]$ be a frame of reference for the global description of Ω (macroscopic scale) and $\mathbf{y} = [y_1, y_2, y_3]$ a frame of reference for Y. The Y module is defined as $Y = \omega \times \left[-\frac{t}{2}, \frac{t}{2}\right]$, where $Y \in \Re^3$ is the elementary cell and $\omega \in \Re^2$ represents the middle plane of the plate (Caillerie, 1984). The ∂Y boundary surface of the elementary cell is shown also in Figure 1.

The basic idea of homogenization consists in introducing averaged quantities representing the macroscopic stress and strain tensors (denoted here respectively as $\mathbf{E}$ and $\mathbf{\Sigma}$), as follows:

$$\mathbf{E} = \langle \boldsymbol{\epsilon} \rangle = \frac{1}{V} \int_Y \boldsymbol{\epsilon}\,(\mathbf{u})\ \mathrm{d}Y \quad \mathbf{\Sigma} = \langle \boldsymbol{\sigma} \rangle = \frac{1}{V} \int_Y \boldsymbol{\sigma}\,\mathrm{d}Y \tag{1}$$

where V stands for the volume of the elementary cell, $\boldsymbol{\epsilon}$ and $\boldsymbol{\sigma}$ stand for

the local quantities (stresses and strains respectively) and $\langle * \rangle$ is the average operator.

According to Anthoine (1995) and Cecchi et al. (2005) the homogenization problem in the linear elastic range in presence of coupled membranal and flexural loads, under the assumption of the Kirchhoff-Love plate theory, can be written as follows:

$$\left.\begin{array}{ll} \operatorname{div} \boldsymbol{\sigma} = \mathbf{0} & (a) \\ \boldsymbol{\sigma} = \boldsymbol{a}(\boldsymbol{y})\boldsymbol{\epsilon} & (b) \\ \boldsymbol{\epsilon} = \mathbf{E} + y_3\boldsymbol{\chi} + \operatorname{sym}\,(\operatorname{grad} \mathbf{u}^{per}) & (c) \\ \boldsymbol{\sigma}\mathbf{e}_3 = 0 \text{ on } \partial Y_3^+ \text{ and } \partial Y_3^- & (d) \\ \boldsymbol{\sigma}\mathbf{n} \text{ antiperiodic on } \partial Y_l & (e) \\ \mathbf{u}^{per} \text{ periodic on } \partial Y_l & (f) \end{array}\right\} \tag{2}$$

where $\boldsymbol{\sigma}$ is the microscopic stress tensor (micro-stress), $\mathbf{u}^{per}$ is a ω-periodic displacement field, $\mathbf{E}$ is the macroscopic in-plane strain tensor, $\boldsymbol{\chi}$ is the out-of-plane strain tensor (curvature tensor), $\boldsymbol{a}(\boldsymbol{y})$ represents a ω-periodic linear elastic constitutive law for the components (masonry units and mortar), as given in equation (2b). Equation (2a) represents the micro-equilibrium for the elementary cell with zero body forces, usually neglected in the framework of homogenization.

Furthermore, in equation (2c), the micro-strain tensor $\boldsymbol{\epsilon}$ is obtained as a linear combination among macroscopic $\mathbf{E}$ and $\boldsymbol{\chi}$ tensors and a periodic strain field. $\mathbf{E}$ and $\boldsymbol{\chi}$ tensors are related to $\boldsymbol{a}(\boldsymbol{y})$ represents a ω-periodic linear elastic constitutive law for the components (masonry units and mortar), as given in equation (2b). Equation (2a) represents the micro-equilibrium for the elementary cell with zero body forces, usually neglected in the framework of homogenization. The macroscopic displacement field components $U_1(x_1, x_2)$, $U_2(x_1, x_2)$ and $U_3(x_1, x_2)$ by means of the classic relations $\mathbf{E}_{\alpha\beta} = \frac{1}{2}\left(U_{\alpha,\beta} + U_{\beta,\alpha}\right)$, with $\mathbf{E}_{i3} = 0$, and $\chi_{\alpha\beta} = -U_{3,\alpha\beta}$ with $\chi_{i3} = 0$, $\alpha, \beta = 1, 2$ and $i = 1, 2, 3$.

Macroscopic homogenized membrane and bending constants can be obtained solving the elastostatic problem (2) and making use of the classic relations:

$$\begin{aligned} \mathbf{N} &= \langle \boldsymbol{\sigma} \rangle^* = \mathbf{A}\mathbf{E} + \mathbf{A}\boldsymbol{\chi} \\ \mathbf{M} &= \langle y_3 \boldsymbol{\sigma} \rangle^* = \mathbf{B}^{\mathbf{T}}\mathbf{E} + \mathbf{D}\boldsymbol{\chi} \end{aligned} \tag{3}$$

where $\mathbf{A}$, $\mathbf{B}$, and $\mathbf{D}$ are the constitutive homogenized plate tensors. Usually, the elementary cell has a central symmetry, hence $\mathbf{B} = \mathbf{0}$. As a rule, a solution for the problem given by equation (2) can be obtained using standard FE packages, as suggested for the in-plane case by Anthoine (1995).

The governing equations in the non-linear case are formally identical to equation (2) provided that a non-linear stress-strain law for the constituent materials is assumed. Extensions to the non-linear case have been provided by e.g. Luciano and Sacco (1997); Pegon and Anthoine (1997); Massart (2003); Massart et al. (2004); Zucchini and Lourenço (2004), etc.

1.1 Closed-form and simplified solutions in the linear elastic range

This section briefly recalls some of the most popular simplified approaches that appeared in the past in the technical literature for obtaining homogenized elastic moduli for masonry. Since the elastostatic problem given in equation (2) cannot be solved in closed form for running bond masonry, several simplifications were assumed in order to obtain "easily" homogenized elastic moduli.

Two-step approaches. One of the first ideas presented, Pande et al. (1989) and Maier et al. (1991), was to substitute the complex geometry of the basic cell with a simplified geometry, so that a closed-form solution for the homogenization problem was possible.

In particular, Pande et al. (1989) presented a model in which a two-step stacked system with alternative isotropic layers was considered (Figure 2). In this way, a so called "two-step homogenization" was obtained. In the first step, a single row of masonry units and vertical mortar joints were taken into consideration and homogenized as a layered system. In the second step, the "intermediate" homogenized material was further homogenized with horizontal joints in order to obtain the final material. In this manner, a very simple mechanical system constituted by elastic springs was obtained and explicit formulas based on classical elasticity concepts were presented.

Obviously, this simplification leads:

1. To underestimate the horizontal stiffness of the homogenized material, since no information on the texture (running bond, stack bond, Flemish bond, etc.) is considered. Furthermore, the inability of the model to consider the regular offset of vertical mortar joints belonging to two consecutive layered unit courses results in significant errors in the case of non-linear analysis;
2. To obtain a homogenized material different if the steps of homogenization are inverted (i.e. if bed joints and masonry units are homogenized in the first step).

Following the idea of a multi-step approach, many other models involving different approximations and ingenious assumptions have been sought, with an increasing large number of papers in the recent years (Pietruszczak and

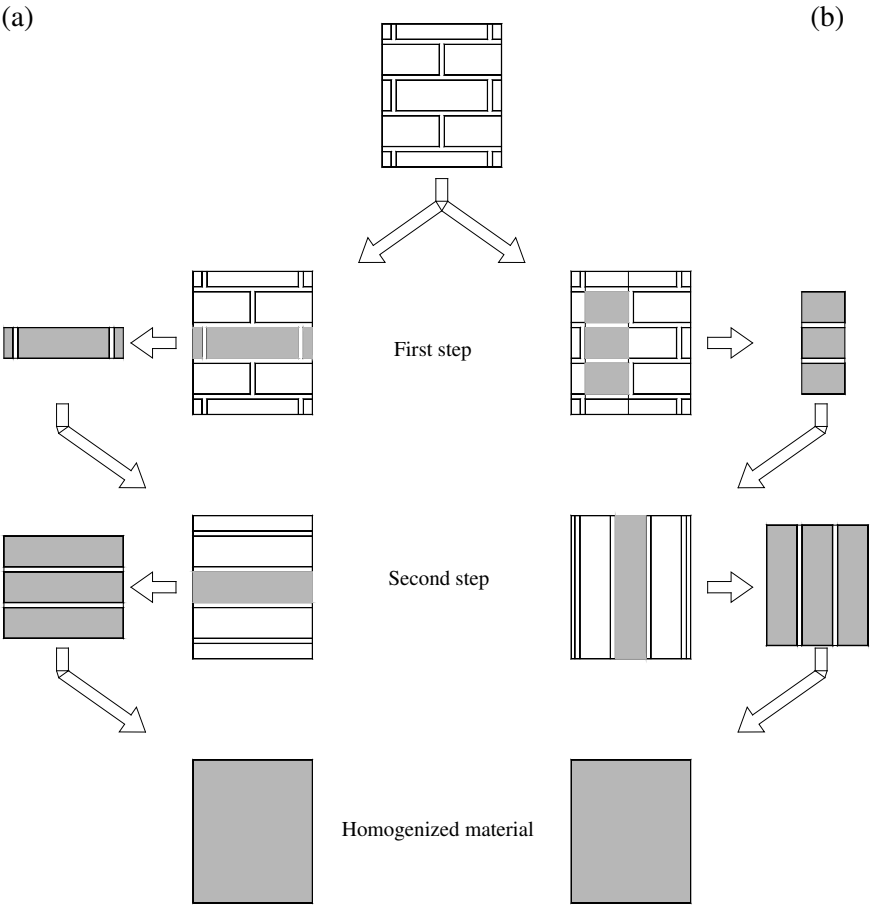

Figure 2. Two-step homogenization

Niu, 1992), where a two-stage homogenization procedure was employed with the head joints considered as uniformly dispersed elastic inclusions and the bed joints assumed to represent a set of continuous weakness.

Reduction of joints to interfaces. A different approach, proposed by de Felice (1995) and Cecchi and Sab (2002), is based on the reduction of joints to interfaces. This idea arose from the observation that masonry units are generally much stiffer than mortar and joints show a small thickness if compared with the size of masonry units.

These studies resulted in the definition of the homogenized masonry constitutive function by means of the introduction of several parameters that measure smallness:

3. ϵ (scale parameter) $\to 0$, which represents the ratio between the size of the cell and the dimension of the overall panel;
4. ξ , representing the ratio between the Young's modulus of the mortar E_m and the Young's modulus of the masonry unit E_b $\left(\xi = \dfrac{E_m}{E_b}\right)$;
5. φ, representing the ratio between the thickness of the joints e and the size of the characteristic module a $\left(\varphi = \dfrac{e}{a}\right)$.

ξ and φ are parameters that take into account the effects of joint sizes and the ratio of deformability of mortar and block. For fixed elastic tensors of both block and mortar and for fixed geometric parameters a, b, t (defined in 1), the so-called "asymptotic case" is obtained when $\xi \to 0$ and $\varphi \to 0$. If φ tends to zero, the joint becomes and interface, whereas if ξ tends to zero the mortar becomes infinitely deformable with respect to the unit. Therefore, the typology of asymptotic problem depends on how ξ and φ tend to zero.

A first simplification usually introduced adopts $\xi = \xi(\varphi)$ and additionally, $\lim_{\varphi \to 0} \xi(\varphi)\varphi^{-1} = \rho \neq 0$. Such asymptotic problem shows cohesive zero thickness interfaces between the masonry units with possible jump of the displacement field. Hence, the field problem may be formulated with reference only to the $\mathbf{a}^a$ elastic tensor of the masonry unit with discontinuity at the interfaces, where the constitutive function is a linear relation between the stresses on the unit surfaces and the jump of the displacement field. Both in de Felice (1995) and Cecchi and Sab (2002), elastic springs with diagonal constitutive tensor $\mathbf{K}$ for the joints are used, so introducing a simplification related to the fact that Poisson effect of the joint is neglected. In particular $\mathbf{K}$ takes the following explicit form:

$$\mathbf{K} = \frac{1}{e}\left(\mu^M \mathbf{I} + \left(\mu^M + \lambda^M\right)(\mathbf{n} \otimes \mathbf{n})\right) \tag{4}$$

where e is the thickness of the joint, $\mathbf{n}$ is the normal to the interface, and μ^M, λ^M are the Lamé constants of mortar.

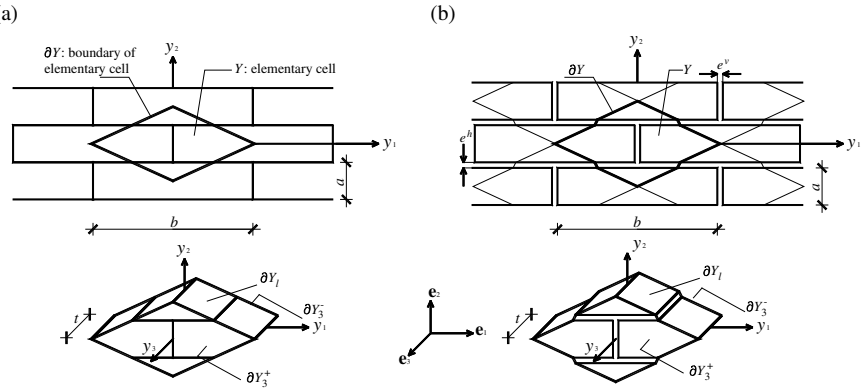

Figure 3. unit cell utilized in de Felice (1995) and Cecchi and Sab (2002). Left: joints reduced to interfaces. Right: actual thickness of the joints.

De Felice (1995) assumed also rigid masonry units, in order to reduce further the complexity of the problem. In this way, see Figure 3-a, this author showed that the problem given by equation (2) can be solved in closed form for running bond masonry and permits to obtain analytical formulas for the homogenized elastic constants, which depend only on the geometry of the elementary cell and on the mechanical properties of joints.

Following this idea, Cecchi and Sab (2002) proposed a multi-parameter homogenization study for the 2D and the 3D in-plane case, removing the hypothesis of rigid masonry units (Figure 3-b). The finite thickness of the joints was considered in an approximated way only in the constitutive relation of the interfaces. A symbolic FE procedure was adopted, in which the elementary cell was discretized by means of a coarse triangular mesh. Here the term symbolic is use to indicate that the homogenization problem was handled in symbolic form, using a mathematical software. In this way, these authors were able to find "quasi-analytical" formulas.

The disadvantages of this approach are the following:

1. The reduction of joints to interfaces, may strongly reduce the accuracy of the results in presence of thick mortar joints and in presence of ξ ratios tending to zero Cecchi et al. (2005).
2. The introduction of elastic masonry units leads to formulas derived from symbolic FE procedures and does not allow solving analytically the homogenization problem.
3. A possible development of the method in the non-linear range can result in non-negligible errors with respect to finite element approaches

and experimental evidences, since the role of joint thickness is lost in the simplifications assumed.

FE procedures. Anthoine (1995) was the first to suggest the utilization of standard FE codes for solving the homogenization problem given by equation (2) in the case of both stacked and running bond masonry. Anthoine (1995, 1997) and Lourenço (1997) also underlined that homogenized moduli depend on the order of the steps and 3D effects are always present.

Cecchi et al. (2005) applied FE procedures to masonry out-of-plane loaded and stressed that:

1. Flexural moduli may significantly differ from membrane moduli, especially in the presence of weak mortar joints. As a consequence, Kirchhoff-Love orthotropic homogenized coefficients cannot be obtained simply by integration of membrane moduli.
2. Cohesive interface closed-form solutions give unreliable results when the ξ ratio is small.

The classical assumptions adopted in the FE method applied to homogenization are the following:

1. Perfect continuity between units and mortar;
2. The periodic displacement that has to be imposed fulfils the constant/linear assumption, at the boundary of the cell, of the macroscopic kinematic descriptors $\mathbf{E}$ and $\boldsymbol{\chi}$.

In this way, considering only a macroscopic strain tensor $\mathbf{E}$ acting, suitable boundary conditions (Figure 4) for $\mathbf{u}^{per}$ periodic and $\boldsymbol{\sigma}\mathbf{n}$ anti-periodic on ∂Y_l (which represents the boundary of the module orthogonal to the middle plane) are imposed, meaning that the elastostatic problem can be formulated only on Y . It is worth noting that several engineering approaches recently presented in the technical literature do not satisfy exactly this hypothesis (Lopez et al., 1999; Zucchini and Lourenço, 2002). In this case, the symmetry of the cell allows to simplify the numerical model and permits to discretize only 1/4 of the elementary cell.

The advantages of the adoption of a FE technique include:

1. The FE solution approximates the actual solution for a suitable refined mesh;
2. Mortar joints thickness is taken into account for the evaluation of the homogenized moduli. This leads to estimate numerically homogenized moduli that can differ from interface moduli;
3. The influence on the homogenized horizontal Young modulus, due to the masonry units staggering, is caught by the model, especially in presence of mortar joints with poor mechanical properties or nonlinear behaviour.

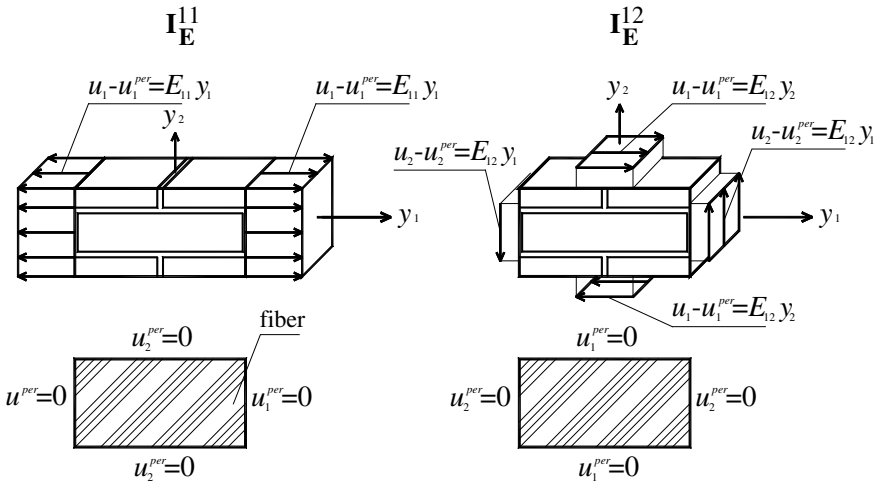

Figure 4. Applied displacement boundary conditions on the elementary cell.

On the other hand, the most severe limitation of the approach is that the computational cost of a FE procedure does not compete favourably with macroscopic approaches when non-linear problems are treated, since the homogenization field problem has to be solved for each Gauss point of each loading step. This leads to handle continuously a "two-size" FE problem (macroscopic and cell level), where the averaged results obtained at a cell level are utilized at a structural level (in the framework of non-linear numerical procedure).

1.2 Simplified stress assumed FE discretization

Simplified models based on a stress assumed FE discretization in the elastic range have been recently proposed by Milani et al. (2006a) and Milani (2011). Essentially, the approach relies into a rough FE discretization of the unit cell, where inside each element a polynomial interpolation of the stress field is a-priori given. Equilibrium inside each element and at the interface between contiguous elements and anti-periodicity conditions are imposed. The solution in the elastic range is simply achieved minimizing the total complementary energy stored into the unit cell, subjected to a certain number of equality constraints representing equilibrium and anti-periodicity.

As shown in Figure 5, one-fourth of the REV is sub-divided into nine

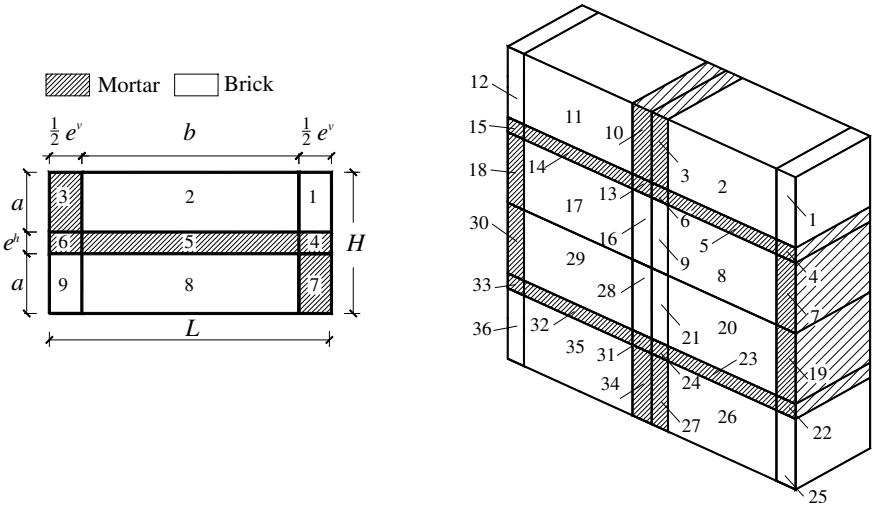

Figure 5. Subdivision in sub domains adopted: Left: subdivision and geometrical characteristics of one-fourth of the elementary cell, Right: subdivision into 36 sub-domains for the entire cell.

geometrical elementary entities (*sub-domains*), so that all the cell is subdivided into 36 sub-domains.

For each sub-domain, polynomial distributions of degree (m) are a priori assumed for the stress components. The generic ij-th component can be written as follows:

$$\sigma_{ij}^{(k)} = \mathbf{X}(\mathbf{y})\mathbf{S}_{ij}^{T} \quad \mathbf{y} \in Y^{K} \tag{5}$$

where:

- $\mathbf{X}(\mathbf{y}) = \lfloor 1 \quad y_1 \quad y_2 \quad y_1^2 \quad y_1 y_2 \quad y_2^2 \quad \ldots \rfloor$;
- $\mathbf{S}_{ij} = \left[S_{ij}^{(1)} \quad S_{ij}^{(2)} \quad S_{ij}^{(3)} \quad S_{ij}^{(4)} \quad S_{ij}^{(5)} \quad S_{ij}^{(6)} \quad \ldots \right]$ is a vector of length $(\widetilde{N}) \quad \left(\widetilde{N} = \dfrac{m^2}{2} + \dfrac{3m}{2} + 1 = \dfrac{(m+1)(m+2)}{2} \right)$ representing the unknown stress parameters;
- Y^k represents the k^{th} sub-domain.

The imposition of equilibrium with zero body forces inside every sub-domain, the continuity of the stress vector on interfaces and anti-periodicity of $\boldsymbol{\sigma}\mathbf{n}$ permit to strongly reduce the total number of independent stress parameters.

In particular, equilibrium has to be imposed everywhere inside each sub-domain, i.e. $\sigma_{ij,j}(x,) = 0$, $i = 1, 2 \forall (x, y) \in$ sub-domain. Since $\sigma_{ij}(x, Y)$ is a

polynomial expression of degree (m), a linear combination of its derivatives $(\mathrm{div}\,\boldsymbol{\sigma})$ is a polynomial of degree $(m-1)$. Therefore equilibrium inside each sub-domain leads to write $(2N)$ linear independent equations in the stress coefficients, where $N = \dfrac{m^2}{2} + \dfrac{3m}{2} + 1 = \dfrac{(m+1)(m+2)}{2}$.

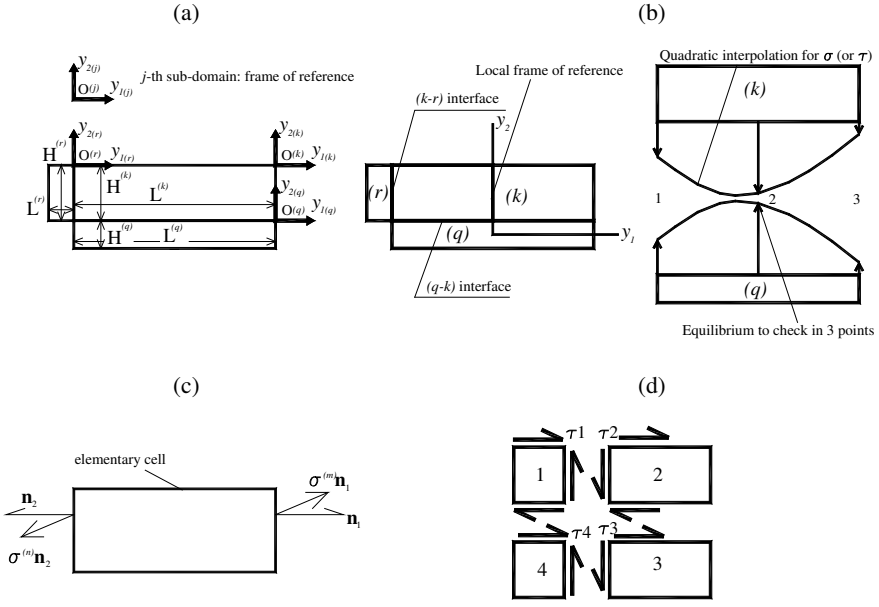

Figure 6. Contiguous sub-domains. -a: geometry and frame of reference of the sub-domains; -b: vertical/horizontal interfaces between adjacent sub-domains; -c: anti-periodicity conditions on the unit cell; -d: linear dependence of some equilibrium equations.

A further reduction of the total unknowns is obtained a priori imposing the continuity of the stress vector on internal interfaces $(\sigma_{ij}^{(k)} n_j + \sigma_{ij}^{(r)} n_j = 0,\ i = 1,2)$ for every (k) and (r) contiguous sub-domains with a common interface of normal $\mathbf{n}$ (6). Being Eqs. (5) polynomial expressions of degree (m) in the abscissa s of the interface, other $2N'$ equations (where $N' = m+1$) in $\hat{\mathbf{S}}^{(k)}$ and $\hat{\mathbf{S}}^{(r)}$ for each $(k \leftrightarrow r)$ interface can be written from (5), see Figure 6-b.

Finally anti-periodicity of $\boldsymbol{\sigma}\mathbf{n}$ on ∂V requires $2N'$ additional equations per pair of external faces $(m)(n)$ (Figure 6-c), i.e. it should be imposed that

stress vectors $\boldsymbol{\sigma}\mathbf{n}$ are opposite on opposite sides of ∂V:

$$\hat{\mathbf{X}}_{ij}^{(m)}(\mathbf{y})\,\hat{\mathbf{S}}^{(m)}\mathbf{n}_1 = -\hat{\mathbf{X}}_{ij}^{(n)}(\mathbf{y})\,\hat{\mathbf{S}}^{(n)}\mathbf{n}_2 \tag{6}$$

Where $\mathbf{n}^{(m)}$ and $\mathbf{n}^{(n)}$ are oriented tensors of the external faces of the paired sub-domains $(m)(n)$.

To conclude, some elementary assemblage operations on the local variables (handled automatically) lead to write the stress vector inside every sub-domain as follows:

$$\widetilde{\boldsymbol{\sigma}}^{(k)} = \widetilde{\mathbf{X}}^{(k)}(\mathbf{y})\,\widetilde{\mathbf{S}} \quad k = 1, \ldots, k^{\max} \tag{7}$$

where:

- $\widetilde{\boldsymbol{\sigma}}^{(k)}$ is the vector of membrane actions inside the k^{th} sub-domain;
- $\widetilde{\mathbf{X}}^{(k)}$ is a $3 \times N_{un}$ matrix which contains only geometrical coefficients; its elements are polynomial forms in the microscopic coordinate $\mathbf{y}$;
- $\widetilde{\mathbf{S}}$ is the vector (of length N_{un}) of the total stress parameters unknown.

The equations written in order to satisfy internal equilibrium, equilibrium on interfaces and anti-periodicity of the stress vector lead to a system of equations $\mathbf{AS} = \mathbf{0}$, where $\mathbf{S}$ is the vector of total stress parameters. Nevertheless, not all the rows of this system are linearly independent. This can be easily shown if four generic rectangular elements with four common interfaces and subjected only to constant non zero shear stress are considered, as reported in Figure 6-d. Internal equilibrium is a priori satisfied, whereas four equations for ensuring equilibrium on interfaces have to be written. Nevertheless, only three of these four equations are linear independent.

Finally, four different models of increasing accuracy ($P_0 \quad P_2 \quad P_3 \quad P_4$) have been obtained increasing the degree of the polynomial expansion.

1.3 Linear elastic case

A preliminary study in the linear elastic range may be done considering the quadratic functional Π of the complementary energy evaluated in the REV. With the stress-assumed discretization previously discussed, an approximation of Π can be written as:

$$\Pi^* = \sum_{k=1}^{k^{\max}} \int_{Y_k} \frac{1}{2} \widetilde{\mathbf{S}}^T \widetilde{\mathbf{X}}^{(k)T}(\mathbf{y})\,\mathbf{C}^{b,m} \widetilde{\mathbf{X}}^{(k)} \widetilde{\mathbf{S}}\,\mathrm{d}Y_k - \sum_j \int_{S_j} \widetilde{\mathbf{S}}^T \widetilde{\mathbf{X}}^{(k)T} \bar{\mathbf{u}}\,\mathrm{d}S_j \tag{8}$$

Where $\mathbf{C}^{b,m}$ is the compliance matrix of units or mortar joints and $\bar{\mathbf{u}}$ is the displacement imposed on the boundary ∂Y of the elementary cell, representing a given macroscopic strain tensor $\mathbf{E}$.

The minimization of the approximated expression of Π leads to the following expression:

$$\begin{aligned}\nabla\Pi^* &= \left(\sum_{k=1}^{k^{\max}} \int_{Y_k} \widetilde{\mathbf{X}}^{(k)T}(\mathbf{y})\, \mathbf{C}^{b,m} \widetilde{\mathbf{X}}^{(k)}\, \mathrm{d}Y_k\right) \widetilde{\mathbf{S}} \\ &\quad - \sum_j \int_{S_j} \widetilde{\mathbf{X}}^{(k)T}(\mathbf{y})\, \bar{\mathbf{u}}\, \mathrm{d}S_j \\ &= \mathbf{C}^{\mathrm{hom}} \widetilde{\mathbf{S}} - \bar{\mathbf{U}} = 0\end{aligned} \tag{9}$$

which enables to find both $\widetilde{\mathbf{S}}$, by factorization of the matrix $\mathbf{C}^{\mathrm{hom}}$ and $\boldsymbol{\Sigma}$, from integration of the local stress field.

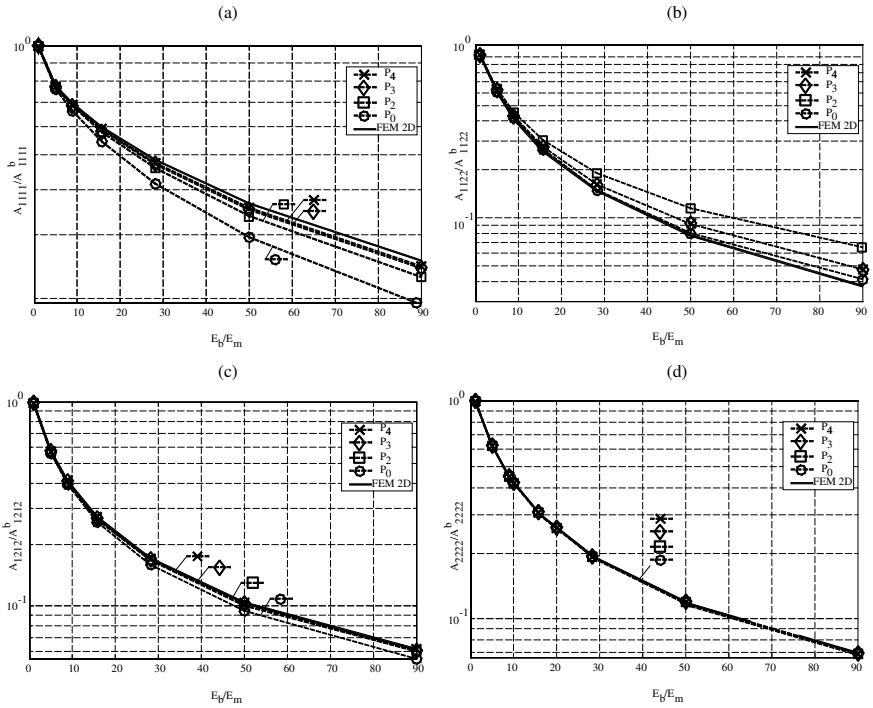

Figure 7. Homogenised in-plane moduli. -a: A_{1111} modulus; -b: A_{1212} modulus; -c: A_{1122} modulus; -d: A_{2222} modulus.

A comparison between the elastic moduli provided by the model proposed and a standard numerical 2D FEM procedure, Anthoine (1995), is

Table 1. Initial mechanical properties assumed for the elastic simulations reported in Figure 7.

	E[N/mm^2] Young modulus	ν Poisson ratio
unit	11000	0.2
mortar	2200	0.25

presented in Figure 7. The dimensions of the units are assumed to be $250 \times 120 \times 55\,\text{mm}^3$ (brick UNI5628/65) and the thickness of mortar joints is equal to 10 mm. The initial mechanical characteristics of materials are reported in Table 1; the simulations are handled keeping the brick Young modulus E_b constant and progressively reducing the mortar Young modulus E_m, so assuming a wide range of E_b/E_m ratios (from 5 to 90), in order to simulate also historical brickwork. Homogenized A_{ijhk} membrane moduli are represented varying E_b/E_m ratio. The homogenized moduli are normalized versus the corresponding moduli of the brick. As it can be noticed, the provided moduli are reliable in a large range of E_b/E_m ratios, even for the simplest model with constant stresses tensor ($P0$). Nevertheless, Figure 7-a shows that a progressively reduced accuracy of the $P0$ model can be noticed for the A_{1111} module, due to the presence of shear stresses in the bed joint.

1.4 Constant Stress Triangular elements discretization of the unit cell

In Milani (2011), an alternative static model relying into the subdivision of the unit cell into 24 constant stress triangular elements and joints reduced to interfaces is presented. Due to the very limited number of optimization variables involved, the model can be handled also without the assistance of a computer.

Joints are reduced to interfaces with zero thickness and blocks are discretized by means of a coarse mesh constituted by three-noded plane-stress elements, Figure 8. The choice of meshing 1/4 of the brick through at least 3 triangular elements is due to the need of reproducing the presence of shear stress in the bed joint (element 2 in Figure 8) in horizontal stretching. All the non-linearity in the RVE is concentrated exclusively on interfaces between adjoining elements both on brick and joint. Brick-brick interfaces allow, at least in principle, the reproduction of blocks failure. The six CST elements used for the discretization of the upper-right 1/4 of the REV are indicated in Figure 14 as 1, 2, 3, 1', 2', 3'.

In the model, the non-dimensional geometrical coefficient ρ indicates the

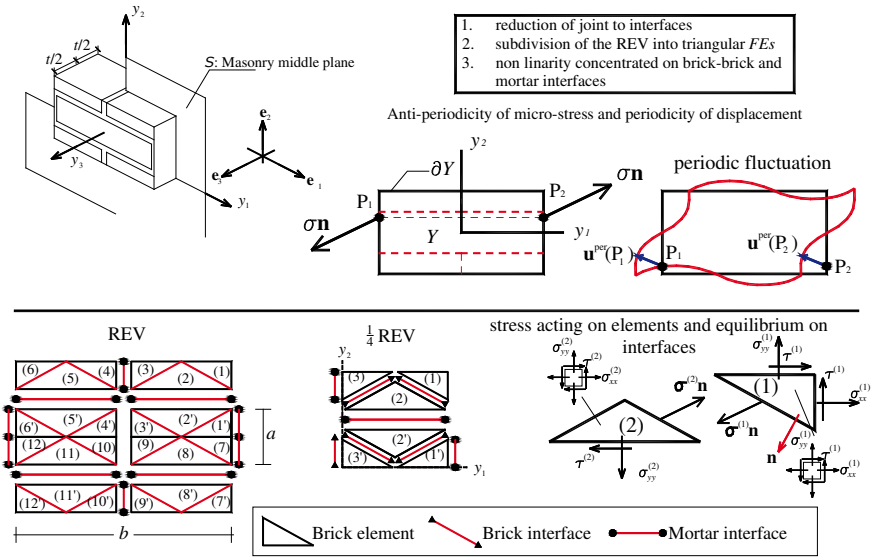

Figure 8. The micro-mechanical model proposed. Subdivision of the REV into 24 CST triangular elements (and 1/4 into 6 elements) and anti-periodicity of the micro-stress field.

ratio between brick semi-length and height, i.e. $\rho = b/2a$ and the superscript (n), with n positive integer, a stress component belonging to the n-th element. In this way, assuming a plane-stress condition, the Cauchy stress tensor inside the n-th CST element $\boldsymbol{\sigma}^{(n)}$ is constituted by the components $\sigma_{xx}^{(n)}$ (horizontal stress), $\sigma_{yy}^{(n)}$ (vertical stress) and $\tau^{(n)}$ (shear stress).

Within the static approach of limit analysis, equilibrium inside each element is a priori satisfied, $\operatorname{div}\boldsymbol{\sigma} = 0$. On the contrary, two equality constraints involving Cauchy stress tensor components of triangular elements must be imposed for each internal interface between adjoining elements.

It can be shown that the imposition of equilibrium on interfaces is represented by a set of 10 equations (being 5 the interfaces for 1/4 of the REV) in 18 unknowns (three stress components for each triangular element).

Having in mind to analyze masonry macroscopic behaviour under combined states of stress acting on its middle plane, all the REV must be considered, as depicted schematically in Figure 8. Anti-periodicity constrains for the stress vector field are written on couples of triangles 1–6, 1'–6', 7–12, 7'–12', 1–7', 3–9', 4–10', 6–12'.

When the whole cell problem is considered, independent variables are

represented by stresses acting on the triangular elements (3 unknowns per element, i.e. 72 unknowns per REV) and the three homogenized stresses Σ_{xx}, Σ_{yy} and Σ_{xy} (75 total optimization variables).

Σ_{xx}, Σ_{yy} and Σ_{xy} are linked with local stress variables by means of the following set of three equations:

$$\begin{aligned}
\Sigma_{xx} &= \frac{1}{A_C}\sum_{i=1}^{N^{tr}} A_{tr}^{(i)}\sigma_{xx}^{(i)} \\
\Sigma_{yy} &= \frac{1}{A_C}\sum_{i=1}^{N^{tr}} A_{tr}^{(i)}\sigma_{yy}^{(i)} \\
\Sigma_{xy} &= \frac{1}{A_C}\sum_{i=1}^{N^{tr}} A_{tr}^{(i)}\tau^{(i)}
\end{aligned} \tag{10}$$

Where, apart quantities already introduced, $A_{tr}^{(i)}$ is the area of the i-th CST element, N^{tr} is the total number of elements in the unit cell and A_C is the total area of the unit cell.

From equilibrium equations, anti-periodicity and (10) a set of linear equations in both the elastic and rigid-plastic problem is obtained.

When dealing with the elastic case, membrane elastic homogenized moduli may be obtained in the same way followed for the polynomial expansion shown in the previous case, i.e. minimizing the complementary energy in the unit cell. In this case, the complementary energy assumes the following quadratic form:

$$\begin{aligned}
\Pi^* = \frac{1}{2}\sum_{i=1}^{N^{tr}} A_{tr}^{(i)}\left[\frac{\sigma_{xx}^{(i)^2}}{E_b} + 2\nu_b\frac{\sigma_{xx}^{(i)}\sigma_{yy}^{(i)}}{E_b} + \frac{\sigma_{yy}^{(i)^2}}{E_b} + \frac{\tau^{(i)^2}}{G_b}\right] \\
+ \frac{1}{2}\sum_{i=1}^{N^I} A_I^{(i)^2}\left[\frac{\sigma_n^{(i)^2}}{E_m} + \frac{\tau^{(i)^2}}{G_m}\right] - A_C\Sigma_{ij}E_{ij}
\end{aligned} \tag{11}$$

Where N^I is the total number of mortar interfaces, $A_I^{(i)}$ is the area of the i-th mortar interface and $\Sigma_{ij}E_{ij}$ is a summation saturating indices i and j (assuming either value x or y) and E_{ij} is a prescribed macroscopic strain component.

Analogously to the previous case, the determination of the membrane elastic moduli may be obtained by a constrained minimization of the complementary energy, which is a quadratic form on the 72 independent microstress variables of the elements and the three variables Σ_{ij} representing the

homogenized stress. Thanks to the very limited number of optimization variables involved, a standard large scale quadratic programming routine is utilized to solve the elastic problem on the unit cell, varying E_b/E_m ratio in a wide range and assuming as initial values for the simulations those reported in Table 1.

Results of the simulations are summarized in Figure 9, where the analytic solution by Lourenço (1996) is also reported, to compare with A_2222 modulus. Essentially, such approach consists in homogenizing a masonry pillar constituted by two half bricks (height h) and a joint with thickness e. For such a structural system it can be proved that the vertical membrane elastic modulus is $A_{2222} = \dfrac{h+e}{(1-\nu_b^2)\,\dfrac{h}{E_b} + (1-\nu_m^2)\,\dfrac{e}{E_m}}$.

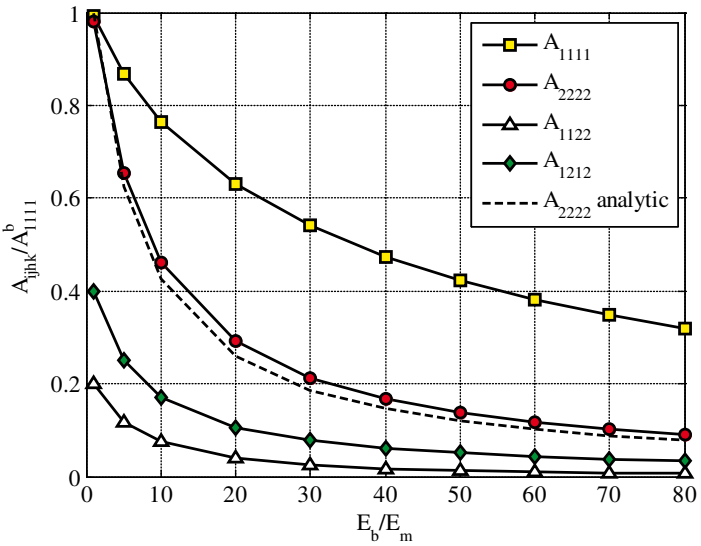

Figure 9. Homogenized in-plane moduli. -a: A_{1111} modulus; -b: A_{1212} modulus; -c: A_{1122} modulus; -d: A_{2222} modulus.

1.5 Homogenized failure surfaces

Both stress assumed approaches previously discussed may be extended in the case of materials exhibiting rigid plastic behaviour, infinite ductility and associated flow rules. This is a classic homogenization problem in the rigid plastic case, for which upper and lower bound theorems have been

provided some decades ago by Suquet (1983) in a general framework. Basing on such theorems, limit analysis combined with homogenization has been extensively applied to masonry structures by e.g. de Buhan and de Felice (1997); Milani et al. (2006a,c); Milani (2011), etc.

De Buhan and de Felice (1997) were the first to apply the kinematic theorem of limit analysis in the framework of masonry homogenization, assuming joints reduced to interfaces with a classic Mohr-Coulomb failure criterion and masonry units infinitely resistant. Milani et al. (2006a,c) and Milani (2011) adopted a static approach, in which either polynomial equilibrated and admissible stress fields were a priori assumed in a finite number of subdomains or a rough discretization with stress constant triangular elements was utilized. In this way, both compressive failure and actual thickness of the joints as well as units crushing may be considered.

These approaches have the following advantages:

1. Masonry homogenized failure surfaces can be recovered making use of well-known linear programming routines and requiring a very limited computational effort;
2. The homogenized failure surfaces so obtained can be implemented in FE limit analysis codes for collapse analysis, without limitations and not requiring to solve a cell problem in each Gauss point at a structural level;
3. They can compete favourably with macroscopic approaches and give relevant information at failure.

On the other hand, some limitations are worth noting:

1. Limit analysis is incapable to give an information on displacements at collapse;
2. As experimental evidences show, frictional behaviour is typically non associated and, at present, mathematical theorems concerning non associated limit analysis applied to homogenization are not available;
3. Masonry behaviour can be quasi-brittle. As a consequence, the assumption of infinite ductility for the constituent materials can be inadequate and preclude the models to be predictive.

Stress assumed approach and polynomial expansion on rectangular sub-domains. The polynomial expansion of the stress field in rectangular sub-domains automatically represents an equilibrated stress field inside the unit cell. To be statically admissible, each point of each subdomain should be subjected to a stress state not violating the material yield. In this framework, the static theorem of limit analysis assures that a point of the failure surface may be found solving the following optimisation

problem:

$$\max\{\hat{\lambda}\} \quad \text{such that} \begin{cases} \hat{\lambda}\mathbf{n}_\Sigma = \dfrac{1}{Y}\displaystyle\sum_{k=1}^{4k^{\max}} \int_Y \widetilde{\mathbf{X}}^{(k)}(\mathbf{y})\,\widetilde{\mathbf{S}}\,\mathrm{d}Y & (a) \\ \mathbf{y} \in Y^k & (b) \\ \widetilde{\boldsymbol{\sigma}} = \widetilde{\mathbf{X}}^{(k)}(\mathbf{y})\,\widetilde{\mathbf{S}} & (c) \\ \widetilde{\boldsymbol{\sigma}}(\mathbf{y}) \in S^k \quad k = 1, \ldots, 4k^{\max} & (d) \end{cases} \tag{12}$$

where

- $\mathbf{n}_\Sigma = \begin{bmatrix} \alpha_{11} & \alpha_{22} & \alpha_{12} \\ \Sigma_{11} & \Sigma_{22} & \Sigma_{12} \end{bmatrix}^T$ is a tensor in the homogenized stress space
- $\hat{\lambda}\mathbf{n}_\Sigma$ represents a macroscopic stress state on the homogenized failure surface $S^{\hom}$, belonging to a straight line from the origin of direction $\mathbf{n}_\Sigma$
- S^k stands for the failure surface of the component (unit or mortar) belonging to the i^{th} sub-domain.
- Y is the area of the elementary cell.

The optimisation problem given by Eqs. (12) is generally non-linear as a consequence of the (possible) non-linearity of the strength functions of the components. In addition, condition Eqs. (12) (d) has to be checked in every point of the domain Y. Nevertheless, as suggested in a classical paper by Belytschko and Hodge (1970), the check could be avoided imposing the material admissibility only where the stress status is the maximum. This is feasible only for the $P0$ and $P1$ models; alternatively, the discretisation proposed here consists in enforcing, in every sub-domain, the admissibility condition in a regular grid of "nodal points" with step $r \times q$ (quasi-lower bound approach).

Within this assumption, the optimisation problem reduces to:

$$\max\{\hat{\lambda}\} \quad \text{such that} \begin{cases} \hat{\lambda}\mathbf{n}_\Sigma = \dfrac{1}{Y}\displaystyle\sum_k \int_Y \widetilde{\mathbf{X}}^{(k)}(\mathbf{y})\,\widetilde{\mathbf{S}}\,\mathrm{d}Y \\ \mathbf{y}^j \equiv \text{nodal point} \\ \widetilde{\boldsymbol{\sigma}}^j = \widetilde{\mathbf{X}}^{(k)}\left(\mathbf{y}^j\right)\widetilde{\mathbf{S}} \\ \widetilde{\boldsymbol{\sigma}}^j \in S^j \quad j = 1, \ldots, rq \\ k = 1, \ldots, 4k^{\max} \end{cases} \tag{13}$$

Optimisation problem (13) generally remains non-linear. In order to use linear pro-gramming algorithms, each of the non-linear inequalities of Eqs. (13) could be approximated by a set of linear inequalities (as proposed in the past, for instance, by Anderheggen and Knöpfel (1972) or Olsen (1998), by replacing the yield surfaces with inscribed hyper polyhedrons. Finally, the convergence of the solution obtained should be checked progressively increasing the number of planes of the approximation, see Sloan (1988); Sloan and Kleeman (1995) and Olsen (1998) and many others.

Alternatively and more efficiently, an iterative procedure may be adopted, taking advantage of the fact that the simplex method proceeds from basic solution to basic solution towards an optimal basic solution, i.e. on the vertices of the hyper polyhedron.

The basic idea of the iterative procedure adopted is the following: in the starting step, a coarse linear approximation of the non-linear failure surfaces of the components is adopted, as shown in Figure 10-a. The application of the simplex method in the optimisation at the i-th step leads to an optimal solution in a corner of the domain.

From the iterative i-th solution point a new tangent plane is added in P' as shown in Figure 10-b, so restarting an $(i+1)^{\text{th}}$ optimisation procedure. The iterations continue until a fixed tolerance in the error between the i^{th} and $(i+1)^{\text{th}}$ solution is reached.

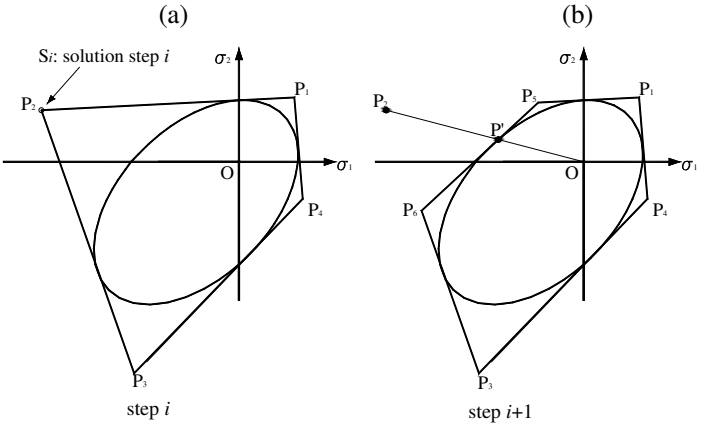

Figure 10. Iterative procedure utilized in the optimization problem.

In Figure 11, the strength domain obtained increasing the degree of the polynomial expansion is represented in the macroscopic stress space with $\Sigma_{12} = 0$; the results are compared with a full finite element limit analysis

on the REV. Mechanical characteristics of the constituent materials are summarized in Table 2; a Mohr-Coulomb failure criterion in plane stress is chosen for mortar joints, while units are supposed infinitely resistant. Units dimensions are 52.5×17.5 mm(length $\times$ height) and mortar joints are 10 mm thick.

Table 2. Mechanical properties assumed for mortar joints (plane stress, units infinitely resistant).

Mortar	
Frictional angle (Φ)	Cohesion (c)
$37°$	1.0028 MPa
$\sigma_t = \frac{2c\cos(\Phi)}{1+\sin(\Phi)}$	$\sigma_c = \frac{2c\cos(\Phi)}{1-\sin(\Phi)}$

As Figure 11 shows, the model with constant stress tensor ($P0$) is unable to reproduce the typical anisotropic behaviour of masonry at failure (Milani et al., 2006a), while the refined models give a progressively increased accuracy of the results (especially $P3$ and $P4$) in comparison with the FE analysis. Therefore, a cubic interpolation $P3$ is at least recommended.

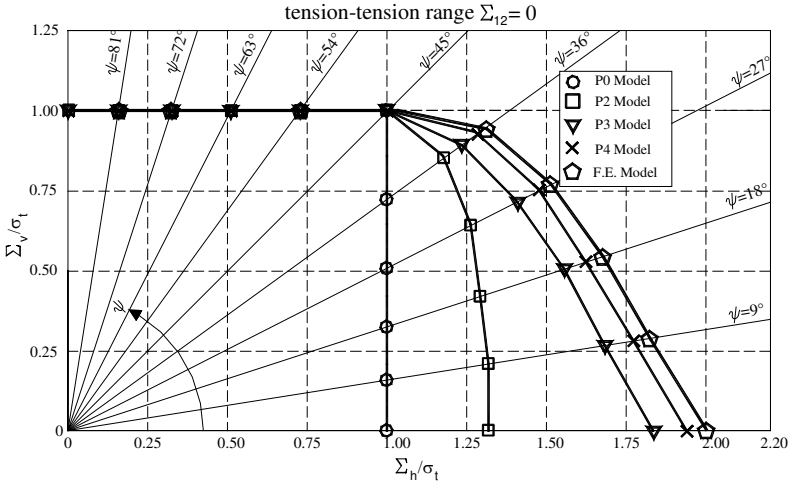

Figure 11. Failure surface in the tension-tension range for the models proposed without shear actions.

Stress assumed approach and CST elements. When dealing with the discretization of the unit cell by means of CST elements and in presence of finite resistance of both interfaces and triangular elements the homogenization problem may be re-written as:

$$\max \lambda$$
$$\text{subject to} \begin{cases} \lambda\alpha = \dfrac{\sum_{i=1}^{24} \sigma_{xx}^{(i)} A_i}{2ab} \\ \lambda\beta = \dfrac{\sum_{i=1}^{24} \sigma_{yy}^{(i)} A_i}{2ab} \\ \lambda\gamma = \dfrac{\sum_{i=1}^{24} \tau^{(i)} A_i}{2ab} \\ \mathbf{A}_{eq}^{I}\mathbf{X} = \mathbf{b}_{eq}^{I} \\ \mathbf{A}_{eq}^{ap}\mathbf{X} = \mathbf{b}_{eq}^{ap} \\ f_E^i\left(\sigma_{xx}^{(i)}, \sigma_{yy}^{(i)}, \tau^{(i)}\right) \leq 0 \, \forall i = 1, \ldots, 24 \\ f_I^i\left(\sigma_I^{(i)}, \tau_I^{(i)}\right) \leq 0 \, \forall i = 1, \ldots, 32 \end{cases} \tag{14}$$

where symbols used in equation (14) have the following meaning:

– α, β and γ indicate the components of the unitary vector $\mathbf{n}_\Sigma$, see Figure 12, in the homogenized membrane stress space. The solution of the optimization problem (14) allows the determination of a point on the homogenized failure surface having coordinates $\Sigma_{xx} = \alpha\lambda$, $\Sigma_{yy} = \beta\lambda$ and $\Sigma_{xy} = \gamma\lambda$. Note that independent variables pass from 75 to 73 introducing the failure multiplier. Usually, masonry in-plane failure surface sections are represented assuming a fixed angle ϑ between the bed joint and the macroscopic horizontal action Σ_{11}. Such sections are obtained keeping ϑ fixed and varying point by point ψ angle, defined as $\psi = \tan^{-1}(\Sigma_{22}/\Sigma_{11})$, where Σ_{22} is the macroscopic vertical action. In this framework, vector $\mathbf{n}_\Sigma$ has the following form:

$$\begin{aligned} \mathbf{n}_\Sigma(1) &= \frac{1}{2}\left(\cos(\psi)\left(1 + \cos(2\vartheta)\right) + \sin(\psi)\left(1 - \cos(2\vartheta)\right)\right) \\ \mathbf{n}_\Sigma(2) &= \frac{1}{2}\left(\cos(\psi)\left(1 - \cos(2\vartheta)\right) + \sin(\psi)\left(1 + \cos(2\vartheta)\right)\right) \\ \mathbf{n}_\Sigma(3) &= \frac{1}{2}\left(\cos(\psi)\cos(2\vartheta) - \sin(\psi)\cos(2\vartheta)\right)\tan(2\vartheta) \end{aligned} \tag{15}$$

- A_i is the area of the i-ith element ($ab/8$ or $ab/16$);
- $\mathbf{X}$ is a 73×1 row vector and collects all the optimization unknowns (elements stress components and collapse multiplier);
- $\mathbf{A}_{eq}^{I} = \mathbf{b}_{eq}^{I}$ is a set of linear equations collecting equilibrium constraints on all interfaces. Since 32 interfaces are present in the discretized REV and 2 equality constraints has to be written for each interface (it has to be ensured that both normal and shear stresses are continuous on the interface), $\mathbf{A}_{eq}^{I}$ is a 64×73 matrix and $\mathbf{b}_{eq}^{I}$ is a 64×1 vector of all zeros.
- $\mathbf{A}_{eq}^{ap}\mathbf{X} = \mathbf{b}_{eq}^{ap}$ collects anti-periodicity conditions and it is therefore a set of 16 equations. Thus $\mathbf{A}_{eq}^{ap}$ is a 16×73 matrix and $\mathbf{b}_{eq}^{ap}$ is a 16×1 vector of all zeros.
- $\mathbf{f}_E^i\left(\sigma_{xx}^{(i)}, \sigma_{yy}^{(i)}, \tau^{(i)}\right) \leq \mathbf{0}$ is a set of non linear inequalities constraints representing the failure surface adopted for the i-th element. Within a linear programming scheme, such failure surfaces are normally linearized. The linearization is usually a lower bound one when a static approach is used, to ensure that a strict lower bound estimation of the collapse load is obtained. Such a lower bound approximation is easily obtained by means of a Delaunay tessellation.
- $\mathbf{f}_I^i\left(\sigma_I^{(i)}, \tau_I^{(i)}\right) \leq 0 \, \forall i = 1, \ldots, 32$ plays the role of $\mathbf{f}_E^i$ for the interfaces. Two typologies of interfaces are present in the model, namely brick-brick interfaces and mortar joints reduce to interfaces. When dealing with the numerical applications reported hereafter, a linearized Lourenço and Rots (1997) failure criterion is adopted for joints reduced to interfaces and a classic Mohr-Coulomb failure criterion is used for brick interfaces. While in the first case a rough approximation of the elliptic cap is assumed (in agreement with Sutcliffe et al. (2001), in the second the constraint is already linear.
- $\sigma_I^{(i)}$ and $\tau_I^{(i)}$ indicate respectively the normal and shear stress acting on interface i.

(14) is a standard linear programming problem and the reader is referred to e.g Anderheggen and Knöpfel (1972) for a critical discussion of efficient (classic) linear programming tools suited for solving (14). On the other hand, it is worth noting that recent trends in limit analysis have demonstrated that the linearization of the strength domain can be circumvented using conic/semidefinite programming (e.g. Krabbenhoft et al. (2005)).

In-plane homogenized failure surfaces. The brickwork considered by Raijmakers and Vermeltfoort (1992) for performing some experimental tests on shear walls is examined. Brick dimensions are $210 \times 52 \times 100\,\mathrm{mm}^3$,

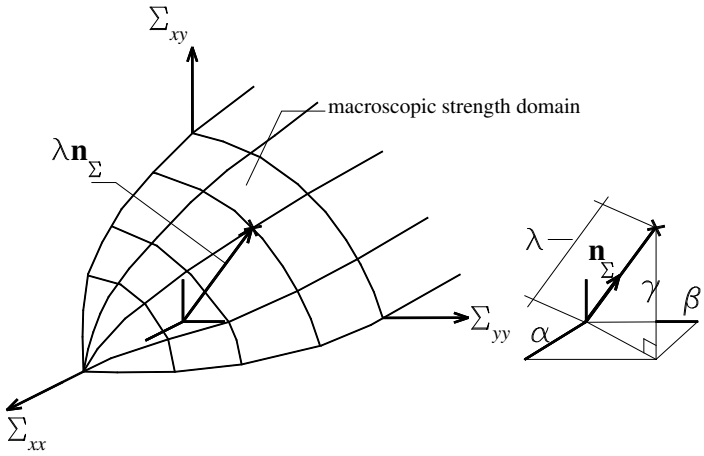

Figure 12. General in-plane load. Meaning of multiplier in the homogenized stress space ($\Sigma_{xx} = \mathbf{n}_\Sigma\,(1)$, $\Sigma_{yy} = \mathbf{n}_\Sigma\,(2)$ and $\Sigma_{xy} = \mathbf{n}_\Sigma\,(3)$)

whereas the thickness of the mortar joints is 10 mm. Such shear walls have been examined through numerical simulations and a micro-mechanical approach by many authors, e.g. Lourenço and Rots (1997); Milani et al. (2006a); Sutcliffe et al. (2001), etc.

It is worth noting that a comparison with a kinematic formulation is possible for joints reduced to interfaces and bricks infinitely resistant. The kinematic formulation, again solved using linear programming, is the following:

$$\left.\begin{aligned} \chi &= \min_{\mathbf{v}} \frac{1}{\Gamma} \int_\Gamma [[\mathbf{v}]]\, \boldsymbol{\sigma}\, \mathrm{d}s \\ \Sigma^0 : \mathbf{D} &= 1 \\ [[\mathbf{v}]] &= \sum_{i=1}^{n} \dot{\lambda}_i \nabla_{\boldsymbol{\sigma}} f^{(i)} \end{aligned}\right\} \tag{16}$$

where χ is the kinematic limit multiplier of the assigned macroscopic stress Σ^0 and $\dot{\lambda}_i$ is the plastic multiplier associated with the (linear) inequality constraint $f^{(i)} \leq 0$ which determines the admissible stress state.

Two models (A and B) for joints are critically examined, see Table (3). They differ only for the compressive cap, which is vertical in model A and with a very prominent shape in model B.

The homogenized surfaces —at different orientations ϑ of the biaxial load with respect to material axes— in the compression-compression re-

Table 3. Raijmakers and Vermeltfoort experimental data. Mechanical properties adopted for mortar joints reduced to interfaces and bricks.

Mortar joints reduced to interfaces (Mohr-Coulomb failure criterion with tension cutoff) and linearized compressive cap)			
		Model A	Model B
cohesion [MPa]	c	$1.4f_t$	
tensile strength [MPa]	f_t	0.25	
compressive strength [MPa]	f_c	10.5	
friction angle [Deg]	Φ	37	
shape of the linearized compressive cap [Deg]	Ψ	30	90
Brick interfaces and triangular brick elements (Mohr-Coulomb failure criterion)			
cohesion [MPa]	c_b	2	
friction angle [Deg]	F_b	45	

gion obtained using the presented static models (results of both models in practice coincide for polynomial expansions with degrees higher than 5) are reported in Figure 13 (Model A) and Figure 14 (Model B), whereas the homogenized behaviour in the tension-tension region is depicted in Figure 15. In this latter case, obviously Model A and B provide the same result. Along with static failure surfaces, the corresponding kinematic strength domains obtained solving (16) are represented. For graphical convenience, kinematic failure surfaces are slightly shifted. As it can be noted, the agreement between the here revised static approaches and the kinematic procedure is almost perfect for all the points inspected. The results show that the homogenized surface depends on the geometrical and mechanical characteristics assumed for the components.

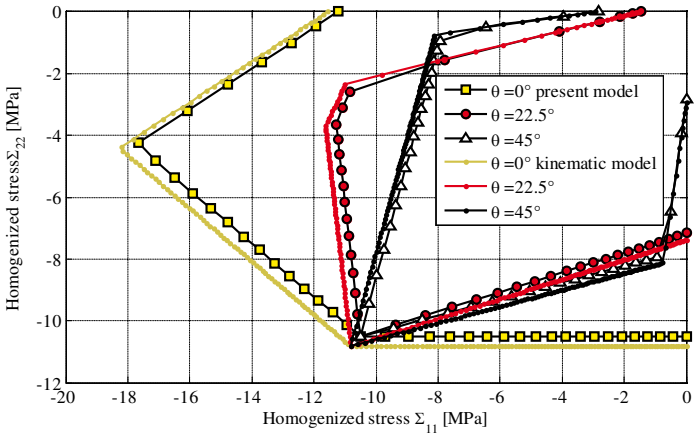

Figure 13. Model A. Compression-compression region. Biaxial strength domain at different orientation of the horizontal action with respect to bed joint direction. Comparison between static approaches and kinematic solution. For graphical convenience, kinematic failure surfaces are slightly shifted from their actual position.

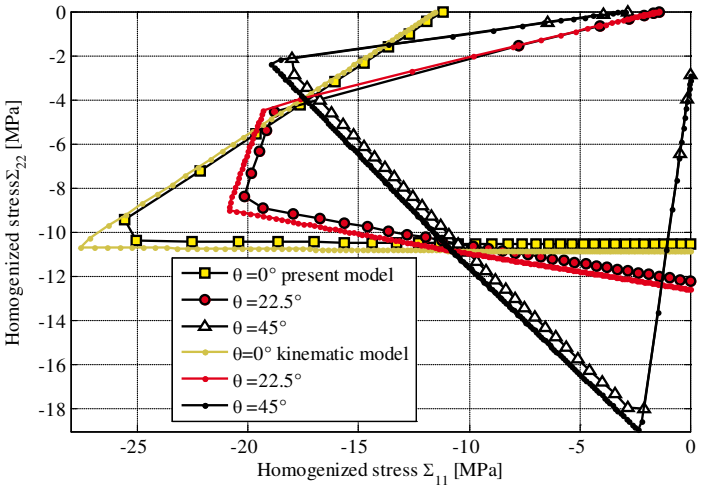

Figure 14. Model B. Compression-compression region. Biaxial strength domain at different orientation of the horizontal action with respect to bed joint direction. Comparison between static approaches and kinematic solution. For graphical convenience, kinematic failure surfaces are slightly shifted from their actual position.

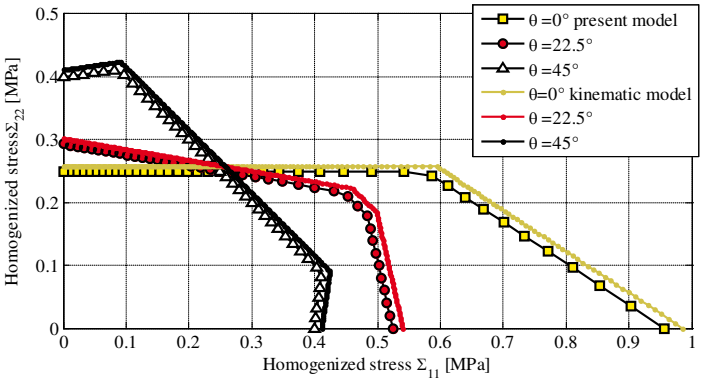

Figure 15. Tension-tension region. Biaxial strength domain at different orientation of the horizontal action with respect to bed joint direction. Comparison between static approaches and kinematic solution. For graphical convenience, kinematic failure surfaces are slightly shifted from their actual position.

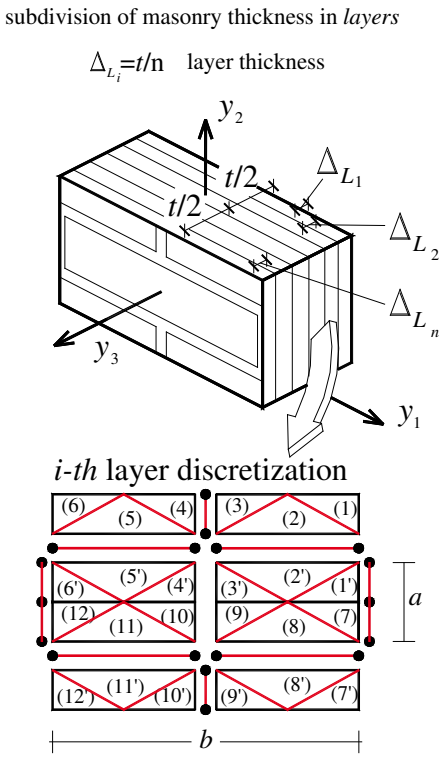

Figure 16. The micro-mechanical model proposed for out-of-plane actions. Subdivision in layers along the thickness and discretization of each layer into triangular equilibrated elements.

Generalization to the out-of-plane case. The generalization of the second static model, presented in this Chapter, to out-of-plane actions (Kirchhoff-Love hypothesis), if performed within the utilization of standard linear programming routines, requires a subdivision (n_L) of the wall thickness t into several layers (Figure 16-a), with a priori fixed constant thickness $\delta_L = t/n_l$ for each layer. Hence, to estimate a point of the failure surface in the bending moment-torque space it is necessary to solve the following linear programming problem:

$$
\begin{aligned}
&\max\{\lambda\}\\
&\text{s.t.}\begin{cases}
\lambda\alpha = \dfrac{\sum\limits_{j=1}^{n_L} \Delta_{L_i}\left(\frac{t+\Delta_{L_i}}{2} - j\Delta_{L_i}\right)\sum\limits_{i=1}^{24}\sigma_{xx}^{(i,j)}A_i}{2ab}\\
\lambda\beta = \dfrac{\sum\limits_{j=1}^{n_L} \Delta_{L_i}\left(\frac{t+\Delta_{L_i}}{2} - j\Delta_{L_i}\right)\sum\limits_{i=1}^{24}\sigma_{yy}^{(i,j)}A_i}{2ab}\\
\lambda\gamma = \dfrac{\sum\limits_{j=1}^{n_L} \Delta_{L_i}\left(\frac{t+\Delta_{L_i}}{2} - j\Delta_{L_i}\right)\sum\limits_{i=1}^{24}\tau^{(i,j)}A_i}{2ab}\\
N_{xx} = \dfrac{\sum\limits_{j=1}^{n_L} \Delta_{L_i}\sum\limits_{i=1}^{24}\sigma_{xx}^{(i,j)}A_i}{2ab} = \Sigma_{xx}t = 0\\
N_{yy} = \dfrac{\sum\limits_{j=1}^{n_L} \Delta_{L_i}\sum\limits_{i=1}^{24}\sigma_{yy}^{(i,j)}A_i}{2ab} = \Sigma_{yy}t = 0\\
N_{xy} = \dfrac{\sum\limits_{j=1}^{n_L} \Delta_{L_i}\sum\limits_{i=1}^{24}\tau^{(i,j)}A_i}{2ab} = \Sigma_{xy}t = 0\\
\mathbf{A}_{eq}^{I}\mathbf{X} = \mathbf{b}_{eq}^{I}\\
\mathbf{A}_{eq}^{ap}\mathbf{X} = \mathbf{b}_{eq}^{ap}\\
f_E^{i,j}\left(\sigma_{xx}^{(i,j)}, \sigma_{yy}^{(i,j)}, \tau^{(i,j)}\right) \le 0 \,\forall i = 1,\ldots,24 \,\forall j = 1,\ldots,n_L\\
f_I^{i,j}\left(\sigma_I^{(i,j)}, \tau_I^{(i,j)}\right) \le 0 \,\forall i = 1,\ldots,32 \,\forall j = 1,\ldots,n_L
\end{cases}
\end{aligned}
\tag{17}
$$

where all the symbols have been already introduced for the in-plane case.

With respect to the in-plane case, the following key issues are worth noting:

- λ is the value of the failure strength in the $M_{xx} - M_{yy} - M_{xy}$ space;
- α, β and γ indicate the components of the unitary vector $\mathbf{n}_\Sigma$, see Figure 12, in the homogenized $M_{xx} - M_{yy} - M_{xy}$ space, in analogy to what stated for the in-plane case;
- $\mathbf{A}^I_{eq}\mathbf{X} = \mathbf{b}^I_{eq}$ collects equilibrium constraints of all interfaces of each layer. Since between contiguous layers no shear stresses are exchanged, such constraints are the same of the in-plane case, one set written for each layer. $\mathbf{A}^I_{eq}$ is a $64n_L \times (72n_L + 1)$ matrix and $\mathbf{b}^I_{eq}$ is a $64n_L \times 1$ vector of all zeros. Analogous considerations can be repeated for the equations set $\mathbf{A}^{ap}_{eq}\mathbf{X} = \mathbf{b}^{ap}_{eq}$, which collects anti-periodicity conditions for each layer. For the out-of-plane case, $\mathbf{A}^{ap}_{eq}$ is a $16n_L \times (72n_L + 1)$ matrix and $\mathbf{b}^{ap}_{eq}$ is a $16n_L \times 1$ vector of all zeros;
- differently to the in-plane case, three additional equality constraints have to be imposed, corresponding to require that homogenized membrane actions $N_{xx} - N_{yy} - N_{xy}$ are equal to zero; - vector $\mathbf{X}$ collects all the unknown stresses of each FE of each layer). Therefore, $\mathbf{X}$ is a vector of length $3 \times 24 \times n_L$.

Finally, it is worth noting that membrane actions are kept, for the sake of simplicity, constant and independent from load multiplier. Consequently, in-plane actions effect optimization only in the evaluation of M_{xx}, M_{yy}, M_{xy} strength domains. Generally, this assumption is technically acceptable for experimental tests where vertical pre compression N_{yy} is constant and applied before out-of-plane actions.

1.6 Out-of-plane homogenized failure surfaces

In the first example, the ultimate masonry horizontal bending, torsion and vertical bending (i.e. M_{xx}, M_{xy} and M_{yy}) are evaluated in absence of pre-compression.

Table 4. Mechanical properties adopted for the out-of-plane numerical simulations in absence of vertical pre-compression (UNI bricks).

Mortar joints reduced to interfaces (Mohr-Coulomb failure criterion)		
friction angle [Deg]	Φ	27
cohesion [MPa]	c	0.132

Standard Italian UNI bricks of dimensions $55 \times 120 \times 250\,\mathrm{mm}^3$ (height $\times$ thickness $\times$ length) and mortar joints reduced to interfaces with a Classic Mohr-coulomb failure criterion are considered. The same simulations have been performed in Cecchi et al. (2007) using a kinematic approach. Mechanical characteristics adopted for joints are summarized in Table 4.

In Figure 17 and Figure 18 respectively, sections $M_{xx} - M_{yy}$ and $M_{xx} - M_{xy}$ of the macroscopic failure surface are reported, at 4 increasing values of n_L, compared with Cecchi et al. (2007) results. The resultant failure surfaces well approximate the upper bound reference surface for $n_L > 10$. hence very coarse discretizations along the thickness may be used. Results show again a dependence on the geometrical and mechanical characteristics assumed for the components.

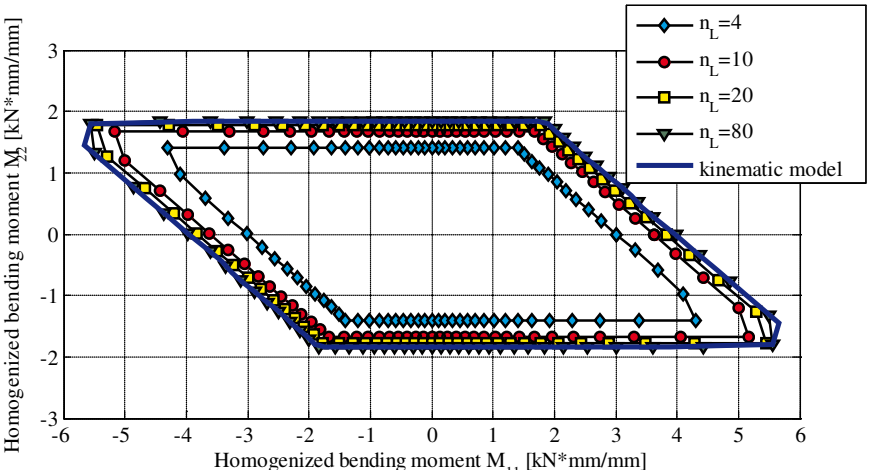

Figure 17. $M_{xx} - M_{yy}$ Failure surface obtained at increasing refinement of the subdivision along the thickness.

2 Structural Level

The homogenized failure surface obtained with the above approaches may be easily coupled with finite element limit analysis codes. Both upper and lower bound approaches have been developed, for in- and out-of-plane loaded masonry walls (Milani et al., 2006b,c) with the aim of providing a full set of numerical data for the design and/or the structural assessment of complex structures. For in-plane loads, the finite element lower bound analysis is based on the equilibrated triangular element bySloan (1988), while the upper bound is based on a modified version of the triangular element with discontinuities of the velocity field in the interfaces by Sloan and Kleeman (1995). The modification takes into account the actual shape of the yield surface for the homogenized material in the interfaces.

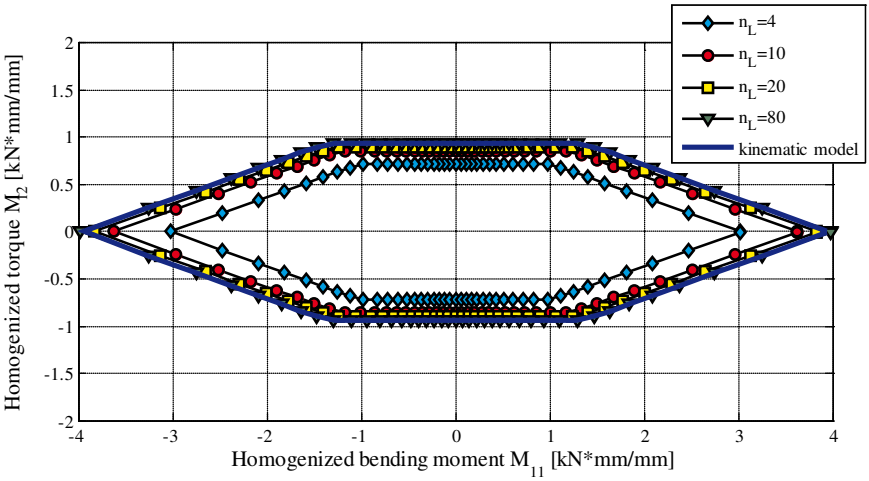

Figure 18. $M_{xx} - M_{xy}$ Failure surface obtained at increasing refinement of the subdivision along the thickness.

When dealing with out-of-plane loads, the triangular plate bending element proposed independently by Hellan (1967) and Herrmann (1967) has been adopted for lower bound calculations, whereas the triangular element proposed by Munro and da Fonseca (1978) has been implemented and employed for the upper bound analyses.

2.1 In-plane loads: shear wall with central opening

The first structural example discussed consists on a windowed masonry shear wall. A set of experimental tests are available from Raijmakers and Vermeltfoort (1992). Two series were tested, corresponding to specimens with and without openings. Here only windowed panels are considered for the sake of conciseness. Two identical walls were tested, labeled as J2G and J3G. The width/height ratio (L/H) of the shear walls is 990/1000 ([mm]/[mm]); the panels were built up with 18 courses of bricks, from which 16 courses were active and 2 were clamped in stiff steel beams, Figure 19. Brick dimensions are $210 \times 52 \times 100\,\mathrm{mm}^3$ and the mortar joints are 10 mm thick. A vertical pre-compression of $0.3\,\mathrm{N/mm}^2$ was applied on the top and its resultant was kept constant during the complete loading procedure. The stiff steel beam did not allow rotations of the top and was subsequently pushed with an increasing horizontal force.

The central opening defines two small relatively weak piers and forces the

compressive strut that develops under horizontal loading to spread around both sides of the opening. The experimental crack pattern as reported by Raijmakers and Vermeltfoort is illustrated in Figure 19-a.

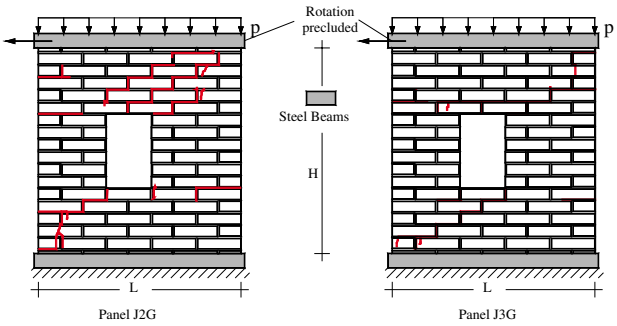

Figure 19. Windowed masonry shear wall by Raijmakers and Vermeltfoort.

For the numerical analysis, a homogenized mesh constituted by 448 elements is utilized. Mechanical properties assumed for the constituent materials are summarized in Table 3 and are taken in agreement with both experimental data provided by Raijmakers and Vermeltfoort (where available) and Lourenço (1996), where the same numerical analyses have been presented within a heterogeneous approach.

In Figure 20, a comparison among collapse load provided by the homogenized limit analysis model proposed in Milani (2011) and here recalled, the heterogeneous approach by Lourenço (1996) and experimental load-displacement curves (2 replicates) is presented. Furthermore, Figure 21 illustrates the limit analysis resultant deformed shape at failure (upper bound solution) and the map of normalized plastic dissipation (representing damage in the framework of limit analysis).

As it is possible to notice, the response provided by limit analysis seems in good agreement with existing literature, both in terms of collapse load predictions and crack pattern.

2.2 Out-of-plane loads: windowed panel in two-way bending

An out-of-plane validation of the homogenization models presented previously is available in Milani et al. (2006c) and Milani (2011).

The panels re-analyzed here consist of solid clay brick masonry. The tests were carried out by Chong et al. (1994) and are denoted by SB. Four different configurations were tested, built in stretcher bond between two stiff abutments with the vertical edges simply supported (allowance for in-plane

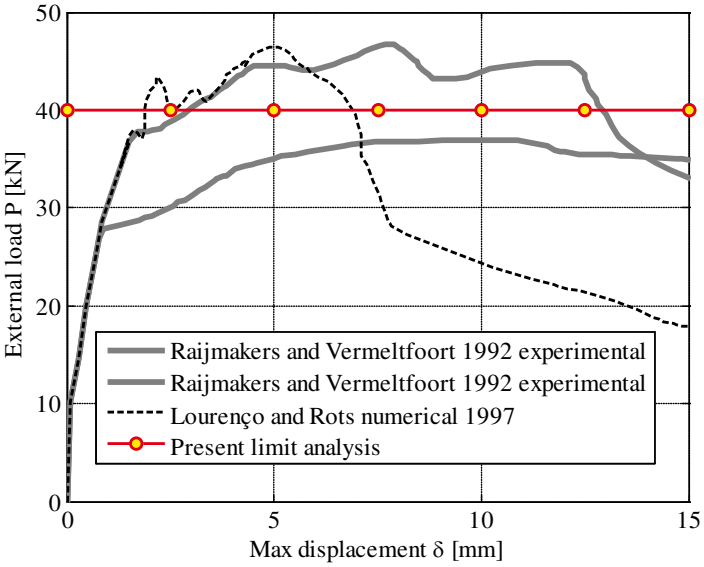

Figure 20. Windowed masonry shear wall by Raijmakers and Vermeltfoort. Comparison among collapse load provided by homogenized limit analysis, a numerical heterogeneous approach and experimental load-displacement curves.

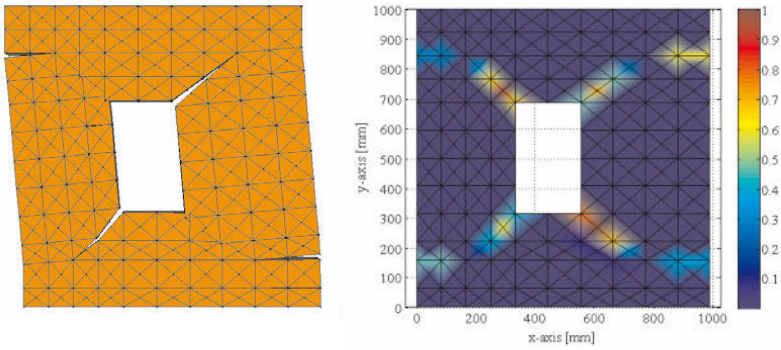

Figure 21. Windowed masonry shear wall by Raijmakers and Vermeltfoort. Left: deformed shape at collapse. Right: normalized plastic dissipation patch.

displacements was provided) and the top edge free. A completely restrained support was provided at the base because of practical difficulties in providing a simple support. The panels were loaded by air-bags until failure with increasing out-of-plane uniform pressure p. The reader is referred to Milani et al. (2006c) for a detailed description of geometric dimensions, loads application, structural FE implementation and discussion of results.

Figure 22 shows typical comparisons between experimental pressure-displacement curves by Chong et al. (1994), numerical pressure displacement curves obtained by means of an orthotropic elasto-plastic macro-model (Lourenço, 2000) and the homogenized limit analysis results (Milani et al., 2006c). In addition, Figure 23 shows typical results of the numerical analysis in terms of principal moment distribution and mechanisms at failure. The agreement with experimental results is worth noting in all cases analysed.

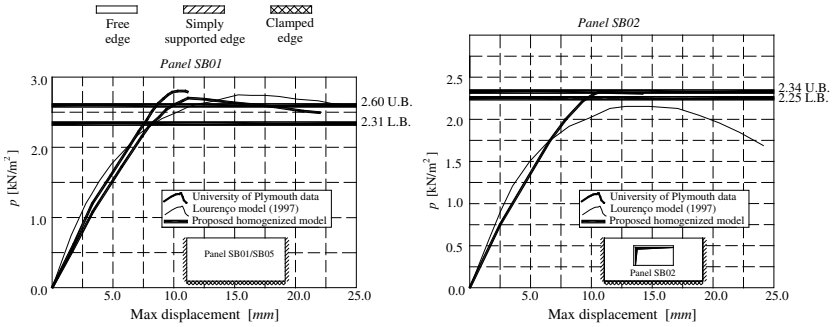

Figure 22. Stress field polynomial expansion approach (out-of-plane model). Comparison between experimental and numerical results obtained, University of Plymouth experimental tests

3 Dynamics and Seismic Behaviour

The seismic response of buildings is particularly difficult to characterize due to its nature, the low number of strong events in a given location, the site effects, the attenuation laws, the non-linear response of the structure, the relevance of execution defects, and many other factors. The seismic action is usually defined in codes via elastic response spectra, which are graphical representations of the maximum value of the response for a single-degree-of-freedom system as a function of the period. From the elastic response spectrum synthetic accelerograms can be generated, which provide the time history of accelerations at the foundations. Recorded accelerograms from

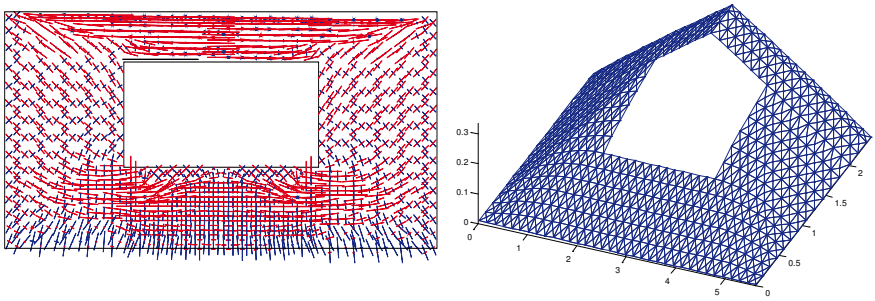

Figure 23. Typical numerical results (Panel SB02) obtained by means of the stress field polynomial expansion approach (out-of-plane model). (a) lower bound results (principal moments at collapse); (b) upper bound results (deformed mesh at collapse).

real earthquakes also exist, being their most relevant characteristics the amplitude, the frequency contents and the duration.

In case of seismic loading on unreinforced masonry buildings, it is certain that non-linear behaviour is triggered at early stages of loading and linear elastic analysis is not an option. Alternative options seem to be push-over methods, as recommended in most codes for earthquake safety assessment, or non-linear time integration methods, which provide complex and time consuming tools hardly available for practitioners. Another much relevant property in case of seismic loading is the presence of floors that provide diaphragmatic action and the so-called "box-behaviour". This possible feature is not usually present in ancient masonry buildings while being present in modern unreinforced masonry buildings, requiring different models of analysis, as addressed next.

3.1 Masonry structures with box behaviour

Modern masonry buildings usually adopt solutions for the slabs that provide considerable in-plane stiffness. This is done by using monolithic solutions for the floors, in concrete and steel, and also by establishing an effective connection between slabs and walls. Moreover, many existing buildings originally constructed with timber floors are capable of providing some diaphragmatic action or have been rehabilitated by stiffening the floors and by providing adequate connections.

The effect of floor diaphragms combined with the in-plane response of structural walls provides box behaviour to the buildings, which usually leads

to good performance when subjected to earthquakes. The first assessment method for seismic analysis of masonry buildings was developed under this simple hypothesis. As result of research studies in former Yugoslavia and the 1976 Friuli earthquake, the POR method was introduced in the Italian region of Friuli-Venezia Giulia, to assess the seismic performance of existing masonry buildings, see Marques and Lourenço (2011). Despite its simplicity, this method was used until very recently in the analysis of existing buildings and in the design of new buildings, in Italy. Its limitations, namely the consideration of an independent storey mechanism, and the 2002 Molise earthquake, clearly stressed the need of methods that consider the overall response of the masonry structures.

Modern regulations, namely Eurocode 8 (CEN, 2004), seriously penalize structural masonry with a low behaviour factor that renders unreinforced masonry impossible, in opposition with experimental findings. Methods inspired in the POR method and based on macro-elements have been developed, particularly in Italy, e.g. Gambarotta and Lagomarsino (1996) and Magenes and Fontana (1998). These methods seem the most appropriate for design and assessment of masonry buildings, given their widespread in commercial software, the simplicity of modelling, the straightforward interpretation of results and the accuracy demonstrated in different validations. The methods are incorporated in the 3Muri [www.stadata.com] and ANDILWall/SAM II [www.crsoft.it/andilwall] computer codes, respectively. While 3Muri formulation is based on the kinematic equilibrium of the macro-elements according to the panel degrees of freedom, SAM II creates an equivalent frame idealization for a global analysis.

The 3Muri and SAM II computer codes perform the safety verification by a nonlinear static (pushover) analysis that simulates the evolution of the structural condition during the earthquake, through application of incremental horizontal forces until collapse. The behaviour of the structure is represented by the so-called "capacity curve", which represents the value of the base shear versus the displacement of a control point (usually the mass centroid of the roof slab). In Marques and Lourenço (2011), a benchmark analysis was carried out demonstrating good agreement of the results for a pushover analysis on two buildings.

To demonstrate the possibilities of construction with unreinforced masonry and the inadequacy of European codes, the seismic safety of buildings with one up to three storeys, based on a pushover analysis carried out in the 3Muri computer code, is considered next. The building configurations studied are shown in Figure 24, namely a one-storey module, and two- and three-storey buildings for semi-detached houses.

Figure 25 illustrates the ultimate response in terms of deformed configu-

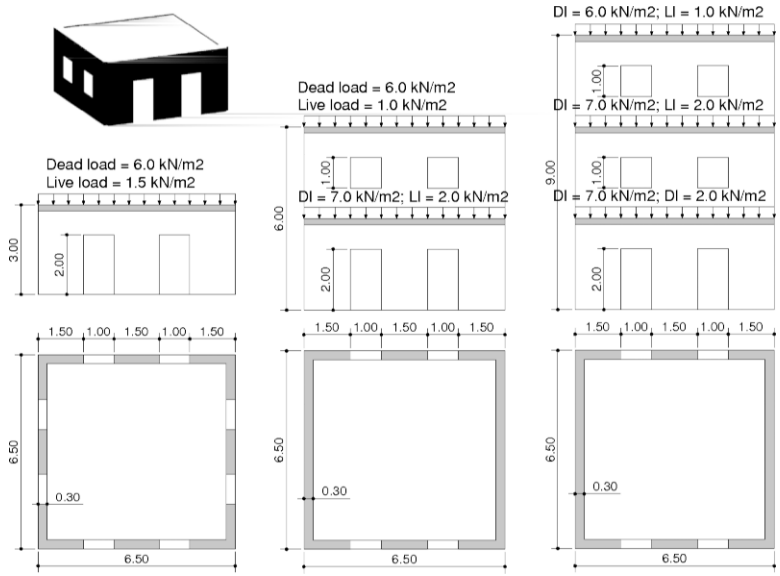

Figure 24. Building configurations studied.

ration and damage of the three buildings, where it can be observed that the collapse mechanisms are essentially induced by flexure, while plastic mechanisms by shear are only found for the three-storey building in spandrels adjacent to the first slab.

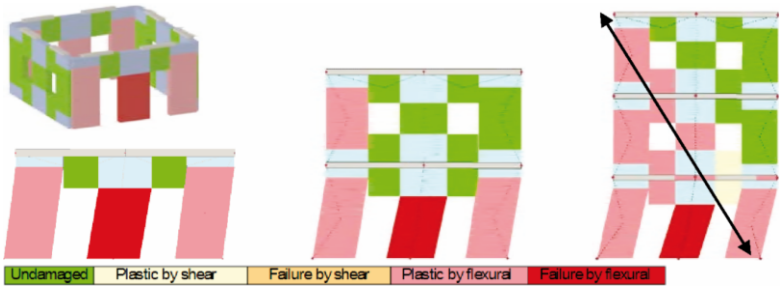

Figure 25. Assessment of ultimate damage and deformed configurations.

Based on the requirements for earthquake resistance imposed by the Italian code OPCM 3431 (2005), and assuming the seismic parameters de-

fined in the Portuguese Annex to Eurocode 8 (CEN, 2004), the possibility to construct the studied buildings in Portugal was evaluated using 3Muri, see Figure 26. Performing an elastic analysis adopting a behaviour factor of 1.5, as recommended by Eurocode 8, provides a safety over conservative assessment, as shown in Figure 27a. A better correspondence between the pushover and linear analysis is achieved by assuming the behaviour factor values proposed by OPCM 3431, as shown in Figure 27b. In the case of the regular building configuration adopted, behaviour factors of 4.0, 3.0 and 3.5, respectively for the one-to-three storey buildings allow a good match between the linear and nonlinear analysis. This example clearly demonstrates the need of adopting adequate analysis techniques for the seismic assessment of unreinforced masonry structures.

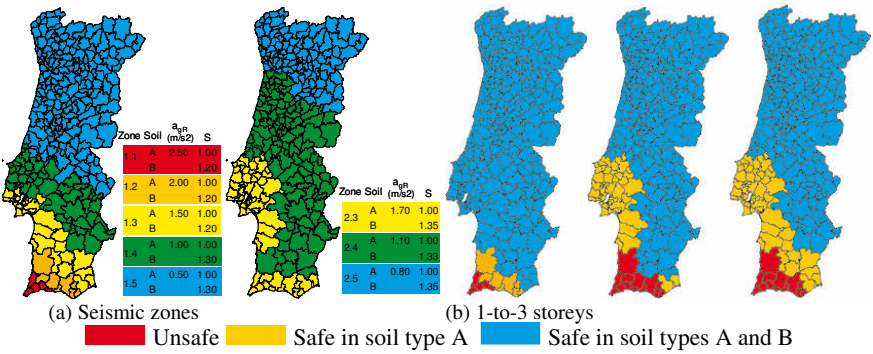

Figure 26. Safety mapping in Portuguese seismic zones by a pushover analysis.

3.2 Masonry structures without box behaviour

Differently from the structures considered in the previous section, unreinforced masonry structures without box behaviour have shown poor performance in many past earthquakes. The reasons for the poor performance are the inherent brittleness, lack of tensile strength, lack of ductility, flexible floor diaphragms and lack of connection between the structural elements. Next, illustrative examples of different analysis tools for the seismic analysis of these structures are presented, see (Lourenço et al., 2011) for additional details.

The first example is the S. Torcato church in Portugal, where limit analysis using macro-blocks was carried out for the seismic performance assessment, as the church exhibits significant damage and requires strengthening.

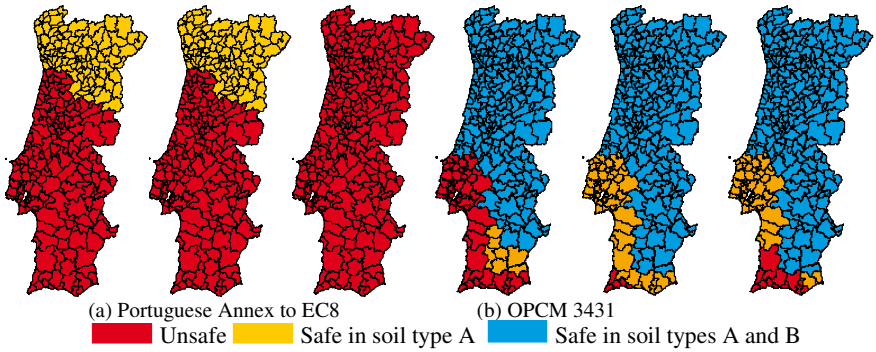

Figure 27. Safety mapping in Portuguese seismic zones by a linear elastic analysis.

In existing masonry buildings partial collapses often occur due to seismic action, generally, with the loss of equilibrium of rigid bodies. In this case study, four mechanisms were defined, based on the inspection and structural analysis of the structure. The mechanisms were partially marked by existing cracks. Figure 28 shows the mechanisms considered in the limit kinematic analysis. According to the limit analysis, the church is safe and the lowest safety factor is equal to 1.69 (with overturning of the tympanum).

This analysis method is conceptually simple and an abacus of possible mechanisms is available at MIBAC 2007 (2007). In the present case, the method is easy to apply as the collapse mechanisms are also partially defined by existing cracking. It is believed that the benefits of using collapse mechanism analysis are the following: (a) the method is intuitive and does not requires advanced knowledge of physics or mechanics, being therefore at reach of most practitioners; (b) the abacus of possible collapse mechanisms and the observation of previous collapses under earthquake action provide are the basis of the inductive approach; (c) the method is conceptually and analytically correct, if the proper collapse mechanisms are selected. It is believed also the method possesses a strong drawback: if wrong collapse mechanisms are selected, the seismic assessment (and related strengthening measures, if applicable) is meaningless. Therefore, practitioners must ensure correct selection of collapse mechanism, either by a detailed inspection of the structure being studied or by adopting more sophisticated analysis methods. This is certainly the case of complex or unusual structures, for which the mechanisms might not be obvious. Another example would be to use pushover analysis or time integration analysis to get more confidence on

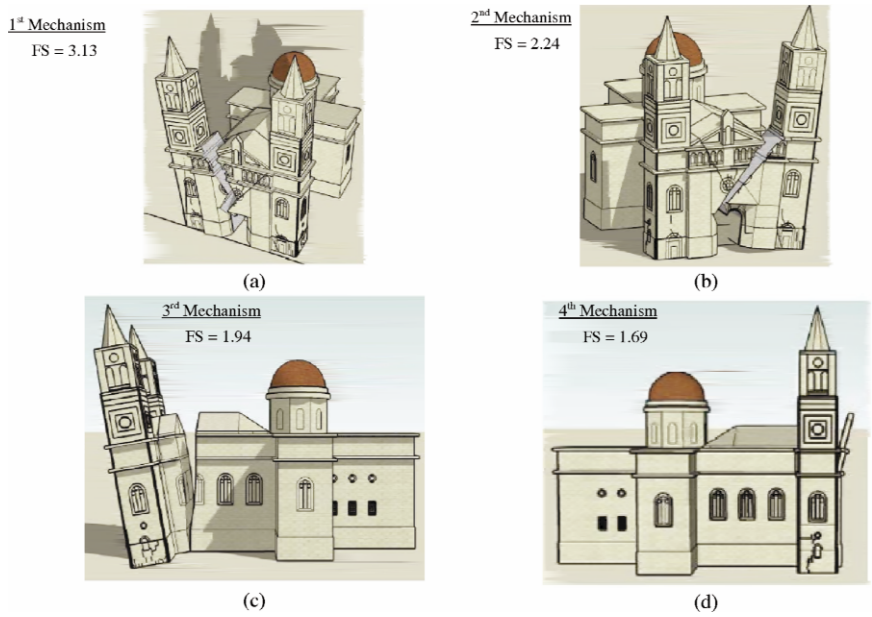

Figure 28. Possible collapse mechanisms: (a) overturning of the left tower; (b) overturning of the right tower; (c) overturning of the façade; (d) overturning of the tympanum. (FS is the safety factor).

collapse mechanisms and then adopt the correct collapse mechanism analysis to calculate the required strengthening.

A second example of application is the Qutb Minar, in New Deli, India. To evaluate its seismic performance different techniques of structural analyses were used, namely non-linear dynamic analysis and non-linear static analysis (pushover analysis). In the analyses different numerical models were considered. Two models were prepared using the Finite Element Method (FEM), both are three-dimensional models but one uses 3D solid elements (Solid Model) while the other one was performed with 3D composite beams (Beam Model). A simplified in-plane model of the minaret based on the Rigid Element Method was also developed. The Rigid Element Method idealizes the masonry structure as a mechanism made of rigid elements and springs (Casolo and Peña, 2007). The numerical models were updated from dynamic identification tests.

In the FEM models, the physical non-linear behaviour of the masonry was simulated using the Total Strain Crack Model detailed in DIANA

(2005), with non-linear behaviour given by a parabolic law in compression and an exponential law in tension (fixed crack model with variable shear retention). In the rigid body and spring model (RBSM), the constitutive law for axial springs is parabolic in compression and bi-linear in tension with softening. A Mohr-Coulomb law was considered for shear springs in order to relate the shear stresses with the axial stresses.

The dynamic analyses were carried out using five artificial accelerograms compatible with the elastic response spectrum for Delhi (PGA = 0.20g). Pushover analyses were carried out considering a uniform acceleration distribution. The load was applied with increasing acceleration in the horizontal direction and a control point at the top of the tower was considered. Figure 29a shows the capacity curves (lateral displacement — seismic coefficient at the base level). Similar behaviour was found with the different models. It can be observed that the average seismic factor is 0.20 and the minaret collapses by overturning at the base.

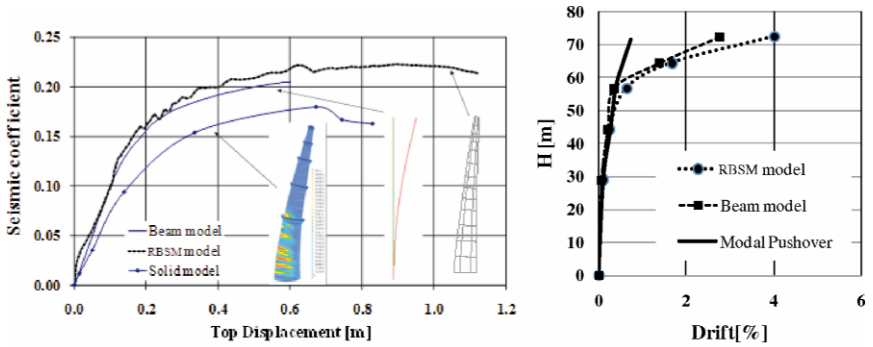

(a) (b)

Figure 29. Results of the pushover analyses: (a) capacity curves of the pushover analyses proportional to the mass; (b) comparison between the drifts obtained through modal pushover analysis and trough dynamic analyses of the Beam and RBSM Models.

In order to study the influence of the distribution of the lateral load in the pushover analysis, additional non-linear static analyses were performed. Four different configurations of lateral loads were considered: (a) linear distribution of the displacement along the height; (b) loads proportional to the first modal shape; (c) adaptive pushover analysis, changing the load distribution according to the changes in the first modal shape during the analysis; (d) modal pushover analysis (Chintanapakdee and Chopra, 2003).

The results of the pushover analyses, namely the failure mode and displacements' distribution along the height, are not in agreement with the non-linear dynamic analysis. Even modal pushover analysis, in which the responses of the first seven modes were combined, is not able to simulate the amplification of the response at higher levels (Figure 29b). This example demonstrates again the need of adopting adequate analysis techniques for the seismic assessment of unreinforced masonry structures.

4 Conclusions

Constraints to be considered in the use of advanced modelling are the cost, the need of an experienced user/engineer, the level of accuracy required, the availability of input data, the need for validation and the use of the results.

As a rule, advanced modelling is a necessary means for understanding the behaviour and damage of (complex) historical masonry constructions and examples have been addressed here. For this purpose, it is necessary to have reliable information on material data, and recommendations are provided in this chapter.

Micro-modelling techniques for masonry structures allow a deep understanding of the mechanical phenomena involved. For large scale applications, macro-block approaches or average continuum mechanics must be adopted and homogenization techniques represent a popular and active field in masonry research. Homogenization techniques represent a popular and active field in masonry research. Several approaches have been recently introduced by different authors and a first attempt to catalogue them and to discuss pros and cons are carried out in this Chapter. Even if it impossible to predict the future of masonry research, this Chapter addresses in detail two different static approaches considered particularly relevant. The first approach is based on a polynomial expansion of the stress field coupled with limit finite elements analysis, whereas the second relies into a discretization of the unit cell by means of a few constant stress finite elements (CST) with joints reduced to interfaces.

Finally, the possibilities of assessment unreinforced masonry structures subjected to seismic loading is addressed using different techniques. It is advocated that linear elastic analysis can hardly be used, as masonry features low tensile strength, and different models must be used in the presence or absence of adequately connected floors, the so-called box behaviour.

In case of box behaviour the available methods have been briefly reviewed. Their performance is good and the knowledge is sound, with some corrections needed in the recent European regulations (Eurocode 8). When box behaviour cannot be guaranteed, the analysis of masonry structures

becomes rather complex. The use of macro-models and limit analysis seems the current trend but difficulties arise in the practical use, namely with respect to validation of the hypothesis of the user and the risk of selecting inadequate failure mechanisms. The non-linear static analysis could be a good and easily understood approach, because it is based on the simple evaluation of the requested deformation with respect to the displacement capacity of the building. This approach is in agreement with the modern provisions for structural assessment. Still, the results obtained from the non-linear static and dynamic analyses indicate quite different response of these structures to earthquakes. It is therefore concluded that non-linear pushover analysis does not simulate correctly the failure mode of masonry structures without box behaviour, even if higher modes are considered via modal pushover analysis.

Bibliography

E. Anderheggen and H. Knöpfel. Finite element limit analysis using linear programming. *International Journal of Solids and Structures*, 8(12): 1413–1431, 1972.

A. Anthoine. Derivation of the in-plane elastic characteristics of masonry through homogenization theory. *International Journal of Solids and Structures*, 32(2):137–163, 1995.

A. Anthoine. Homogenization of periodic masonry: plane stress, generalized plane strain or 3d modelling? *Communications in numerical methods in engineering*, 13(5):319–326, 1997.

T. Belytschko and P.G. Hodge. Plane stress limit analysis by finite elements. *Journal of the Engineering Mechanics Division*, 96(6):931–944, 1970.

D. Caillerie. Thin elastic and periodic plates. *Mathematical Methods in the Applied Sciences*, 6(1):159–191, 1984.

S. Casolo and F. Peña. Rigid element model for in-plane dynamics of masonry walls considering hysteretic behaviour and damage. *Earthquake engineering & structural dynamics*, 36(8):1029–1048, 2007.

CEB-FIP. *Model Code 90.* Thomas Telford Ltd., UK, 1993.

A. Cecchi and K. Sab. A multi-parameter homogenization study for modelling elastic masonry. *European Journal of Mechanics-A/Solids*, 21(2): 249–268, 2002.

A. Cecchi, G. Milani, and A. Tralli. Validation of analytical multiparameter homogenization models for out-of-plane loaded masonry walls by means of the finite element method. *Journal of engineering mechanics*, 131(2): 185–198, 2005.

A. Cecchi, G. Milani, and A. Tralli. A Reissner–Mindlin limit analysis model for out-of-plane loaded running bond masonry walls. *International journal of solids and structures*, 44(5):1438–1460, 2007.

CEN. *Eurocode 8: Design of structures for earthquake resistance, Part 1: General rules, seismic action and rules for buildings*. European Committee for Standardization, Belgium, 2004.

CEN. *Eurocode 6: Design of masonry structures, Part 1–1: General rules for reinforced and unreinforced masonry structures*. European Committee for Standardization, Belgium, 2005.

C. Chintanapakdee and A.K. Chopra. Evaluation of modal pushover analysis using generic frames. *Earthquake engineering & structural dynamics*, 32(3):417–442, 2003.

V.L. Chong, C. Southcombe, and I.M. May. The behaviour of laterally loaded masonry panels with openings. In *3th Int. Masonry Conf. Proc. Brit. Mas. Soc.*, pages 178–182, London, 1994.

P. de Buhan and G. de Felice. A homogenization approach to the ultimate strength of brick masonry. *Journal of the Mechanics and Physics of Solids*, 45(7):1085–1104, 1997.

G. de Felice. Metodi di omogeneizzazione per sistemi regolari di corpi rigidi. In *Proceedings of the XII AIMETA Congress. Naples, Italy*, pages 3–6, 1995.

DIANA. Displacement method ANAlyser, 2005. release 9.1, CD-ROM, Netherlands.

L. Gambarotta and S. Lagomarsino. On the dynamic response of masonry walls (in Italian). In *Proc. National Congress "La Meccanica delle Murature tra Teoria e Progetto"*, Messina, 1996.

K. Hellan. Analysis of elastic plates in flexure by a simplified finite element method. Number 46 in Acta polytechnica Scandinavica. Norges tekniske vitenskapsakademi, 1967.

L.R. Herrmann. Finite-element bending analysis for plates. *Journal Engineering Mechanics Division*, 93:13–26, 1967.

H.K. Hilsdorf. Investigation into the failure mechanism of brick masonry loaded in axial compression. In F.H. Johnson, editor, *Designing, engineering and constructing with masonry products*, pages 34–41. Gulf Publishing Company, Houston, Texas, 1969.

G. Hoffman and P. Schubert. Compressive strength of masonry parallel to the bed joints. In N.G. Shrive and A. Huizer, editors, *Proc. 10th Int. Brick and Block Masonry Conf.*, pages 1453–1462, Calgary, Alberta, 1994.

K. Krabbenhoft, A.V. Lyamin, M. Hjiaj, and S.W. Sloan. A new discontinuous upper bound limit analysis formulation. *International Journal for Numerical Methods in Engineering*, 63(7):1069–1088, 2005.

J. Lopez, S. Oller, E. Onate, and J. Lubliner. A homogeneous constitutive model for masonry. *International journal for numerical methods in engineering*, 46(10):1651–1671, 1999.

P.B. Lourenço. *Computational strategies for masonry structures*. PhD thesis, Delft University of Technology, the Netherlands, 1996. Available from `www.civil.uminho.pt/masonry`.

P.B. Lourenço. On the use of homogenisation techniques for the analysis of masonry structures. *Masonry International*, 11(1):26–32, 1997.

P.B. Lourenço. Experimental and numerical issues in the modelling of the mechanical behaviour of masonry. In P. Roca and et al., editors, *Proc. Structural analysis of historical constructions II, CIMNE*, pages 57–91, Barcelona, 1998a.

P.B. Lourenço. Sensitivity analysis of masonry structures. In *Proc. 8th Canadian Masonry Symp.*, pages 563–574, Jasper, Canada, 1998b.

P.B. Lourenço. Anisotropic softening model for masonry plates and shells. *Journal of Structural Engineering*, 126(9):1008–1016, 2000.

P.B. Lourenço. Computations on historic masonry structures. *Progress in Structural Engineering and Materials*, 4(3):301–319, 2002.

P.B. Lourenço and J.L. Pina-Henriques. Validation of analytical and continuum numerical methods for estimating the compressive strength of masonry. *Computers & structures*, 84(29):1977–1989, 2006.

P.B. Lourenço and L.F. Ramos. Characterization of cyclic behavior of dry masonry joints. *Journal of Structural Engineering*, 130(5):779–786, 2004.

P.B. Lourenço and J.G. Rots. A multi-surface interface model for the analysis of masonry structures. *Journal of engineering mechanics*, 123(7): 660–668, 1997.

P.B. Lourenço, J.O. Barros, and J.T. Oliveira. Shear testing of stack bonded masonry. *Construction and Building Materials*, 18(2):125–132, 2004.

P.B. Lourenço, J.C. Almeida, and J.A. Barros. Experimental investigation of bricks under uniaxial tensile testing. *Masonry International*, 18(1): 11–20, 2005.

P.B. Lourenço, G. Milani, A. Tralli, and A. Zucchini. Analysis of masonry structures: review of and recent trends in homogenization techniques this article is one of a selection of papers published in this special issue on masonry. *Canadian Journal of Civil Engineering*, 34(11):1443–1457, 2007.

P.B. Lourenço, N. Mendes, L.F. Ramos, and D.V. Oliveira. Analysis of masonry structures without box behavior. *International Journal of Architectural Heritage*, 5(4-5):369–382, 2011.

R. Luciano and E. Sacco. Homogenization technique and damage model for old masonry material. *International Journal of Solids and Structures*, 34 (24):3191–3208, 1997.

G. Magenes and A.D. Fontana. Simplified non-linear seismic analysis of masonry buildings. In *Proc. British Masonry Society*, number 8, pages 190–195, 1998.

G. Maier, E. Papa, and A. Nappi. On damage and failure of unit masonry. In *Proc. Experimental and numerical methods in earthquake engineering*, pages 223–245, Brussels and Luxembourg, 1991. Balkema Editions.

R. Marques and P.B. Lourenço. Possibilities and comparison of structural component models for the seismic assessment of modern unreinforced masonry buildings. *Computers & Structures*, 89(21):2079–2091, 2011.

T.J. Massart. *Multi-scale modeling of damage in masonry structures*. PhD thesis, University of Bruxelles, Belgium, 2003.

T.J. Massart, R.H.J. Peerlings, and M.G.D. Geers. Mesoscopic modeling of failure and damage-induced anisotropy in brick masonry. *European Journal of Mechanics-A/Solids*, 23(5):719–735, 2004.

N. Mendes. *Seismic assessment of ancient masonry buildings: Shaking table tests and numerical analysis*. PhD thesis, University of Minho, Portugal, 2012.

MIBAC 2007. *Guidelines for the evaluation and mitigation of seismic risk to cultural heritage*. Ministry for Cultural Heritage and Activities, Gangemi Editore, Rome, Italy, 2007.

G. Milani. Simple lower bound limit analysis homogenization model for in-and out-of-plane loaded masonry walls. *Construction and Building Materials*, 25(12):4426–4443, 2011.

G. Milani, P.B. Lourenço, and A. Tralli. Homogenised limit analysis of masonry walls, part I: Failure surfaces. *Computers & structures*, 84(3–4):166–180, 2006a.

G. Milani, P.B. Lourenço, and A. Tralli. Homogenised limit analysis of masonry walls, part II: Structural examples. *Computers & structures*, 84 (3–4):181–195, 2006b.

G. Milani, P.B. Lourenço, and A. Tralli. Homogenization approach for the limit analysis of out-of-plane loaded masonry walls. *Journal of structural engineering*, 132(10):1650–1663, 2006c.

J. Munro and A.M.A. da Fonseca. Yield line method by finite elements and linear programming. *Structural Engineer*, 56(2), 1978.

P.C. Olsen. The influence of the linearisation of the yield surface on the load-bearing capacity of reinforced concrete slabs. *Computer methods in applied mechanics and engineering*, 162(1):351–358, 1998.

OPCM 3431 . *Technical regulations for the design, assessment and seismic adaptation of buildings*. Gazzetta Ufficiale Serie Generale n.107 del 10/05/2005, Italy, 2005.

G.N. Pande, J.X. Liang, and J. Middleton. Equivalent elastic moduli for brick masonry. *Computers and Geotechnics*, 8(3):243–265, 1989.

M. Paulo-Pereira. *Assessment of the seismic performance of building enclosures (in Portuguese)*. PhD thesis, University of Minho, Portugal, 2012.

P. Pegon and A. Anthoine. Numerical strategies for solving continuum damage problems with softening: application to the homogenization of masonry. *Computers & structures*, 64(1):623–642, 1997.

PIET-70. *P.I.E.T. 70 Masonry work*. Prescriptions from Instituto Eduardo Torroja. Consejo Superior de Investigaciones Científicas, Madrid (in Spanish), 1971.

S. Pietruszczak and X. Niu. A mathematical description of macroscopic behaviour of brick masonry. *International journal of solids and structures*, 29(5):531–546, 1992.

T.M.J. Raijmakers and A.T. Vermeltfoort. Deformation controlled tests in masonry shear walls. *Report B-92*, 1156, 1992. TNO-Bouw,Delft, The Netherlands (in Dutch).

J.G. Rots, editor. *Structural masonry: An experimental/numerical basis for practical design rules*. Balkema, Rotterdam, the Netherlands, 1997.

P. Schubert. The influence of mortar on the strength of masonry. In J.W. de Courcy, editor, *Proc. 8th Int. Brick and Block Masonry Conf.*, pages 162–174, London, 1988. Elsevier Applied Science.

S.W. Sloan. Lower bound limit analysis using finite elements and linear programming. *International Journal for Numerical and Analytical Methods in Geomechanics*, 12(1):61–77, 1988.

S.W. Sloan and P.W. Kleeman. Upper bound limit analysis using discontinuous velocity fields. *Computer Methods in Applied Mechanics and Engineering*, 127(1):293–314, 1995.

P. Suquet. Analyse limite et homogeneisation. *Comptes Rendus de l'Academie des Sciences-Series IIB–Mechanics*, 296:1355–1358, 1983.

D.J. Sutcliffe, H.S. Yu, and A.W. Page. Lower bound limit analysis of unreinforced masonry shear walls. *Computers & Structures*, 79(14):1295–1312, 2001.

M. Tomazevic. *Earthquake-resistant design of masonry buildings*. Imperial College Press, London, 1999.

R. van der Pluijm. *Out-of-plane bending of masonry: Behavior and Strenght*. PhD thesis, Eindhoven University of Technology, The Netherlands, 1999.

G. Vasconcelos and P.B. Lourenço. In-plane experimental behavior of stone masonry walls under cyclic loading. *Journal of structural engineering*, 135(10):1269–1277, 2009.

G. Vasconcelos, P.B. Lourenço, C.A.S. Alves, and J. Pamplona. Experimental characterization of the tensile behaviour of granites. *International journal of rock mechanics and mining sciences*, 45(2):268–277, 2008.

A. Zucchini and P.B. Lourenço. A micro-mechanical model for the homogenisation of masonry. *International Journal of Solids and Structures*, 39(12):3233–3255, 2002.

A. Zucchini and P.B. Lourenço. A coupled homogenisation–damage model for masonry cracking. *Computers & structures*, 82(11):917–929, 2004.